

Entropy Production and Phase Transitions
far from Equilibrium
with Emphasis on Wet Granular Matter

Dissertation
zur Erlangung des Doktorgrades
der Mathematisch-Naturwissenschaftlichen Fakultäten
der Georg-August-Universität zu Göttingen

vorgelegt von
Axel Hager-Fingerle
aus Nürnberg

Göttingen 2007

D 7

Referent: Prof. Dr. Stephan Herminghaus

Korreferentin: Prof. Dr. Annette Zippelius

Tag der mündlichen Prüfung: 11. Dezember 2007

To Svenja

Abstract

This thesis investigates irreversible dynamics. It is shown analytically that the recent Fluctuation Theorem extends to relativistic dynamics. In the analytic consideration of non-relativistic granular gases with broken time-reversal symmetry we find violations of the Fluctuation Theorem for large fluctuations. This is confirmed by simulations of wet granular matter in driven stationary states. It is shown that the theorem persists to hold for small fluctuations, which explains earlier reports of confirmation in literature as a consequence of their measurement range. The particle interaction in wet granular matter is experimentally shown to be hysteretic with the formation and rupture of capillary bridges. The measured dissipation is quantified by the rupture length and energy of the bridges. For a kinematic description of wet granular matter based on these experimental findings, the Enskog factor is generalized analytically to a set of six factors, which account for the hysteretic interaction in a statistical description. Such a statistical and, moreover, continuum description is made possible by the analytical and numerical computations of the Kolmogorov-Sinai entropy, which demonstrates the substantial increase of dynamical chaos due to the capillary interaction in wet granular matter. On this basis, the equation of state of wet granular matter is derived analytically. A van-der-Waals-like mechanical instability is predicted, and verified in simulations and experiments. In the simulations, the instability leads to the breakup of capillary bridges. This nonequilibrium dynamics is described analytically by a mean-field theory in quantitative agreement with the simulations. The experimentally determined critical point of this instability agrees quantitatively with the theory. A novel method, which allows to measure the velocity distribution in nonequilibrium steady states of granular matter based on the Mössbauer effect, is suggested. In a first measurement, an exponential velocity distribution is observed for the fluid-like state. It is demonstrated that the global instantaneous state of the dynamical capillary network in wet granular matter is observable by electrical conductivity, when an ionic liquid is added. This allows to detect the transition of wet granular matter from the solid to the fluid state in the bulk, excluding surface effects, and to demonstrate experimentally with unprecedented precision that this transition is discontinuous and hysteretic with respect to the external driving. Simulations and experiments show that this nonequilibrium transition sets in at a critical *acceleration* of the external driving. Furthermore, the transition from the fluid-like to the gaseous state of wet granular matter is demonstrated experimentally and by simulations. In both approaches it is shown quantitatively that this transition is determined by a critical *velocity* of the driving, which is directly related to the capillary energy. States of fluid/gas coexistence, which emerge in experiments and simulations are explained analytically as subcritical instabilities in the balance of power. Applying the derived equation of state, the spatial distributions of temperature, density and dissipation are computed. Order parameters are measured, and the global phase diagram of the nonequilibrium states and transitions of wet granular matter is presented.

Zusammenfassung

In dieser Dissertationsschrift wird irreversible Dynamik untersucht. Es wird analytisch gezeigt, dass das jüngst entwickelte Fluktuationstheorem auf relativistische Dynamik erweiterbar ist. Die analytische Betrachtung nicht-relativistischer granularer Gase mit gebrochener Zeitumkehrsymmetrie zeigt dagegen, dass das Fluktuationstheorem durch große Fluktuationen verletzt wird. Dies wird durch Simulationen feuchter Granulate in getriebenen Zuständen bestätigt. Es wird gezeigt, dass das Theorem für kleine Fluktuationen weiterhin Bestand hat, wodurch frühere Bestätigungen in der Literatur durch ihren Messbereich erklärt werden. Es wird experimentell nachgewiesen, dass die Teilchenwechselwirkung in feuchten Granulaten hysteretisch ist durch die Bildung und das Reißen von Kapillarbrücken. Die gemessene Dissipation wird quantitativ durch die Abrisslänge und -energie der Brücken beschrieben. Auf dieser Basis wird für die Kinematik feuchter Granulate der Enskog-Faktor analytisch erweitert zu einem Satz von sechs Faktoren, die eine statistische Beschreibung der hysteretischen Wechselwirkung ermöglichen. Die Zulässigkeit einer statistischen und ferner hydrodynamischen Beschreibung ist das Ergebnis analytischer und numerischer Berechnungen der Kolmogorov-Sinai-Entropie, welche eine erhebliche Zunahme des dynamischen Chaos durch die Kapillarwechselwirkung in feuchten Granulaten zeigt. Auf dieser Grundlage wird die Zustandsgleichung feuchter Granulate analytisch hergeleitet und eine van-der-Waals-ähnliche Instabilität vorhergesagt. Diese wird in Simulationen und Experimenten nachgewiesen. In der Simulation führt diese Instabilität zum Aufbrechen von Kapillarbrücken, deren zeitliche Entwicklung analytisch in Molekularfeldnäherung berechnet wird mit dem Ergebnis quantitativer Übereinstimmung. Die experimentelle Bestimmung des kritischen Punktes der Instabilität ist in quantitativer Übereinstimmung mit der Theorie. Eine neue Methode zur Messung der Geschwindigkeitsverteilung in granularen Nichtgleichgewichtszuständen unter Anwendung des Mössbauereffekts wird vorgeschlagen. Eine erste Messung zeigt eine exponentielle Verteilung im granularen Fluid. Eine direkte Messung des globalen Zustands des dynamischen Kapillarnetzwerkes im feuchten Granulat wird durch Benetzung mit ionischen Flüssigkeiten durchgeführt. Dies ermöglicht, den Übergang feuchter Granulate vom festen in den fluiden Zustand im Volumen zu beobachten. Dadurch kann mit bislang unerreichter Präzision experimentell nachgewiesen werden, dass dieser Phasenübergang diskontinuierlich und hysteretisch ist. Weiter zeigen Numerik und Experiment, dass dieser Nichtgleichgewichtsübergang bei einer kritischen *Beschleunigung* der äußeren Anregung auftritt. Es wird ferner der Übergang feuchter Granulate vom fluiden in den gasförmigen Zustand in Experimenten und Simulationen gezeigt. In beiden Zugängen wird quantitativ nachgewiesen, dass dieser Übergang bei einer kritischen *Geschwindigkeit* der Anregung einsetzt, welche direkt aus der Kapillarenergie folgt. Fluid/Gas-Koexistenzen treten in Experimenten und Simulationen auf und werden analytisch als subkritische Instabilität des Energieflusses erklärt. Unter Anwendung der Zustandsgleichung werden räumliche Temperatur-, Dichte- und Dissipationsverteilungen berechnet. Ordnungsparameter werden gemessen und ein umfassendes Phasendiagramm der Nichtgleichgewichtszustände und Phasenübergänge feuchter Granulate wird erstellt.

Aus demselben Grunde ist unser Leben in der Kindheit so unendlich bedeutend, in jener Zeit ist uns alles gleich wichtig, wir hören alles, wir sehen alles, bei allen Eindrücken ist Gleichmäßigkeit, statt dass wir späterhin absichtlicher werden, uns mit dem Einzelnen ausschließlich beschäftigen, das klare Gold der Anschauung für das Papiergeld der Bücherdefinitionen mühsam einwechseln und an Lebensbreite gewinnen, was wir an Lebenstiefe verlieren.

Heinrich Heine
Die Harzreise

Table of Contents

Abstract	i
Zusammenfassung	iii
1 Irreversibility as the Starting Point	1
1.1 Music as an Example of Irreversibility in Perception	1
1.2 Equilibrium Statistics and Thermodynamics	2
1.3 Nonequilibrium: Broken Detailed Balance	3
1.3.1 The Fluctuation Theorem	4
1.3.2 The Kolmogorov-Sinai Entropy	4
1.3.3 The Lyapunov Exponents and How It is All Connected	4
1.3.4 Nonequilibrium Statistical Mechanics and Hydrodynamics	5
1.3.5 Phase Transitions far from Equilibrium	5
1.4 Outline of this Thesis	5
2 Relativistic Fluctuation Theorems	9
2.1 A Human Question Put in Physical Terms	9
2.2 The General Stochastic Formulation of Fluctuation Theorems	11
2.2.1 The Integral Fluctuation Theorem	11
2.2.2 The Detailed Fluctuation Theorem	13
2.3 Special-Relativistic Brownian Motion	14
2.4 Fluctuation Theorems for High Energy Physics	16
2.4.1 Generalizations in the Framework of Special Relativity	18
2.4.2 First Explicit Example: The Commuting Brownian Particle	18
2.5 Generalizations in the Framework of General Relativity	22
2.5.1 Cosmological Fluctuation Theorem	23
2.5.2 Additional Theorems for the Einstein-de Sitter Universe	24
2.5.3 Second Explicit Example: The Expanding Universe	25
2.6 Conclusions	27
2.7 Appendix: Treating the Truncated Moment Problem	28
3 The Paradigm System: Wet Granular Matter	31
3.1 Dry and Wet Granular Matter	31

3.2	The Mechanisms of Dissipation in Wet Granular Matter	33
3.3	The Time-Resolved Measurement of Single Bridge Dynamics	39
3.4	The Minimal Capillary Model	46
3.4.1	The Experimental Basis	46
3.4.2	The Force Law	46
3.4.3	Fundamental Properties	47
3.4.4	Qualitative Change of Material Properties Caused by Wetting Liquids	47
3.4.5	Qualitative Changes in the Granular Dynamics	48
3.5	Conclusions	51
4	Fluctuation Theorem and Phase Transitions in One Dimension	53
4.1	Elementary Phase Space Evolution under Driving	53
4.2	The Fluctuation Theorem for a Non-Dissipative Gas	56
4.3	‘Violation’ of the Fluctuation Theorem for a Dissipative Gas	57
4.4	Suggestion for a Definition of Entropy for Systems far from Equilibrium . . .	61
4.5	The Direct Observation of the Fluid/Gas Transition	65
4.6	The Symplecticity of Wet Granular Matter	68
4.6.1	Generalization of the Dellago-Posch Formula to Wet Granular Matter	68
4.6.2	The Proof of Symplecticity	72
4.6.3	The Proof of Conjugate Pairing of the Lyapunov Exponents	72
4.7	The Kolmogorov-Sinai Entropy as an ‘Order Parameter’	73
4.8	Conclusions	75
5	The Kolmogorov-Sinai Entropy: Wetting Increases Chaoticity	77
5.1	The Dynamical System Perspective	77
5.2	The Minimal and the Extended Capillary Model	79
5.3	How to Relate the Two-Particle System to the N -Particle System	82
5.4	The Ensemble Average	85
5.5	The Expansion of Velocity Space	87
5.6	Results for the Kolmogorov-Sinai Entropy	88
5.7	The One-Dimensional System as an Exceptional Case	96
5.7.1	The Cluster-Internal Chaoticity	97
5.7.2	Remark on Numerical Techniques and the Dimensionality	99
5.8	A Diagrammatic Approach to Entropy Production	100
5.9	Conclusions	103
6	Unclustering Transition in Freely Cooling Wet Granular Matter	105
6.1	Introduction	105
6.2	Numerical Observation of the Transition	106
6.3	Analytic Description of the Full Cooling Scenario	107
6.4	The Thermal Decoupling	112
6.5	Energy and Entropy	112

6.6	A Simplified Visualization	113
6.7	Inelastic Collisions and Unequal Particle Masses	114
6.8	Conclusions	114
6.9	Appendix: A Comment on the Notion of Clusters	115
7	The Equation of State of Wet Granular Matter	117
7.1	The Nonequilibrium State	118
7.2	Dry Spheres as the Starting Point	120
7.2.1	The Dense Limit	123
7.2.2	The Dilute and Moderately Dense Regime	126
7.3	The Pair Correlation under the Hysteretic Interaction	131
7.3.1	The Hysteretic Coupling	131
7.3.2	Switching On the Force of Capillary Bridges	136
7.4	The Equation of State and the Critical Point	137
7.4.1	Frozen Degrees of Freedom	138
7.4.2	The Pressure of Wet Granular Matter	140
7.5	Conclusions	145
7.6	Appendix A: The Background Contribution g_B	145
7.6.1	The Weighting Factors	145
7.6.2	The Configuration Space	146
7.7	Appendix B: Explicit Expressions for the Pair Correlation	151
7.7.1	High Density	151
7.7.2	Low and Moderate Density	152
7.8	Appendix C: Self-Consistency of Bridge Coordination K	153
7.9	Appendix D: Contact Correlation Near Jamming	153
7.10	Appendix E: On the Contact Correlation in Dilute Hard Disc Systems	155
8	The Critical Point of Wet Granular Matter	159
8.1	Conductivity as Experimental Order Parameter of the Liquid Network	160
8.1.1	The Measurement Method	160
8.1.2	The Experimental System	160
8.2	The Solid/Fluid Transition	162
8.2.1	The Granular Temperature	164
8.2.2	Capillary Strengthening and the Hysteretic Fluidization	169
8.3	The Critical Point	170
8.3.1	The Critical Density	170
8.3.2	The Critical Temperature	174
8.4	Conclusions	179
8.5	Appendix A: Analytic Solution of the Granular Heat Equation	179
8.6	Appendix B: Experimental Cross-Checks	183
8.6.1	Exclusion of Artifacts due to the Inelastic Heat Production	183
8.6.2	Exclusion of Gravitational Artifacts	183

9	The Velocity Distribution Measured by the Mössbauer Effect	187
9.1	The Mössbauer Effect from the Point of View of Granular Physics	187
9.2	The Principal Effects for Mössbauer Spectroscopy	188
9.2.1	The Source of γ -Quanta	188
9.2.2	Phonons - The Quanta of Lattice Vibrations	189
9.2.3	The Mössbauer - Lamb Factor	190
9.2.4	Natural Line Width	192
9.2.5	Longitudinal and Transverse Doppler Shift	192
9.2.6	The Chemical Isomer Shift	193
9.2.7	The Electric Quadrupole Splitting	193
9.2.8	Magnetic Splitting	194
9.3	Granular Glass Spheres with Highly Enriched ^{57}Fe	194
9.3.1	Production of $^{57}\text{Fe}_2\text{O}_3$ Powder	194
9.3.2	Production of Glass Melt with Enriched ^{57}Fe	195
9.3.3	Production of Spherically Shaped Particles	195
9.4	The Granular Mössbauer Setup	196
9.4.1	The Atomic Density and the Effective Absorber Thickness	196
9.4.2	The Mössbauer Spectrum at Rest	197
9.5	The Transmission Integral for the Granular Mössbauer Effect	198
9.5.1	The Emission Distribution of the Source	198
9.5.2	The Transmission Distribution of the Absorption	198
9.5.3	The Granular Velocity Distribution	199
9.6	Reconstruction of the Velocity Distribution	200
9.7	How to Measure Translation and Rotation of Granular Particles	204
9.8	Conclusions	205
10	Phase Transitions and Coexistence far from Equilibrium	207
10.1	Balance Equations	208
10.1.1	The Phase Space Flow of Wet Granular Matter	208
10.1.2	The Pseudo-Liouville Operator for the Hysteretic Bridge Dynamics	210
10.1.3	Projected Phase Space Density	211
10.1.4	Hysteretic Enskog Correlation for a Closed Evolution Equation	212
10.1.5	The Hydrodynamic Fields	213
10.2	Stationary States of Wet Granular Matter	214
10.3	Simulated Phase Diagram and the Hysteretic Interaction	218
10.4	Order Parameters to Detect the Transition Lines	220
10.4.1	An Order Parameter for Phase Coexistence	220
10.4.2	A Dynamical Order Parameter for Fluidization and Sublimation	221
10.5	Universality with respect to the Force Law	222
10.6	The Continuum Solutions	225
10.6.1	The Energetic Sinks	226

10.6.2 The Energetic Source	226
10.6.3 Stable Solutions	227
10.6.4 Comparison of Analytic and Simulation Results	229
10.7 The Coarsening Dynamics of the Coexistence State	231
10.8 Conclusions	234
10.9 Appendix: Comment on Model Details	234
11 Concluding Summary and Outlook	237
References	241
Acknowledgments	255
List of Publications and Meetings	257
Curriculum Vitae	259

Chapter 1

Irreversibility as the Starting Point

The scientific motivation of this dissertation originates from irreversibility. The homo sapiens preferably applies symmetries [222] in her or his perception and thinking, and in physics the time-reversal symmetry (and its later precise formulation as the CPT theorem in quantum field theory [210]) is among the highest principles¹. Research on nonequilibrium processes, which are irreversible and violate the time-reversal symmetry, was substantially stimulated by the Fluctuation Theorem of G. Gallavotti and E.G.D. Cohen [89] in recent years. This theorem is fascinating as it explains increments of entropy² for reversible chaotic dynamics, and revived the discussion on the apparent conflict between microscopic reversibility and macroscopic irreversibility, formulated, e.g., as the Loschmidt paradox [145] more than a century ago. Among the various answers to the question how irreversibility can emerge from fundamentally reversible laws, the H-Theorem of L. Boltzmann (1872) was the first. Here entropy grows because correlations of particles prior to their collision are ignored. In this thesis the entropy production in a *dissipative* gas will be investigated in Chap. 5 in terms of the Kolmogorov-Sinai entropy. Another classical explanation, dating back to Boltzmann and further emphasized by the Ehrenfests, suggests that entropy rises because its initial value was exceptionally low, due to the initial condition defined by the cosmic Big Bang³. Chap. 2 presents a modern stochastic formulation of the Fluctuation Theorem in this classical context of cosmic expansion, in order to find the relativistic influence on entropy production. It turns out that for such a relativistic Ornstein-Uhlenbeck process, the cosmological expansion acts in the cosmic frame of reference exactly as an additional viscous damping.

1.1 Music as an Example of Irreversibility in Perception

Let us have for the beginning a pleasurable look on irreversibility by studying music. We all would agree that a master piece of music has a well defined direction in time, usually the reverse direction is not pleasant at all. The Fluctuation Theorem measures irreversibility by comparing the probability of forward and backward transition rates, as will be defined and investigated in detail in Chap. 2. We consider the probability that the note n follows

¹Symmetry principles guide physics since 1905. From a positivistic point of view, one might regard Einstein's Special Theory of Relativity as a mere reinvention of the results of Maxwell (whose equations on electrodynamics obey the Poincaré symmetry group), Poincaré, and Lorentz (having published his famous transformation in 1904). Of course, this point of view misses what is essential for physics. Physics aims at revealing the principle behind experiments, which is for this case the Poincaré symmetry group: "The 1905 Special Theory of Relativity was the beginning of a general acceptance of symmetry principles as a valid basis for physical theories." (S. Weinberg [235]).

²In the Gallavotti-Cohen Fluctuation Theorem, entropy is associated to the contraction of phase space.

³In the philosophical literature [167] this is referred to as the "past hypothesis".

Tune	$S_+^{(2)}$	$S_-^{(2)}$	$\Delta S^{(2)}/\overline{S}^{(2)}$
Sisters Act	0.318	0.324	-0.019
Der Mond ist aufgegangen	0.312	0.307	+0.016
Bach's Toccata (beginning)	0.605	0.607	-0.003
US national anthem	0.528	0.516	+0.023

Table 1.1: Test for irreversibility in music. $S_{\pm}^{(\alpha)}$ measures the complexity of transitions with memory of length α , so that $S^{(\alpha)} = 0$ for a predictable tune (for example a scale) and $S^{(\alpha)} = 1$ for complete unpredictability. There is no significant asymmetry with respect to time-reversal (similar results for higher α). Quite satisfactorily, J. S. Bach exhibits the highest complexity.

after a sequence N_α of α notes. The entropy production per note may then be defined as in [25] by averaging the negative logarithm of this transition probability over all preceding strings of notes N_α and ‘final states’ n , weighted by the probability of their joined occurrence. Mathematically, we are free to do the same computation for the piece of music reversed in time. Results for the forward entropy production $S_+^{(\alpha)}$ and the reverse direction, $S_-^{(\alpha)}$, are given in Tab. 1.1. In the case of “Toccata and Fugue” of J. S. Bach, we restrict ourselves to the beginning of the Toccata (the dramatic opening of the organ). As we can see, not only the laws of physics, but also those of music show to a high degree time-reversal symmetry, with respect to the definition of entropy applied, indicating that the irreversibility of music is caused by our previous knowledge (which is not included in the comparatively ignorant $S_{\pm}^{(\alpha)}$) and our perception⁴.

The physical origin of irreversibility is the intrinsic probabilistic nature of quantum measurements⁵. The indeterminacy on the smallest scales is exponentially amplified by classical chaos, and necessitates the statistical description of many-particle systems. This thesis is devoted to the part played by classical physics for irreversible dynamics.

1.2 Equilibrium Statistics and Thermodynamics

The existing (micro-/grand-) canonical ensemble theory provides a statistical description of stationary states with Hamiltonian or quantum dynamics in the thermodynamic limit⁶. A general dynamical system is said to fulfill detailed balance, if its microscopic transition currents cancel pairwise, i.e. the probability fluxes $j(A \rightarrow B)$ and $j(B \rightarrow A)$ between any pair (A, B) of configurations or states are balanced,

$$j(A \rightarrow B) = P(A) P_{\text{trans}}^{\text{dt}}(A \rightarrow B) = P(B) P_{\text{trans}}^{\text{dt}}(B \rightarrow A) = j(B \rightarrow A), \quad (1.1)$$

as is sketched in panel (A) of Fig. 1.1. This is for example true for a quantum system when Fermi's golden rule describes the transition rates⁷. In other words, detailed balance means *microscopic reversibility*⁸. The classical example is the Glauber dynamics [100] of the Ising

⁴This is obviously related to the exciting question for a physical explanation why the human brain, subject to the reversible laws of physics, does not remember the future.

⁵These may be regarded as quantum fluctuations, as the ‘collapse’ of a quantum state, or as the unitary time-evolution of relative quantum states according to H. Everett (1957).

⁶Here we think for example of the explanation by T. D. Lee and C. N. Yang (1952) for phase transitions as the non-analytic behavior of the grand canonical potential (and hence, of the pressure) due to the distribution of the zeros of the partition function in the complex plane of the fugacity.

⁷The symmetry of the transition matrix $P_{\text{trans}}^{\text{dt}}(i \mapsto j)$ is a stronger condition than detailed balance for the stationary state, as this implies uniformity.

⁸In the case of a stochastic model such dynamics is referred to as a reversible Markov process.

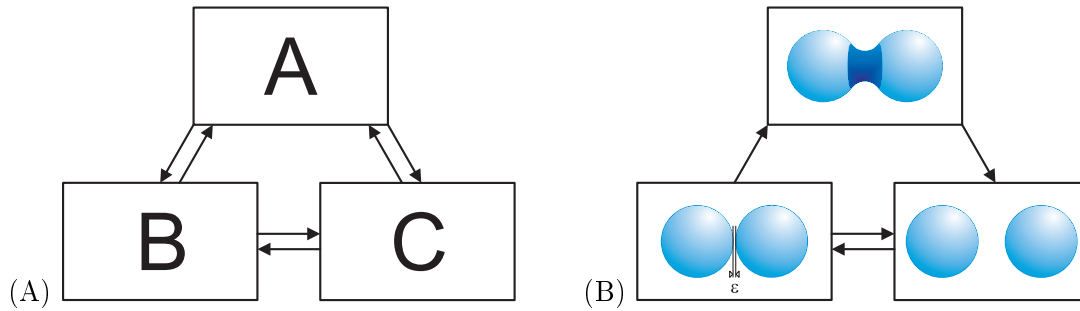


Figure 1.1: Equilibrium systems fulfill the principle of detailed balance, which states that the forward and backward channels for changes of the system state cancel pairwise in the stationary state. In wet granular matter this principle is violated by the hysteric liquid bridge interaction, which is the formal reason why wet granular matter is a dynamical system out of equilibrium.

model in the stationary state. A biophysical counterexample are ionic channels, where gating may be investigated by observing violations of detailed balance statistically [185]. On the macroscopic scale, an equilibrium system is homogeneous with respect to all its intensive thermodynamic variables. Certainly, equilibrium is an idealized concept⁹. To the benefit of structure formation and self-organization, systems out of equilibrium predominate. The universe is under cosmic expansion, the solar system is powered by the sun, metabolism defines living organisms, and the production of numerical results (which reduces entropy) by a processor is entropically overcompensated by the production of heat. As the boundaries of such open or dissipative systems are essential to provide mass or energy currents, there cannot be a thermodynamic limit, and the question naturally arises whether the established concepts of equilibrium can be generalized. This includes the important concept of entropy, which developed along with the theory of equilibrium thermodynamics¹⁰, and there is at present an open debate on the concept and definition of entropy in nonequilibrium situations [151].

1.3 Nonequilibrium: Broken Detailed Balance

Dynamical systems which violate detailed balance are said to be out of equilibrium [116]. Granular matter is a very actively studied example of such a dissipative non-Hamiltonian system, in which the equations of motion have broken time-reversal symmetry. The breaking of time-reversal is exceptionally obvious for wet granular matter, as shown in Fig. 1.1B. Two particles covered by a liquid film interact *hysteretically* with the formation and rupture of a capillary bridge [114].

⁹As R. Kubo pointed out in a lecture [132], thermo-“dynamics” is really a theory of “thermostatics”.

¹⁰The historic starting point is S. Carnot’s consideration of general reversible processes in 1824. The first formulation, $dS_{\text{Clausius}} = \delta Q/T$, as well as the name entropy from the Greek “entrepein” (transform) and “tropé” (potential for transformation) was given by R. Clausius in 1850. We owe J. W. Gibbs, 1876, the general expression $S_{\text{Gibbs}} = - \int f \ln f \, d\text{vol}(\Gamma)$ for an arbitrary ensemble density f . The Gibbs formula was rederived in 1948 by C. Shannon in the context of information theory. In 1877 L. Boltzmann introduced the configuration entropy $S_{\text{Boltzmann}} = k_B \ln \Omega$, where Ω is the number of microscopic configurations. With A. Einstein [73], we may interpret Ω as the number of microscopic realizations belonging to the same macroscopic state.

1.3.1 The Fluctuation Theorem

The aforementioned Fluctuation Theorem [89] requires microscopic time-reversal. It predicts that the probability to observe a reduction of entropy, $-\Delta s < 0$, as compared to the positive increment $+\Delta s$, is exponentially small:

$$\frac{\text{Prob}(-\Delta s)}{\text{Prob}(+\Delta s)} = \exp\left(\frac{-\Delta s}{k_B}\right). \quad (1.2)$$

It came therefore as a surprise when S. Aumaître *et al.* (with simulations in [10]) and K. Feitosa and N. Menon (experimentally in [78]) reported the observation of the Fluctuation Theorem for granular matter, which does not meet the requirement of a time-reversal map.

1.3.2 The Kolmogorov-Sinai Entropy

A second requirement of the Fluctuation Theorem is chaoticity. A measure for dynamical chaos is the Kolmogorov-Sinai entropy h_{KS} . Its definition is as follows [61]. Suppose we are given a partition W_i of phase space $\{\Gamma\}$ (for example hypercubes with linear dimension ϵ). Denote the probability to find the trajectory $\Gamma(t)$ of the system in $(W_{i_0}, W_{i_1}, W_{i_2}, \dots)$ at times $(0, \Delta t, 2\Delta t, \dots)$ by $P(i_0, \dots, i_n)$. It is then natural to define the entropy per time step as

$$h(\{W_i\}) = - \lim_{n \rightarrow \infty} \frac{1}{n} \sum_{i_0, \dots, i_n} P(i_0, \dots, i_n) \ln P(i_0, \dots, i_n). \quad (1.3)$$

In order to have an entropy independent of the choice of the partition W_i , the Kolmogorov-Sinai entropy is defined as the supremum of all partitions:

$$h_{\text{KS}} = \sup_{\{W_i\}} h(\{W_i\}). \quad (1.4)$$

For a time-continuous system one takes the limit $\Delta t \rightarrow 0$. The Kolmogorov-Sinai entropy gives the rate at which correlations decay exponentially in time.

1.3.3 The Lyapunov Exponents and How It is All Connected

The Kolmogorov-Sinai entropy is very closely related to the Lyapunov exponents λ_j , which describe the exponential rate at which perturbations grow ($\lambda_j > 0$) or shrink ($\lambda_j < 0$), to be defined in the Chaps. 4 and 5. For a closed system, the sum of *all positive* exponents is equal to the Kolmogorov-Sinai entropy [170]:

$$h_{\text{KS}} = \sum_{\lambda_j > 0} \lambda_j. \quad (1.5)$$

Entropy production is identified with phase space contraction in the Gallavotti-Cohen Fluctuation Theorem [90]. On long time scales, the mean phase space contraction rate is equal to the sum of *all* Lyapunov exponents. The latter is according to (1.5) equal to $h_{\text{KS}} - h_{\text{KS}}^\dagger$, where h_{KS}^\dagger is the Kolmogorov-Sinai entropy of the time-reversed system. For wet granular matter there is no time-reversal map due to the unidirectional arrows in Fig. 1.1B.

Just to mention one remarkable dynamical property, wet granular matter is dissipative and at the same time (everywhere locally) symplectic¹¹ with respect to the particle positions and momenta in phase space. The symplecticity implies that the sum of all Lyapunov exponents is zero. This is for example not fulfilled for dry granular matter modeled by inelastic collisions.

¹¹By symplectic it is meant throughout this thesis that the tangent space dynamics, restricted to the

1.3.4 Nonequilibrium Statistical Mechanics and Hydrodynamics

The statistical description of equilibrium is motivated by the impossibility to observe the full microscopic dynamics of collective systems, and justified by chaoticity¹². Complexity remains to be the motivation for a statistical description far from equilibrium, and dynamical chaos persists to be its rigorous foundation: in order for the system to be properly described by distribution functions and for macroscopic fields to approach well-defined (local) values, the system has to be sufficiently chaotic [61, 64]. This is – besides the Fluctuation Theorem – another reason to quantify the chaoticity of nonequilibrium systems.

Given the requirement of dynamical chaos, with statistical methods a macroscopic or hydrodynamic continuum description may be derived, for instance using the Boltzmann-Enskog kinetic theory. This is well established [106] for systems fulfilling microscopic time-reversal symmetry. Hereby the Enskog factor, which describes particle correlations, is a non-trivial function of density. It is therefore preferable to generalize and apply this machinery to the hysteretic interaction in wet granular matter. Furthermore, to solve the continuum equations, one is interested in constitutive equations, such as the equation of state relating pressure to temperature and density. The existence of such an equation of state is by far not obvious for dissipative systems [113].

1.3.5 Phase Transitions far from Equilibrium

By virtue of its hysteretic interaction, wet granular matter has an intrinsic energy scale (as will be shown in Chap. 3). It is therefore among the most widespread dissipative collective systems [160, 122, 114]: e.g. as wet sand on the beach, in geology, and pharmaceutical production. The extraction of a defined energy in particle collisions is also a model for planetary formation, as has been investigated in microgravity experiments flown onboard the space shuttle [22].

At the same time, phase transitions are among the most interesting phenomena in thermodynamics and statistical physics, since unexpected cooperative properties arise from elementary interaction laws. It is natural to ask if the hysteretic interaction of wet granular matter gives rise to phase transitions, and whether, e.g., states of phase coexistence are possible which would generalize the established concept of a first order transition to nonequilibrium. As a geological phenomenon, wet granulates exhibit a number of striking dynamical transformations, such as soil liquefaction due to earthquakes [191, 98, 114].

In spite of its widespread relevance, the nonequilibrium dynamics and transitions of wet granular matter have hardly been subject of scientific investigation. The fundamental approach based on dynamical system theory to this nonequilibrium system is lacking. Much of the experimental, analytical and numerical work presented in this thesis is therefore devoted to the dynamics of wet granular matter and the systematic description of its nonequilibrium phase transitions, where there has been no unifying phase diagram before.

1.4 Outline of this Thesis

Nonequilibrium statistics and dynamics, especially for wet granular matter as a nonlinear dynamical system, are developed in the Chaps. 2, 3, 4, 5, 7, and 9. Based on these results,

continuous phase space of position and momentum, conserves the symplectic form S , as discussed in the Chaps. 4, 5, and 10. The full dynamics includes the hysteretic discrete bridge status, for which reason there is no time-reversal map for wet granular matter. Symplecticity is therefore understood as a local property, and not in the global sense of symplectic manifolds.

¹²The existence of a measure in phase space, which is defined as the infinite time average of the trajectory, is the Birkhoff ergodic theorem [20]. Ergodicity then leads to the microcanonical distribution.

the nonequilibrium phase transitions of wet granular matter are described in the Chaps. 6, 8, and 10.

We begin with the Fluctuation Theorem which is introduced in Chap. 2. Since dissipative gases occur in the accretion disks of stellar formation, we take the opportunity to generalize the Fluctuation Theorem to account for relativistic particle motion. This allows us furthermore to prove Fluctuation Theorems under cosmic expansion as motivated by the historical remark above. Here the physical meaning of time-reversal for a stochastic process with multiplicative coupling is clarified. In Chap. 3 the hysteretic interaction of wet granular matter is quantified theoretically and confirmed experimentally. The reported experiment resolves in time the hysteretic formation of single capillary bridges. This leads us to the Minimal Capillary Model [114] for the hysteretic particle interaction in wet granular matter, which will be applied prevalently in simulations and for analytic computations in this thesis. A first simulation result shows the very different structures which emerge from a gas with the ‘wet’ hysteretic interaction as compared to inelastic collisions that model dry granular matter. In Chap. 4 we begin with the stationary states of wet granular matter in one dimension based on the Minimal Capillary Model. The conflict between the broken time-reversal in the granular dynamics, and the Fluctuation Theorem having been observed in literature [10, 78], is resolved. It is shown that the Fluctuation Theorem is fulfilled only for small fluctuations of entropy. At high fluctuations the functional form of the Fluctuation Theorem (1.2) is violated. For wet granular matter, this violation is shown to be directly related to a nonequilibrium phase transition, the fluid/gas transition. The Lyapunov spectrum and the Kolmogorov-Sinai entropy are computed across this fluid/gas transition. The Kolmogorov-Sinai entropy is found to decrease with temperature because the dynamical chaos is enhanced by the hysteretic bridges in fluid clusters, which evaporate at higher temperature. This numerical observation is directly continued by the analytic computation of the Kolmogorov-Sinai entropy for the wet granular gas (general w.r.t. the dimensionality $D > 1$) in the following Chap. 5. The exceptional case $D = 1$ is mapped to a ‘wet billiard’ and the Lyapunov spectrum is computed numerically. The Kolmogorov-Sinai entropy is found to be greater than one in units of the system collision frequency, which extends the molecular chaos hypothesis for this nonequilibrium system, and opens the road to generalize the Boltzmann-Enskog kinetic approach by taking broken detailed balance into account. This is done for the free cooling in one dimension in Chap. 6. The bridge energy density, as well as the binding and rupture frequencies are computed analytically on the mean-field level. In quantitative agreement with simulations, it is found that the capillary network undergoes an unclustering transition above a critical density, with the segregation of dense granular droplets. In two dimensions the persistent microscopic probability fluxes of the hysteretic interaction are solved for the steady nonequilibrium state in Chap. 7. The analytical result is a set of pair correlation functions near contact. These detailed correlation functions depend on the bond status and generalize the Enskog factor to allow for the hysteretic dynamics. An explicit formula for the bridge coordination number is derived. For the solid state of wet granular matter, the formula is compared with configurations resulting from simulations and very good agreement is found. The equation of state of wet granular matter is derived analytically, which gives the pressure in wet granular matter as a function of the granular temperature and densities, ranging from gas to jamming. A van-der-Waals-like mechanical instability is shown to exist. The critical point is directly related to the length and energy scale of the hysteretic interaction. This theoretical prediction is followed by an experiment in Chap. 8, which uses an ionic liquid, so that the global state of the capillary network in driven wet granular matter is detected by electrical conductivity. The phase segregation, driven by the mechanical instability below the critical point, is clearly observed. Quantitative agreement of the critical density and the

critical temperature with the theoretical predictions is found. The experimental method is furthermore applied to demonstrate that the solid/fluid transition in wet granular matter is discontinuous with respect to the driving force. The velocity distribution is required for many computations, such as the Fluctuation Theorem, the equation of state and the Kolmogorov-Sinai entropy. For this, a novel experimental method is suggested based on the Mössbauer effect in Chap. 9. A first measurement shows its feasibility, and an exponential velocity distribution in the volume of a granular fluid is observed. The theoretically established dynamical chaos and the analytic computation of the hysteretic pair correlation function enables the Boltzmann-Enskog kinematic approach to wet granular matter, and leads to a continuum description in Chap. 10. The theory explains the fluid/gas transition in wet granular matter. Order parameters are defined, and the global phase diagram of wet granular matter is derived from experiment and simulation in quantitative agreement. Besides nonequilibrium states of single phases, the phase diagram contains regions of fluid/gas and solid/gas coexistence. For the fluid/gas coexistence the profiles of temperature, density and dissipation are derived from the continuum theory and the equation of state. Finally, the coalescence dynamics of granular droplets is discussed.

The results of each chapter are outlined at the beginning and summarized in the conclusions of the chapter. Chap. 11 summarizes the results obtained in this thesis and gives a brief outlook to future research. Parts of this thesis are published in [79, 82, 81, 83, 80, 84, 86] and have contributed to [85].

Chapter 2

Relativistic Fluctuation Theorems

Dissipative gases, forming the central topic of this thesis, occur in accretion disks [38] and the circumstellar formation of planetesimals [127], for which initial state relativistic particle motion is required. Guided by the interest in entropy production, we follow the introductory remarks in the last chapter on the Ehrenfests and investigate the Second Law in special relativistic and cosmological context¹. This provides an opportunity to concisely introduce the Fluctuation Theorem, which will be reverted to in the following chapter.

To reveal how nonequilibrium physics and relativity theory intertwine, this chapter studies relativistic Brownian motion under cosmic expansion. Two Fluctuation Theorems for the entropy Δs , which is locally produced in this extreme nonequilibrium situation, are presented and proven. The first, $\langle e^{-\Delta s} \rangle = 1$, is a generalization of the Second Law of thermodynamics, which remains valid at relativistic particle energies and under high cosmic expansion rates. From this relation it follows that the probability to observe a local reduction of entropy is exponentially small even if the universe was to recollapse. For the special case of the Einstein-de Sitter universe an additional relation, $\langle e^{-\Delta s - \Delta h} \rangle = 1$, is derived which holds simultaneously with the first relation and where Δh is proportional to the Hubble constant. Furthermore, the Fluctuation Theorems are shown to provide a physical criterion to resolve the known discretization dilemma arising in special-relativistic Brownian motion. Explicit examples and a general method for the computation of non-Gaussian entropy fluctuations are provided.

2.1 A Human Question Put in Physical Terms

The physical basis of the direction of time has been discussed at least since Boltzmann's H-Theorem in 1872. A priori, the thermodynamic arrow of time has to be distinguished from the possibility of a prime direction of time defined by the expansion of the universe [243]. By now we know that due to the dominating dark energy component of about 72%, our universe is very likely to expand forever [209, 18]. Yet the fascinating cosmological arrow of time could not be based on firm theoretical ground [107, 166, 108, 2, 34]. So one may still ask: Is it a mere coincidence that our memory strictly refers to times when the size of the universe was smaller? Put in physical terms, the guiding question of this chapter is: Does the cosmic expansion rate effect the production of entropy by nonequilibrium processes? While a general theory of nonequilibrium thermodynamics does not exist, Fluctuation Theorems provide a unique starting point to develop the means to address such a fundamental question. First progress in the description of entropy production and giant fluctuations beyond linear-response was

¹The results of this chapter are published in [79].

made in the 1970s [23], and major advance was achieved in recent years with the derivation of Fluctuation Theorems for various classes of systems [75, 89, 90, 137, 229, 199, 125, 124, 126]. Fluctuation Theorems generalize the Second Law of thermodynamics. The Second Law states that the Gibbs entropy S of an ensemble may not decrease,

$$\Delta S \geq 0 \text{ at any time.} \quad (2.1)$$

The Fluctuation Theorems naturally extend the concept of entropy and allow statements about the probability to observe isolated “violations” of (2.1). To this end the Fluctuation Theorems assign a change Δs of entropy to an observation of few or even single particles. When a nonequilibrium system of finite size is observed, the entropy Δs produced within a certain time interval is a fluctuating quantity. The founders of statistical mechanics, L. Boltzmann and J.W. Gibbs were well aware that the Second Law holds only for the entropy $\Delta S = \langle \Delta s \rangle$ of an infinite ensemble. The angle brackets denote the ensemble average over observations of equal systems. Boltzmann mentioned the possibility of “violations”, $\Delta s < 0$, in his famous reply to the Poincaré recurrence objection (in a written argument with E. Zermelo) and designated the Second Law as a theorem of probability (“Wahrscheinlichkeitssatz”), emphasizing that the Second Law cannot be expected to hold for few particles [24]. *Loco citato*, he referred to Gibbs [99] who had concluded: “The impossibility of an uncompensated decrease of entropy seems to be reduced to an improbability.” It is this improbability that is quantified by Fluctuation Theorems.

For the steady state of strongly chaotic systems the detailed Fluctuation Theorem,

$$\frac{\text{Prob}(\Delta s = +a)}{\text{Prob}(\Delta s = -a)} = \exp\left(\frac{a}{k_B}\right) \text{ for any } a, \quad (2.2)$$

was proven in the limit of infinite observation time [89, 90]. The detailed Fluctuation Theorem (2.2) was also derived in [137] for a non-relativistic particle in contact with a heat bath at temperature T . Initially, only the external change in the bath entropy, $\Delta s_e = \Delta Q/T$ with the energy ΔQ dissipated into the surrounding bath, was taken into account [137, 229]. In [199] it was pointed out that when the particle is assigned an intrinsic entropy $s_s = -k_B \ln P$ (with the particle’s phase space density P), the sum of intrinsic and external entropy, $\Delta s = \Delta s_s + \Delta s_e$, obeys the Fluctuation Theorem (2.2) even for finite observation time². This is the definition of entropy applied throughout this chapter. Furthermore, for non-stationary states in the presence of time-dependent driving forces, an integral Fluctuation Theorem of the form

$$\left\langle e^{-\Delta s/k_B} \right\rangle = 1, \quad (2.3)$$

was proven and linked to the Jarzynski relation [125, 124, 126]. Technically, the averaging over observations, $\langle \dots \rangle$, is a path integral over trajectories, which is explained in the following section.

The detailed Fluctuation Theorem (2.2), the integral Fluctuation Theorem (2.3), and the Second Law of thermodynamics (2.1) form a consistent hierarchy of statements: from Eq. (2.2) follows (2.3) by integrating over a , and Eq. (2.3) implies (2.1) by virtue of the Jensen inequality.

We proceed as follows. A modern stochastic formulation of the Fluctuation Theorem is given in the following section. The recent unification [51, 66, 67] of Einstein’s 1905 publications

²In the earlier Fluctuation Theorem of Evans and Searles a similar term was added to the dissipation function (Eq. (2.6) in [77]), that is not present in the Gallavotti-Cohen Fluctuation Theorem [89, 90], resulting in a Fluctuation Theorem for chaotic systems which holds for finite time. For the stochastic formulation of finite time Fluctuation Theorems such a term was considered in [150], Eqs. (5.9) and (5.11).

on Brownian motion [71] and special relativity [72] is briefly reviewed in the following Sec. 2.3. Based on these findings, the results of Sec. 2.4 are twofold. First, for the relativistic Brownian processes of [66] and [67], we reconcile the Fluctuation Theorems (2.2) and (2.3), which have become a paradigm of nonequilibrium physics, with special relativity. For the similar process suggested in [51], Fluctuation Theorems follow by analogous reasoning. In [66] and [67] it was pointed out that the relativistic time dilation leads to multiplicative coupling, necessitating a careful choice of the discretization rule. We show explicitly that there is one relativistic detailed Fluctuation Theorem (2.2) and one relativistic integral Fluctuation Theorem (2.3) valid for all choices. Second, we shall find the physically correct expression for the entropy production following from relativistic Fluctuation Theorems when the Hänggi-Klimontovich discretization rule is applied. In Sec. 2.5 we go beyond special relativity with a set of two general-relativistic integral Fluctuation Theorems for the cosmological standard model. These expose clearly the role of cosmic expansion in entropy production. We shall identify the entropy production which is solely due to the Hubble expansion of space. Such entropy producing processes dominate when the expansion rate of the universe exceeds the particle scattering rate, for instance in an early inflationary phase after the big bang. The Secs. 2.4 and 2.5 conclude each with examples where we explicitly compute the non-Gaussian fluctuations $P(\Delta s)$, $P(\Delta s_s)$ and $P(\Delta s_e)$ of entropy production.

2.2 The General Stochastic Formulation of Fluctuation Theorems

This section gives a general derivation of the Fluctuation Theorem for stochastic processes and emphasizes that every broken symmetry implies a Fluctuation Theorem.

2.2.1 The Integral Fluctuation Theorem

Let $\mathbf{\Gamma}(t)$ denote the state of the observed system, which performs a time continuous stochastic process under the influence of a thermal environment. Its stochastic dynamics are described completely by the probability distribution $P[\mathbf{\Gamma}, \mathbf{C}]$, which gives the probability to observe a certain system trajectory $\mathbf{\Gamma}$. This probability depends on the environmental conditions: \mathbf{C} describes a set of external parameters, such as the environmental temperature $T(t)$, external forces (for example acting on a charged system by an electric field $\mathbf{E}(t)$), or – as we shall consider finally in the general-relativistic case – the curvature of spacetime. All these external parameters may vary during the process, so that $\mathbf{C}(t)$ is a deterministic protocol. The general idea underlying stochastic formulations of Fluctuation Theorems is as follows. Consider an arbitrary transformation \mathcal{T} , which does not leave the physical dynamics (represented by a Langevin or Fokker-Planck equation) invariant. While $P[\mathbf{\Gamma}, \mathbf{C}]$ describes the dynamics of the original stochastic system, the transformed stochastic dynamics will be given by another probability distribution $\tilde{P}[\mathbf{\Gamma}, \mathbf{C}]$. Assuming P and \tilde{P} to have the same support, we define

$$\Delta s[\mathbf{\Gamma}, \mathbf{C}] \equiv k_B \ln P[\mathbf{\Gamma}, \mathbf{C}] - k_B \ln \tilde{P}[\mathbf{\Gamma}, \mathbf{C}] , \quad (2.4)$$

to quantify the symmetry breaking of the transformation \mathcal{T} for every trajectory $\mathbf{\Gamma}$. For the quantity Δs defined in (2.4), an integral Fluctuation Theorem of the form (2.3) is a mathematical identity,

$$\left\langle e^{-\Delta s/k_B} \right\rangle = \int \mathcal{D}[\mathbf{\Gamma}] P[\mathbf{\Gamma}, \mathbf{C}] e^{-\Delta s/k_B} = \int \mathcal{D}[\mathbf{\Gamma}] \tilde{P}[\mathbf{\Gamma}, \mathbf{C}] = 1 .$$

The path integration $\int \mathcal{D}[\mathbf{\Gamma}]$ covers all continuous functions $\mathbf{\Gamma}$, weighted by the probability $P[\mathbf{\Gamma}, \mathbf{C}]$.

We are interested in a Fluctuation Theorem that quantifies the irreversibility of the stochastic process. This is why we choose the transformation \mathcal{T} to be time reversal³,

$$\begin{aligned}\tilde{P}[\mathbf{\Gamma}, \mathbf{C}] &= P[\tilde{\mathbf{\Gamma}}, \tilde{\mathbf{C}}], \\ \text{with } \tilde{\mathbf{\Gamma}}(+t) &= \mathbf{\Gamma}(-t) \\ \text{and } \tilde{\mathbf{C}}(+t) &= \mathbf{C}(-t) \text{ for all } t.\end{aligned}$$

To get a result on the total entropy production, the transformation \mathcal{T} acts globally by reversing both, the stochastic system trajectory $\mathbf{\Gamma}$ and the time dependence of the environment \mathbf{C} .

The probability $P[\mathbf{\Gamma}, \mathbf{C}]$ to observe a stochastic trajectory $[\mathbf{\Gamma}]_{-\tau}^{+\tau}$ in the time interval $(-\tau, +\tau)$ depends on the initial conditions, which are given by $\mathbf{\Gamma}(-\tau)$ for a Markov process or by the history $[\mathbf{\Gamma}]_{-\tau-T}^{-\tau}$ for a system with memory time T (which may be infinite):

$$\begin{aligned}P[\mathbf{\Gamma}, \mathbf{C}] &= P_{\text{in}} P_{\text{F}} , & (2.5) \\ \text{with } P_{\text{in}} &= \begin{cases} P(\mathbf{\Gamma}, \mathbf{C})|_{-\tau}, & \text{if Markovian} \\ P[\mathbf{\Gamma}, \mathbf{C}]_{-\tau-T}^{-\tau}, & \text{if with memory} \end{cases} \\ \text{and } P_{\text{F}} &= P([\mathbf{\Gamma}, \mathbf{C}]_{-\tau}^{+\tau} | \text{in}) .\end{aligned}$$

We refer to the initial state or the history as the in-state of the system, which is distributed according to the first factor P_{in} in (2.5). The second factor P_{F} is the (forward) propagator on the time interval $(-\tau, +\tau)$ under the influence of the thermal environment. Analogously, the time-reversed probability is written as

$$\tilde{P}[\mathbf{\Gamma}, \mathbf{C}] = \tilde{P}[\tilde{\mathbf{\Gamma}}, \tilde{\mathbf{C}}] = P_{\text{out}} P_{\text{R}} . \quad (2.6)$$

Inserting (2.5) and (2.6) in (2.4), Δs decomposes into the sum

$$\Delta s = \Delta s_{\text{s}} + \Delta s_{\text{e}} , \quad (2.7)$$

$$\text{with } \Delta s_{\text{s}} = -k_{\text{B}} \ln P_{\text{out}} + k_{\text{B}} \ln P_{\text{in}} , \quad (2.8)$$

$$\text{and } \Delta s_{\text{e}} = k_{\text{B}} \ln \frac{P_{\text{F}}}{P_{\text{R}}} . \quad (2.9)$$

The first term (2.8) is the change of the system entropy $s_{\text{s}} = -k_{\text{B}} \ln P_j$ as the system state changes from “ $j = \text{in}$ ” to “ $j = \text{out}$ ”. The expression $s_{\text{s}}(P_j) = -k_{\text{B}} \ln P_j$ for the system entropy was suggested in [199] for a Markov process and is a widely accepted definition because s_{s} resembles the Boltzmann entropy and $S_{\text{s}} = \langle s_{\text{s}} \rangle = -k_{\text{B}} \langle \ln P_j \rangle$ coincides with the Gibbs entropy of the ensemble P_j .

The second term (2.9) is a Crooks relation [48, 49, 42] defined by the forward and reversed time evolution under the stochastic influence of the thermal environment. We have to show that Δs_{e} as introduced in (2.9) equals exactly the entropy produced in the thermal environment, so that $\Delta s = \Delta s_{\text{s}} + \Delta s_{\text{e}}$ is the total entropy production. A major objective of this chapter is to evaluate (2.9) for a thermal environment at relativistic energies to adjudicate on the physical interpretation as environmental entropy.

For Markov processes, such as the relativistic Brownian motion discussed in the next

³If $\mathbf{\Gamma}$ is the phase space vector (\mathbf{x}, \mathbf{p}) , the momenta are inverted, $\tilde{\mathbf{\Gamma}}(t) = (\mathbf{x}(-t), -\mathbf{p}(-t))$.

section, the forward and reverse propagators are infinite products of transition probabilities,

$$P_F = \lim_{n \rightarrow \infty} \prod_{k=1}^n P_{\text{trans}}^{\Delta t_k}(\Gamma_{k-1} \mapsto \Gamma_k, \mathbf{C}(\Delta t_k)) \text{ and}$$

$$P_R = \lim_{n \rightarrow \infty} \prod_{k=1}^n P_{\text{trans}}^{\Delta t_k}(\Gamma_k \mapsto \Gamma_{k-1}, \mathbf{C}(\Delta t_k)) ,$$

so that entropy production is local in time: For the environmental entropy follows

$$\Delta s_e = \int_{-\tau}^{+\tau} \dot{s}_e(t) dt \quad \text{with}$$

$$\dot{s}_e(t) dt = k_B \ln \frac{P_{\text{trans}}^{\text{dt}}(\Gamma^- \mapsto \Gamma^+, \mathbf{C}(t))}{P_{\text{trans}}^{\text{dt}}(\tilde{\Gamma}^- \mapsto \tilde{\Gamma}^+, \mathbf{C}(t))} , \quad (2.10)$$

and the change in system entropy is $\Delta s_s = s_s(+\tau) - s_s(-\tau)$ with $s_s(t) = -k_B \ln P(\Gamma(t), \mathbf{C}(t))$. The probability density $P(\Gamma, t) = P(\Gamma, \mathbf{C}(t))$ evolves according to the continuity equation,

$$\partial_t P(\Gamma, t) + \nabla_{\Gamma} \circ \mathbf{j}(\Gamma, t) = 0 , \quad (2.11)$$

with the probability current

$$\mathbf{j}(\Gamma, t) = \sum_{n=0}^{\infty} \frac{(-\nabla_{\Gamma})^n}{n!} \circ \mathbf{M}_{n+1}(\Gamma, t) P(\Gamma, t) . \quad (2.12)$$

The Helfand moments \mathbf{M}_n are tensors of order n which are related to the transition probability $P_{\text{trans}}^{\text{dt}}$ by [183]

$$\mathbf{M}_n(\Gamma, t) dt = \int (\Gamma' - \Gamma)^n P_{\text{trans}}^{\text{dt}}(\Gamma \mapsto \Gamma', \mathbf{C}(t)) d\Gamma' .$$

The higher moments are present only if the heat bath in which the system is embedded is out of equilibrium. A possible system for relativistic Brownian motion is an electron which couples by Compton scattering to a gas of photons. We assume that such a heat bath is in local equilibrium so that we have a well-defined temperature $T(\mathbf{x}, t)$ yielding an isotropic diffusion $\mathbf{M}_2 \propto T \mathbb{1}$ with vanishing higher moments, $\mathbf{M}_n = 0$ for $n > 2$. Equation (2.11) then reduces to the Fokker-Planck equation and the transition probabilities are Gaussian.

2.2.2 The Detailed Fluctuation Theorem

While the integral Fluctuation Theorem derived above holds for arbitrary environmental conditions \mathbf{C} , the stronger detailed Fluctuation Theorem (2.2) holds if the deterministic protocol is invariant under time-reversal, $\mathbf{C} = \tilde{\mathbf{C}}$. The general derivation for the quantity Δs defined in (2.4) is also done conveniently by path integration. The probability to observe a production of entropy $\Delta s = a k_B$ is

$$\begin{aligned} & \text{Prob}(\Delta s = a k_B) \\ &= \int P[\Gamma, \mathbf{C}] \delta(\Delta s[\Gamma, \mathbf{C}] = a k_B) \mathcal{D}[\Gamma] \\ &= \int P[\tilde{\Gamma}, \tilde{\mathbf{C}}] e^{\Delta s/k_B} \delta(\Delta s[\Gamma, \mathbf{C}] = a k_B) \mathcal{D}[\Gamma] \\ &= e^a \int P[\tilde{\Gamma}, \tilde{\mathbf{C}}] \delta(\Delta s[\Gamma, \mathbf{C}] = a k_B) \mathcal{D}[\Gamma] \\ &= e^a \int P[\tilde{\Gamma}, \tilde{\mathbf{C}}] \delta(\Delta s[\tilde{\Gamma}, \tilde{\mathbf{C}}] = -a k_B) \mathcal{D}[\tilde{\Gamma}] . \end{aligned}$$

In the second and last equality we exploited Eq. (2.4). Using the trivial fact that the path integration can be reordered in time, we arrive at

$$\text{Prob}(\Delta s = a k_B) = e^a \int P[\Gamma, \tilde{\mathbf{C}}] \delta(\Delta s[\Gamma, \tilde{\mathbf{C}}] = -a k_B) \mathcal{D}[\Gamma] .$$

Comparing this result with the probability

$$\text{Prob}(\Delta s = -a k_B) = \int P[\Gamma, \mathbf{C}] \delta(\Delta s[\Gamma, \mathbf{C}] = -a k_B) \mathcal{D}[\Gamma]$$

to observe a reduction $\Delta s = -a k_B$, yields the detailed Fluctuation Theorem (2.2) for any symmetric protocol, $\mathbf{C} = \tilde{\mathbf{C}}$. Therefore the detailed Fluctuation Theorem holds not only in the steady state, which the system reaches under time-independent forcing, $\mathbf{C}(t) = \text{const}$, but also for example in periodically changing conditions that are symmetric with respect to the observed time-frame $(-\tau, +\tau)$.

We conclude this general derivation of Fluctuation Theorems with the remark that the presented formulation gives a unifying perspective on the distinct Fluctuation Theorems of [199] and [152]. Equation (6) in [152] is generalized by Eq. (2.4), while the Eqs. (2.8) and (2.9) correspond to the decomposition of entropy according to the Eqs. (5) and (14) in [199] respectively.

2.3 Special-Relativistic Brownian Motion

The derivation of the Fluctuation Theorems (2.2) and (2.3) in Sec. 2.2 uses the abstract expression (2.10) for the entropy production \dot{s}_e in the embedding heat bath. As emphasized before, this expression has to be evaluated for a physical process to allow for a physical interpretation as entropy. An instructive process is relativistic Brownian motion.

To minimize technicalities, we consider first the one-dimensional special-relativistic motion of a particle with rest mass m in a heat bath at temperature T . The generalization to higher spatial dimensions is straightforward. Even if we would allow the particle to equilibrate with its environment, the mean squared velocity may not obey the non-relativistic law $\langle v^2 \rangle = k_B T / m$ in the high temperature limit, since the finite speed of light defines an insurmountable upper bound. The special-relativistic nonequilibrium Brownian motion, giving rise to bounded velocity distributions, has been set forth in [51, 66, 67] using both, the language of stochastic differential equations (relativistic Langevin equations) and the language of probability densities (relativistic Fokker-Planck equations). Simulations of this relativistic stochastic process have been applied to analyze scattering experiments of quark-gluon plasma [227]. As in the familiar non-relativistic case [183], a deterministic force F_d acts on the particle in the rest frame of the heat bath,

$$dp_d = F_d dt = -\nu p dt , \tag{2.13}$$

so that the time scale of dissipation is $1/\nu$. In the relativistic generalization (2.13), the non-relativistic momentum mv is replaced by $p = p^1 = mv/\sqrt{1 - v^2/c^2}$, which is the spatial component of the relativistic momentum vector p^α . As common, Greek indices refer to temporal ($\alpha = 0$) and spatial components. The signature of the Minkowski metric tensor is $\eta_{\alpha\beta} = \eta^{\alpha\beta} = \text{diag}(-1, 1)$. Moreover, Einstein's summation convention is invoked throughout.

Since the rest mass is not altered in elastic collisions, $p^\alpha p_\alpha = -(mc)^2 = \text{const}$, the change in the momentum vector dp^α is always “orthogonal” to p_α in the sense of

$$p_\alpha dp^\alpha = 0 . \quad (2.14)$$

This means that the classical particle cannot leave its mass shell $p^\alpha p_\alpha = -(mc)^2$, which is nothing but its dispersion relation,

$$E = p^0 c = \sqrt{(mc^2)^2 + (pc)^2} . \quad (2.15)$$

The general solution of (2.14) is the projection $dp^\alpha = (\delta^\alpha_\beta + p^\alpha p_\beta / (mc)^2) \xi^\beta$ of an arbitrary Lorentz vector ξ^β . It is readily confirmed that the choice

$$dp^\alpha_d = -m\nu \left(\delta^\alpha_\beta + \frac{p^\alpha p_\beta}{(mc)^2} \right) v^\beta_{\text{bath}} d\tau \quad (2.16)$$

reduces to Eq. (2.13) in the rest frame of the bath with the bath velocity vector $v^\alpha_{\text{bath}} = (c, 0)$ and the particle’s proper time τ . Hence, Eq. (2.16) is the generalized Lorentz-invariant deterministic part of the Brownian motion⁴.

The description of relativistic Brownian motion is completed by Lorentz-invariant stochastic changes dp^α_s of the momentum caused by the impacts of the surrounding heat bath at temperature T . The derivation is guided by two principles: first, the relativistic momentum is the proper quantity performing a Wiener process, since it is physically exchanged and additive, whereas the velocity is well-known not to be additive in special relativity. The second postulate demands that the distribution is Gaussian in the instantaneous rest frame of the particle. This connects the relativistic Brownian motion to the non-relativistic case. These principles determine the exchanged momenta dp^α_s to be distributed according to (cf. Eq. (35c) in [66])

$$P_{\text{coll}}(p^\mu, dp^\nu_s) = \frac{mc \delta(p_\beta dp^\beta_s)}{2\sqrt{\pi} \mathcal{D} d\tau} \exp\left(-\frac{dp^\alpha_s dp_{s\alpha}}{4\mathcal{D} d\tau}\right). \quad (2.17)$$

The Dirac distribution $\delta(p_\beta dp^\beta_s)$ in (2.17) guarantees that the mass-shell condition (2.14) is also fulfilled by the stochastic impacts, since they are elastic. While the relativistic momentum p is additive and unbounded, the velocity is restricted to the open interval $(-c, +c)$. This can be seen by the elegant relation $v/c^2 = p/E$ in the rest frame of the bath, which is equivalent to

$$dx = \frac{pc}{\sqrt{(mc)^2 + p^2}} dt . \quad (2.18)$$

As mentioned before in the context of the general Kramers-Moyal expansion (2.12), the bath temperature T is defined by the Einstein relation,

$$\mathcal{D} = k_B T m \nu , \quad (2.19)$$

with the momentum diffusion constant \mathcal{D} (cf. Eq. (59) in [66]).

⁴Equation (16) in [66] contains an identically vanishing term.

2.4 Fluctuation Theorems for High Energy Physics

We have now the manifestly Lorentz-invariant Langevin equation

$$dp^\alpha = dp_d^\alpha + dp_s^\alpha \quad (2.20)$$

with the deterministic part given by (2.16) and the stochastic part described by (2.17) at hand. Specifying (2.20) to the rest frame of the bath yields

$$dp = -\nu p dt + dp_s . \quad (2.21)$$

The probability density of the exchanged momenta dp_s is found by integrating out the dp_s^0 -component in (2.17), cf. [66]:

$$P_{\text{coll}}(p, dp_s) = \frac{\exp\left(-dp_s^2/(4\mathcal{D}\sqrt{1+\frac{p^2}{(mc)^2}}dt)\right)}{2\sqrt{\pi\mathcal{D}dt}\sqrt{1+\frac{p^2}{(mc)^2}}} . \quad (2.22)$$

This exhibits the discretization dilemma: A discretization rule has to be imposed on (2.22) since relativistic invariance does not determine whether p in (2.22) refers to the particle momentum p_- before the collision (pre-point rule of Itô), to the post-point $p_+ = p_- + dp$ (Hänggi-Klimontovich), or to the midpoint $(p_- + p_+)/2$ (Fisk-Stratonovich).

The Eqs. (2.18), (2.21) and (2.22) establish the relativistic stochastic motion of the Brownian particle in phase space. The corresponding transition probability is uniquely determined by the discretization rule:

$$P_{\text{trans}}^{\text{dt}} \left(\begin{array}{l} x \mapsto x + dx \\ p \mapsto p + dp \end{array} \right) = \frac{\delta\left(dx - \frac{pc^2}{E}dt\right)}{2\sqrt{\pi\mathcal{D}E}dt/mc^2} \\ \times \exp\left(-\frac{\left(dp + \nu p dt - (1-\kappa)\frac{\mathcal{D}}{mc^2}\frac{dE}{dp}dt\right)^2}{4\mathcal{D}E}dt/mc^2\right) . \quad (2.23)$$

The discretization is contained in the parameter κ , $0 \leq \kappa \leq 1$. Hänggi-Klimontovich, Fisk-Stratonovich, or Itô correspond to the values $\kappa = 0$, $\frac{1}{2}$, or 1 respectively.

Let us now investigate the consequences for entropy production arising out of the special-relativistic discretization dilemma. As derived in Sec. 2.2, the total entropy is a sum of the particle intrinsic entropy $s_s(t) = -k_B \ln P(x(t), p(t), t)$ with the particle's nonequilibrium phase space density $P(x, p, t)$, and the external entropy s_e of the ambient heat bath at temperature T .

Inserting the probability current (2.12) in momentum space

$$j_p(x, p, t) = -\left(\nu p + \kappa\frac{\mathcal{D}}{mc^2}\frac{dE}{dp}\right)P(x, p, t) - \frac{\mathcal{D}E}{mc^2}\frac{\partial P(x, p, t)}{\partial p} \quad (2.24)$$

in the differential ds_s of the particle entropy $s_s(t) = -k_B \ln P(x(t), p(t), t)$ we find the equation of motion (generalizing Eq. (7) in [199]) for s_s ,

$$ds_s = ds_s|_{\kappa=0} + \kappa k_B d \ln E . \quad (2.25)$$

Here we have isolated the second term which depends on the discretization rule applied.

The entropy production ds_e in the bath follows by contrasting the transition probabilities of the trajectory $\mathbf{\Gamma} = (x, p)$ with its time-reverse $\tilde{\mathbf{\Gamma}} = (\tilde{x}, -\tilde{p})$ to extract the irreversible

part, $\ln P_{\text{trans}}^{\text{dt}}(\mathbf{\Gamma}^- \mapsto \mathbf{\Gamma}^+) - \ln P_{\text{trans}}^{\text{dt}}(\tilde{\mathbf{\Gamma}}^- \mapsto \tilde{\mathbf{\Gamma}}^+)$, causing the dissipation (2.10). From a brief computation we find:

$$\begin{aligned} ds_e &= k_B \ln \frac{P_{\text{trans}}^{\text{dt}} \left(\begin{array}{l} x \mapsto x + dx \\ p \mapsto p + dp \end{array} \right)}{P_{\text{trans}}^{\text{dt}} \left(\begin{array}{l} x + dx \mapsto x \\ -p - dp \mapsto -p \end{array} \right)} \\ &= -\frac{dE}{T} - \kappa k_B d \ln E . \end{aligned} \quad (2.26)$$

The Eqs. (2.25) and (2.26) reveal that although the relativistic Brownian motion is physically inequivalent depending on κ , the fluctuations of the total entropy $s = s_s + s_e$ are independent of κ . Explicitly, the change of the total entropy is

$$\frac{ds}{k_B} = -\frac{\partial \ln P}{\partial t} dt - \frac{\partial \ln P}{\partial x} dx + \frac{mc^2 j_p}{\mathcal{O}EP} dp .$$

Two technical comments are here in order. First, when computing ds_e in (2.26) the notation has to carefully distinguish between initial $\mathbf{\Gamma}^-$ and finale state $\mathbf{\Gamma}^+$, and one should consider the quotient $P(\mathbf{\Gamma}^- \rightarrow \mathbf{\Gamma}^- + d\mathbf{\Gamma})/P(\mathbf{\Gamma}^- + d\mathbf{\Gamma} \rightarrow \mathbf{\Gamma}^-)$ as done in (2.26). Writing the back transition in the numerator in the form $P(\mathbf{\Gamma}^+ \rightarrow \mathbf{\Gamma}^+ - d\mathbf{\Gamma})$ would be correct yet unfavorable for evaluation, because common $\mathbf{\Gamma}^-$ -factors could not be canceled out. In transforming $P(\mathbf{\Gamma}^+ \rightarrow \mathbf{\Gamma}^+ - d\mathbf{\Gamma})$ to $P(\mathbf{\Gamma}^- + d\mathbf{\Gamma} \rightarrow \mathbf{\Gamma}^-)$ the known spurious drift of the multiplicative coupling has to be taken into account [183]. Second, the discretization term in (2.26) can be absorbed by defining a more complicated fluctuation-dissipation theorem, however in this dissertation we use exclusively the Einstein relation (2.19).

The path integration of the results (2.25) and (2.26) according to Subsec. 2.2 yields the detailed Fluctuation Theorem (2.2) for time-symmetric environments, and the integral Fluctuation Theorem (2.3) for arbitrary environmental conditions, with entropy fluctuations Δs observed over finite time. Therewith we have proven relativistic Fluctuation Theorems that are unaffected by the discretization dilemma.

Furthermore, we are now in a position to address the physical choice of κ by virtue of the Fluctuation Theorem. Because of energy conservation, the energy $-dE$ in (2.26) lost by the particle equals the heat dQ gained by the ambient bath:

$$ds_e = \frac{dQ}{T} - \kappa k_B d \ln E . \quad (2.27)$$

In the non-relativistic regime the particle energy $E = mc^2 + E_{\text{kin}}$ is dominated by the energy of the rest mass m so that the second term in (2.27) vanishes for $mc^2 \gg E_{\text{kin}}$,

$$d \ln E = \frac{E_{\text{kin}}}{mc^2 + E_{\text{kin}}} d \ln E_{\text{kin}} ,$$

and we recover the non-relativistic Fluctuation Theorems [199]. At arbitrary relativistic energies (2.15) the Hänggi-Klimontovich rule, $\kappa = 0$, entails the correct expression for the entropy

$$ds_e = \frac{dQ}{T} , \quad (2.28)$$

which is produced in the heat bath.

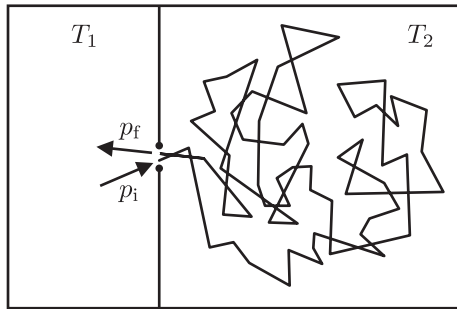


Figure 2.1: A Brownian particle commuting between different thermal environments. The non-Gaussian fluctuations of entropy occurring in this system can be evaluated analytically (cf. Figs. 2.2 and 2.3).

2.4.1 Generalizations in the Framework of Special Relativity

To generalize the Fluctuation Theorems to D spatial dimensions, momentum and force in Eq. (2.13) are simply substituted by their spatial vectors and the Greek indices in the Lorentz-invariant Eqs. (2.16) and (2.17) take values up to D . After integrating out the temporal component p^0 , the distribution (2.22) is found to contain a quadratic form \underline{A} instead of the square in the exponent (cf. Eq. (15) in [67]) with tensor components

$$A_{ij} = \delta_{ij} - \frac{c^2}{E^2} p_i p_j . \quad (2.29)$$

The Fluctuation Theorems follow using the fact that \mathbf{p} is an eigenvector of \underline{A} . No complications are caused by allowing an inhomogeneous heat bath, where the temperature T and the dissipation rate ν vary in space. As far as the integral Fluctuation Theorem (2.3) is concerned, a bath temperature evolving in time is also permitted (as part of the environmental condition $\mathbf{C}(t)$ in Sec. 2.2). Since the time-asymmetric part enters (2.28), the dissipation rate ν may be an even function of the momentum, $\nu(\mathbf{p}) = \nu(-\mathbf{p})$. This is of physical relevance since ν is known not to be constant even for most non-relativistic processes [176]. As mentioned in the general derivation of Sec. 2.2, an arbitrary time-dependent external force $F_e(t)$ (being also part of the environmental condition $\mathbf{C}(t)$ defined in the rest frame of the bath) does not pose a problem. After adding $F_e(t)$ to the deterministic force F_d in (2.13) we find the expression $ds_e = dQ/T$ with the heat $dQ = -dE + F_e dx$. This is the First Law of thermodynamics stated in the frame of the bath.

2.4.2 First Explicit Example: The Commuting Brownian Particle

We give (to the author's knowledge) the first example where the non-Gaussian fluctuations of particle entropy Δs_s , environmental entropy Δs_e , and total entropy Δs can be evaluated exactly. A complementary method which allows the general numerical computation of fluctuations by iteration will be proposed in the context of a cosmological example in 2.5.3.

Consider two heat baths at temperatures T_1 and T_2 with a Brownian particle moving initially in T_1 . After the equilibration time, its momentum p_i (in units of mc) will be distributed according to the Jüttner-Maxwell distribution $\varphi(p_i, T_1)$ [128], where

$$\begin{aligned} \varphi(p, T) &= C^{-1} e^{-E(p)/T} = C^{-1} e^{-\sqrt{1+p^2}/T} \\ &= \frac{e^{-p^2/(T+T\sqrt{1+p^2})}}{Z(T)} \end{aligned} \quad (2.30)$$

is the equilibrium solution of the Brownian motion presented in Sec. 2.3. The last formulation in (2.30) (following from $\sqrt{1+p^2}-1 = p^2/(1+\sqrt{1+p^2})$) is convenient for the low momentum limit. To keep formulas concise, we measure heat in units of mc^2 and entropy in units of k_B , so that temperature T is measured in units of mc^2/k_B . The relativistic partition sum $Z(T)$ equals

$$Z(T) = 2 \exp(1/T) K_1(1/T) , \quad (2.31)$$

with K_1 being the first modified Bessel function of the second kind. The Brownian particle can pass to the bath T_2 through an opening (cf. Fig. 2.1). This opening is small enough to keep the baths at different temperatures and to ensure that the Brownian particle spends enough time in T_2 before returning to T_1 . So its momentum p_f on return has become uncorrelated to the initial value p_i and is distributed according to $\varphi(p_f, T_2)$. The change of the particle entropy Δs_s and the environmental entropy Δs_e during the relaxation of the Brownian particle in T_2 can be expressed using φ :

$$\Delta s_s = s_s(t_f) - s_s(t_i) = \ln \frac{\varphi(p_i, T_1)}{\varphi(p_f, T_2)} \quad (2.32a)$$

$$\Delta s_e = \frac{\Delta Q}{T_2} = \ln \frac{\varphi(p_f, T_2)}{\varphi(p_i, T_2)} \quad (2.32b)$$

$$\Delta s = \Delta s_s + \Delta s_e = \ln \frac{\varphi(p_i, T_1)}{\varphi(p_i, T_2)} \quad (2.32c)$$

The total entropy Δs in (2.32c) follows from the above definitions of particle entropy (2.32a) and environmental entropy⁵ (2.32b). From the resulting expression (2.32c) we find the macroscopic Gibbs entropy,

$$\Delta S = \langle \Delta s \rangle = \int \varphi(p_i, T_1) \ln \frac{\varphi(p_i, T_1)}{\varphi(p_i, T_2)} dp_i ,$$

to equal the relative entropy of the baths,

$$\Delta S = S_{\text{KL}}(T_1 \| T_2) , \quad (2.33)$$

which is also known as the Kullback-Leibler distance [136, 135].

The trajectory entropies (2.32) depend only on the pair (p_i, p_f) of initial and end point in momentum space. Therefore the distributions $P(\Delta s)$, $P(\Delta s_s)$ and $P(\Delta s_e)$ follow not from path integrals but ordinary integrals such as

$$P(\Delta s_e) = \int \varphi(p_i, T_1) \varphi(p_f, T_2) \delta(\Delta s_e - \Delta s_e(p_i, p_f)) dp_i dp_f ,$$

where the expression $\Delta s_e(p_i, p_f)$ (2.32b) is inserted in the Dirac delta function to sum over all trajectories yielding a certain entropy increment Δs_e . Because of its physical relevance, we begin with the explicit non-relativistic results, $T \ll mc^2/k_B$, when φ (2.30) becomes the Maxwell-Boltzmann distribution:

$$P(\Delta s) = \frac{\Theta(A(\Delta s - s_0))}{\sqrt{\pi A}(\Delta s - s_0)} e^{-\frac{\Delta s - s_0}{A}} \quad (2.34a)$$

$$P(\Delta s_s) = \frac{K_0(|\Delta s_s - s_0|)}{\pi} \quad (2.34b)$$

$$P(\Delta s_e) = \frac{\sqrt{\alpha}}{\pi} e^{\Delta s_e \frac{1-\alpha}{2}} K_0\left(|\Delta s_e| \frac{1+\alpha}{2}\right) \quad (2.34c)$$

⁵ Aside from the physical expression $\Delta Q/T$ used in (2.32b), the expression $\ln(\varphi(p_f, T)/\varphi(p_i, T))$ in terms of the equilibrium distribution φ is directly related to the definition (2.10) by the principle of detailed balance, $\varphi(p_i, T) P_{\text{trans}}^{(\Delta t)}(p_i \mapsto p_f, T) = \varphi(p_f, T) P_{\text{trans}}^{(\Delta t)}(p_f \mapsto p_i, T)$, because the baths themselves are in local equilibrium.

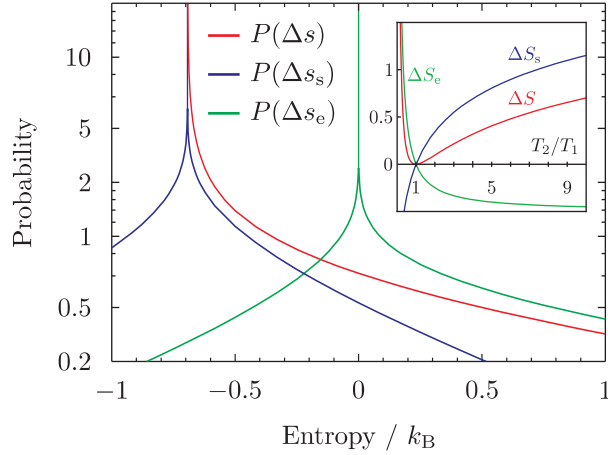


Figure 2.2: The exact expressions (2.34) for the distribution of particle entropy Δs_s (blue), environmental entropy Δs_e (green), and total entropy $\Delta s = \Delta s_s + \Delta s_e$ (red). The plot is for $T_1 = 4T_2 \ll mc^2/k_B$. The inset shows the dependence on the temperature ratio for the macroscopic entropies (2.35): $\Delta S_s = \langle \Delta s_s \rangle$, $\Delta S_e = \langle \Delta s_e \rangle$, and $\Delta S = \Delta S_s + \Delta S_e$ which is non-negative according to the Second Law of thermodynamics (2.1).

The abbreviations $A = \alpha^{-1} - 1$ and $s_0 = \frac{1}{2} \ln \alpha$ contain the dependence on the temperature ratio $\alpha = T_2/T_1$. The Heaviside step function is denoted by Θ . The distribution functions (2.34) are plotted in Fig. 2.2. With the Bessel function K_0 appearing in (2.34), the distributions for Δs_s and Δs_e have logarithmic divergences at s_0 and 0 respectively. The distribution of Δs has the stronger inverse square root divergence as Δs approaches s_0 from above and vanishes below s_0 . From (2.34a) the integral Fluctuation Theorem (2.3) can be verified directly, while the detailed Fluctuation Theorem (2.2) is obviously not fulfilled (as it has to be since the embedding temperature for the Brownian particle changes randomly with time). We remark that (2.34a) is not simply the convolution of (2.34b) and (2.34c) because Δs_s and Δs_e are highly correlated.

The macroscopic entropies $\Delta S_s = \langle \Delta s_s \rangle$, $\Delta S_e = \langle \Delta s_e \rangle$, and $\Delta S = \langle \Delta s \rangle = \Delta S_s + \Delta S_e \geq 0$ are the mean values of the distributions (2.34):

$$\Delta S_s = s_0 = \frac{\ln \alpha}{2} \quad (2.35a)$$

$$\Delta S_e = \frac{\alpha^{-1} - 1}{2} \quad (2.35b)$$

After the Brownian particle has visited both reservoirs once, the total macroscopic entropy increment has the symmetric form

$$\Delta S(T_1 \rightarrow T_2 \rightarrow T_1) = \Delta S(T_2 \rightarrow T_1 \rightarrow T_2) = \frac{(T_1 - T_2)^2}{2T_1 T_2} > 0. \quad (2.36)$$

In the relativistic regime, mc^2 defines a third energy scale, so that the results no longer depend only on the ratio of temperatures. The singularity at $\Delta s = s_0$ is shifted to the position

$$s_0 = \ln \frac{Z(T_2)}{Z(T_1)} \quad (2.37)$$

in terms of the partition sum (2.31). The first relativistic correction of the partition sum is

$$Z(T) = \sqrt{2\pi T} \left(1 + \frac{3}{8}T + \mathcal{O}(T^2) \right), \quad (2.38)$$

so that s_0 depends on the temperature difference $\Delta T = T_2 - T_1$ in first order:

$$s_0 = \frac{1}{2} \ln \frac{T_2}{T_1} + \frac{3}{8} \Delta T + \mathcal{O}(T_1^2, T_2^2). \quad (2.39)$$

In the ultra-relativistic regime, $T \gg mc^2/k_B$, the partition sum becomes linear in T ,

$$Z(T) = 2T + 2 + \mathcal{O}(1/T), \quad (2.40)$$

so that the position s_0 of the singularity depends on the ratio of temperatures as in the non-relativistic limit and reaches twice its non-relativistic value,

$$\lim_{k_B T \gg mc^2} s_0 = 2 \lim_{k_B T \ll mc^2} s_0 = \ln \frac{T_2}{T_1}. \quad (2.41)$$

The relativistic distribution functions are sums of Bessel functions. For example the system entropy Δs is distributed at arbitrary temperatures T_1 and T_2 according to

$$P(\Delta s_s) = \frac{1}{N(T_1, T_2)} \begin{cases} f(T_1, T_2, |\Delta s_s - s_0|), & \Delta s > s_0 \\ f(T_2, T_1, |\Delta s_s - s_0|), & \Delta s < s_0 \end{cases}. \quad (2.42)$$

The normalization factor in (2.42) is

$$N(T_1, T_2) = \frac{Z(T_1)Z(T_2)}{2\sqrt{T_1 T_2}} \quad (2.43)$$

and the function f in (2.42) is defined by the integral

$$f(a, b, z) = e^{-z} \int_0^\infty dx \frac{e^{-x}}{\sqrt{x}\sqrt{x+2z}} \frac{1+ax/2}{\sqrt{1+ax/4}} \frac{1+b(x/2+z)}{\sqrt{1+b(x/4+z/2)}}. \quad (2.44)$$

The non-relativistic limit (2.34b) follows from $f(0, 0, z) = K_0(z)$ and $N(0, 0) = \pi$. The first relativistic corrections are

$$\begin{aligned} P(\Delta s) &= g_0(\Delta s_s - s_0) \\ &+ \bar{T} g_1(\Delta s_s - s_0) \\ &+ \Delta T g_2(\Delta s_s - s_0) + \mathcal{O}(T_1^2, T_2^2, T_1 T_2), \end{aligned} \quad (2.45)$$

with the mean temperature $\bar{T} = (T_1 + T_2)/2$ and the temperature difference $\Delta T = T_2 - T_1$. We remark that the functions

$$g_0(z) = \frac{K_0(|z|)}{\pi} \quad (2.46a)$$

$$g_1(z) = \frac{3}{4\pi} (|z|K_1(|z|) - K_0(|z|)) \quad (2.46b)$$

$$g_2(z) = \frac{3}{8\pi} z K_0(|z|) \quad (2.46c)$$

exhibit the symmetry $T_1 \leftrightarrow T_2$ of the system, $g_1(-z) = g_1(z)$, $g_2(-z) = -g_2(z)$, and preserve the normalization at any order, $\int_{-\infty}^\infty g_j(z) dz = \delta_{0,j}$.

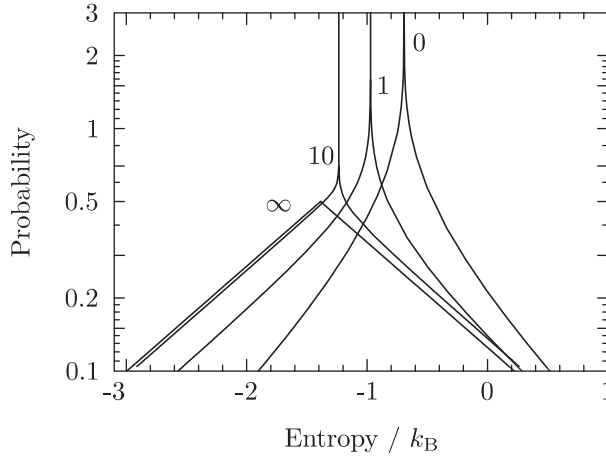


Figure 2.3: This plot shows the distribution of system entropy, $P(\Delta s_s)$, as we pass from the non-relativistic regime to the ultra-relativistic regime. The parameter attached to each graph is $k_B \sqrt{T_1 T_2} / (mc^2)$ which assumes the values zero (non-relativistic limit), 1, 10 and ∞ (ultra-relativistic limit). As we approach the ultra-relativistic limit, the mean doubles and the spread of fluctuations widens, but does not diverge. The logarithmic peak reduces to a kink. Note that we are discussing the classical relativistic regime. Quantum corrections, depending on the particle spin, are expected when pair creation sets in.

In the ultra-relativistic limit, we find $N \rightarrow 2\sqrt{T_1 T_2}$ (2.43) and $f(T_1, T_2, z) \rightarrow \sqrt{T_1 T_2} e^{-z}$ (2.44), so that

$$P(\Delta s_s) = \frac{e^{-|\Delta s_s - s_0|}}{2} \quad (2.47)$$

is an exponential distribution. It is only in the ultra-relativistic limit that the logarithmic divergence at s_0 vanishes in favor of a kink (cf. Fig 2.3). In the intermediate relativistic regime ($k_B T \approx mc^2$) the distribution $P(\Delta s_s)$ has skewness. The exact distribution (2.42) is shown for a fixed temperature ratio $T_1 = 4T_2$ as the geometric mean $\sqrt{T_1 T_2}$ is increased from zero (non-relativistic limit) to infinity (ultra-relativistic limit) in Fig 2.3.

2.5 Generalizations in the Framework of General Relativity

The monotonic increase of entropy is a fundamental principle of physics and the universe is known to expand, as was discovered by E. Hubble in 1929. The discussion whether there is a direct connection between these observations has never stopped [107, 166, 108, 2, 34]. Therefore we aspire a formulation of the Fluctuation Theorem consistent with general relativity, but we restrict ourselves to the class of Friedmann-Lemaître models, which describe a spatially homogeneous and isotropic, expanding or contracting universe. The corresponding line element (given by the Robertson-Walker metric) is $-dt^2 + dr^2$. The important difference compared to special relativity is that the spatial part, dr^2 , is scaled by a time dependent factor $R(t)$ describing the expansion or contraction of the universe:

$$dr^2 = R^2(t) h_{ij}(\xi) d\xi^i d\xi^j. \quad (2.48)$$

The Latin indices describe spatial components numbered by 1 to 3. We do not have to deal with the details of the metric tensor \mathbf{h} describing the spatial curvature. The result will

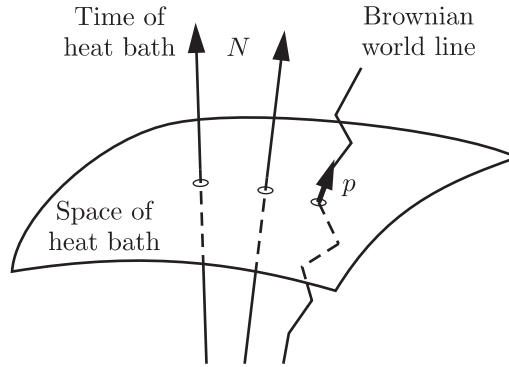


Figure 2.4: A sketch of spacetime showing a spatial slice of the heat bath at fixed time and the world line of a Brownian particle in a (locally) expanding universe.

be valid for all possible geometries. The expansion rate $H(t) = \dot{R}(t)/R(t)$, named Hubble function, is one of the most important quantities in cosmology and its present value is a direct observable [169]. The typical frame for a cosmic heat bath is the frame of the cosmic microwave background.

2.5.1 Cosmological Fluctuation Theorem

In general relativity, the correct equations of motion include the covariant differential Dp of the momentum. (Denoting by p the 4-vector, the components of Dp are $Dp^\alpha = dp^\alpha + \Gamma_{\mu\nu}^\alpha p^\mu dx^\nu$.) Its spatial components replace the left hand side of (2.21) and can be split up into a spatially covariant part, ${}^{(3)}D\mathbf{p}$, and a contribution due to the time-dependent scaling:

$$D\mathbf{p} = {}^{(3)}D\mathbf{p} + H(t) \mathbf{p} dt . \quad (2.49)$$

Therefore the covariant Langevin equation, generalizing Eq. (2.21) to be valid in an expanding or contracting universe of arbitrary spatial geometry, reads

$${}^{(3)}D\mathbf{p} = - [\nu(\mathbf{p}, t) + H(t)] \mathbf{p} dt + {}^{(3)}D\mathbf{p}_s . \quad (2.50)$$

Herein, H enters as an additional damping term, which has caused the cooling during the expansion of our universe and is responsible for the cosmological red shift. The distribution of the stochastic impacts ${}^{(3)}D\mathbf{p}_s$ is found after substituting h_{ij} for the Euclidean metric δ_{ij} in (2.29). Applying the time-reversal map, we find that Eq. (2.28) gains a second term due to the cosmic expansion:

$$\begin{aligned} ds_e &= -\frac{dE}{T} - \frac{\|\mathbf{p}\|^2}{ET} d \ln R \\ &= -\frac{dE}{T} - H \frac{(\mathbf{p}, d\mathbf{r})}{T} \\ &= ds_e^{(\text{particle})} + ds_e^{(\text{cosmic})} . \end{aligned} \quad (2.51)$$

The numerator $(\mathbf{p}, d\mathbf{r})$ in (2.51) is the canonical line integral (canonical one-form) in phase space. The integral Fluctuation Theorem (2.3) extends to an expanding ($H > 0$) or contracting ($H < 0$) spacetime when this second term is taken into account. It has a clear geometric interpretation: the Hubble function is the external curvature of space,

$$DN = H d\mathbf{r} , \quad (2.52)$$

with N being the time-like normal vector to the space of the heat bath as depicted in Fig. 2.4. Put more formally, $DN = \underline{S}d\mathbf{r}$ with the second fundamental form \underline{S} , which is due to the maximum symmetry of space a scalar and equal to H . This permits the second term in (2.51) to be written as

$$ds_e^{(\text{cosmic})} = -\frac{(p, DN)}{T}.$$

Since the particle energy $E = p^0 = -p_0 = -(p, N)$ is the zero component of the 4-vector p , the first term in (2.51) equals the differential

$$ds_e^{(\text{particle})} = \frac{d(p, N)}{T} = \frac{(Dp, N) + (p, DN)}{T},$$

such that the sum of both terms is

$$ds_e = \frac{(Dp, N)}{T}. \quad (2.53)$$

It is natural to think of the numerator (Dp, N) as the heat $dQ = Tds_e$ exchanged with the bath, since it is the projection of the exchanged 4-momentum Dp on the local energy component N of the heat bath.

Cosmology is an example for the breaking of the First Law, $-dE = d(p, N) \neq (Dp, N) = dQ$, by non-static metrics. So we find ourselves in a remarkable situation: There is no First Law in cosmology, while the Second Law and furthermore the integral Fluctuation Theorem hold.

The isolated cosmological entropy term $ds_e^{(\text{cosmic})}$ in (2.51) would indeed undergo a change of sign if the expansion turned into contraction. But in the entire bath entropy (2.53) the geodesic flow N enters as a projection, which does not imply a change of sign if N was to contract. Eventually, a decreasing total entropy $s = s_s + s_e$ is always exponentially unlikely as expressed by the integral Fluctuation Theorem (2.3).

2.5.2 Additional Theorems for the Einstein-de Sitter Universe

So far, we applied the time-reversal transformation to arrive at $\langle e^{-\Delta s} \rangle = 1$. As emphasized at the outset of the general derivation in Sec. 2.2, we are free to choose any other transformation from the mathematical point of view. Then the function in the exponent will no longer equal the entropy Δs . For instance, if the system is invariant under the chosen transformation, we will get the trivial result $\langle e^0 \rangle = 1$. But for physically sensible transformations, the Fluctuation Theorem will remunerate us with non-trivial relations. In order to derive a Fluctuation Theorem that contains the cosmic expansion rate H , let us choose a local time-reversal transformation, which acts only on the local particle dynamics and leaves the sign of the global cosmic expansion rate H unchanged. Repeating the computation of Sec. 2.5.1 with the transformation $\tilde{H} = H$ (local time reversal) instead of $\tilde{H} = -H$ (global time reversal) yields

$$\langle e^{-(\Delta s + \Delta h)} \rangle = 1, \quad \text{with } \Delta h = \frac{AH}{T}. \quad (2.54)$$

The additional term Δh is proportional to the Hubble constant, the inverse temperature and the action $A = \int ((\mathbf{p}, \mathbf{v}) - \Delta E) dt$ of the energy change $\Delta E = \dot{E}/\nu$.

This demonstrates that the Fluctuation Theorem is an efficient technique to design relations that include those physical observables, which are most interesting for a given system or experiment. The second general relativistic Fluctuation Theorem (2.54) holds in addition to

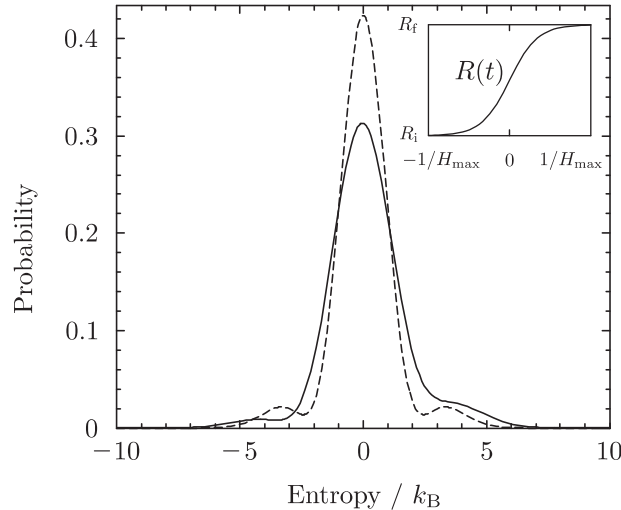


Figure 2.5: The distribution of particle entropy Δs_p is shown for a cosmic inflationary phase. The system starts in equilibrium at time $t = -1/\nu$ with temperature T_i , undergoes a period of inflation centered at $t = 0$ (cf. the inset), and equilibrates again until the time $1/\nu$ with the lower bath temperature T_f . The maximum of the Hubble function is $H_{\max} = 100\nu$ for the distribution shown in solid line. The case of a static universe with zero mean entropy is plotted in dashed line. This system is described completely by the ratio H_{\max}/ν of the cosmic expansion rate and the thermal relaxation rate, the temperature to mass ratio $k_B T_{\text{mean}}/(mc^2) = 10$, and the inflation factor $R_f/R_i = 2$.

(2.3). At first glance one might be surprised that there is an infinity of Fluctuation Theorems, all constraining the fluctuations of Δs . But since the distribution function $P(\Delta s)$ is a point in the infinite dimensional (Banach) space of integrable functions, there has to be an infinity of physical constraints to determine $P(\Delta s)$ uniquely.

In many interesting stages of the cosmic evolution, such as the early (hypothetical) inflationary phase and the future phase of accelerated expansion, the size of the universe grows exponentially with time so that H is constant. During these periods the cosmic impact on the local relativistic Brownian motion with (2.49) is time-independent. We can therefore immediately infer from the general derivation in Sec. 2.2.2, that for these phases of the cosmic evolution the stronger detailed formulations of the Fluctuation Theorem hold as well.

2.5.3 Second Explicit Example: The Expanding Universe

The cosmological Fluctuation Theorems of the Secs. 2.5.1 and 2.5.2 restrict the entropy fluctuations Δs caused by a relativistic particle. In this section we compute the detailed distribution of fluctuations explicitly for evolving cosmic environments.

The entropy change $ds = ds_s + ds_e^{(\text{particle})} + ds_e^{(\text{cosmic})}$ has contributions of the system entropy, $s_s = -\ln P$, and by heat exchange, $ds_e = dQ/T$. Since there is no First Law, $dE + dQ \neq 0$, for the time dependent cosmic metric, the heat contribution ds_e splits up in a term due to the change of particle energy, $ds_e^{(\text{particle})} = -dE/T$, and a cosmological term, $ds_e^{(\text{cosmic})} = -p^2 H dt / (ET)$, as derived in Eq. (2.51). The method to compute distributions of fluctuations will be presented for the particle term, $s_e^{(\text{particle})}$, which we abbreviate by s_p . It is straight forward to apply the method to the other terms.

To compute the distribution $P(\Delta s_p, \Delta t)$ of produced entropy Δs_p , we have to sum up $ds_p = -dE/T(t)$ over the observation time Δt . Therefore we have to evolve the process $p(t)$ while book keeping the change of entropy s_p . This is done by extending the Fokker-Planck equation to evolve the joint distribution $P(p, s_p, t)$. The evolution of entropy s_p is directly related to the dynamical variable p by the differential $ds_p = -dE(p)/T(t)$, since relativistic Brownian motion is restricted to the mass-shell (2.15). The similar evolution of $P(p, E, t)$ is easily determined. One method is to include the Helfand moments $\langle dE \rangle$, $\langle dE^2 \rangle$, and $\langle dE dp \rangle$ into the probability current (2.12), from which we find the Fokker-Planck equation $\partial_t P + \partial_p j_p + \partial_E j_E = 0$ for $P(p, E, t)$. The correlation $\langle dE dp \rangle$ is important because dE is not independent from dp on the mass-shell. Equivalently, we can proceed using the Fokker-Planck equation $\partial_t P + \partial_p j_p = 0$ for $P(p, t)$ with the current (2.24) and substitute every differentiation ∂_p by $\partial_p + \frac{\partial E}{\partial p} \partial_E$ so that the probability current is tangential to the mass-shell. After identifying $\partial_{s_e} = -T \partial_E$ (2.28) we arrive at the Fokker-Planck equation

$$\begin{aligned} \frac{1}{\nu} \partial_t P &= F_0(\partial_p - \frac{E'(p)}{T} \partial_{s_p}) P \\ &= \left[F_0(\partial_p) - F_1(\partial_p) \partial_{s_p} + F_2 \cdot \partial_{s_p}^2 \right] P \end{aligned} \quad (2.55)$$

for the distribution $P(p, s_p, t)$. The momentum operator is

$$F_0(\partial_p) = \lambda + (\lambda + T/E)p\partial_p + ET\partial_p^2 .$$

The entropic extensions of the Fokker-Planck Eq. (2.55) are

$$F_1(\partial_p) = 1 + \lambda F_2 + 2p\partial_p \text{ and } F_2 = p^2/(ET) .$$

The function $\lambda(t) = 1 + H(t)/\nu$ contains the cosmic driving by expansion. This function of time is deterministic since we can safely neglect the back reaction of our tiny system on the cosmic evolution. The entropy fluctuations $P(\Delta s_p, \Delta t)$ follow from (2.55) when solved for the initial condition

$$P(p, s_p, t)|_{t=0} = \delta(s_p) P_0(p) \quad (2.56)$$

and after integrating out the momentum p :

$$P(\Delta s_p, \Delta t) = \int_{\mathbb{R}} P(p, \Delta s_p, \Delta t) dp . \quad (2.57)$$

The Fokker-Planck Eq. (2.55) is solved by orthogonal functions. We expand the distribution $P(p, s_p, t)$ in a series of Hermite polynomials with respect to the entropy dependence, so that the two-dimensional Fokker-Planck (2.55) for $P(p, s_p, t)$ reduces to an one-dimensional system for the coefficients $a_k(p, t)$. The coefficients $a_k(p, t)$ are simple linear combinations of the moments $M_l(p, t)$,

$$M_l(p, t) = \int P(p, s_p, t) s_p^l ds_p ,$$

so that the singular initial condition (2.56) are represented by $M_0(p, 0) = P_0(p)$ and $M_l(p, 0) = 0$ for all $l > 0$ in a regular way. From (2.55) follows after integrating by parts a hierarchy of differential equations for the moments $M_l(p, t)$:

$$\frac{1}{\nu} \partial_t M_l = F_0(\partial_p) M_l + l F_1(\partial_p) M_{l-1} + l(l-1) F_2 M_{l-2} . \quad (2.58)$$

The case $l = 0$ reduces to the Fokker-Planck equation for the momentum, $M_0(p, t) \equiv P(p, t)$. Since (2.58) is a parabolic differential equation, numerical solutions for the $M_l(p, t)$ can be obtained by standard techniques. Integrating p , we have the moments $m_l(\Delta t) = \int M_l(p, \Delta t) dp$ for the distribution of entropy (2.57). After computing iteratively a sufficient number of moments m_l , the probability distribution for the entropy (2.57) can be reconstructed by the algorithm presented in appendix 2.7.

Let us illustrate (2.57) for a universe undergoing a transient inflation as sketched in the inset of Fig. 2.5. Such a transition of the scale factor ranging from R_i to R_f according to

$$R(\tau) = \frac{R_i e^{-\tau} + R_f e^{\tau}}{e^{-\tau} + e^{\tau}}$$

is a common toy-model for particle creation in quantum field theory [21]. The peak of the Hubble function shall be H_{\max} , so that $\tau = tH_{\max}/I$. The inflation factor is $I = 2(\sqrt{R_f} - \sqrt{R_i})/(\sqrt{R_f} + \sqrt{R_i})$. Neglecting quantum effects, the thermal heat bath, which may consist of photons or other massless particles, cools proportional to the inverse scale factor [234],

$$T(t) = \frac{T_{\text{mean}}}{R_i^{-1} + R_f^{-1}} \frac{2}{R(t)}.$$

We choose the mean temperature T_{mean} in the relativistic regime, $k_B T_{\text{mean}} = 10mc^2$. The universe inflates by the factor $R_f/R_i = 2$. The cosmic forcing of the system depends on the ratio of the relaxation rate ν and the expansion rate H_{\max} . For the nonequilibrium distribution of the particle entropy Δs_p shown as solid line in Fig. 2.5 the dimensionless control parameter H_{\max}/ν equals 100. As reference, the symmetric distribution of the relativistic equilibrium with $H_{\max} = 0$ is plotted in dashed line. When H_{\max}/ν assumes the values 1, 10 and 100, the width σ_{s_p} of the distribution $P(\Delta s_p)$ increases monotonically, being equal to 1.45, 1.48 and 1.64 respectively. In contrast, the mean ΔS_p is not monotonic and assumes the values 0.68, 0.69 and 0.15 respectively. Five moments have been computed to construct Fig. 2.5.

2.6 Conclusions

Relativistic Fluctuation Theorems have been established that remain valid for high temperatures or low masses, $mc^2 \ll k_B T$. The integral Fluctuation Theorem, $\langle e^{-\Delta s} \rangle = 1$, was found to hold also in the framework of general relativity as far as the cosmic expansion is concerned.

With the additional Fluctuation Theorem $\langle e^{-\Delta s - \Delta h} \rangle = 1$ and the numerical example of Sec. 2.5.3 we can answer the question raised in the introduction: yes, the cosmic expansion has an influence on the total entropy fluctuations Δs , and the mean values of individual terms such as the particle contribution $\Delta s_e^{(\text{particle})}$ can undergo a change of sign for cosmic contraction. However the relation $\langle e^{-\Delta s} \rangle = 1$ holds, which implies the Second Law, $\Delta S = \langle \Delta s \rangle > 0$, so that for a macroscopic system the sign of ΔS is independent of the cosmological evolution. We have the remarkable situation that the First Law is violated by cosmic expansion, while the Second Law and moreover the Fluctuation Theorem hold.

On the theoretical road ahead, one may expect integral Fluctuation Theorems to hold for arbitrary time-dependent and inhomogeneous fields, such as gravitational waves, when the concise expression (2.53) is applied. For the process originally introduced in [51], the weaker inequality (2.1) has been proven recently [182] under general conditions.

Experimentally, the change of the environmental entropy $\Delta s_e = -\Delta E/T$ can be measured by detecting single particles after a sequence of elastic collisions, i.e. collisions without decay or excitation of internal degrees of freedom. Such collisions are observed for heavy quarks

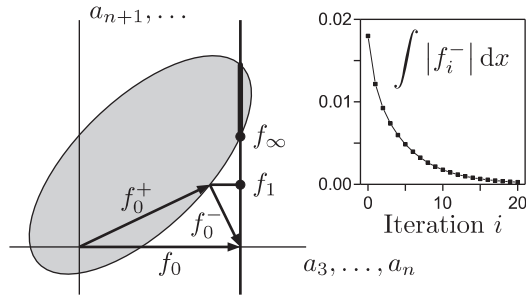


Figure 2.6: A sketch of the space spanned by the functions (2.61). The first n coefficients a_3, \dots, a_n are predetermined by the known moments (vertical line). The higher coefficients a_{n+1}, \dots are determined iteratively. The shaded region represents the non-linear (convex) space of non-negative functions. The inset shows the rapid convergence of the algorithm.

(for instance the charm quark) which traverse the expanding quark-gluon plasma created by heavy-ion collisions. Nonequilibrium thermodynamical descriptions are being developed at present for these relativistic media [227]. Moreover, the relativistic Fluctuation Theorem is not only subject of high energy physics and cosmology. The special-relativistic Fluctuation Theorem can be tested with a high-precision spectroscopy experiment by shining a laser on an excited granulate of glass or reflecting steel beads, so that the granulate serves as a heat bath and the photons are the ultra-relativistic “Brownian” particles which scatter inelastically due to the Doppler shift⁶. The environmental entropy $\Delta s_e = -\Delta E/T$ then follows from the measurement of the frequency shift $\Delta\nu = \Delta E/h$.

2.7 Appendix: Treating the Truncated Moment Problem

In order to reconstruct a distribution function, we are interested in an efficient algorithm that generates uniquely out of $n \geq 2$ given moments m_k a continuous and non-negative function f on the real line, so that

$$\int_{\mathbb{R}} f(x) x^k dx = m_k \text{ for } k \leq n, \text{ and} \quad (2.59)$$

$$\left| \int_{\mathbb{R}} f(x) H_k dx \right| = \text{minimal for } k > n. \quad (2.60)$$

In (2.60) the Hermite polynomials $H_k(y) = \sum_{l=0}^k h_{kl} y^l$ are written in the variable $y = (x - m_1)/\sqrt{2}\sigma$ rescaled by the width $\sigma = \sqrt{m_2 - m_1^2}$. The truncated moment problem (2.59) has to be augmented by the complementary condition (2.60) for uniqueness. Functions solving the Eqs. (2.59) are readily given by

$$f(x) = \frac{e^{-y^2}}{\sqrt{2\pi}\sigma} \left(1 + \sum_{k=3}^{\infty} \frac{a_k}{2^n n!} H_k(y) \right). \quad (2.61)$$

By virtue of the orthogonality of the Hermite polynomials, the first n coefficients $a_k = \langle H_k \rangle_f = \int f H_k dx = \sum_{l=0}^k h_{kl} m_l$ are directly determined by the known moments m_l . If one was to truncate the series (2.61) after the n 's coefficient, the resulting function f_0 may take negative values. If so, we use this negative part $f_0^- = f_0 \Theta(-f_0)$ of the function $f_0 = f_0^+ + f_0^-$ to

⁶Cf. the introductory discussions of Chap. 9, in which case the photon is *absorbed* and not scattered.

determine the higher coefficients to be $a_k = -\langle H_k \rangle_{f_0^-}$ for $k > n$. This yields a new function $f_1 = f_1^+ + f_1^-$ with a smaller negative part f_1^- . Iteratively one approaches the desired solution f_∞ with arbitrary precision (cf. Fig. 2.6).

We will use the Hermite expansion (2.61) in the following chapter (cf. Sec. 4.3) also for granular matter.

Chapter 3

The Paradigm System: Wet Granular Matter

The hysteretic interaction between a pair of wetted spheres has been pointed out in the first chapter (cf. Fig. 1.1B) as a mechanism that breaks time-reversal symmetry. In the present chapter, the *hysteretic pair interaction* between wetted surfaces is quantified theoretically and experimentally verified. The formation and rupture of single liquid bridges is temporally resolved. The impact velocities are chosen to cover the range of typical particle velocities in agitated wet granular matter. The results will therefore form the basis for the analytic and numerical modeling of many-particle systems in the following chapters, where we will furthermore compare theoretical predictions on the collective macroscopic dynamics with experiments. For this program the particle interaction is determined in this chapter, so that there will be no free parameters left in the following modeling and experimental comparisons. It is shown that the hysteretic formation and rupture of liquid capillary bridges between adjacent grains accounts for most relevant cases of wet granular matter. The various dissipation mechanisms are discussed with particular emphasis on their relevance. Variations of the rupture energy loss with the impact energy are quantified and discussed. From the broken time-reversal symmetry, observed experimentally, we arrive at the Minimal Capillary Model which describes wet granular matter by the bridge energy E_{cb} and rupture length s_{crit} as the interaction parameters.

The first section introduces dry and wet granular matter. In the Sec. 3.2 the mechanisms of dissipation in wet granular matter are discussed theoretically. The results of the single bridge experiment are presented in Sec. 3.3. This leads us to the Minimal Capillary Model in Sec. 3.4 which is directly applied in a first simulation showing the different structures formed in dry and wet granular matter.

3.1 Dry and Wet Granular Matter

Granular materials are truly ubiquitous, on earth and in space. They form the rings of Saturn, and are present in nature as sand and mineral resources for example. The industrial handling of granular materials accounts for about 10% of the world wide energy consumption [68]. The reason for such an energetic investment is intrinsic to the granular materials: granular matter is a *dissipative* system. The dissipation is caused by the vast number of internal degrees of freedom which each granular particle possesses. To consider a well-defined example, a glass sphere with 1 millimeter in diameter consists of more than 10^{19} SiO_2 molecules. Shaking such glass beads creates a ‘heat bath’ represented by the chaotic center-of-mass motion of the grains, which easily corresponds to giga- or even tera-Kelvins when converted

to temperature using Boltzmann's constant. At the same time the internal degrees remain largely at ambient temperatures, and provide an energetic sink. This strong nonequilibrium situation has attracted much scientific interest within the last 25 years¹ (cf. [105, 123, 27, 114] and references therein, just to mention a few). Beside the physical importance of granular matter as a model nonequilibrium systems and its industrial relevance, it is noteworthy that the mesoscopic and macroscopic granular materials have the benefit to be well accessible to controlled experiments. The vigorously shaken dilute state is a granular gas which allows for a Boltzmann-Enskog description yet is, unlike a 'usual' gas of molecules, out of equilibrium with, e.g., non-Maxwellian velocity distributions [113]. The 'fluid'-like state at milder shaking shows further rich nonequilibrium phenomena, such as the Brazil nut effect [184] and states of granular oscillons [225]. The interest in granular materials among the soft-matter community increased within the last years, as it has been widely recognized that many concepts which are well established for colloidal systems and glasses apply as well to granular systems [213, 43, 27, 14, 153], and vice versa [161, 7, 33, 130]. Furthermore, both colloidal and granular matter play a certain role as models for other systems which are too complex to be tractable. In particular, granular systems are of great interest in the context of dynamical systems far from thermal equilibrium [78, 10, 114].

The scientific interest in *wet* granular matter strongly increased in recent years² [215, 216, 143, 205, 206, 217, 119, 144, 237, 122, 198, 87, 114, 120, 142, 163]. The term 'soft matter' applies particularly well to wet granulates, which can be shaped to stable structures ([220], Fig. 3.10B), but yield to rather small shear stress [119, 158, 179, 196, 181]. This plasticity stands out against dry granulates, such as the sand in an hourglass, which runs through the orifice like a fluid ([68], Fig. 3.10A). While earlier studies [119, 163] focused on the stability of the static state, the investigation of the dynamics of wet granular matter has just begun [198, 87, 114]. The change in bulk properties is due to a fundamental change of the underlying particle interaction. In the wet system, small liquid capillary bridges form between adjacent grains, exerting an attractive force upon them by means of the surface tension of the liquid [144, 204]. It is clear that these only form when the liquid wets the material the grains consist of, which is well fulfilled for most sands. When a wet granulate is being sheared, or otherwise mechanically agitated, the repeated formation and rupture of the many liquid objects inside gives rise to considerable dissipation, which is then experienced as a noticeable resistance to the external drive imposed on the material. In order to understand the mechanical properties of wet granular matter, it is thus indispensable to understand the dissipation processes connected to the liquid capillary bridges in detail.

The hysteretic formation and rupture of liquid bridges has been emphasized in the first chapter as a mechanism which breaks the time-reversal symmetry of a hard sphere system. Since a liquid bridge mediates an attractive force between particles, wet granular matter interacts by *hysteretic forces*, as has been introduced in the scientific literature in [198, 87, 114]. With these hysteretic forces, the interaction and dissipation in wet granular matter is of qualitative different nature [114] compared to dry granular matter. In collision of dry particles a certain *fraction* of the initial kinetic energy is dissipated into the atomic degrees of freedom of the particles. This is in sharp contrast to the hysteretic interaction in wet granular matter. A liquid bridge is formed between particles in contact. Being stretched between moving particles, the bridge bears a defined maximal potential energy. With the rupture of the capillary bridge, this intrinsic energy ΔE_{cb} is dissipated into the molecular degrees of freedom of the liquid.

¹The first scientific investigations of granular materials started much earlier, usually credited to R. A. Bagnold [11] about 70 years ago.

²There exist individual pioneering scientific works among which [40], e.g., dates forty years back, as well as engineering results [188].

Wet granular matter has therefore an *intrinsic energy scale*, as will be discussed theoretically in the following section and confirmed experimentally under realistic impact conditions in this chapter.

3.2 The Mechanisms of Dissipation in Wet Granular Matter

This section discusses five different mechanisms (and regimes) by which energy is dissipated in the wet granular dynamics.

Inelastic Collisions. — Collisions of macroscopic particles are inelastic. This dissipation is responsible for the fact that even the perfectly dry granulate in the hourglass behaves distinctly different from a regular fluid. Some fraction of the kinetic energy of the grains is transferred at each impact to the microscopic degrees of freedom on atomic scale. The heat bath represented by the chaotic motion of the grains corresponds to giga- or tera-Kelvins as emphasized above. In collisions, this heat bath is coupled to the room-temperature heat bath of the internal degrees of freedom of the particles, for example by the excitation of the particles' phonon spectrum. Some of the most striking features of granular motion owe to this intrinsic nonequilibrium character.

On the level of a continuum description, an elastic and an inelastic force component can be distinguished in the collision of particles. The continuum theoretic description of a sphere pressed against a flat wall (or equivalently up to a factor $1/\sqrt{2}$, when two spheres exchange forces) was derived by H. Hertz in 1882. The surface separation is denoted by s throughout this thesis (cf. Fig. 3.1A). The elastic Hertz force for a compression $\xi = -s > 0$ reads

$$F_{\text{elastic}} = c_1 \xi^{3/2} . \quad (3.1)$$

The coefficient $c_1 = \sqrt{2R_{\text{eff}}} E/3(1 - \nu^2)$ contains the Young modulus E , the Poisson ratio ν , and the Derjaguin relation

$$R_{\text{eff}}^{-1} = (R_1^{-1} + R_2^{-1})/2 . \quad (3.2)$$

This is the quasi static force, while collisions at finite impact velocity give rise to a dissipative force, since the particles are macroscopic which allows for internal friction. The viscoelastic generalization of Eq. (3.1) has the additional term [27]

$$F_{\text{visco}} = c_2 \xi^{1/2} \dot{\xi} . \quad (3.3)$$

The restitution coefficient ε quantifies the dissipation caused by inelastic forces, and is defined as the residual fraction of the momentum, i.e. the ratio of the momenta after and before the impact,

$$\varepsilon = \frac{p_f}{p_i} = \frac{-\dot{\xi}(t_{\text{coll}})}{\dot{\xi}(0)} . \quad (3.4)$$

Integrating the viscoelastic forces (3.1) and (3.3) shows that this ratio is fairly independent of the initial kinetic energy of the grains in a wide range, and tends to be smaller for large energies [27]. The associated loss in energy is

$$\Delta E_{\text{inelastic}} = E_0(1 - \varepsilon^2) , \quad (3.5)$$

with the initial energy (in the center-of-mass system) denoted by E_0 .

Other mechanism of dissipation in 'dry' collisions, such as plastic deformations, can be included to further reduce the factor $1 - \varepsilon^2$. The most important aspect of this dissipation mechanism is that the energy lost in the impacts, $\Delta E_{\text{inelastic}}$, scales with the impact energy, E_0 . There is thus no specific energy scale set by this process.

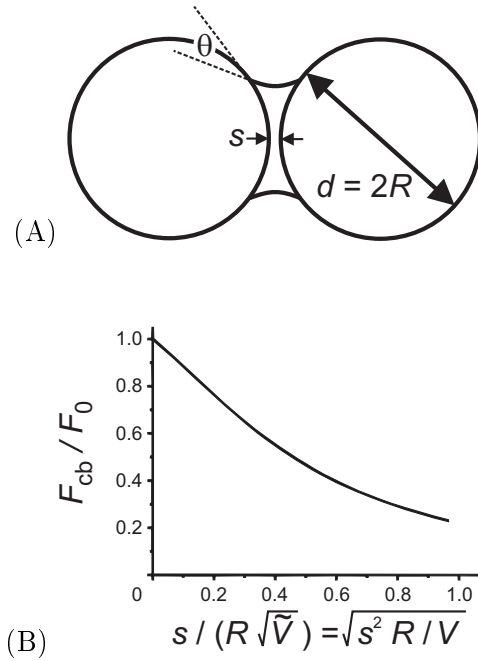


Figure 3.1: (A) A liquid capillary bridge between two spherical ‘grains’ of radius R . The capillary bridge can span a certain distance between the grains, until it pinches off at a critical distance which depends upon the liquid volume in the bridge. (B) A typical force-vs-distance curve observed as a liquid bridge has formed. It is shown as normalized with respect to the contact force, $F_0 = 2\pi\gamma R \cos \theta$.

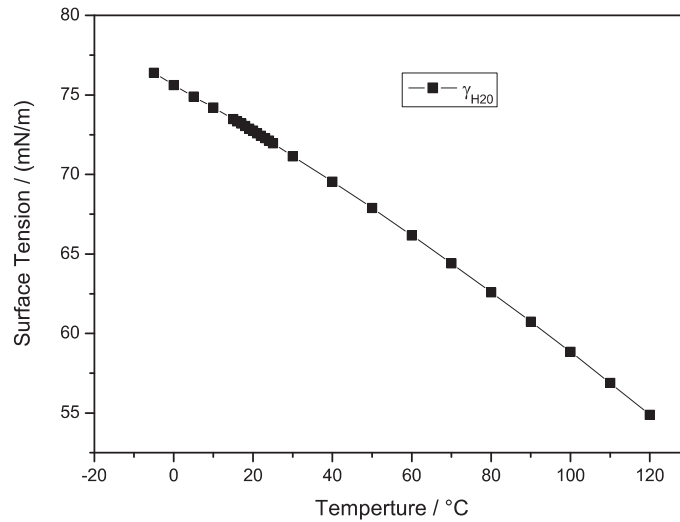


Figure 3.2: Surface tension of water at different temperature [140]. Water is an ubiquitous as well as exceptional fluid in many respects. When used to wet granular materials, its high surface tension and simultaneously low viscosity allows for a clear-cut approach to wet granular matter, where capillary forces dominate over viscous forces, as described quantitatively by the smallness of the capillary number $Ca = \frac{\eta v}{\gamma}$.

The Capillary Interaction. — Contrary to the inelastic collision, the liquid capillary bridges which are present in a wet granulate do provide their own energy scale. This is due to their characteristic dynamics of bridge formation and rupture. When two wet grains approach each other, the liquid adsorbed on their surface will not react until they come into contact. At this point, liquid is rapidly dragged to the area of contact due to the interfacial forces, and a capillary bridge forms. When the grains withdraw from each other after the impact, the bridge remains intact for quite some distance, exerting an attractive force upon the grains. This is illustrated in Fig. 3.1A for the idealized case of spherical grains. The angle θ is the contact angle the liquid makes with the grain material, and characterizes its wetting properties. For complete wetting, we have $\theta = 0$. At a certain critical separation of the grain surfaces, which shall be denoted by s_{crit} throughout this thesis, the bridge ruptures and distributes its liquid content back onto the grain surfaces. The rupture length s_{crit} depends on the liquid volume of the capillary bridge, If $\tilde{V} = V/R^3$ is the normalized liquid volume of a bridge between spherical grains of radius R , and $\tilde{s} = s/R$ is the normalized separation of the grain surfaces, rupture occurs at

$$\tilde{s}_{\text{crit}} = \left(1 + \frac{\theta}{2}\right) \left(\tilde{V}^{1/3} + 0.1\tilde{V}^{2/3}\right) \quad (3.6)$$

in good approximation [237].

A typical force-vs-distance curve is shown schematically in Fig. 3.1B. The force is normalized with respect to the contact force,

$$F_0 = 2\pi R\gamma \cos \theta , \quad (3.7)$$

where γ is the surface tension of the liquid ([237], cf. Fig. 3.2 for the surface tension of water). It should be noted that the capillary force easily exceeds the gravitational force of the particle. For instance, the capillary force (3.7) caused by water acting on a glass sphere of 1 millimeter diameter is 17 times its weight. Since there is no liquid bridge (and thus no force) when the grains are approaching, the energy lost in the entire process of formation and rupture of the liquid bridge is given by the area under the descending curve,

$$\Delta E_{\text{cb}} = \int_0^{s_{\text{crit}}} F(s) \, ds . \quad (3.8)$$

For spherical grains, the shape of this curve is well known in the quasi-static case [237]. It corresponds to the force exerted by a rotationally symmetric minimal surface spanned between the spheres, where the liquid volume of the bridge and the contact angle are the main geometric parameters. A good approximation is

$$F = \frac{F_0}{1 + 1.05S + 2.5S^2} , \quad (3.9)$$

where $S = \tilde{s}/\sqrt{\tilde{V}}$ [237]. This is in fact the curve displayed in Fig. 3.1B. It terminates at $S_{\text{crit}} = \tilde{s}_{\text{crit}}/\sqrt{\tilde{V}}$ as given by Eq. (3.6). Using this approximation, we can evaluate the integral and obtain

$$\Delta E_{\text{cb}} = 0.67 F_0 R \sqrt{\tilde{V}} \arctan(0.35 + 1.68S_{\text{crit}}) \quad (3.10)$$

for complete wetting ($\theta = 0$). S_{crit} is at least of order unity, such that the $\arctan(\dots) \approx 1.1$ or larger in (3.10), and it never goes beyond 1.57. Hence a reasonable approximation is

$$\Delta E_{\text{cb}} \approx F_0 R \sqrt{\tilde{V}} . \quad (3.11)$$

Given the fact that we have neglected side effects such as contact angle hysteresis, this should be as good as it gets.

The presence of a defined energy loss, which does not scale with the impact energies of the colliding grains, has dramatic consequences for the collective physical properties of the system. Most prominently, it will be shown in the following chapters to lead to phase transitions which occur when the granular temperature is comparable to the energy loss. It is illustrative to express the fixed energy loss in terms of an energy-dependent restitution coefficient. We readily obtain

$$\varepsilon_{\text{cb}} = \sqrt{1 - \frac{\Delta E_{\text{cb}}}{E}}, \quad (3.12)$$

where ΔE_{cb} is constant. Obviously, ε becomes zero when $E = \Delta E_{\text{cb}}$. As a consequence, an energy-driven phase transition may be anticipated when the granular temperature comes close to ΔE_{cb} (cf. Chaps. 4 and 10). This is not the case in a dry system described by a constant restitution coefficient.

If the impact dynamics is sufficiently slow as compared to the dynamics of bridge formation and rupture, we may assume that the dynamic force-vs-distance curve corresponds to the quasi-static case, as represented by Eq. (3.9). However, when we consider dynamical processes, as they take place in a sheared or otherwise agitated wet granular material, we have to discuss the influence of this dynamics on ΔE_{cb} . In doing so, we will also have to consider the energy loss due to damping in the liquid.

Quadratic Damping. — Starting in the moment when the thin wetting layers of the interacting particles touch, the interjacent liquid is moved laterally outwards, as the surfaces of the particles come closer to contact. The Reynolds number for the liquid phase is, in the case of water, $\text{Re}_{\text{water}} = \rho_{\text{water}} v R / \eta_{\text{water}} \approx 223$ ($\eta_{\text{water}} = 0.894 \text{ mN s/m}^2$, $\rho_{\text{water}} = 998 \text{ kg/m}^3$, $v = 0.4 \text{ m/s}$). Therefore the kinetic term in the Navier-Stokes is not negligible, which describes the propagation of a circular pressure front moving outwards from the impact point. This sound wave is rapidly damped due to the shear mode imposed by the boundary condition in the extremely shallow liquid film. The details of the spatially separated attenuation is without relevance for the particle. (At this point, the experiment could be even done with superfluid helium.) The energy emitted into the liquid film is taken from the particle by the local damping force $F_{\text{inertia}} \propto -v^2$, which is necessary to squeeze out the liquid against its inertial resistance. For a general force $F(s, v)$, there is no explicit time dependence in (the relative component of) the equation of motion³, $\dot{v} = F/m_{\text{red}}$, so that one can substitute $v(t)$ in favor of $v(s)$ using $v'v = \dot{v}$ to arrive at

$$v'(s) = \frac{F(s, v(s))}{m_{\text{red}}v(s)}. \quad (3.13)$$

(This is actually a generalization of the differential $p = \partial L / \partial v$ defining the canonical momentum, since Eq. (3.13), $p dv = F ds$, holds for dissipative forces.) For the kinetic damping, $F_{\text{inertia}} \propto -v^2$, Eq. (3.13) implies that the velocity falls off exponentially with the intrusion. When the cross section $2\pi R(s_{\text{film}} - s)$, $0 < s < s_{\text{film}}$, of the sphere dipped into the film is taken into account, we find $F_{\text{inertia}} = -\pi R(s_{\text{film}} - s)\rho_{\text{water}}v^2$. Thus the velocity at contact decays exponentially with the film thickness s_{film} according to $v_c = v_0 \exp[-\pi\rho_{\text{water}}Rs_{\text{film}}^2/(2m_{\text{red}})]$. Furthermore, the lateral flow u speeds up⁴ as the surfaces come closer according to the continu-

³We write the reduced mass so that the cases of particle-particle interaction and the collision with the wall (of ‘infinite’ mass, $m_{\text{red}} = m$) are included.

⁴For particle-wall collisions, and for large capillary bridges, the backflow of liquid gives rise to an experimentally visible tapering of the capillary bridge at the wall, whereas the equilibrium shape would be broader at the wall.

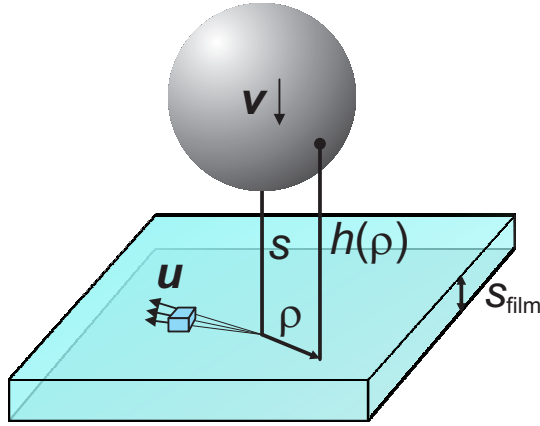


Figure 3.3: Sketch of a wetted spherical particle approaching a wetted wall. This impact dynamics is discussed theoretically in Sec. 3.2 and studied experimentally in Sec. 3.3. As shall be convention throughout this thesis, the variable s denotes the minimal separation of surfaces, here between particle and wall at $\rho = 0$, $h(0) = s$.

ity equation (for incompressible wetting liquid), $\text{div } \mathbf{v} = 0$: $us \approx v(s_{\text{film}} - s)$ in linear approximation. This gives rise to a spatial dependent force, $F_{\text{inertia}}(s, v) = -\pi R \rho_{\text{water}} v^2 (s_{\text{film}} - s)^2 / s$, which is easily integrated according to Eq. (3.13):

$$v_c \approx v_0 \left(\frac{r}{s_{\text{film}}} \right)^{\frac{3s_{\text{film}}^2 \rho_{\text{water}}}{4R^2 \rho_{\text{grain}}}}, \quad (3.14)$$

where the (small) roughness $r (\ll s_{\text{film}})$ is the lower integration bound. Hence the dissipated energy, $\Delta E \propto v_0^2 - v_c^2$ is

$$\Delta E_{\text{inertia}} = E_0 \frac{3 \rho_{\text{water}}}{2 \rho_{\text{grain}}} \left(\frac{s_{\text{film}}}{R} \right)^2 \ln \frac{s_{\text{film}}}{r}. \quad (3.15)$$

Compared to Eq. (3.14), we could safely neglect the fourth order in s_{film}/R in the expression (3.15). A factor of two for approach and retraction is included. So for glass spheres and the rather high film thickness of $s_{\text{film}} \approx 100 \mu\text{m}$ used in the single particle experiment to ensure homogeneity, we find $\Delta E_{\text{inertia}} \approx 2.7 E_0 (s_{\text{film}}/R)^2$. It is of great importance to realize that this is simply another contribution to the restitution coefficient. Since $1 - \varepsilon^2 \approx 2(1 - \varepsilon) = 2 \sum_j \Delta \varepsilon_j$, the restitution coefficient is reduced by

$$\Delta \varepsilon_{\text{inertia}} = 0.3 \left(\frac{s_{\text{film}}}{R} \right)^2 \ln \frac{s_{\text{film}}}{r} \approx 1.4 \left(\frac{s_{\text{film}}}{R} \right)^2 = 0.014, \quad (3.16)$$

without a qualitative change of the particle interaction.

Linear Damping of Viscous Dissipation. — The essential difference compared to the previously regarded damping force, $F_{\text{inertia}} \propto -v^2$, is that the viscous damping is linear in v : $F_{\text{visc}} = -vm_{\text{red}} f(s)$. Thus, according to Eq. (3.13), the velocity does not decay exponentially with distance, but algebraically or even logarithmically (for $f(s) \propto 1/s$):

$$v(s) = v_0 - \int f(s) ds. \quad (3.17)$$

Hence the loss in energy, $\Delta E \propto v_0^2 - v_c^2$, has one term which is independent of the initial energy and could give rise to the sticking of the particles.

The viscous dissipation is caused by the lateral flow of the wetting liquid. This flow is driven by the time-dependent boundaries of the two colliding spheres, or by one sphere and a flat wall. Such viscous friction falls in the class of lubrication problems, which are described by the Stokes equation, $\nabla P = \eta \Delta \mathbf{u}$, in the plane parallel to the wall that we consider as the collision partner (cf. Fig 3.3). The result for no-slip boundary conditions is the classical Reynolds equation (derived by O. Reynolds in 1886 [180]), which is here stated in polar coordinates with the radial coordinate ρ , so that (the Laplace operator is $\Delta = \rho^{-1} \partial_\rho \rho \partial_\rho$) according to the axial symmetry of the problem (cf. Fig. 3.3):

$$\eta^{-1} \rho^{-1} \partial_\rho (\rho h^3(\rho, t) \partial_\rho P) = 6U \partial_\rho h(\rho, t) + 12 \partial_t h(\rho, t) . \quad (3.18)$$

The U describes the tangential motion of the sphere, which we neglect to arrive at the main contribution which is due to the perpendicular approach, $\partial_t h < 0$, of the sphere. The solution of Eq. (3.18) is the pressure $P(\rho, t)$, which gives the viscous force after being integrated over the part of the boundary of the sphere, which is wetted by the capillary bond to the wall. Inserting the locally curved shape of the sphere, $h(\rho, t) = s(t) + r^2/(2R)$, and integrating the Reynolds equation (3.18) twice over ρ , yields the viscous force [74]

$$F_{\text{visc}} = \frac{3\pi}{2} R^2 \eta \frac{v}{s} \quad (3.19)$$

for spherical grains, where η is the viscosity of the liquid and v is the relative velocity of the grains at impact. The overwhelming part of the viscous dissipation falls in the withdrawal regime, since $s_{\text{crit}} \gg s_{\text{film}}$. If viscous forces are dominant, the equation of motion during withdrawal reads $F_{\text{visc}} = -m\dot{s}$, with the grain mass m , and the dot indicating the derivative with respect to time. Direct integration leads to

$$\Delta E_{\text{visc}} = m v_{\text{visc}} \int_r^{s_{\text{crit}}} \frac{\dot{s}}{s} ds = \frac{1}{2} m v_{\text{visc}}^2 \ln \frac{s_{\text{crit}}}{r} \left(2 \frac{v}{v_{\text{visc}}} - \ln \frac{s_{\text{crit}}}{r} \right) , \quad (3.20)$$

where v denotes the velocity directly after the impact and r is the lower cutoff parameter, which is bounded away from zero by the roughness of the grains [114] as applied before. Here

$$v_{\text{visc}} = \frac{9\eta}{8\rho R} \quad (3.21)$$

is a characteristic velocity, where ρ_{grain} is the density of the grain material. If $v = v_{\text{visc}} \ln \frac{s_{\text{crit}}}{r}$, the grains stick together in the sense that their kinetic energy is not sufficient to supply the *viscous* energy required for reaching the rupture distance, s_{crit} , even at zero surface tension. If v is considerably larger, one obtains the known result [114]

$$\Delta E_{\text{visc}} \approx \frac{3\pi}{2} R^2 \eta v \ln \frac{s_{\text{crit}}}{r} . \quad (3.22)$$

Eq. (3.20) may as well be expressed in terms of an energy dependent restitution coefficient as

$$\varepsilon_{\text{visc}} = 1 - \sqrt{\frac{E_{\text{visc}}}{E}} , \quad (3.23)$$

where $E_{\text{visc}} = \frac{m}{2} [v_{\text{visc}} \ln(s_{\text{crit}}/r)]^2$ is the impact energy below which sticking occurs. We see from the Eqs. (3.12) and (3.23) that there are great similarities between the capillary and the viscous effects, and both strongly differ from the scale-free energy loss encountered with the

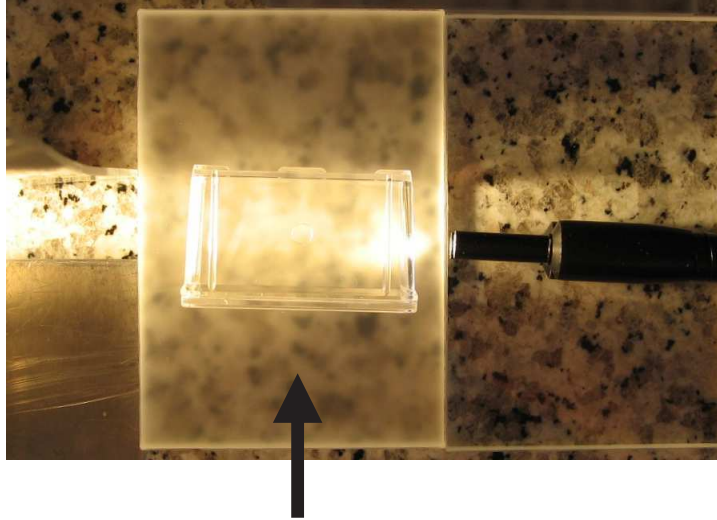


Figure 3.4: Top view of the experimental setup. The high speed camera views the scene from the bottom end of this picture (arrow). The scene is illuminated either through a slit from the left or a cold light source from the right, so that reflections from the sidewalls of the cavity are avoided. The cavity was dry when this picture was taken, which is why the roughed bottom plate has appears hazy (compared to the perfectly flat plate to its right). For the wet experiment the cavity was vapor saturated and

dry systems. The smallness of the Capillary number⁵, $Ca = \eta_{\text{water}}v/\gamma_{\text{water}} = 0.0012 \ll 1$, ($v = 10$ cm/s) indicates that the capillary bridge energy ΔE_{cb} dominates over the viscous energy E_{visc} . It is the main motivation of the experiment reported in this chapter to determine the relative relevance of these two dissipation mechanisms under realistic dynamical – and therefore nonequilibrium – conditions.

The Friction in Air. — If not evacuated, the granular particles move in a gas phase of finite viscosity. For air the viscosity is $\eta_{\text{air}} = 18.4 \mu\text{Pa s}$ at 20°C . The imposed resistance force is $F_{\text{air}} = -6\pi\eta_{\text{air}}vR$ (Stokes friction) if $Re_{\text{air}} = \rho_{\text{air}}vR/\eta_{\text{air}}$ is small, otherwise $F_{\text{air}} \approx 0.71\rho_{\text{air}}R^2v^2$ under turbulence. For a realistic system, such as the reported experiment of this chapter, Re_{air} is of the order of 10. ($\rho_{\text{air}} = 1.204$ kg/m³).

3.3 The Time-resolved Measurement of Collision and Single Bridge Interaction

In order to investigate to what extent the concepts discussed above in Sec. 3.2 apply under realistic conditions, we have performed an experiment particularly designed to map the conditions in agitated wet granular matter as closely as possible. As model grains, we have used spherical glass beads with radius $R = 1$ mm. The surface of each glass sphere has been wetted with the fine mist generated from (Millipore) water by a piezo spray.

The spheres fell freely in a closed box (30.4 cm³ in volume, shown from top in Fig. 3.4) filled with water saturated air. As the initial height is $h_i = 29$ mm, the impact velocities were on the order of a few cm/sec, which corresponds to typical granular temperatures in agitated

⁵The capillary regime is also discussed in the review article [114], cf. especially Fig. 7 therein.

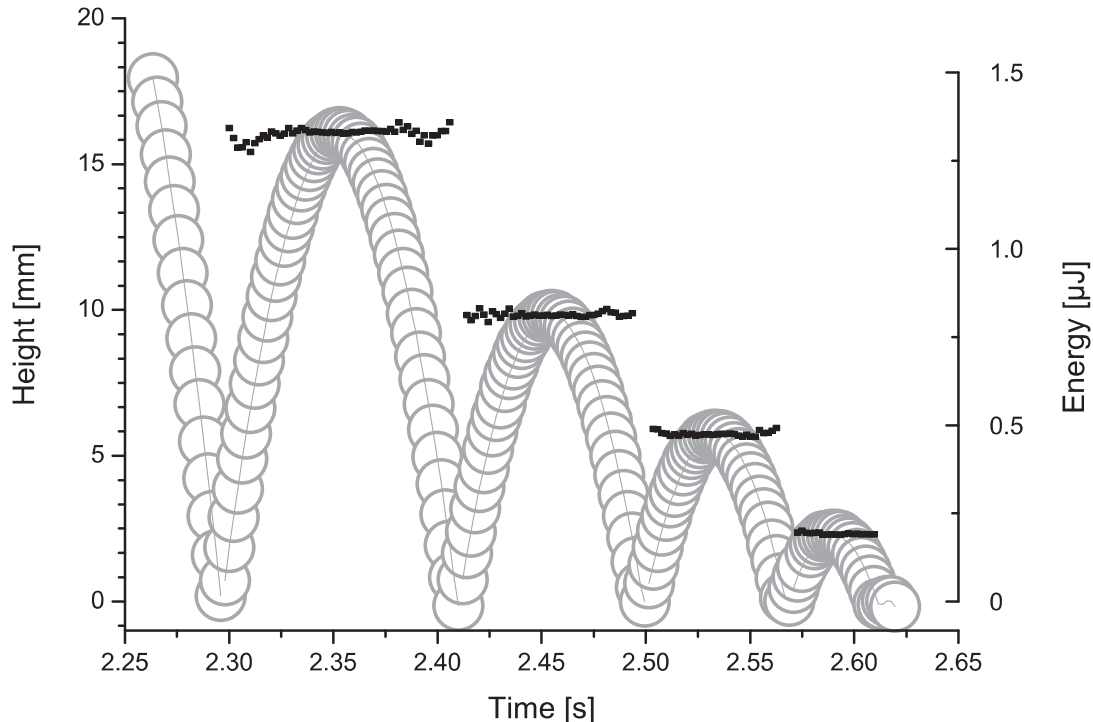


Figure 3.5: An experimental run as captured by a fast camera yields the trajectory of a single wetted glass bead bouncing on a wetted glass plate within a vapor saturated environment. The size of the circle corresponds to the actual size of the glass sphere (1.94 mm in diameter), and the positions shown have been traced optically by a camera with Complementary-metal-oxide-semiconductor (CMOS) sensor at 491.29 frames per second. From the trajectories, we can derive the total energy as a function of time. The superimposed black squares is the instantaneously measured sum of potential and kinetic energy, deduced from height and velocity. Note that firstly, there is no air-friction damping the ballistic branches of the trajectory, and secondly, the particle undergoes bound oscillations at the very end of the trajectory. These type of motions will play a certain role in the analytical treatment of Kolmogorov-Sinai entropy in Chap. 5.

granulates. With this initial velocity the spheres collided with a wet horizontal glass plate, with defined roughness amplitude ($r = \sqrt{\langle h_0^2 \rangle} \approx 1 \mu\text{m}$) to ensure a low contact angle⁶.

The motion of the glass spheres was recorded with a fast CMOS camera, the images were subsequently analyzed by standard image processing techniques.

Since all arguments put forward above concerning forces between two spherical grains apply as well to forces between a sphere and a flat wall, we have studied the latter because of its better experimental accessibility. We just have to keep in mind that in formulas developed for two spherical grains, the radius of the sphere must be multiplied by two. This corresponds to the well-known Derjaguin approximation (3.2). Although this is not an highly accurate expression for the system under study [237], it provides a reasonable approximation since other effects, like contact angle hysteresis, give rise to larger uncertainties [114].

The result is shown in Fig. 3.5. The height of a bouncing glass sphere is plotted as a function of time (circles). On the same time scale, the total energy as obtained from the

⁶The contact angle θ' may be described according to the Wentzel law $\cos \theta' = r \cos \theta$, with r the increased microscopic surface area divided by the geometric surface area.

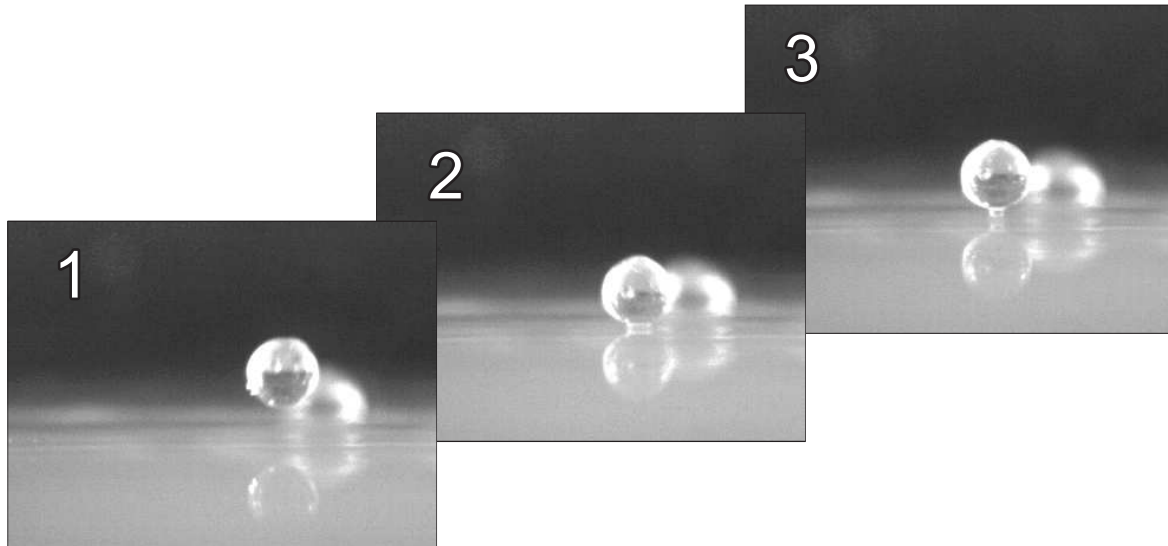


Figure 3.6: Irreversibility at work: as pointed out in Sec. 1.3, the system undergoes temporally directed transitions. The three consecutive images are taken around the time of impact with the bottom glass plate. The hysteretic character of the bridge is clearly seen. The time elapsed between two consecutive images is 2.04 ms. (1) The particle approaches the glass plate freely. (2) The liquid bridge is formed almost instantaneously (compared to the particle motion) as the covering wetting films overlap. At this point in time, the attractive capillary force is switched on. (3) The particle is bound by the liquid bridge to the plate.

instantaneous velocity and height is indicated by the black squares. While there is some scattering in the vicinity of the impacts, mostly due to the finite delay between consecutive images, the energy is observed to be constant with high accuracy away from the impacts, allowing for an accurate determination of the energy level of each bounce.

Below in Fig. 3.6, we show three consecutive closeup images in the ultimate temporal vicinity of an impact with the glass plate. The time elapsed between the images is 2.04 ms. The hysteretic character of the capillary bridge formation and rupture is clearly visible from its absence before the impact (left) and its persistence afterwards (right). The wet surfaces approach freely, until the surface films touch. Then, on a very short time scale which is far below one millisecond, the liquid accumulates around the contact due to capillary forces which minimize the Free Energy of the liquid/air interface. A capillary bridge grows out at the contact and mediates an attractive force because of its negative Laplace pressure. This liquid bridge is stretched but remains intact (or even continues to grow in volume) as the surfaces move apart. Therefore the particles are subject to an attractive force until a certain critical separation s_{crit} is reached, where liquid bridges becomes unstable and ruptures. Associated with this elongation is the hysteretic loss of energy, ΔE_{cb} .

From the difference in the energy levels of consecutive bounces, we can deduce the energy ΔE_{cb} lost in the impact with the glass plate. For a quantitative analysis, we have to consider as well the energy loss due to viscous friction in the air, ΔE_{air} . Using Stokes' formula, it is straightforward to see that

$$\Delta E_{\text{air}} \approx \frac{4\pi R\eta_{\text{air}}}{g} \left(\frac{2E}{m} \right)^{3/2} \quad (3.24)$$

where η_{air} is the viscosity of air. This is valid at low Reynolds numbers. We have $\text{Re}_{\text{air}} \approx v/v_{\text{visc, air}} \approx \sqrt{H/15.6\mu\text{m}}$, where H is the height of the bounce, such that Re_{air} reaches values

at most up to 30 in our experiment. Since turbulence sets in only at much higher Re_{air} [218], we can safely assume Eq. (3.24) to describe our system well.

The most convenient way of analyzing the data is to plot the energy of each bounce as a function of the energy of the previous one. Taking all dissipation mechanisms into account, we obtain

$$E_{n+1} = \varepsilon^2 E_n - \Delta E_{\text{cb}} - \Delta E_{\text{visc}} - \Delta E_{\text{air}} \quad (3.25)$$

where n numbers the bounces, and the last two terms depend upon E_n . The result is displayed in Fig. 3.8A. The full squares represent the results for E_{n+1} as obtained from the experiment, while the open circles have been corrected for ΔE_{air} according to Eq. (3.24), which is known without any free parameters. As one can clearly see, the correction is of minor importance, as suggested already by the energy data from the trajectories in Fig. 3.5. From Eq. (3.22), we see that the viscous energy loss in the liquid is of order mv_0v , which is readily checked to be below 3 nJ in our experiments. It is thus even smaller than the viscous dissipation in the air, and will henceforth be neglected. The experimental error of the results displayed in Fig. 3.8A is well below the size of the symbols.

The three data points for the largest energies lie on a straight line within errors. From the slope of this line, we obtain the restitution coefficient connected to the solid impact of the glass sphere with the bottom plate. The result is $\varepsilon = 0.82 \pm 0.02$. Interpreting the intercept with the vertical axis as the capillary bridge energy, we obtain $\Delta E_{\text{cb}} = 0.07 \pm 0.02 \mu\text{J}$. However, this intercept can be determined in principle for each pair of consecutive energy levels, E_n . The corresponding results for ΔE_{cb} are shown in the inset of Fig. 3.8A as a function of the incident energy. The deviation of the datum point at lowest energy from the straight line in the main panel transforms into a pronounced increase of ΔE_{cb} at low energy.

From the few times at which we could capture the formation of a bridge with the camera, we could estimate the bridge volume assuming an axisymmetric shape. For the bridge at the slowest impact, we obtained $\tilde{V} = 0.25 \pm 0.06$ for the dimensionless volume. Together with Eq. (3.11) this leads to $\Delta E_{\text{cb}} = 0.214 \pm 0.056 \mu\text{J}$, where we have assumed complete wetting ($\theta = 0$). This result is indicated by the shaded area in the inset of Fig. 3.8A and compares very favorably with the experimental value obtained at low impact energy.

The reduction of ΔE_{cb} at larger impact energies may be understood when one considers the dynamics of formation of the bridge. There is some time needed for the liquid to rearrange from the thick wetting layer around the contact point into the liquid capillary bridge structure. The entire process spans several time scales, starting from the microsecond range at individual asperities of the grain roughness [245] to ripening processes on the scale of minutes [131]. Consequently, although the impact duration of the glass sphere with the bottom is sufficient to form a small bridge, the volume of the latter will be larger when it has more time to form. The characteristic time scale of the early stage of bridge formation can be estimated from the typical height of the bridge at contact, which is $\tilde{h} = h/R \approx \sqrt{\tilde{V}/2\pi} \approx 0.2$. Knowing that viscous damping is of minor importance, we consider the dispersion relation of undamped capillary waves, $\omega^2 = \gamma q^3 / \rho_{\text{water}}$. With $q \approx 1/h$ we obtain the time scale $\tau = 1/\omega \approx 3.3 \times 10^{-4}$ sec. It is straightforward to calculate the kinetic impact energy E_τ at which the solid surfaces are closer than h for a duration equal to τ . We obtain

$$E_\tau = \frac{8\pi R^2 \gamma \rho_{\text{grain}}}{3\tilde{h} \rho_{\text{water}}} \approx 780 \text{ nJ} \quad (3.26)$$

which is of the same order as the transition seen in the inset of Fig. 3.8A.

However, the dynamics not only of bridge formation, but also of bridge rupture gives rise to variations in ΔE_{cb} . If the solid surfaces withdraw rapidly, the formation of the extended

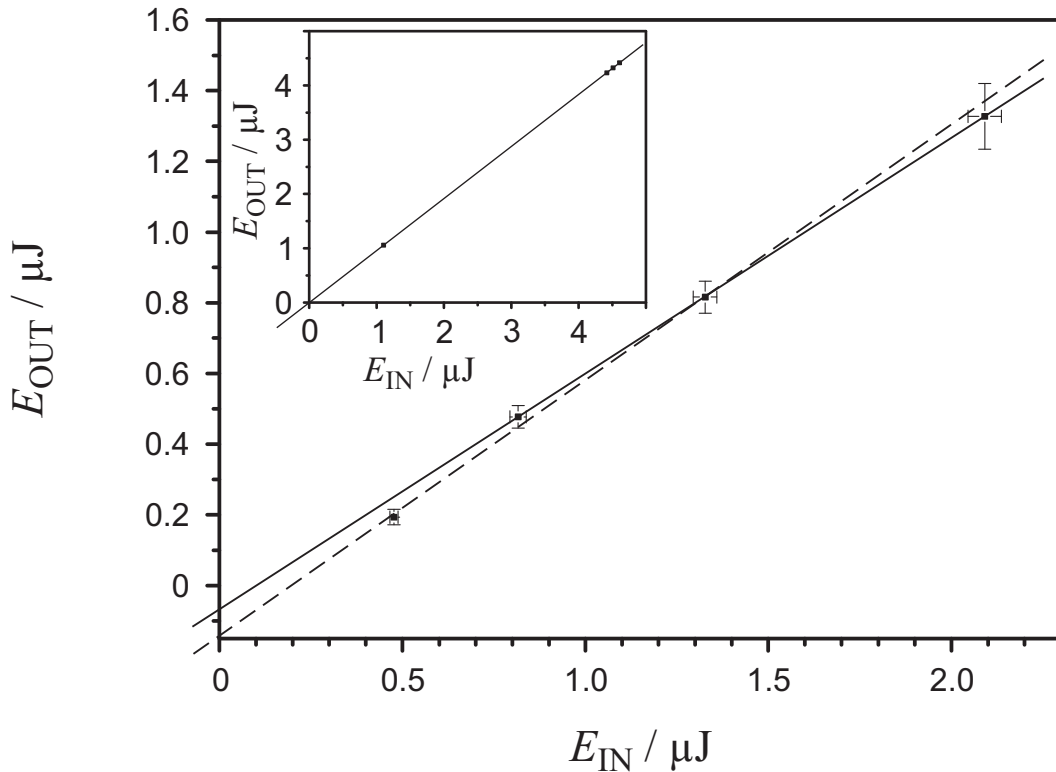


Figure 3.7: Final energy as a function of initial energy, $E_{\text{OUT}} = \varepsilon^2 E_{\text{IN}} - \Delta E$, at four impacts. The main panel shows the energies extracted directly from the experimental run (shown in Fig. 3.5). The particle energy has been computed between subsequent collisions from the trajectory of the wetted sphere as it bouncing against a wetted glass plate. There is a clear negative intercept which corresponds to an energy loss, ΔE , which does not vanish at low impact energies, so that the sphere finally sticks to the glass plate. The dashed line is a fit to all four points assuming an equal energy loss ΔE for all four collision events. This mean bond energy is $\Delta E = (141 \pm 36)\text{nJ}$. Although this dashed fit falls within the (too conservative) error bars, deduced from the scattering of instantaneous energy measurements, a closer look at the measured energies clearly reveals two regimes: the first three collisions fall perfectly on the solid line. For these collision events the ripening time of the capillary bridge is above the time the bridge exists before it ruptures. Hence, the bridge volume is reduced compared to the final fourth impact, for which the interaction time is above the capillary ripening time (cf. computation in text). The inset shows the analogous experiment in a very dry environment heated to 40°C . The points are collisions of one glass bead for different initial heights (not collisions consecutive in time on a single trajectory). There is no measurable intercept. (The slope is higher in the absence of (3.16) and because the glass plate used had a smooth surface).

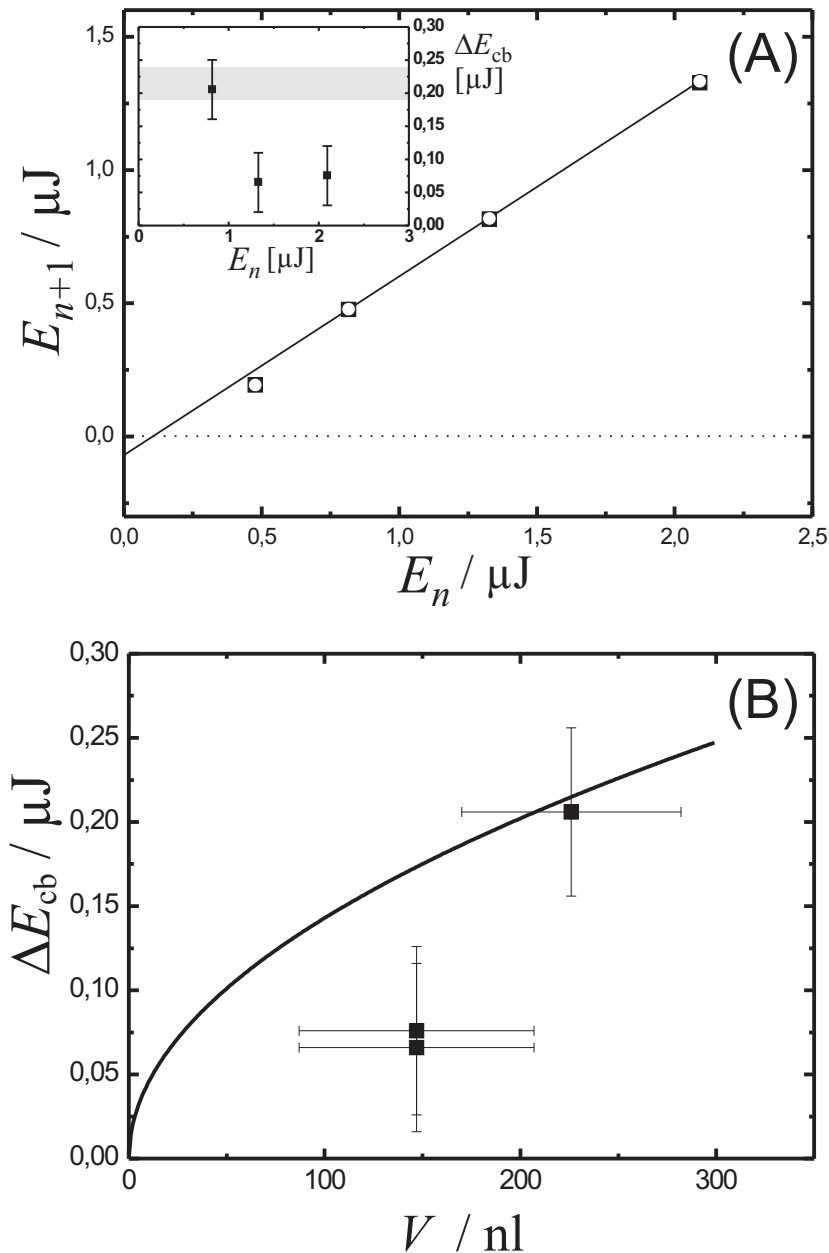


Figure 3.8: (A) The ‘return map’ of total energies between impacts as shown before in Fig. 3.7, but with air friction (and the even smaller viscous damping) being corrected (open circles). The accuracy of the measurement is sufficient for the deviation of the datum point at smallest energy from the line to be significant. It points to finite-time effects in the dynamics of bridge formation and rupture. (B) The energy loss associated with bridge rupture as a function of bridge volume, which was determined independently from images taken around the impacts. The solid curve represents the quasi-static limit (Eq. (3.11)), without fitting parameters. Although this equation relies on considerable approximations, the deviation of the data points at smaller volume is clearly significant.

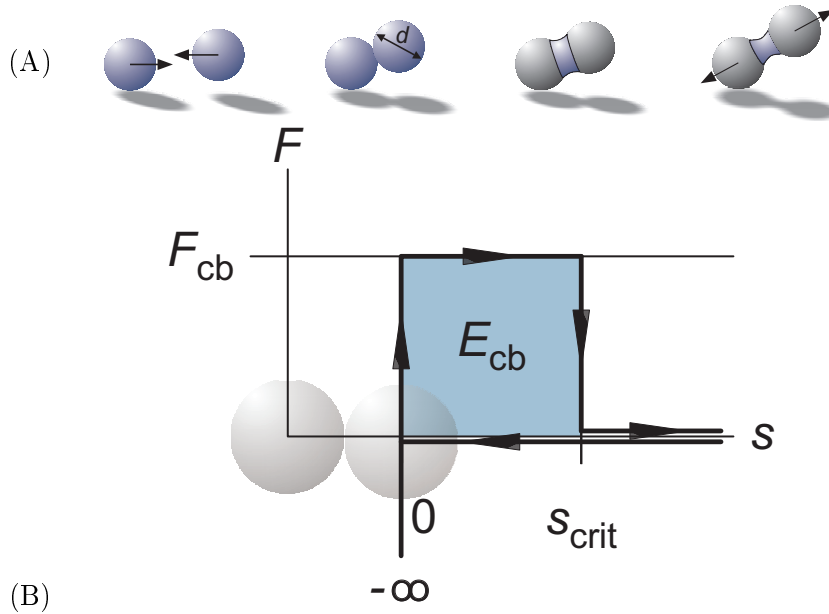


Figure 3.9: The hysteretic interaction via capillary bridges. (A) illustrates the formation of a capillary bridge. In (B) we see the hysteresis loop associated with the formation and rupture of a capillary bridge. The two fundamental interaction parameters are the maximal capillary bridge energy E_{cb} , and the maximal bridge length s_{crit} . The rupture length s_{crit} is largely exaggerated for the purpose of illustration. The Minimal Capillary model [114] incorporates the hysteresis, characterized by rupture length and rupture energy, while a constant bridge force is assumed for simplicity. (In Chap. 10 we will see that details of the force law are indeed largely irrelevant.)

neck will be impeded and the bridge is expected to pinch off at a separation which is smaller than the ‘quasi-static’ s_{crit} . This reduces the upper limit of the integral in Eq. (3.8), and thus the value of ΔE_{cb} . By measuring the bridge volumes for different impacts independently, we can distinguish these two effects. This is shown in Fig. 3.8B, where ΔE_{cb} is plotted as a function of the bridge volume, as determined from images close to the respective impacts. The solid line represents Eq. (3.11) and has no fitting parameters. Good agreement is found for the larger bridge volume, which corresponds to the leftmost point in the inset of Fig. 3.8A. At smaller volume, ΔE_{cb} is indeed reduced, but this reduction is much stronger than predicted by the solid line, which represents the quasi-equilibrium shapes.

If we finally return to the conversion of the energy loss into an energy-dependent restitution coefficient, we see that the variations in ΔE_{cb} will cause $\varepsilon(E)$ to decrease even stronger with decreasing impact energy than suggested by Eq. (3.12). This stresses again the qualitative differences to the dry systems, where $\varepsilon(E)$ tends to be decreasing with *increasing* impact energy. When one looks at the results in the main panel of Fig. 3.8A, one might not anticipate that the small negative intercept with the vertical axis should be of any importance for the collective behavior of many spheres. Quite surprisingly, the dramatic mechanical differences between dry and wet sand show that this is nevertheless the case.

3.4 The Minimal Capillary Model

3.4.1 The Experimental Basis

We have demonstrated in the last section experimentally, that the capillary interaction between curved wetted surfaces gives rise to a defined bond energy E_{cb} . (The Δ in ΔE_{cb} is henceforth suppressed to shorten notation.) This energy is *not* taken from the relative motion of the particles in the moment of the collision, but transferred into the surface energy of the capillary bridge being stretched as the particles move. The sum of granular energy and capillary energy is conserved as long as the bridge remains intact. The formation and rupture of capillary bridges is spatially separated (cf. Fig. 3.6). This implies that the capillary force is switched on and off hysteretically. When the surface separation exceeds the intrinsic length scale s_{crit} , the bridge ruptures and the surface energy E_{cb} is irreversibly lost. We have therewith shown that the interaction in wet granular matter is dominated by

- the hysteretic formation and rupture of capillary bridges, which are characterized by their
- rupture length, s_{crit} , and the associated
- capillary energy, E_{cb} , which is dissipated in the event of rupture.

Note that this mechanism of dissipation does not rely on the viscosity of the wetting liquid, but on its surface tension γ .

The measurement resolved the dynamics down to 1 ms. The liquid bridge volume in this setup would correspond to a liquid volume fraction (in relation to the total jammed granular volume) of approximately $W = 11\%$ if six liquid bridges⁷ of this size were residing on one particle in a solid configuration of wet granular matter. The liquid bridge volume has been deliberately chosen to be sufficiently high in order to resolve the bridge energy on the micro-Joule scale by observing the wet granular kinematics. The formation of the liquid bridge itself was found not to be resolved on the millisecond time scale. Hence, this puts an upper bound on the initial formation time of the capillary bridge, which will be even faster for the liquid content $W \leq 2\%$ we will work with in this thesis. On the other hand, the stretching of the capillary bridge up to its critical length has been clearly resolved, so that we may apply in the analytic and numerical modeling a separation of time scales, assuming an instantaneous bridge formation.

3.4.2 The Force Law

For analytic computations and numerical simulations of the full many-particle system presented in this thesis, we will apply the Minimal Capillary Model [114], which assumes that the capillary force is constant, $F_{cb} = E_{cb}/s_{crit}$. This model has been found to reproduce experimental results, e.g. for the shearing of wet granular matter [87]. The wet granular interaction is consequently described by two parameters, the intrinsic length scale s_{crit} and energy scale E_{cb} . These parameters are not free but uniquely determined for the chosen wet granular matter: namely by the surface tension γ of the wetting liquid, the contact angle θ , the amount of added liquid, and the particle size, according to the expressions (3.6) and (3.10). Figure 3.9 illustrates the Minimal Capillary Model which incorporates the three important properties summarized above in 3.4.1.

⁷Six is a typical value [114] and equal to the coordination number of isostatic networks in three dimensions, as is discussed in Chap. 7.

We will furthermore investigate the dependence of dynamical and transition properties on the details of the force law in this thesis. Variation of the Minimal Capillary Model will be computed for the Kolmogorov-Sinai entropy (cf. the Extended Capillary Model in Chap. 5), and for the nonequilibrium phase diagram of wet granular matter (cf. the square-well potential in Chap. 10). We will show in these computations that the simplifying assumption of a constant force is well justified. Furthermore, we find in all experimental results presented in this thesis support without contradiction for the Minimal Capillary Model.

3.4.3 Fundamental Properties

By virtue of this hysteretic interaction wet granular matter is a remarkable system, where the following aspects are found to concur. Its widespread relevance in geology, industry and astrophysics has been pointed out in the first chapter. There the peculiar dynamical property to be (everywhere locally) symplectic and still dissipative has been mentioned (and will be proven in Chap. 4). This means that the wet granular dynamics is close to a Hamiltonian system and still dissipative with $E_{cb} > 0$. The dissipation is experimentally controlled by the choice of the wetting liquids, since according to the Eqs. (3.7) and (3.10) we have $E_{cb} \propto \gamma$ depending on the surface tension γ . The symplecticity is related to the fact that in wet granular matter the mechanism of dissipation is not ‘hidden’ in the moment of the collision, but present in the particle dynamics as finite hysteretic forces. The hysteretic capillary forces largely influence the chaoticity (as will be derived in the Chaps. 4 and 5). Finally, the intrinsic energy scale set by the hysteretic loss will be shown to cause nonequilibrium transition (in the Chaps. 4, 6, 8, and notably 10). With these properties wet granular matter may be regarded as a paradigm system to study entropy production, nonequilibrium dynamics, and transitions.

3.4.4 Qualitative Change of Material Properties Caused by Wetting Liquids

Dry sand trickles easily through chinks and crevices, as everyone knows well from the hour glass, or just personal experience. However, the addition of small amounts of liquid are sufficient to transform it into a plastic (or, more precisely, a viscoplastic) material. The same is true for all granular matter when a few volume percent of liquid are added, provided the latter wets the grains well and the grains are not too large.

As we have disclosed in the preceding sections of this chapter that there is a qualitative change in the dissipative interaction caused by the wetting additive, which is quantified by the capillary bridge energy E_{cb} , the rupture length s_{crit} , and the bridge force E_{cb}/s_{crit} , we can envisage that this particle-particle interaction will lead to entirely different macroscopic material properties for *wet* and *dry* granular matter. Before we investigate this change quantitatively on the level of many-particle systems in this thesis, we briefly allude to the following examples by visual inspection.

First and indubitably the most popular wet-granular-effect is the stability of sand castles, which cannot be built from dry, but only from wetted sand. In an architectural object such as the one pictured in Fig. 3.10B, the liquid bridge topology in the bulk exceeds the isostatic value of six bonds per particle, so that this liquid bridge network is stable as long as the bulk stress does not exceed the liquid bridge force on the level of single capillary bridges. This internal liquid structure is studied in [197] by means of tomography measurements at the European Synchrotron Radiation Facility in Grenoble, which the author has had the pleasure to attend once.

While sand castles represent a static state frozen far from equilibrium, a second and slightly more dynamical example occurs with shifting sand dunes. These are continuously reshaped

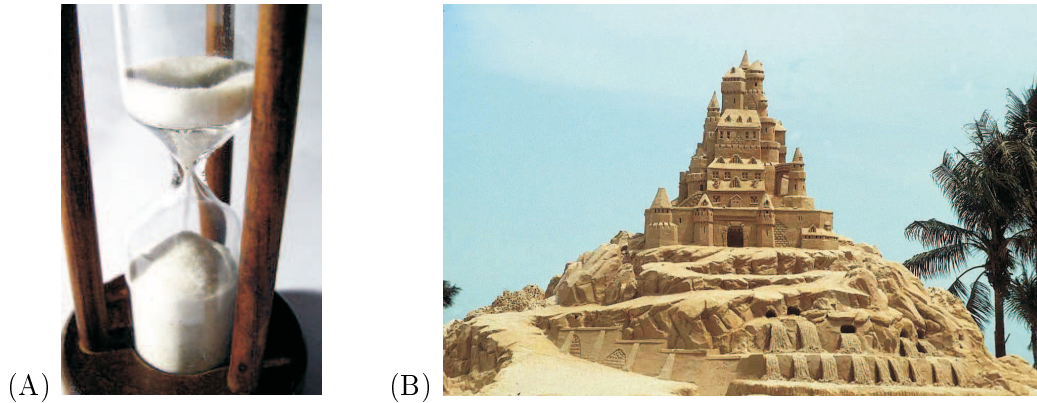


Figure 3.10: (A) Dry granular matter has no plasticity and streams, very reminiscent to a fluid, through the constriction of an hourglass (Copyright provided by ‘WilHei’, aboutpixel.de). (B) shows an example of what is probably the most famous steady state of wet granular matter: a sand castles on the beach. This stability of wet granular matter under gravity shows its resistance against shear stress (Copyright provided by D. Erny, picture-newsletter).

by saltation, an eolian sand transport in which individual grains are lifted and hit back the surface to release others, observed on Earth [15] as well as on Mars [168]. Yet this transport process comes to rest in the Namib desert at about 200 days a year in the early morning hours [139]. At that time cold thermohaline circulation at the Skeleton Coast has cooled the sea air, letting moisture condensate to form coastal sea fogs, which move inland over the ridges of the dunes to wet their surfaces.

3.4.5 Qualitative Changes of Dynamics: Solid, Gas and Flocculation in Wet Granular Matter

As a dynamical example, let us take a first look at a simulation which takes capillary bridges into account, with the hysteretic interaction as established experimentally in Sec. 3.3 and summarized in Sec. 3.4.1. Results from various simulation techniques will be quantitatively analyzed in the context of analytical and experimental results in the following chapters. The Figs. 3.11 and 3.12 show snapshots of typical two-dimensional structures which result in freely evolving granulates (without gravity), jargonized as the ‘free cooling state’. We will quantitatively describe a free cooling process in Chap. 6. Here we are interested in the qualitative difference of the structures which emerge in dry and wet granular matter. In both cases, the granulate was prepared initially to fill approximately the left half of the quadratic simulation domain homogeneously with an area covering of 68%. The initial velocity distribution is a Maxwellian of temperature T_0 . Figure 3.11 is the ‘dry’ structure resulting from inelastic collisions with a constant coefficient of restitution, $\varepsilon = 0.9$ (cf. the first paragraph in 3.2), while the quite different structure in Fig. 3.12 is a result of the hysteretic interaction.

Dry granulates have in particular an instability to form density inhomogeneities. This is so because for particles which happen to be in a region of slightly increased density, the mean free paths are shorter, so that dissipation by collisions is enhanced, until the particles have largely lost their relative kinetic energies. The correlated center of mass motion of the region remains. At the same time faster particles from dilute regions bump into the cold dense regions, compress it further, and get stuck inside due to the increased number of collision partners. As a result dense clouds and voids are formed, visible in the simulation snap shot of two million particles in Fig. 3.11. It is emphasized that this simulation assumed a constant

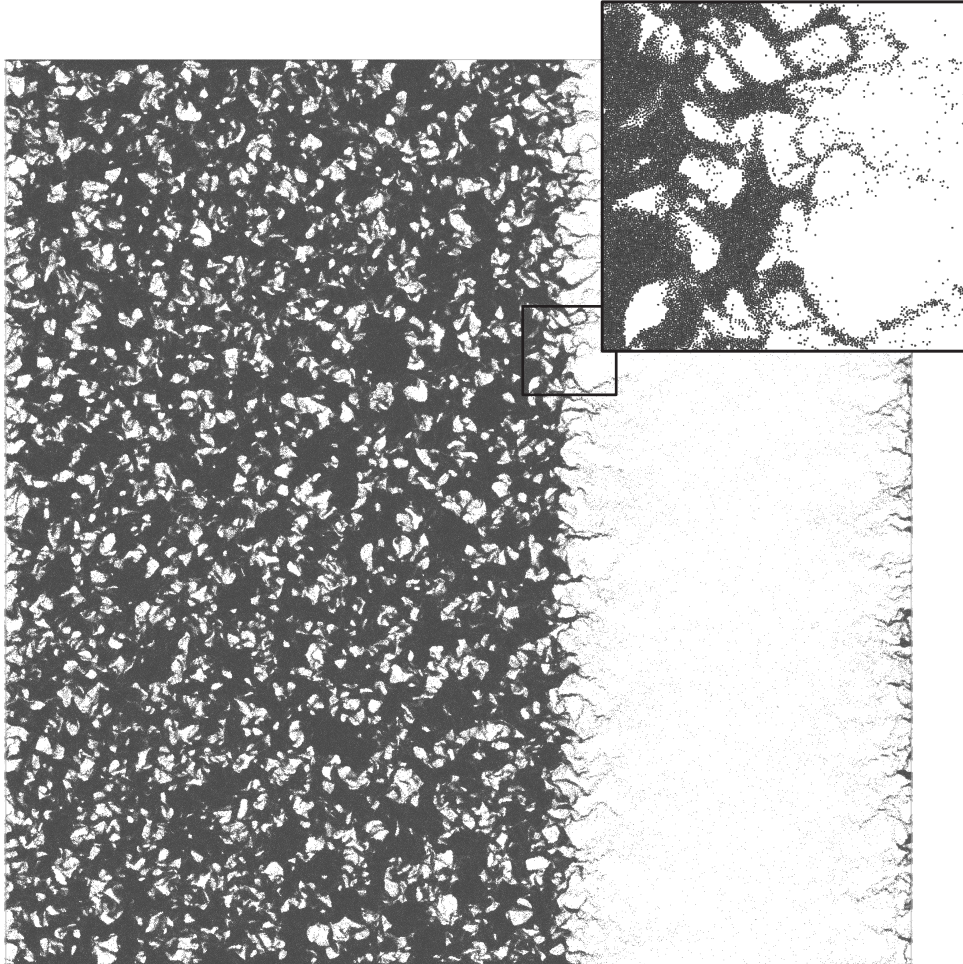


Figure 3.11: **Dry** granular matter: a snap shot of two million discs colliding inelastically with a constant coefficient of restitution. In each particle-particle collision, 10% of the energy in the center of mass system is dissipated. The discs were initially distributed homogeneously, with 68% covering fraction, in a subdomain spanning approximately half of the full rectangular simulation domain on the left. The initial velocity distribution was a Maxwellian. The subdomain expanded and formed the filamentous structures at the boundaries, of which the inset provides a closeup view. The interior exhibits dense packed clouds and voids. The simulation domain has cylindrical topology with periodic boundaries connecting left and right, while there are reflecting boundaries at the top and bottom end of the domain.

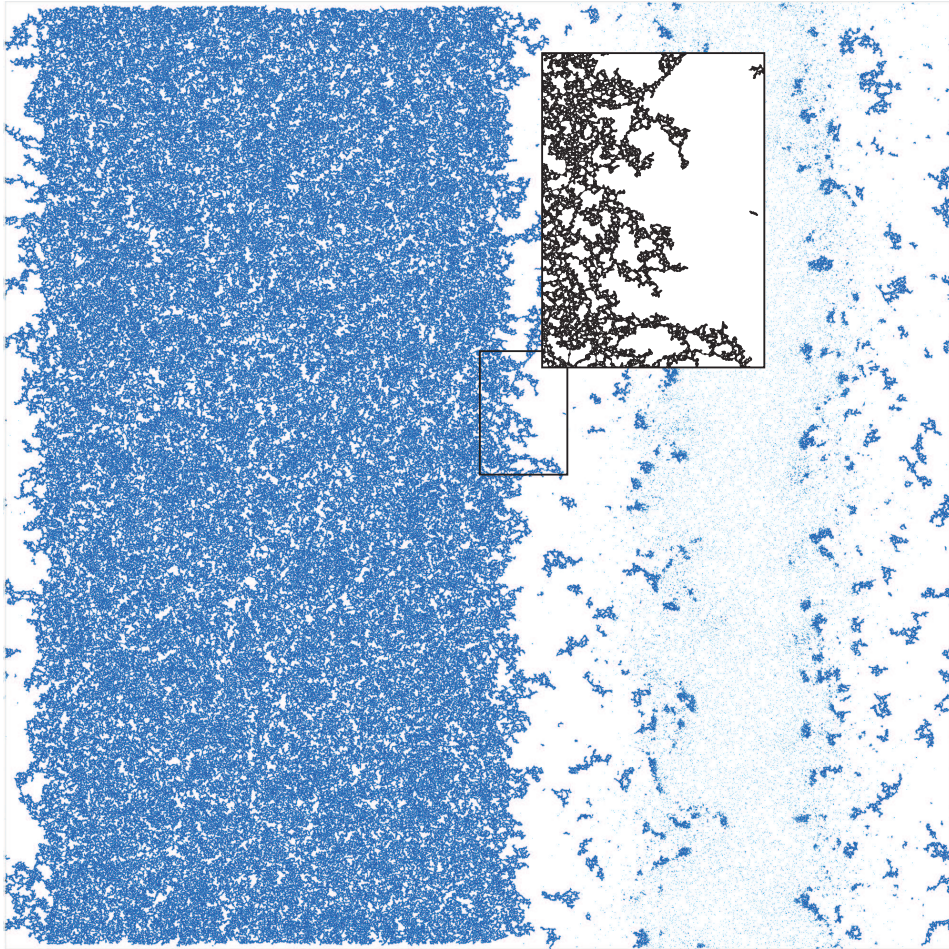


Figure 3.12: **Wet** granular matter: the very different structure which emerges from the hysteretic interaction with capillary bridge energy E_{cb} , when compared to Fig. 3.11. The spatial initial distribution was as in Fig. 3.11 (for a smaller system of one million particles). The initial temperature was chosen to be 20 times higher than the bridge energy. A shock wave of gas particles is emitted out of the initial subdomain in the very beginning. At the time shown, the hysteretic formation and rupture of liquid bonds has cooled the dense block on the left to its final frozen state ($T \ll E_{cb}$), while the gas emitted in the beginning is confined between growing flocculent clusters which shield the gas layer from the dense block. The bridge coordination number is close to four in the frozen block, which is the isostatic value for two-dimensional systems. The zoom-in shows the internal liquid network structure which is the microscopic origin of the bulk stability of wet granular matter, also in three dimensions when wet sand is used to mold a sandcastle on the beach (cf. Fig. 3.10B.)

coefficient of restitution, so that the system has no intrinsic energy scale, and time is scalable: i.e. with higher initial velocities the dynamics speeds up, but the resulting structure is the very same.

Very much different is the situation with wet granular matter. At high granular temperatures, $T \gg E_{cb}$, the system behaves as a gas of hard spheres. For granular temperatures below the intrinsic energy E_{cb} , the capillary bridges form a stable network which endows the plasticity to this solid state. Such a frozen state we see on the left hand-side of Fig. 3.12. In this region of high initial density, the rapid formation and rupture of capillary bridges has cooled the material, resulting in a wide meshed stable network. The enlarged region shows the capillary bridges in black, while the blue particles are masked out in the inset. This allows us to directly view the underlying capillary network, which has a fractal appearance⁸. In contrast, the dilute stripe on the right-hand side is filled by fast particles, which escaped initially (at $T_0 = 20E_{cb}$) from the dense region on the left, to form a gas phase. Since the simulation domain has periodic boundary conditions in the horizontal direction, the gas is confined by and coexists with the solid material. At the interface, the particles are at low density and low temperature, which causes them to form fluffs of wet granular matter which precipitate out of the gas. We will encounter frequently in this thesis different phases, such as the wet granular gas or solid, whose clearly distinguishable state will be shown to result from the intrinsic length and energy scales of the capillary interaction established in this chapter.

The density instability in dry granular gases creates beautiful clouds, but hardly allows to introduce the notion of a solid clusters with boundaries defined in a topological sense by connectivity. In contrast, the wet granular interaction forms networks, where the liquid bridges naturally define the neighborhood relations. The number of liquid bonds residing on a particle are 4.1 in the dense regime of Fig. 3.12, which compares nicely to the value $2D = 4$ of a two-dimensional network that is isostatic (meaning roughly speaking that the network is stable and has no redundant bonds, cf. Proposition 2.2 in [44]). We will address the liquid bridge coordination when we derive the equation of state in Chap. 7. The liquid bonds also play a crucial role for the chaotic properties, as is quantified in the following two chapters.

3.5 Conclusions

Dry and wet granular matter are dissipative systems. The fundamentally different particle interaction in wet granular matter has been discussed theoretically and confirmed experimentally in this chapter. It has been demonstrated that the impact dynamics between wet surfaces dissipates a defined amount of energy E_{cb} . This enables the sticking of particles, in contrast to the restitution model of dry granular matter which is scale-free for energy. Wet granular matter is for this reason a paradigm dissipative system, which includes astrophysical models of planetary formation. Particles interact hysteretically with the formation of capillary bridges at contact, and their rupture at a positive separation s_{crit} . This length scale and the bond energy, E_{cb} , necessary to break the liquid bridge, characterize wet granular matter. Both parameters have been quantified in the experiment and are according to the hysteresis incorporated in the Minimal Capillary Model. Therewith the particle interaction in wet granular dynamics has been clarified. The formation of stable network configurations has been demonstrated in a two-dimensional simulation. The results of this chapter about the wet-particle interaction allow us to proceed with the analytic and numerical investigation of dynamical and bulk properties far from equilibrium in the following chapters.

⁸This structure is at present investigated in cooperation with S. Ulrich (U. Göttingen) and K. Röller (MPI DS Göttingen).

Chapter 4

The Fluctuation Theorem and Phase Transitions in One Dimension

The Fluctuation Theorem is shown to hold for small fluctuations Δs in driven steady states of dissipative gases. Small means $\Delta s < Nm \langle v^2 \rangle / T$, where N is the number of particles, m the particle mass, T the granular temperature, and v the driving speed. For higher fluctuations, substantial deviation from the functional form of the Fluctuation Theorem are predicted by a minimal analytic model and observed in simulations. This resolves the contradiction between the derivation of the Fluctuation Theorem based on time-reversal symmetry [89], and numerical reports of the Fluctuation Theorem for granular gases which were limited to small fluctuations [10]. For wet granular matter, it is shown numerically that the onset of the deviations coincides with the critical driving, where a nonequilibrium transition is discovered. The granular temperature is shown to rise discontinuously by three orders of magnitude from a fluid state with $T \approx 2E_{cb}$ to a gaseous state, as $m \langle v^2 \rangle / 4$ exceeds the capillary energy E_{cb} . The number of wet clusters scales close to the evaporation with the driving velocity with an exponent close to $1/3$. The evaporation of wet clusters provides an opportunity to measure the influence of the hysteretic capillary forces on the chaoticity of the dynamics. This is quantified by the Kolmogorov-Sinai entropy which is computed across the transition. Remarkably, the slower fluid dynamics is found to have a higher Kolmogorov-Sinai entropy production rate than the gas. This is the first numerical observation of the increase in chaos by the presence of capillary bridges, which is directly continued by the analytic computation in the following chapter.

This chapter begins with the analytic confirmation of the Fluctuation Theorem for an equilibrium, non-dissipative gas in the Secs 4.1 and 4.2. The ‘violation’ is described analytically for a nonequilibrium state in Sec. 4.3. In Sec. 4.4 the distribution of the energy exchanged at the boundaries, ΔE , is derived from simulation over eight orders of magnitude. A minimal construction to recover the Fluctuation Theorem by modifying the Clausius relation $\Delta s(\Delta E)$ for nonequilibrium states is discussed. Sec. 4.5 presents the numerical results of the fluid/gas transition. In Sec. 4.6 the Dellago-Posch formula for the computation of Lyapunov exponents is generalized to take the hysteretic capillary bridge formation into account. With the explicit matrices for the tangent space evolution, the full Lyapunov spectrum and the Kolmogorov-Sinai entropy are computed as a function of driving.

4.1 Elementary Phase Space Evolution under Driving

To maintain a dissipative system, such as granular matter, in a stationary nonequilibrium state, power must be steadily injected by an external driving. This is done in experiments

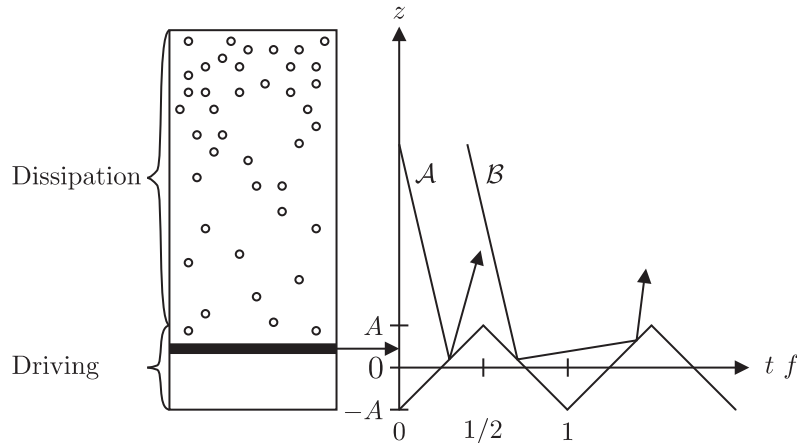


Figure 4.1: A dissipative granular gas driven by a moving boundary, symbolized as black bar at the bottom of the left figure. On the right side a space-time plot shows the vertical motion of the boundary and two particle trajectories, denoted by \mathcal{A} and \mathcal{B} . While in \mathcal{A} energy is gained from the boundary, the trajectory \mathcal{B} collides first with the wall in the phase of expansion when heat is extracted.

with dry and wet granulates¹ by a vibrating boundary or wall which injects energy through its collisions with the grains. A realistic motion of the wall is continuous in space, so that there is a period of time for inward and outward movement. An ‘ideal’ sawtooth profile with infinite withdrawal speed is not suitable: it would violate the Fluctuation Theorem from the start, because the probability for entropy reduction (by extracting energy) would be identical zero². The wall we consider for this section shall have a triangular driving signal as is shown in Fig. 4.1. Generalizations, to e.g. sinusoidal motion, are possible but mathematically cumbersome. The main result can be obtained with the more tractable triangular driving.

To keep it as simple as possible we neglect the influence of gravity. (As a general law the Fluctuation Theorem should hold in microgravity environments, too.) We assume the granular gas to be sufficiently dilute, so that we can neglect particle collisions within the region where power is exchanged with the wall.

Looking at the first half period of the driving motion in the time interval $[0, \frac{1}{2f}]$, we can immediately write down the phase space transformation for particles that will not hit the wall,

$$\begin{pmatrix} z(\frac{1}{2f}) \\ \dot{z}(\frac{1}{2f}) \end{pmatrix} = \begin{pmatrix} 1 & \frac{1}{2f} \\ 0 & 1 \end{pmatrix} \begin{pmatrix} z(0) \\ \dot{z}(0) \end{pmatrix}, \quad (4.1)$$

and those (such as particle \mathcal{A} in Fig. 4.1) that hit the upwards moving wall,

$$\begin{pmatrix} z(\frac{1}{2f}) \\ \dot{z}(\frac{1}{2f}) \end{pmatrix} = - \begin{pmatrix} 1 & \frac{1}{2f} \\ 0 & 1 \end{pmatrix} \begin{pmatrix} z(0) \\ \dot{z}(0) \end{pmatrix} + 2 \begin{pmatrix} \frac{v}{2f} - A \\ v \end{pmatrix}. \quad (4.2)$$

Herein $v = 4Af$ is the constant amplitude of the wall velocity at frequency f . As often in

¹A method used in simulations and theory to achieve a stationary state is to add a stochastic force term to the equations of motion [221]. This is theoretically favorable, however more realistic is to drive the system from the boundaries.

²This would imply that the left-hand side of (1.2) is zero in contradiction to the strictly positive exponential on the right-hand side.

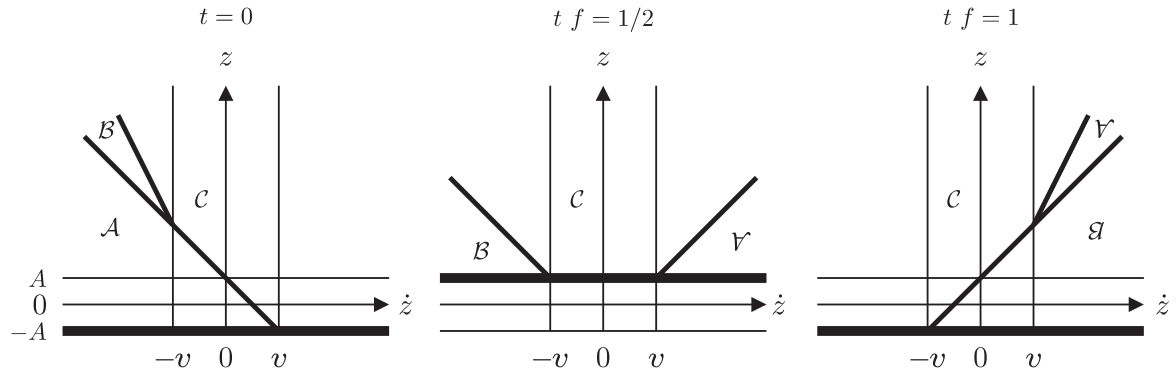


Figure 4.2: The evolution of phase space under the influence of the driving boundary shown as the black bar at the bottom. The upside down letters are to illustrate that these phase space regions have undergone a collision with the boundary (which rotates them by π with respect to their initial orientation at time zero).

this thesis, the boundary motion with velocity $v(t)$ is used to define a temperature scale³,

$$T_{\text{wall}} = \frac{m \langle v^2 \rangle}{2k_{\text{B}}}, \quad (4.3)$$

which is set by the motion of the wall. The condition for a collision with the inwards moving wall,

$$A - z(0) - \frac{1}{2f} \dot{z}(0) > 0, \quad (4.4)$$

defines a region in phase space which we denote by \mathcal{A} . Similarly, all trajectories \mathcal{B} (cf. Fig. 4.1 for an example) are at time $\frac{1}{2f}$ in the region

$$-A - z\left(\frac{1}{2f}\right) - \frac{1}{2f} \dot{z}\left(\frac{1}{2f}\right) > 0 \quad (4.5)$$

of phase space, so that they collide with the wall as it moves downwards in the time interval $[\frac{1}{2f}, \frac{1}{f}]$. Particles moving freely in the second half period obey

$$\begin{pmatrix} z(1/f) \\ \dot{z}(1/f) \end{pmatrix} = \begin{pmatrix} 1 & \frac{1}{2f} \\ 0 & 1 \end{pmatrix} \begin{pmatrix} z(\frac{1}{2f}) \\ \dot{z}(\frac{1}{2f}) \end{pmatrix}, \quad (4.6)$$

while those in the region \mathcal{B} evolve according to

$$\begin{pmatrix} z(1/f) \\ \dot{z}(1/f) \end{pmatrix} = - \begin{pmatrix} 1 & \frac{1}{2f} \\ 0 & 1 \end{pmatrix} \begin{pmatrix} z(\frac{1}{2f}) \\ \dot{z}(\frac{1}{2f}) \end{pmatrix} - 2 \begin{pmatrix} \frac{v}{2f} - A \\ v \end{pmatrix}. \quad (4.7)$$

These transformations can be clearly visualized in phase space, as done in Fig. 4.2.

We note in passing that the determinants of all transformations are unity. The particle-wall system is a Hamiltonian system with a time dependent Hamilton function. Therefore the phase space volume is conserved but energy is not.

³The notion of a wall temperatures is used in the Chaps. 8 and 10.

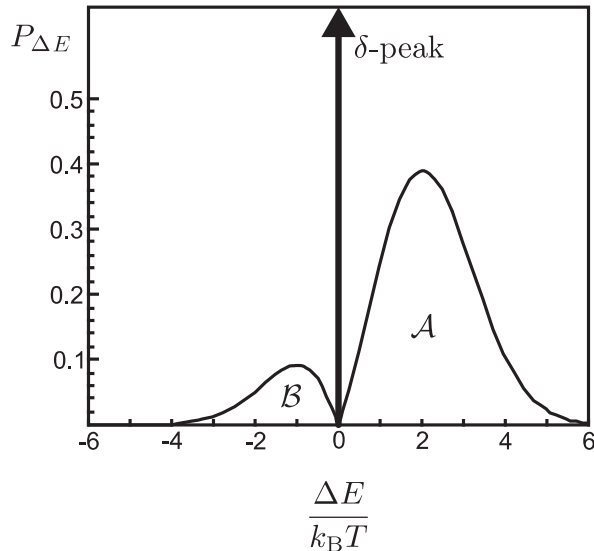


Figure 4.3: The distribution of energy exchanged within one driving cycle according to Eq. (4.10). The δ -peak at $\Delta E = 0$ stems from the phase space region \mathcal{C} , while the positive and negative values of ΔE are due to \mathcal{A} and \mathcal{B} respectively. (This plot is for the dimensionless parameters $b = c = 0.5$.)

We denote by ΔE the energy brought into the gas by the wall within one period of agitation. The distribution of ΔE follows from the phase space distribution of the particles, $f_p(z, \dot{z})$, at the beginning of the driving period and the change in velocity caused by the wall. Denoting the final velocity after one period of driving for a particle with initial state (z, \dot{z}) by $v_f(z, \dot{z})$, the distribution of exchanged energy ΔE is

$$P_{\Delta E}(\Delta E) = \int dz d\dot{z} f_p(z, \dot{z}) \delta\left(\Delta E - m(v_f(z, \dot{z})^2 - \dot{z}^2)/2\right). \quad (4.8)$$

Depending on whether the initial phase space point (z, \dot{z}) lies within the domain \mathcal{A} or \mathcal{B} of Fig. 4.2, the final velocity v_f is given by the second line of (4.2) or (4.7) respectively. In \mathcal{A} we have energy injection ($2mv(v - \dot{z}) > 0$) and in \mathcal{B} energy extraction ($2mv(v + \dot{z}) < 0$). In the region \mathcal{C} the velocity is unchanged so that these particles contribute to $\Delta E = 0$. The distribution of ΔE will therefore have a delta-peak at zero.

4.2 Explicit Demonstration of the Fluctuation Theorem for a Non-dissipative Gas

We first confirm the Fluctuation Theorem explicitly for an equilibrated gas with conservative forces that fulfills detailed balance, so that the phase space distribution is the equilibrium Maxwell-Boltzmann distribution⁴ with temperature T :

$$f_p(\dot{z}) = n_z \sqrt{\frac{m}{2\pi k_B T}} e^{-\frac{m \dot{z}^2}{2k_B T}}. \quad (4.9)$$

⁴The Maxwell velocity distribution follows by setting the probability current of the Fokker-Planck equation equal to zero, which is the condition of detailed balance (cf. e.g. Eq. (4.50) in [183]).

The distribution of energy exchange, which results from (4.8) when (4.9) is inserted, reads

$$P_{\Delta E}(\Delta E) = (1 - ab) \delta(\Delta E) + \frac{b}{16} \frac{|\Delta E|}{(k_B T_{\text{gm}})^2} e^{-\left(\frac{\Delta E}{4k_B T_{\text{gm}}} - c\right)^2}. \quad (4.10)$$

There are two independent physical parameters: the wall velocity or equivalently the wall ‘temperature’ $T_{\text{wall}} = mv^2/(2k_B)$, and the gas temperature T . In the exponent of (4.10) appears their geometric mean,

$$T_{\text{gm}} = \sqrt{T_{\text{wall}} T}. \quad (4.11)$$

In the result (4.10) we used the following dimensionless abbreviations:

$$a = e^{-c^2} + \sqrt{\pi} c \operatorname{erf}(c) \quad (4.12)$$

$$b = \frac{n_z}{f} \sqrt{\frac{k_B T}{2\pi m}} \quad (4.13)$$

$$c = \sqrt{\frac{T_{\text{wall}}}{T}}. \quad (4.14)$$

Although the underlying velocity distribution is Gaussian, the distribution (4.10) for the exchanged energy ΔE has quite some structure. The first term in (4.10) is the delta-peak with probability mass $(1 - ab)$ due to particles that miss the wall in one period. These particles are located in the region of the phase space denoted by \mathcal{C} in Fig. 4.2. The region \mathcal{A} gives rise to the instances of positive ΔE , which are more frequent than the converse events \mathcal{B} . With Eq. (4.10) we can readily verify the relation of the Fluctuation Theorem for any $\Delta E \neq 0$. Taking the quotient of the probabilities to observe the events $-\Delta E$ and $+\Delta E$, the quadratic terms and the wall temperature drop out in the exponent of (4.10), with the result:

$$\frac{P_{\Delta E}(-\Delta E)}{P_{\Delta E}(\Delta E)} = e^{-\frac{\Delta E}{k_B T}}. \quad (4.15)$$

After inserting $\Delta s = \Delta E/T$ in (4.15) and transforming the probability distribution, we arrive at the relation

$$\frac{P_{\Delta s}(-\Delta s)}{P_{\Delta s}(\Delta s)} = e^{-\frac{\Delta s}{k_B}} \quad (4.16)$$

of the Fluctuation Theorem for entropy⁵ production, which expresses that the observation of entropy reduction is exponentially unlikely as discussed in Chap. 2.

4.3 ‘Violation’ of the Fluctuation Theorem for a Dissipative Gas

In the last section we have been heating a gas of particles, that fulfills detailed balance, by the fast, non-adiabatic motion of the driving wall. How is the situation with dissipative systems, such as dry or wet granular gases? Their equations of motion have no time-reversal symmetry: reversing the momenta does not lead back to the earlier system state. However, time-reversal symmetry is the essential requirement in derivations of Fluctuation Theorems for dynamical systems [77, 89, 90].

⁵Following the common notation in the literature and of Chap. 2, the fluctuating entropy on short time scales is denote by lower case Δs . In contrast, the mean entropy per driving cycle is $\Delta S = \langle \Delta s \rangle > 0$.

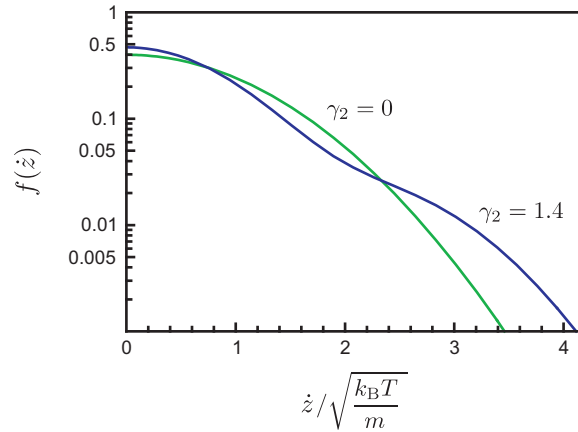


Figure 4.4: Deviation of the velocity distribution as described by the kurtosis excess γ_2 .

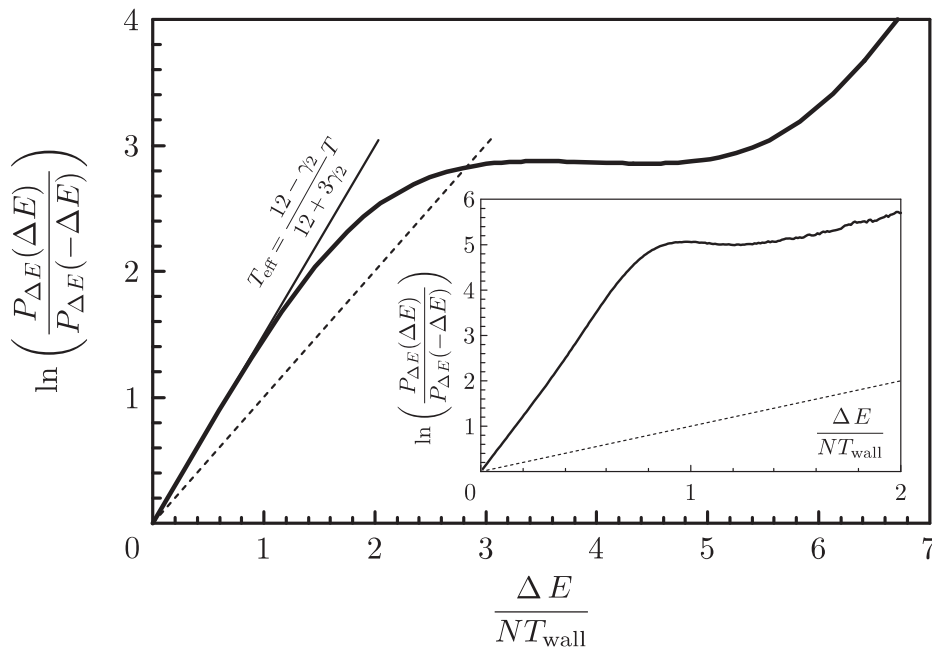


Figure 4.5: ‘Violation’ of the Fluctuation Theorem. In a dissipative system with broken time reversal symmetry, the assumptions of the Fluctuation Theorem are not fulfilled. The reported experimental [78] and numerical [10] confirmations were limited to small fluctuation. The present analytic model and the simulation (inset) resolve deviations at higher energies. The inset results from a simulation of wet granular matter in one dimension. The kurtosis excess is $\gamma_2 = 1.4$ in the main panel.

The more surprising were reports on the experimental [78] and numerical [10] confirmation of the relation (4.15) of the Fluctuation Theorem for dry granular gases. We therefore generalize the analysis of the previous section. In dissipative gases, the velocity distribution deviates from a Gaussian [78, 27]. For a general particle velocity distribution $f_p(\dot{z})$, the distribution of power fluctuations is, according to the phase space consideration in 4.1 and Eq. (4.8):

$$\begin{aligned} P_{\Delta E}(\Delta E) &= C \delta(\Delta E) + \frac{n_z}{2f} \sum_{\tilde{v}=\pm v} \frac{1}{2m|\tilde{v}|} \int_{\tilde{v}-\dot{z}>0} d\dot{z} f_p(\dot{z}) (\tilde{v} - \dot{z}) \delta\left(\frac{\Delta E}{2m\tilde{v}} - \tilde{v} + \dot{z}\right) \\ &= C \delta(\Delta E) + \frac{n_z}{16mf} \frac{|\Delta E|}{k_B T_{\text{wall}}} f_p \left[\left(v - \frac{\Delta E}{2mv} \right) \text{sgn}(\Delta E) \right]. \end{aligned} \quad (4.17)$$

For a Maxwellian f_p , Eq. (4.17) reduces to the result (4.10). The constant C is determined by normalization and f in the denominator is the shaking frequency. From Eq. (4.17) we see immediately that the quotient of the probabilities to observe fluctuations $\pm\Delta E$, expressed in the general velocity distribution f_p , is equal to

$$\frac{P_{\Delta E}(-\Delta E)}{P_{\Delta E}(\Delta E)} = \frac{f_p\left(\frac{\Delta E}{2mv} + v\right)}{f_p\left(\frac{\Delta E}{2mv} - v\right)}. \quad (4.18)$$

As a controlled departure from equilibrium we consider deviations from the Maxwell distribution as described by higher cumulants. This is conveniently done by an expansion of the velocity distribution f_p in Hermite polynomials⁶, as introduced in Sec. 2.7:

$$f_p(\dot{z}) = \sqrt{\frac{m}{2\pi k_B T}} \left(1 + \frac{\gamma_2}{96} H_4 \left(\sqrt{\frac{m\dot{z}^2}{2k_B T}} \right) \right) \exp\left(-\frac{m\dot{z}^2}{2k_B T}\right). \quad (4.19)$$

Herein the first order measure for nonequilibrium is the kurtosis excess γ_2 , $0 < \gamma_2 < 4$, which has been observed to assume positive values in simulations of dry and wet granular matter in one dimension [241]. Figure 4.4 shows how probability mass is shifted away from the center (at zero velocity) for $\gamma_2 > 0$ without increasing the granular temperature T . Plugging the velocity distribution (4.19) in the general expression⁷ (4.18) we find that the Fluctuation Theorem (4.15) is *violated*: Writing the first terms of an expansion in energy explicitly, yields

$$\ln\left(\frac{P_{\Delta E}(\Delta E)}{P_{\Delta E}(-\Delta E)}\right) = \frac{\Delta E}{T_{\text{eff}}} + \frac{\gamma_2}{162} \frac{432 - 72\gamma_2 - 29\gamma_2^2}{(\gamma_2 + 4)^3} \left(\frac{\Delta E}{T_{\text{eff}}}\right)^3 + \mathcal{O}\left(\frac{\Delta E}{T_{\text{eff}}}\right)^5. \quad (4.20)$$

The functional form of the Fluctuation Theorem is extended by non-linear order terms. The denominator abbreviated by T_{eff} in the analytic result (4.20) is

$$T_{\text{eff}} = \frac{12 - \gamma_2}{12 + 3\gamma_2} T. \quad (4.21)$$

T_{eff} deviates the more from the granular temperature T , the further we are away from equilibrium as described by γ_2 . The analytic result therefore predicts the initial slope to deviate from the inverse temperature of the granular system. A deviation of the temperature T_{eff} , which was defined by the slope of the Fluctuation Theorem, from the granular temperature T , has been also observed in the experiment of K. Feitosa and N. Menon [78].

⁶Similar expansions of the velocity distribution frequently use Sonine polynomials (which are associated Laguerre polynomials) [27].

⁷To reduce the number of free parameters, we assume an ideal coupling to the wall by equating wall temperature and granular temperature.

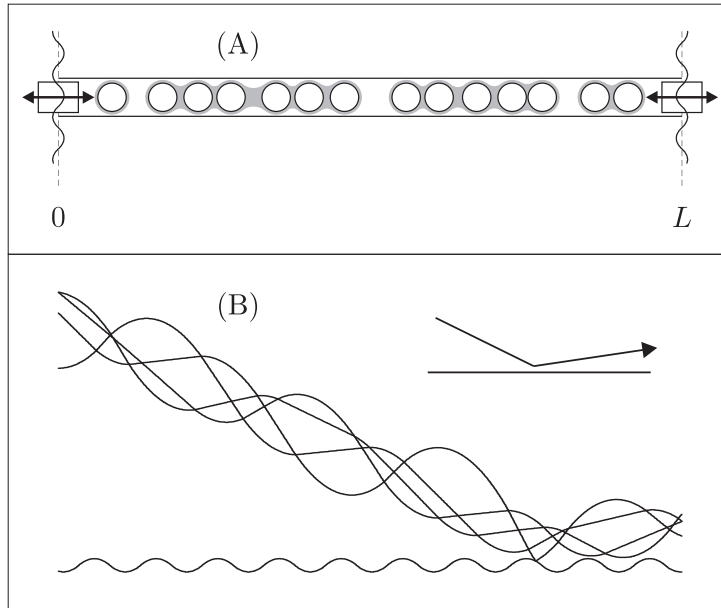


Figure 4.6: (A) A sketch of wet granular matter in one dimension. The system is dissipative due to the hysteretic liquid bridge interaction. A stationary state is maintained by the periodic shaking of the boundaries. (B) A space-time plot with time increasing to the left. We see a small cluster of 4 particles interacting with an oscillating boundary. On average the boundaries inject energy into the system. Here we observe the rarer case when energy flows out of the system. (The inset arrow illustrates the center of mass motion of the cluster.)

Furthermore, this experiment [78] was interpreted as the confirmation of the functional form (4.15) of the Fluctuation Theorem, according to which the right-hand side of (4.20) should be a linear function in ΔE . The full functional form according to the analytic model for the nonequilibrium state (4.19) is shown in Fig. 4.5. For low energies exchanged with the boundary, the linear relations seems to hold. However at higher energies per particle, $\Delta E/N$, which are of the order of the wall temperature, T_{wall} , or above, there are substantial deviations. The inset in Fig. 4.5 shows a simulation result of wet granular matter. The qualitative agreement to the simple analytic model is obvious, and as good as can be expected, since we used the kurtosis as the only parameter to describe the nonequilibrium state. (To compare with the analytic description based on the one-particle distribution function, the exchanged energy per particle is shown on the abscissa in both plots of Fig. 4.5.)

Therewith the seeming conflict between the requirements for the Fluctuation Theorem and the observation is resolved by the analytic model in general and by the simulation in the case of wet granular matter: the functional form of the Fluctuation Theorem holds as an approximation for small fluctuations, whereas at higher energies a revision is needed. This revision is addressed in the following section for wet granular matter.

4.4 Suggestion for a Definition of Entropy for Systems far from Equilibrium

We have seen in the last section (in Eq. (4.20)) that the probability to observe a reduction in entropy $\Delta s < 0$ with Δs defined⁸ by

$$\Delta s = \frac{\Delta E}{T} \quad (4.22)$$

(and k_B set equal to unity to shorten notation) does not fulfill the Fluctuation Theorem

$$\Delta s = \ln \frac{P_{\Delta s}(\Delta s)}{P_{\Delta s}(-\Delta s)}, \quad (4.23)$$

according to which the relation

$$\frac{\Delta E}{T} = \Delta s = \ln \frac{P_{\Delta s}(\Delta s)}{P_{\Delta s}(-\Delta s)} = \ln \frac{P_{\Delta E}(\Delta E)}{P_{\Delta E}(-\Delta E)} \quad (4.24)$$

is predicted. In this section, a suggestion is worked out how the Fluctuation Theorem can be recovered for wet granular. We assume for this section that the Fluctuation Theorem bears the potential of being more general, while the Clausius expression is limited to equilibrium. We thus intend to construct a modified quantity $\Delta \tilde{s}$ which fulfills the Fluctuation Theorem and reduces to the Clausius expression in equilibrium.

We start with the following observation: It has been shown in the Secs. 4.2 (Eq. (4.15)) and 4.3 (Eq. 4.20) that the ratio of probabilities,

$$\Delta \tilde{s}(\Delta E) := \ln \frac{P_{\Delta E}(\Delta E)}{P_{\Delta E}(-\Delta E)}, \quad (4.25)$$

converges to the Clausius definition of entropy (4.22), $\Delta \tilde{s} \rightarrow \Delta s$, as equilibrium is approached. The Clausius definition is well known to be limited to equilibrium. In the important search for a generalized definition of entropy, which is directly observable in nonequilibrium experiments, it is therefore admissible to study the ratio $\Delta \tilde{s}$, *defined* by Eq. (4.25), as a candidate for a generalized definition of entropy, which could remain valid for experiments far from equilibrium.

As stated in beginning of this section, we demand that this new quantity $\Delta \tilde{s}$ fulfills the Fluctuation Theorem (4.23). First we note that $\Delta \tilde{s}$ according to (4.25) already fulfills the Fluctuation Theorem (4.23) if the Jacobian $d(\Delta \tilde{s})/d(\Delta E)$ of the odd function $\Delta \tilde{s}(\Delta E)$ (4.20) can be canceled out in the fraction (4.23). This is possible if the function $\Delta \tilde{s}$ grows monotonically with the exchanged energy ΔE , so that the function $\Delta \tilde{s}(\Delta E)$ is injective, i.e. we have contributions to $\Delta \tilde{s}$ from one value ΔE in the general transformation rule for probabilities,

$$P_{\Delta \tilde{s}}(x) = \int_{-\infty}^{\infty} P_{\Delta E}(y) \delta(x - \Delta \tilde{s}(y)) dy, \quad (4.26)$$

which then reduces to $P_{\Delta s}(\Delta s) = P_{\Delta E}(\Delta E) / [d(\Delta s)/d(\Delta E)]$.

However we have seen with the example in Fig. 4.5 that the function $\Delta \tilde{s}(\Delta E)$ is in general *not* monotonic, but has horizontal or negative slope. For this reason, the occurrence of such extrema in $\Delta \tilde{s}(\Delta E)$ is investigated systematically by (event-driven) simulations of wet

⁸This is the Clausius definition of entropy which has been applied in the aforementioned publications [78, 10].

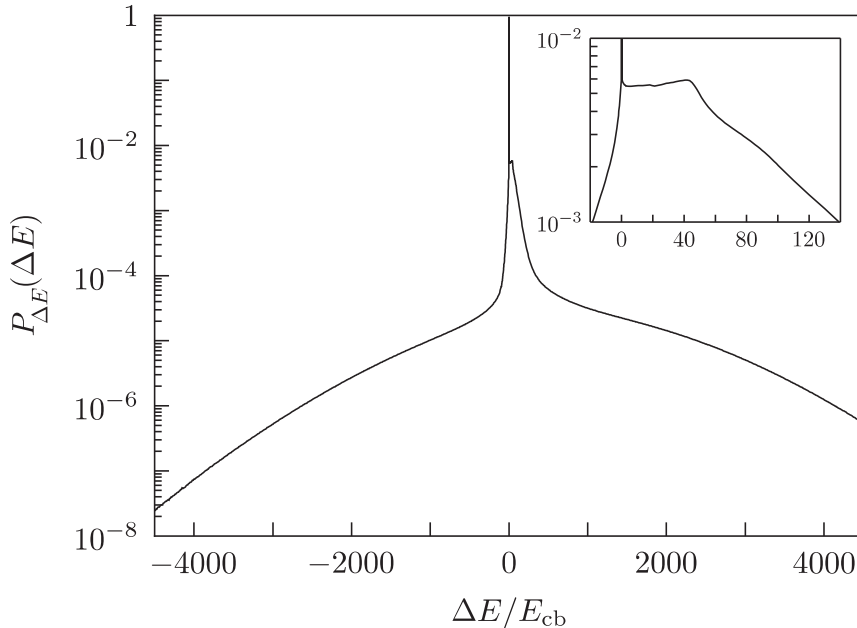


Figure 4.7: The distribution of exchanged energy with the boundaries. This distribution has been measured by simulating more than 10^{11} driving periods at $v^{\text{rms}} = 2.03\sqrt{E_{\text{cb}}/m}$. ΔE is the energy exchanged within one period. At $\Delta E = 0$ a very pronounced delta-peak is clearly resolved (cf. the inset), as predicted by the phase space evolution in Sec. 4.1. Almost all probability mass is contained in the delta-peak. (Note the logarithmic scale of probability).

granular matter. The 1D system is driven by parabola segments as shown in Fig. 4.6, similar to the sinusoidal driving in most experiments⁹. The driving velocity is characterized by $v^{\text{rms}} = \sqrt{\langle v^2 \rangle}$. As the control parameter the driving amplitude A is varied at fixed frequency f , so that $v^{\text{rms}} = 8Af/\sqrt{3}$. It is indispensable to choose unequal masses in the one-dimensional simulation. Otherwise the momentum of a single particle colliding with a cluster transmits the cluster ballistically up to the last particle on the other end of the cluster¹⁰. In order to avoid this Newton-cradle effect in favor of a homogeneous state, we choose incommensurable masses,

$$\frac{m_j}{\bar{m}} = 1 + \delta \sin(j \varphi_G) ,$$

with the irrational golden angle $\varphi_G = 2\pi/(1 + \sqrt{5})$ and polydispersity $\delta = 1/10$. The dry limit of such a 1D system without the hysteretic interaction has been investigated intensively within the last five years¹¹ [162, 39], so that we have a well-defined starting point to introduce dissipation by the capillary bridges.

The distribution $P_{\Delta E}(\Delta E)$ of the exchanged energy is measured in the simulation. Figure 4.7 presents the numerical result for the driving velocity $v^{\text{rms}} = 2.03\sqrt{E_{\text{cb}}/m}$. The delta-peak at $\Delta E = 0$ is present in the simulation as predicted by the analytical models (cf. Eqs. (4.10) and (4.17)). To resolve the extremely rare events of high energy exchange,

⁹ $N = 100$ particles are driven symmetrically from both ends. The dimensionless density of the system is chosen to be $n_z s_{\text{crit}} = 1$.

¹⁰This last particle would then be ejected from the cluster with the rupture of a capillary bridge if the kinetic energy exceeds the capillary energy.

¹¹Especially the diffusive transport of heat has been investigated in [162, 39].

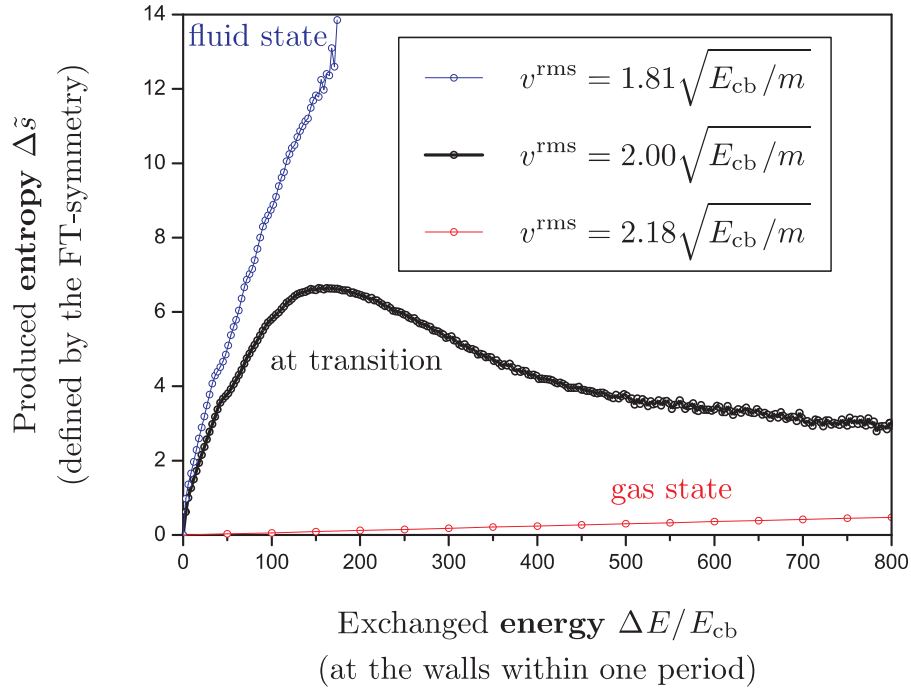


Figure 4.8: Simulation results on the function $\Delta\tilde{s}(\Delta E)$, defined by Eq. (4.25). Depending on the state of the system, branches are observed along which the ‘entropy’ $\Delta\tilde{s}$ decreases as more energy ΔE is injected.

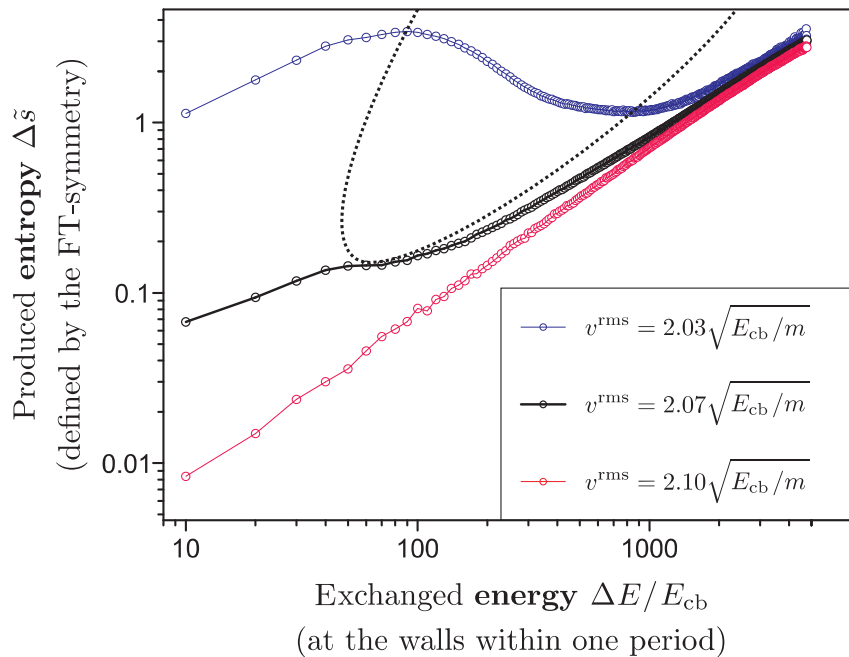


Figure 4.9: A close-up of Fig. 4.8 showing three nonequilibrium steady states of wet granular matter which differ slightly in the driving velocity. On this double logarithmic plot we see the existence of a critical driving velocity close to $v^{\text{rms}} = 2.07\sqrt{E_{\text{cb}}/m}$, below which the function $\Delta\tilde{s}(\Delta E)$ develops negative slopes. Branches of negative slope define the region contoured by the dashed line. The minimum of this region is the critical velocity, where simulations show an abrupt rise of the granular temperature (cf. Fig. 4.11).

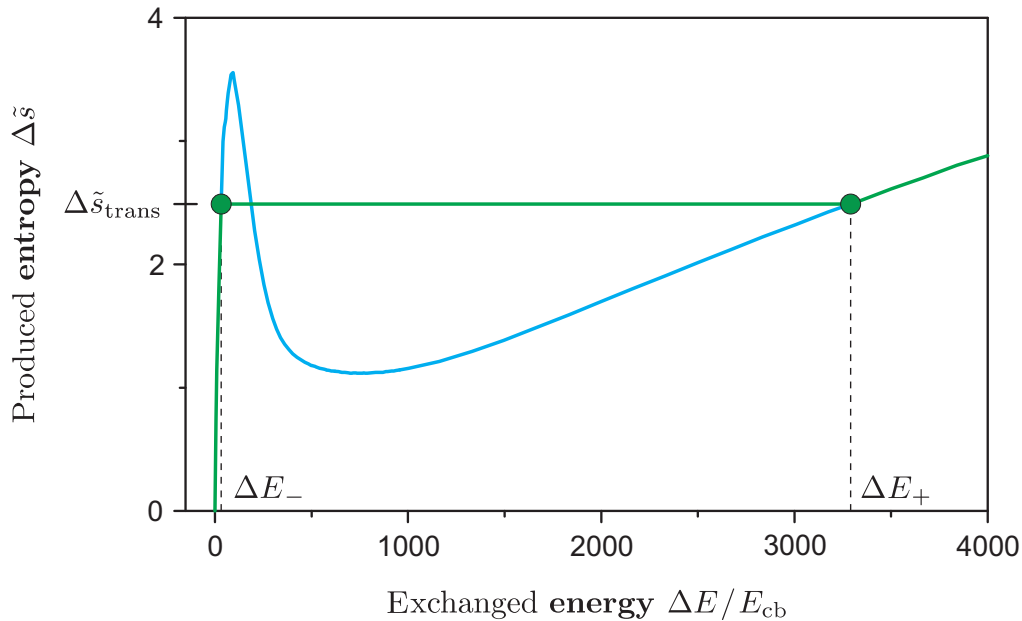


Figure 4.10: The construction of a function $\Delta s(\Delta E)$ which fulfills the Fluctuation Theorem. In equilibrium, this function reduces to the Clausius entropy $\Delta E/T$. The blue curve is $\Delta \tilde{s}$ which results according to Eq. (4.25) from the distribution $P_{\Delta E}$, which has been measured in the simulation (cf. Fig. 4.7) at driving $v^{\text{rms}} = 2.03\sqrt{E_{\text{cb}}/m}$. The green curve is the constructed function Δs , such that the Fluctuation Theorem is fulfilled.

the event driven simulation was run for 10^{11} driving cycles to have sufficient statistics. The measured probabilities span eight orders of magnitude. Using Eq. (4.25) the function $\Delta \tilde{s}$ is inferred from $P_{\Delta E}$. The results presented in Fig. 4.8 show that small changes of the driving leads to qualitative changes in $\Delta \tilde{s}(\Delta E)$. While for the lower and higher driving velocities (blue and red curve) $\Delta \tilde{s}$ is monotonic and close to linear, the intermediate driving parameter $v^{\text{rms}} = 2.00\sqrt{E_{\text{cb}}/m}$ leads to a maximum (black curve). As we investigate the vicinity of this parameter value, shown as double logarithmic plot in Fig. 4.9, we observe that $\Delta \tilde{s}$ has a universal asymptote at high energies. Moreover, there is a critical velocity of the driving below which $\Delta \tilde{s}$ is non-monotonic¹². The domain of negative slope is indicated by the dotted curve in the Δs - ΔE plane of Fig. 4.9.

To have the Fluctuation Theorem fulfilled, it is suggested to construct a modified function $\Delta s(\Delta E)$ out of $\Delta \tilde{s}(\Delta E)$ as follows. Inserting the general expression for the transformation of probabilities (4.26) in the relation (4.23) we find the functional condition

$$x = \ln \frac{P_{\Delta s}(x)}{P_{\Delta s}(-x)} = \ln \frac{\int_0^\infty P_{\Delta E}(y) \delta(\Delta s(y) - x) dy}{\int_0^\infty P_{\Delta E}(y) \delta(\Delta s(y) + x) dy} \quad (4.27)$$

which has to be fulfilled for all $x > 0$. A minimal construction of $\Delta s(\Delta E)$ out of $\Delta \tilde{s}(\Delta E)$, such that the Fluctuation Theorem (4.27) holds, replaces the branch of negative slope by a horizontal line. The Fluctuation Theorem (4.27) determines the position of this line uniquely by the implicit equation

¹²For weak driving the granular temperature is low, so that large fluctuations ΔE are extremely rare. For this reason the function $\Delta \tilde{s}(\Delta E)$ ends from the physical point of at a value ΔE of the order of TN , which is before the theoretical maximum.

$$\Delta\tilde{s}_{\text{trans}} = \ln \frac{\int_{E_-(\Delta\tilde{s}_{\text{trans}})}^{E_+(\Delta\tilde{s}_{\text{trans}})} P_{\Delta E}(y) dy}{\int_{E_-(\Delta\tilde{s}_{\text{trans}})}^{E_+(\Delta\tilde{s}_{\text{trans}})} P_{\Delta E}(-y) dy}, \quad (4.28)$$

as a consequence of Eq. (4.27). Figure 4.10 shows this construction carried out at $v^{\text{rms}} = 2.03\sqrt{E_{\text{cb}}/m}$. The probability distribution $P_{\Delta E}(\Delta E)$ (shown before in Fig. 4.10) and Eq. (4.25) lead to the blue curve for $\Delta\tilde{s}$. For the constructed function Δs shown in green, the ‘loop’ of the blue curve has been replaced by a horizontal line. This function Δs fulfills the Fluctuation Theorem (4.23). The construction is reminiscent to the Maxwell construction (used in equilibrium thermodynamics in the different case of a van-der-Waals loop). At this point the question arises whether this construction has the physical meaning of a discontinuous transition. The following section shows by simulations of wet granular matter the existence of a discontinuous transition.

4.5 The Direct Observation of the Fluid/Gas Transition

We have constructed a function $\Delta s(\Delta E)$, shown in Fig. 4.10, which fulfills the Fluctuation Theorem (4.23) for the dissipative wet granular gas and reduces in equilibrium to the Clausius expression (4.22) of entropy. In order to assess if one may interpret this function as a candidate for entropy, we consider the derivatives

$$\frac{1}{T_{\text{eff}}} = \frac{\partial s}{\partial E}, \quad (4.29)$$

which would predict a discontinuous change in the granular temperature according to the different slopes at the points marked by circles in Fig. 4.10. The effective temperatures, defined by the slope of Δs , have the values $T_{\text{eff},-} = (22 \pm 4)E_{\text{cb}}$ and $T_{\text{eff},+} = (1800 \pm 90)E_{\text{cb}}$. We therefore measure the granular temperature T in the simulation as the driving amplitude is varied. The protocol of the simulation is to increase the amplitude in small steps. Data is not collected until there is no measurable drift in the granular temperature $T(t)$, so that we are in the nonequilibrium steady state at any time of measurement. The result is shown in Fig. 4.11. We observe a rapid increase of the granular temperature at a certain driving amplitude A_c , which is shown as upper abscissa. The abscissa at the bottom is the root mean square driving velocity. The transition point is close to the value $v^{\text{rms}} = 2\sqrt{E_{\text{cb}}/m}$, which is where the negative slope, discussed in the preceding section (cf. e.g. Fig. 4.9), occurs in the relation of the Fluctuation Theorem. The number of transient clusters N_{cl} , defined by the connectivity of capillary bridges, shows a power-law form, $N_{\text{cl}}^{\infty} - N_{\text{cl}} \propto (A - A_c)^{\beta}$. The data points available in the vicinity of the critical point span one order of magnitude and are plotted on logarithmic scales in Fig. 4.12. The slope of the red line is 1/3.

So far frequency has been kept constant. In general, the driving allows for two independent parameters, which are controlled in an experimental situation as acceleration a and frequency f . The transition points in the plane spanned by these control parameters are shown in Fig. 4.13 and fall on a line through origin, $a = 4\sqrt{3}v^{\text{rms}}f$. This demonstrates that the fluid/gas transition in one dimension is determined by the driving velocity v^{rms} , or equivalently by the wall temperature T_{wall} defined in Eq. (4.3). The critical wall temperature, $T_{c, \text{wall}} = (2.1 \pm 0.1)E_{\text{cb}}$, is in proportion to the capillary energy E_{cb} as there is no other energy scale in the simulation.

It should be noted that simulation with capillary bridges to the driving walls have also been performed: All numerical results reported above have been found to hold for hydrophobic and hydrophilic boundary conditions. Furthermore, simulations taking gravity into account have shown no influence on the critical driving velocity, provided the capillary force is equal

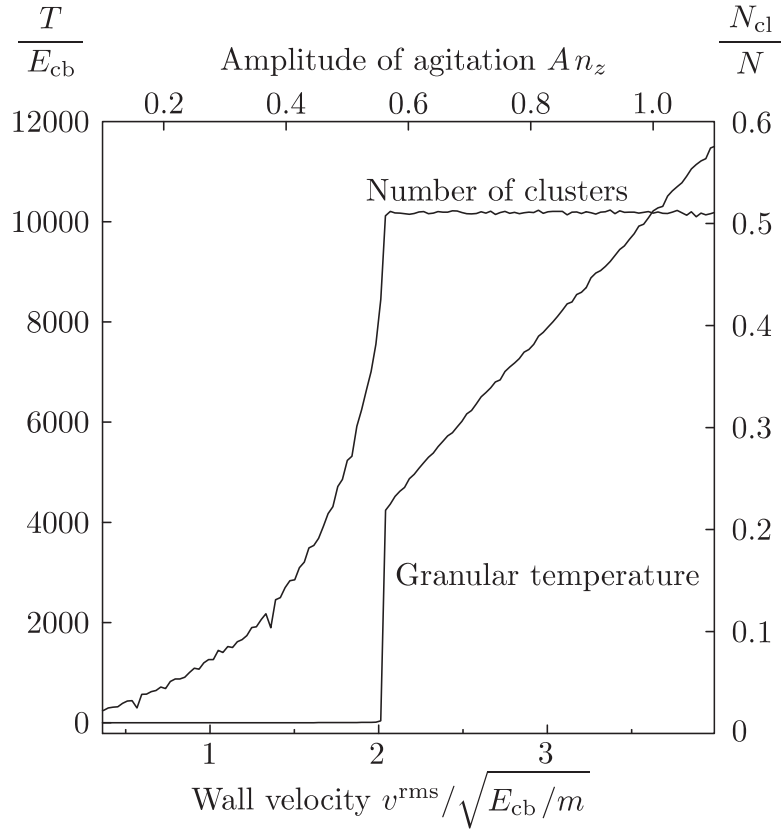


Figure 4.11: The fluid/gas transition of wet granular matter, observed in simulations of a one-dimensional system as depicted in Fig. 4.6. The frequency of the boundary motion is fixed while its amplitude A is increased. At the amplitude $A_c n_z \approx 0.55$, with the density $n_z = L/N$, the granular temperature increases discontinuously. To the left of the transition point, at $A n_z = 0.53$, the granular ‘fluid’ has the temperature $T = (2.8 \pm 0.2)E_{\text{cb}}$, where E_{cb} is the maximal potential energy stored in a liquid bridge prior to rupture. At the transition the granular temperature increases by three orders of magnitude. The second ordinate on the right gives the number of transient clusters, N_{cl} , defined by the connectivity of capillary bonds. It exhibits a power-law behavior at the transition.

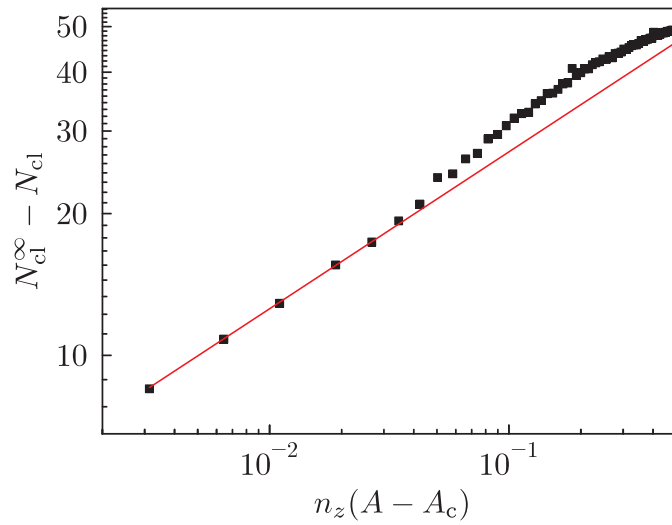


Figure 4.12: The number of clusters at the fluid/gas transition, shown before in Fig. 4.11, in the vicinity of the transition on logarithmic scales. The red line has slope 1/3.

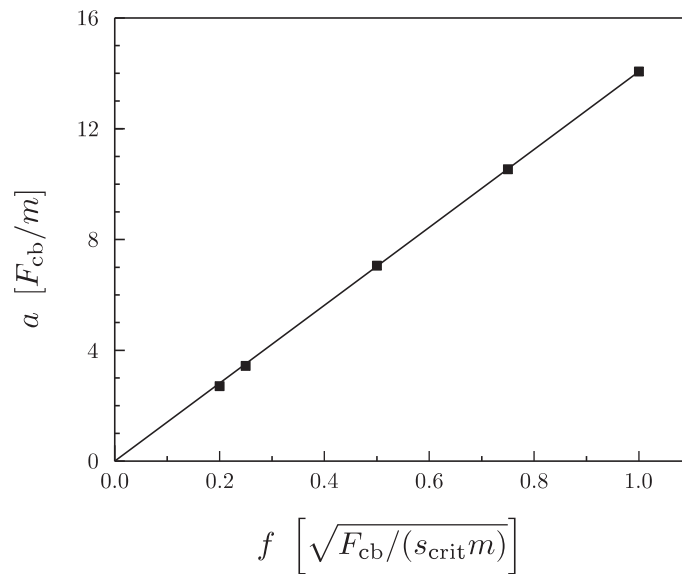


Figure 4.13: The fluid/gas transition for different amplitudes and different frequencies of the driving. The transition line is shown in the plane spanned by acceleration and frequency, which are direct observables in an experiment. If the fluid/gas transition would depend on the force, F_{cb} , of the capillary bridges, the transition points would form a horizontal line in this plot with the acceleration on the ordinate. The acceleration $a = 32Af^2 = 4\sqrt{3}v^{rms}f$ is found to grow linearly with the frequency f , so that the transition is determined by a critical velocity, which is close to $v^{rms} = 2\sqrt{E_{cb}/m}$. (cf. Fig.4.11).

or greater than the gravitational force of one particle. The one-dimensional simulations show no phase coexistence and no hysteresis of the fluid/gas transition when the control parameters are changed slowly as described above.

The fluid/gas transition in wet granular matter will be extended to higher dimension in Chap. 10, in conjunction with experiments and an continuum description. It is interesting to note that – analogously to the coexistence of two different densities described by the equilibrium Maxwell construction – the two different slopes at the points marked by circles in the construction of Fig. 4.10 correspond to the coexistence of two different effective temperature, $T_{\text{eff},-}$ and $T_{\text{eff},+}$ (cf. Eq. 4.29). Since the effective temperatures is known to be scaled as compared to the granular temperature (described by Eq. (4.21)), we consider the ratio which is equal to $T_{\text{eff},+}/T_{\text{eff},-} = 82$. Such a coexistence state will be actually reported in Chap. 10 for the two-dimensional system. An analytic description of the discontinuous fluid/gas transition is also presented in Chap. 10. As emphasized in the introduction, in order to develop an analytic statistical description of wet granular matter as a nonequilibrium system, it is essential to study the chaoticity of the system. This will be considered in the following sections below.

4.6 The Symplecticity of Wet Granular Matter

Similar to the case of the Fluctuation Theorem discussed in this chapter, it is lucid to perform the explicit proof of the (local) symplectic structure of wet granular in $D = 1$ dimension. This is done in the present section. Using the explicit result of the proof, we can readily perform the numerical computation of the Lyapunov spectrum and the Kolmogorov-Sinai entropy for the one-dimensional driven system. This prepares and complements the analytic computation of the Kolmogorov-Sinai entropy in higher dimensions in following chapter. We will finally take the opportunity to combine the nonequilibrium transition of the last section with the Kolmogorov-Sinai entropy, which will be computed as an ‘order parameter’ of the fluid/gas transition.

4.6.1 Generalization of the Dellago-Posch Formula to Wet Granular Matter

The classical Benettin algorithm [17] for the computation of Lyapunov spectra (which rests on the “multiplicative ergodic theorem” for cocycles of V. I. Oseledec [164]) has been generalized in [53, 54, 55, 56] to include the discrete collision events occurring in a gas of hard spheres. Here the Dellago-Posch formula is further generalized to take the formation and breaking of liquid bonds into account. Formation and rupture events are present as submanifolds of codimension one in phase space (cf. Fig 4.14), because they are determined by a single condition for the radial distance. The system has a smooth Hamiltonian evolution, $\Phi_{j-1}^{(\Delta t)}$, prior to any event and again after the event, $\Phi_j^{(\Delta t)}$:

$$\Phi_j^{(0)} = \text{identity} \quad (4.30)$$

$$\partial_t \Phi_j^{(\Delta t)}(\mathbf{\Gamma}) = \mathbf{F}_j \left(\Phi_j^{(\Delta t)}(\mathbf{\Gamma}) \right) \quad (4.31)$$

within the regions denoted by C_j in Fig. 4.14, so that

$$\mathbf{\Gamma}(t + \Delta t) = \Phi_j^{(\Delta t)}(\mathbf{\Gamma}(t)) \quad (4.32)$$

solves the canonical equations of motion within C_j ,

$$\dot{\mathbf{\Gamma}} = \mathbf{F}_j(\mathbf{\Gamma}) \quad (4.33)$$

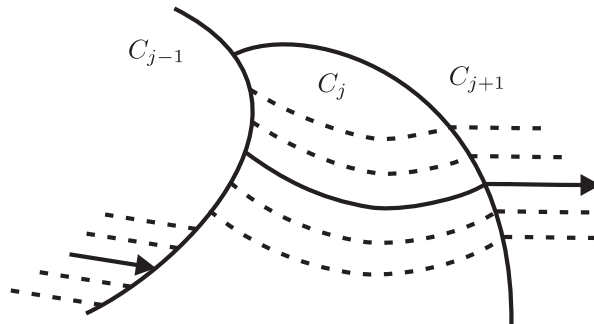


Figure 4.14: A general phase space with discrete events when the flow crosses from one smooth part C_j to another C_{j+1} . In wet granular matter made of hard particles the phase space flow is discontinuous (left crossing) in collisions and not differentiable (right crossing) when a liquid bridge ruptures.

with the symplectic form (being represented by) S and the local Hamiltonian H_j which is generating the phase space flow,

$$\mathbf{F}_j = S \nabla H_j . \quad (4.34)$$

The tangent space dynamics describes the evolution of small perturbations of the initial phase space point. We first look at the unperturbed trajectory, and then at the perturbation. The full evolution to a state $\mathbf{\Gamma}(t) \in C_j$ including the (binding or rupture) event M_j is the composition

$$\mathbf{\Gamma}(t) = \Phi^{(t)}(\mathbf{\Gamma}(0)) = \Phi_j^{(t-t_j)} \circ M_j \circ \Phi_{j-1}^{(t_j-t_{j-1})} \circ \dots \quad (4.35)$$

where t_j denotes the time the unperturbed trajectory undergoes the event M_j . While the unperturbed trajectory evolves from event to event, $\mathbf{\Gamma}(t_{j-1}+) \mapsto \mathbf{\Gamma}(t_j+)$, the change of perturbations $\delta\mathbf{\Gamma}$ is given by the Jacobian $\partial\mathbf{\Gamma}(t_j+)/\partial\mathbf{\Gamma}(t_{j-1}+)$. The $+$ expresses that $\mathbf{\Gamma}(t_j+)$ refers to the system state directly after the time-discrete event M_j has occurred. When computing this Jacobian we have to differentiate (4.35) and bear in mind that the event time t_j depends on the preceding state $\mathbf{\Gamma}(t_{j-1}+)$. Using the Eqs. (4.30) and (4.31), the differentiation yields immediately the general formula

$$\begin{aligned} & \frac{\partial\mathbf{\Gamma}(t_j+)}{\partial\mathbf{\Gamma}(t_{j-1}+)} \\ = & \left[-\mathbf{F}_j(\mathbf{\Gamma}(t_j+)) + \frac{\partial M_j(\mathbf{\Gamma})}{\partial\mathbf{\Gamma}} \mathbf{F}_{j-1}(\mathbf{\Gamma}(t_j+)) \right] \frac{\partial t_j}{\partial\mathbf{\Gamma}(t_{j-1}+)} \\ + & \frac{\partial M_j(\mathbf{\Gamma})}{\partial\mathbf{\Gamma}} \frac{\partial\Phi_{j-1}^{(t_j-t_{j-1})}(\mathbf{\Gamma})}{\partial\mathbf{\Gamma}(t_{j-1}+)} . \end{aligned} \quad (4.36)$$

We specify Eq. (4.36) to the case of the Minimal Capillary Model in one dimension. Since the Minimal Capillary Model assumes the liquid bridge force to be independent of the particle separation, the accelerations \mathbf{a}_j are constant within the continuous regions of phase C_j and the flow vector is $\mathbf{F}_j = (\mathbf{v}, \mathbf{a}_j)^T$. (Here $(.,.)$ denotes the extended vector and not a scalar product.) When two particles with masses m_1 and m_2 collide, the time-discrete change $\mathbf{\Gamma} \mapsto M(\mathbf{\Gamma})$ in

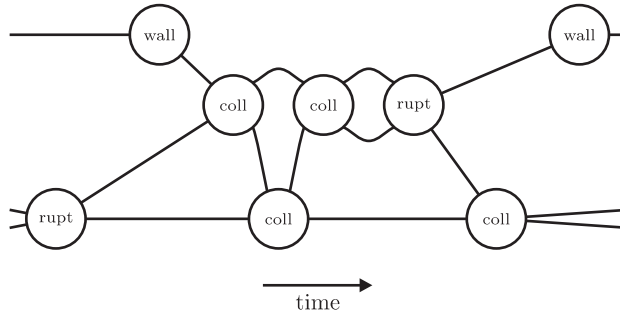


Figure 4.15: The multiplication of stability matrices within a given event topology. Each line corresponds to the free continuous motion given by (4.42) and each circle depicts a time-discrete event given by (4.43), (4.45), or (4.46). The evolution does not require global time slices. The tangent space dynamics is described by a sequence of matrices, which can be directly read off this graph, as described in the text leading to Eq. (4.47). (Only the initial time, t_i , and final time, t_f , have to be globally equal for all particles.)

phase space is linear and perturbations

$$\delta\mathbf{\Gamma} = \begin{pmatrix} \delta x_1 \\ \delta v_1 \\ \delta x_2 \\ \delta v_2 \end{pmatrix} \quad (4.37)$$

evolve according to the matrix

$$\frac{\partial M}{\partial \mathbf{\Gamma}} = \begin{pmatrix} 1 & 0 & 0 & 0 \\ 0 & \alpha & 0 & r_2 \\ 0 & 0 & 1 & 0 \\ 0 & r_1 & 0 & -\alpha \end{pmatrix}, \quad (4.38)$$

with $\alpha = \frac{m_1 - m_2}{m_1 + m_2}$ and $r_{1,2} = \frac{2m_{1,2}}{m_1 + m_2}$. The collision time $t_j = t_j(\mathbf{\Gamma}(t_{j-1}+))$ is computed conveniently from the implicit condition $h(\mathbf{\Gamma}(t_{j-1}+), t_j) = 0$ with $h(t) = x_1(\mathbf{\Gamma}_1(t_{j-1}+), t) - x_2(\mathbf{\Gamma}_2(t_{j-1}+), t)$:

$$\frac{\partial t_j}{\partial \mathbf{\Gamma}(t_{j-1}+)} = -\frac{\partial h / \partial \mathbf{\Gamma}}{\partial h / \partial t_j}. \quad (4.39)$$

For the Minimal Capillary Model this yields

$$\frac{\partial t_j}{\partial \mathbf{\Gamma}(t_{j-1}+)} = \frac{(1, \Delta t_1, -1, -\Delta t_2)}{v_2(t_{j-}) - v_1(t_{j-})}, \quad (4.40)$$

where $\Delta t_{1,2}$ are the times elapsed since the colliding particles have participated in a collision or rupture event. Such a temporal decomposition of the preceding particle state is shown as a graph¹³ in Fig. 4.15. The lines have temporal length Δt_j and each vertex (circle) represents an event M_j . The denominator of (4.40) is the relative velocity in the instant before the collision.

¹³Such a localized evolution is implemented in efficient event-driven simulations. Combined with the so-called heap structure to organize the events, this is the building principle of event-driven simulations.

Inserting (4.38) and (4.40) in the general expression (4.36) one ends up with a product of matrices,

$$\frac{\partial \mathbf{\Gamma}(t_{j+})}{\partial \mathbf{\Gamma}(t_{j-1+})} = M_{\text{coll}} \mathbf{C} \quad (4.41)$$

that describes the shearing of phase space in the continuous part of the evolution,

$$\mathbf{C} = \begin{pmatrix} 1 & \Delta t_1 & 0 & 0 \\ 0 & 1 & 0 & 0 \\ 0 & 0 & 1 & \Delta t_2 \\ 0 & 0 & 0 & 1 \end{pmatrix}, \quad (4.42)$$

and a matrix for the subsequent time-discrete collision event

$$M_{\text{coll}} = \begin{pmatrix} \alpha & 0 & r_2 & 0 \\ g_1 & \alpha & -g_1 & r_2 \\ r_1 & 0 & -\alpha & 0 \\ -g_2 & r_1 & g_2 & -\alpha \end{pmatrix}. \quad (4.43)$$

The abbreviations g_1 and g_2 describe the influence of the hysteretic interaction forces, and read

$$g_1 = \frac{a_1^- - a_1^+ - r_2(a_1^- - a_2^-)}{v_2^- - v_1^-}. \quad (4.44)$$

In g_2 the subindices 1 and 2 are exchanged as compared to g_1 in Eq. (4.44). The superscript + and - indicate quantities directly before and after the collision respectively. Analogously, one finds the matrix for the rupture event,

$$M_{\text{rupt}} = \begin{pmatrix} 1 & 0 & 0 & 0 \\ g_1 & 1 & -g_1 & 0 \\ r_1 & 0 & 1 & 0 \\ -g_2 & 0 & g_2 & 1 \end{pmatrix}, \quad (4.45)$$

(with $r_{1,2} = 0$ in (4.44)) and the matrix for the wall collision,

$$M_{\text{wall}} = \begin{pmatrix} -1 & 0 \\ \frac{2a^-}{v^- - v_w} & -1 \end{pmatrix}, \quad (4.46)$$

(which acts on one particle) where v_w is the wall velocity (which is unchanged due to the wall's infinite mass) at the impact.

We denote by \mathbf{C}^j , $M_{\text{coll}}^{(jk)}$, $M_{\text{rupt}}^{(jk)}$, and $M_{\text{wall}}^{(jk)}$ the matrices as defined above and extended to system size by zeros off the diagonal and unity on the diagonal in the rows and columns of particles $l \neq j, k$. With these explicit matrices, we can for any system trajectory directly write down the generalized Dellago-Posch formula for wet granular matter, which takes the binding and rupture events into account. As an example, we consider the event sequence shown as a graph in Fig. 4.15. We number the three particles (visible as lines during the period of continuous phase space flow) in the graph from top to bottom by superscript (1), ..., (3). Time increases from left to right in the graph, whereas in a product of matrices the outer right acts first. Therefore time increases from right to left in the product sequence of matrices:

$$M(t_i, t_f) = \frac{\partial \mathbf{\Gamma}(t_f)}{\partial \mathbf{\Gamma}(t_i)} = \dots M_{\text{coll}}^{(23)} \mathbf{C}^{(2)} \mathbf{C}^{(1)} \mathbf{C}^{(3)} M_{\text{coll}}^{(12)} \mathbf{C}^{(2)} \mathbf{C}^{(1)} M_{\text{wall}}^{(1)} \mathbf{C}^{(1)} M_{\text{rupt}}^{(23)} \mathbf{C}^{(3)} \mathbf{C}^{(2)} \quad (4.47)$$

Therewith we have the tangent space evolution of wet granular matter explicitly. Note that matrices acting on different particles commute. This general procedure is not limited to the one-dimensional system, and we will evaluate the product sequence in the following chapter for $D > 2$.

4.6.2 The Proof of Symplecticity

(Local) Symplecticity is the property

$$\mathbf{M}^T \mathbf{S} \mathbf{M} = \mathbf{S} , \quad (4.48)$$

which expresses that the tangent space evolution \mathbf{M} preserves the symplectic form (represented by the matrix) \mathbf{S} . We have been using the position-velocity representation of phase space throughout this chapter (which is furthermore appropriate for the following numerical computation), in which \mathbf{S} has the representation (as before restricted to the two-particle subspace)

$$\mathbf{S} = \begin{pmatrix} 0 & -m_1 & 0 & 0 \\ \frac{1}{m_1} & 0 & 0 & 0 \\ 0 & 0 & 0 & -m_2 \\ 0 & 0 & \frac{1}{m_2} & 0 \end{pmatrix} . \quad (4.49)$$

The fundamental properties of \mathbf{S} are

$$\mathbf{S}^2 = -\mathbf{I} \quad (4.50)$$

and

$$\det \mathbf{S} = 1 . \quad (4.51)$$

(The unity matrix is denoted by \mathbf{I} .) Symplecticity is a group property, i.e. with symplectic matrices \mathbf{M}_1 and \mathbf{M}_2 , the composed matrix $\mathbf{M}_1 \circ \mathbf{M}_2$ is as well symplectic, as is obvious using (4.48). Therefore an arbitrary wet granular trajectory is symplectic if and only if all matrices $\mathbf{M}_{\text{event}}$ associated with discrete events preserve the symplectic structure (4.48). This follows by inserting the explicit representations (4.43), (4.45), (4.46), and (4.49) in Eq. (4.48). Hence, the dynamics of wet granular matter is (everywhere locally) symplectic.

4.6.3 The Proof of Conjugate Pairing of the Lyapunov Exponents

Conjugate pairing refers to the property of a dynamical system to have its Lyapunov exponents in pairs $\pm\lambda_j$. This follows from the symplectic properties (4.48), (4.50), and (4.51), as is shown in what follows.

The Lyapunov exponents are the limits

$$\{\lambda_1, \lambda_2, \dots\} = \lim_{t \rightarrow \infty} \frac{1}{2t} \ln (\text{spec } \mathbf{M}^T \mathbf{M}) , \quad (4.52)$$

where the stability matrix $\mathbf{M} = \mathbf{M}(t) = \frac{\partial \mathbf{\Gamma}(t)}{\partial \mathbf{\Gamma}(0)}$ follows from the diagrammatic rules, which we have discussed in Sec. 4.6.1 and Fig. 4.15. Denoting the eigenvalues by $\sigma_j = e^{2\lambda_j}$, the spectrum is the zero set of the characteristic polynomial

$$\det(\mathbf{M}^T \mathbf{M} - \sigma \mathbf{I}) = 0 . \quad (4.53)$$

The conjugate pairing rule then states, that whenever $\sigma = \sigma_j > 0$ solves (4.53), $\sigma = 1/\sigma_j$ is another solution.

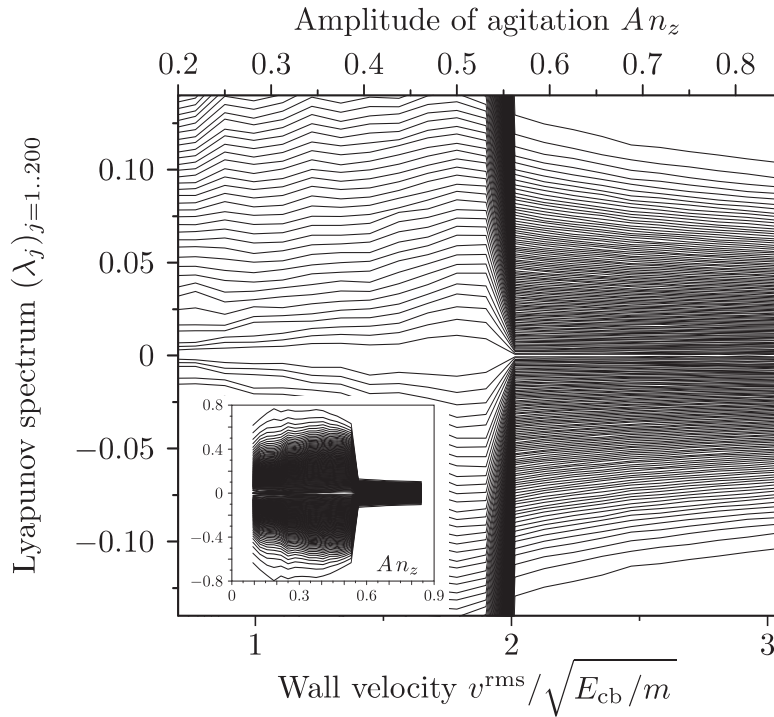


Figure 4.16: The Lyapunov spectrum of wet granular matter across the fluid/gas transition. The spectrum obeys conjugate pairing, $\lambda_j + \lambda_{2N-j+1} = 0$, since this dissipative system is symplectic, as proven in the Secs. 4.6.2 and 4.6.3.

The following direct computation shows that σ^{-1} is indeed a simultaneous solution of Eq. (4.53):

$$\begin{aligned}
 \det(\mathbf{M}^T \mathbf{M} - \sigma \mathbf{I}) &= \det(\mathbf{M}^T \mathbf{M} \mathbf{S} - \sigma \mathbf{S}) \\
 &= \det(\mathbf{M}^T \mathbf{M} \mathbf{S} - \sigma \mathbf{M}^T \mathbf{S} \mathbf{M}) \\
 &= \det(\mathbf{M}) \det(\mathbf{M} \mathbf{S} - \sigma \mathbf{S} \mathbf{M}) \\
 &= \det(\mathbf{M}) \det(\mathbf{S}(\mathbf{M} \mathbf{S} - \sigma \mathbf{S} \mathbf{M}) \mathbf{S}) \\
 &= \det(\mathbf{M}) \det(-\mathbf{S} \mathbf{M} + \sigma \mathbf{M} \mathbf{S}) \\
 &= \det(-\mathbf{M}^T \mathbf{S} \mathbf{M} + \sigma \mathbf{M}^T \mathbf{M} \mathbf{S}) \\
 &= \det(-\mathbf{S} + \sigma \mathbf{M}^T \mathbf{M} \mathbf{S}) \\
 &= \det(\sigma \mathbf{M}^T \mathbf{M} - \mathbf{I}) \\
 &= \sigma^{2N} \det(\mathbf{M}^T \mathbf{M} - \frac{1}{\sigma} \mathbf{I}) .
 \end{aligned}$$

Hence, the Lyapunov spectrum of wet granular matter is of the form $(\lambda_1, \lambda_2, \dots, -\lambda_2, -\lambda_1)$.

4.7 The Kolmogorov-Sinai Entropy as an ‘Order Parameter’ of Nonequilibrium Phase Transition

We found a discontinuous transition in Sec. 4.5, which we refer to as the fluid/gas transition of wet granular matter, because the fluid state has a granular temperature equal to few multiples of the capillary bond energy, and the gas temperature is more than three orders of magnitudes

above E_{cb} . The wet granular fluid consists of transient clusters of particles, connected by the capillary bridges. In the gas state the bridge force is too weak to have a significant influence on the particle motion, so that the fast hysteretic formation and rupture of capillary bridges cools the system homogeneously. In this section we are interested to see the Lyapunov spectrum in conjunction with this nonequilibrium transition. Since the transition causes the clusters to evaporate, we can observe the influence of the capillary bridges on the chaoticity of the wet granular dynamics which is quantified by the Kolmogorov-Sinai entropy. Intuitively, one might expect the gas phase to be more chaotic than the fluid.

To compute the Lyapunov spectrum, we use the generalized Dellago-Posch formula of wet granular matter, as derived above with Eq. (4.47). The principal idea is as follows: The computer simulates the phase space trajectory of wet granular matter, deduces from the event sequence (represented by a graph as in Fig. 4.15) the sequence of matrices (cf. Eq. (4.47)), and multiplies them all. The numerical realization needs some refinement, since there are millions of matrices in Eq. (4.47). From multiplication to multiplication the entries grow or decrease exponentially depending on the directions in tangent space which stretch or shrink. To avoid an over- or underflow in the floating point representation of numbers, a product sequence of 50 matrices is QR -decomposed into a product of an orthogonal matrix Q and a triangular matrix R . The computation is then continued with Q as the initial matrix, since Q is of order unity and contains the Lyapunov vectors sorted from fastest growth to fastest decrease. The logarithm of the diagonal elements of R are the finite time Lyapunov exponents λ_j , which are added up over the long simulation time for each Lyapunov vector separately.

The result is shown in Fig. 4.16. On the vertical axis the Lyapunov exponents λ_j are plotted. Since the system has $N = 100$ particles in $D = 1$ dimensions, there are 200 independent directions in tangent space spanned by the Lyapunov vectors. Each Lyapunov vector, has its characteristic rate of growth, λ_j (or shrinkage if λ_j is negative). As we vary the driving amplitude A (upper abscissa) at fixed frequency f , we measure the Lyapunov exponents λ_j as functions of the driving. The lower abscissa shows the driving velocity, where we see that at the critical value of the driving the spectrum changes completely. The figure shows a zoom-in so that we can see the individual functions $\lambda_j(v^{\text{rms}})$ in the fluid phase, $v^{\text{rms}} < 2\sqrt{E_{cb}/m}$. First, we observe that the spectrum is symmetric with respect to the line $\lambda = 0$, as derived analytically above in 4.6.2 and 4.6.3. Furthermore, we see that the lowest Lyapunov exponents (around zero) form band structures at low driving. The lowest three Lyapunov exponents form one bundle which breaks up as the driving is increased. The fourth and the fifth exponent (counted from zero) form a pair of exponents at weak driving. Such band structures have been termed Hydrodynamic Lyapunov Modes [56] and attracted recent attention. The inset displays the full extent of the spectrum which – as we see clearly – collapses to smaller values at the transition to the gas state.

From the full Lyapunov spectrum, the Kolmogorov-Sinai entropy follows immediately, which is the sum of all the positive exponents as mentioned in the introduction (Eq. (1.5)) according to the Pesin-Theorem [170]. The Kolmogorov-Sinai entropy of wet granular matter as a function of the driving is shown in Fig. 4.17, across the fluid/gas transition. The error bars are deduced from the deviation of $\sum_j \lambda_j$ from the theoretical value zero. (In the gas state, the error bars are more than one order of magnitude below the symbol size.) The Kolmogorov-Sinai entropy has a maximum value within the fluid state, and falls off very rapidly at the transition to the gas.

It is emphasized that the Lyapunov spectrum (in Fig. 4.16) and the Kolmogorov-Sinai entropy (in Fig. 4.17) are given in units of the (constant) shaking frequency f , so that the presented result gives h_{KS} in ‘absolute units’ and has *not* been divided by the collisions frequency, which largely increases in the gas state. Therefore $1/h_{KS}$ is the time scale for the

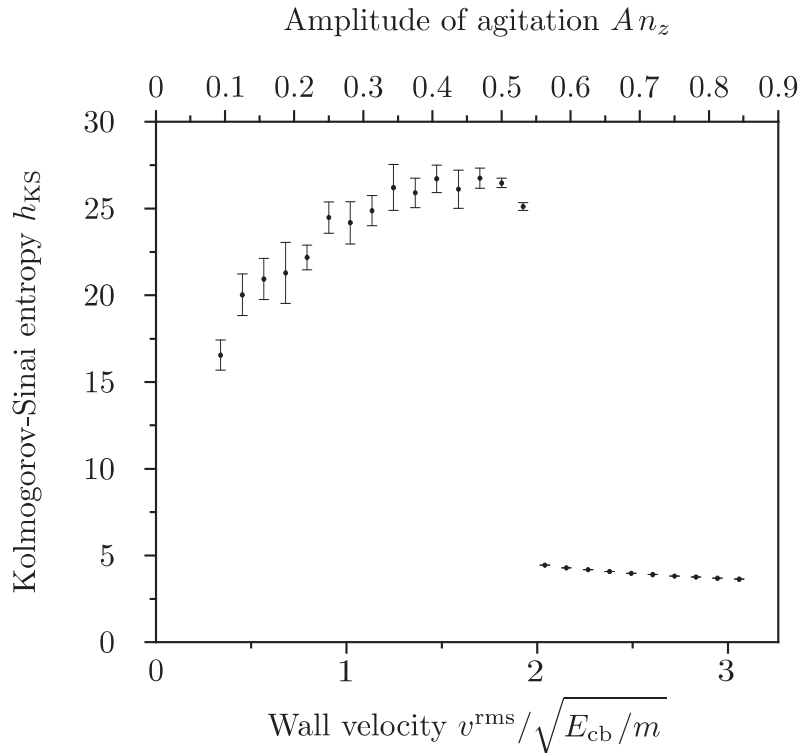


Figure 4.17: The Kolmogorov-Sinai entropy of wet granular matter in the vicinity of the fluid/gas transition.

decay of correlation due to the chaoticity of the dynamics. The kinematic time scale, set by the particle velocity and collision frequency, decreases in the gas state as described by the increase of temperature in Fig. 4.11. We have therefore the remarkable result, that in spite of the substantial *decrease* in the kinematic time scale, the time scale of chaoticity, $1/h_{\text{KS}}$, *increases* in the gas state. This might appear at first glance to be counterintuitive. However it should be considered that in the gas state the clusters formed by capillary bridges break up. The influence of the capillary bridges on the dynamics is marginal at $T \gg E_{\text{cb}}$. Thus the present numerical result points towards a substantial influence of the capillary bridges, such that the effect of the increased collision frequency is over-compensated: the higher the capillary energy, E_{cb} , compared to the granular temperature, T , the more chaotic is the dynamics of wet granular matter. In the following chapter the influence of the capillary bridges on the Kolmogorov-Sinai entropy is quantified analytically as a function of E_{cb}/T .

4.8 Conclusions

The Fluctuation Theorem has been investigated analytically and numerically in this chapter. While for a conservative gas the Fluctuation Theorem was shown to hold, the non-equilibrium state of a dissipative gas violates the Fluctuation Theorem at high values of exchanged energies and entropies. This deviation has been derived for a minimal change in the Maxwell velocity distribution described by the kurtosis, and observed in simulations. This is consistent with the fact, that the requirement of time-reversal symmetry for the Fluctuation Theorem to hold, is not fulfilled in a dissipative gas. Moreover, this result resolves the seeming conflict between the lacking requirement and reports of the Fluctuation Theorem being fulfilled at

smaller fluctuations in earlier experiments [78] and simulations [10].

The distribution of exchanged energies has been systematically investigated in simulations of wet granular matter. The occurrence of negative slopes, that violate the functional form of the Fluctuation Theorem, were shown to coincide with a discontinuous transition in the temperature of the steady nonequilibrium state. Based on simulation results, a minimal construction to alter the Clausius relation between entropy and energy has been discussed, which reduces to $\Delta s = \Delta E/T$ in equilibrium and allows to generalize the Fluctuation Theorem for wet granular matter.

We finally employed the evaporation of wet clusters in the fluid/gas transition to quantify the influence of capillary bridges on the granular chaoticity: The Kolmogorov-Sinai entropy has been determined across the transition. We found that the chaoticity increases as E_{cb}/T increases from gas to fluid, because of the presence of capillary bonds. This physically relevant observation and the mathematical concept to evolve tangent space by an infinite product of matrices (Eq. (4.47)), are continued in the analytic computation of the Kolmogorov-Sinai entropy as a function of E_{cb}/T in the following chapter.

Chapter 5

The Kolmogorov-Sinai Entropy: Wetting Increases Chaoticity

Common knowledge about wet granular matter might be due to childhood experiences in building sandcastles, which imparts knowledge about the striking influence a wetting additive has on the quasi-static mechanical properties of dense granulates. Let us be complementary in this chapter: we investigate the dilute granular gas at $T \gg E_{cb}$. Rather surprisingly, the influence of the liquid bridge formation is dramatic, also in this gaseous limit.

We will derive an analytic expression for the Kolmogorov-Sinai entropy, the measure for chaos in non-linear systems, applied to dilute wet granular matter. Our results shall be general with respect to spatial dimensionality $D \geq 2$. The grains are modeled as hard spheres and the influence of the wetting liquid is described according to the Capillary Model, in which dissipation is due to the hysteretic cohesion force of capillary bridges. The Kolmogorov-Sinai entropy is expanded in a series with respect to density. We find a rapid increase of the leading term when liquid is added. This demonstrates the sensitivity of the granular dynamics to humidity, and shows that the liquid significantly increases the chaoticity of the granular gas. The Lyapunov spectrum, which exhibits the symplectic symmetries of the wet granular dynamics, is computed numerically for the exceptional case of $D = 1$.

Before performing the detailed computation, let us anticipate from physical intuition what we expect. The qualitatively novel aspect, introduced by the wetting liquid, is the possibility of sticking collisions. Obviously at the critical energy of sticking, a strong influence on the future course of the trajectory is exerted by the capillary bridge. We therefore expect these critical slice of phase space to contribute the most to the Kolmogorov-Sinai entropy. Based on the preceding chapter, the presentation is self-contained including the definition of the Kolmogorov-Sinai entropy in terms of the Lyapunov spectrum¹.

5.1 The Dynamical System Perspective

The field of granular physics has undergone considerable progress in recent times [101, 27]. As part of soft matter physics, granulates have inspired the development of nonequilibrium statistical mechanics [65, 149]. Its potential to the foundation of physics can hardly be overestimated, since granular gases provide a road away from the well-developed Boltzmann-Enskog theory of conservative gases towards dissipative systems far from thermal equilibrium. In connection with geophysics, some aspects of landslides may be understood in terms of

¹Further reference on dynamical systems are the classical review articles [187], [200], [69], and [95], as well as the books of Gaspard [94] und Dorfman [61].

solid/liquid phase transitions of wet granular matter (cf. the Chaps. 8 and 10, and [114]), and wet granular gases are of technological relevance in granulators, pelletizers, and other instances in process engineering.

Wet granular gases are systems consisting of mesoscopic particles and a liquid phase wetting the particles. Despite their importance, the theory of wet granular matter is still nascent. There is a growing number of experimental [211, 141] and numerical work [52, 181] on this subject, but the hysteretic nature of the liquid bridge interaction (as established in Chap. 3 and [114]) was not taken into account in the modeling. We stress that the attraction force mediated by capillary bridges is not a function of distance but depends on the collision history. The theory of wet granular matter advanced with recent simulation and models describing the free cooling state [241, 80]. To the best of our knowledge, the hysteretic dissipative dynamics of wet granular matter was treated analytically for the first time in Fingerle *et al.* [83]. In the present chapter this approach is presented in detail, which treats the wet granulate as a complex dynamical system and uses powerful tools available in this area. Such is the Lyapunov spectrum,

$$\lambda_j = \lim_{t \rightarrow \infty} \frac{1}{t} \ln \frac{\delta\Gamma_j(t)}{\delta\Gamma_j(0)}, \quad (5.1)$$

where j numbers the degrees of freedom in phase space, as introduced in Chap. 4. It gives the rate of exponential divergence or convergence of two equal copies of the system in phase space, $\delta\Gamma_j(t) = \Gamma_j^{(1)}(t) - \Gamma_j^{(2)}(t)$, with perturbed initial conditions $\delta\Gamma_j(0)$. A positive Lyapunov exponent indicates chaotic behavior, i.e. sensitive dependence on the initial conditions [129]. Since we are dealing with a closed system, the sum of all positive Lyapunov exponents equals the Kolmogorov-Sinai entropy (KS entropy) [170, 171, 69].

The KS entropy is an indispensable tool in the modern description of dynamical systems. Firstly, from it we learn about the degree of chaoticity because its inverse is the time scale of predictability. Secondly, this dynamical entropy is a well-defined quantity for both equilibrium and nonequilibrium systems. Thirdly, when tiny deviations of initial conditions that were not observable in the beginning are enlarged by the evolution, this can be interpreted as the production of information about the initial conditions. Finally, the KS entropy is known to be related to macroscopic properties such as transport coefficients [93, 96, 62, 12, 36, 37, 231].

Our objective is to compute the KS entropy for the wet granular gas. Pioneering work has been done by H. van Beijeren, J. R. Dorfman *et al.* [226, 63] in the analytic treatment of sums of Lyapunov exponents for the gas of hard elastic spheres. Here a generalization of the method suggested in [226] is developed.

This chapter is organized as follows. In Sec. 5.2 we describe the hysteretic interaction of wet granulates, introducing the extended capillary model. This interaction allows the sticking of particles by attractive forces in contrast to the restitution model for dry granulates which assumes that a certain fraction of energy is lost instantaneously by inelastic collisions. In Sec. 5.3 we use the terminology developed in Sec. 5.2 to relate the behavior of the two-particle system to the full N -particle system. Thereby we are lead to determine the probability distribution for colliding pairs of particles in Sec. 5.4. In Sec. 5.5 we derive the formula that expresses the expansion of velocity space as a function of the two-particle initial conditions for arbitrary spatial dimension. In Sec. 5.6 the results of the Secs. 5.3-5.5 are combined to accomplish the computation of the KS entropy. Section 5.7 points out why, surprisingly, the one-dimensional stationary state is more complex. In Sec. 5.8 the relation between the KS entropy and the Gibbs entropy is discussed.

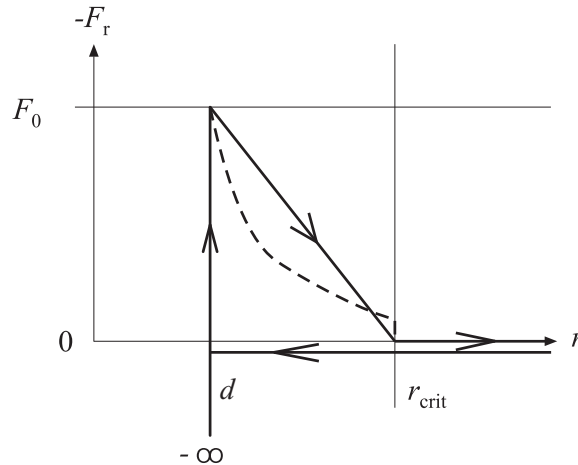


Figure 5.1: Radial forces between a pair of wetted spheres. Solid line: The radial force of the Extended Capillary Model is plotted versus the center distance r . There is no interaction between the particles as they approach. After the collision applies $\vec{F}(r) = -F_0 \frac{r_{\text{crit}} - r}{r_{\text{crit}} - d} \frac{\vec{r}}{r}$ for $r \in (d, r_{\text{crit}})$, otherwise there is no force. Dashed line: Experiments yield a decreasing force law (according to Eq. (3.9) and [207, 237]) with a discontinuity at the rupture. Therefore the even simpler Minimal Capillary Model (cf. Sec. 3.4) which assumes a constant force that drops to zero at the critical separation is a good alternative approximation. The hysteretic interaction is the relevant property which is described by both the Minimal and the Extended Capillary Model.

5.2 The Minimal and the Extended Capillary Model

We have experimentally confirmed the Capillary Model for the dynamics of wet granulates in Chap. 3, and it will be applied here. The system consists of hard spherical grains with equal diameter d and equal mass m . These are covered by a liquid film, so that every time two particles touch, a liquid bridge is formed. The Capillary Model assumes that bridges are formed instantaneously. As we focus on the dilute gas, we may restrict our considerations to pair interactions.

Experiments and computations (cf. Chap. 3 and [207, 237]) yield a capillary force law, $F(s)$, that is excellently described by Eq. (3.9) with s being the surface separation (expressed in the natural length unit of the liquid bridge volume, V_{cb} , as $S = s\sqrt{d/(2V_{\text{cb}})}$ in Eq. (3.9)). The Capillary Model assumes that the bridge pinches off at a critical surface separation $s = s_{\text{crit}}$ (i.e. at a distance $r_{\text{crit}} = d + s_{\text{crit}}$ of the centers). To leading order, the rupture distance s_{crit} equals the cubic root of the bridge volume V_{cb} . The energy that was stored in the stretched liquid bridge before the rupture is dissipated into the liquid and lost for the granular motion. We emphasize that this is the only dissipative mechanism in the Capillary Model and effects due to the viscosity of the liquid are explicitly ignored, as established and discussed in detail in Chap. 3. In the moment of the rupture, the system is non-Hamiltonian because the atomic degrees of freedom of the liquid to which energy flows are masked out in the description of the granular dynamics. Of course the forces acting on the grains are finite at the rupture, so that the trajectories (as functions of time) are continuous in the granular phase space and differentiable with respect to the initial state before the rupture.

By a collision we denote the moment when two particles in the entire N -particle system touch each other. Since we are interested in statistical statements and a point in time is of measure zero, we can assume without loss of generality that there is a unique sequence of

collisions. For a certain pair of colliding particles, we refer to the “collision cycle” as the time interval $[t_i, t_f]$ that comprises the collision of these two particles. The collision cycle starts at t_i when the last particle of the two breaks free from its former collision partner and ends at t_f in the moment when the liquid bridge between them ruptures.

During its collision cycle the radial motion of the two-particle system traverses a hysteresis loop. This is shown in Fig. 5.1 for the force (3.9) (dashed line) and for a simpler force law (solid line). The solid line in Fig. 5.1 falls off linearly with the surface separation s . This is the Extended Capillary Model in contrast to the Minimal Capillary Model (cf. Sec. 3.4 and [87]) which assumes a constant force. The corresponding hysteretic ‘potential’ of the Extended Capillary Model is

$$\frac{\phi(r)}{E_{cb}} = \begin{cases} -1, & d < r \text{ before first collision,} \\ -\left(\frac{r_{crit}-r}{r_{crit}-d}\right)^2, & d < r \leq r_{crit} \text{ after collision,} \\ 0, & r_{crit} \leq r \text{ after collision,} \\ \infty, & r < d. \end{cases} \quad (5.2)$$

In both, the Minimal and the Extended Capillary Model, the hysteretic loss of energy, i.e. the area $E_{cb} = -\int_d^{d+s_{crit}} F_r dr$ in Fig. 5.1, is a characteristic system property. When the energy in the center of mass system is below E_{cb} , colliding particles will form a stable bound state with periodic collisions. With faster relative motion the liquid bridge exists for a finite time until the particles scatter off each other. We define a corresponding relative velocity v_{cb} by $E_{cb} = mv_{cb}^2/4$ (with the additional factor 1/2 because $m/2$ is the reduced mass). From this point on we distinguish between scattering events and collisions leading to bound states. For the scattering, the restitution coefficient $\epsilon = v_f/v_i$ of the Capillary Model is an *increasing* function of the initial energy or velocity:

$$\epsilon(E_i) = \sqrt{1 - \frac{E_{cb}}{E_i}} \text{ or } \epsilon(v_i) = \sqrt{1 - \frac{v_{cb}^2}{v_i^2}}. \quad (5.3)$$

The binding threshold E_{cb} of the Capillary Model ² contrasts sharply with the widespread models for dry granules that assume either a constant or with increasing velocity *decreasing* coefficient of restitution for the collision of viscoelastic particles [27].

Let us denote by v_{crit} the critical modulus of the relative velocity $\vec{v}_i \equiv \vec{v}_1 - \vec{v}_2$, that determines whether the incoming particles will form a bound state or scatter. For head-on collisions (impact parameter $b = 0$) $v_{crit} = v_{cb}$, otherwise $v_{crit} > v_{cb}$ since there is additional energy in the rotary motion. The next step is to determine v_{crit} as a function of b .

Determination of the Critical Velocity

The bridge interaction is a central force problem. If v_i is lower than v_{cb} , the effective potential

$$\phi_{eff}(r) = \frac{mb^2v_i^2}{4r^2} + \phi(r) \quad (5.4)$$

(of the liquid bridge potential given by (5.2)) does not reach a maximum in r after the collision and leads to a bound state. For most $v_i > v_{cb}$ the particles scatter, but there are some bound cases with high angular momenta, corresponding to high impact parameters. Figure 5.2 shows three effective potentials for a given initial velocity v_i and different impact parameters b . In the case drawn with solid lines, b and v_i fulfill the critical relation $v_i = v_{crit}(b)$. For the higher b (fine dotted line in Fig. 5.2) we have $v_i < v_{crit}(b)$ so that a bound system is formed. Hence

²In the capillary regime described in [114], the dissipation by inelastic collisions [27] is dominated by the hysteretic liquid bridge interaction as we have seen in Chap. 3.

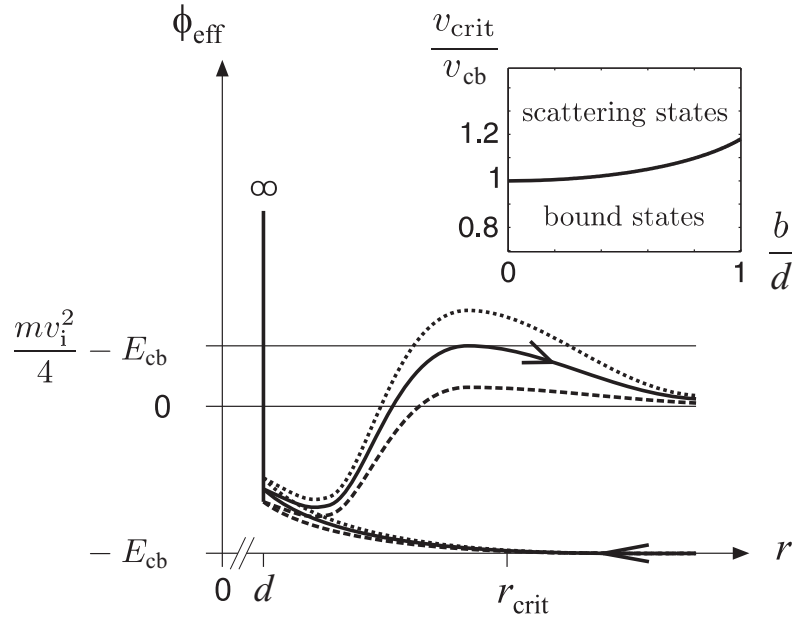


Figure 5.2: The effective potential for $v_i > v_{cb}$ and three different impact parameters. For the solid line in the middle b and v_i are critical. For the higher b (fine dotted line) the particles are bound, for a lower b (roughly dotted line) they scatter. The inset shows the complete space of collision parameters. The critical velocity v_{crit} (plotted in units of v_{cb} for $r_{crit} = d$) as a function of the scaled impact parameter b/d divides the plane in bound and scattering states.

the criterion is that $\phi_{eff}(r)$ touches the asymptotic energy $E_{cb} - m v_i^2/4$ in a single point. For the Extended Capillary Model it is possible to calculate these intersections explicitly. These are the roots of $(E_{cb} - m v_i^2/4 + \phi_{eff}) r^2$, which is a fourth order polynomial in r with one trivial root at $r = 0$ and another unphysical root for $r < d$. So there are two real roots for the bound state which turn into a complex conjugated pair of roots for the scattering state. (Since the derivative of ϕ_{eff} is continuous and negative at $r = r_{crit}$, the turning point r_{max} of a bound state follows correctly from this analytic consideration to be $r_{max} < r_{crit}$ without the need to take the non-analytic point $r = r_{crit}$ of ϕ_{eff} into account.) The easiest way is to compute the discriminant of the fourth order polynomial $(E_{cb} - m v_i^2/4 + \phi_{eff}) r^2$, which is equal to

$$\begin{aligned}
& 16v^4 \underline{b^4} \\
& + (8v^6 - 4v^4(5\gamma + 9) + v^2(27 + 18\gamma - \gamma^2)) \underline{b^2} \\
& - v^6 + v^8 + 3v^6\gamma + 3v^4(\gamma - 1)\gamma + v^2(\gamma - 3)\gamma^2 - \gamma^3,
\end{aligned}$$

with $\gamma = d \frac{2r_{crit} - d}{(r_{crit} - d)^2}$. The discriminant vanishes as the two physical roots coincide. Since the impact parameter b enters the problem only through the angular momentum term in (5.4), the discriminant is a quadratic function of b^2 . Therefore it is elementary to give $b_{crit}(v_i)$ as the inverse function of $v_{crit}(b)$ explicitly:

$$\frac{b_{crit}(v_i)}{d} = \frac{\sqrt{-8 - 20\delta^2 + \delta^4 + 16w^2 + 20\delta^2 w^2 - 8w^4 - \delta(8 + \delta^2 - 8w^2)^{3/2}}}{4\sqrt{2}w(\delta - 1)}, \quad (5.5)$$

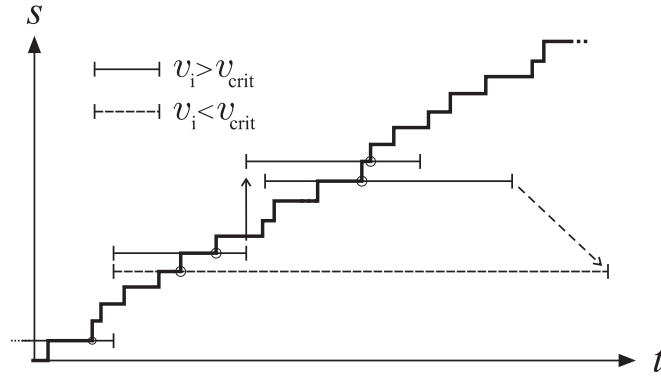


Figure 5.3: The collision sequence $s(t)$ and the collision cycles: the step function $s(t)$ is the total number of collisions in the entire N -particle system until time t . The horizontal solid and dashed bars symbolize the collision cycles for scattering and bound pairs respectively. For the derivation is important that overlapping cycles affect different pairs of particles. The dashed arrow indicates a third particle that hits and breaks up a bound two-particle state.

with $\delta = \frac{r_{\text{crit}}}{r_{\text{crit}} - d}$ and $w = \frac{v_i}{v_{\text{cb}}}$. This function is plotted as inset in Fig. 5.2. Much more concise is the corresponding function for the Minimal Capillary Model:

$$v_{\text{crit}}(b) = \frac{v_{\text{cb}}}{\sqrt{1 - \frac{b^2}{r_{\text{crit}}^2}}}. \quad (5.6)$$

In the following sections including the main results (5.40)-(5.43) of this chapter, we shall be completely general without the need to specify for the Minimal or Extended Capillary Model.

5.3 How to Relate the Two-Particle System to the N -Particle System

In the previous section we have shown how on the level of two-particle interactions the most important property of the real wet granular gas, namely the hysteretic binding and breaking of liquid bridges, can be modeled. Further, we have seen that the bond energy of the liquid bridge gives rise to the sticking of particles. In this section we treat the many-particle system.

Let ν denote the mean collision frequency per particle. If the modulus of the initial relative velocity v_i is lower than v_{crit} , so that particles stick together, the collision cycle is not terminated until a third particle bumps into the bound two-particle system. We assume that the outstate of such a three-particle event contains free particles, because the formation of higher mass clusters is rare in the gas-like state (cf. Fig. 5.11). The pair interactions taking place in the N -particle system may be envisaged as shown in Fig. 5.3. The number of collisions up to time t is denoted by $s(t)$. Since $s(t)$ is strictly monotonic its inverse $t(s)$ exists. The collision rate of the system, $s/t(s)$, tends for $s \rightarrow \infty$ to $N\nu/2$ (each collision involves two particles). To have the steps visible Fig. 5.3 has been drawn for low N . The horizontal bars represent the concept of collision cycles introduced in the last section. There are two particles which are going to collide. As the beginning of the collision cycle we take the time when the last of these two particles has ruptured its liquid bridge connection to some previous collision partner. The collision cycle will end when these two particles rupture the liquid bridge between them. Thus a solid arrow in Fig. 5.3 shows that one of the particles which

just finished its collision cycle immediately begins another one. The dashed arrow indicates that a third particle (that came out of another collision cycle) ends a bound two-particle state.

With this picture in mind the computation of the KS entropy can be tackled. As stated by Pesin's theorem the KS entropy equals the sum of all positive Lyapunov exponents, because the system is closed and sufficient chaotic [170, 171]. Lyapunov exponents describe the rate at which a certain direction in phase space grows or shrinks for large times. There is a orthogonal set of Lyapunov vectors ξ_j describing the direction while the associated Lyapunov exponent λ_j describes the exponential rate

$$\xi_j(t) \simeq \xi_j(0) e^{\lambda_j t} \quad (5.7)$$

for long times t . According to the sign of λ_j one speaks of stable and unstable directions. The deviations in the initial conditions are infinitesimal small, i.e. the Lyapunov exponents characterize the tangent space map associated with a certain trajectory. In an ergodic system the Lyapunov spectrum $\{\lambda_j\}$ is independent of the trajectory according to Oseledec's theorem [164, 165]. There is no doubt about the ergodicity of the gas of $N \gg 1$ hard spheres [202].

Since in a dilute system the free flight time and the mean free path are large compared to the interaction time and the range r_{crit} of the interaction, perturbations of velocities are amplified as compared to spatial deviations [226]. This is not to be understood as a neglect of the spatial Lyapunov exponents. The Capillary Model is symplectic (cf. Chap. 4), so that for each positive exponent λ_j there is a negative exponent $\lambda_k = -\lambda_j$ and the fact that the spatial deviations remain small means that the spatial directions mainly contain negative Lyapunov exponents, while the positive ones are assigned to velocities. So the conjecture is that the velocity space coincides (approximately) with the unstable manifold of the system. Based on this conjecture the KS entropy, h_{KS} , is given by the logarithmic volume growth rate in velocity space:

$$h_{\text{KS}} = \lim_{s \rightarrow \infty} \frac{1}{t(s)} \ln \left| \det \prod_{i=1}^s M_i \right|. \quad (5.8)$$

The deviation matrix M_i of the i 's collision cycle is restricted to velocity space, so that it describes the evolution of velocity perturbations. There are three crucial points here: (i) This limit exists by virtue of Oseledec's multiplicative ergodic theorem [164, 165]. (ii) We have an unique collision sequence. (iii) Although there are pair interactions occurring with time overlaps, there is no ordering problem when writing down the total deviations as a product of collision cycles, because the coexisting liquid bridge interactions affect always disjoint pairs (by the assumption that there are two-particle clusters only) and deviation matrices of disjoint pairs commute. Therefore the matrices M_i can describe the full collision cycle of a single pair of particles, ignoring all other interactions taking place simultaneously in the N -particle system. This temporal decomposition has also been discussed in the context of Fig. 4.15 in the last chapter. Our approach differs from [226], because the Capillary Model has a hysteretic interaction with finite interaction time. The dry limit follows by turning off the interaction, $E_{\text{cb}} \rightarrow 0$, as a special case.

The expression (5.8) can be simplified dramatically:

$$\begin{aligned}
\frac{h_{\text{KS}}}{N} &= \frac{1}{N} \lim_{s \rightarrow \infty} \frac{1}{t(s)} \ln \left| \det \prod_{i=1}^s M_i \right| \\
&= \frac{1}{N} \lim_{s \rightarrow \infty} \frac{1}{t(s)} \sum_{i=1}^s \ln |\det M_i| \\
&= \frac{1}{N} \lim_{s \rightarrow \infty} \frac{s}{t(s)} \frac{\sum_{i=1}^s \ln |\det M_i|}{s} \\
&= \frac{\nu}{2} \langle \ln |\det M| \rangle .
\end{aligned} \tag{5.9}$$

Herein the brackets $\langle \dots \rangle$ denote averaging over the two-particle phase space only.

Since we expect the Lyapunov exponents to be of the order of the collision frequency ν , they are (according to the limit in (5.8)) only well-defined if we let the system evolve for a time

$$t_{\text{Lyapunov}} \gg \frac{1}{\nu} = t_{\text{coll}} .$$

In the subsequent discussion we will point out that this can be fulfilled even if there was no external driving mechanism to keep the dissipative system in a stationary state. Clearly, without a thermostat the system cools, $\dot{T} < 0$, [241, 80]. The collision frequency ν is of the order $|\dot{T}|/E_{\text{cb}}$. On the other hand, cooling will be irrelevant on time scales below $t_{\text{cool}} = T/|\dot{T}|$. So the hierarchy

$$t_{\text{coll}} \ll t_{\text{Lyapunov}} \ll t_{\text{cool}}$$

of time scales can be fulfilled if

$$E_{\text{cb}} \ll T . \tag{5.10}$$

This implies that for weak liquid bridges as compared to the thermal energy we may speak of a Lyapunov spectrum independently from the question of the thermostat. No additional limitation is set, since the condition (5.10) is already required to be consistent with the gas state (displaying mainly single particles instead of clusters as confirmed by the simulation in Fig. 5.11) which is studied in this chapter.

Two tasks remain. The determination of the probability distribution for the formula (5.9) is done in the next section. To make use of momentum conservation the subspace is spanned by the center of mass position $\vec{R} \equiv \frac{\vec{r}_1 + \vec{r}_2}{2}$ and velocity $\vec{V} \equiv \frac{\vec{v}_1 + \vec{v}_2}{2}$ of the two-particle system, as well as the distance $\vec{r} \equiv \vec{r}_1 - \vec{r}_2$ between the centers of the spheres and their relative velocity $\vec{v} \equiv \vec{v}_1 - \vec{v}_2$. The last step is to compute for any spatial dimension D the matrix M appearing in (5.9), which maps for a specific point in the $4D$ -dimensional phase space $(\vec{R}, \vec{r}, \vec{V}, \vec{v})$ the initial velocity deviations

$$\begin{pmatrix} \delta \vec{V}_i \\ \delta \vec{v}_i \end{pmatrix}$$

from the beginning of the collision cycle to the final deviations

$$\begin{pmatrix} \delta \vec{V}_f \\ \delta \vec{v}_f \end{pmatrix} = M \begin{pmatrix} \delta \vec{V}_i \\ \delta \vec{v}_i \end{pmatrix} \tag{5.11}$$

at the end of the collision cycle. This is done in Sec. 5.5.

Before we derive the joint probability density a comment on the velocity distribution itself is in order. It is well-known that for dissipative gases the velocity distribution can deviate

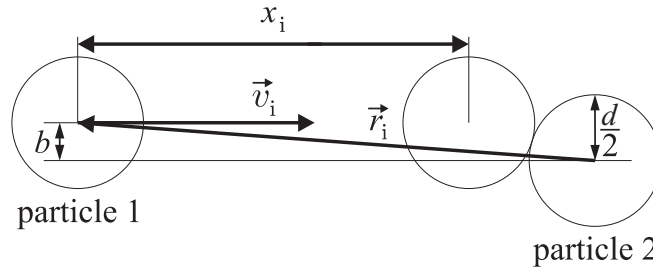


Figure 5.4: The relative coordinate system with respect to particle 2.

from the Maxwell-Boltzmann velocity distribution [113] depending on the state and driving mechanism. For explicit results we shall use the Maxwell-Boltzmann velocity distribution,

$$\begin{aligned}
 P(v_1, v_2) d^D v_1 d^D v_2 &= \left(\frac{\alpha}{\pi}\right)^D e^{-\alpha(v_1^2 + v_2^2)} d^D v_1 d^D v_2 \\
 &= \left(\frac{\alpha}{\pi}\right)^D e^{-\alpha(2V_i^2 + \frac{1}{2}v_i^2)} d^D V_i d^D v_i \\
 &= P(V_i, v_i) d^D V_i d^D v_i
 \end{aligned} \tag{5.12}$$

with $\alpha = \frac{m}{2T}$. The result for the KS entropy will also be given in a form that is readily evaluated for any velocity distribution. For the distribution (5.12) the modulus v_i of the initial relative velocity is distributed according to

$$P(v_i) dv_i = \frac{2 \left(\frac{\alpha}{2}\right)^{\frac{D}{2}}}{\Gamma\left(\frac{D}{2}\right)} v_i^{D-1} e^{-\frac{\alpha}{2}v_i^2} dv_i. \tag{5.13}$$

5.4 The Ensemble Average

We determine the probability distribution for two particles under the condition that they will collide in the future. Therefore we depict the initial configuration of an arbitrary pair of particles in relative coordinates $\vec{r}_i = \vec{r}_1 - \vec{r}_2$ as follows (Fig. 5.4): we rotate our coordinate frame such that the horizontal axis is per definition

$$\vec{e}_x \equiv \frac{\vec{v}_i}{v_i}, \tag{5.14}$$

with the initial relative velocity $\vec{v}_i = \vec{v}_1 - \vec{v}_2$. This means that particle 2 rests in the origin while particle 1 moves horizontally to the right. Clearly, the particles will collide if and only if

- (i) the impact parameter is low enough,
$$b = \sqrt{r_i^2 - \left(\vec{r}_i, \frac{\vec{v}_i}{v_i}\right)^2} \leq d,$$
- (ii) and particle 1 is to the left of particle 2,
$$(\vec{r}_i, \vec{v}_i) < 0.$$

For any pair of velocities \vec{v}_1, \vec{v}_2 , there are initial relative spatial positions that lead to a collision. So we have to integrate over the entire velocity space $\mathbb{R}^D \times \mathbb{R}^D$,

$$\left(\frac{\alpha}{\pi}\right)^D \int_{\mathbb{R}^D} d^D v_1 \int_{\mathbb{R}^D} d^D v_2 e^{-\alpha(v_1^2 + v_2^2)}. \tag{5.15}$$

We take condition (i) into account by integrating the impact parameter over the interval $[0, d]$. From the conventional assumption of molecular chaos (i.e. the positions and velocities of two particles are uncorrelated) follows that the impact is uniformly distributed within the cross section,

$$P(b) db = (D-1) \frac{b^{D-2} db}{d^{D-1}}, \quad 0 < b < d. \quad (5.16)$$

Further, we need to know the horizontal distance $x_i > 0$ to the collision point. Together with the impact parameter b this determines the relative spatial position completely in the plane of incidence, since according to (ii), $\vec{r} = b \vec{e}_y - (x_i + \sqrt{d^2 - b^2}) \vec{e}_x$ always points to the left.

The probability distribution of x_i follows from the distance covered by the particles in the laboratory frame. Denoting by x_1 and x_2 the length that particle 1 and 2, respectively, have traveled in the laboratory frame since the beginning of the collision cycle, we have the equal time condition

$$\frac{x_1}{v_1} = t_{\text{free}} = \frac{x_2}{v_2}, \quad (5.17)$$

where t_{free} stands for the time of free flight that both particles have in common. From this follows for the initial separation of particles

$$x_i = v_i t_{\text{free}} = \frac{v_i}{v_1} x_1. \quad (5.18)$$

The probability density of the traveled distances x_1 and x_2 are known in a gas to be

$$e^{-x_j/l} \frac{dx_j}{l}, \quad j = 1, 2. \quad (5.19)$$

The length scale l is the mean free path in the laboratory frame. Hence, under the assumption of molecular chaos the probability density of the initial separation x_i is

$$\begin{aligned} P(x_i | v_1, v_2) &= C \int_0^\infty \frac{dx_1}{l} \int_0^\infty \frac{dx_2}{l} e^{-(x_1+x_2)/l} \\ &\quad \times \delta\left(x_i - x_1 \frac{v_i}{v_1}\right) \delta\left(\frac{x_1}{v_1} - \frac{x_2}{v_2}\right) \\ &= C' e^{-\frac{x_i}{l} \frac{v_1+v_2}{v_i}} \end{aligned} \quad (5.20)$$

up to a normalization factor. Obviously this yields the integration

$$\frac{v_1 + v_2}{v_i} \int_0^\infty \frac{dx_i}{l} e^{-\frac{x_i}{l} \frac{v_1+v_2}{v_i}} \quad (5.21)$$

as part of the ensemble average. Putting (5.15), (5.16) and (5.21) together we can compute arbitrary expectation values:

$$\begin{aligned} \langle \dots \rangle &= (D-1) \left(\frac{\alpha}{\pi}\right)^D \int_{\mathbb{R}^D} d^D v_1 \int_{\mathbb{R}^D} d^D v_2 \frac{v_1 + v_2}{v_i} \\ &\quad \times \int_0^d \frac{db}{d^{D-1}} b^{D-2} \int_0^\infty \frac{dx_i}{l} \\ &\quad \times e^{-\alpha(v_1^2+v_2^2) - \frac{x_i}{l} \frac{v_1+v_2}{v_i}} \dots \end{aligned} \quad (5.22)$$

with $v_i = \|\vec{v}_1 - \vec{v}_2\|$. In passing we take a look at the distribution of x_i in Fig. 5.5. The joint distribution (5.22) implies that x_i is approximately distributed according to an exponential fall off, as one may expect, because the distances in the laboratory frame follow such a law. However there are differences: the mean is lower, e.g. $\langle x_i \rangle \approx 0.71 l$ for $D = 2$, and the distribution falls off faster than exponentially for small x_i (cf. [226]).

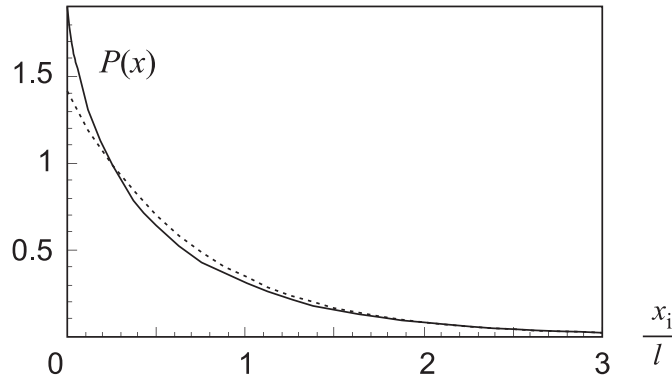


Figure 5.5: The distribution of x_i after averaging out the velocities. The dashed curve is an exponential distribution with the same mean. Clearly $P(x_i)$ deviates from an exponential at distances x_i below the mean free path l .

5.5 The Expansion of Velocity Space

We aim to compute the determinant of the matrix M as defined by Eq. (5.11). There are always two distinct deviation matrices M_{bound} for $v_i < v_{\text{crit}}$ and M_{scatt} for $v_i > v_{\text{crit}}$, so that the phase space average naturally decomposes into

$$\begin{aligned} \langle \ln |\det M| \rangle &= \langle \ln |\det M_{\text{bound}}| \rangle_{v_i < v_{\text{crit}}} \\ &+ \langle \ln |\det M_{\text{scatt}}| \rangle_{v_i > v_{\text{crit}}} . \end{aligned}$$

After determining these matrices, Eq. (5.9) will enable us to compute

$$\frac{h_{\text{KS}}}{N} = \frac{\nu}{2} \left[\langle \ln |\det M_{\text{bound}}| \rangle_{v_i < v_{\text{crit}}} + \langle \ln |\det M_{\text{scatt}}| \rangle_{v_i > v_{\text{crit}}} \right] . \quad (5.23)$$

Because of momentum conservation, $\vec{V}_i = \vec{V}_f$, the matrix M is of the blocked form

$$M = \begin{pmatrix} \mathbf{1}_D & \Theta_D \\ \Theta_D & M' \end{pmatrix} ,$$

where $\mathbf{1}_D$ and Θ_D are unity and zero matrices of dimension $D \times D$ respectively. Therefore the only contribution to the growth in velocity space stems from the relative velocities,

$$\det M = \det M' . \quad (5.24)$$

The final relative velocity ³ is

$$\vec{v}_f = \sqrt{v_i^2 - v_{\text{cb}}^2} (\cos \vartheta \vec{e}_x + \sin \vartheta \vec{e}_y) . \quad (5.25)$$

As defined in (5.14) \vec{e}_x points in the direction of the incoming velocity and $\vec{e}_y = \vec{e}_x \times \frac{\vec{r} \times \vec{v}_i}{\|\vec{r} \times \vec{v}_i\|} = \frac{\vec{r} v_i^2 - \vec{v}_i (\vec{r} \cdot \vec{v}_i)}{\|\vec{r} v_i^2 - \vec{v}_i (\vec{r} \cdot \vec{v}_i)\|}$ is the orthogonal vector spanning the plan of motion, such that

$$\vec{r} = -X_i \vec{e}_x + b \vec{e}_y$$

³Note that in this context v_{cb} is given by $mv_{\text{cb}}^2/4 = \phi + E_{\text{cb}}$ as a function of r for the case of sticking particles, when 'final' does not refer to the rupture event.

with $X_i = x_i + x_{\text{col}}$ and $x_{\text{col}} = -(\vec{r}_{\text{col}}, \vec{e}_x) = \sqrt{d^2 - b^2}$ is the x -distance of the particles in the moment of collision.

When considering deviations of (5.25) one has to take into account contributions due to the change of the angle ⁴ $\vartheta = \vartheta(b(\vec{r}, \vec{v}_i), v)$,

$$\delta\vartheta = \frac{\partial\vartheta}{\partial b}\delta b + \frac{\partial\vartheta}{\partial b} \frac{X_i}{v_i} \delta v_y + \frac{\partial\vartheta}{\partial v_i} \delta v_x, \quad (5.26)$$

as well as contributions caused by rotations and inclinations of the orbital plane of motion:

$$\begin{pmatrix} \delta\vec{e}_x \\ \delta\vec{e}_y \\ \delta\vec{e}_z \\ \vdots \end{pmatrix} = \begin{pmatrix} 0 & \frac{\delta v_y}{v_i} & \frac{\delta v_z}{v_i} & \cdots \\ -\frac{\delta v_y}{v_i} & 0 & \frac{X_i}{b} \frac{\delta v_z}{v_i} & \cdots \\ -\frac{\delta v_z}{v_i} & -\frac{X_i}{b} \frac{\delta v_z}{v_i} & 0 & \cdots \\ \vdots & \vdots & \vdots & \ddots \end{pmatrix} \begin{pmatrix} \vec{e}_x \\ \vec{e}_y \\ \vec{e}_z \\ \vdots \end{pmatrix}. \quad (5.27)$$

The Eqs. (5.26) and (5.27) hold for arbitrary spatial dimension D . The resulting deviation matrix M' is rather complicated:

$$M' = \begin{pmatrix} \frac{\cos\vartheta}{\epsilon} - \epsilon v_i \vartheta_v \sin\vartheta & -(1 + X_i \vartheta_b) \epsilon \sin\vartheta & 0 & \cdots \\ \frac{\sin\vartheta}{\epsilon} + \epsilon v_i \vartheta_v \cos\vartheta & +(1 + X_i \vartheta_b) \epsilon \cos\vartheta & 0 & \cdots \\ 0 & 0 & \epsilon \left(\cos\vartheta + \frac{X_i}{b} \sin\vartheta \right) & 0 \cdots \\ \vdots & \vdots & 0 & \epsilon \left(\cos\vartheta + \frac{X_i}{b} \sin\vartheta \right) \\ & & \vdots & \ddots \end{pmatrix} \quad (5.28)$$

with the restitution coefficient (5.3) and the abbreviations $\vartheta_b \equiv \frac{\partial\vartheta}{\partial b}$, $\vartheta_v \equiv \frac{\partial\vartheta}{\partial v}$. The determinant of M (which equals M' , cf. Eq. (5.24)) is surprisingly simple:

$$\det M = \left(-1 + x_i \frac{\partial\vartheta}{\partial b} \right) \left(1 - \frac{v_{\text{cb}}^2}{v_i^2} \right)^{\frac{D}{2}-1} \times \left(1 + \frac{x_i}{b} \sin\vartheta \right)^{D-2}, \quad (5.29)$$

where we eliminated $x_{\text{coll}} \ll x_i$ using

$$\begin{aligned} x_{\text{coll}} \vartheta_b &\approx -2 \\ \frac{x_{\text{coll}}}{b} \sin\vartheta &\approx 2 - 2 \frac{b^2}{d^2} \\ \cos\vartheta &\approx 2 \frac{b^2}{d^2} - 1. \end{aligned}$$

This reduces in the dry case, $v_{\text{cb}} = 0$, to the expressions (18) ($D=2$) and (19) ($D=3$) in [226]. The first factor in (5.29) is always non-zero since $\frac{\partial\vartheta}{\partial b} < 0$.

5.6 Results for the Kolmogorov-Sinai Entropy

In Fig. 5.6 the relative dynamic $\vec{r}(t)$ (which equals the motion of one of the two particles in the center of mass system up to a factor of 2) is sketched. In both cases, the determinant of

⁴One has to distinguish between the variation of the function b (as given in item (i) on page 85), $\delta b(\vec{r}_i, \vec{v}_i) = \delta(\vec{r}_i, \vec{e}_y) = \delta b - \frac{X_i}{v_i} \delta v_y$, and $\delta b = (\delta\vec{r}_i, \vec{e}_y)$ as an opportune notation for the spatial deviation δy .

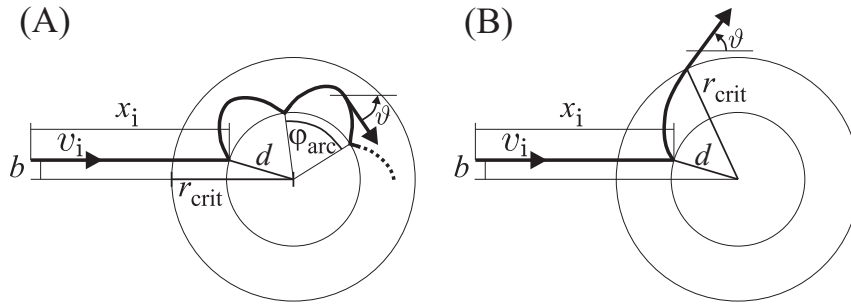


Figure 5.6: The relative motion for (A) sticking and (B) scattering.

M is of the form (5.29), but the meaning of the angle $\vartheta(b, v_i)$ is quite different. For impact velocities above the critical value, ϑ is the scattering angle

$$\begin{aligned} \vartheta_{\text{scatter}}(b, v_i) &= \pi - \arcsin \frac{b}{d} \\ &\quad - \arcsin \frac{b}{r_{\text{crit}} \sqrt{1 - \left(\frac{v_{\text{cb}}}{v_i}\right)^2}} \\ &\quad - \int_d^{r_{\text{crit}}} d\varphi_\phi(r), \end{aligned}$$

whereas for $v_i < v_{\text{critical}}$ the angle ϑ is a function of time,

$$\begin{aligned} \vartheta_{\text{bound}}(t_3, b, v_i) &= \frac{\pi}{2} - \arcsin \frac{b}{d} \\ &\quad - t_3 \frac{\varphi_{\text{arc}}(b, v_i)}{t_{\text{arc}}(b, v_i)} - \varphi_{\text{osc}}(t_3, b, v_i). \end{aligned}$$

Here t_3 denotes the time during which the two-particle systems remains bound until it is freed by a third particle. The angle between two contacts $\varphi_{\text{arc}}(b, v_i)$ equals $2 \int_d^{r_{\text{max}}(b, v_i)} d\varphi_\phi(r)$ and there is a similar integral for the time t_{arc} it takes to run through one arc. The index ϕ ought to remind us that the potential (5.2) enters only through these integral expressions. For $t_3 \gg t_{\text{arc}}$ the angle ϑ_{bound} grows linearly with time, while the bound oscillations φ_{osc} are negligible.

Depending on the details of the interaction potential, φ_{arc} and t_{arc} can grow beyond all bounds as the pair (b, v_i) approaches the critical line $(b, v_{\text{crit}}(b))$ (cf. Fig. 5.2) in the bound regime (from below). This singular behavior occurs in the Extended Capillary Model (linear force, Fig. 5.1), whereas in the Minimal Capillary Model (constant force) both quantities remain finite. Close to the divergence the motion is an outward directed spiral, so that the turning point is never reached and the periodic collisions end. The interaction time can also diverge for scattering states (reaching the critical line in Fig. 5.2 from top), but this singularity is integrable with respect to velocity. In the bound case the divergence is cut off by the third particle and because of angular momentum conservation we have the estimate

$$\vartheta_{\text{bound}}(t_3, b, v_i) \leq \text{const} + \frac{t_3 b v_i}{d^2}. \quad (5.30)$$

We will use the right-hand side as an approximation. The stopping time t_3 is a random variable itself and distributed according to

$$\frac{V_i}{l'} e^{-\frac{v_i}{l'} t_3} dt_3, \quad (5.31)$$

for a given center of mass velocity V_i of the bound system. There is a smaller mean free path l' for the bound two-particle system: since its total cross section changes with time the effective diameter d_{eff} is $\frac{3}{2}d$ so that the mean center-center distance at contact is $\frac{5}{4}d$. Another factor of $\sqrt{\frac{2}{3}}$ is caused by the mass ratio [97], thus

$$l' = \left(\frac{4}{5}\right)^{D-1} \sqrt{\frac{2}{3}} l. \quad (5.32)$$

In the following, we shall evaluate averages that are linear in t_3 , so that we can forthwith substitute the expectation value, $\bar{t}_3 = \frac{l'}{V_i}$, of the distribution (5.31). Then from (5.30) follows

$$\frac{\partial \vartheta_{\text{bound}}}{\partial b}(v_i) \approx \frac{v_i l'}{V_i d^2}. \quad (5.33)$$

In both cases, binding and scattering, $\frac{\partial \vartheta}{\partial b}$ is at least of the order of $\frac{1}{d}$, while x_i is of the order of the mean free path

$$l = \frac{\Gamma\left(\frac{D+1}{2}\right)}{\sqrt{2\pi}^{\frac{D-1}{2}}} (d^{D-1} n)^{-1}, \quad (5.34)$$

with n being the number density of grains. Formulas for the mean free path are well established [35] and other characteristic quantities for the motion of tracer particles are also available [97]. We remark that investigating the trajectories of tracer particles is a promising technique for the experimental confirmation of results presented in this chapter.

Our goal is to expand the KS entropy in the small dimensionless parameter $nd^D \ll 1$. So this is an expansion for the dilute wet granular system. The unity in the first and the last factor in (5.29) contributes to the KS entropy only in linear and higher orders, while we are interested in the logarithmic and zeroth order terms:

$$\begin{aligned} |\det M| &= x_i \left| \frac{\partial \vartheta}{\partial b} \right| \left(1 - \frac{v_{\text{cb}}^2}{v_i^2} \theta(v_i - v_{\text{crit}}) \right)^{\frac{D}{2}-1} \\ &\times \left(\frac{x_i}{b} \sin \vartheta \right)^{D-2}. \end{aligned} \quad (5.35)$$

With the step function θ , Eq. (5.35) is valid for scattering and binding, because we assume that the collision with the third particle rethermalize the two-particle system, so that the next collision cycle starts with the same initial distribution. This is to say that the third particle is regarded as a signal to break the bound state, as is shown in relative coordinates in Fig. 5.7. Since the 'third' particles have an energy of the order of the granular temperature $T \gg E_{\text{cb}}$ we can safely neglect the formation of bound states of three or more particles (cf. Fig. 5.11). A cluster size expansion will be discussed at the end of this section.

After introducing the appropriate length scales l and d we are lead to examine

$$\begin{aligned} \frac{h_{\text{KS}}}{N} &= \frac{\nu}{2} \left[(D-1) \ln \frac{l}{d} - (D-2) \left\langle \ln \frac{b}{d} \right\rangle \right. \\ &+ (D-1) \left\langle \ln \frac{x_i}{l} \right\rangle \\ &+ \left\langle \ln \left(d \left| \frac{\partial \vartheta_{\text{bound}}}{\partial b} \right| \right) \right\rangle_{v_i < v_{\text{crit}}} \\ &+ \left\langle \left(\frac{D}{2} - 1 \right) \ln \epsilon + \ln \left(d \left| \frac{\partial \vartheta_{\text{scatt}}}{\partial b} \right| \right) \right\rangle_{v_i > v_{\text{crit}}} \\ &+ (D-2) \langle \ln |\sin \vartheta| \rangle \left. \right]. \end{aligned} \quad (5.36)$$

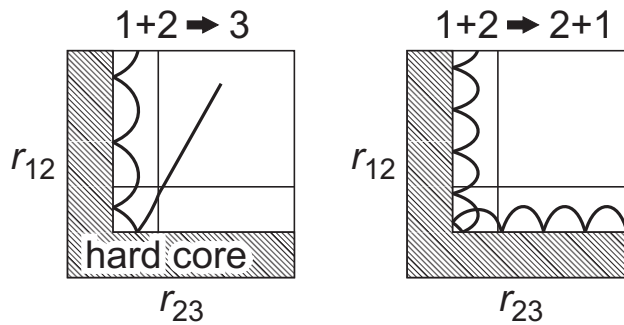


Figure 5.7: The left panel shows the typical case at gas temperatures $T \gg E_{cb}$: a bound state is broken by a third particle. In the computation we use the collision between a bound state and a third particle as the event which terminates the bound state. The possibility shown in the right panel, to have a bound states in the final state after a collision, is exponentially rare at high temperature.

The first two terms in the square bracket yield

$$-\ln nd^D - C_D, \quad (5.37)$$

with a numerical constant $C_D = \frac{D-1}{2} \ln 2 + \frac{(D-1)^2}{2} \ln \pi - \frac{D-2}{D-1} - (D-1) \ln \Gamma\left(\frac{D+1}{2}\right)$. This is independent of the ensemble average and the interaction potential.

If x_i was distributed exponentially with mean l , the third term in (5.36) would give rise to the negative of Euler's constant, $-\gamma_{\text{Euler}} \approx -0.5772$, independent of the dimensionality of the problem. As discussed before, lower values of x_i are favored. That is why we find by numerical computation a lower expectation value, e.g. for $D = 2$:

$$\left\langle \ln \frac{x_i}{l} \right\rangle \approx -1.01. \quad (5.38)$$

The fourth term in (5.36) is (cf. Eq. (5.33))

$$\begin{aligned} & \left\langle \ln \left(d \left| \frac{\partial \vartheta_{\text{bound}}}{\partial b} \right| \right) \right\rangle_{v_i < v_{\text{crit}}} \\ &= - \left(\ln nd^D + \tilde{C}_D \right) \langle 1 \rangle_{v_i < v_{\text{crit}}} \\ & \quad + \left\langle \ln \frac{v_i}{V_i} \right\rangle_{v_i < v_{\text{crit}}}, \end{aligned} \quad (5.39)$$

with the numerical constant $\tilde{C}_D = (D-1) \ln \frac{5}{4} + \frac{\ln 3}{2} + \frac{D-1}{2} \ln \pi - \ln \Gamma\left(\frac{D+1}{2}\right)$.

Together with (5.37) the logarithm $\ln nd^D$ herein forms the leading term of the density expansion. Therefore the logarithm $\ln nd^D$ in (5.39) is a correction of the leading term as it is known for the dry case [226]. The KS entropy has the following density expansion:

$$\frac{h_{\text{KS}}}{N} = -\nu A_D \ln nd^D + \nu B_D + \mathcal{O}(nd^D), \quad (5.40)$$

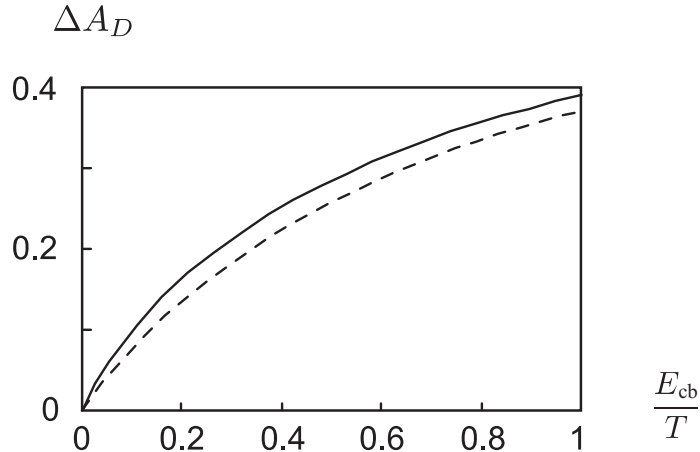


Figure 5.8: The increase $\Delta A_D = \frac{P_{\text{bound}}}{2}$ of the leading coefficient $A_D = \frac{D-1}{2} + \Delta A_D$: The solid line is for two, the dashed line for three dimensions D . Since $A = \frac{D-1}{2}$ in the absence of the liquid bridge interaction we recover the result for dry granulates as a special case. With the approximation for the wet granular gas used in the derivations one is restricted to temperatures above the bridge energy E_{cb} . Otherwise the method applied has to be extended to take clusters of more than two particles sticking together into account. The far extreme case, $E_{\text{cb}} \gg T$, is known as the so-called sticky gas.

with the leading coefficient

$$\begin{aligned}
 A_D &= A_D \left(\frac{E_{\text{cb}}}{T}, \frac{r_{\text{crit}}}{d} \right) \\
 &= \frac{D-1}{2} + \frac{D-1}{\Gamma(\frac{D}{2})} \left(\frac{m}{4T} \right)^{\frac{D}{2}} \\
 &\quad \times \int_0^d \frac{db}{d^{D-1}} b^{D-2} \int_0^{v_{\text{crit}}(b)} dv v^{D-1} e^{-\frac{m}{4T}v^2}, \quad (5.41)
 \end{aligned}$$

and the density independent part

$$\begin{aligned}
 B_D &= \frac{1}{2} \left[-C_D + (D-1) \langle \ln \frac{x_i}{l} \rangle - \tilde{C}_D \langle 1 \rangle_{v_i < v_{\text{crit}}} \right. \\
 &\quad \left. + \langle \ln \frac{v_i}{V_i} \rangle_{v_i < v_{\text{crit}}} + \langle \ln \left(d \left| \frac{\partial v_{\text{scatt}}}{\partial b} \right| \right) \rangle_{v_i > v_{\text{crit}}} \right. \\
 &\quad \left. + (D-2) \left(\frac{\langle \ln \epsilon \rangle_{v_i > v_{\text{crit}}}}{2} + \langle \ln |\sin \vartheta| \rangle \right) \right]. \quad (5.42)
 \end{aligned}$$

The general form of the leading term, valid for any velocity distribution, is

$$A_D = \frac{D-1}{2} + \frac{P_{\text{bound}}}{2}. \quad (5.43)$$

We want to emphasize that so far all results of this section are general with respect to the spatial dimensionality of the problem and the details of the particle interaction. The probability $P_{\text{bound}} = \langle 1 \rangle_{v_i < v_{\text{crit}}}$ in (5.43) is given by integrating velocity and impact factor over the bound states in Fig. 5.2. Only here the detailed interaction models (5.5) and (5.6) enter the problem. The velocity distribution for this integration may also be taken directly from an experiment, as the one described in Chap. 9.

Let us now turn to explicit results. For the Gaussian velocity distribution (5.13) and odd spatial dimensions the velocity integral of P_{bound} is an incomplete Gamma function. In even dimensions the integral is elementary, yielding for $D = 2$

$$A_2(\varepsilon, \gamma) = 1 - \frac{1}{2} \int_0^1 dx e^{-\varepsilon f(x, \gamma)}, \quad \varepsilon = \frac{E_{\text{cb}}}{T},$$

as a function of the bridge energy over granular temperature, ε , and the wetting content, $\gamma = r_{\text{crit}}/d \geq 1$. The remaining integration variable is the impact parameter, $x = b/d$. The excess of the critical energy over the bridge energy, $f(x, \gamma) = E_{\text{crit}}/E_{\text{cb}}$, depends on the model details. In the Minimal Capillary Model from Eq. (5.6) follows

$$f(x, \gamma) = \left(1 - \frac{x^2}{\gamma^2}\right)^{-1}.$$

The coefficient A_D of the Minimal Capillary Model is plotted in Fig. 5.8 as a function of the liquid bridge energy for two and three dimensions. Very similar curves follow from the Extended Capillary Model. For the plot the limit of short liquid bridges, $r_{\text{crit}} = d$, was chosen. This corresponds to a small amount of liquid that is just sufficient to wet the surface roughness of realistic spheres. Independent of $r_{\text{crit}}/d \geq 1$, in the dry limit (or equivalently the high temperature limit) A_D approaches $(D - 1)/2$, which is the known result for hard spheres [226]. For a higher content of wetting liquid, $r_{\text{crit}}/d > 1$, the dependence of the leading term on the binding energy becomes flatter, but in an experimental situation there is a simultaneous gain in E_{cb} when liquid is added. Varying the surface tension of water by adding a salt to the wetting solution is an experimentally feasible way to measure this curve directly with a fixed amount of wetting liquid, such that r_{crit}/d can be kept constant and E_{cb} increases according to Eq. 3.10.

From this graph we see the sensitive dependence of the KS entropy on the cohesion force of the wetting liquid. To gain analytic insight we investigate exemplarily the two-dimensional case plotted. Substituting $z = 1/(1 - x^2)$ gives

$$A_2(\varepsilon, 1) = 1 - \frac{1}{4} \int_1^\infty \frac{dz}{z^2} \frac{e^{-\varepsilon z}}{\sqrt{1 - 1/z}} \quad (5.44)$$

Splitting up the integration at $z = 1/\varepsilon$ allows to separate the non-analytic part.

$$\begin{aligned} A_2(\varepsilon, 1) = 1 & - \frac{\varepsilon}{4} \int_1^\infty \frac{dz}{z^2} \frac{e^{-z}}{\sqrt{1 - \varepsilon/z}} \\ & - \frac{1}{4} \int_1^{\frac{1}{\varepsilon}} \frac{dz}{z^2} \frac{e^{-\varepsilon z}}{\sqrt{1 - 1/z}} \end{aligned} \quad (5.45)$$

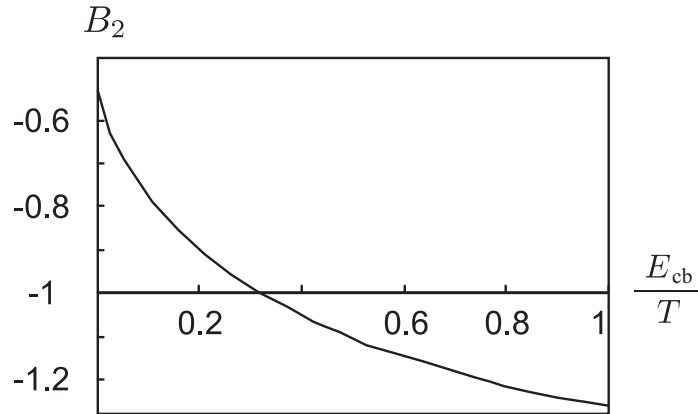
The first integral in (5.45) can be expanded in powers of $\varepsilon \in [0, 1)$ since $z > 1$. The second integral equals 2 for $\varepsilon \rightarrow 0$, while its first derivative has a logarithmic divergence:

$$A_2(\varepsilon, 1) = \frac{1}{2} + \varepsilon \left(C - \frac{\ln \varepsilon}{4} \right) + \mathcal{O}(\varepsilon^2). \quad (5.46)$$

The constant C is $\int_1^\infty \exp(-z)/4z + \ln 2/2 + (1 - 1/e)/4 \approx 0.56$. This shows that the slope of A_2 is vertical at $E_{\text{cb}} = 0$.

Let us finally look at the next higher order term B_D of the density expansion. For simplicity we restrict ourselves to the case $D = 2$, so that

$$\begin{aligned} B_2 = & \frac{1}{2} \left[-C_2 + \left\langle \ln \frac{x_i}{l} \right\rangle - \tilde{C}_2 \langle 1 \rangle_{v_i < v_{\text{crit}}} + \left\langle \ln \frac{v_i}{V_i} \right\rangle_{v_i < v_{\text{crit}}} \right. \\ & \left. + \left\langle \ln \left(d \left| \frac{\partial \vartheta_{\text{scatt}}}{\partial b} \right| \right) \right\rangle_{v_i > v_{\text{crit}}} \right]. \end{aligned} \quad (5.47)$$


 Figure 5.9: The coefficient B_2 of the density expansion (5.40).

The last term in (5.47) is exactly equal to unity in the limit of dry granulates,

$$\begin{aligned} & \lim_{E_{cb} \rightarrow 0} \left\langle \ln \left(d \left| \frac{\partial \vartheta_{\text{scatt}}}{\partial b} \right| \right) \right\rangle_{v_i > v_{\text{crit}}} \\ &= \int_0^d \frac{db}{d} \ln \frac{2}{\sqrt{1 - (b/d)^2}} = 1, \end{aligned}$$

but decreases as the critical velocity increases when we turn on the liquid bridge interaction. The coefficient B_2 for the zeroth order in the expansion (5.40) is plotted in Fig. 5.9.

It is known for the dry limit [226], that the accordance of B_D with numerical simulation cannot keep up with the successful confirmation of A_D . The origin of this discrepancy is the assumption that the unstable manifold coincides with velocity space and it is quite involved to improve on that [50]. In the dry limit our method yields $B_2 = -0.52(8)$, which is lower than the analytical estimate ($B_2 = 0.1045$) and the simulated result ($B_2 = 0.679$) of [226].

From the knowledge of the coefficients A_D and B_D follows the KS entropy in the dilute system for various wetting contents as shown in Fig. 5.10 for $D = 2$.

The Cluster Expansion

In Eq. (5.23) we considered events including bound states of two particles ($a + b + c \rightarrow ab + c \rightarrow a + b + c$) and scattering events ($a + b \rightarrow a + b$) by writing

$$\begin{aligned} \langle \ln |\det M| \rangle &= \langle \ln |\det M_{\text{bound}}| \rangle_{v_i < v_{\text{crit}}} \\ &+ \langle \ln |\det M_{\text{scatt}}| \rangle_{v_i > v_{\text{crit}}} . \end{aligned} \quad (5.48)$$

The first term is proportional to P_{bound} which led to Eq. (5.43). Here we wish to point out how to generalize the computation of the KS entropy to include clusters of higher particle number. All equalities in (10) hold for arbitrary types of events, when M_i denotes the deviation matrix associated with the i th event and ν is the generalized event frequency. Referring to the event type by T we reorder the averaging. Collecting the events of type T by introducing $\delta_{\text{type}(j),T}$ (which is unity for an event T and otherwise zero) we write $\langle \dots \rangle_T$ for $\langle \dots \delta_{\text{type}(j),T} \rangle$:

$$\frac{2}{\nu N} h_{\text{KS}} = \langle \ln |\det M| \rangle = \sum_T \langle \ln |\det M_T| \rangle_T . \quad (5.49)$$

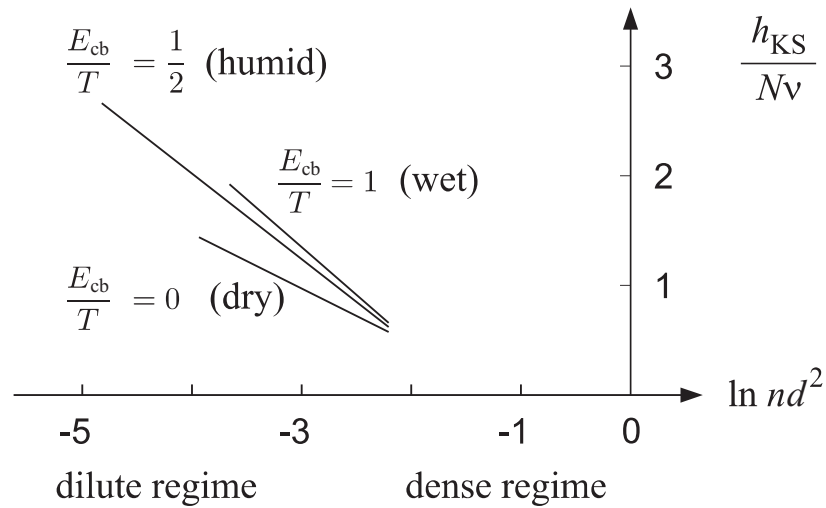


Figure 5.10: The two-dimensional KS entropy as a function of the density for three different bridge energies E_{cb} . This energy depends on the amount of wetting liquid added to the granular gas as is indicated in the plot. Another way to change E_{cb} is to add a salt or a surfactant.

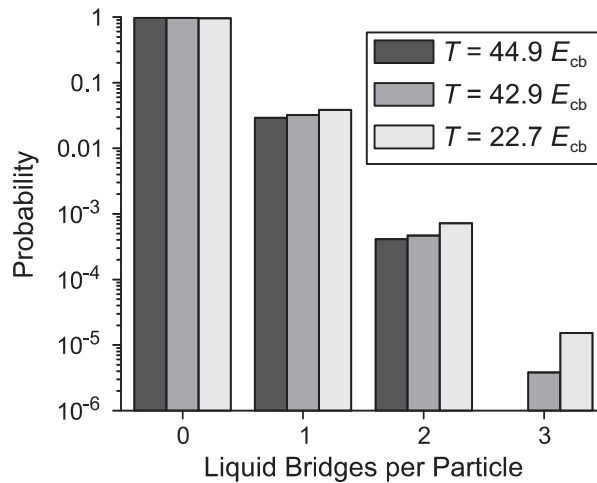


Figure 5.11: The probability for a sphere to have a certain number of liquid bonds ending on its surface. This distribution is derived from a three dimensional molecular dynamics simulation of a wet granular gas with an occupied volume fraction of 3.9%, which corresponds to $nd^3 = 0.074$. The granular temperature T has been varied as indicated. The probability for two liquid bridges ending on one particle, as necessary for a three-particle-cluster, is suppressed by more than three orders of magnitude. An analytic approach to the KS entropy is favorable because the direct numerical integration suffers from high computing times for the full tangent space dynamics and yields noisy results [239]. The liquid bond distribution shown is a robust and reliable single-particle quantity.

The summation can be written as a systematic expansion in the cluster size:

$$\left\{ \begin{array}{l} a + b \rightarrow a + b \\ \\ a + b + c \rightarrow ab + c \\ \\ \vdots \end{array} \right. \begin{array}{l} \rightarrow \\ \nearrow \\ \rightarrow \\ \searrow \\ \rightarrow \end{array} \left\{ \begin{array}{l} a + b + c \\ \\ \left\{ \begin{array}{l} ac + b \\ bc + a \\ ab + c \end{array} \right. \\ \\ abc \end{array} \right. \begin{array}{l} (T_1) \\ (T_2) \\ (T_3) \\ (T_4) \\ (T_5) \\ (T_6) \end{array}$$

with the events T_1 and T_2 considered before in (5.48). The events T_j with $j > 2$ result in new many-particle-clusters which are exponentially rare components of the wet granular gas as is evident from Fig. 5.11. We remark that the scattering of a bound state (T_5) prolongs the mean bond time t_3 to become $t'_3 = \alpha t_3$, with $\alpha = 1 + 2P_{T_5} + 3P_{T_5}^2 + \dots = 1/(1 - P_{T_5})^2$. The unity in front of this series corresponds to breaking the bound state in its first collision (T_2), the second term corresponds to one scattering event of the bound pair and the following terms to multiscattering. The contribution to the KS entropy is proportional to the logarithm of this time, $\ln t'_3 = \ln t_3 - 2 \ln(1 - P_{T_5})$. The first term $\ln t_3 \propto -\ln(nd^D)$ is the wet granular contribution to the leading coefficient A as identified in Eq. (44). The second term gives a correction to the B -coefficient which is of the order $P_{T_5} = \mathcal{O}(\sqrt{E_{cb}/T^3})$ for three dimensions.

This concludes our discussion of systems of two and higher spatial dimensionality. Before we turn to a general diagrammatic description of entropy production, it is pointed out in the following section why the case $D = 1$ has to be treated as an exceptional case for the computation of the KS entropy.

5.7 The One-Dimensional System as an Exceptional Case

Here we discuss why, contrary to what we might expect, the one-dimensional gas is more complex.

The ‘dry term’, $(D-1)/2$, in Eq. (5.43) predicts the correct result for one spatial dimension in the absence of the capillary interaction, namely zero KS entropy: After the coordination transformation $y_i = x_i - \sum_{k=1}^{i-1} d_k$, the particles transform to point-like objects. In collisions they exchange their velocities if they have equal masses, so that after renumbering, the particles can be regarded as moving ballistically. Obviously this *dry* system is integrable and has therefore all its Lyapunov exponents equal to zero, which implies $h_{KS} = 0$. Also the one-dimensional system with arbitrary masses is linearly (not exponentially) unstable with respect to perturbations of the initial conditions, so that the one-dimensional system is not chaotic until it is wetted.

We have seen in this chapter that the wetting liquid has a stronger influence in two dimensions (logarithmic divergence of the slope shown in Eq. (5.46)) than in three dimensions. In one spatial dimension the wet effect is even stronger, and of qualitative different nature. While the free cooling state presented in the following Chap. 6 inherits its randomness from the initial state, the thermostated steady state has to be sufficiently chaotic in order to be homogeneous without cluster growth. This is not fulfilled in one dimension. In the derivation for $D > 1$, we could assume that the high granular temperature prevents clustering in the stationary state due to the intrinsic chaoticity (for which reason the scenario on the left-hand side in Fig. 5.7 dominates for $D > 1$ dimensions). Yet in one dimension, a bound state cannot

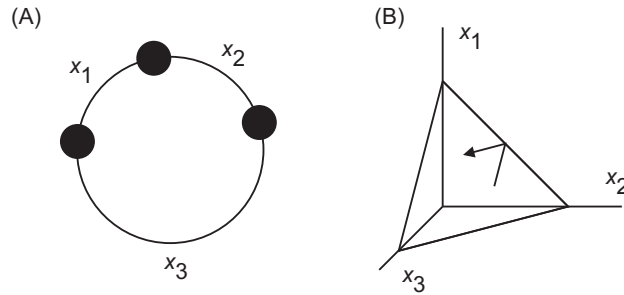


Figure 5.12: Without liquid bridges the 1D-system is equal to a triangular billiard, which is integrable. (A) shows an example of a three-particle system with periodic boundary conditions. (B) Plotting the relative coordinates x_j in Cartesian coordinates, the isochores dynamics is restricted to the triangular plane.

be broken up by a third particle. If the particle masses are too similar or even equal, Newton's cradle effect causes a simple exchange of the binding partners. For this reason the wet term in Eq. (5.43) gives the correct contribution from 2-clusters, however bigger clusters are not negligible for $D = 1$ even at $T \gg E_{cb}$.

One might think at first glance that here a numerical factor greater but still of the order of unity might be sufficient to describe the influence due to n -clusters for $n > 2$. This is not the case because there is a dramatic difference between a 2-cluster and a n -cluster for $n > 2$ from the point of view of dynamical systems. While a 2-cluster is an integrable subsystem, in any dimension and for all force laws⁵, already the one-dimensional 3-cluster forms a chaotic subsystem with positive Lyapunov exponents.

5.7.1 The Cluster-Internal Chaoticity

This chaoticity caused by the bridge interaction can be represented by an equivalent dynamical system as is shown in the Figs. 5.12 and 5.13. Figure 5.12 shows that a dry system of three particles, represented in relative coordinates x_j , is equivalent to a triangular billiard: system is constrained to the plane $\sum_j x_j = L$. Because of its flat boundaries the triangular billiard is integrable, and hence $h_{KS} = 0$. With the liquid bridge interaction, the stable clusters are located in the the wedges of this triangular billiard (cf. Fig. 5.13B). However, the trajectory is parabolic under the force of the capillary bridge. Therefore the system is equivalent to a single point particle which moves under gravity in the wedge (illustrated in Fig. 5.13C). This dynamical system has six degrees of freedom, four of which correspond to vanishing Lyapunov exponents due to conservation laws (as is explained in the context of the explicit numerical spectrum in the following paragraph). Because of the symplectic symmetry of the spectrum there is one pair of nonzero Lyapunov exponent, $(\lambda_1, -\lambda_1)$, and the KS entropy is $\lambda_1 > 0$. The generalization to $N > 3$ particles is straightforward: the configuration space is in general an $(N - 1)$ -simplex instead of the triangle for $N = 3$.

The full Lyapunov spectrum of a 1D system with $N = 10$ particles is computed numerically with an event-driven algorithm, and shown in Fig. 5.14. To measure the Lyapunov exponents, the system is kept in a stationary state by a Gaussian thermostat. The spectrum is computed by evolving not only the phase space trajectory, but also the tangent space dynamics, as derived in Sec. 4.6.1. After a certain number of collisions, the stability matrix M of the

⁵The two-body problem is, analogous to the Kepler problem, integrable in relative coordinates, as there is a sufficient number of first integrals of motion.

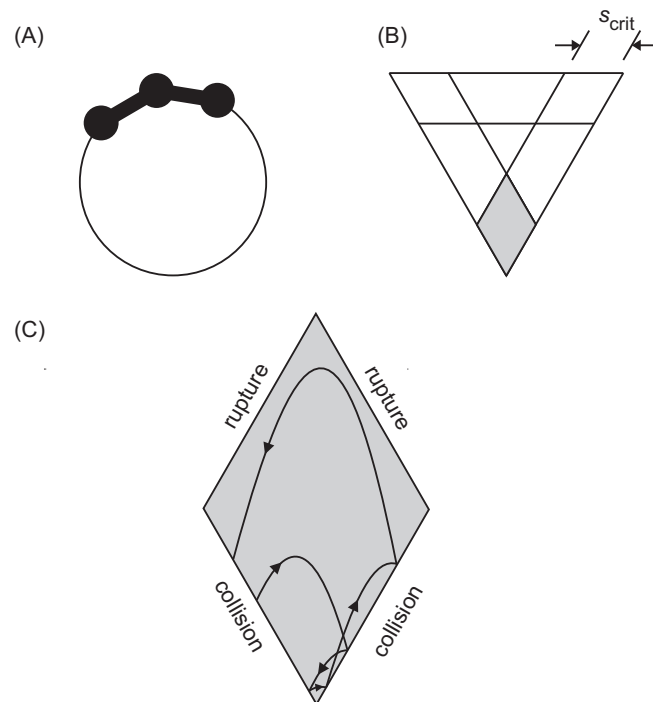


Figure 5.13: (A) With the liquid bridge interaction, the 3-clusters configurations are located in the wedges of the triangular configuration space. (B) One out the three possible cluster configuration is shown in gray. As long as the energy is insufficient to break a capillary bond, the system is equivalent to a single mass point moving ballistically in a wedge under gravity, as is shown in (C). With the parabola trajectories due to the capillary force, the system has one positive exponent, one negative (of equal magnitude), and four Lyapunov exponents equal to zero.

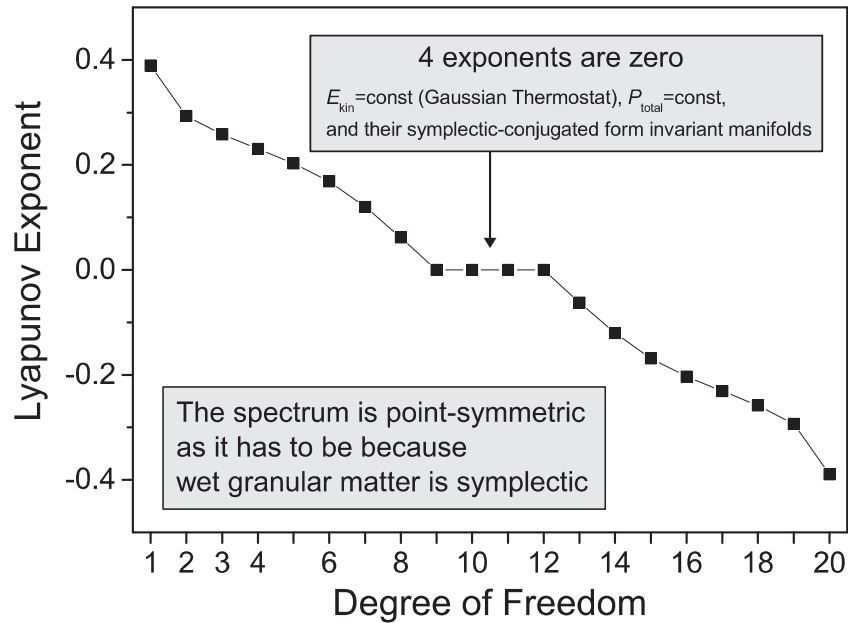


Figure 5.14: The Lyapunov spectrum of ten wet granular particles with a Gaussian thermostat in one spatial dimension under periodic boundary conditions.

deviations in tangent space has very large and very small value according to the stable and unstable directions. The matrix is QR -decomposed to retain the directions (the eigenvectors of $M^T M$) and the logarithmic growth rates, as discussed in Sec. 4.7. The tangent space evolution is continued with the eigenvectors as initial values, so that these eigenvectors are aligned to the stable and unstable manifolds in phase space. Since wet granular matter is symplectic, the Lyapunov spectrum is point-symmetric (cf. proof in 4.6.2), as is confirmed here numerically with high accuracy. Because of energy conservation (due to the thermostat) and momentum conservation (pair interaction under periodic boundary condition), we have two conserved quantities, and in addition their symplectic conjugated directions⁶ with vanishing growth. For this reason there are in total four Lyapunov exponents equal to zero. Note that this is not the case with the spectrum computed for the system driven by shaking boundaries in Sec. 4.7. Here all exponents are bounded away from zero, because the boundaries break translation invariance and energy is not constant but fluctuates (cf. 4.7), as investigated in detail in the context of the Fluctuation Theorem in the Secs. 4.3 and 4.4.

5.7.2 Remark on Numerical Techniques and the Dimensionality

While the liquid bridge coordination shown in Fig. 5.11 is a robust numerical quantity also for the time-driven simulation method, this is not the case for the sensitive Lyapunov spectrum of a many particle system for the following reason. The direct integration algorithm has to adapt the time steps to allow for an accurate integration of the extremely short contact repulsion. With these fine integration steps it takes extremely long until the system has explored its high dimensional phase space as is necessary for reliable Lyapunov spectra. Associated with the high number of integration steps is an increase of the numerical error. The superior event-driven technique can simulate the dynamics according to the Capillary Model of wet

⁶For energy conservation, the conjugated direction is the translation along the phase space trajectory itself. Cf. p. 24 in [94] on the relation between symmetry and vanishing exponents.

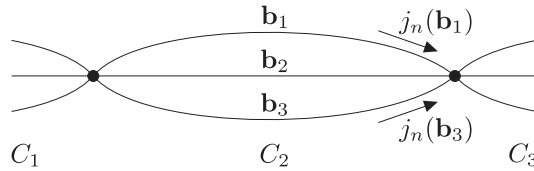


Figure 5.15: Topology of the state space. In this sketch the continuous part C is plotted to the right and the discrete part D extends vertically. The continuous parts C_σ are in general not one-dimensional so that the shown connectivity is a simplified example.

granular matter in one-dimension only. This stresses the significance of an analytic approach, as the one presented in this chapter for $D \geq 2$, while for $D = 1$ numerical methods are complementary.

5.8 A Diagrammatic Approach to Entropy Production

The general expression for the entropy produced by piecewise smooth dynamical systems is derived. Its connection to the Kolmogorov-Sinai entropy is pointed out. The case of wet granular matter as a piecewise Hamiltonian system is discussed.

We consider a general dynamical system. Its space of states, M , may not only contain a continuous phase space $C = \{\Gamma\}$, but also discrete degrees of freedom $D = \{\mathbf{b}\}$, so that in general:

$$\text{State Space } M = \{\Gamma, \mathbf{b}\} . \quad (5.50)$$

In connection with the Fluctuation Theorem, theorists have most often considered smooth dynamical systems, such as the non-Hamiltonian sheared fluid of the seminal work [89] and the presentment [187]. A smooth dynamical system possesses a smooth vector field $\mathbf{F}(\Gamma)$, so that the physical dynamics are generated by the following system of non-linear first order differential equations: $\dot{\Gamma} = \mathbf{F}(\Gamma)$. We proceed to the important case when the generator \mathbf{F} is not smooth everywhere. The flow only needs to be smooth within certain subsets C_σ :

$$\dot{\Gamma} = \mathbf{F}(\Gamma, \mathbf{b}) \quad (5.51)$$

$$\mathbf{b} = \text{const for } \Gamma \in C_\sigma . \quad (5.52)$$

The subsets C_σ tessellate the entire continuous part C of the state space:

$$C = \bigcup_{\sigma} \bar{C}_\sigma . \quad (5.53)$$

At the borders ∂C_σ of C_σ , the discrete part \mathbf{b} of the system may alter, $\mathbf{b} \mapsto \mathbf{b}'$, so that the direction of the flow has a discontinuity, $\mathbf{F}(\Gamma, \mathbf{b}) \mapsto \mathbf{F}(\Gamma, \mathbf{b}')$.

This is all we need to know to compute the entropy production. Entropy is defined as the Gibbs-Shannon functional of the probability distribution $P(\Gamma, \mathbf{b})$ on the state space M :

$$S(t) = - \sum_D \int_C P \ln P \, dv . \quad (5.54)$$

First, we split up the integration in a sum of integrals over the C_σ . Second, we use the conservation of probability within each C_σ , as is expressed by the continuity equation,

$$\begin{aligned} \partial_t P + \text{div } \mathbf{j} &= 0 , \\ \mathbf{j} &= P\mathbf{F} . \end{aligned}$$

Finally, we integrate by parts twice, taking the boundary terms into account.

$$\begin{aligned} \dot{S} &= \sum_{\sigma} \sum_{D_{\sigma}} \left(\int_{C_{\sigma}} P \operatorname{div} \mathbf{F} \, dv + \int_{\partial C_{\sigma}} j_n \ln P \, d\mu \right) \\ &\quad - \sum_{\sigma} \sum_{D_{\sigma}} \int_{\partial C_{\sigma}} j_n \, d\mu \end{aligned} \quad (5.55)$$

Herein, $F_n = (\mathbf{F}, \mathbf{n})$ is the normal component \mathbf{n} of the generator \mathbf{F} . The last term in (5.55) is identical zero, since the probability current $j_n = (\mathbf{j}, \mathbf{n})$ crossing the boundaries is conserved. So we have the result

$$\begin{aligned} \dot{S} &= \sum_D \int_C P \operatorname{div} \mathbf{F} \, dv \\ &\quad + \sum_{\sigma} \sum_{D_{\sigma}} \int_{\partial C_{\sigma}} j_n \ln P \, d\mu . \end{aligned} \quad (5.56)$$

Since the probability for leaving C_{σ} across the border element $d\mu$ within time dt is $j_n \, d\mu \, dt$, we can write (5.56) in the concise form

$$\dot{S} = \langle \operatorname{div} \mathbf{F} \rangle + \sum_{\sigma} \sum_{\mathbf{b} \in D_{\sigma}} \nu_{\sigma}(\mathbf{b}) \langle \ln P \rangle_{\sigma, \mathbf{b}} , \quad (5.57)$$

with the bulk average

$$\langle \dots \rangle = \sum_D \int_C \dots P \, dv ,$$

and the border average

$$\langle \dots \rangle_{\sigma, \mathbf{b}} = \frac{\int_{\partial C_{\sigma}} \dots j_n \, d\mu}{\int_{\partial C_{\sigma}} j_n \, d\mu} . \quad (5.58)$$

The denominator in (5.58) is the escape rate $\nu_{\sigma}(\mathbf{b})$ of C_{σ} through the channel \mathbf{b} . Note that the sign of ν_{σ} is positive for a deterministic ensemble flow leaving C_{σ} , and negative if the flow \mathbf{F} points to the interior of C_{σ} .

With (5.57) we have generalized the common result for smooth systems, in which case there is only the divergence term: Smooth dynamical systems produce entropy by phase space contraction.

An instructive example of the additional term is the wet granular gas: The rate ν_{bound} at which the binding state is entered, is the collision frequency times the probability for sticking, $\nu_{\text{bound}} = \nu_{\text{coll}} P_{\text{bound}}$. Furthermore, the probability P that the binding state is occupied, has to be proportional to some power of the system density. This allows an abstract view on the result on the Kolmogorov-Sinai entropy. All we used was the multi-sheet structure of phase space.

In the case of smooth dynamical systems the divergence is the sum of *all* Lyapunov exponents and the Kolmogorov-Sinai entropy is the sum of the positive ones. Hence, we can relate the Gibbs-Shannon entropy and the Kolmogorov-Sinai entropy by

$$\dot{S} = h_{\text{KS}} - h_{\text{KS}}^{\dagger} . \quad (5.59)$$

The dagger (\dagger) refers to the time-reversed system, which has the signs of all Lyapunov exponents reversed. Equation (5.59) also holds for piecewise smooth and reversible systems.

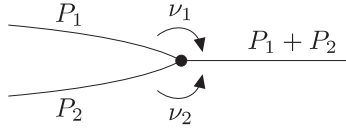


Figure 5.16: The elementary event of information loss.

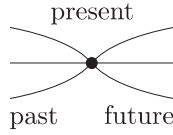


Figure 5.17: Change of entropy at vertex.

Focusing on the case of wet granular matter at any density and in any dimension, the first term in (5.57) is absent, since the system is piecewise Hamiltonian and Hamiltonian systems conserve phase space (Liouville theorem). When we go to higher densities, there will be bigger and bigger clusters, and the transition from one binding configuration to another yields escape rate terms analogous to the one discussed above. When a collision between grain i and j takes place, the initial configuration can be bounded (1) or unbounded (2). Eventually, there will always be a bridge. This situation is sketched in Fig. 5.16. According to (5.57) the entropy lost by the system in this process is

$$\dot{S} = \nu_1 \ln P_1 + \nu_2 \ln P_2 - (\nu_1 + \nu_2) \ln(P_1 + P_2) . \quad (5.60)$$

For equal transition rates $\nu_1 = \nu_2 = \nu$ and equal occupation probabilities $P_1 = P_2 = P$, this results in $\ln 2$, as on my have expected according to the binary nature information is stored in the capillary bond.

Collection of Diagrammatic Formulas The entropy produced by a piecewise smooth dynamical system is $-\dot{S}$ with

$$\begin{aligned} \dot{S} &= \langle \text{div } \mathbf{F} \rangle \\ &+ \sum_i \nu_i^{(\text{out})} \ln P_i - \sum_f \nu_f^{(\text{in})} \ln P_f . \end{aligned} \quad (5.61)$$

The summation runs over initial decay channels (i) and future branches (f). This sum over histories is sketched in Fig. 5.17. The conservation of probability across the vertex (always fulfilled) constrains

$$\sum_i \nu_i^{(\text{out})} = \sum_f \nu_f^{(\text{in})} .$$

The conservation of phase space across the vertex (holds for our model of wet granular matter, but not for the restitution model) constrains

$$\sum_i P_i = \sum_f P_f .$$

5.9 Conclusions

We worked out the effect of the capillary interaction on the chaoticity of the granular dynamics. Liquid bridges give rise to radial hysteretic force over finite distance. The detailed distance dependence was found to be of minor importance in the comparison of the Minimal and the Extended Capillary Model, whereas the decisive property is the extraction of the bridge energy, which is independent of the initial velocity in contrast to the restitution model of dry granulates. As part of the computation, the explicit distribution of relative particle separations prior to collision was derived, which deviates from a simple exponential (Eq. (5.20) and Fig. 5.5).

An enhanced chaotic dynamics of the wet granular system as compared to dry spheres was derived analytically. The leading term in the expansion of the KS entropy with respect to density is sensitive to the sticking of particles. It was shown that the prolonged interaction time of stable pairs enforces the exponential separation in velocity space. The continuous but in general not differentiable transition to the dry limiting case has been established. The exceptional one-dimensional case could be mapped to the equivalent dynamics of a ‘wet billiard’, and the Lyapunov spectrum was computed numerically.

The dynamical property derived in this chapter recommends the wet granular system as a suitable candidate for a Gallavotti-Cohen-type Fluctuation Theorem [89, 90], since the requirement of chaoticity is met. Future work can therefore concentrate on the generalization regarding the broken time-reversibility (pointed out in Chap. 4). Moreover, the presented result on the increased chaoticity extends the molecular chaos hypothesis to the nonequilibrium states of wet granular matter, so that we can generalize a Boltzmann-Enskog-type kinetic theory by taking the hysteretic interaction into account in the following Chaps. 6, 7, and 10.

The rigorous derivation of phenomenological laws such as the Navier-Stokes equation for viscous flow and the Fourier law for heat transport is a fundamental problem under intense discussion. Relations between the Lyapunov spectrum of the microscopic dynamics and macroscopic properties such as viscosity and heat conductivity have been established within the last years, most detailed for the Lorentz gas [93, 96, 62, 12, 36, 37, 231]. The importance of such relations is apparent from the fact they bridge the gap between microscopic reversibility and macroscopic irreversibility challenging physicists since L. Boltzmann. It is natural that future work extends transport relations for the hysteretic interaction, based on the result for the KS entropy.

A further interesting problem is the computation of the KS entropy for dense wet granulates, since this might lead to a novel description of clustering – as a nonequilibrium phase transition – in terms of the Lyapunov spectrum. Yet this problem is challenging as it needs new concepts, because the identification of the velocity space with the instable manifold is limited to the dilute gas. Here the general diagrammatic approach in the last Sec. 5.8 of this chapter may serve as a starting point.

Chapter 6

Unclustering Transition in Freely Cooling Wet Granular Matter

As in Chap. 4 we start with the 1D system¹. In the present chapter it is demonstrated analytically and by extensive simulations that above a critical density, the clustering of wet granular matter under isochoric conditions is not monotonic in time, but undergoes a sharp unclustering transition. At this point the liquid bridge connections, which are homogeneously distributed in the hot initial state, suddenly break at certain locations and cold granular droplets precipitate out of the homogeneous initial state. These droplets have an intrinsic size, which depends on the density of the initial gas. The formation of these droplets interrupts the clustering process, and the number of clusters can easily rise by more than one order of magnitude. This transition takes place when the granular temperature comes close to the energy scale set by the capillary interaction. After this precipitation, the resulting gas of droplets undergoes sticky coalescence events, so that the systems converges asymptotically to the scaling law of the sticky gas. This asymptote is shown to be universal when time is scaled with density. The velocity distribution of clusters is shown to be close to an exponential, while the thermal particle motion inside clusters is Gaussian.

6.1 Introduction

For more than a century, attempts have been made to extend thermodynamics to systems out of equilibrium. Some progress has been achieved recently with the advent of so-called fluctuation theorems [75, 89, 90, 125, 199], but we still lack a general method to feasibly derive macroscopic properties from the microscopic interaction. Due to its dissipative nature, granular matter is a paradigmatic system of nonequilibrium physics and the dry case has been

¹The case of three-dimensional free cooling is a current joint project in cooperation with S. Ulrich (U. Göttingen) and K. Röller (MPI DS Göttingen).

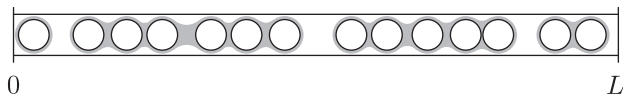


Figure 6.1: A schematic representation of wet granular matter in one dimension. For an interval of length L' we denote by L the configuration length, which is reduced by the sum of all particle diameters, $L = L' - L_{\text{jamming}}$.

studied extensively [105, 123, 155, 101, 27, 16]. In this chapter wet granular matter is presented as an example of a dissipative and piecewise Hamiltonian system. An analytic method is proposed to predict macroscopic quantities for such systems based on the computation of conditional probabilities. In quantitative agreement with direct simulations we will find a self-organized unclustering transition in cooling wet granular matter.

As has been shown in Chap. 3, capillary bridges give rise to a hysteretic interaction force: for a bridge to form, adjacent grains must touch, but as their separation x is increased again, the bridge remains and exerts an attractive force $F_{cb}(x)$ until it ruptures when a critical distance s_{crit} is reached². This entails dissipation even without the liquid to be viscous, since the energy $E_{cb} = \int_0^{s_{crit}} F_{cb}(x) dx$ is lost whenever a bridge is formed and then ruptured again [207]. The increased chaoticity of this dynamical system as compared to the dry gas of spheres has been demonstrated in Chap. 5. The dilute wet granular system has been recently shown to cluster monotonically in time [241]. Here we focus on the dense case, when many particles interact, such that the collision frequency is on the order of, or even larger than, the average inverse life time of a capillary bridge. In this chapter, we will adopt what has been termed the Minimal Capillary Model (cf. Chap. 3 and [114, 87]), in which F_{cb} is assumed to be constant as the liquid bridge is stretched, as introduced in Chap. 3. There we observed with the flocculent structures emerging in 2D wet granular matter in 3.4.5, that the free cooling is quite complex in higher dimensions. In this chapter we restrict ourselves to dimensionality $D = 1$ to simplify the analysis. This furthermore allows us to simulate the Minimal Capillary Model for large systems at high densities. This is possible because the Capillary Model can be exactly realized by the event-driven technique³ for $D = 1$. The chosen dimensionality will eventually turn out not to be a significant restriction, since the transition established theoretically in this chapter is reported for a three-dimensional experiment in Chap. 8.

The Sticky Gas Scaling Law

Before we solve the full dynamics, we remind of a simple scaling analysis [88] which allows to determine the low temperature asymptotic at late times, when each collision leads to the sticking of particles. The collision frequency in the system is quadratic in the number of clusters, N_{cl}^2 , and proportional to the mean cluster velocity $\propto \sqrt{T/M}$. The cluster mass M is inversely proportional to the number of clusters because of mass conservation. The temperature is constant, because each sticky collision eliminates one degree of freedom. Hence,

$$\dot{N}_{cl} = -f_{bind} \propto -N_{cl}^{5/2}, \quad (6.1)$$

which is readily integrated to

$$N_{cl} \propto t^{-2/3}. \quad (6.2)$$

As is shown and explained analytically in the following sections, the cooling scenario of *dense* wet granular matter is surprisingly different. With a dense system, we think of particles which have a mean separation which is less than the critical length of the liquid bridge, s_{crit} .

6.2 Numerical Observation of the Transition

In order to set the stage for the scenario to be studied, we consider an initial state consisting of an ideal gas of N equal particles at temperature $T(0) = T_i \gg E_{cb}$, i.e. the velocities of

²Quantities referring to capillary bonds, such as the number of bonds (N_{cb}) and the bond energy (E_{cb}) are denoted by the subindex ‘cb’.

³In dimensions $D > 1$, the interaction has to be simplified for the event-driven simulation technique, which causes artifacts at high densities discussed in Chap. 10.

particles at random positions are distributed according to Maxwell. The Boltzmann constant is set to unity. We define a cluster as a sequence of particles connected by liquid bridges. There are no liquid bonds initially, so that the number of ‘clusters’ is $N_{\text{cl}}(0) = N$. Obviously in one dimension we have $N = N_{\text{cl}} + N_{\text{cb}}$ at any time, where N_{cb} denotes the number of capillary bridges. Note that we consider the isochoric system with fixed configuration length L (cf. Fig. 6.1). The number of clusters N_{cl} changes in each rupture and binding event. In the macroscopic limit, $N \rightarrow \infty$, relative fluctuations vanish and the number of clusters N_{cl} becomes a smooth function of time. The simulations were performed with $N = 10^7$ particles in order to obtain good statistics. The high number of particles is the reason why all results reported hold for periodic as well as elastic boundary conditions.

A log-log plot of the number of clusters N_{cl} as a function of time is shown in Fig. 6.2A, where the density of particles is varied as an additional parameter. We can clearly distinguish four stages: starting from the ideal gas configuration of N particles at temperature $T_i = 10E_{\text{cb}}$, the number of clusters decreases as the first bonds are formed. This corresponds to the initial decline which is universal for all densities, $\rho = N/L$, on the scaled time axis, $\tau = \rho s_{\text{crit}} t$. In the second stage, the ongoing fast rearrangements of clusters cool down the system. The number of clusters fluctuates around a constant value which depends on the particle density only. As the third stage, we observe, quite unexpectedly at first glance, an unclustering transition that sets in when the granular temperature T reaches E_{cb} . At high density, the number of clusters may increase suddenly by roughly an order of magnitude. In the final stage, almost all collisions lead to stable clusters since $T \ll E_{\text{cb}}$, yielding a self similar power-law reminiscent of the ‘sticky gas’ [32]. Quite remarkable is the asymptotic data collapse for all densities when plotted versus τ . The intermediate stages distinguish the free cooling of dense wet granular matter from the monotonic clustering of dry granular gases [16].

There is a handy argument for the appearance of the unclustering peaks at densities $N/L > 3/s_{\text{crit}}$: on the plateau, clusters are formed mainly due to the geometric confinement L , while the liquid bridge force is too weak to have a significant influence on the granular motion at the initially high temperatures. Later, with less energy being stored in the liquid bridges, the clusters contract in their spatial extension and break up into smaller units. The cooling granulate condenses to ‘droplets’⁴. Since there is space for more of these shorter clusters, N_{cl} increases. This is obviously a direct consequence of the isochoric setting.

6.3 Analytic Description of the Full Cooling Scenario

Let us now attempt a mean-field-type description of our system. Every time a liquid bridge is formed, the number of clusters decreases by one and a rupture event implies the increase of N_{cl} by unity. Hence

$$\dot{N}_{\text{cl}} = f_{\text{rupt}} - f_{\text{bind}} , \quad (6.3)$$

where the rupture frequency f_{rupt} and binding frequency f_{bind} are the transition rates for the processes $N_{\text{cl}} \mapsto N_{\text{cl}} \pm 1$. The hysteretic interaction of the Minimal Capillary Model reduces the system energy E by the bridge energy E_{cb} , where a fraction γ is dissipated in the formation of the bridge,

$$\dot{E} = -E_{\text{cb}} (\gamma f_{\text{bind}} + (1 - \gamma) f_{\text{rupt}}) . \quad (6.4)$$

To solve the set of differential equations (6.3) and (6.4) we use the simplifying assumption that the cooling state can be described by a single granular temperature $T \equiv \langle v^2 \rangle$, so that the

⁴The experimental observation of a related effect has been reported in [98].

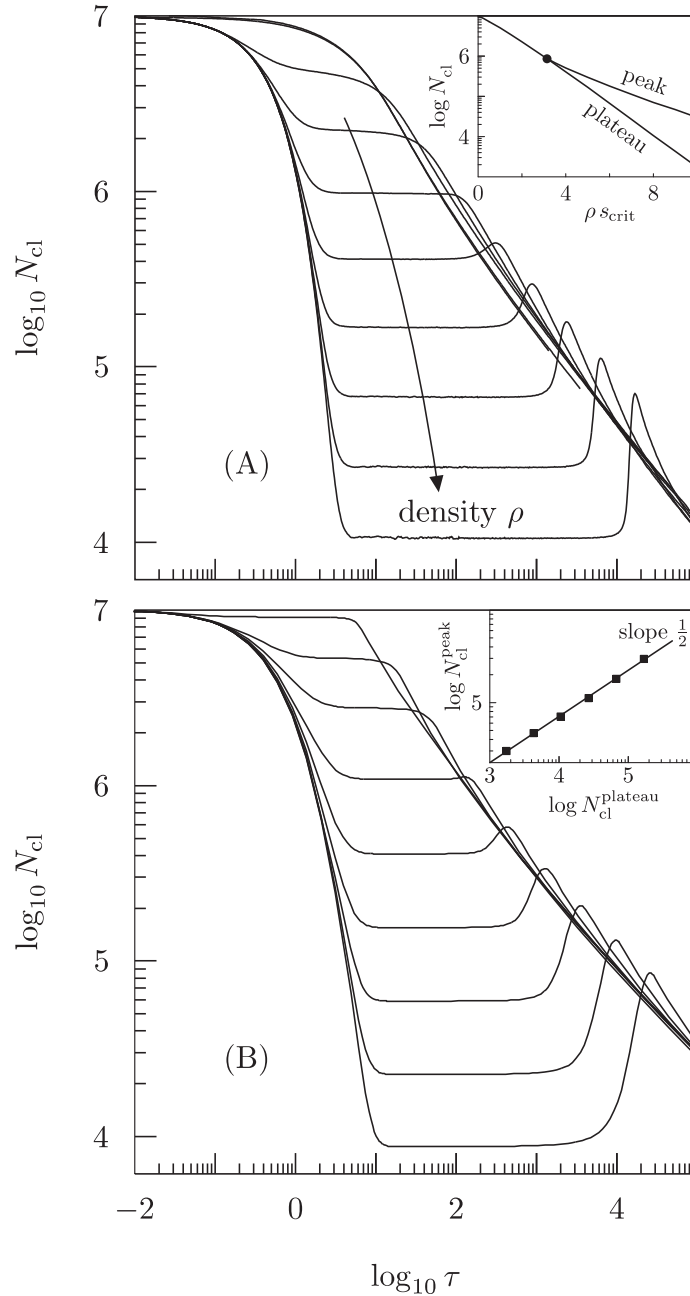


Figure 6.2: The evolution of the number of clusters in an isochoric ensemble of wet granular matter is shown for nine different densities. The log-log plot (A) results from direct simulations and (B) shows solutions of the differential equation (6.3). The dimensionless density ρs_{crit} assumes the values $1/10, 1, 2, \dots, 8$. Plot (A) includes also the density $1/20$, which differs from $1/10$ by less than the line width representing the dilute limit $\rho s_{crit} \rightarrow 0$. Dense systems exhibit a plateau as long as the granular temperature T is higher than the bond energy E_{cb} . Later, the cohesion force mediated by the liquid bridges becomes significant and leads to the contraction of the liquid bridges. Consequently, formerly big clusters break up into several contracted droplets. This unclustering transition is visible as a peak in the function $N_{cl}(t)$. In the final asymptotic stage these small clusters regroup in 'sticky gas' collisions. The insets show the emergence of the peak as the density ρs_{crit} is increased (A) and the scaling relation between N_{cl}^{peak} and $N_{cl}^{plateau}$ (B). Note the collapse on the same universal asymptote when plotted w.r.t. $\tau = \rho s_{crit} t$ for all densities. (The mass scale is set by the particle mass so that the natural time unit is $s_{crit}/\sqrt{E_{cb}}$.)

kinetic energy E_{kin} is $NT/2$. The particles define the mass unit. The potential energy stored within the liquid bridges is $E_{\text{bond}} = N_{\text{cb}}E_{\text{cb}}(\langle x \rangle_{\text{bond}}/s_{\text{crit}} - \gamma)$, since the liquid bridge force is assumed constant in the Minimal Capillary Model. In the following we derive expressions for the frequencies f_{rupt} , f_{bind} and the wet granular energy $E = E_{\text{kin}} + E_{\text{bond}}$ in terms of the present number of clusters and the granular temperature. This allows to replace E by T as an independent variable, and the evolution equations (6.3) and (6.4) become independent of γ since the granular motion is determined uniquely by the liquid bridge forces.

The expectation value $\langle x \rangle_{\text{bond}}$ has to be computed using the distribution of interparticle distances x under the condition of a liquid bond. In the dense system the particle collision frequency is exponentially larger than the cooling rate. This separation of time scales justifies to use a canonical distribution $\sim \exp(-W(x)/T)$ inside the clusters. $W(x)$ includes the energy stored in the bridge and the work done against the external pressure $P = NT/L$. Normalizing according to the condition $x < s_{\text{crit}}$, we obtain the distribution of bond lengths x :

$$p_{\text{bond}}(x) = \frac{\alpha}{s_{\text{crit}}} \frac{e^{-\alpha \frac{x}{s_{\text{crit}}}}}{1 - e^{-\alpha}} \quad \text{with } \alpha = \frac{E_{\text{cb}}}{T} + \rho s_{\text{crit}}. \quad (6.5)$$

The first application of this distribution is to compute the mean bridge length

$$\frac{\langle x \rangle_{\text{bond}}}{s_{\text{crit}}} = \frac{1}{\alpha} - \frac{1}{e^{\alpha} - 1}, \quad (6.6)$$

and hence the system energy E as a function of T and N_{cl} :

$$E = N \frac{T}{2} + N_{\text{cb}} E_{\text{cb}} \left(\frac{1}{\alpha} - \frac{1}{e^{\alpha} - 1} \right). \quad (6.7)$$

At low granular temperatures, $T \ll E_{\text{cb}}$, Eq. (6.7) yields $E = NT/2 + N_{\text{cb}}T + \mathcal{O}(T/E_{\text{cb}})$. Thus we recover the equipartition theorem of equilibrium physics [117] as a limiting case: in the low temperature limit few liquid bridges break and the system is asymptotically Hamiltonian. The kinetic degrees of freedom are quadratic in the Hamiltonian having mean energy $T/2$, while each liquid bridge has a linear potential with mean energy T .

The rupture frequency of a liquid bridge is the probability $p_{\text{bond}}(s_{\text{crit}})$ (for the bridge being stretched to its maximum length) multiplied by the mean relative velocity in the direction to break the bridge, $\langle \dot{x} \theta(\dot{x}) \rangle$ (with the Heaviside step function θ). The separation of time scales mentioned above implies that the velocities within a cluster follow a Maxwellian distribution, so that $\langle \dot{x} \theta(\dot{x}) \rangle = \sqrt{T/\pi}$, as confirmed by simulations. This gives the system rupture frequency

$$f_{\text{rupt}} = \frac{N_{\text{cb}}\alpha}{s_{\text{crit}}} \sqrt{\frac{T}{\pi}} \frac{1}{e^{\alpha} - 1}. \quad (6.8)$$

It is proportional to the Bose-Einstein factor because the rupture dissipates packages of energy E_{cb} into the wetting liquid just as a Planck radiator emits photons. The only task remaining is to find the explicit expression for the binding frequency. The mean number of particles within a cluster is $m = N/N_{\text{cl}}$. We denote by y the gap length between neighboring clusters. Since the mean-field approach neglects correlation in the spatial distribution of clusters, the probability for neighboring clusters to have a separation between y and $y + dy$ is $\exp(-y/\langle y \rangle_{\text{gap}}) dy/\langle y \rangle_{\text{gap}}$. The cluster collision frequency is this probability at contact, $y = 0$, times the cluster velocity factor $\langle \dot{y} \theta(\dot{y}) \rangle$. Hence the system binding frequency caused by the translational motion of clusters is $f_{\text{bind}}^{\text{trans}} = N_{\text{cl}} \sqrt{T/m\pi}/\langle y \rangle_{\text{gap}}$. The mean cluster separation $\langle y \rangle_{\text{gap}}$ follows from the isochoric condition $L = N_{\text{cb}} \langle x \rangle_{\text{bond}} + N_{\text{cl}} \langle y \rangle_{\text{gap}}$. With $f_{\text{bind}}^{\text{trans}}$

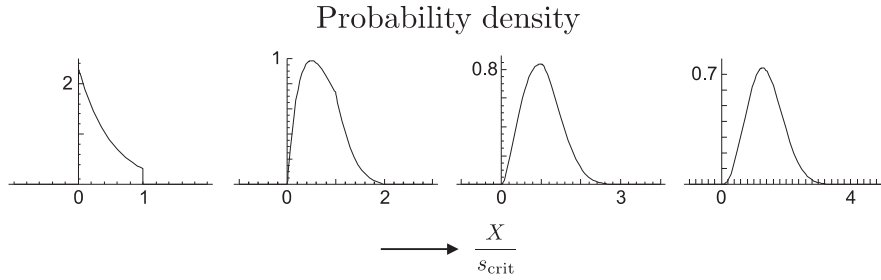


Figure 6.3: Length fluctuations of a cluster made up of $m = 2, 3, 4, 5$ particles. The distribution converges according to the central limit theorem quickly to a Gaussian. In these plots $\alpha = 2$ was chosen. On the horizontal axis the cluster length X is plotted in units of s_{crit} .

we have taken the translation of clusters into account. This describes one out of m degrees of freedom each cluster possesses. Finally, we treat the remaining $m - 1$ oscillatory modes causing fluctuations of the total cluster length X . Since the distribution function for the length x of a single liquid bridge (Eq. (6.5)) is known, the fluctuations of the total length X of an m -cluster are given by convoluting p_{bond} with itself $m - 1$ times. According to the central limit theorem, the distribution of the length fluctuations converges rapidly to a Gaussian with increasing m (Fig. 6.3). Therefore in the relevant case of large m , the cluster length X obeys the normal-distribution $p_{\text{cl}}(X)$ with mean $\langle X \rangle_{\text{cl}} = (m - 1) \langle x \rangle_{\text{bond}}$ and width

$$\sigma_X = \sqrt{(m - 1)} s_{\text{crit}} \sqrt{\frac{1}{\alpha^2} - \frac{\frac{1}{2}}{\cosh \alpha - 1}}. \quad (6.9)$$

The consideration of time scales also implies the equal thermal excitation of all modes. This gives the second term, $f_{\text{bind}}^{\text{osc}} = N_{\text{cl}}(m - 1) \sqrt{T/m\pi} p_{\text{cl}}(\langle X \rangle_{\text{cl}} + \langle y \rangle_{\text{gap}})$, for the binding frequency, which describes the merger of clusters by short range length fluctuations. This binding mechanism dominates in the hot and dense system, whereas the probability $p_{\text{cl}}(\langle X \rangle_{\text{cl}} + \langle y \rangle_{\text{gap}})$ to close the gap $\langle y \rangle_{\text{gap}}$ by length fluctuations is over-exponentially suppressed at late times. With the total binding frequency, $f_{\text{bind}} = f_{\text{bind}}^{\text{trans}} + f_{\text{bind}}^{\text{osc}}$, the derivation of the mean-field theory is completed. We have now a closed set of non-linear differential equations without free parameters at hand determining the time evolution of macroscopic quantities such as the granular temperature and the number of clusters:

$$\dot{N}_{\text{cl}} = f_{\text{rupt}} - f_{\text{bind}} \quad (6.10a)$$

$$\dot{T} = - \frac{(s_{\text{crit}} - \langle x \rangle_{\text{bond}}) f_{\text{rupt}} + \langle x \rangle_{\text{bond}} f_{\text{bind}}}{\frac{N s_{\text{crit}}}{2E_{\text{cb}}} + (N - N_{\text{cl}}) \frac{d\langle x \rangle_{\text{bond}}}{dT}} \quad (6.10b)$$

The solution of $N_{\text{cl}}(t)$ according to the theory is confronted with direct simulations at various densities in Fig. 6.2. While the upper plot (A) results from full simulations of 10^7 particles, (B) shows solutions of the differential equations (6.10) for the same initial data and densities. Both approaches clearly exhibit the unclustering effect. With both methods the plateau and peak height is found to obey a square root scaling law. (The dots in the inset of Fig. 6.2B result from simulations). The explanation of this scaling turns out to be far from straightforward, and will be as part of the author's future research left to a forthcoming publication.

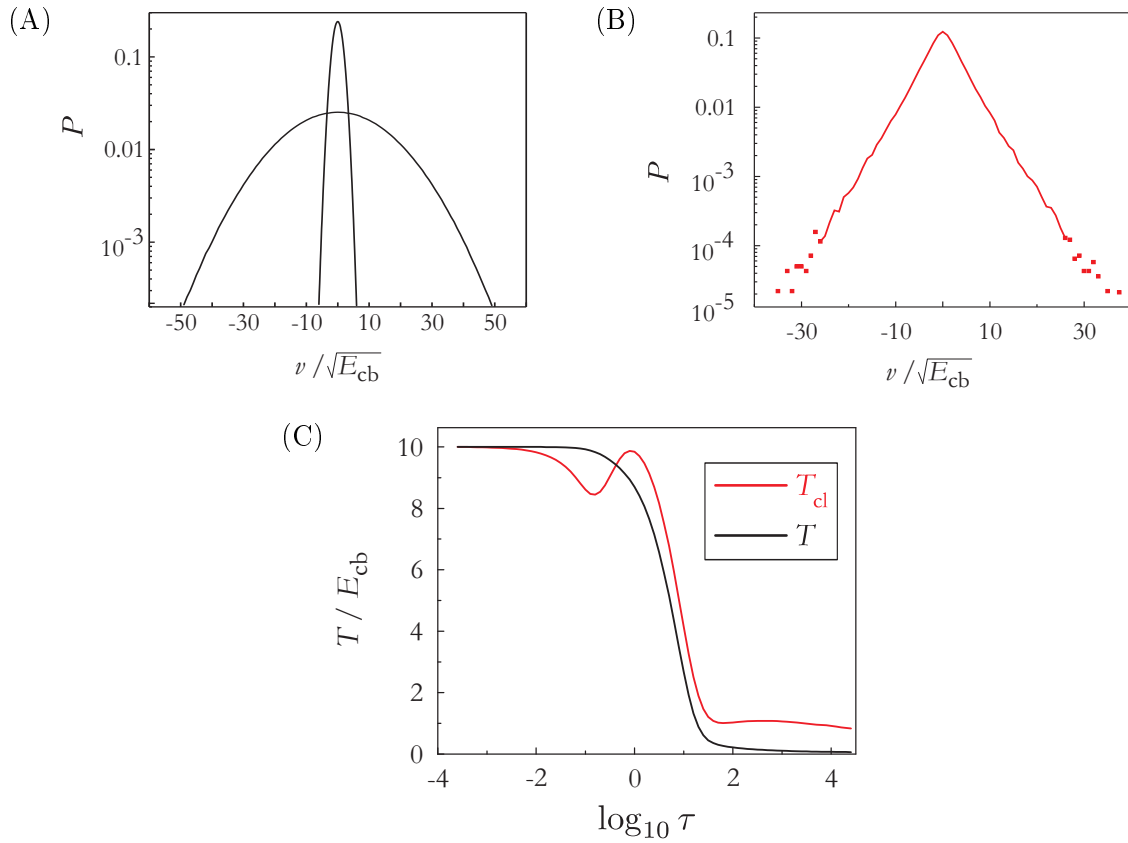


Figure 6.4: The thermalization of the cluster motion and the internal degrees of freedom of a cluster decouple at late times. (A) Initially, the particles are given an equilibrium velocity distribution. As the system cools, the Gaussian shape is conserved for the oscillatory degrees of freedom inside a cluster, because a stable cluster is a chaotic Hamiltonian subsystem (cf. the result 5.7.1 in Chap. 5 on the cluster intrinsic dynamics). (B) Velocity distribution for the center of masses of clusters in the scaling (sticky gas) regime, for density $\rho s_{\text{crit}} = 1$. In sharp contrast to (A), this nonequilibrium distribution has exponential tails. (C) Development of two different temperatures in the free cooling of a one-dimensional system with dimensionless density $s_{\text{crit}}\rho = 1$. The total system temperature $T = (1 - \frac{N_{\text{cl}}}{N})T_{\text{osc}} + \frac{N_{\text{cl}}}{N}T_{\text{cl}} \approx T_{\text{osc}}$ includes all degrees of freedom, and the temperature T_{cl} is defined by the center of mass motion of the clusters. (The apparent reheating at the onset of clustering is due to the fact that the fastest particles are the first to find a binding partner.)

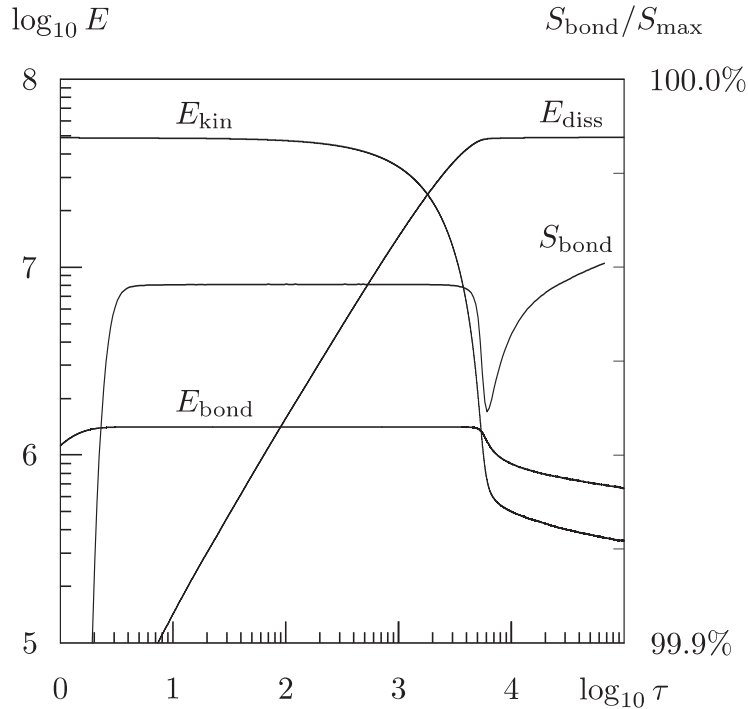


Figure 6.5: The unclustering transition is also present in entropy and energy measurements. Note the crossing of potential energy E_{bond} and kinetic energy E_{kin} at the transition.

6.4 The Thermal Decoupling

There are differences in the time scales between simulation and mean-field theory. This is because the oscillatory and translational modes do not have the same temperature as has been assumed for simplicity. Indeed, the direct simulation reveals that $T_{\text{cl}} > T_{\text{osc}}$ at late times, as is shown in Fig. 6.4C. Here T_{cl} is the temperature as derived from the translatory (i.e. center of mass) motion of clusters. This inequality is understood easily: when clusters bind, the energy of the eliminated translational degree of freedom is distributed among the energies of the new oscillatory degree of freedom and the liquid bridge potential. This yields a lower temperature T_{osc} within the clusters. It is straightforward to split up the first term, $E_{\text{kin}} = NT/2$, on the right hand side of (6.7) into $E_{\text{kin}} = E_{\text{trans}} + E_{\text{osc}}$ to account for this. With the lower internal temperature T_{osc} (cf. Fig. 6.4), the rupture events are suppressed in the final phase of the free cooling, which explains the steeper slope of Fig. 6.2A.

6.5 Energy and Entropy

Aside from the number of clusters, energetic as well as entropic signatures of the unclustering transition may be traced. In the phase space of wet granular matter, symplectic collision and rupture events are connected by smooth Hamiltonian trajectory segments. This gives the system the mathematically beautiful property to be dissipative and still to conserve its canonical phase space volume. Because there is no contraction of phase space (\mathbf{x}, \mathbf{p}) , there is also no associated entropy production, as it is the case for inelastic collision models of dry granular matter [156]. The system state is given by $(\mathbf{x}, \mathbf{p}, \mathbf{b})$, which includes the bond status $\mathbf{b} = (b_1, b_2, \dots)$, $b_j = 0, 1$. Figure 6.5 shows the Gibbs entropy S_{bond} of the distribution of

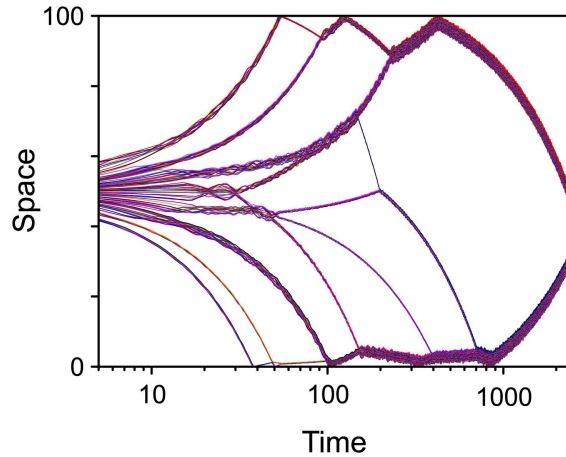


Figure 6.6: A highly simplistic picture of the unclustering peak. The initial cluster is overheated. In the real experiment (presented here theoretically and realized in Chap. 8), the isochoric condition forces the cluster to reduce its granular temperature until it reaches the granular bond energy. Then the capillary force destabilizes the thermal motion of the granular gas and leads to the break-up of clusters into smaller droplets. These granular droplets have an increased mean free path which suspends the clustering until these droplets aggregate in the final state, which is the reason for the self-similar sticky gas asymptotic. Note that in this spacetime plot, the visual inspection is simplified by increasing the mean free path manually at $t = 0$. Each color represents the trajectories of an individual particle, of which there are only 50 in this small system.

bridge bonds. With the formation of the first liquid bridges, S_{bond} raises quickly from zero close to its equilibrium value S_{max} . At the transition the isolated entropy S_{bond} decreases abruptly, indicating this simple structure formation process, and finally grows towards its equilibrium value. Of course, the total entropy production is never negative. Most of the entropy is not produced by the evolution of the wet granular system $(\mathbf{x}, \mathbf{p}, \mathbf{b})$, but caused by the energy $E_{\text{diss}}(t) = E(0) - E(t)$ which is dissipated into the wetting liquid. The importance to sum up the system and environmental entropies has been recognized recently for the formulation of fluctuation theorems [199]. For wet granular matter the environmental entropy production, $\Delta S_{\text{liq}} = E_{\text{diss}}/T_{\text{liq}}$, dominates since its peculiarity is the smallness of the liquid temperature T_{liq} by more than 10 orders of magnitude in comparison with the granular temperature T in realistic experiments (cf. Chap. 3 and [87]).

6.6 A Simplified Visualization

We can (strongly simplified) illustrate the droplet formation by inspecting the space-time paths of 50 particles originating out of an overheated cluster on a logarithmic time scale as shown in Fig. 6.6. Here the voids between droplets are exaggerated for the purpose of illustration by manually increasing the system size⁵ at $t = 0$. We can clearly see the formation of smaller droplets out of the initial state, which finally recollect.

⁵We remark that the system has reflecting boundaries which influence the final state of such a small system as the one shown, while reflecting and periodic boundaries give equal free cooling dynamics for a huge system as the one simulated above.

6.7 Inelastic Collisions and Unequal Particle Masses

Simulations have also been performed beyond the Minimal Capillary Model by combining bridge interaction with inelastic particle collisions. For restitution coefficients between 0.8 and 1.0, the higher cooling rate merely shifts the unclustering peak to earlier times. With restitution coefficients below 0.5, the peak is covered by the initial decline so that the monotonic behavior of dry granular matter is recovered. To observe the transition at lower restitution the initial temperature has to be increased beyond $10E_{cb}$. The unclustering process for inelastic systems is shown in Fig. 8.7 of Chap. 8 in the context of the experimental demonstration of the unclustering effect. Furthermore, it has been ensured that the results reported in this chapter are reproducible with unequal particle masses (random mass distributions as well as alternating masses).

6.8 Conclusions

A transition in the capillary connectivity of dense cooling wet granular matter has been discovered numerically and described analytically. The transition sets in when the overheated liquid network has cooled down to the energy scale set by the capillary interaction. The homogeneous wet granulate breaks up into isolated granular droplets, as described in quantitative agreement by the presented mean-field theory⁶. This precipitation of granular droplets out of the homogeneous gas opens up voids that prolong the mean free path. This was shown to be essential in the computation of the collision frequency since the clustering is suspended at this time in the free evolution. Here the unclustering peak is observed. In the final state of the free cooling, the droplets agglomerate with self-similar mass-time dependence. This asymptote was shown to be universal when time is rescaled by density in Fig. 6.2. The position of the unclustering peak is determined by the granular temperature with $T \approx E_{cb}/4$.

The unclustering effect was shown to require a critical density. Expressed in linear dimensions, the mean particle separation \bar{s} has to be less than one third of the rupture length of the bridge, s_{crit} . We shall find similar conditions for instabilities in two (Chap. 7) and three dimensions (Chap. 8).

The particle motion inside clusters was shown to have a Gaussian velocity distribution also at late times, which is a consequence of the cluster-internal chaoticity discussed in the preceding Sec. 5.7. The cluster velocities were shown to follow an exponential distribution over three orders of magnitude.

The numerical confirmation of the mean field theory derived above makes it a promising starting point for higher dimensional generalization (cf. the ‘Equation of State’ in Chap. 7), and extensions to stationary states which exhibit strong spatial inhomogeneities such as phase separation which we shall encounter in Chap. 10. The experimental confirmation of the presented unclustering transition is reported in Chap. 8. One may expect that the method of conditional probabilities applied here is neither limited to one spatial dimension nor wet granular matter at all, but applicable to the entire class of dissipative and piecewise Hamiltonian systems. It would be interesting to formulate and prove a fluctuation theorem for this class of systems with broken time-reversal symmetry.

⁶The description has spatial dependence in so far it distinguishes connected domains (described by x above) and unconnected domains (y) which coexist.

6.9 Appendix: A Comment on the Notion of Clusters

Here it is pointed out that the local definition of a ‘stable bond’ by inspecting the kinetic energy of a bond pair in its center of mass system is inconsistent with the equations of motion. At first glance, one might be misled by intuition to think of a separation of variables: the center of mass motion and the relative motion. However, as is well-known, this is only possible for 2-particle clusters, since the two-body problem is integrable (for any radial force law), while the three body-problem is generically chaotic; and wet granular matter is a N -particle system with $N \gg 2$. As the simplest counter example we consider for the moment three particles on a line obeying the Minimal Capillary Model. If there was only a single capillary bond in the system, the stability argument would hold. As soon as the center particle is bonded to both sides, the bridge forces cancel. The center particle moves freely, rendering the local energetic criterion irrelevant. If one was still to define a number of “stable” clusters, $N_{\text{cl}} = N - (N - N_{\text{cl}})\text{erf}\sqrt{E_{\text{cb}}/T}$,⁷ there appears even both, a peak and a minimum, for $\kappa \geq 2$ in the single-temperature model described above.

To summarize, three reasons are stated why the natural objects emerging in dense wet granular matter, for which we are free to agree upon some name – be it “cluster”, “network” or another term – ought to be defined by the capillary topology: Firstly, the equations of motion do not allow for a unique local criterion of stable bonds. Secondly, the instantaneous topology is a direct experimental observable, as is demonstrated in Chap. 8. Thirdly, an approach that starts with the definition of a cluster by a certain energy, forestalls the result of a transition at this energy. Rather, it is most natural to approach wet granular matter as a dynamical system, which demands an enlargement of the state space so that the *instantaneous* bridge status is included in order to describe the *hysteretic* formation and rupture of bridges. With the bridge topology as an impartial order parameter it is possible to detect the critical point at $T \approx E_{\text{cb}}/4$ avoiding any circular reasoning.

⁷ $(N - N_{\text{cl}})\text{erf}\sqrt{\kappa E_{\text{cb}}/T}$ is the number of “stable” bonds.

Chapter 7

Pair Correlation and Equation of State of Wet Granular Matter — The Theoretical Prediction of the Critical Point

In this chapter an expression is presented for the near-contact pair correlation function of D -dimensional weakly polydisperse hard spheres, which arises from elementary free-volume arguments. Its derivative at contact agrees very well with presented simulations for $D = 2$. For jammed states, the expression predicts that the number of exact contacts is equal to $2D$, in agreement with established simulations. When the particles are wetted, they interact by the formation and rupture of liquid capillary bridges. Since formation and rupture events of capillary bonds are well separated in configuration space, the interaction is *hysteretic* with a characteristic energy loss E_{cb} . The pair correlation is strongly affected by this capillary interaction depending on the liquid-bond status of neighboring particles. A theory is derived for the nonequilibrium probability currents of the capillary interaction which determines the pair correlation function near contact. This finally yields an analytic expression for the equation of state, $P = P(N/V, T)$, of wet granular matter for $D = 2$, valid in the complete density range from gas to jamming. Driven wet granular matter exhibits a van-der-Waals-like unstable branch at granular temperatures $T < T_c$ corresponding to a first order segregation transition of clusters. For the realistic rupture length of the liquid bridge, $s_{crit} = 0.07d$, the critical point is located at $T_c = 0.274E_{cb}$. While the critical temperature weakly depends on the rupture length, the critical density ϕ_c is shown to scale with s_{crit} according to $s_{crit} = 4d(\sqrt{\phi_J/\phi_c} - 1)$. The segregation transition is closely related to the precipitation of granular droplets reported for the free cooling of one-dimensional wet granular matter in Chap. 6, and extends the effect to higher dimensional systems. Since the limiting case of sticky bonds, $E_{cb} \gg T$, is of relevance for aggregation in general, simulations have been performed which show very good agreement with the theoretically predicted coordination K of capillary bonds as a function of the bond length s_{crit} . This result implies that particles that stick at the surface, $s_{crit} = 0$, form isostatic clusters. An extension of the theory in which the bridge coordination number K plays the role of a self-consistent mean-field is proposed.

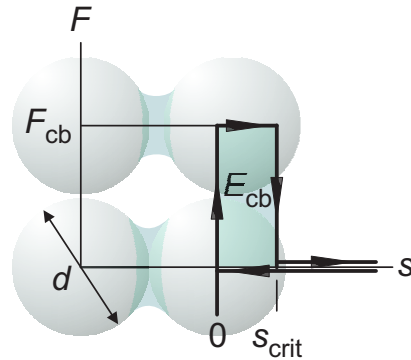


Figure 7.1: The hysteretic interaction in wet granular matter, as established experimentally in Chap. 3. In this chapter we apply this Minimal Capillary Model to derive the equation of state. Capillary bridges form at contact and mediate an attractive force F_{cb} . At the bridge length s_{crit} the bridge becomes unstable and pinches off. The hysteretic interaction by capillary bridges causes a well-defined loss of energy denoted by E_{cb} . While the particle diameter d is the only length scale for dry granulates, in wet granular matter there is a second scale set by s_{crit} . A realistic value is $s_{crit} \approx 0.07d$, which is realized when 1% of the jamming volume is added by a wetting liquid (with zero contact angle). Furthermore, the bond energy E_{cb} defines an intrinsic energy scale, which is absent in dry granulates. As is shown in this chapter, the length and energy scale set by the capillary interaction give rise to a phase transition with a critical density ϕ_c and a critical granular temperature T_c .

7.1 The Nonequilibrium State

The influence of capillary bridges on the microscopic structure has been discussed in Chap. 3. There we observed that the processes of formation and rupture of liquid bridges cause substantial changes in the mechanical properties of the granular material. Because of the generality of the effects, it has become common to study systems with spherical grains (usually glass beads in experiments), in order to ease theoretical modeling and to avoid side effects. We decided to follow this approach.

In this chapter we show analytically that the peculiar interaction by capillary bridges gives rise to a first order transition, and we compute the critical density and the critical temperature. We shall focus on the two dimensional case, but many concepts carry over to dimensionality $D = 3$. Since there is no clear observation of a first order phase transition in the hard-sphere fluid for $D \leq 2$ [19, 154], the added liquid leads to a qualitative change. More importantly, this transition is determined entirely by the geometric and energetic properties of the capillary bridges.

A dry system of N hard spheres with diameter d confined to an area or volume V has no intrinsic energy scale, so that the equation of state is of the form $P = T f(N/V)$ with the temperature $T = \langle mv_i v_i \rangle$ and a nonlinear density dependence, f . The defined size of hard particles is conveniently used to restate the density $n = N/V$ as the dimensionless occupied fraction $\phi = \sigma_D n d^D / (2^D D)$ (σ_D the surface of a D -dimensional unit sphere), which is the area fraction $\phi = \frac{\pi}{4} n d^2$ for two, and volume fraction $\phi = \frac{\pi}{6} n d^3$ for three dimensions.

The capillary interaction of wet granular matter has a well-defined binding energy E_{cb} [237], and it has been demonstrated experimentally in Chap. 3 under realistic dynamical conditions with impact velocities typical for strongly fluidized wet granular matter that the hysteretic character of the interaction is essential: the dominant mechanism of dissipation

is the hysteretic formation and rupture of capillary bridges, the energy E_{cb} of which is irreversibly taken from the kinetic energy of the granular motion whenever a liquid bridge ruptures [114]. There the bridge energy has been quantified, according to which E_{cb} is proportional $d^2\sqrt{W}$ (cf. Eq. (3.10)). W is the volume fraction of the added liquid with respect to the total volume of the jammed granular sample. Figure 7.1 illustrates the hysteresis of the Minimal Capillary Model, which assumes a constant bridge force F_{cb} as discussed in Chap. 3, and is applied in this chapter. This may appear as an oversimplification at first glance, but there is increasing experimental evidence that the details of the force law are insignificant for the collective dynamics on which we focus here [114], as also confirmed from the point of view of dynamical systems theory in Chap. 5 where the Minimal and the Extended Capillary Model yielded very similar results. The strongest experimental support for the Minimal Capillary Model under dynamical conditions is due to the quantitative experimental confirmation of the unclustering transition in Chap. 8 and the fluid/gas coexistence of wet granular matter in Chap. 10.

Obviously, an external energy current has to be continuously injected to drive the system into a nonequilibrium steady state. In the equilibrium limit, $E_{cb} \rightarrow 0$, we will have a pressure of the form $P = T f(\phi)$. It is the objective of this chapter to derive the equation of state for the hysteretic liquid bridge interaction of wet granular matter in such a driven state. In view of the intrinsic energy scale E_{cb} , this relation has to be of the form $P = P(\phi, T/E_{cb})$.

The equation of state is understood as an intrinsic property of homogeneous wet granular matter, kept in a stationary nonequilibrium state of granular temperature T . With this given temperature we may subsume various ways in which the system can be externally driven to compensate for the dissipation by rupturing liquid bridges, so that this granular temperature T is maintained over many particle diameters.

We remark that in most experimental situations involving wet granular matter, the granular temperature is a nonlinear, even discontinuous, response depending on the details of the driving, such as boundary motion or air flow in air-fluidized beds. In this chapter we deliberately regard the granular temperature as the *control parameter*, so that the theoretical description of the boundary coupling is conveniently separated. Yet we emphasize that for the full description of an experimental situation one has to insert the equation of state into the equation for the external energy input, and then solve for the granular temperature as the *nonlinear response* to the external driving.

We aim at describing the steady nonequilibrium states of wet granular matter, which are so multifaceted that at first glance one might think that aside from density and granular temperature further physical parameters are necessary in order to describe such a state. Yet as simulations have shown, states of wet granular matter far from equilibrium are very well described analytically by a granular temperature T assuming a Gaussian velocity distribution as we did in Chap. 6, neglecting higher cumulants¹. Furthermore, it is known that the self-organized velocity distribution of free cooling wet granular matter has a vanishing fourth cumulant [241]. We point out that the condition of a locally isotropic and homogeneous state used in this chapter implies that the temperature field may vary only slowly over many particle diameters so that there is no strong influence by a heat current, which would otherwise be considered as a third parameter of the local nonequilibrium state.

Throughout this study, we allow for a certain polydispersity, $0 \leq \Delta d/d < 0.1$. (For higher polydispersity, the dense system undergoes a kinetic glass transition [192, 193]). First of all,

¹It is straightforward to use a velocity distribution with more cumulants as parameters, such as for example Eq. (4.19), at all places where expectation values of velocities are evaluated (for instance in the Eqs. (6.8) and (7.60)). The resulting equation of state will then have the cumulants as additional parameters describing the nonequilibrium steady state.

polydispersity is frequently used in simulations and experiments to prevent the monocrystalline state. Secondly, most systems of practical relevance exhibit some polydispersity. Another characteristic of 'real' granulates is that the surfaces of the grains are not ideal, bearing certain roughness. This does, however, only change the amount of liquid which must be added in order to achieve the capillary interaction: first some liquid is required to fill the crevices and tiny recesses in the grain surfaces, until the grains effectively have a smooth liquid coating, which is then completely wetted by all additional liquid. For glass beads, as those used in most of the experiments, this is typically the case above a volume fraction $W_{\min} = 0.1\%$. We also require an upper limit on the volume fraction of the wetting liquid, so that the maximal length s_{crit} of liquid bridges is of the order or below the polydispersity Δd of the spheres. This is to demand that $s_{\text{crit}}/d \approx \sqrt[3]{W}/3$ is smaller than $\Delta d/d < 0.1$, so that $W < W_{\max} = 2.8\%$. This happens to closely coincide with the upper limit set on the liquid content to ensure that neighboring capillary bridge do not merge [197]. For this range of the liquid content the capillary interaction is a truly pairwise interaction with the capillary force acting radially between pairs of particles. Another implication of roughness is that there is a substantial tangential friction between adjacent grains. This means that in principle one has to include all rotational degrees of freedom in the kinetic considerations for any statistical physical treatment of our system. However, we are here focusing on the effects due to the liquid capillary bridges, which mediate central forces. These do not couple to the (tangential) rotational modes. We therefore expect that the rotational degrees of freedom play, in our system, the role of a spectator heat bath which follows the translational dynamics, but does not influence it greatly, aside from a quantitative increase of the granular specific heat. In fact, experiments and simulations of wet granular systems (cf. Chaps. 8 and 10) show that this approach yields remarkable agreement with experimental data. In this chapter, we thus completely neglect all rotational degrees of freedom.

7.2 Dry Spheres as the Starting Point

Before we add the wetting liquid to the hard sphere system, we investigate the dry case in this section and derive expressions for the pair correlation near contact, which will be extended to the wet case in the following section.

Due to their finite size, the positions of hard spheres are not distributed independently from each other, as it is the case for the point-particles of the ideal gas. The configuration space of N spheres is not V^N , but restricted to a concave subset in which the systems moves chaotically as a high dimensional billiard. With the absence of an intrinsic energy scale, the dry system is athermal, which means that a change in temperature is equivalent to rescaling the time axis. The excluded volume gives rise to correlations in the particle positions, which are measured by the pair correlation function. Denoting by $n = N/V$ the mean macroscopic particle density and by $n_{\text{m}}(\mathbf{r}) = \sum_i^N \delta(\mathbf{r} - \mathbf{r}_i)$ the microscopic density, the isotropic pair correlation $G(r)$ is defined as the probability

$$\langle n_{\text{m}}(\mathbf{r}) \rangle_{\text{particle at } 0} \text{ d vol} = n G(|\mathbf{r}|) \text{ d vol} = n g(s) \text{ d vol} \quad (7.1)$$

to find the center of a particle in the shell $\text{d vol} = \sigma_D r^{(D-1)} dr$ of radius $r = r_i + r_j + s$ and thickness $dr = ds$ centered around a reference particle. We have conveniently subtracted the particle radii $r_i + r_j$ in the last equality of (7.1), so that $s > 0$ is the surface separation. The function $g(s)$ is advantageous for polydispersity scattered around the mean diameter d ², because of its defined contact point, $s = 0$, which is smeared out in the function $G(r)$.

²We do not distinguish between the mean value and the root mean square of the diameter (relevant to the Voronoï area), because they differ only by $(\Delta d/d)^2/2 < 5 \times 10^{-3}$.

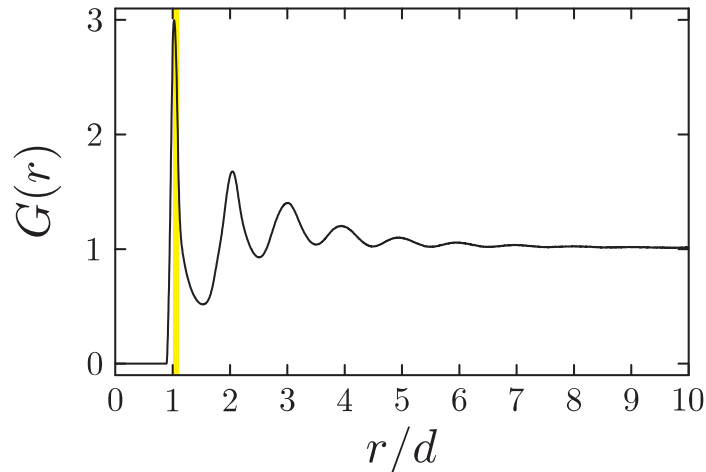


Figure 7.2: The pair correlation of wet granular matter in a fluidized state resulting from a molecular dynamics-type simulation in $D = 2$ dimensions (with driving acceleration $\Gamma = 15$). The correlation function $G(r)$ vanishes in the range $(0, d)$ where the finite particle size leads to excluded volume. We use the function $g(s)$ with the surface separation s of neighboring particles as it is convenient for wet granular matter where interstitial liquid bridges have the length s . Note that this is not exactly identical to the function $G(d+s)$ shifted by one particle diameter d , since a realistic granular system has some polydispersity Δd around the mean diameter d . Aside from kinetic contributions, the pressure is due to the interaction forces which become dominant with increasing density. The internal forces in wet granular matter are short-ranged. Therefore our interest focuses on the sharp fall-off in the indicated range $0 < s < s_{\text{crit}}$ of capillary interaction. This highlighted region indicates the typical range of s_{crit} , and corresponds to the region highlighted in Fig. 7.4. Furthermore, we derive more detailed correlation functions, $g^{\text{u}}(s)$ and $g^{\text{b}}(s)$, for unbound and capillary connected pairs, respectively, in order to describe the hysteretic interaction in wet granular matter.

Furthermore it is the natural way to describe an interstitial liquid bridge between the considered pair of particles, with s the length of the bridge. For a certain liquid volume per particle and contact angle of the wetting liquid, there is a well defined critical bridge length s_{crit} at which the bridge becomes unstable and ruptures. The mean density n is factored out in (7.1) so that the dimensionless g would be equal to unity for all separations if there was no particle-particle correlation. Figure 7.2 shows the pair correlation of a fluidized state in which long range order is lost, so that $g(s)$, respectively $G(r)$, tends to unity for $r \gg d$.

The forces in wet granular matter, hard-core repulsion and liquid bridge attraction, are short-ranged and radial, acting between pairs of particles over a separation range $0 < s < s_{\text{crit}}$ with $s_{\text{crit}} \ll d$. We are therefore interested in the short-range behavior of the pair correlation $g(s)$ up to leading order in s/d . For such short particle separations the pair correlation $g(s)$ is (up to a normalization constant) just the probability to find next neighbors at a separation s . Put in equivalent words: decomposing the pair correlation function $g(s) = \sum_{k=1}^{\infty} g_k(s)$ in contributions g_k of the k 's shell of Voronoï neighbors, we have $g(s) = g_1(s)$ in the range of interest, $0 < s < s_{\text{crit}} \ll d$. To shorten notation we suppress the subindex 1.

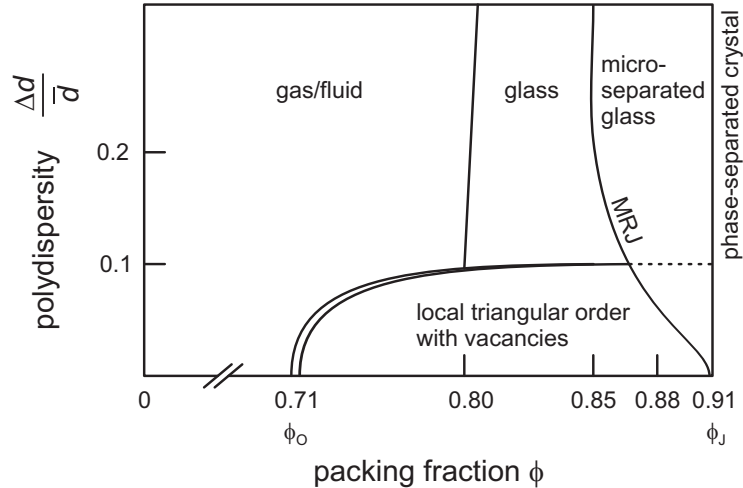


Figure 7.3: This plot reviews [193], [58] (Fig. 15 therein), and [212]. The athermal transitions shown are properties of the configuration space of hard discs. Since the wet granular dynamics takes place in this configuration space, results for hard discs form the starting point for a theory of wet granular matter in two dimensions. At low (gas) and moderate (fluid) densities ϕ , the configuration space is probed ergodically and the system has low shear viscosity. As density is increased, the system gets trapped in a disordered state (glass for polydispersity above 0.1), or in a state with local triangular order. Both transitions, the glass transition (vertical line at $\phi \approx 0.80$) and the ordering transition (curved line ending at $\phi_0 = 0.71$) can be detected by the rapid increase of the shear viscosity η (cf. [91] for the ordering transition). While there is an athermal first order transition in three dimensions, it is at present discussed in the literature whether the transition region (double lines ending at ϕ_0) represents a fluid/solid coexistence (corresponding to a weak first order transition with a small jump of the entropy per particle) or if there is an intermediate hexatic phase (according to the Kosterlitz-Thouless-Halperin-Nelson-Young scenario) [19, 154]. As the packing fraction ϕ is increased further, the islands to which the system is confined in the configuration space shrink to points. This jamming limit can be detected by the divergence of the pressure P (at fixed granular temperature) under compression (for example using the particle expansion of the Lubachevsky-Stillinger algorithm). The maximal random jammed state (MRJ, for strict jamming as defined by Torquato, Truskett, and Debenedetti [219]) is the vertical curve at the right. Densities higher than MRJ are deep in the glassy regime. From the thermodynamic point of view, the system would cluster in phases separated according to the particle size, but this eutectic freezing-transition is kinetically suppressed [58] and unreachable.

7.2.1 The Dense Limit

Figure 7.3 gives an overview of results by [193], [58] (Fig. 15 therein), and [212] for the phases of the two-dimensional system depending on density and polydispersity. For polydispersity below 0.1, there are two density regimes separated by the ordering transition at ϕ_o ³. These transitions are a purely geometric property (i.e. excluded volume effect) of the configuration space and are therefore athermal. To compute the radial next-neighbor distribution at densities above the critical density, $\phi > \phi_o$, we consider the Voronoï tessellation of the system, which embeds each particle into a convex polygonal cell. The sizes $\{V_i\}$ of the Voronoï cells scale as $(d + s)^D$, where the particle separation is denoted by s . For instance in $D = 2$, the area of a single Voronoï cell in the ensemble is given by $\sum_j (2(d + s_j)(d + s_{j+1}) - [(d + s_j)^2 + (d + s_{j+1})^2] \cos \alpha_j) / (8 \sin \alpha_j)$. This formula holds for direct and indirect Voronoï neighbors, and averaging over the angles α_j between neighbors yields $C(d + s)^2$ on the mean-field level, where we use a single separation s in accordance with the assumption of an isotropic state. (The assumption of isotropy will be relaxed in the discussion of clustering in wet granular matter in Sec. 7.4.1.) In what follows we eliminate the geometry factor C in favor of the jamming density. The mean cell size $\sum_i^N V_i/N = V/N = 1/n$ is exactly the inverse density n . Hence,

$$\left\langle \left(1 + \frac{s}{d}\right)^D \right\rangle = \frac{n(s \rightarrow 0)}{n} = \frac{\phi(s \rightarrow 0)}{\phi}, \quad (7.2)$$

where the triangle brackets denote averaging over next neighbors which are in contact ($s \rightarrow 0$) with the center particle at the jamming density $\phi(s \rightarrow 0)$. We refer to those pairs of particles which come into contact at jamming as neighbors of type A, i.e the surface separation s_A of A-neighbors is

$$s_A = 0 \text{ at } \phi = \phi_J. \quad (7.3)$$

In the monodisperse limit for $D = 2$, ϕ_J assumes the value of the triangular crystal, $\phi_{\max} = \pi/(2\sqrt{3}) = 0.91$. Polydispersity decreases the (maximal random) jamming density ϕ_J and increases the critical density ϕ_o for the onset of triangular order as shown in Fig. 7.3⁴

Contribution to the Contact Correlation: The A-Neighbors

Since the Voronoï cells exchange their free volume, $V - V_{\min} \propto (1 + \frac{s}{d})^D - 1$, and the total volume is conserved we assume an exponential distribution of the free volume, which is well confirmed by experiments with dry granulates [6]. The conditions (7.2) and (7.3) determine the A-neighbor distribution uniquely:

$$P_A(s) \, d \text{ vol}(s) = \frac{D/(\sigma_D d^D)}{\phi_J/\phi - 1} \exp\left(-\frac{(1 + \frac{s}{d})^D - 1}{\phi_J/\phi - 1}\right) d \text{ vol}(s). \quad (7.4)$$

The volume element for $D = 2$ is

$$d \text{ vol}(s) = \sigma_D r^{(D-1)} dr = \pi d (1 + s/d) ds. \quad (7.5)$$

³Numerics reported at present [19, 154] could not distinguish between a weak first order transition (with constant pressure at ϕ_o), and two subsequent continuous transitions (with slowly increasing pressure at ϕ_o).

⁴For monodisperse discs, $\Delta d = 0$, amorphous states have been reported to exist at $\phi = 0.805$ and local jamming is possible at $\phi = 0.844$ [238], while collective jamming occurs not until $\phi = 0.88$ [60]. An extreme and quite nice example for artificial constructions which are stable at densities far below ϕ_{\max} is the Kagomé lattice which has ordered defects.

The contribution g_A which A-neighbors give to the pair correlation is equal to the A-neighbor distribution P_A (7.4) up to a prefactor, so that

$$g_A(s) = g_c^{\text{at}} \exp\left(-\frac{\left(1 + \frac{s}{d}\right)^D - 1}{\phi_J/\phi - 1}\right) \quad (7.6)$$

is determined as soon as we know the athermal contact value, $g_c^{\text{at}} = g_A(0)$. This contact value follows from the classical free volume theory [190] (which was based on [29]),

$$\frac{P}{nT} = \frac{D}{\phi_J/\phi - 1} + \mathcal{O}(1), \quad (7.7)$$

in conjunction with the general relation between the particle-wall correlation $g_{\text{wall}}^{\text{at}}$ and the pair correlation g_c^{at} ,

$$\frac{P}{nT} = g_{\text{wall}}^{\text{at}} = 1 + 2^{D-1}\phi g_c^{\text{at}}. \quad (7.8)$$

As a consequence, we obtain

$$\frac{2^{D-1}}{D}\phi g_c^{\text{at}} = \frac{1}{\phi_J/\phi - 1} \quad (7.9)$$

close to jamming. Expression (7.9) is exact for $D = 1$, and has been confirmed as the asymptotic behavior of the diverging pressure close to jamming for $D = 2$ [148, 91] in event-driven simulation with accuracy 10^{-4} . We remark that this expression is not limited to weak polydispersity and has been confirmed for polydispersity far above 0.1 in the glass state [208, 57]. An independent elementary derivation of Eq. (7.7) is given for $D = 2$ in Appendix 7.9.

Inserting (7.9) in (7.6), we have as the first central result a closed expression for the near-contact pair correlation of neighbors which form exact contacts in the jamming limit (so-called A-neighbors):

$$g_A(s) = g_c^{\text{at}} \exp\left(-\frac{2^{D-1}}{D}\phi g_c^{\text{at}} \left[\left(1 + \frac{s}{d}\right)^D - 1\right]\right). \quad (7.10)$$

Eq. (7.10) implies for the derivative at contact,

$$d g_A'(0) = -2^{D-1}\phi g_A^2(0), \quad (7.11)$$

a quadratic dependence on the contact value $g_c^{\text{at}} = g_A(0)$. Eq. (7.11) can be viewed as a consequence of normalization: the height of the contact peak is g_c^{at} and so the width is of the order $1/g_c^{\text{at}}$, which means that the negative slope is of the order g_c^2 . In fact, writing the A-neighbor correlation function $g_A(s)$ in terms of the contact value g_c^{at} , as we did in (7.10), is the natural form to express the density dependence of g_A because this manifests that the coordination number of A-neighbors is density independent:

$$\begin{aligned} K_A &= n \int g_A \, d\text{vol} \\ &= \frac{2^D}{d} D \phi g_c^{\text{at}} \int_{s=0}^{\infty} \exp\left(-\frac{2^{D-1}}{D}\phi g_c^{\text{at}} \left[\left(1 + \frac{s}{d}\right)^D - 1\right]\right) \left(1 + \frac{s}{d}\right)^{D-1} ds \\ &= 2D. \end{aligned} \quad (7.12)$$

More significantly, K_A equals exactly the isostatic contact value $2D$, which is obviously correct for particles on a line ($D = 1$) and is the accepted value for ideal discs and spheres in $D = 2$ and $D = 3$ dimensions respectively [59, 58, 153]. The finding (7.12) is an essential confirmation of consistency of our approach, since it is independent from conventional arguments based on the rank of the rigidity matrix (which accounts for global constraints on the degrees of freedom) [59].

As the contact value g_c^{at} (7.9) grows to infinity in the jamming limit, $\phi \rightarrow \phi_J$, the constant integral (7.12) implies that $n g_A(s)$ becomes a delta distribution with 'weight' $2D$ at contact, $s = 0$.

The Background Contribution: The B-Neighbors

The configuration space is spanned by all particle positions $\{\mathbf{r}_i\}$. Consequently, a jammed configuration is – aside from a small fraction of rattlers⁵ – an isolated configuration point, and the set of jammed configuration is a set of discrete points. When the density is slightly relaxed, a finite system remains confined to a finite environment around the jamming point (cf. [46], p. 35). As density is lowered further, these environments are no longer isolated so that the system is able to migrate between these 'islands of jamming'.

The stability analysis of contact networks [186, 44, 45, 59, 60] has put forth the result that frictionless spheres (except for the singular limiting case of a monodisperse crystal) jam strictly in an isostatic packing with $2D$ contacts per particle on average, as confirmed numerically [59] for $D = 3$, be the state random (glass regime in Fig. 7.3) or locally ordered. Therefore we can identify within an island of jamming on average four neighboring particles in $D = 2$ dimensions which are close to the reference particle, and which will be in contact with the reference particle, $s_A \rightarrow 0$, in the jamming limit, $\phi \rightarrow \phi_J$. These are the A-neighbors with the contribution g_A to the pair correlation derived in (7.10). Furthermore, it is a mathematical fact that any discrete set of points in flat two-dimensional space has on average six Delaunay/Voronoi neighbors [157], two of which have no contact to the reference particle, $g_B(0) = 0$. Hence, on the mean field level the following picture arises: Beside the four A-neighbors there are two B-neighbors which are sterically hindered by other particles from further approach to the reference particle. Summing up the contributions of A- and B-neighbors,

$$g^{\text{dense}}(s) = g_A(s) + g_B(s) , \quad (7.13)$$

gives us the pair correlation function near contact. The pair correlation near contact which arises from these blocked states, g_B , is discussed in detail in appendix 7.6. The essential result is that the configuration space of blocked states tends quadratically to zero in s_B , so that to leading order the normalization of two B-neighbors for $D = 2$ determines the B-contribution in (7.13):

$$\begin{aligned} g_B(s_B) &= \mathcal{N} P_B(s_B) \\ &= \frac{1}{\phi c_B^3} \left(\frac{s_B}{d} \right)^2 e^{-[(1+\frac{s}{d})^2 - 1]/c_B} \left[1 + \mathcal{O} \left(\frac{s_B}{d} \right) \right] \end{aligned} \quad (7.14)$$

with $c_B = \phi_{\text{max}}/\phi - 1$. In Fig. 7.4 the resulting near-contact pair correlation 7.13 for the dense regime is shown as the sum of g_A and g_B .

⁵Typically one or two percent for packings produced by the Lubachevsky-Stillinger algorithm (Lubachevsky [147] for 2D, [59] for 3D)

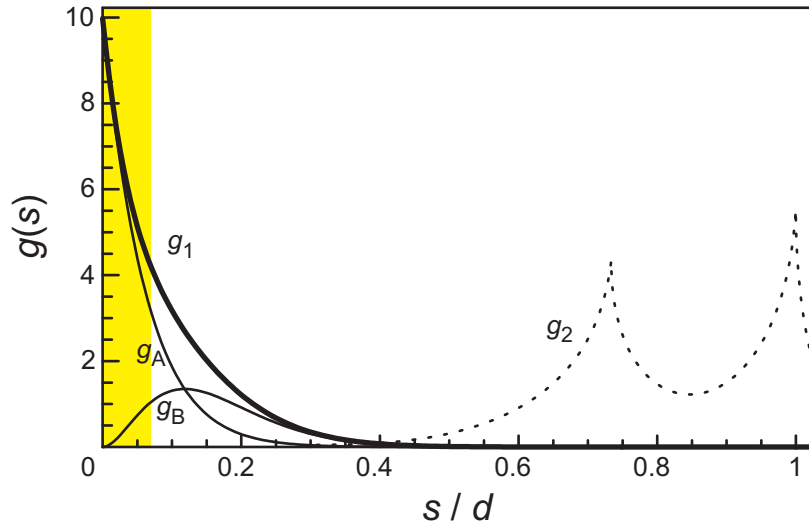


Figure 7.4: The pair correlation near contact resulting from free-volume considerations. Close to jamming we distinguish between neighbors which form exact contacts in the jamming limit (contribution g_A , Eq. (7.10)) and those that are blocked at positive separation s (curve g_B , Eq. (7.14)). The near-contact correlation is the sum of both contributions. For this plot the density is chosen to $\phi = 0.8$. The dashed curve sketches a typical second shell consisting of the second Voronoï neighbors. They are out of the interaction range, $0 < s < s_{\text{crit}}$, which is indicated by the highlighted stripe.

7.2.2 The Dilute and Moderately Dense Regime

In this part we turn to the free rheological regime, $0 < \phi < \phi_o$. When two spheres are closer than one diameter, $s < d$, they shield each other from certain collisions events. If one was to neglect three-particle correlations, the isotropic bombardment by ‘third’ particles gives rise to the well-known attractive depletion force first proposed by S. Asakura and F. Oosawa [4, 5]. As is evident from Fig. 7.5, summing up equal contributions over the accessible cross section is equivalent to the pressure exerted onto the submanifold indicated by the solid line in Fig. 7.5C and denoted by Σ .

This depletion force, as well as the liquid bridge force which we will take into account in the next section, will affect the pair correlation function. A systematic way to study this effect has been worked out by Hansen *et al.* [172], resulting in a Fokker-Planck equation for the two-particle distribution function. After integrating out the momenta and the center of mass coordinates, one finds that the depletion force as well as other non-entropic pair forces (such as the liquid bridge force), give rise to a Boltzmann factor,

$$g(s) \propto \exp\left(-\frac{V(s)}{T}\right). \quad (7.15)$$

For the depletion force

$$F_{\text{depl}} = -V'_{\text{depl}} = T n g_c^{\text{at}} \Sigma, \quad (7.16)$$

where

$$n g_c^{\text{at}} \Sigma ds = \frac{dV_{\text{conf}}}{V_{\text{conf}}} = -d \ln g(s) \quad (7.17)$$

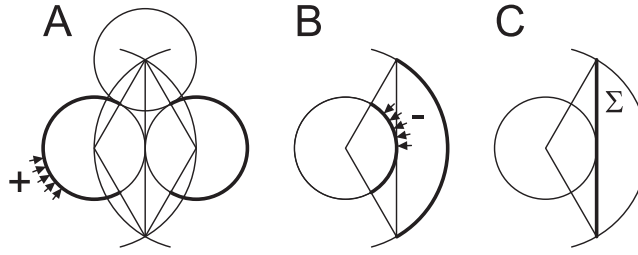


Figure 7.5: Origin of the depletion force attracting neighboring particles that are separated by less than a particle diameter. One may either think of this as an entropic force, due to the decrease of excluded volume when the shells of excluded volume overlap. Equivalently one may view this as the net force due to isotropic bombardment. Obviously, the integration over the solid arc in A is up to a sign equivalent to the integration in plot B. In B the integration is over the outer solid arc, which is the configuration space of the third particle's coordinate at impact. Since the integration in B is projected by a cos-factor to give the axial symmetric force component, we can equivalently drop the cos-factor and integrate over the submanifold indicated by the solid line Σ in C.

is the infinitesimal logarithmic change of the excluded area (or the configuration space per particle, V_{conf}), when the particles are separated by $s < d$, and Σ denotes the size of the corresponding section (line or area) in Fig. 7.5C. At contact, $s = 0$, the size of the integration section Σ is

$$\Sigma = \frac{\sigma_{D-1}}{D-1} \left(\frac{\sqrt{3}}{2} d \right)^{D-1}, \quad (7.18)$$

which yields V_{depl} to leading order in s . The depletion effect with the potential

$$\frac{V_{\text{depl}}}{T} = \frac{9}{2} \phi g_c^{\text{at}} \frac{s}{d} \left(1 - \frac{s}{3d} - \left(\frac{s}{3d} \right)^2 \right) \quad (7.19)$$

for $D = 3$ has been confirmed in [214] by computer simulations. Polydispersity is known to have a minor effect on the depletion attraction [104]. For $D = 1$ (7.17) gives the Poisson distribution $V_{\text{depl}}/T = \phi g_c^{\text{at}} s/d$ which is exact only for $D = 1$.

In two dimensions, the depletion potential is

$$\frac{V_{\text{depl}}}{T} = \frac{2}{\pi} \phi g_c^{\text{at}} \left(4 \arctan \frac{\gamma_{\text{vol}}}{W} + \gamma_{\text{vol}} W - C \right) \quad (7.20)$$

$$= 2g_c^{\text{at}} \frac{\phi}{\phi_{\text{max}}} \frac{s}{d} + \mathcal{O} \left(\frac{s}{d} \right)^2 \quad (7.21)$$

for $D = 2$ with $\gamma_{\text{vol}}(s) = 1 + s/d$, the square root $W(s) = \sqrt{(1 - s/d)(3 + s/d)}$ and the constant $C = 2\pi/3 + \sqrt{3}$ to have $V_{\text{depl}} = 0$ at $s = 0$. The first line (7.20) is valid for $0 \leq s \leq d$, and the second line (7.21) suffices for the region of interest, $0 \leq s \leq s_{\text{crit}} \ll d$. For the application of results on the near-contact decay of the pair correlation function, such as (7.21), we prefer the exponential notation (used before in the dense case (7.10)) because it is most elegant to perform volume integration:

$$g_{\text{AO}}^{\text{dilute}}(s) = g_c^{\text{at}} \exp \left(- \frac{\phi}{\phi_{\text{max}}} g_c^{\text{at}} \left[\left(1 + \frac{s}{d} \right)^2 - 1 \right] \right) \left[1 + \mathcal{O} \left(\frac{s_{\text{B}}}{d} \right)^2 \right] \quad (7.22)$$

for $D = 2$. In this notation the dilute and dense behavior of the pair correlation are conveniently compared, showing that the result (7.22) for the gaseous/fluid regime differs by the factor $1/\phi_{\max} = 1.10$ in the exponent from the dense result (7.10) close to jamming, so that according to (7.22) the depletion force falls-off slower than the configuration density ϕg_c^{at} . We will now show that this is due to an over-estimation of the depletion force, caused by neglecting correlated three-particle events: when the plane of incidence of the third particle closely coincides with the symmetry plane Σ , the incoming particle will hit in short sequence the pair of particles considered, which increases very effectively the exchange of momentum, i.e. the depletion attraction is reduced.

To determine analytically and numerically the effect of correlated collisions which correct the Asakura-Oosawa result (7.22) we define the dimensionless measure

$$Z = \frac{4}{\pi} \frac{F_{\text{depl}}}{nTdg_c^{\text{at}}} = -\frac{dg_c'}{\phi g_c^2}, \quad (7.23)$$

for which the Asakura-Oosawa approach (7.16) and (7.18) gives $Z_{\text{AO}} = \frac{4}{\pi}\sqrt{3} \approx 2.205$ (Line A in Fig. 7.7). When we take correlated three-particle events into account, there are three contributions. Firstly, an attractive contribution $Z_1 > 0$ due to collisions on the front side of the pair, indicated by '1' in Fig. 7.6, which fall in the range $-\pi/2 < \varphi < \pi/2$. The corresponding value Z_1 is easily integrated. Isotropy of the state demands that the angle α between the symmetry axis of the pair $P'P$ and the incoming momentum \mathbf{p}_i is uniformly distributed, as well as the impact parameter b (cf. Fig. 7.6). These collision parameters are related by $(\alpha, b) = (\varphi + \theta, d \sin \theta)$ to the position φ on P and the angle of incidence θ with respect to the normal of P, which implies that φ is uniformly distributed and θ is weighted by the cosine-factor $\cos \theta$. Integration over $-\pi/2 < \varphi < \pi/2$ yields the axial force contribution

$$F_1 = 2Tng_c^{\text{at}}d, \quad (7.24)$$

so that $Z_1 = 8/\pi \approx 2.546$.

Secondly, the attraction is weakened by collisions hitting P in the remaining range $\pi/2 < |\varphi| < \varphi_{\max}(s)$ (which we refer to as the 'broad side') giving rise to $Z_2 < 0$. At contact $\varphi_{\max}(s = 0)$ is $2\pi/3$. For these collisions the incidence is shadowed by the partner particle P' so that the angle of incidence θ is restricted to $-\pi/2 < \theta < \theta_{\max}(\varphi)$. (Confer the collision event '2' in Fig. 7.6.) Some trigonometry determines $\theta_{\max}(s, \varphi)$ by the relation

$$(1 + \gamma_{\text{vol}}(s) \cos \varphi) \sin \theta_{\max} = 1 - \gamma_{\text{vol}}(s) \cos \theta_{\max} \sin \varphi, \quad (7.25)$$

which allows for an explicit function of φ at $s = 0$:

$$2 \cos \theta_{\max}(\varphi) = \tan \frac{\varphi}{2} - \sqrt{1 + 2 \cos \varphi}. \quad (7.26)$$

After integrating over the impact momenta p_i in the rest frame of P, the axial force imposed on P is

$$F_2(s) = \frac{4}{\pi} Tng_c^{\text{at}}d \int_{\pi/2}^{\varphi_{\max}(s)} d\varphi \cos \varphi \int_{-\pi/2}^{\theta_{\max}(\varphi)} d\theta \cos^2 \theta, \quad (7.27)$$

where the $\cos \varphi$ projects the force on the symmetry axis of the pair PP'. The $\cos \theta$ factor appears quadratically in the integrand (7.27) because of the cosine-distribution (or equivalent, because the Enskog collision frequency is proportional to the radial velocity $(p_i/m) \cos \theta$), and

the transferred momentum which is $p_i \cos \theta$. Symmetry allows us to integrate over the upper half, $\pi/2 < \varphi < \varphi_{\max}(s)$ in (7.27) and multiply by 2 with the general result

$$Z_2(s) = \frac{8}{\pi} \int_{\pi/2}^{\varphi_{\max}(s)} d\varphi \cos \varphi \left[\frac{1}{2} + \frac{\theta_{\max}(s, \varphi)}{\pi} + \frac{\sin 2\theta_{\max}(s, \varphi)}{2\pi} \right], \quad (7.28)$$

and the numerical value $Z_2(0) = -0.32813(9)$.

Thirdly, the most obvious and important correction on the three-particle level comes from double collisions denoted by 3 in Fig. 7.6. The third particle hits first P' (gray arrow in Fig. 7.6) from the broad side at $\varphi' \in (\pi/2, \theta_{\max})$. The radial component $p_i \cos \theta'$ of its incoming momentum p_i is transferred to P', which is why the third particle moves on tangentially to the circular cross section of P' with momentum $p_i \sin \theta'$ to collide shortly afterwards with particle P. Here the momentum transferred is the radial component with respect to P, $p_i \sin \theta' \cos \theta$, so that

$$F_3(s) = \frac{4}{\pi} Tng_c^{\text{at}} d \int_{\pi/2}^{\varphi_{\max}(s)} d\varphi' \cos \varphi(\varphi') \cos \theta(s, \varphi') \int_0^{\theta_{\max}(s, \varphi')} d\theta' \cos \theta' \sin \theta'. \quad (7.29)$$

The collision point on P' described by $\varphi'(\varphi)$ is related to φ (the subsequent collision point on P) by $\cos(\varphi' - \varphi) = 1 + \gamma_{\text{vol}}(s) \cos \varphi$. The incident angle θ on P is independent of θ' and given by $\sin \theta(s, \varphi') = 1 + \gamma_{\text{vol}}(s) \cos \varphi'$. After the elementary θ' -integration we find

$$Z_3(s) = \frac{8}{\pi^2} \int_{\pi/2}^{\varphi_{\max}(s)} d\varphi' \cos \varphi(\varphi') \cos \theta(s, \varphi') \sin^2 \theta_{\max}(s, \varphi'), \quad (7.30)$$

and $Z_3(0) = -0.091593(7)$. Summing up the three contributions gives $Z_{\text{corr}} = \sum_{i=1}^3 Z_i \approx 2.127$ which is shown as the line B in Fig. 7.7.

Based on the numerical data presented in Fig. 7.7, we shall in the sequel assume the value

$$Z_{\text{sim}} = 2. \quad (7.31)$$

By virtue of good statistics the simulation at $\phi = 0.097$ gave $Z_{\text{sim}} = 2.0009 \pm 0.0050$, and Fig. 7.7 suggest this result to hold with few percent limits very well over the entire density regime $0 < \phi < \phi_0$ considered in this subsection. The value $Z = 2$ determines the near-contact pair correlation uniquely to be

$$g^{\text{dilute}}(s) = g_c^{\text{at}} \exp \left(-\phi g_c^{\text{at}} \left[\left(1 + \frac{s}{d} \right)^2 - 1 \right] \right) \left[1 + \mathcal{O} \left(\frac{s_B}{d} \right)^2 \right] \quad (7.32)$$

for $D = 2$. Satisfactorily, this result (7.32) has exactly the same functional dependence on the configuration density ϕg_c^{at} as the formula put forward for the dense case (7.10) in the previous subsection. While three-particle collisions are obviously important since they shift Z in the right direction, no analytic explanation for this coincidence corresponding to the value $Z = 2$ is provided at present. Yet we shall see in the next section that any value other than $Z = 2$ would lead to inconsistencies when we introduce the liquid bridge interaction.

We finally remark that the result (7.32) strongly differs from the 'Poissonian fluid' [70], for which the contact correlation $g_c^{\text{at}} - 1 > 0$ is ignored. Even at the lowest density ($\phi = 0.1$) considered in Fig. 7.7 the Poisson fluid would give $Z_{\text{Poisson}}(\phi = 0.1) = 1.7$ which is 15% below the simulation value, and the deviation from $Z = 2$ grows with density ϕ .

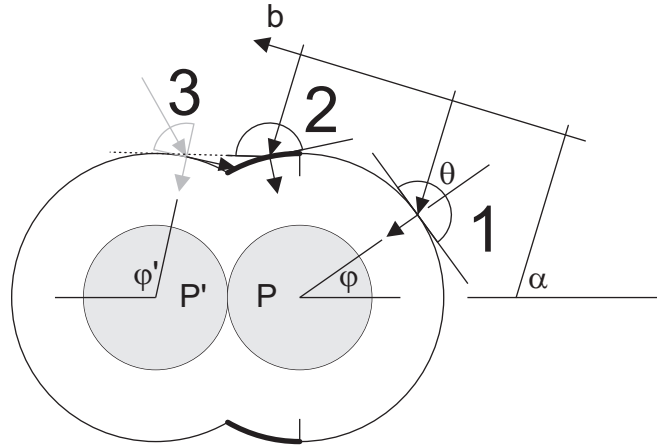


Figure 7.6: Three contributions to the effective force between a pair of particles P and P'. The collisions events 1 are attractive, while the events 2 cause a weaker repulsive forces. Furthermore the attraction is weakened by the temporally correlated collisions events 3.

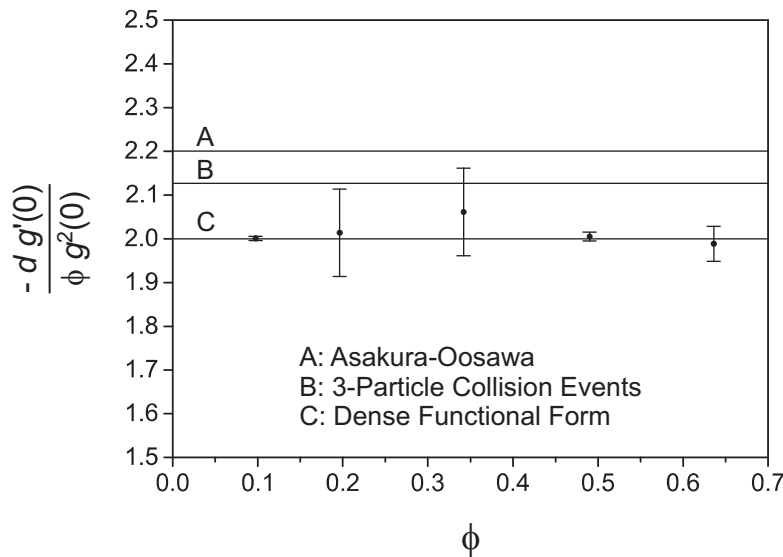


Figure 7.7: Functional test of the near-contact pair correlation (7.32). The vertical axis is proportional to the depletion force, $F_{\text{depl}} \propto -d \ln g/ds$ at contact, divided by the configuration density ϕg_c^{at} . This fraction Z is predicted to be density independent by (7.32) and to assume the value $Z = 2$ (line C). Line A corresponds to the classical Asakura-Oosawa result, which is only valid for large beads immersed in a bath of small beads. In line B the corrections due to temporally correlated collisions events (derived in the text) have been taken into account. These events occur when a third particle of equal size strikes a pair of particles with a given separation $s \ll d$ as sketched in Fig. 7.6. We proceed using the value $Z = 2$ (line C) because it agrees best with the simulation. Furthermore, $Z = 2$ corresponds to a near contact correlation function which is of exactly the same form as the function g_A we use in the dense case, when expressed in terms of the configuration density $\phi g_c^{\text{at}}(\phi)$.

7.3 The Pair Correlation under the Hysteretic Interaction

In this section we dress up the pair correlation function in order to describe the status of the liquid-bonds which are created and ruptured hysteretically in wet granular matter. We will proceed in two steps: first, we introduce in part 7.3.1 the liquid bridges as hysteretic but forceless objects which follow the unperturbed particle dynamics. As a result, a direct relation of the dynamical system and the limiting case of isostatic granular packings [60, 153] at rest is found. In 7.3.2 we turn on the liquid bridge force to its physical value, so that the bridges unfold their back-reaction on the granular dynamics. In the limit of low granular temperatures, $T \ll E_{cb}$, the particles stick together. For this frozen state of wet granular matter the bridge coordination K is computed analytically as a function of the rupture length s_{crit} , and we find very good agreement with simulations.

7.3.1 The Hysteretic Coupling

Due to the hysteretic interaction, the pair correlation g is no longer a function of the particle separation s . In order to include the knowledge about the collision history the configuration space has to be enlarged in two respects: Obviously we distinguish between pairs with and without liquid bridges, which we denote by superscript indices, $g^b(s)$ and $g^u(s)$ respectively, for ‘bridged’ and ‘unbridged’ neighbors (cf. Fig. 7.8). In addition, time reversal-symmetry is broken by the formation of the capillary bridge at contact. Hence we distinguish approaching pairs (with a negative relative velocity) which might collide and form a liquid bridge in the future, and those that move apart so that they can rupture the liquid-bond in the future. This relative velocity is denoted by a subscript arrow.

As we discuss the radial pair distribution, contact and rupture become the important points on the s -axis of the pair correlation function. At these points the functions g^b and g^u are coupled according to the hysteretic transition of the bond status. We use an intuitive notation, writing ‘c’ and ‘r’ in the subscript for contact and rupture distance, respectively:

$$\begin{aligned}
 g_{c \leftarrow \textcircled{v}}^u &= \begin{cases} \text{The probability for a pair} \\ \text{at rupture distance} \\ \text{approaching without bridge.} \end{cases} \\
 g_{\textcircled{c} \rightarrow r}^b &= \begin{cases} \text{The probability for a pair} \\ \text{at contact} \\ \text{moving away with bridge.} \end{cases} \\
 &\text{etc.}
 \end{aligned}$$

A configuration at contact, $s = 0$ (or to be more precise: the right-sided limit $s = 0+$), is denoted by a circled \textcircled{c} , and the rupture at $s = s_{\text{crit}}$ by the circled \textcircled{v} . The uncircled letter allows to conveniently indicate the direction of motion with the arrow. Infinitesimally close to contact, there are four detailed correlation values: the bridge-connected and the unconnected states, either particularized by the sign of the relative velocity. The same is true for the left-sided limit $s = s_{\text{crit}} -$ of the rupture point. An infinitesimal distance beyond this point, at $s = s_{\text{crit}} +$, there is only the unbound state possible with the two signs for incoming and outgoing velocities. This gives us in total ten detailed pair correlation coefficients. These are determined by the following ten equations describing the hysteretic flow of probability, as it we can be read off from Fig. 7.8:

Conditions on the contact shell

$$g_{\textcircled{c} \rightarrow r}^u = 0 \tag{7.33}$$

$$g_{\textcircled{c} \rightarrow r}^b = g_{\textcircled{c} \leftarrow r}^u + g_{\textcircled{c} \leftarrow r}^b \tag{7.34}$$

The Eq. (7.33) expresses that no particles rebound without a liquid-bond, but rather that all return with a bridge as stated by (7.34). This implies that the particle number is conserved in collisions (in contrast to the absorbent dynamics modeled in [241] for $D = 1$).

Domain of capillary interaction

$$g_{\mathcal{C}}^b = \gamma^b(s_{\text{crit}}) g_{\mathcal{C}}^b \quad (7.35)$$

$$g_{\mathcal{C}}^u = \gamma^u(s_{\text{crit}}) g_{\mathcal{C}}^u \quad (7.36)$$

$$g_{\mathcal{C} \rightarrow \mathcal{C}}^u = \gamma_{\text{pass}} g_{\mathcal{C} \leftarrow \mathcal{C}}^u \quad (7.37)$$

The functions $\gamma^u(s)$ and $\gamma^b(s)$ take into account the near-contact decay of the pair correlation without and with liquid bond, respectively. The last Eq. (7.37) describes spectator grains, i.e. grains which pass through the domain of possible capillary interaction without bridge formation. The fraction of these passing particles, $\gamma_{\text{pass}} = 1 - (1 + s_{\text{crit}}/d)^{1-D}$ ($= 1/(1 + d/s_{\text{crit}})$ for $D = 2$) equals the gap between the considered cross section $(2d + 2s_{\text{crit}})^{D-1}$ of the capillary interaction and the hard-core cross section $(2d)^{D-1}$.

Conditions on the rupture shell

$$g_{\mathcal{C} \leftarrow \mathcal{C}}^b = 0 \quad (7.38)$$

$$g_{\mathcal{C} \leftarrow \mathcal{C}}^u = g_{\mathcal{C} \leftarrow \mathcal{C}}^u \quad (7.39)$$

$$g_{\mathcal{C} \rightarrow \mathcal{C}}^b + g_{\mathcal{C} \rightarrow \mathcal{C}}^u = g_{\mathcal{C} \leftarrow \mathcal{C}}^u \quad (7.40)$$

The Eqs. (7.38, 7.39) state that only unbound particles enter the domain of capillary interaction, and (7.40) describes the rupture of a capillary bridge when the pair escapes from the domain.

The hysteretic capillary dynamics is coupled to the hard particle dynamics by the source term of new unbound pairs of particles entering the capillary interaction range:

Source Term

$$g_{\mathcal{C} \leftarrow \mathcal{C}}^u + g_{\mathcal{C} \leftarrow \mathcal{C}}^u / \gamma^u(s_{\text{crit}}) = (1 - K/K_{\text{sites}}) g_{\mathcal{C}}^{\text{at}} \quad (7.41)$$

The left-hand side is the current of approaching unbound neighbors (measured at contact). If all neighbors were unconnected, $K = 0$, this current would equal the dry value $g_{\mathcal{C}}^{\text{at}}$. But since there are K neighbors with bonds out of the K_{sites} 'docking sites' which are sterically accessible for liquid bonds, the remaining unconnected fraction is $1 - K/K_{\text{sites}}$.

The final tenth equation is the stationary state condition, which demands that the rupture frequency equals the binding frequency:

Stationary state condition

$$f_{\text{bind}} = f_{\text{rupt}} \quad (7.42)$$

These frequencies follow from the probability to have a particle on the collision or rupture shell, respectively, multiplied by the radial component of the relative velocity under the condition that the particle moves in the appropriate direction for the event to occur. This is analogous to the case $D = 1$ in Chap. 6, with the only difference that here we have to integrate over shells:

$$f_{\text{bind}} = 2^{D+1} D \sqrt{\frac{T}{\pi}} \frac{\phi}{d} g_{\mathcal{C} \leftarrow \mathcal{C}}^u, \text{ and} \quad (7.43)$$

$$f_{\text{rupt}} = 2^{D+1} D \sqrt{\frac{T}{\pi}} \frac{\phi}{d} g_{\mathcal{C} \rightarrow \mathcal{C}}^b \gamma_{\text{vol}}(s_{\text{crit}}) \quad (7.44)$$

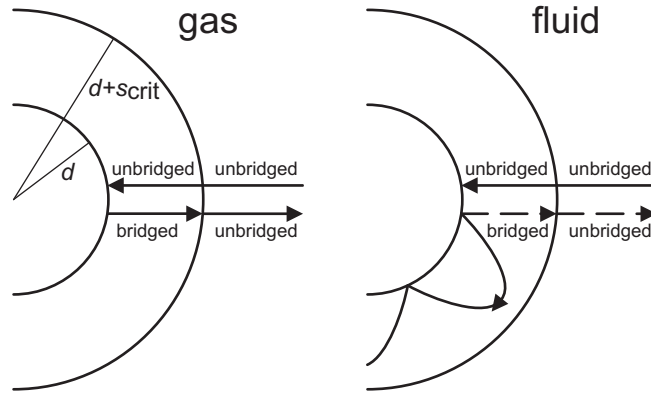


Figure 7.8: The hysteretic interaction in a wet granular gas or fluid can either lead to scattering or bound states. Note that the formation and rupture of the liquid bridge is spatially separated, which gives rise to a hysteretic loss and a coupling between the pair correlation functions g^b for neighbors with and without, g^u , capillary bridge. In this sketch the maximal liquid bridge length s_{crit} is drawn largely exaggerated. For a typical volume fraction of 1% wetting liquid added to the volume of jammed granular matter one finds $s_{\text{crit}}/d \approx 0.07$ [114].

The volume factor $\gamma_{\text{vol}}(s) = (1 + s/d)^{(D-1)}$ takes the increased size of the outer rupture shell as compared to the inner binding shell into account.

Eliminating those correlation coefficients that are identically zero (7.33, 7.38), we can arrange the coupling equations for the domain of capillary interaction as a 6×6 matrix system:

$$\begin{array}{l}
 \text{Collision:} \\
 \text{With Bridge:} \\
 \text{Unconnected:} \\
 \text{Stationarity:} \\
 \text{Spectators:} \\
 \text{Source:}
 \end{array}
 \begin{pmatrix}
 1 & 1 & -1 & 0 & 0 & 0 \\
 0 & \gamma^b & \gamma^b & 0 & -1 & 0 \\
 \gamma^u & 0 & 0 & -1 & 0 & -1 \\
 -1 & 0 & 0 & 0 & \gamma_{\text{vol}} & 0 \\
 0 & 0 & 0 & -1 & 0 & \gamma_{\text{pass}} \\
 1 & 0 & 0 & 0 & 0 & 1/\gamma^u
 \end{pmatrix}
 \circ
 \begin{pmatrix}
 g_{\text{c} \leftarrow \text{r}}^u \\
 g_{\text{c} \leftarrow \text{r}}^b \\
 g_{\text{c} \rightarrow \text{r}}^b \\
 g_{\text{c} \rightarrow \text{r}}^u \\
 g_{\text{c} \rightarrow \text{r}}^b \\
 g_{\text{c} \leftarrow \text{r}}^u
 \end{pmatrix}
 = (1 - K/K_{\text{sites}}) g_{\text{c}}^{\text{at}}
 \begin{pmatrix}
 0 \\
 0 \\
 0 \\
 0 \\
 0 \\
 1
 \end{pmatrix}
 \quad (7.45)$$

The γ -functions in the matrix are to be evaluated at $s = s_{\text{crit}}$. As it has to be on physical grounds, this system is non-singular with determinant $(1 + s_{\text{crit}}/d)^{D-1} (2 + \gamma_{\text{pass}}) \gamma^b(s_{\text{crit}}) > 0$.

The last row of the system (7.45) describes the creation of new liquid bridges as discussed before in the context of the equivalent Eq. (7.41). We remark that here we used that the correlation g_{c}^{at} of the dry system at contact has equal contributions from positive and negative relative velocities, immediately before and after the collision, which is still true for the wetted elastic particles we consider. This symmetry between positive and negative radial relative velocities is broken if one wishes to introduce a restitution coefficient $0 < \epsilon < 1$ to model inelastic collisions: the contact correlation of positive velocities is then increased by a factor $1/\epsilon$ as compared to the negatives.

One should see clearly the very different meaning of K and K_{sites} . The dynamical quantity K is the *number of instantaneously existing capillary bonds*:

$$K = 2^D D \phi \frac{g_{\text{c}}^b}{d} \int_0^{s_{\text{crit}}} \gamma^b(s) \gamma_{\text{vol}}(s) ds . \quad (7.46)$$

K rapidly decays close to zero in dilute systems. As K comes closer to the value of K_{sites} in a very dense system, the binding frequency $f_{\text{bind}} \propto g_{\text{c} \leftarrow \text{r}}^u \propto K - K_{\text{sites}}$ (7.43) goes to

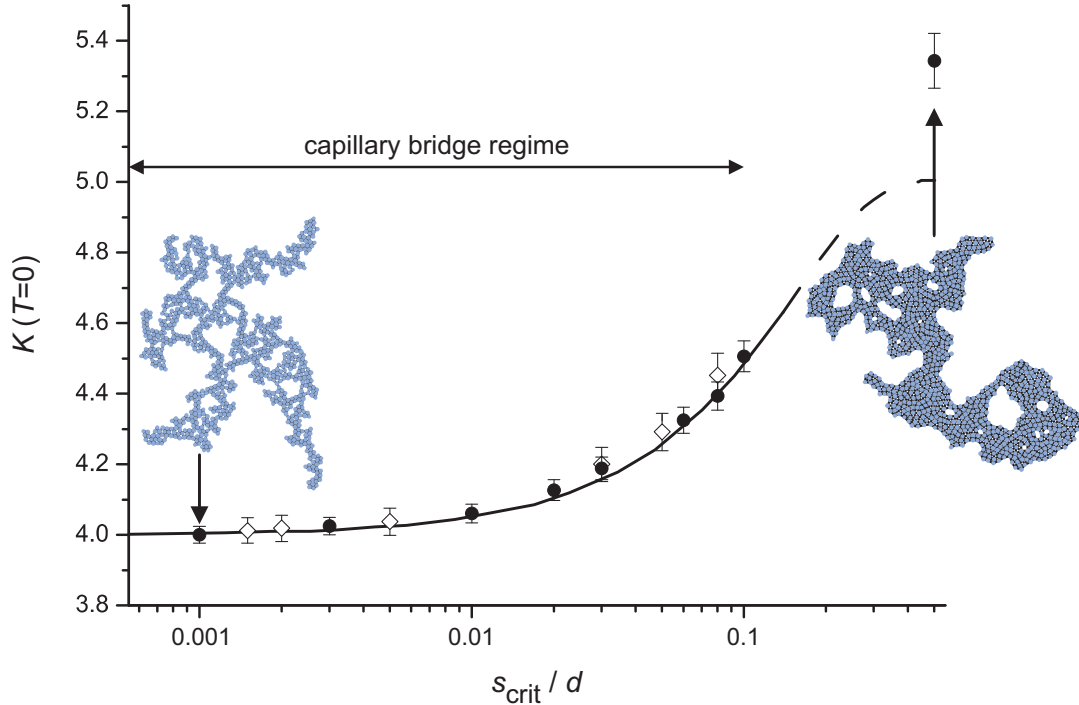


Figure 7.9: The capillary bridge coordination K in the low temperature limit, $T \ll E_{cb}$. As proven in the text, K converges to the athermal function $K_{\text{sites}}(\phi, s_{\text{crit}})$ in this low temperature limit. The solid line is $K_{\text{sites}}(\phi_0, s_{\text{crit}})$ over a wide range of maximal bridge lengths s_{crit} . Points represent final states of free cooling simulations with 1000 particles of uniformly distributed polydispersity $\Delta d = 0.06d$. The open symbols are clusters with winding number one (cylindrical topology), connected over one periodic boundary on a rectangular domain. Such structures have internal tensile strength which necessitates a slightly increased coordination, visible as a small shift compared to the closed symbols which represent localized clusters (as the two examples drawn in the plot). As predicted by Eq. (7.51) of the presented theory, the structures emerging with exact contacts, $s_{\text{crit}} \rightarrow 0$, are found to be precisely isostatic, $K_{\text{sites}} = 4$. The line is the analytic result (7.50), for which very good agreement is found with the simulations over the entire range of the capillary bridge regime, $0 < s < 0.2r$ (with r the particle radius), which is indicated in the figure. Beyond this regime, the theory does not hold because in the derivation we limited ourselves to the leading order in s_{crit}/d . More importantly, the rupture length s_{crit} cannot be further increased beyond the capillary regime by simply increasing the liquid content in the granular sample. As mentioned in the introduction, liquid bridges residing on the same sphere would rather merge [197] into more complicated objects.

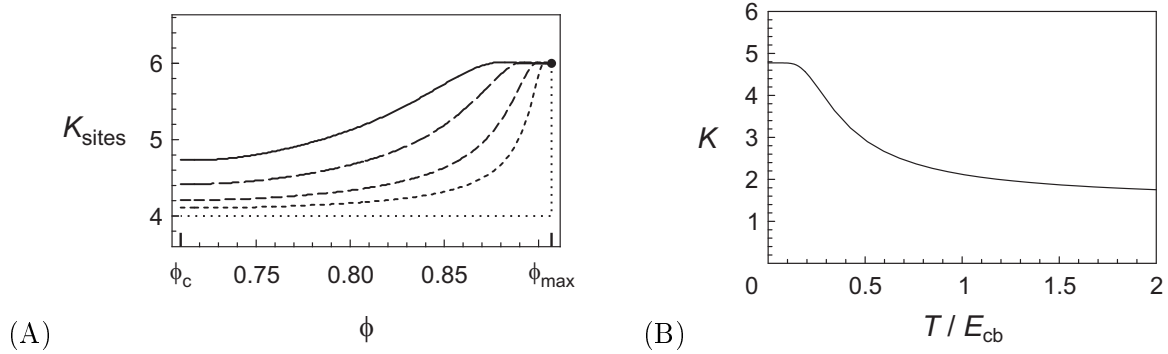


Figure 7.10: (A) The maximum number of 'docking sites' for capillary bonds on a particle, K_{sites} , which is possible in two dimensions given the pinch-off length s_{crit} of capillary bridges and the density ϕ . K_{sites} is independent of the temperature because it is a pure geometric quantity: the number of possible neighboring sites. Here K_{sites} is shown as a function of ϕ for different s_{crit} ranging from $s_{\text{crit}}/d = 0.07$ (solid curve), 0.04, 0.02, to 0.01 (short dashes). As is shown in the text, K_{sites} is the coordination number in the zero temperature limit. While the mean coordination number K rapidly goes to zero with density for finite temperature, the zero-temperature limit is ≥ 4 for all densities, because the system clusters. The dotted curve represents the limit $s_{\text{crit}} \rightarrow 0$. The longer s_{crit} the closer K_{sites} comes to six, the number of next neighbors in two dimensions. In the limit $s_{\text{crit}} \rightarrow 0$ the coordination K_{sites} converges to the number of exact contacts which is precisely four. (B) The capillary bridge coordination K drops down in the vicinity of the critical temperature as clustered structures break up. For this plot the mean density is chosen to be $\phi = 0.75$.

zero because steric hindrance prohibits the formation of further capillary contacts: $K - K_{\text{sites}}$ gives the number of vacant sites for capillary bonds. Therefore K_{sites} is the maximum number of 'docking sites' for capillary bonds. It is a pure geometric property and grows with s_{crit} , because $s_{\text{crit}} > 0$ still allows for a slight rearrangement of particles in the formation of new capillary bridges without breaking existing ones. In the limit $s_{\text{crit}} \rightarrow 0$, K_{sites} is the number of 'contact sites'. We therefore expect K_{sites} to equal the number of exact contacts, $2D = 4$. So let us compute $K_{\text{sites}}(\phi, s_{\text{crit}})$ in the following paragraph.

The maximum number of possible bonds, K_{sites} , is an athermal function of density ϕ and the critical liquid bridge length s_{crit} . We determine K_{sites} from the obvious fact, that the granular dynamics is unaffected by the introduction of forceless bridges: for $\gamma^b = \gamma^u$ we recover the dry contact correlation $g_{\text{c}}^b + g_{\text{c}}^u = g_{\text{c}}^{\text{at}}$. This is the athermal limit, or high temperature limit of wet granular matter.

$$\text{High temperature limit} \begin{cases} \gamma^b = \gamma^u \\ g_{\text{c}}^b + g_{\text{c}}^u = g_{\text{c}}^{\text{at}} \end{cases} \quad (7.47)$$

From the hysteretic bridge system (7.45) follows in this forceless or high granular temperature limit (7.47):

$$\left(1 - \frac{\gamma^u \gamma_{\text{vol}}}{1 + \gamma_{\text{pass}}}\right) K_{\text{sites}} = (1 + \gamma^u \gamma_{\text{vol}}) K \quad \text{and} \quad (7.48)$$

$$g_{\text{c}}^b = \frac{g_{\text{c}}^{\text{at}}}{1 + \gamma^u \gamma_{\text{vol}}}. \quad (7.49)$$

The γ -functions with the argument s suppressed are understood to be evaluated at $s = s_{\text{crit}}$.

Inserting the Eqs. (7.48) and (7.49) in (7.46) yields

$$K_{\text{sites}} = 2^D D \phi g_{\text{c}}^{\text{at}} \frac{\int_0^{s_{\text{crit}}} \gamma^{\text{u}}(s_{\text{crit}}) \gamma_{\text{vol}}(s_{\text{crit}}) ds/d}{1 - \gamma^{\text{u}} \gamma_{\text{vol}} / (1 + \gamma_{\text{pass}})} \quad (7.50)$$

$$= 4 \frac{1 - \gamma^{\text{u}} + \mathcal{O}(s_{\text{crit}}^3)}{1 - \gamma^{\text{u}} + \mathcal{O}(s_{\text{crit}}^2)} = 4 + \mathcal{O}(s_{\text{crit}}) . \quad (7.51)$$

In the last line we have set $D = 2$, so that we could use (7.10) and (7.14). The result (7.51) is the second important consistency test. Finding the number of exact contacts in the jamming limit to equal four in (7.12) showed the consistency of the free-volume argument applied there. Here in (7.51) we find for any density that the different function K_{sites} for the number of possible bridges sites equals four as well when $s_{\text{crit}} = 0$. This is as intuitively expected and a confirmation of the consistency between the hysteretic system (7.45) and the near-contact pair correlation. In view of the numerical finding $Z_{\text{sim}} = 2$ for the derivative at contact of the pair correlation (as defined in (7.23)) we remark that the entirely analytic description by the hysteretic system gives in general $K_{\text{sites}} = 8/Z + \mathcal{O}(s_{\text{crit}})$, which is why the consistency is non-trivial and the finding $Z_{\text{sim}} = 2$ fits favorably into the entire picture.

Thus the hysteretic system (7.45) provides a direct connection between the static granular properties captured in K_{sites} and the granular system in motion at positive granular temperature which we are treating in general. We remind that K_{sites} is determined by the steric self-hindrance and therefore a pure geometric property independent of the granular temperature. When inspecting a snapshot of a close granular packing we can find local cases of contact coordination ($s_{\text{crit}} = 0$) higher than four. These are fluctuations within the granular ensemble, while K_{sites} and K are mean-field quantities. Of course, for a finite bridge length $s_{\text{crit}} > 0$, a mean bridge coordination $K \in (0, K_{\text{sites}})$ with K_{sites} higher than four is possible due to elongated bridges, as described by (7.50). Before we evaluated the expression (7.50) of K_{sites} for positive s_{crit} (plotted in Fig. 7.9), it is enlightening to switch on the capillary forces in the following section because this allows us to apply K_{sites} to 'frozen' wet granular matter.

7.3.2 Switching On the Force of Capillary Bridges

Under the attraction of a liquid bridge, the pair correlation $g^{\text{b}}(s)$ of connected neighbors falls off faster than $g^{\text{u}}(s)$ for unbound particles, depending on the granular temperature T/E_{cb} compared to the bridge energy. The logarithmic derivative of the radial pair correlation is to be interpreted as the effective radial force [112, 111], $\beta F = \partial_s \ln g(s)$, as discussed before in Sec. 7.2.2. This exponential dependence can be justified as the solution of the Fokker-Planck equation derived in [172]. Moreover, in the context of the hysteretic interaction of wet granular matter this exponential factor has been successfully applied in the case $D = 1$ (cf. Eq. (6.5) in Chap. 6). Therefore we proceed by switching on the liquid bridge force to the physical value of the Minimal Capillary Model (cf. 3 and [114]), $F_{\text{b}} = E_{\text{cb}}/s_{\text{crit}}$, including this exponential in the short-range dependence of the pair correlation function for bridges neighbors:

$$\gamma^{\text{b}}(s, T) = \gamma^{\text{u}}(s) \exp\left(-\frac{E_{\text{cb}}}{T} \frac{s}{s_{\text{crit}}}\right) . \quad (7.52)$$

At low granular temperatures this exponential gives rise to shorter average bridge lengths, and describes the reduced probability that a bridge reaches its critical length s_{crit} . Therefore the hysteretic system (7.45) describes the sticking of particles and the onset of clustering.

We have discussed in the previous Sec. 7.3.1 that steric effects in the dynamical system limit the mean number of bonds to a maximum of K_{sites} , and we derived that K_{sites} converges to the number of isostatic contacts in the limit $s_{\text{crit}} \rightarrow 0$. Here this connection is put on

firm grounds with a clear physical interpretation attributed to K_{sites} : K_{sites} is the bridge coordination K of solid wet granular matter.

Proof of $K \rightarrow K_{\text{sites}}$ in the low temperature limit. Solving (7.45) for K/K_{sites} , we obtain

$$\frac{K(T, s_{\text{crit}}, \phi)}{K_{\text{sites}}(s_{\text{crit}}, \phi)} = \frac{1}{1 + X(T)/Y(T)}, \quad (7.53)$$

with

$$X(T) = \gamma^b(s_{\text{crit}}, T) K_{\text{sites}} (\gamma_{\text{pass}} + 2)\gamma_{\text{vol}} \text{ and} \quad (7.54)$$

$$Y(T) = 8I(T) \phi g_{\text{c}}^{\text{at}} (\gamma_{\text{pass}} + 1), \quad (7.55)$$

where $I(T)$ stands for the integral over bond states,

$$I(T) = \int_{s=0}^{s_{\text{crit}}} \gamma^b \gamma_{\text{vol}} ds/d = \int_{s=0}^{s_{\text{crit}}} e^{-\frac{E_{\text{cb}}s}{Ts_{\text{crit}}}} \gamma^u \gamma_{\text{vol}} ds/d = \frac{T s_{\text{crit}}}{E_{\text{cb}}d} + \mathcal{O}(T^2), \quad (7.56)$$

which goes linearly to zero, while $\gamma^b(T) \propto e^{-E_{\text{cb}}/T}$ vanishes for $T \rightarrow 0$ faster than any power of T . Hence $X/Y \rightarrow 0$ so that Eq. (7.53) implies

$$\lim_{T \rightarrow 0} K = K_{\text{sites}} \quad (7.57)$$

as conjectured.

This low temperature limit ($T \ll E_{\text{cb}}$) is of general interest since it represents a sticky gas of ideal spheres, which serves as a model for aggregation in various areas of physics [173] and astrophysics [22]: once two particles had contact, the remaining degree of freedom is tangential motion. The analytic prediction of formula (7.51) is $K_{\text{sites}} = 4$ in the limit of exact contacts, $s_{\text{crit}} = 0$. In order to evaluate (7.50) for positive s_{crit} we insert the near-contact decay γ^u given by the general results (7.10), (7.14), and (7.32), setting $D = 2$. The explicit expression for γ^u , which we use throughout this thesis for results without free parameters, is given in the appendix 7.7. Here we take into account known formulas for the contact value g_{c}^{at} at low densities, as well as higher corrections to the free volume theory. Inserting this expression in (7.50) results in the curve shown in Fig. 7.9. We have performed simulations in this low-temperature limit. The wet granular matter was initially prepared in a gas state with $T = 50E_{\text{cb}}$ and cooled by the formation and rupture of bonds. The insets in Fig. 7.9 show final states when the granular temperature T is more than one order of magnitude below E_{cb} and no further change in the configuration was observed on exponential time scales. The symbols in Fig. 7.9 have been measured in this final state. In perfect agreement with the prediction of Eq. (7.51), we find in the contact limit, $s_{\text{crit}} \rightarrow 0$, the coordination to be exactly 4. Moreover, the increase in the number of bonds per particle with the increase of the maximal bridge length s_{crit} is found to be in very good agreement with the simulations.

Further analytic results for high densities are shown in Fig. 7.10 (A). As is intuitively clear and shown by the family of curves in Fig. 7.10 (A), the convergence of the limit $s_{\text{crit}} \rightarrow 0$ is not uniform with respect to density, since K_{sites} is pinned to the kissing number 6 of the monodisperse crystal density at ϕ_{max} .

7.4 The Equation of State and the Critical Point

We are now in the position to derive the equation of state, $P = P(T, \phi)$, for wet granular matter with capillary bonds tensile up to the rupture length s_{crit} . The cohesion of capillary

bridges will reduce the pressure as compared to a dry hard-sphere system of equal temperature. By virtue of Eq. (7.53), we have the bridge coordination number K as a function of density ϕ and granular temperature T . Since in the Minimal Capillary Model the bridge force is assumed to be independent of the bridge length s , the knowledge of the mean number of bridges K will allow us to evaluate the reduction of the pressure due to cohesion. Furthermore, the particle-particle collisions are enhanced by the bridge attraction, increasing the contact correlation. The contact correlation g_{\odot}^{wet} for wet granular matter derives from the Eqs. (7.45) and (7.46):

$$g_{\odot}^{\text{wet}} = g_{\odot}^{\text{at}} \frac{(1 + \gamma_{\text{pass}})(1 + \gamma^{\text{b}}\gamma_{\text{vol}}) I^{\text{u}}}{(1 + \gamma_{\text{pass}} - \gamma^{\text{u}}\gamma_{\text{vol}})I^{\text{b}} + (2 + \gamma_{\text{pass}})\gamma^{\text{b}}\gamma_{\text{vol}}I^{\text{u}}} \quad (7.58)$$

with the integrals

$$I^{\text{u/b}} = \int_0^{s_{\text{crit}}} \gamma^{\text{u/b}}(s) \gamma_{\text{vol}}(s) ds . \quad (7.59)$$

The analytic expression (7.58) for the contact correlation of wet granular matter, g_{\odot}^{wet} , is indeed strictly greater than the one of the dry system, g_{\odot}^{at} , to which it converges in the high temperature limit when the capillary energy E_{cb} is small compared to the granular temperature T . This limit follows obviously from (7.58) because the functions with superscript index 'b' turn into those with 'u' for $T \gg E_{\text{cb}}$. In the low temperature limit, liquid bonds oscillate with an amplitude proportional to the kinetic energy which equals T on average, so that the probability to find the particles at contact, g_{\odot}^{wet} , grows proportional to $1/T$, as can be derived easily from (7.58) using the expansion (7.56).

7.4.1 Frozen Degrees of Freedom

As the system starts to cluster at temperatures close to E_{cb} , voids remain between the clusters with linear dimensions large compared to the particle diameter. Clearly, this growing length scale, which is set by the sizes of clusters and voids, is not captured by the short-range behavior of the pair correlation function. Here we advance the theory beyond the level of two-particle correlations to take correlation on large scales, such as the collective particle motion in a cluster, in an approximative fashion into account.

The collective motion of a cluster is due to stable capillary bonds which impose constraints, such that the internal degrees of freedom of clusters are frozen. Since K is the number of instantaneous capillary bridges of which the fraction $\text{erf}(\sqrt{E_{\text{cb}}/T})$ with kinetic energies below E_{cb} forms stable bonds, we have

$$K_{\text{frozen}} = K \text{erf} \left(\sqrt{\frac{E_{\text{cb}}}{T}} \right) \quad (7.60)$$

for the number of frozen degrees of freedom.

We are interested in the density of the remaining degrees of freedom. The idea is simple and powerful: As a general mathematical property of triangulations, there are on average precisely six Voronoï neighbors [157], independent of density or ordering. In Fig. 7.11 we can observe that the Voronoï neighbors with stable bonds contribute less to the area $1/n$ of the Voronoï cell. This picture suggest a two-fluid model with frozen and free neighborhoods as the two constituents. The fraction of frozen and free triangulation bonds is proportional to K_{frozen} and K_{free} respectively, and the area contributions associated to each bond sum up to the total size of the Voronoï cell:

$$K_{\text{frozen}} + K_{\text{free}} = 6 \quad (7.61)$$

$$\frac{K_{\text{frozen}}}{n_{\text{frozen}}} + \frac{K_{\text{free}}}{n_{\text{free}}} = \frac{6}{n} . \quad (7.62)$$

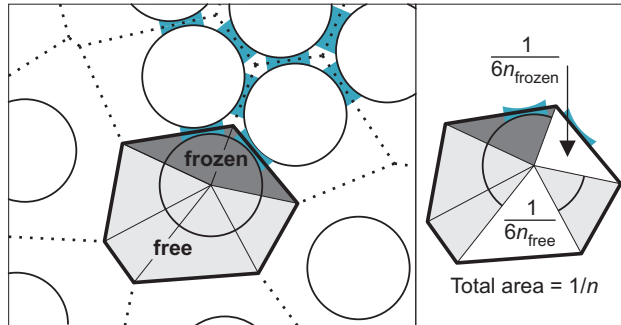


Figure 7.11: A local configuration of two-dimensional wet granular matter at moderate density. The cell borders are located at one half of the surface separation for polydisperse diameters (not half center distance), so that each cell contains one particle completely. Since there is one particle in each Voronoï cell, the mean area equals the inverse density. In Sec. 7.2.1 we have used the Voronoï tessellation to compute the derivative of the pair correlation at contact for a dry and dense system. For such a dense system, the Voronoï cell resembles a hexagon with a size proportional to $(d + s)^2$, where s is the particle separation. In wet granular matter, we distinguish the densities n_{free} and n_{frozen} associated with the binding status of the capillary interaction. A stable capillary bond contributes $1/(6n_{\text{frozen}})$ to the cell area, $1/n$, and thus less than an unconnected neighborhood with $1/(6n_{\text{free}})$ does. The areas sum up to the cell size, so that these densities are related as expressed by the Eqs. (7.61) and (7.62).

Because of this reciprocal sum rule for the densities one may call this a reciprocal two-fluid model. The densities $n_{\text{free}} < n < n_{\text{frozen}}$ introduced by Eq. (7.62), generalize the mean density n by decomposing the volume $1/n$ per particle into bound and free neighborhoods on the mean-field level. $1/(6n)$ is the average volume of a neighborhood, since there are six neighborhoods on average. The contribution of a free Voronoï neighbor is $1/(6n_{\text{free}})$, and $1/(6n_{\text{frozen}})$ is the contribution of a neighborhood frozen by a capillary bridge. Put in physical terms, n_{frozen} is the local density inside a cluster.

The density n_{frozen} of the stable bond component follows analogously to (7.2) when averaged with the additional exponential factor (7.52) due to the capillary force:

$$\left\langle \left(1 + \frac{s}{d}\right)^D \right\rangle_{\text{frozen}} = \frac{n_{\text{J}}}{n_{\text{frozen}}} \quad (7.63)$$

$$\langle \dots \rangle_{\text{frozen}} = \frac{\int_0^{s_{\text{crit}}} \dots \gamma_{\text{frozen}}(s) \gamma_{\text{vol}}(s) ds}{\int_0^{s_{\text{crit}}} \gamma_{\text{frozen}}(s) \gamma_{\text{vol}}(s) ds} \quad (7.64)$$

$$\gamma_{\text{frozen}}(s) = \exp\left(-\phi g_{\text{c}}^{\text{at}} \left[\left(1 + \frac{s}{d}\right)^D - 1\right] - \frac{E_{\text{cb}}}{T} \frac{s}{s_{\text{crit}}}\right) \quad (7.65)$$

Without affecting the leading order in s/d one is free to replace the last s in the exponent (7.65) by $s + s^2/(2d)$, so that the integral (7.63) is elementary resulting in

$$\frac{n_{\text{J}}}{n_{\text{frozen}}} - 1 = \left[\left(1 + \frac{s_{\text{crit}}}{d}\right)^D - 1\right] \left(\frac{1}{\alpha} - \frac{1}{e^{\alpha} - 1}\right) \quad (7.66)$$

$$\text{with } \alpha = \left[\left(1 + \frac{s_{\text{crit}}}{d}\right)^D - 1\right] \left(\phi g_{\text{c}}^{\text{at}} + \frac{E_{\text{cb}}}{T} \frac{d}{Ds_{\text{crit}}}\right). \quad (7.67)$$

We point out that Eq. (7.66) implies Eq. (6.6) in Chap. 6 for $D = 1$.

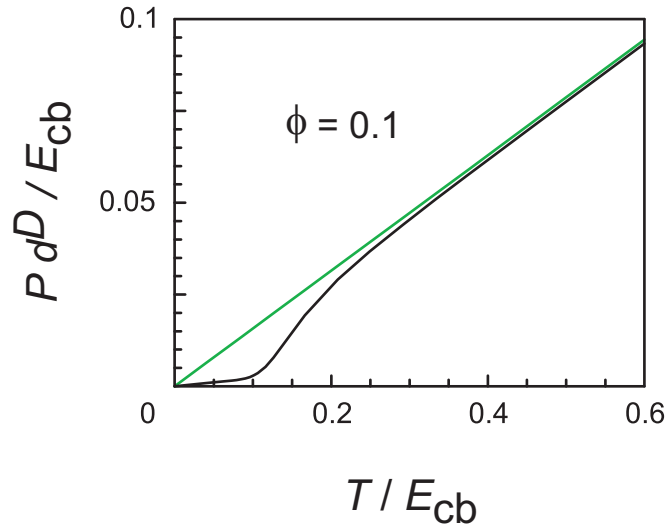


Figure 7.12: The pressure P of wet granular matter is shown as function of the granular temperature T . The dimensionality is $D = 2$ and the covered area fraction is $\phi = 0.1$, so that at high temperatures the system is a dilute gas. The maximum bridge length is $s_{\text{crit}} = 0.07d$. The behavior below the critical temperature $T_c = 0.274E_{\text{cb}}$ of wet granular can be understood in the following way: the system agglutinates to clusters. With these effective particles the pressure is reduced according to the reduced number density of effective particles. The breakup of clusters is reflected by the rising pressure around T_c . The straight line is the athermal pressure of hard discs, $P^{\text{dry}} = n g_{\text{wall}}^{\text{at}} T$ which is reached asymptotically when the granular temperature is higher than the energy scale E_{cb} set by the capillary interaction.

From the Eqs. (7.53), (7.60)-(7.62), and (7.66)-(7.67) follows the density of degrees of freedom which are not frozen out by capillary bonds, $n_{\text{free}}(T, s_{\text{crit}}, \phi)$. One may regard n_{free} as the density of clusters.

We remark that the two-fluid model of neighborhoods is the only concept presented in this theory of wet granular matter which cannot be generalized in a straight forward manner to three dimensions, because for $D = 3$ the number of Voronoï neighbors is not a universal constant (such as 6 for $D = 2$ and 2 for $D = 1$), but depends on the granular order (reaching its minimum value 12 for close packing and its maximum of approximately 15.5 in the ideal gas limit) [8]. The reason for this is that three-dimensional space cannot be filled with tetrahedrons, while flat space can be tiled by triangles. As a consequence, the number of constituents in the two-fluid model of neighborhoods would not be conserved for $D = 3$ and the numerator on the right-hand side of (7.62) is not a constant.

7.4.2 The Pressure of Wet Granular Matter

Here we arrive at the pressure $P(T, \phi)$ using the density $n_{\text{free}}(T, \phi)$ (7.61) of degrees of freedom, the coordination $K(T, \phi)$ (7.53), and the contact correlation $g_{\text{c}}^{\text{wet}}(T, \phi)$ (7.58). The pressure is the trace of the stress tensor

$$P = -\frac{1}{D} \text{tr} \underline{\underline{\sigma}}. \quad (7.68)$$

The stress tensor $\underline{\underline{\sigma}} = \underline{\underline{\sigma}}^{\text{kin}} + \underline{\underline{\sigma}}^{\text{force}}$ describes the flow of momentum. The kinetic term has components $\sigma_{i,j}^{\text{kin}} = -\sum_k^N \langle m v_i^{(k)} v_j^{(k)} \delta(\mathbf{r} - \mathbf{r}^{(k)}) \rangle$. With the granular temperature $T = \langle m v_i v_i \rangle$, its trace yields nT for uncorrelated particle motion (as in an ideal gas). In general we have

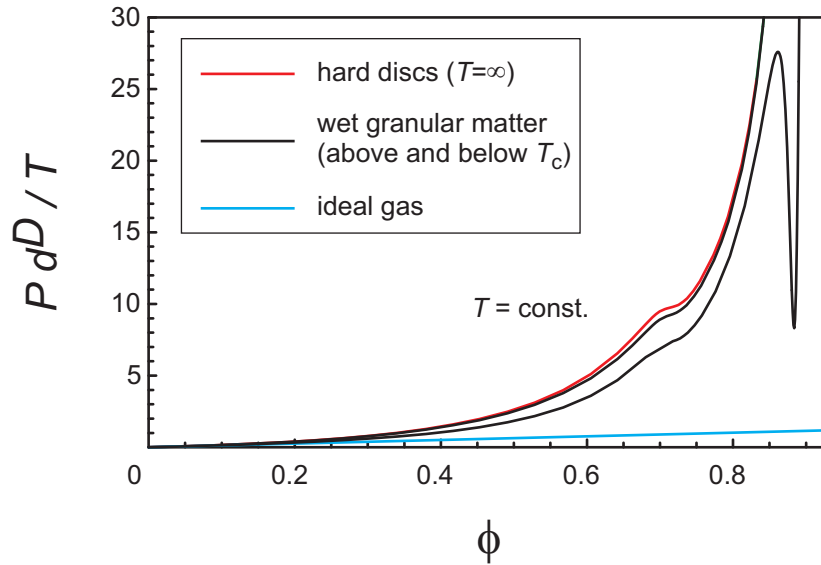


Figure 7.13: Isotherms of wet granular matter for the realistic rupture length $s_{\text{crit}} = 0.07d$. In the high temperature limit the liquid bridges forfeit their influence on the dynamics, so that the equation of state reduces to the hard sphere pressure. This can be seen by the two black isotherms of wet granular matter, of which the higher is at $T = E_{\text{cb}}$ and converges to the top curve in the limit $T \gg E_{\text{cb}}$. The lower black isotherm is at $T = 0.2E_{\text{cb}}$ and exhibits an unstable branch. The critical point is at $T_c \approx 0.274E_{\text{cb}}$ (cf. Fig. 7.14 for a close-up).

the kinetic contribution

$$P^{\text{kin}} = n_{\text{free}}T \quad (7.69)$$

wherein there frozen degrees of freedom have been taken out. For moderate densities, one may interpret (7.69) as the kinetic contribution to the pressure due to a gas of clusters.

The interparticle forces \mathbf{F} give rise to the Cauchy tensor $\underline{\underline{\sigma}}^{\text{force}}$, which is the tensor product of the center-to-center vector \mathbf{r} and the pair force \mathbf{F} ,

$$\underline{\underline{\sigma}}^{\text{force}} = \frac{n_{\text{free}}}{2} \langle \mathbf{F} \otimes \mathbf{r} \rangle, \quad (7.70)$$

so that $\underline{\underline{\sigma}}^{\text{force}}$ is diagonal for radial forces. The factor 1/2 assigns half of the momentum current to either of the interaction particles, i.e. $\mathbf{r}/2$ may be seen as the transport vector within the Voronoï cell. The Cauchy tensor (7.70) has contributions only by the unfrozen pairs of particles with density n_{free} , because in frozen neighborhoods the repulsive momentum exchanged in collisions is exactly balanced by the bridge attraction under the time average on the right-hand side of (7.70).

A comment on the significance of the reciprocal two-fluid model as represented by Eq. (7.61) and (7.62) is in order here. We consider for instance a compressed state of wet granular matter with K_{frozen} around five and K_{free} around unity. While K_{free} is small, the prefactor n_{free} in (7.70) is not necessarily small. From (7.61) and (7.62) follows that both, n_{free} and n_{frozen} , converge to n_J as the system gets jammed ($n \rightarrow n_J$), so that the repulsive dominated state is correctly described by the Cauchy tensor (7.70) which grows beyond all bounds as $n \rightarrow n_J$. If one had (in contradiction to the additivity of areas) summed up densities linearly instead of the reciprocal sum rule (7.62), the free density would vanish or could even become negative under such conditions.

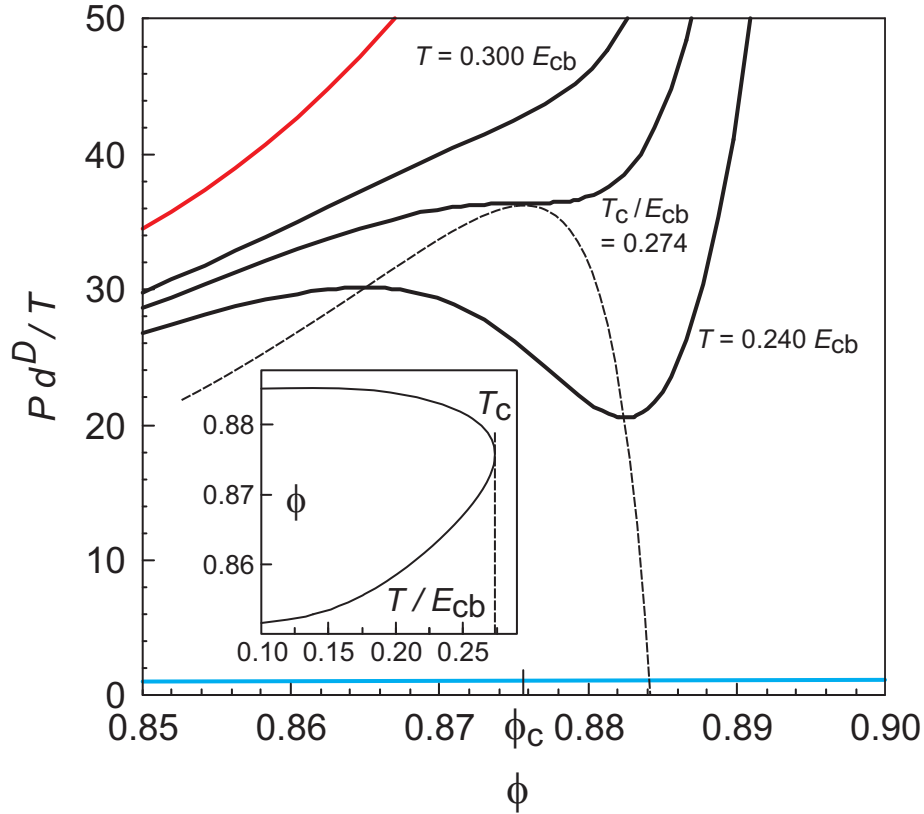


Figure 7.14: A close-up of the transition region in wet granular matter. The dashed line in the main panel is the spinodal of the homogeneously driven wet granular system in $D = 2$ dimensions. The solid black lines are wet granular isotherms around the critical point, which is located at $T_{\text{crit}} = 0.273(5)E_{\text{cb}}$ for $s_{\text{crit}} = 0.07d$. The change of the critical point with the amount of added liquid (represented by s_{crit}) is shown in Fig. 7.15. The curve in the upper left corner is the athermal pressure P^{dry} of the hard disc system [148] without liquid bridges, and the line at the bottom is the ideal gas pressure ($P^{\text{id}D}(\phi)$ has a defined slope). $P^{\text{dry}} = g_{\text{C}}^{\text{at}} P^{\text{id}}$ is increased compared to the ideal gas by the Enskog factor g_{C}^{at} . The pressure of wet granular matter is reduced compared to the dry system P^{dry} due to the capillary cohesion. The inset shows the spinodal in the temperature-density plane, where the critical temperature can be clearly determined.

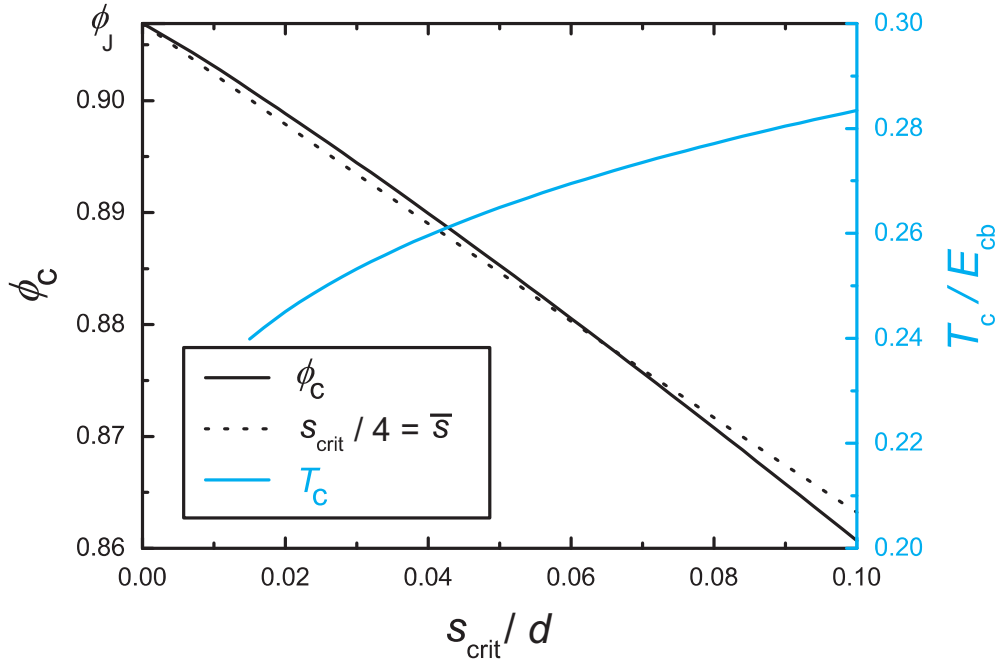


Figure 7.15: The influence of the rupture length s_{crit} on the position of the critical point in the phase diagram Fig. 7.14 of wet granular matter. The position of the critical point is described by the critical parameters (ϕ_c, T_c) , which are plotted on the left and right vertical axis respectively. Solid lines result from the full theory (7.74) by solving for the intersection of $\partial_\phi P(\phi, T) = 0$ and $\partial_\phi^2 P(\phi, T) = 0$. For the critical temperature we find a very mild variation with the rupture length, so that over the entire physically relevant range of capillary interaction we have $T_c \approx E_{\text{cb}}/4$. The influence of the rupture length s_{crit} on the critical density ϕ_c can be understood very clearly with the help of the dashed line. The dashed line is the implicit equation $s_{\text{crit}} = 4\bar{s}(\phi)$ for the density ϕ , which is expressed in terms of the mean particle separation $\bar{s}(\phi) = d \left(\sqrt[3]{\phi_J/\phi} - 1 \right)$. Since the dashed line closely follows the full theory, the critical density is such that the mean particle separation scales with the rupture length s_{crit} . This shows that both intrinsic characteristics of the capillary interaction, the rupture length and the bridge energy E_{cb} , determine the critical point of wet granular matter.

It is finally easy to determine the time average on the right-hand side of (7.70) for the two different forces acting in wet granular matter, the delta-force in collisions of hard particles and the flat force $F_{\text{cb}} = E_{\text{cb}}/s_{\text{crit}}$ of the capillary bonds. In a collision at time t_{coll} the radial momentum $\Delta\mathbf{p}$ is transferred instantaneously:

$$\langle \mathbf{F}_{\text{coll}} \otimes \mathbf{r} \rangle = \langle \Delta\mathbf{p} \otimes \mathbf{r} \delta(t - t_{\text{coll}}) \rangle = \mathbb{1} \langle \Delta p(\mathbf{r}, -\mathbf{v}) \theta((\mathbf{r}, -\mathbf{v})) \delta(r - d) \rangle = -\mathbb{1} g_{\text{c}}^{\text{wet}} n \sigma_D d^D T. \quad (7.71)$$

In the last equality the δ -function gives rise to the contact correlation $g_{\text{c}}^{\text{wet}}$ and the trivial integration of angles leaves $\sigma_D d^{D-1}$. $\mathbb{1}$ is the unity matrix and θ is the Heaviside step function. Inserting (7.71) in (7.70) and taking the trace (7.68) yields

$$P_{\text{coll}} = 2^{D-1} n_{\text{free}} T \phi g_{\text{c}}^{\text{wet}}. \quad (7.72)$$

The cohesive virial due to capillary bridges is

$$\langle \mathbf{F}_{\text{cb}} \otimes \mathbf{r} \rangle = \left\langle K \frac{E_{\text{cb}}}{s_{\text{crit}}} \frac{\mathbf{r} \otimes \mathbf{r}}{r} \right\rangle = \frac{\mathbb{1}}{D} K \frac{E_{\text{cb}}}{s_{\text{crit}}} \langle d + s \rangle \approx \frac{\mathbb{1}}{D} K \frac{E_{\text{cb}}}{s_{\text{crit}}} d. \quad (7.73)$$

Hence the final result

$$P = n_{\text{free}} T \left(1 + 2^{D-1} \phi g_{\text{c}}^{\text{wet}} \right) - n_{\text{free}} E_{\text{cb}} \frac{K}{2D} \frac{d}{s_{\text{crit}}}, \quad (7.74)$$

where the last term is the bridge cohesion (7.73). Since n_{free} , the contact correlation $g_{\text{c}}^{\text{wet}}$ and K have been derived explicitly in (7.61), (7.58) and (7.53) as functions of ϕ and T , we have the equation of state for wet granular matter, $P = P(\phi, T)$.

The Figs. 7.12 and 7.13 show the analytic result (7.74) as a function of the granular temperature T and the density ϕ . In the high temperature limit wet granular matter behaves as a hard-spheres system. Below the critical point granular clusters are predicted to segregate due to the mechanically unstable branch of the pressure as a function of density, which appears in Fig. 7.13 below the critical temperature. Figure 7.14 provides a close-up of the critical point of wet granular matter and its spinodal. The critical density of this transition is high, because the particles have to be close enough in order to form a dynamical capillary network. As we show in Fig. 7.15, the critical density is determined by the length scale of capillary bridges, such that the rupture length s_{crit} scales with the mean particle separation \bar{s} . Moreover, the rupture length is approximately four times the mean particle separation, $s_{\text{crit}} \approx 4\bar{s}$ (dashed line shown in Fig. 7.15 for comparison). This result is to be compared with the very same ratio for the reported critical density of the unclustering effect in Chap. 6: in the free cooling of dense one-dimension wet granular matter, the granular network was found to break up into granular droplets which precipitate out of the homogeneous initial state, as soon as the density exceeded a critical value. This critical density was shown numerically and analytically to be set by $s_{\text{crit}} \approx 3\bar{s}$ in Chap. 6. The different prefactor is due to the additional cooling dynamics and the dimensionality $D = 1$. The theory of wet granular matter presented in this chapter predicts this transition to persist in higher dimensions.

As we shorten the rupture length s_{crit} (which can be easily done experimentally by evaporating the wetting liquid), the dry system is approached in such a way that the spinodal narrows in the $T - \phi$ plane and is shifted to the jamming point, where it eventually shrinks to a line and vanishes. Figure 7.15 shows the convergence of the critical density to the jamming density. Since the capillary bridge regime sets an upper limit on the rupture length, the critical point is confined on the density axis between the ordering transition at ϕ_0 and the jamming density ϕ_J . The critical temperature almost exclusively depends on the bridge energy, according to $T_c \approx E_{\text{cb}}/4$, over the entire capillary regime.

With this discussion of transitions occurring in wet granular matter the presentation of the theory for wet granular matter is completed for this chapter. The reader may find in appendix 7.8 a brief methodical extension of the theory where a self-consistent equation is derived for future works.

7.5 Conclusions

Starting with the hard-sphere fluid, an expression (7.10) for the narrowing of the near contact pair correlation was derived, which describes in the jamming limit the delta-peak of $2D$ isostatic contacts per particle, in agreement with the accepted value of simulations. In the gas and fluid regime the fall-off predicted by this expression for the pair correlation at contact was found to be well confirmed by simulations. We then addressed the nonequilibrium case of wet granular matter by the introduction of capillary bridges which are formed hysteretically. The Enskog description in terms of the pair-correlation function was extended with six different non-vanishing correlation coefficients which take the bridge status into account and allow for the hysteretic dissipative dynamics. The coordination number of bonds was computed analytically as a function of the rupture length of the capillary bridges, the granular temperature, and the density. The limiting case of strong bonds led to the sticky gas dynamics for which simulations have been performed which showed very good agreement with the analytic prediction of the coordination number. Based on the derived expressions for the contact correlation and the bridge coordination, we finally computed the pressure of wet granular matter analytically as a function of density and granular temperature. Here the method of the reciprocal two-fluid was put forward, which describes the effective degrees of freedoms in order to take the correlated motion of particles glued to clusters into account. The isotherms of wet granular matter were found to have an unstable branch which gives rise to the segregation of dense clusters. The critical temperature of this transition was derived to be approximately one quarter of the capillary bond energy. The critical density is directly related to the pinch-off distance of the capillary bridges. The close relation to the unclustering effect reported for one dimension in Chap. 6 was pointed out, for which reason the latter effect persists also in higher dimensions.

Clearly it will be interesting to probe the critical point of wet granular matter experimentally and by direct simulations. As was shown in this chapter, the position of the critical point is determined by the length and energy of the capillary bridges. These quantities can be controlled accurately in an experiment of shaken wet granular matter. This experiment is reported in Chap. 8. Future measurements of the critical temperature will allow to discern between extensions such as the nonlinear coupling discussed in appendix 7.8.

Future analytic work includes the background contribution g_B in the dense regime, since our numerics indicate that the pair correlation is flatter near the contact as predicted by g_A alone. This task might be addressed in conjunction with the analogous background contribution in three dimensions, for which in the jamming limit an integrable power-law divergence, $g_B \propto 1/s^\delta$, has been reported in numerical studies (with $\delta = 0.5$ [201] or $\delta = 0.6$ [59]) and experiments [9], but is as well lacking a theoretical explanation at present.

7.6 Appendix A: The Background Contribution g_B

7.6.1 The Weighting Factors

With g_A in (7.10) we considered the four (cf. Eq. (7.12)) A-neighbors, which form isostatic contacts at jamming, $s_A \rightarrow 0$ for $\phi \rightarrow \phi_J$ (7.3), and are separated by s_A according to Eq. (7.4)

before jamming. Analogously, the separation s_B of the two B-neighbors is weighted by

$$P_B(s_B) \propto \exp\left(-\frac{\left(1 + \frac{s_B}{d}\right)^2 - 1}{\phi_{\max}/\phi - 1}\right). \quad (7.75)$$

While in Eq. (7.4) the denominator in the exponential is $c_A = \phi_J/\phi - 1$ so that $s_A \rightarrow 0$ at the jamming density, in Eq. (7.75) the denominator is $c_B = \phi_{\max}/\phi - 1$ since the blocked B is only forced to form a contact, $s_B \rightarrow 0$, for a perfect crystal with $\phi \rightarrow \phi_{\max}$. Of course this limit is kinematically unreachable because the system comes to rest at the jamming density $\phi_J < \phi_{\max}$. ϕ_{\max} would be reached. We note that c_B is a small dimensionless quantity: for $\phi > \phi_0 = 0.71$ we have $0 < c_B < 0.2774$.

Close to jamming, the B-neighbors are fixed in space by particles other than the reference particle. Except for arch-like constructions which are rare for frictionless particles, and would include second Voronoï neighbors keeping B at a separation larger than our region of interest, $s_B > s_{\text{crit}}$, this hindrance is due to the A-neighbors. Therefore the probability $g_B(s_B)$ to find a B-neighbor at separation s_B from the reference particle (sketched with hatching in Fig. 7.17) is given by the integral over all configurations where four A-neighbors hinder two B-neighbors.

The configurations will be weighted by a phase space factor C and the exponential factor P_B . We are above the ordering density ϕ_0 , so that the neighborhood has (by definition of the phase) hexagonal order as sketched in the inset of Fig. 7.16. Projecting the configurations with the two B-neighbors blocked (gray subset in Fig. 7.16) on a single θ -axis, we find the configuration space factor

$$C(\theta) = \frac{3(5\pi - 6\theta)}{2\pi^2}. \quad (7.76)$$

In the sequel we abbreviate

$$\gamma_{\text{vol}}(s) \propto 1 + s/d. \quad (7.77)$$

for the volume factor (7.75) in $D = 2$. Wide gaps of length s_B are exponentially suppressed by P_B .

7.6.2 The Configuration Space

Let us now address the configuration space plotted in Fig. 7.17. If the opening angle θ of the A-neighbors exceeded $\theta_T(s_A)$,

$$\cos \frac{\theta_T(s_A)}{2} = \frac{\sqrt{s_A(2d + s_A)}}{d + s_A}, \quad (7.78)$$

the B-particle could slip through and turn into an A-neighbor, which is defined by having a free path towards the reference particle. This transition corresponds to the neck connecting different jamming island in the configuration space. Only along the line \overline{PQ} in Fig. 7.17 defined by $\theta = \theta_C(s_A)$,

$$\cos \frac{\theta_C(s_A)}{2} = \frac{s_A + d}{2d}, \quad (7.79)$$

the B-neighbor can touch the reference particle, so that $s_B = 0$. The Eqs. (7.78) and (7.79) define the upper boundary of the domain of integration for all s_A ,

$$\theta_{\max}(s_A) = \begin{cases} \theta_C(s_A) & s_A/d \leq \sqrt{2} - 1 \\ \theta_T(s_A) & s_A/d \geq \sqrt{2} - 1 \end{cases}, \quad (7.80)$$

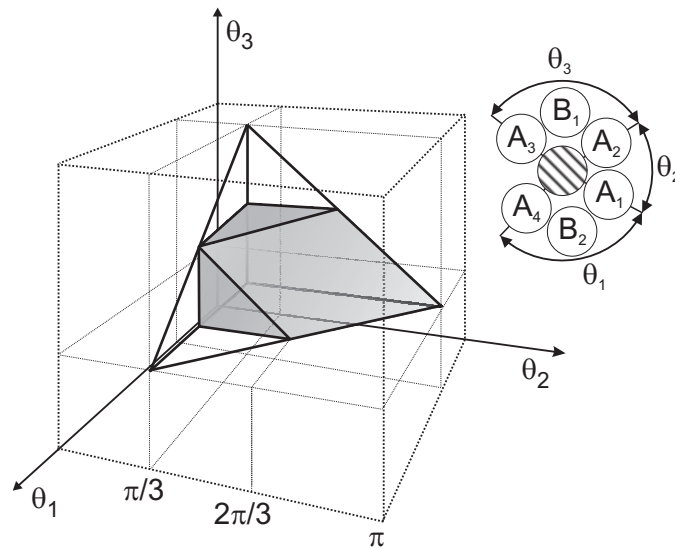


Figure 7.16: The angular configuration space of four neighbors close to the reference particle. These we denote as A-neighbors. The faceted inner subset shown in gray is the subspace conditioned to the property that two further particles, the B-neighbors, are hindered by the A-particles in approaching the reference particle. The projection of this subset onto an θ -axis (for the angle between a blocking A-pair, θ_1 or θ_3 in this example) gives rise to a linear configuration space factor $C(\theta)$. Obviously a B-neighbor acts like a wedge driven between two A-neighbors, and therefore increases θ . This is taken into account by the weighting factor $P_B(s_B)$ which favors shorter separations s_B between the particle B and the reference particle, depending on the density ϕ .

which is continuously differentiable but not smooth at the point Q.

The lower boundary is

$$\cos \frac{\theta_S(s_A, s_B)}{2} = \frac{(s_A + d)^2 + s_B^2 + 2ds_B}{2(s_A + d)(s_B + d)}, \quad (7.81)$$

where B hits A.

The simple lower bound on θ ,

$$\cos \frac{\theta_{\min}(s_A)}{2} = \sqrt{1 - \left(\frac{d/2}{d + s_A}\right)^2}, \quad (7.82)$$

which ensures that the A-neighbors do not overlap is without applicatory relevance, as it implies that the B-neighbor is pushed out to $s_B/d > \sqrt{3} - 1 \approx 0.73$. This is suppressed in the dense regime $\phi > \phi_o$ by the factor F of Eq. (7.75).

The configuration space ends to its right in a cusp where the lower and upper bound intersect at

$$s_A^{\text{cusp}}(s_B) = \sqrt{s_B^2 + 2ds_B + 2d^2} - d. \quad (7.83)$$

This cusp converges to the point Q for $s_B \rightarrow 0$.

With the integration bounds (7.80), (7.81), (7.83), and the weighting factors (7.75), (7.76) we have

$$g_B(s_B) = \mathcal{N} P_B(s_B) \left[\int_0^{s_A^{\text{cusp}}(s_B)} ds_A P_A(s_A) \gamma_{\text{vol}}(s_A) \int_{\theta_S(s_A, s_B)}^{\theta_{\max}(s_A)} d\theta C(\theta) \right]^2 \quad (7.84)$$

$$= \mathcal{N} P_B(s_B) \left[\frac{s_B}{d} I_1(n) + \left(\frac{s_B}{d}\right)^2 I_2(n) + \mathcal{O}\left(\left(\frac{s_B}{d}\right)^3\right) \right]^2. \quad (7.85)$$

We emphasize that the configuration space (s_A, θ) describes the relative position of one A-neighbor sketched symmetrically in Fig. 7.17. Since there are two independent A-neighbors involved, their configuration is the direct product $(s_{A1}, \theta_1) \times (s_{A2}, \theta_2)$. On this account the configuration integral is squared in (7.84), with the important consequence that the leading order in $g_B(s_B)$ is quadratical. The normalization constant \mathcal{N} is determined by the knowledge that there are two B-neighbors. While the exponential prefactor dominates the long range decay, we expand the near-contact increase in s_B/d . Substituting the dimensionless area $z_A = ((1 + s_A/d)^2 - 1)/c_A$ for integration in favor of the particle separation s_A , the expressions I_i , $i = 1, 2$ are of the form

$$I_i = c_A \int_0^{1/c_A} e^{-z_A} f_i(c_A z_A) dz_A \quad (7.86)$$

with

$$f_1(x) = \frac{3(x-1)\alpha(x)}{2\pi^2 \sqrt{(3-x)(x+1)}} \quad (7.87)$$

$$\frac{f_2(x)}{f_1(x)} = \frac{2}{x-3} - \frac{2}{x-1} + \frac{6\sqrt{x+1}}{\alpha(x)\sqrt{3-x}} - \frac{6\sqrt{3-x}}{\alpha(x)\sqrt{x+1}} - 1 \quad (7.88)$$

$$\alpha(x) = \pi - 12 \arcsin \frac{\sqrt{x+1}}{2}$$

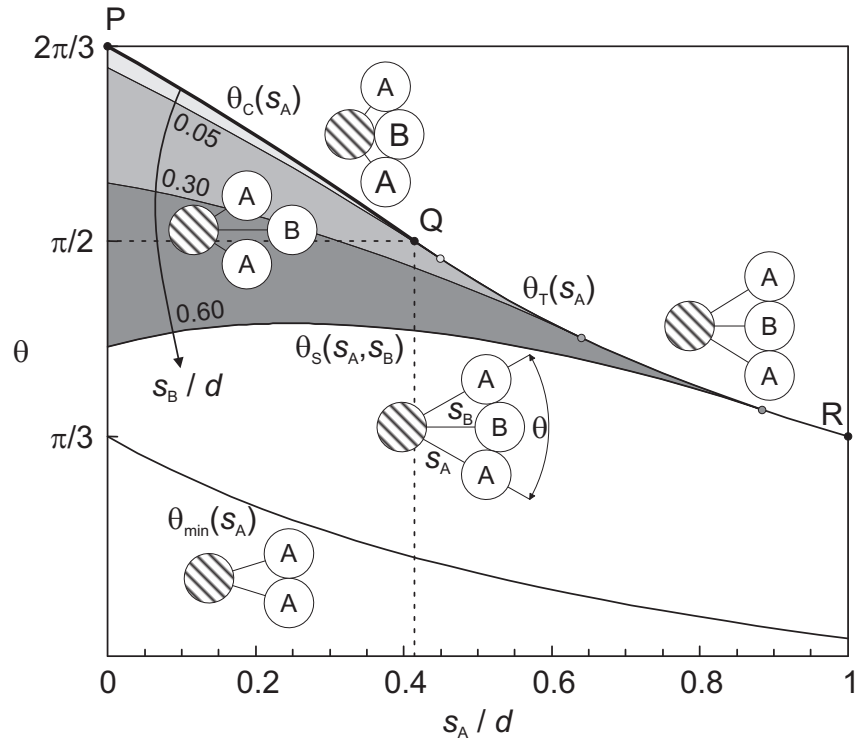


Figure 7.17: A section of the configuration space of neighboring particles. Within the gray domain the particle denoted by B is blocked: the two neighbors labeled A sterically hinder the particle B from approaching the reference particle (shaded). Only at the boundary $\theta_C(s_A)$ (curve \overline{PQ} ranging from $[s_A, \theta]_P = [0, 2\pi/3]$ to $[s_A, \theta]_Q = [(\sqrt{2} - 1)d, \pi/2]$) the B-neighbor can touch the reference particle. The probability $g_B(s_B)$ to find a B-neighbor at a separation s_B follows from integrating over the gray domain, which grows with increasing s_B . The lower bound, $\theta_S(s_A, s_B)$, is plotted for the values $s_B = 0.05, 0.30,$ and 0.60 . Large areas spanned by this neighborhood are exponentially rare the higher the mean density ϕ , so that the probability distribution in this plot concentrates in the vicinity of the upper left corner P as we come closer to the jamming limit. At the line \overline{QR} the B-neighbor slips through and turns into an A-neighbor, so that \overline{QR} is the transit to another jamming island in configuration space. The corresponding transition rate is proportional to the probability density along \overline{QR} and therefore vanishes in the jamming limit.

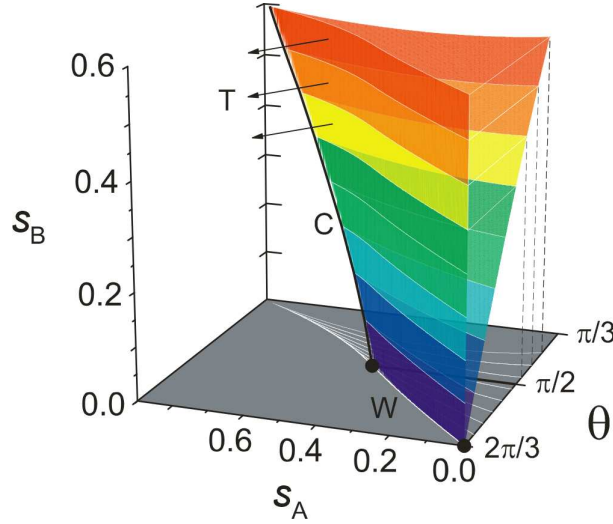


Figure 7.18: The s_A - θ -plot of Fig. 7.17 with the full s_B dependence shown on the additional vertical axis.

The integrals I_i can be treated by expanding the functions $f_i = \sum_{\nu} f_i^{(\nu)} x^{\nu}$:

$$I_i = \sum_{\nu=0}^{\infty} f_i^{(\nu)} c_A^{\nu+1} \underbrace{\int_0^{1/c_A} e^{-z} z^{\nu} dz}_{=\nu! - \Gamma(\nu+1, 1/c_A)}. \quad (7.89)$$

All incomplete Gamma functions can be eliminated by virtue of the recurrence relation (cf. (6.5.2) and (6.5.22) in [1])

$$\Gamma(\nu+1, 1/c_A) = \nu \Gamma(\nu, 1/c_A) + (-1)^{\nu} c_A^{-\nu} e^{-1/c_A}. \quad (7.90)$$

As is apparent from the recurrence relation, the result will be of the form

$$I_i = R_i(c_A) + e^{-1/c_A} S_i(c_A). \quad (7.91)$$

The regular part, for instance in first order of s_B/d ,

$$R_1(c_A) = c_A \frac{\sqrt{3}}{2\pi} + c_A^2 \frac{9 - 2\sqrt{3}\pi}{3\pi^2} + c_A^3 \frac{-27 + 2\sqrt{3}\pi}{3\pi^2} + \dots, \quad (7.92)$$

is a series expansion about the point of jamming, $c_A = 0$. It is asymptotically diverging due to the factorial which appears in the recurrence relation. Fortunately this does not restrain us from an excellent approximation, since for the relevant density, $\phi > \phi_o$, the quality of the expansion increases for more than 10 terms in the expansion (cf. panel (a) of the Fig. 7.19). The second part in (7.91), for which the first order of s_B/d is given by

$$S_1(c_A) = c_A \frac{\sqrt{3}}{2\pi} + c_A^2 \frac{9 - 2\sqrt{3}\pi}{3\pi^2} + c_A^3 \frac{-27 + 2\sqrt{3}\pi}{3\pi^2} + \dots, \quad (7.93)$$

and has a positive radius of convergence (cf. panel (b) in Fig. 7.19). This part is over-exponentially suppressed by the prefactor $\exp -1/c_A$ close to jamming.

In the application to wet granular matter the sub-leading order $(s_B/d)^3 < 4 \cdot 10^{-4}$ is negligible for a realistic value of $s \leq s_{\text{crit}} \approx 0.07d$, whereby we have the concise result

$$g_B(s_B) = \mathcal{N} e^{-z_B} z_B^2 + \mathcal{O}(z_B^3) \quad (7.94)$$

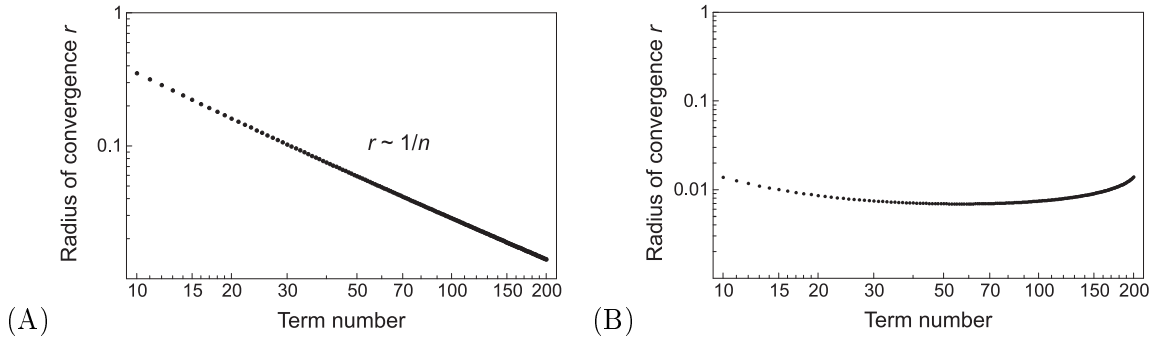


Figure 7.19: The radii of convergence r_k for expansions around the jamming point. The contribution blocked B-neighbors give to the pair correlation can be expanded in a series around the jamming point, $c_A = 0$. The radius of convergence is given by the Cauchy-Hadamard formula $r_j = 1/\sqrt[j]{K_j}$ for the term $K_j(s_B/d)^j$. (A) The asymptotic divergence of the R -series in (7.92) poses no practical problem since few terms (less than 10) give sufficient accuracy. (B) The S -series in (7.92) converges.

with the abbreviation $z_B = ((1 + s_B/d)^2 - 1)/c_B$ and $1/c_B \approx \phi g_c^{\text{at}}$. The normalization $8\phi \frac{c_B}{2} \int g_B dz_B = 2$ according the two B-neighbors determines \mathcal{N} in (7.94). Hence the result (7.14).

7.7 Appendix B: Explicit Expressions for the Pair Correlation in Two Dimensions without free Parameters

In our general derivation of the theory of wet granular matter we distinguished between the jamming density ϕ_J and the (highest possible) crystalline packing $\phi_{\text{max}} = \pi/(2\sqrt{3})$ achieved in monodisperse domains. The exact value of the jamming density ϕ_J depends on many details such as the distribution of polydispersity and the jamming protocol for the increase of density. When we want to give explicit results without free parameters on the bridge coordination $K(T, \phi, s_{\text{crit}})$ and the equation of state $P = P(T, \phi, s_{\text{crit}})$ we do this for weak polydispersity, where the difference between ϕ_J and ϕ_{max} is negligible and the limiting case of 'dry' discs has been studied extensively.

7.7.1 High Density

For monodisperse 'dry' discs, $\phi_J = \phi_{\text{max}}$, there are higher order corrections to the free volume result (7.9) available in the literature which are incorporated in the final results on the bridge coordination and the equation of state for wet granular matter. These corrections are expansions with respect to $x = \phi_J - \phi$ fitted to simulations:

$$g_c^{\text{dense}} = \left(\frac{1}{x} + a_0 + a_2 x^2 + \dots \right) \frac{\phi_J}{\phi} = \left(\frac{1}{x} + a_0 + a_2 x^2 + \dots \right) \left(1 + \frac{x}{\phi_J} + \dots \right) \quad (7.95)$$

Equation (7.95) holds in the dense regime, $\phi_o < \phi < \phi_{\text{max}}$, above $\phi_o = 0.71$. The numerical coefficients are $a_0 = -1.07$ and $a_2 = 5.89$ [148], confirmed by our own simulations. Similar empirical expressions are also available for polydisperse discs in the glass state (Eq. (6) in [58]).

D	Scaled Particle Theory		Heuristic Fits	
	g_c^{at}	$g_{\text{wall}}^{\text{at}}$	g_c^{at}	$g_{\text{wall}}^{\text{at}}$
1	$\frac{1}{1-\phi}$	$\frac{1}{1-\phi}$	$\frac{1}{1-\phi}$	$\frac{1}{1-\phi}$
2	$\frac{1-\phi/2}{(1-\phi)^2}$	$\frac{1}{(1-\phi)^2}$	$\frac{1-7\phi/16}{(1-\phi)^2} - \frac{\phi^3/128}{(1-\phi)^4}$	$\frac{1+\phi^2/8}{(1-\phi)^2} - \frac{\phi^4/64}{(1-\phi)^4}$
3	$\frac{1-\phi/2+\phi^2/4}{(1-\phi)^3}$	$\frac{1+\phi+\phi^2}{(1-\phi)^3}$	$\frac{1-\phi/2}{(1-\phi)^3}$	$\frac{1+\phi+\phi^2-\phi^3}{(1-\phi)^3}$

Table 7.1: The particle-particle correlation g_c^{at} and the particle-wall correlation $g_{\text{wall}}^{\text{at}}$ at contact for different spatial dimensions valid up to moderate densities. The center column shows the results of the Scaled Particle Theory and the right column contains the exact expression for one dimension, and heuristic expressions [13] of Henderson [110] for two dimensions and Carnahan-Starling [31] in three dimensions.

7.7.2 Low and Moderate Density

For the analytic treatment an explicit expression for the contact correlation g_c^{at} in Eq. (7.32) is needed (as the counterpart to the dense expression (7.95)). Aside from the trivial one-dimensional case ⁶, exact expressions for the contact correlation of hard spheres are unknown for the dilute regime. Yet there are well-established approximations in the literature resulting from Scaled Particle theory [178, 109], from the virial expansions [177], as solutions of the Percus-Yevick closure [106], as well as heuristic expressions [194] such as the Carnahan-Starling formula with corrections to better fit simulation results (cf. Tab. 7.1).

As in the dense regime 7.7.1 we shall use the Henderson-Luding expression [148, 110] (cf. also the earlier work [230])

$$g_c^{\text{dilute}} = \frac{1-7\phi/16}{(1-\phi)^2} - \frac{\phi^3/128}{(1-\phi)^4} \quad (7.96)$$

for the uncaged regime, $0 < \phi < \phi_o$, and the merging function $m(\phi) = 1/(1 + \exp((\phi_o - \phi)/m_0))$ with a cross-over width $m_0 = 0.0111$ to smoothly connect the dense (7.95) and dilute (7.96) expressions [148]:

$$g(s) = m(\phi) g^{\text{dilute}}(s) + (1 - m(\phi)) g^{\text{dense}}(s) \quad (7.97)$$

with $g^{\text{dilute}}(0) = g_c^{\text{dilute}}$ and $g^{\text{dense}}(0) = g_c^{\text{dense}}$ as given by the Eqs. (7.95) and (7.96). The near-contact decay has been established in the Eqs. (7.10) and (7.14) for $\phi > \phi_o$, and in Eq. (7.32) for $0 < \phi < \phi_o$:

$$g^{\text{dilute}}(s) = g_c^{\text{at}} \gamma_{\text{dilute}}^{\text{u}} \quad \text{and} \quad (7.98)$$

$$g^{\text{dense}}(s) = g_c^{\text{at}} \gamma_{\text{dense}}^{\text{u}} = g_c^{\text{at}} \gamma_{\text{dilute}}^{\text{u}} \left[1 + \left(\phi g_c^{\text{at}} \frac{s}{d} \right)^2 \right] \quad (7.99)$$

up to leading order in s_{crit} with

$$\gamma^{\text{u}}(s)_{\text{dilute}} = \exp \left(-\phi g_c^{\text{at}} \left[\left(1 + \frac{s}{d} \right)^2 - 1 \right] \right). \quad (7.100)$$

⁶The configuration space of the one-dimensional gas is $L - Nd$, so that the equation of state is $P(L - Nd) = NT$. Comparison with the general expression $P = g_{\text{wall}}^{\text{at}} nT$ yields $g_{\text{wall}}^{\text{at}} = (1 - \phi)^{-1}$.

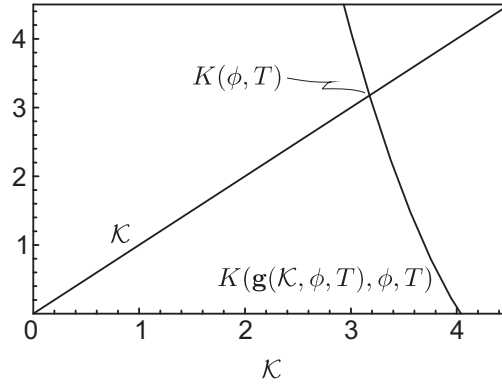


Figure 7.20: A typical graphical solution of the self-consistent equation (7.102). Here the density is chosen to be $\phi = 0.6$ and the granular temperature is $T = 0.2E_{cb}$.

With the contact expressions (7.95, 7.96), as well as the short-range decay formulas (7.10, 7.32), we have sufficient information on the dry system over the entire density range. We may therefore proceed by introducing the hysteretic capillary bridges.

7.8 Appendix C: Self-Consistency of Bridge Coordination K

All results presented so far on the coordination $K(\phi, T)$ and pressure $P(\phi, T)$ allowed explicit analytic results. Here we want to demonstrate how to treat more complicated source terms of the hysteretic system (7.45) numerically. Such an extension of the theory could be motivated as follows. The current of free (unbound) approaching particles could be a function of the free density n_{free} instead of the mean density, since some of the unconnected neighbors traverse the voids between clusters, so that Eq. (7.41) is changed to

$$\phi g_{\text{c} \leftarrow \text{r}}^{\text{u}} + \phi g_{\text{c} \leftarrow \text{r}}^{\text{u}} / \gamma^{\text{u}}(s_{\text{crit}}) = (1 - K/K_{\text{sites}}) \phi_{\text{free}} g_{\text{c}}^{\text{at}}(\phi_{\text{free}}). \quad (7.101)$$

Obviously this approach is a lower estimate for the current of freely approaching particles, which is why (7.101) is considered as a methodical example rather than a physical competitor to the theory presented above.

With the altered Eq. (7.101) the hysteretic system (7.45) can still be solved analytically to find the correlation coefficients $\mathbf{g} = \{g_{\text{c} \leftarrow \text{r}}^{\text{u}}, g_{\text{c} \leftarrow \text{r}}^{\text{b}}, g_{\text{c} \rightarrow \text{r}}^{\text{b}}, g_{\text{c} \rightarrow \text{r}}^{\text{u}}, g_{\text{c} \rightarrow \text{r}}^{\text{b}}, g_{\text{c} \rightarrow \text{r}}^{\text{u}}\}$. Unlike before, due to the coupling (7.101) and the Eqs. (7.60)-(7.62), the correlations \mathbf{g} are a highly nonlinear function of K . Therefore Eq. (7.46) becomes a nonlinear self-consistent equation:

$$K(\mathbf{g}(\mathcal{K}, \phi, T), \phi, T) = \mathcal{K}. \quad (7.102)$$

The physical value $K(\phi, T)$ of the coordination is the solution \mathcal{K} of (7.102). The numerical solution of (7.102) is found to be very robust, as Fig. 7.20 indicates. Plugging the resulting self-consistent $K(\phi, T)$ back into the equation for the pressure (7.74) of wet granular matter, we find that the critical point is shifted from $T_c = 0.273(5)E_{cb}$ to $T_c = 0.216(5)E_{cb}$. This reduction of the critical temperature is intuitively clear since with less particles arriving to form bonds, the wet granular matter 'evaporates' at lower granular temperatures.

7.9 Appendix D: Contact Correlation Near Jamming

In the jammed state of weakly polydisperse particles, $\phi \rightarrow \phi_J \approx \phi_{\text{max}}$, the A-neighbors form exact contacts, $s_A = 0$, so that the $g_A(s_A) \propto \delta(s_A)$ has a delta peak at zero and the contact

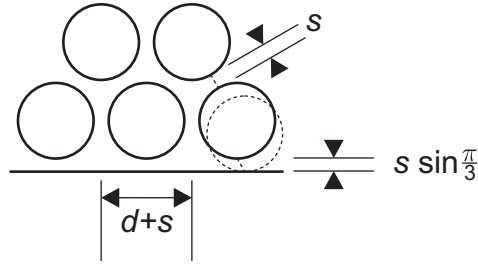


Figure 7.21: A sketch of the dry system around close packing. The particles are equally distributed in the direction of the approximate triangular lattice vectors. As we rotate the coordinate frame to be aligned with the wall, we see that the free configuration space per particle is $(d + s) s \sin \frac{\pi}{3}$.

value g_c^{at} is infinite. When the density is reduced by scaling the particle position by a factor $\alpha > 1$, the particle separation s_A and the density ϕ are related by

$$(\phi_{\text{max}}/\phi)^{1/D} = \alpha = 1 + s/d. \quad (7.103)$$

Denoting the particle-wall correlation by $g_{\text{wall}}^{\text{at}}$, the probability to find a particle with contact to the wall can be read off Fig. 7.21 to be

$$n g_{\text{wall}}^{\text{at}} = \frac{1}{(d + s) s \sin \frac{\pi}{3}} = \frac{2}{\sqrt{3}} \frac{1}{(d + s) s} \quad (7.104)$$

Inserting (7.103) we find the particle-wall contact correlation to be

$$\begin{aligned} g_{\text{wall}}^{\text{at}} &= \frac{1}{1 - \sqrt{\phi/\phi_{\text{max}}}} \\ &= \frac{2}{\phi_{\text{max}}/\phi - 1} \text{ asympt. for } \phi \rightarrow \phi_{\text{max}}. \end{aligned} \quad (7.105)$$

The pressure P of the hard sphere fluid follows by taking the trace of the pressure tensor, which yields a kinetic term (the ideal gas term) and second contribution from the hard-core repulsion (which is proportional to the particle-particle contact correlation g_c^{at} . Cf. also Eq. (7.74) for the special case without bridges, $K = 0$):

$$\frac{P}{nT} = 1 + 2^{D-1} \phi g_c^{\text{at}}. \quad (7.106)$$

In complete analogy⁷, the pressure P can also be computed from particle-wall collisions:

$$\frac{P}{nT} = g_{\text{wall}}^{\text{at}}. \quad (7.107)$$

After equating (7.106) and (7.107), from formula (7.105) follows the asymptotic expression for the particle-particle correlation,

$$\begin{aligned} g_c^{\text{at}} &= \frac{1}{2\sqrt{\phi} (\sqrt{\phi_{\text{max}}} - \sqrt{\phi})} \\ &= \frac{1}{\phi_{\text{max}} - \phi} \text{ asympt. for } \phi \rightarrow \phi_{\text{max}}, \end{aligned} \quad (7.108)$$

We remark that the Eqs. (7.106) and (7.107) are not restricted to high densities, $\phi > \phi_0$.

⁷The probability to find a particle in contact to the wall is $n g_{\text{wall}}^{\text{at}}$ where $g_{\text{wall}}^{\text{at}}$ is the particle-wall contact correlation analogueous to the particle-particle correlation g_c^{at} . In a hard sphere systems without cohesion, momentum is exchanged with the walls in collisions where the normal component changes by $2p_n$ which gives rise to the momentum flow $n g_{\text{wall}}^{\text{at}} \langle 2p_n v_n \theta(v_n) \rangle = n g_{\text{wall}}^{\text{at}} \langle m v_n^2 \rangle = n g_{\text{wall}}^{\text{at}} T$ at the boundaries.

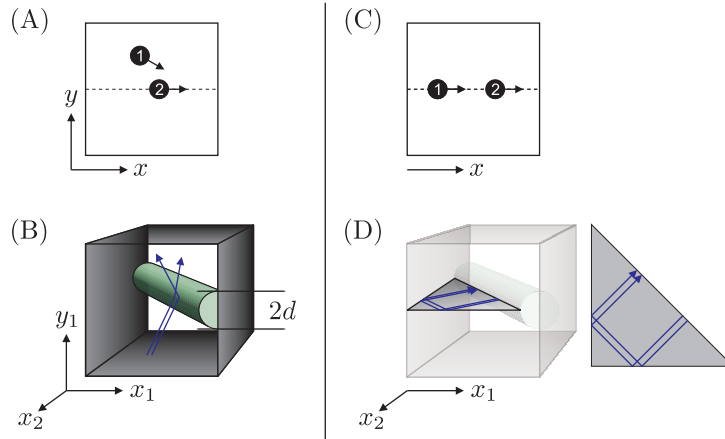


Figure 7.22: An illustrative two-particle system. In (A) particle 1 moves freely in the box and particle 2 moves on the dashed line. The resulting configuration space is sketched in (B). The system is chaotic and very similar to the Sinai billiard. Chaoticity means that two close initial configurations are separated exponentially in time, as illustrated by the blue trajectories in (B). The one-dimensional system (C) (with both particles moving on a line) is integrable. Velocity perturbations grow linear in time, spatial perturbations do not grow at all as shown in (D).

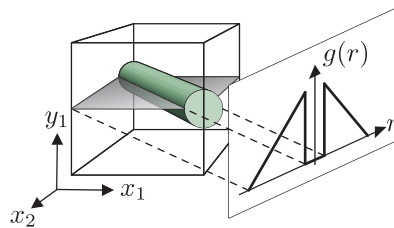


Figure 7.23: The two-particle correlation function caused by the excluded volume (green cylinder). The piecewise linear correlation function follows assuming ergodicity, so that the free volume is equally visited by the system. A general property caused by the excluded volume of finite size particles is the peak in the two-particle correlation function at contact.

7.10 Appendix E: On the Contact Correlation in Dilute Hard Disc Systems

Why is there a peak at contact?

An instructive system that exhibits excluded volume effects consists of two hard discs moving in a box with one disc restricted to move on a horizontal line as shown in Fig. 7.22 (A). This system is tractable because it has three degrees of freedom. Its three dimensional configuration space is shown in Fig. 7.22 (B). This simple example allows to follow a general property of the two-particle correlation function: at the particle-particle contact the correlation jumps from zero to a peak value. To see this we project the probability mass of the full configuration space onto the one-particle space (of particle 2) as done geometrically in Fig. 7.23.

Scaled Particle Theory

A classical and lucid way to derive the contact value $g_{pp}(\phi) = g(d+, \phi)$ is provided by the Scaled Particle Theory put forward by Reiss, Frisch and Lebowitz [178]. For a recent extension see [115]. Here one considers the probability $p_0(\phi, \lambda)$ to find no particle center within a randomly positioned sphere of radius λ . For monodisperse particles of radius d there can be at most one particle center within a sphere of radius $\lambda \leq d/2$, so that

$$p_0(\lambda, \phi) = 1 - n w_D \lambda^D \text{ for } 0 \leq \lambda \leq d/2, \quad (7.109)$$

where w_D is the volume of the unit sphere. Logarithmic derivatives of probabilities are in general conditional probabilities, and so is $-\mathrm{d} \ln p_0$ the probability to find a particle center within two shells of radii λ and $\lambda + \mathrm{d}\lambda$, given that there is no particle center in the inner shell. Since this conditional probability is proportional to the particle density n and the volume $\mathrm{d}V = w_D \mathrm{d}\lambda^D$ between the shells, one defines a function $G(\lambda, \phi)$ by the relation $-\partial \ln p_0 / \partial \lambda = G(\lambda, \phi) n \partial V / \partial \lambda$, so that $G(\lambda, \phi)$ is the contact correlation between a particle and a hollow cavity with radius $\lambda - d/2$. The general concept of the Scaled Particle Theory is to study the analytic properties of $G(\lambda, \phi)$ as a function of λ . From (7.109) follows

$$G(\lambda, \phi) = \frac{1}{p_0(\phi, \lambda)} = \frac{1}{1 - \left(\frac{2\lambda}{d}\right)^D \phi} \text{ for } 0 \leq \lambda \leq d/2. \quad (7.110)$$

For a hard sphere system without attractive forces the contact correlation between a hollow sphere of diameter d and a particle equals the correlation between two particles, so that the particle-particle contact correlation is

$$g_{\mathrm{pp}}(\phi) = g(d+, \phi) = G(d, \phi). \quad (7.111)$$

Furthermore, a flat wall is nothing but a sphere with infinite radius, so that the particle-wall contact correlation is

$$g_{\mathrm{pw}}(\phi) = G(\infty, \phi). \quad (7.112)$$

Equating the local pressure in the volume (which is the trace of the stress tensor depending on the particle-particle correlation g_{pp}) and the pressure measure at the boundaries (where the particle-wall contact correlation g_{pw} enters the computation) one finds the relation [106]

$$g_{\mathrm{pw}}(\phi) = 1 + 2^{D-1} \phi g_{\mathrm{pp}}(\phi). \quad (7.113)$$

Because of the Eqs. (7.111) and (7.112), Eq. (7.113) relates $G(d, \phi)$ and $G(\infty, \phi)$. This suggests to expand the function $G(\lambda, \phi)$ in powers of $1/\lambda$:

$$G(\lambda, \phi) = \sum_{j=0}^{D-1} G_j(\phi) \lambda^{-j}. \quad (7.114)$$

The coefficients G_j have a direct physical interpretation as pressure, surface tension and line tension [115]. Note that such an ansatz is reasonable for the differentiable void-particle correlation G , whereas the particle-particle correlation g of hard spheres is discontinuous as we have seen before, because voids are compressible but the particles are not. The value $G(d/2, \phi)$ and its first derivative $G'(d/2, \phi)$ given by (7.110), together with the relation (7.113), determine the three coefficients G_j for $D = 3$ spatial dimensions. The resulting expressions for g_{pp} and g_{pw} are shown in Tab. 7.1 for various spatial dimensions. Aside from the trivial one-dimensional case⁸, exact expressions for the contact correlation of hard discs and spheres are unknown. The last column presents the heuristic fits to simulations suggested by Henderson [13, 110, 31].

The Influence of Polydispersity on the Contact Correlation

Most granular media are polydisperse⁹, and the hard sphere system is the basis for the equation of state for wetted spheres. Let us briefly discuss how one can obtain explicit results on the two-particle contact correlation in such dry polydisperse media. From the trace of the stress tensor follows the local pressure of a hard sphere systems,

$$\frac{P}{nT} = 1 + 2^{D-1} \phi \left\langle \frac{\left(\frac{d_1+d_2}{2}\right)^D}{\mu_D} g_{\mathrm{pp}}(d_1, d_2, \phi) \right\rangle, \quad (7.115)$$

where brackets denote averaging over the quenched disorder of size polydispersity. The detailed contact function $g_{\mathrm{pp}}(d_1, d_2, \phi)$ is the correlation for a pair of particles with diameters d_1 and d_2 . The information about

⁸The configuration space of the one-dimensional gas is $L - N \langle d \rangle$, so that the equation of state is $P(L - N \langle d \rangle) = NT$. Comparison with the general expression $P = g_{\mathrm{pw}} n T$ yields $g_{\mathrm{pw}} = (1 - \phi)^{-1}$.

⁹Polydispersity influences the compactivity of the undriven solid state and reduces the liquid bridge coordination number. Therefore the fluidization transition under vertical sinusoidal driving sets in at a higher acceleration Γ_{crit} for less polydisperse media, as verified by the author experimentally: a highly monodisperse system of 500 $\mu\mathrm{m}$ spheres undergoes the solid-fluid transition at a peak acceleration $\Gamma_{\mathrm{crit}} \approx 6.5$ (at 200 Hz shaking frequency, cf. Chap. 8), while a system with 6% polydispersity fluidizes at $\Gamma_{\mathrm{crit}} \approx 2$ (cf. Chap. 10). Both systems have been wetted with 1% water.

the distribution of particle sizes in the medium is captured in the moments $\mu_k = \langle d^k \rangle$. The moment $\mu_D = \langle d^D \rangle$ in the denominator of (7.115) stems from the definition of ϕ as the occupied volume, $\phi = \frac{\text{vol}_{\text{occ}}}{\text{vol}_{\text{sys}}} = \frac{N \langle \text{vol}_{\text{sph}}(d) \rangle}{\text{vol}_{\text{sys}}}$. The numerator $(d_1 + d_2/2)^D$ results from the radial integration in the stress tensor.

Santos, Yuste and de Haro [194] have suggested a method which is mathematically similar to the Scaled Particle Theory: The contact correlation $g_{\text{pp}}(d_1, d_2, \phi)$ for a pair of particles is expanded in powers of the mean inverse diameter:

$$g_{\text{pp}}(d_1, d_2, \phi) = \sum_{n=0}^D H_n(\phi) z^n, \quad \text{with } z = \frac{2}{d_1^{-1} + d_2^{-1}} \frac{\mu_{D-1}}{\mu_D}. \quad (7.116)$$

From the point of view of billards, $g_{\text{pp}}(d_1, d_2, \phi)$ is the probability distribution on the boundary of the configuration space. This boundary is locally an geometrical object with codimension 1 and $D-1$ dimensions of the boundary have a non-vanishing curvature. The ansatz (7.116) is just an expansion in the local mean curvature of the boundary of the configuration space. To generalize the result to arbitrary dimensions we collect the moments in (7.115) and arrive at

$$\frac{P}{nT} = 1 + \phi \sum_{n=0}^D 2^{n-1} H_n \sum_{k=0}^{D-n} \binom{D-n}{k} \frac{\mu_{k+n} \mu_{D-k} \mu_{D-1}^n}{\mu_D^{n+1}}, \quad (7.117)$$

Analogous to the Scaled Particle Theory, we equate the pressure in the volume and the pressure measured at the system walls. The particle-wall correlation for a particle of diameter d is $g_{\text{pw}}(d, \phi) = g_{\text{pp}}(d, \infty, \phi)$, so that

$$\frac{P}{nT} = \langle g_{\text{pw}}(d, \phi) \rangle = \sum_{k=0}^D 2^k H_k \frac{\mu_k \mu_{D-1}^k}{\mu_D}. \quad (7.118)$$

Comparison of (7.117) and (7.118) yields equations for the coefficients H_k . Furthermore, the monodisperse limit (with $z = 1$ in the ansatz (7.116)) is known,

$$g_{\text{pp}}(d, d, \phi) = \sum_{n=0}^D H_n(\phi) = g_{\text{pp}}(d, \phi), \quad (7.119)$$

and the limit of a bidisperse system with a point-particle component (so that $z = 0$ in the ansatz (7.116)) determines the zero coefficient to be

$$g_{\text{pp}}(d, 0, \phi) = H_0(\phi) = \frac{1}{1-\phi}, \quad (7.120)$$

because a point particle can visit every niche of the unoccupied system space which volume fraction is $1 - \phi$. The Eqs. (7.117)-(7.120) determine all coefficients H_k . For $D = 2$ we find the coefficients to be

$$H_1 = (2 - \phi) g_{\text{pp}} - \frac{2 - \phi/2}{1 - \phi}, \quad H_2 = \frac{1 - \phi/2}{1 - \phi} - (1 - \phi) g_{\text{pp}}. \quad (7.121)$$

Chapter 8

The Critical Point of Wet Granular Matter

— The Quantitative Experimental Confirmation

In this chapter, the experimental observation of the critical point in fluidized wet granular matter is reported. The experimental data show quantitatively that the critical density and temperature are set by the length and energy of the capillary bridges. This confirms the theoretical predictions of the Chaps. 6 and 7. The experiment is sensitive to the global state of the capillary network: 10^5 small steel spheres are wetted with an ionic liquid solution while agitated vertically. The global electrical conductivity, $\Sigma = 1/R$, of the capillary network is measured. R is shown to be a well-suited order parameter for the instantaneous liquid bridge topology and the nonequilibrium states of wet granular matter. The method is in particular advantageous because transitions of the bulk structure are detected, where optical methods are limited to surface effect. Furthermore, this chapter reports precise measurements of the hysteresis in the fluidization/solidification transition of wet granular matter. The experimentally observed sharp step in $R(\Gamma)$ at the fluidization transition, $\Delta\Gamma_{\text{SF}}/\Gamma_{\text{SF}} \sim 10^{-4}$, demonstrates for the first time clearly that the solid to fluid transition is a discontinuous nonequilibrium transition. The capillary network is shown to significantly strengthen after solidification, which retards fluidization and explains the large lag of fluidization at Γ_{SF} as compared to solidification at Γ_{FS} . It is demonstrated that this hysteresis can almost double the driving acceleration, $\Gamma_{\text{SF}} \approx 1.9\Gamma_{\text{FS}}$. Moreover, the temporal fluctuations $\langle (R(t) - \bar{R})^2 \rangle$ allow the direct observation of the granular temperature T : the fluctuations are theoretically derived to be proportional to \sqrt{T} . In the experiments, the granular temperature is shown to vanish quadratically in the driving velocity at the solidification, and to jump discontinuously at the fluidization.

Section 8.1 presents the concept of assessing the nonequilibrium states by virtue of the electrical conductivity of the capillary network. We begin with the mildly driven states in Sec. 8.2, where the discontinuous fluidization, the solidification and their hysteresis are demonstrated. The location of the critical point in the density-temperature plane is determined experimentally in Sec. 8.3. Conclusions are given Sec. 8.4. The granular heat equation is solved analytically for the experimental geometry in appendix 8.5. Important experimental cross-checks are reported in the appendix 8.6.

8.1 Conductivity as an Experimental Order Parameter of the Capillary Network

The capillary network plays a crucial role for the mechanical stability of wet granular matter at rest, as discussed in the Secs. 3.4.4 and 3.4.5. In the solid state, the granular motion is frozen by the rigidity constraints of the capillary network. The failure of the capillary network gives rise to the fluidization transition [87, 114], which is a nonequilibrium transition from the disordered solid state to the driven granular fluid. This process is reminiscent of soil liquefaction which can lead to land slides.

A further nonequilibrium transition is the unclustering effect observed in simulations and described analytically in the free cooling of wet granular matter of Chap. 6 in one dimension. Closely related is the segregation transition derived theoretically for steady states in two dimensions by the equation of state in Chap. 7. Both transitions are mechanical instabilities, as described by the van-der-Waals-like loop for the wet granular isotherms. These transitions are predictions of the theory developed in this thesis for nonequilibrium states. In order to verify them experimentally, it is desirable to have an instantaneous experimental measure for the capillary network structure, which allows to follow such transitions in real-time.

8.1.1 The Measurement Method

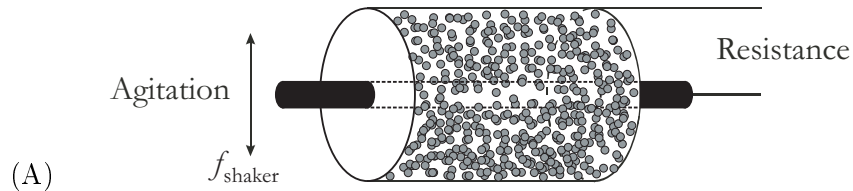
This is realized by an electrically conductive wetting liquid of high surface tension, which wets steel spheres. So we have the capillary bridges for the wet dynamics, and simultaneously, the electrical conductivity due to the capillary network. As an essential precondition, the author found that the contact resistance between *dry* steel spheres (with the quarter of a millimeter in radius) is more than five orders of magnitude higher than the resistance with the capillary bridges formed at the contact points. This is due to the few metal atoms forming a common electron band in the point-like contact. In contrast, the capillary bridge (around the mechanical contact point) electrically contacts the spheres with a cross section which is of the order of the particle radius. Therefore each capillary bridge contributes as a bond of finite resistance to the capillary network. For this reason, the global resistance R of this wet granular matter is a direct measure for the global connectivity of the microscopic capillary network, and R serves as an order parameter of the dynamical capillary network. It is emphasized that this method is sensitive to the bulk structure, while optical methods are limited to surface effects.

Moreover, the electrical signal captures the instantaneous state of the network, which is under permanent formation and rupture of capillary bonds. This dynamics leads to measurable temporal fluctuations $R(t)$. These fluctuations about the mean resistance, \overline{R} , are directly related to the binding and rupture frequency of the capillary bonds. Since these frequencies are known functions of the granular temperature T , we can measure relative changes of the granular temperature. With a time-resolved measurement of the resistance, $R(t)$, we can follow the changes in the bulk *coordination of the capillary network* and (up to a constant factor) the *granular temperature* of wet granular matter in any accessible nonequilibrium state.

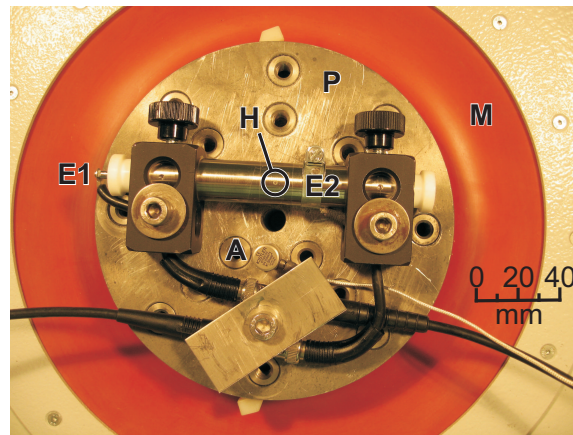
8.1.2 The Experimental System

The granular material consists of small hardened steel spheres¹ with radius $R = 250\mu\text{m}$. The particles are monodisperse, with size deviation $\Delta R/R \approx 2 \times 10^{-3}$. Such particles are commercially available for micro ball bearings and pen balls, so that their spherical shape is

¹The steel grade is AISI 420 C, which has the high Rockwell hardness 60 HRC.



(A)



(B)

Figure 8.1: A granulate of steel spheres is wetted by an conductive liquid. The conductivity is an order parameter of the capillary network, and allows to determine the state of wet granular matter. (A) Sketch of the horizontal cylindrical cell, which is set under sinusoidal vertical motion. (B) Top view of the experimental setup. It is constructed to withstand the vis inertiae acting at accelerations up to $100 g$. The granulate consists of 1.12×10^5 stainless steel spheres with radius $r = 250 \mu\text{m}$ inside the horizontal cylinder. The inner rod electrode E1 protrudes at the left end of the cylindrical cell. The cell is gastight, sealed by PTFE plugs at the left and right end. Both electrodes, the inner and the outer cylindrical electrode E2, are made of stainless steel with which the particles have a restitution coefficient $\epsilon_{pw} = 0.85$. The hole H of 1 mm diameter is used to inject the wetting solution with a syringe needle, and closed during the experiment. The cell and an acceleration sensor A are mounted on the plate P of an electromagnetically driven shaking system. M is an elastic membrane, which allows for sinusoidal motion of the entire setup perpendicular to the image plane at frequencies from 100 to 300 Hz, and accelerations up to $50 g$. The conductivity of the granulate is measured continuously (10^5 samples per second) as a function of the driving frequency and acceleration.

of high precisions. The particles used have deviations from sphericity, $\Delta R = \sum_{l,m} a_{l,m} Y_l^m$, with amplitudes $a_l \approx 0.12 \mu\text{m}$ at long scales ($l = 1-15$), which reduce to the level of $0.05 \mu\text{m}$ at short scales ($l = 50-500$). The granulate is shaken vertically in a horizontal cylinder made of unhardened stainless steel, which serves as the outer electrode (cf. Fig. 8.1). The inner electrode is a rod of the same material along the symmetry axis of the cylinder, which contributes as well as the outer cylinder in the mechanical excitation of the granular medium. The jammed state of the system was found to have a packing fraction $\phi_J = 0.62$, which is slightly below the maximal random jammed density in a box ($\phi = 0.63$) or under periodic boundary conditions ($\phi = 0.64$) [60], because of the more complicated boundary geometry². The density in the cell is chosen according to the predicted critical densities (in the Chaps. 6 and 7). There, the critical density is predicted to be a function of the rupture length, s_{crit} (cf. Fig. 7.15). The wet granular dynamics is measured under isochoric conditions at overall densities $\phi = 0.923\phi_J$ and $\phi = 0.939\phi_J$ expressed in units of the jamming density ϕ_J . The dimensionless system size is designed to be rather big, with $N = 1.12 \times 10^5$ spheres and an inner length $L = 280R$ of the cylindrical cavity holding the granulate. The inner diameter is $D = 64R$, and the radial separation of the electrodes is $24R$. The prolonged geometry yields good statistics for the electrical resistance measurement combined with a very homogeneous mechanical driving of the granulate. It has been furthermore scrutinized that all effects reported in this chapter are reproducible in smaller cells of the same geometry, scaled down to half the volume, as well as to the tenth of the full volume, while the particle radius R was kept. Hence finite size or spurious boundary effects are excluded.

A very dry initial state is prepared by heating the cleaned steel spheres to 250°C for several hours. At approximately 50°C the particles are filled in the cell. The cell is closed by gastight plugs of polytetrafluoroethylene (PTFE) at its ends. A defined amount of the wetting and conductive liquid is injected through a small hole (item H in Fig. 8.1B) with a syringe needle, and sealed during the measurement.

8.2 The Solid/Fluid Transition

The granulate is initially brought in the fluid state at a driving frequency of $f_{\text{shaker}} = 100 \text{ Hz}$. The resistance and the acceleration, measured by means of a piezo sensor mounted on the system, are recorded 10^5 times a second. From this data the acceleration $\Gamma(t) = a(t)/g$ and the resistance $R(t)$ is deduce for each single driving cycle. As throughout this thesis, the dimensionless Γ (without explicit time-dependence) denotes the peak acceleration. As it is shown in Fig. 8.2A by the dashed line, the acceleration of the driving is then continuously reduced at fixed frequency f_{shaker} . At the critical acceleration $\Gamma_{\text{FS}} = 4.72$, the resistance sharply falls off to the plateau value R_{solid} of the solid state.

The amplitude of the driving is then increased again, linearly in time over more than 10 minutes. Within that period the solid system is annealed, which strengthens the capillary network by further increasing the number of capillary bonds per particle. This strongly increases the critical acceleration necessary to fluidize the wet granular matter. At $\Gamma_{\text{FS}} = 8.74$ the solid state abruptly breaks up within a quarter of a second. The red squares superimposed in Fig. 8.2 within this short period of time, show the data points underlying the measured resistance curve, separated 10 ms in time. It is seen that the breakup first accelerates starting with the points of constant frequency being close-by, reaches a maximum, and finally decelerates again. Expressed in the dimensionless acceleration Γ of the external driving, the

²This shows also that the granulate does not crystallize.

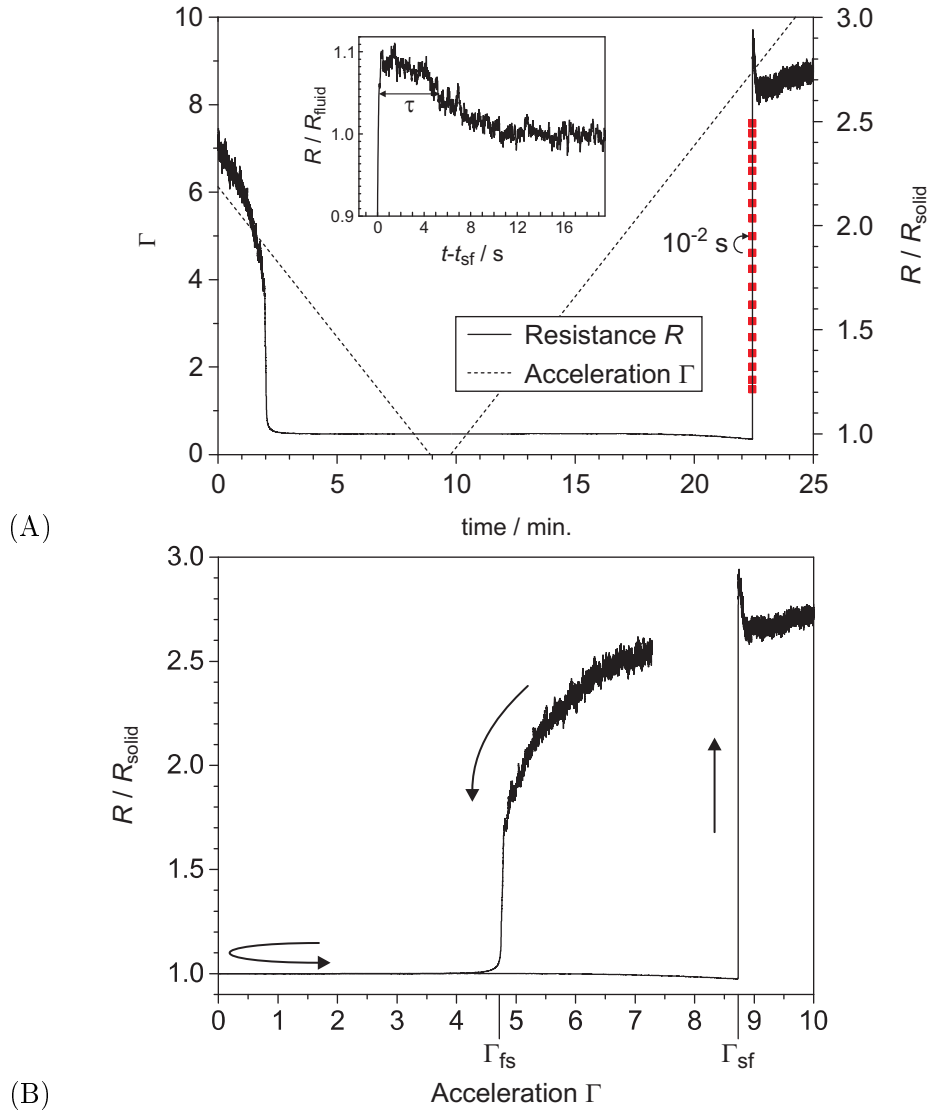


Figure 8.2: The fluid/solid and solid/fluid transition in wet granular matter. The acceleration (dashed line) is reduced continuously (early times in (A)), so that the fluidized wet granular matter enters the solid state with a sharp fall-off in the resistance at $\Gamma_{\text{FS}} = 4.72$, as indicated in panel (B) where the data is plotted as a function of the dimensionless driving force Γ . At this point the granular motion, in the sense of particles interchanging their relative locations, comes to rest. Because of the increased relaxation time, the granular matter is not in a stationary state at Γ_{FS} , and R crosses over to R_{solid} . The slower the protocol for the ramping of Γ , the steeper is the slope at Γ_{FS} , so that in the steady state limit, the solidification point has vertical slope for infinitesimally slow change of Γ . (As is shown in Sec. 8.2.1, the solidification point is determined best by the direct measurement of the granular temperature T , which allows a finite protocol.) The acceleration is then slowly ramped up again (late times in (A)) over more than 10 minutes. The more time the wet granular matter is given under this annealing, the higher is the critical acceleration, Γ_{SF} , necessary to break the capillary network in the abrupt fluidization transition. The strengthening of the capillary network in the granular annealing gives rise to the strong hysteresis, which is observed for this transition in (B). For the slow ramping shown here, $\Gamma_{\text{SF}} = 8.74$ is increased by a factor of 1.85 compared to the reversed transition at Γ_{FS} , which is independent of the granular history.

sharpness of the fluidization edge is

$$\frac{\Delta\Gamma_{\text{SF}}}{\Gamma_{\text{SF}}} = 3 \times 10^{-4} . \quad (8.1)$$

This gives unprecedented experimental evidence that the solid/fluid transition in wet granular matter is a prominent example for a *discontinuous* transition far from equilibrium. We remark that the sharpness of this transition has become possible because the transition has been observed in the volume, and not on the surface where few particles, participating in surface melting effects, are subject to strong fluctuations. The fluidization transition is a collective phenomenon far from equilibrium which involves all 10^5 particles. If we assume that this transition is accompanied by a propagating front, the velocity of the latter can be estimated from the length of the cylinder, which yields

$$v_{\text{prop}} \approx 30 \text{ cm/s} \approx 12f_{\text{shaker}}R = 6f_{\text{shaker}}d . \quad (8.2)$$

Since the densely packed state has a coordination number close to 6 [60, 114], this is what one would expect for a particle that undergoes one ring-collision with its neighbors per driving cycle. (In a collision the momentum is exchanged over the center-center distance $2R = d$.)

The hysteresis in the solid/fluid transition can be studied by varying the speed of the driving protocol. For the slow ramping (over minutes as shown in Fig. 8.2), Γ_{SF} is increased by a factor of 1.85 compared to the reversed Γ_{FS} . The latter is found to be independent of the granular history. As we speed up the ramping by a factor of 100, the fluidization point Γ_{SF} reduces from 8.74 to 5.2. Without time to ‘anneal’ voids in the granular solid, the transition becomes asymptotically reversible, such that the fluidization converges to the point of solidification, $\Gamma_{\text{SF}} \rightarrow \Gamma_{\text{FS}} = 4.72$. The strengthening of the capillary network during the period of ‘granular annealing’ is the reason for the strong hysteresis in the solid/fluid transition.

Immediately after the fluidization, the resistance shows a sharp overshooting. The nascent fluidized granulate has a higher resistance, which relaxes to the resistance R_{fluid} as is shown in the inset of Fig. 8.2A. As we compare the full width at half maximum of this overshooting, we find that this relaxation time is $\tau = 5.2$ seconds, independent of the ramp speed (τ as indicated for the slow run in Fig. 8.2A and the 100 times faster run in Fig. 8.9). Therefore τ is the *intrinsic* relaxation time of the wet granular system. The pronounced fluctuations around the value R_{fluid} reflect the rupture frequency of capillary bonds in the fluid state. The sudden increase in resistance by almost a factor of three at the fluidization edge is due to the reduced coordination number in the fluid state. The mean coordination number in the fluidized state can be estimated from the known value $K_{\text{S}} \approx 6$ in the solid state, and the increase of resistance³ by the factor $R_{\text{fluid}}/R_{\text{solid}} = 2.65$, to be $K_{\text{F}} \approx 2.3$. In this context we remind that the fluidized granular matter is confined to the high density $\phi = 0.923\phi_{\text{J}}$.

8.2.1 The Granular Temperature

In this section it is shown that the granular temperature can be directly measured up to a constant factor. The basic idea is that the frequency, at which capillary bonds are formed and broken, gives rise to defined and measurable fluctuations in the resistance of wet granular matter. Quantitatively, we have the relation (cf. the Eqs. (7.43) and (7.44))

$$f_{\text{rupt/bind}} = G_{\text{rupt/bind}}(\phi)\sqrt{T} \quad (8.3)$$

³The time scale for the formation of a liquid bridge (as discussed in detail in Chap. 3) is much shorter than the time scale for transport of liquid on the surface of the sphere [87]. The reduction of the coordination number is therefore not accompanied by an increase of the bridge volume. If we assume that the liquid bridges have equal volume, we have the linear relation $R_{\text{fluid}}/R_{\text{solid}} = \Sigma_{\text{solid}}/\Sigma_{\text{fluid}} = K_{\text{S}}/K_{\text{F}}$.

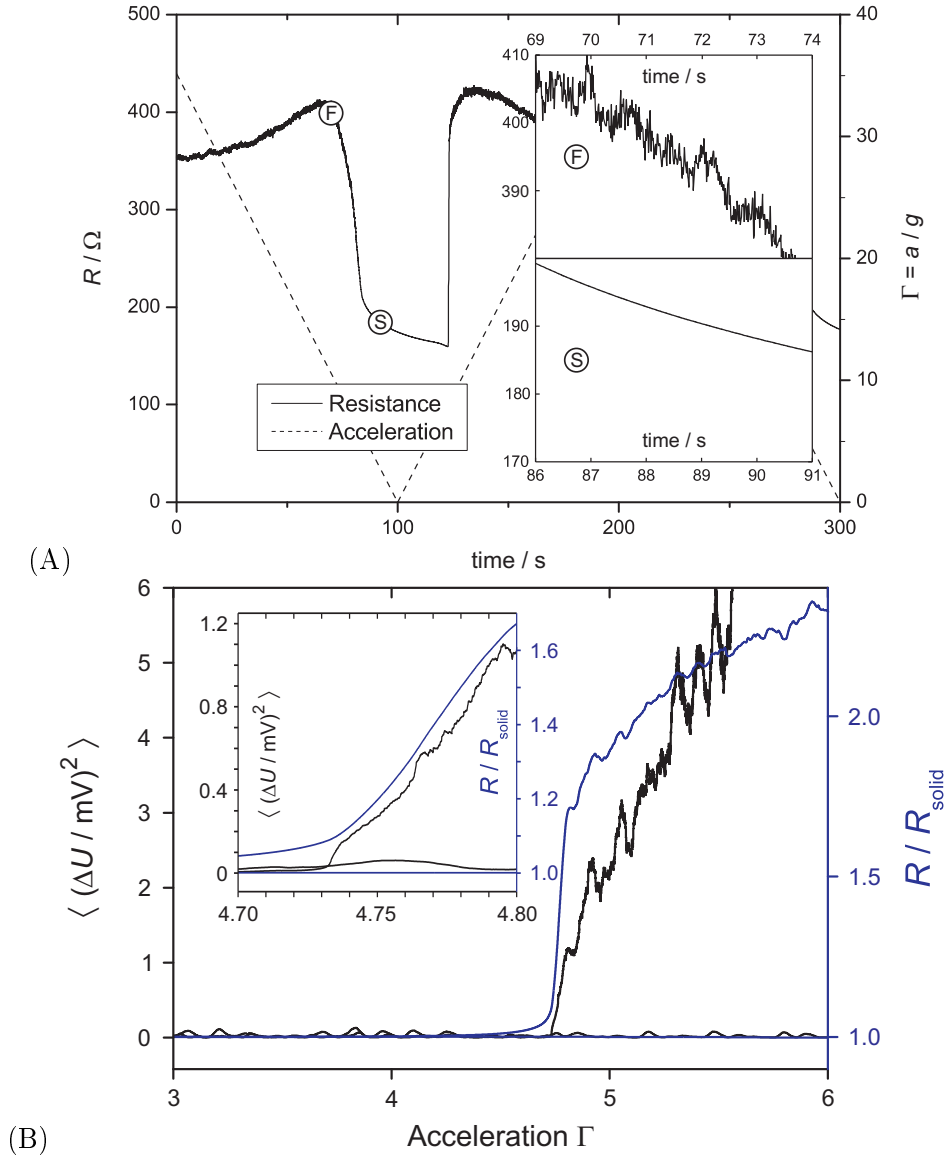


Figure 8.3: (A) Fluctuations in the resistance. The temporal fluctuations originate from binding and rupture events of the capillary network. The binding and rupturing frequency is proportional to the square root of the granular temperature T . This is why these fluctuations provide a direct measure for T . The fluctuations are very pronounced in the fluid state F and vanish in the solid state S. The inset S shows the absence of fluctuations on the same scale as the inset for the fluid F. (B) Measurement of the fluctuations (black curve) at the solidification point Γ_{FS} . The resistance R (blue curve) crosses over to R_{solid} because of the finite ramping speed. In contrast, the fluctuations measure the particle motion and allow to determine the point of solidification even at a finite ramping speed. The granular temperature is given, up to a constant factor, by the voltage fluctuations $\langle \Delta U^2 \rangle \propto \sqrt{T}$ at the cell. The fluctuations $\langle \Delta U^2 \rangle = M^{-1} \sum_{j=1}^M \Delta U_j^2$ shown here result from $M = 300$ driving cycles at 100 Hz. The inset provides a close-up at finer voltage scale. It shows that the fluctuations $\langle \Delta U^2 \rangle$ go linearly to zero at in the vicinity of the solidification point. This shows that the granular temperature is quadratically related to the driving velocity, $v \propto f_{\text{shaker}} A$, of the boundaries (cf. Eq. (8.12)).

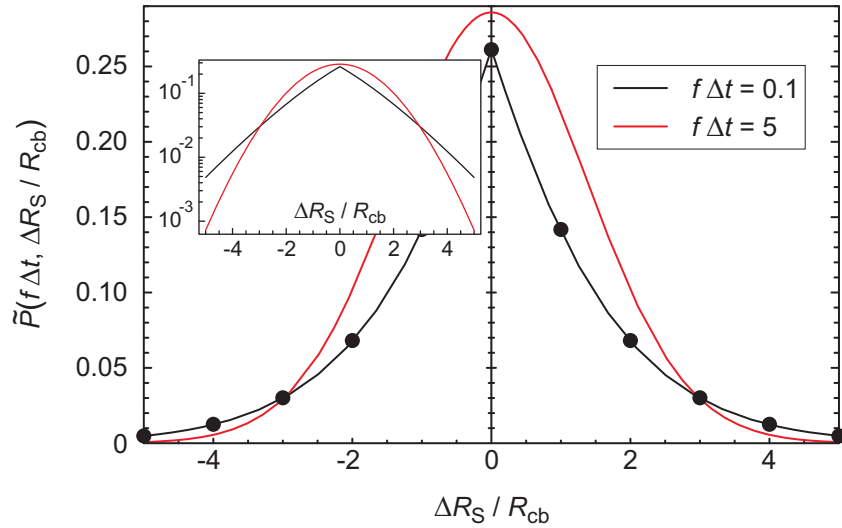


Figure 8.4: On short time scales, below the typical time f^{-1} of the binding and rupture frequency, $f = f_{\text{rupt}} = f_{\text{bind}}$, the fluctuations of the wet granular resistance, ΔR_S , obey a double Poisson process (black distribution). On longer time scales, this rapidly converges to Gaussian noise (red curve). The information about the granular temperature is in principle captured on all time scales by the width of the distribution. Equation (8.10) states that the granular temperature is proportional to the fourth power of the width.

between the granular temperature T and the frequencies of the binding and rupture events. The factor $G_{\text{rupt/bind}} \propto \phi g_{\text{rupt/bind}}(\phi)$ in (8.3) depends on the density ϕ (also through the pair correlation g , which is a function of the density as well). Since the experimental system is isochoric, G is a constant. The resistance $R(t)$ performs a stochastic process,

$$\dot{R} = -(R - \bar{R})/\tau + \dot{R}_S \quad (8.4)$$

around the mean value \bar{R} with the relaxation time τ as introduced before in Sec. 8.2. The stochastic term R_S in the Langevin Eq. (8.4) is caused by the rearrangements of the dynamic capillary network. Here the granular temperature enters: if we assume that the breaking and formation of a single capillary bond perturbs the global resistance by a small constant $\pm R_{\text{cb}}$, we have $R_S = R_S^+ - R_S^-$ with the two Poisson processes $R_S^{+/-}$, which account respectively for the rupture events (by increasing the resistance) and the binding events (by reducing the resistance):

$$\langle \dot{R}_S^{+/-} \rangle = R_{\text{cb}} f_{\text{rupt/bind}} , \quad (8.5)$$

with the (temporal) Poisson distributions

$$\text{Prob}(\Delta R_S^{+/-} = k R_{\text{cb}}) = e^{-f_{\text{rupt/bind}} \Delta t} (f_{\text{rupt/bind}} \Delta t)^k / k! , \quad (8.6)$$

where $\Delta t = t_2 - t_1$ and $\Delta R_S^{+/-} = R_S^{+/-}(t_2) - R_S^{+/-}(t_1)$. In the stationary state (i.e. we change the external driving slowly enough, and do not perform a free cooling experiment) we have $f = f_{\text{rupt}} = f_{\text{bind}}$. The fluctuations in $R_S(t)$ have a distribution

$$P(f \Delta t, \Delta R/R_{\text{cb}} = k) = \text{Prob}(R(t_2) - R(t_1) = k R_{\text{cb}}) . \quad (8.7)$$

To arrive at this distribution, we sum over the probability to have k^- new bonds and k^+ broken bonds (which is given by Eq. (8.6)), for a given net change k with $k = k^+ - k^-$. This sum can be written as a hypergeometric series ${}_pF_q$:

$$P(f \Delta t, k) = \frac{e^{-2f \Delta t}}{|k|!} (f \Delta t)^{|k|} {}_0F_1(|k| + 1; (f \Delta t)^2) . \quad (8.8)$$

The distribution (8.8) is shown in Fig. 8.4. The function is scaled to $\tilde{P}(k) = \sqrt{f \Delta t} P(k\sqrt{f \Delta t})$ in order to compare different time scales Δt . While the fluctuations on short time scales (of the order of the event frequency f) obey the more complicated distribution (8.8), the long-time behavior has a Gaussian noise amplitude with zero mean,

$$\langle \Delta R_S \rangle = (f_{\text{rupt}} - f_{\text{bind}}) \Delta t = 0 , \quad (8.9)$$

and variance

$$\langle \Delta R_S^2 \rangle = R_{\text{cb}}^2 (f_{\text{rupt}} + f_{\text{bind}}) \Delta t \propto \sqrt{T} \Delta t . \quad (8.10)$$

This consideration shows that it is not necessary to resolve individual rupture events, which occur in the experimental system up to gigahertz rates for fast driving. The fluctuations of the resistance, $\langle \Delta R_S^2 \rangle$, are proportional to the square root of the granular temperature as described by Eq. (8.10). (This is not akin to the velocity distribution where the variance is linear in temperature.)

The granular cell is connected to the power source with a large series resistance, so that we can (equivalently to Eq. (8.10)) measure the fluctuations of the cell voltage:

$$\langle \Delta U^2 \rangle \propto \sqrt{T} \Delta t . \quad (8.11)$$

The solid state is characterized by iso- or hyperstatic [60] constraints imposed by the capillary bonds, which freeze the relative motion of the granular particles (and give rise to the plastic material property as discussed in Sec. 3.4). We therefore expect the wet granular solid to have zero fluctuations, also at positive driving. This is actually seen in the experiment: the black curve in Fig. 8.3B are the measured fluctuations, which vanish at a precisely defined driving acceleration Γ . This allows to clearly determine the solidification of wet granular matter. In contrast, the resistance $R(\Gamma)$ (blue curve) crosses over, which does not clearly determine the transition for a finite ramping speed. This is so because the wet granular fluid is not in its steady state, as the rearrangements slow down close to the solidification, while the ramping speed is kept constant. Therefore the value of the resistance R is also not the steady state value, but crosses over to R_{solid} .

Furthermore, we see in Fig. 8.6 (red curve) that the fluctuations go linearly to zero at Γ_{FS} , so that according to Eq. (8.11), $\Gamma - \Gamma_{\text{FS}} \propto \sqrt{T}$. The experimental protocol for the driving keeps the frequency f_{shaker} fixed and changes the driving amplitude A , so that the driving acceleration $\Gamma \propto A f_{\text{shaker}}^2$ is proportional to the velocity of the driving boundaries, $v_{\text{D}} = A f_{\text{shaker}}$. Hence the experimental finding: the granular temperature vanishes at the solidification according to

$$(v - v_{\text{FS}})^2 \propto T . \quad (8.12)$$

A quadratic relation is obviously expected based on dimensional analysis.

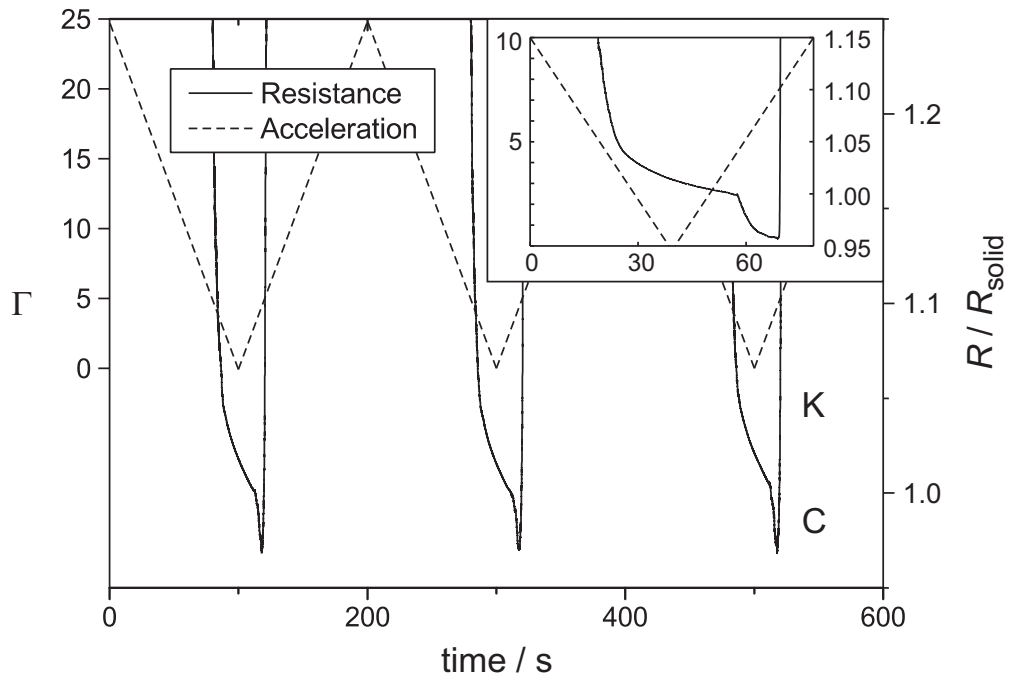


Figure 8.5: The strengthening of the capillary network, which precedes the solid/fluid transition. Each S/F transition is preceded by an annealing process, which increases the homogeneity of the capillary network in the wet granular matter and increases the capillary coordination. This granular annealing manifests in the dip (labeled C) of the resistance $R(T)$ prior to the breaking of the capillary network at the fluidization edge (labeled K). When the acceleration is increased within a minute or less, the dip can set in abruptly, as is shown in the inset. The increase in conductivity by five percent does not reflect the increase in the coordination of the capillary network, which is much stronger since the fixed amount of wetting liquid is shared by the capillary bonds. The contact force F_{cb} of a capillary bond depends weakly on the liquid volume of the individual capillary bridge [114].

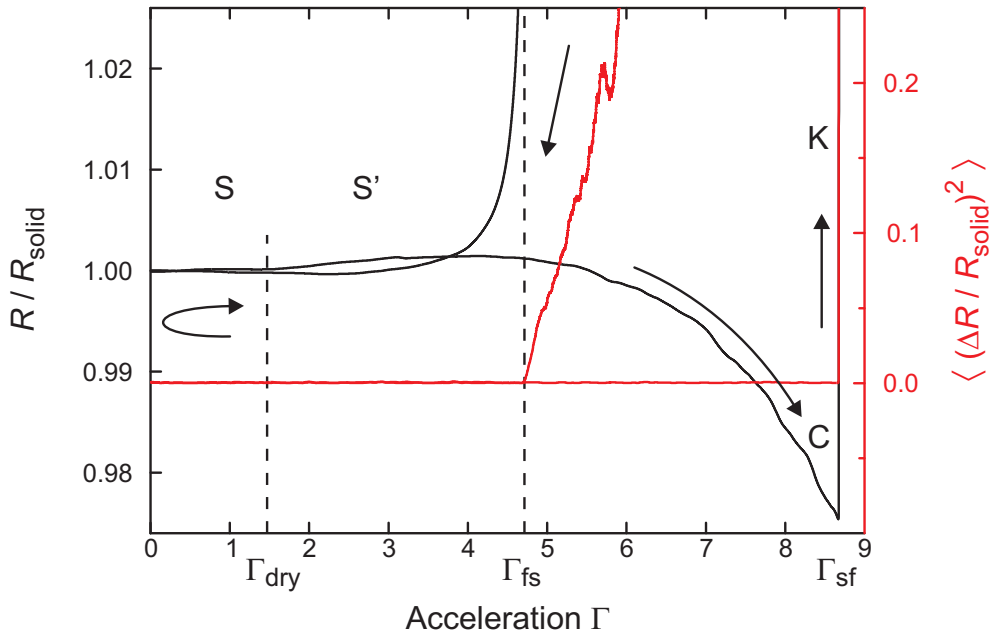


Figure 8.6: A look inside the capillary network. The high quality of the data allows to deeply zoom inside the solid/fluid hysteresis. At the fluidization transition the resistance (black curve) has a rapid cross over structure, and the granular temperature (observed as the fluctuations shown in the red curve) goes linearly to zero. The granular temperature T remains zero throughout the solid state. The integration time for the fluctuations in resistance, which are proportional to \sqrt{T} , is 10 s ($M = 1000$ driving cycles). At the solid/fluid transition, the capillary network breaks up, which causes the abrupt jump in the resistance. The granular temperature is found to be also discontinuous at this transition.

8.2.2 Capillary Strengthening and the Hysteretic Fluidization

The solid state exhibits also a certain dynamics, which can be resolved by virtue of the resistance measurements. As a general finding, the resistance reduces in the solid state. This strongly indicates that the capillary bridges grow on a longer time scale, which is of the order of one minute. Further, there are two distinct regimes. When the ramping is fast, i.e. one minute or less, there is a very reproducible sudden drop in the resistance, prior to the breakup of the network at the fluidization. Typical examples of this rearrangement are shown Fig. 8.5. The main panel shows a sequence of three ramps. The sharp dip in the resistance is clearly visible. The inset with the finer time scale suggests that there are two different mechanism for the reduction in R .

The quality of the data shown in Fig. 8.2 allows to zoom in by two orders of magnitude, which reveals the change of the resistance $R(t)$ within the solid state in Fig. 8.6. This is the regime when the ramping speed is slow, with one driving cycle lasting more than ten minutes. Here we find that the sudden drop in the resistance does not occur. Let us have a look at the full cycle beginning with the fluid state. The branch of $R(\Gamma)$ in Fig. 8.6, along which the driving amplitude is reduced (where the arrow points downwards and to the left), has a pole-like functional form on this scale with the rapid fall-off located precisely at the solidification point Γ_{FS} , where the granular temperature $T(\Gamma)$ (red line) simultaneously vanishes. As the external driving increases again in the solid state denoted by S, the capillary bridges are hardly exposed to stretching forces until the point $\Gamma_{\text{dry}} \approx 1.4$, at which the dry granulate

would fluidize. Beyond that point, fluidization is prevented by the capillary attraction. The slight increase in resistance corresponds to few out of a thousand capillary bonds, which break beyond this point. The degrees of freedom released by these broken capillary bonds cause local rearrangements of bonds in the capillary network, still at unmeasurable granular temperature. With these slight rearrangements within the solid state denoted by S' , the wet granular system evolves within a tiny subspace of the configuration space towards more and more stable configurations, because the weakest links within the granular sample are the first to break and being replaced. It is reasonable to assume that the speed of this evolution, which strengthens the capillary network, is approximately linear in the driving amplitude, $\dot{R} \propto -\Gamma$. This explains why we observe the parabolic reduction of resistance, $\Delta R(\Gamma) \propto -\Gamma^2$, until fluidization suddenly sets in at Γ_{SF} . This period of the capillary network evolution (labeled C) can be seen as a competition between the rate of strengthening and the rate at which the driving is increased. For this reason it is clear that a slower increase of the driving prolongs the compactification period, and causes the pronounced hysteresis of the solid/fluid transition.

The red curve in Fig. 8.6 shows the fluctuations also at the fluidization transition at Γ_{SF} . At this transition point we see clearly that the fluctuations rise (as the resistance R shown in black) discontinuously. We can therefore conclude the investigation of the hysteretic solid/fluid transitions, by pointing out that in the direction of solidification the granular temperature goes quadratically to zero (Eq. (8.12) with the driving. By contrast, the granular temperature is discontinuous for the reversed direction at the fluidization transition.

8.3 The Critical Point

The Chaps. 6 and 7 led independently to the theoretical prediction of a critical point in dense wet granular matter. Above a critical density a transition in the capillary network has been observed in simulations of freely cooling wet granular matter in agreement with an analytical model (Chap. 6). An explicit equation of state for the homogeneously driven steady state of wet granular matter has been derived in Chap. 7, which predicts the existence of a critical point by the onset of a van-der-Waals instability. Both theories predict the critical density ϕ_c to be set by the rupture length of the capillary bridge such that the mean separation, \bar{s} , is below the bond length s_{crit} : the one-dimensional free cooling shows $\bar{s} \approx s_{crit}/3$ for the critical density. The equation of state predicts $\bar{s} \approx s_{crit}/4$ for the critical point (in two dimensions). The critical temperature T_c is predicted to be closely equal to $E_{cb}/4$ in both cases, the free cooling and the steady state. Free cooling simulations below the critical density (monotonic) and above the critical density (with the unclustering peak) are shown in Fig. 8.7A. The panel B shows simulations which take in addition to the Minimal Capillary Model a restitution coefficient into account. The theoretical spinodal, derived from the equation of state in Chap. 7, is shown in Fig. 8.7C. This section reports the experimental observation of the critical point in wet granular matter.

8.3.1 The Critical Density

The critical density has been theoretically predicted to be set by the rupture length of the capillary bridge, s_{crit} , which is the natural length scale of the capillary interaction (cf. Fig. 8.7). In order to detect the critical point one can gradually increase the density ϕ , while scanning through the granular temperature T , until the segregation transition is observed. With the

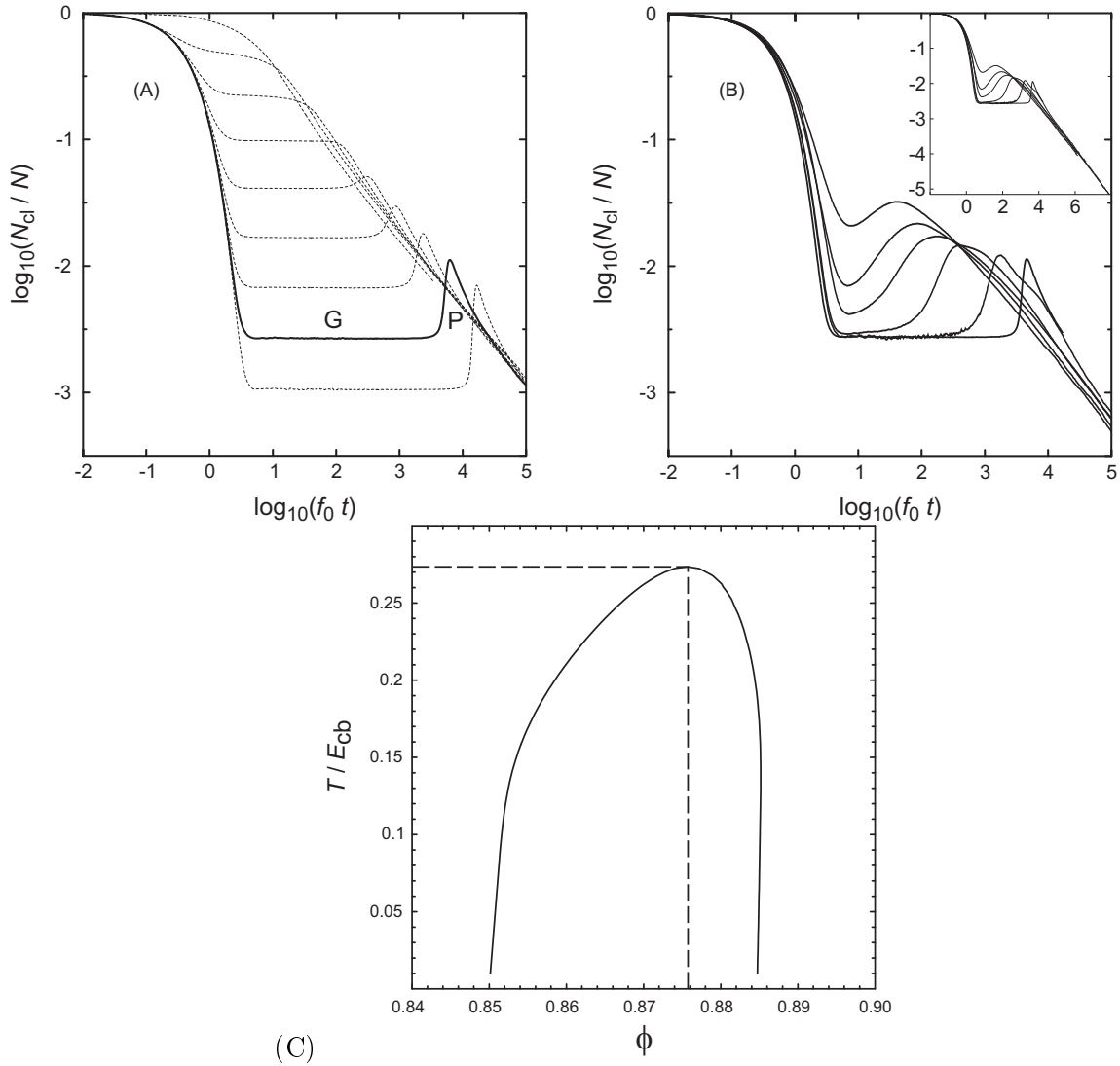


Figure 8.7: Theoretical predictions for the existence of a critical point. (A) The free-cooling simulation of 10^7 particles in one dimension presented in Chap. 6. The experimental findings shown in the Figs. 8.8 and 8.9 can be directly compared with the unclustering transition observed in the free-cooling simulation. In the initial state of the simulation all particles were separated. After few collisions per particle, the system reaches the plateau G at high temperature in complete analogy to the plateau found in the experiment. Here the capillary network depends only on density. The dashed lines show simulation runs with different densities. The denser the system the deeper is the plateau level. As the temperature comes close to $T_c \approx E_{cb}/4$, granular droplets were observed to precipitate out of the hot and homogeneous state G. The peak value at P gives the number of granular droplets N_{cl} over the particle number N . This segregation effect sets in only after a critical density has been exceeded, as we find in the experiment. In one dimension and under the cooling dynamics, the transition set in when the system was dense enough to have $\bar{s} < s_{crit}/3$. (B) Free cooling simulation with a restitution coefficient ϵ_{pp} for inelastic particle collisions. The peak is shifted to earlier times because the cooling process is accelerated by the additional dissipative mechanism. ϵ_{pp} assumes the values 1.0, 0.999, 0.99, 0.95, 0.90, and 0.80. The apparent broadening of the peak is due to the logarithmic time scale. (C) The theoretically predicted spinodal for wet granular matter in two dimensions, as derived in Chap. 7. In order to compare systems of different dimensionalities, the critical density has to be expressed in terms of the mean particle separation. The theoretical prediction is $\bar{s} \approx s_{crit}/4$, with a minor dependence on the capillary energy (cf. Chap. 7, Fig. 7.15).

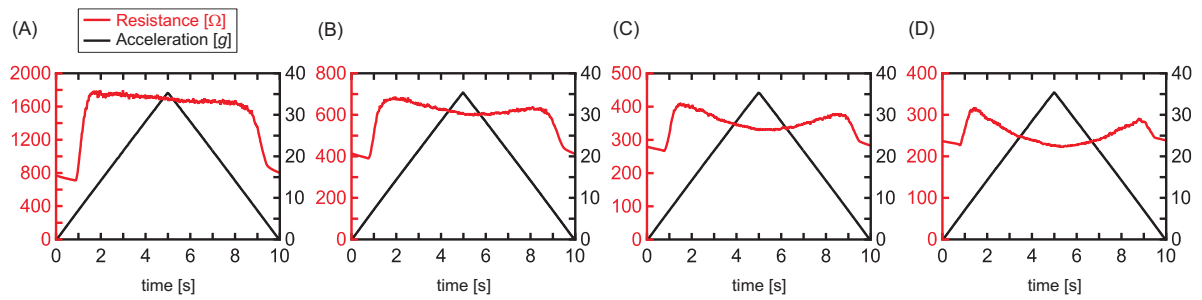


Figure 8.8: Measurement of the critical density. The granular temperature is varied in each measurement (A) to (D). The density can be equivalently expressed as the mean particle separation \bar{s} . Below the critical density, \bar{s} is longer than a certain fraction of the capillary bond length denoted by s_{crit} . The system is isochoric, such that \bar{s} is kept fixed. As we increase the liquid content from (A) to (D) – and therewith the maximal bond length s_{crit} – we find that at $s_{\text{crit}}/\bar{s} \approx 4$, between the cases (A) and (B), a peak develops. This is the critical point. The density is sufficiently high so that the range of the capillary interaction can cause a density instability. Yet this is only possible if the capillary bridge energy is not exceeded by the granular temperature T . At strong driving (around the time stamp $t = 5$ s), the granular particles move randomly. The particles remain instantaneously connected by the elongated bridges. This ‘passive’ capillary network causes the observed reduction of the resistance, visible as the plateau in the center of each measurement. As the driving amplitude is reduced, the granular temperature T is also reduced. When T comes close to the capillary bridge energy E_{cb} , granular droplets precipitate out of the dense granular gas, as has been predicted theoretically in Chap. 6. Between the dense droplets voids remain, which increase the resistance and cause the observed peak in $R(\Gamma)$.

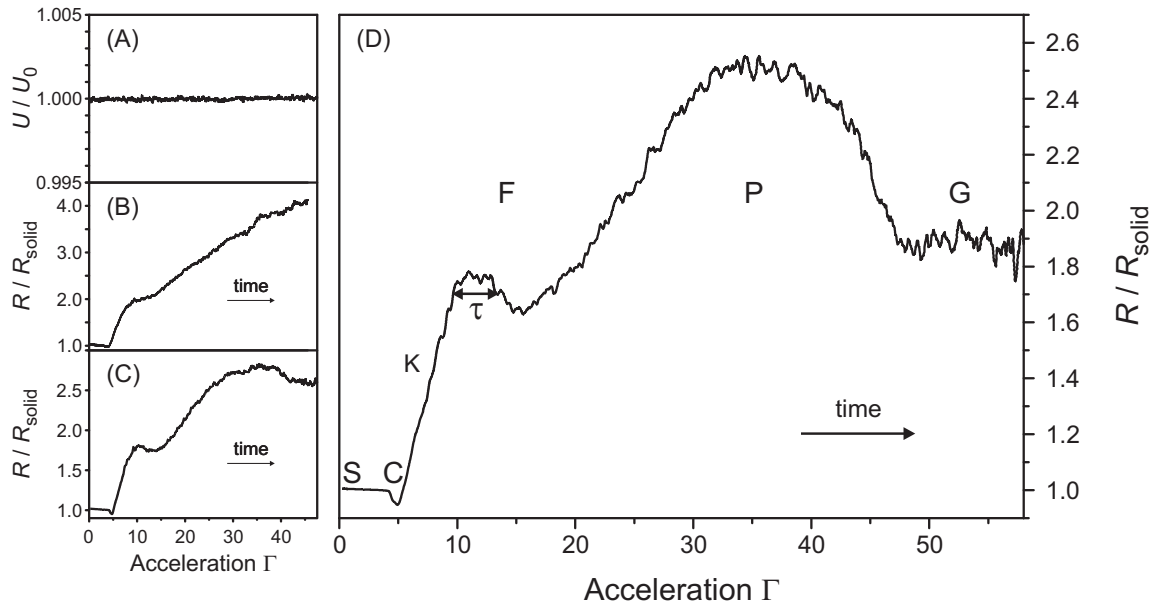


Figure 8.9: Measurement of the critical density at higher frequency. (A) In the perfectly dry system, there is no measurable resistance, the voltage drop at the cell equals the source with subpercent precisions and with a series resistance of $1 \text{ M}\Omega$. Hence $R \gg 100 \text{ M}\Omega$. (B) After $40 \mu\text{l}$ of wetting and conductive solution has been added and mixed, the solid/fluid transition becomes clearly visible. This corresponds to a liquid fraction $W = 0.33\%$ with respect to the jamming volume of the sample. Beyond the fluidization, the resistance increases as the connectivity of the capillary network decreases towards the random state at high granular temperature. This shows that we are still below the critical point. (C) With $60 \mu\text{l}$ liquid ($W = 0.49\%$), we observe the first appearance of the segregation peak P. At $80 \mu\text{l}$ ($W = 0.66\%$), the peak P is fully developed as shown in the main panel (D). The higher bond energy and the higher driving frequency ($f_{\text{shaker}} = 200 \text{ Hz}$ as compared to 100 Hz in Fig. 8.8) lead to a clear separation of the fluidization edge K and the segregation peak P. The homogeneous state G is characterized by a plateau of the resistance. The value of the plateau only depends on the geometric ratio between mean particle separation and maximal capillary bridge length, s_{crit}/\bar{s} , and is independent of the granular temperature T because the capillary bonds have no influence on granular dynamics. This homogeneous state G is not a gas in the sense of a dilute system, since the density is constant throughout the experiment. Rather, G is energetically a gas state with $T \gg T_c > E_{\text{cb}}$. With the homogeneous distribution of particles, we have a highly linked dynamical network of capillary bonds which facilitate the reduction in resistance. At the critical temperature, $T = T_c \approx E_{\text{cb}}/4$, dense granular droplets precipitate out of the homogeneous state Chap. 6 due to a mechanical instability, similar as described by the equation of state for the stationary state in Chap. 7. The voids which open up in-between the droplets, give rise to the pronounced peak P of the resistances. In the denser system shown before in Fig. 8.8 the segregation peak P closely coincided with the fluidization edge K for two reasons. First, the capillary bridges are shorter at the critical point and have therefore less bond energy. Secondly, the segregation peak is shifted to lower Γ because of the lower driving frequency at 100 Hz .

increase of density ϕ , the mean particle separation

$$\bar{s} = 2R \left(\sqrt[3]{\frac{\phi_J}{\phi}} - 1 \right) \quad (8.13)$$

is reduced. The segregation transition is predicted to set in when \bar{s} is below s_{crit} . Equivalently, one can perform the experiment with the increase of s_{crit} by increasing the liquid volume, while keeping density ϕ fixed. Since the liquid content can be controlled very precisely within an isochoric cell, we have conducted the experiment in the latter way: the mean separation is fixed with $\bar{s} = 10.6 \mu\text{m}$ (for the denser system at $\phi = 0.939\phi_J$) and $\bar{s} = 13.55 \mu\text{m}$ (for the less dense system at $\phi = 0.939\phi_J$), while s_{crit} is increased.

We observe the onset of the peak shortly before $60 \mu\text{l}$ wetting solution has been added in the latter system (cf. the panels (B) and (C) in Fig. 8.9 where the peak develops). Since the jammed volume of the sample is $V_{\text{sys}} = 12.18 \text{ ml}$, the liquid fraction is $W = 0.49\%$ with respect to the solid state at ϕ_J . For complete wetting (zero contact angle) this yields a rupture distance (cf. Eq. (8) in [114])

$$s_{\text{crit}} = 1.31 W^{1/3} R = 0.223 R = 55.7 \mu\text{m} . \quad (8.14)$$

Hence we can report the experimental finding:

$$\frac{s_{\text{crit}}}{\bar{s}} = 4.1 \pm 0.1 . \quad (8.15)$$

The uncertainty in this result is due to the theoretical formula (8.14), applied to the present dynamical conditions. In the denser system with $\phi = 0.939\phi_J$, the mean particle separation is $\bar{s} = 10.6 \mu\text{m}$, and we find the peak shortly before the liquid content has reached $W = 0.29\%$, as shown in Fig. 8.8. This amount of wetting liquid corresponds to $s_{\text{crit}} = 46.9 \mu\text{m}$, so that here we find from Fig. 8.8A and B in concordance: $3.1 < \frac{s_{\text{crit}}}{\bar{s}} < 4.4$.

The last run shown in Fig. 8.8D is for higher liquid content, $W = 1.64\%$. Here we see that the dynamical capillary network has almost reached the conductivity of the solid state. This shows that with the increase of the maximal capillary bond length, s_{crit} , the coordination number has been increased in the dense isochoric system, close to the value $K \approx 6$ even under dynamical conditions.

The finding that the mean particle separation has to be significantly smaller than the rupture length of the capillary bond for the precipitation to set in (as also predicted by the theoretical computations in the Chaps. 6 and 7) is a direct consequence of the *hysteretic* formation and rupture of the capillary bridges. The high ramping speed (5 seconds) in the experiment shown in Fig. 8.8 can be regarded as to mimic the free cooling state of Chap. 6.

8.3.2 The Critical Temperature

In this section we compare the critical temperature T_c for the segregation transition (shortly below the critical point) with the bond energy E_{cb} of a capillary bridge.

While the capillary force weakly depends on the liquid content W , the capillary energy is proportional to $E_{\text{cb}} \propto \sqrt{W}$ [237]. In the denser system, $\phi = 0.939\phi_J$, the capillary bridge is shorter at the critical point, as compared to the system at $\phi = 0.923\phi_J$. With this lower energy $E_{\text{cb}} \approx 2 \text{ nJ}$, the segregation peak almost coincided with the fluidization edge (cf. Fig. 8.8). In the less dense system the capillary bridge is longer at the critical point, which increases the capillary energy to 3.7 nJ .

The onset of fluidization at Γ_{SF} and the solidification at Γ_{FS} , depend on the acceleration of the driving. In contrast, the cluster segregation is predicted by the preceding theories

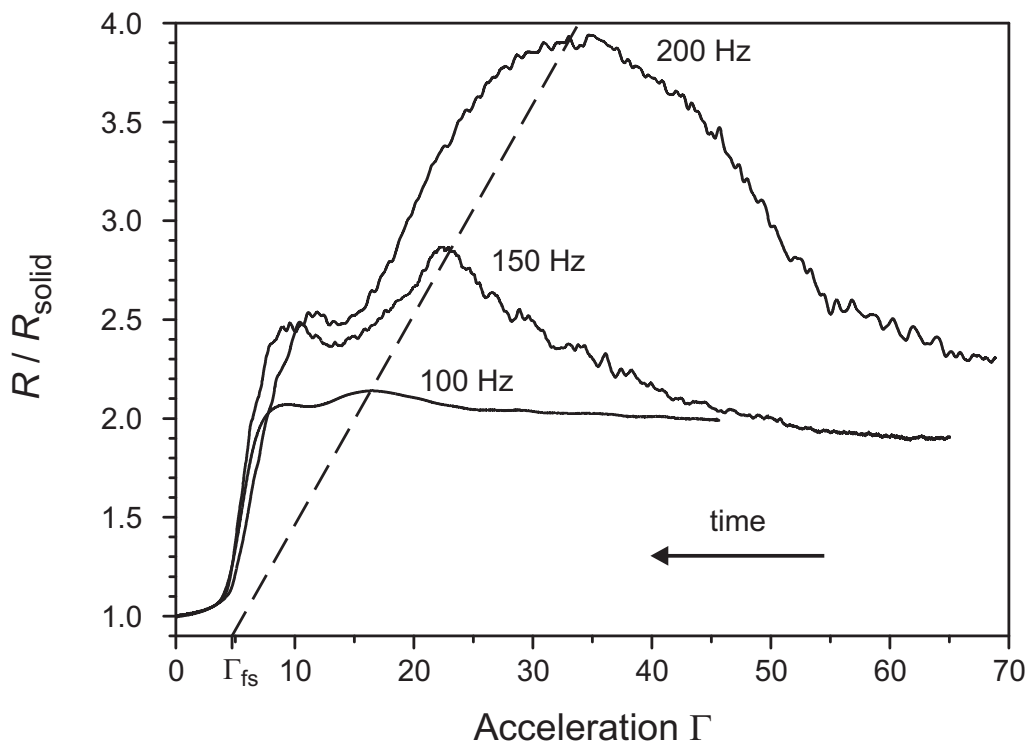


Figure 8.10: Direct measurement of the unclustering peak. The segregation of granular droplets give rise to the increase in R . The solidification point, Γ_{FS} , is independent of the driving frequency because the fluid/solid transition is determined by the *force* of the capillary network. In clear contrast, the peak of the segregation transition is shifted (dashed line) with the driving frequency. The full data set in Fig. 8.11 shows that this transition is determined by a *critical granular temperature*, $T_c \approx E_{cb}/4$, as predicted by the theories in the Chaps. 6 and 7. These measurements have been taken with $100 \mu\text{l}$ of solution, which is equal to the liquid fraction $W = 0.82\%$. Note that the dashed line goes to zero at solidification, since this is the point where T vanishes.

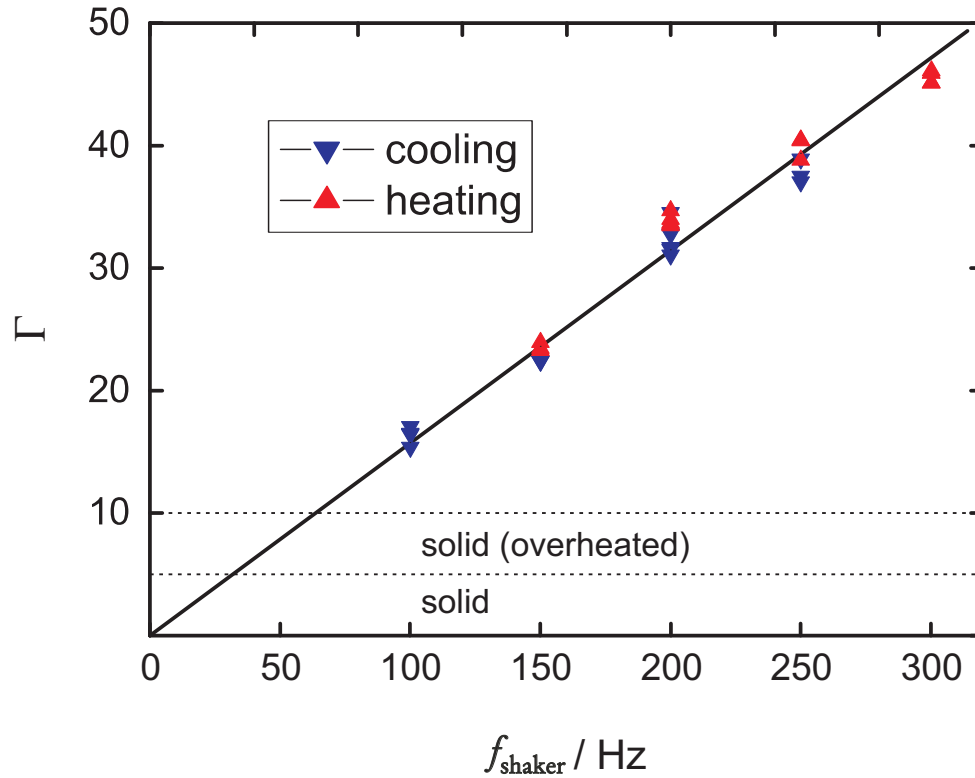


Figure 8.11: The location of the segregation (unclustering) transition as a function of the driving frequency. As we have shown, the solid/fluid transition sets in at a critical acceleration Γ_{crit} . In contrast, the peak of the segregation transition is not determined by acceleration (vertical axis). All data fall on a line through the origin, so that the segregation transition is determined by a critical *velocity* of the driving: $\Gamma = v_{\text{crit}}\omega/g = (2\pi v_{\text{crit}}/g)f_{\text{shaker}}$, with constant v_{crit} . The energy corresponding to this driving velocity is $E_{\text{drive}} = v_{\text{crit}}^2 m/2 = 15.24 \pm 0.40$ nJ, when multiplied with the particle mass m . This is the critical energy associated with the boundary motion in the vertical direction of shaking. This corresponds to a boundary temperature $T_{\text{max}} = \varepsilon_{\text{pw}}^2 m \langle v_{\text{drive}}^2 \rangle / 3 = \varepsilon_{\text{pw}} m \langle v_{\text{crit}}^2 \rangle / 6 = 3.67$ nJ. The granular temperature inside the cell follows from the granular heat equation, and has a mean temperature between 0.75 nJ and 1.45 nJ. The capillary bridge energy is $E_{\text{cb}} = 3.27$ nJ for this liquid content. Hence $2.25 < E_{\text{cb}}/T_{\text{crit}} < 4.39$, of which the upper bound is the better estimate.

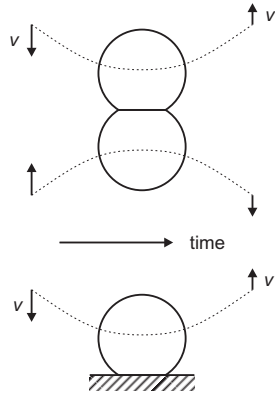


Figure 8.12: While a direct measurement of the restitution coefficient in particle-particle collisions is not feasible, it is easily measured using the symmetry of the interaction. In the center-of-mass system of the colliding pair, the second particle can be replaced by a hard flat wall of infinite mass. In such a way the restitution coefficient ε for particle-particle collisions is easily measured

presented in this thesis to be determined by energy, not by the driving force. The energy scale, expressed by the granular temperature T , is proportional to the squared velocity of the driving. We therefore expect the peak of the cluster segregation to be determined by the driving velocity. The driving velocity is linear in f_{shaker} , whereas the acceleration is quadratic in f_{shaker} : $\Gamma = 4\pi A f_{\text{shaker}}^2 / g$. Increasing the driving frequency yields a higher granular temperature for the same acceleration. Figure (8.10) demonstrates that the segregation peak is indeed shifted by the increase of the capillary energy and can be further shifted by the driving frequency. This shows that the segregation transition is determined by energy, while the fluidization transition is determined by force.

We aim to quantify the critical energy in terms of the critical ‘granular temperature’ T_c for the segregation transition. Figure 8.11 shows the acceleration Γ_{peak} at which the cluster segregation is observed for different frequencies. The data follow a straight line through the origin which shows that

$$\Gamma_{\text{peak}} = A\omega^2/g = (A\omega)\omega/g = 2\pi v_{\text{shaker}} f_{\text{shaker}} \quad (8.16)$$

defines the critical velocity of the driving, v_{shaker} .

As has been shown in Sec. 8.2, the solid/fluid transition is increased as compared to the fluid/solid transition due to compactification. At 100 Hz the fluidization threshold for the solid/fluid transition comes very close to the peak of the segregation transition. The overlay with the fluidization edge spuriously shifts the peak to higher accelerations. For this reason Fig. (8.11) does not include a ‘heating’ run at 100 Hz.

Now that we have measured the critical velocity of the driving v_{shaker} , we wish to relate the driving velocity to the granular temperature, so that we arrive at the critical granular temperature, T_c . This is accomplished in the following.

Computation of the Granular Temperature in the Cell

Since in the experimental systems the mean particle separation is below the rupture length of the capillary bonds, we can focus on the inelasticity described by the restitution coefficient ε . The direct measurement of the restitution coefficient for particle-particle collisions is not

feasible, because it is extremely difficult to control the impact parameter $b \ll R = 250 \mu\text{m}$ at such small length scales. Fortunately this is not necessary. Due to symmetry, the deformation of a head-on particle-particle collision causes a flat deformation of the particles as sketched in Fig. 8.12. The very same inelastic dynamics can therefore be achieved with a hard flat wall. The experimental result is $\varepsilon_{\text{pp}} = 0.96$ for the particle-particle restitution, and $\varepsilon_{\text{pw}} = 0.85$ for the particle-electrode collisions.

The motion of the electrodes defines the boundary value of the ‘granular temperature’ T_{G} . We derive the boundary temperature as function of the driving frequency and acceleration. The granular temperature is defined by the mean squared velocity vector \mathbf{v} , according to

$$T = \frac{m}{3} \langle \mathbf{v}^2 \rangle . \quad (8.17)$$

This definition of the granular temperature is analogous to the temperature of a molecular gas, where the particle mass m is the mass of the granular particles. While the particle motion in the bulk is chaotic, the boundary motion is neither isotropic nor stochastic, but vertical and periodic with amplitude A and frequency $\omega = 2\pi f_{\text{drive}}$:

$$\mathbf{v}(t) = \mathbf{e}_z A_0 \omega \sin(\omega t) . \quad (8.18)$$

In collisions with the boundaries, momentum is exchanged normal to the boundary surface, such that the boundary motion feeds energy into the normal direction, \mathbf{n} , with $\mathbf{n} \cdot \mathbf{e}_z = \sin \varphi$. Hence the granular temperature as ‘seen’ from a particle at the boundary is

$$T_{\text{boundary}}(\varphi) = T_{\text{max}} \sin^2 \varphi \text{ with} \quad (8.19)$$

$$T_{\text{max}} = \frac{\varepsilon_{\text{pw}}^2 m g^2 \Gamma_{\text{peak}}^2}{24\pi^2 f_{\text{shaker}}^2} . \quad (8.20)$$

The restitution coefficient ε_{pw} accounts for the inelasticity in the coupling between particle and wall. In this context we remark that the critical driving amplitude $A(t) = A_0 \sin(\omega t)$ is $A_0 = 370 \mu\text{m}$ at 100 Hz and reduces to $A_0 = 110 \mu\text{m}$ at 300 Hz, so that the A_0 is close to but still below the particle size of $500 \mu\text{m}$. In Eq. (8.19), the amplitude has been substituted in favor of the acceleration $\Gamma = A_0 \omega^2 / g$, which is directly measured in the experiment.

From the slope in Fig. 8.11 follows the boundary temperature (8.19) with

$$T_{\text{max}} = 3.67 \text{ nJ} , \quad (8.21)$$

according to (8.20).

The granular temperature in the bulk follows from the granular heat equation solved with the anisotropic Dirichlet boundary condition $T(\varphi) = T_{\text{max}} \sin^2 \varphi$ (8.19), as is done analytically in the Appendix 8.5. The boundary condition (8.19) defines a good lower estimate for the mean temperature \bar{T} . We can furthermore set an upper limit on the mean temperature assuming that the granular temperature is isotropic on the boundary, $T(\varphi) = T_{\text{max}}$. This would be the case if tangential friction would feed energy into the granulate as effective as the normal forces do. As is shown in the appendix 8.5, the isotropic boundary conditions yield $\bar{T} = 0.396 T_{\text{max}}$, while the normal coupling gives $\bar{T} = 0.203 T_{\text{max}}$.

The volume V_{cb} of a capillary bridge is related to the liquid content $W = 0.82\%$ by (Eq. (18) in [114])

$$V_{\text{cb}} = R^3 \tilde{V}_{\text{cb}} = R^3 \frac{8\pi W}{3K_{\text{J}} \phi_{\text{J}}} \approx 0.29 \text{ nl} , \quad (8.22)$$

(which is approx. 16 n mol) with $K_J \approx 6$. Expressed in units of the capillary energy (Eq. (20) in [114] for complete wetting, $\theta = 0$)

$$E_{cb} \approx 5.5 \sqrt{\tilde{V}_{cb} \gamma R^2} \approx 3.27 \text{ nJ} , \quad (8.23)$$

we can put the following bounds on the mean granular temperature at the critical point:

$$\frac{E_{cb}}{4.4} < T_c < \frac{E_{cb}}{2.25} . \quad (8.24)$$

Since the tangential coupling is not expected to be as effective as the normal coupling, the critical granular temperature is closer to the lower bound on the left-hand side of (8.24). This experimental result on the critical behavior of the three-dimensional wet granular system noticeably agrees with the theoretical predictions $T_c \approx E_{cb}/4$ which were given for one (cf. Chap. 6) and two (cf. Chap. 7) dimensions.

Schematic Representation of Nonequilibrium States

Before we conclude, a schematic overview of the nonequilibrium states observed in wet granular matter as the external driving is increased and decreased again, is provided in Fig. 8.13. This depiction reemphasizes that in the isochoric system the resistance R (measured in the experiment) and the number of clusters N_{cl} (determined in the simulation) are monotonically related. This is why we the peak in the experiment (shown in Fig. 8.9) is the direct observation of the theoretically predicted unclustering transition, as shown in Fig. 8.7 and derived Chap. 6.

8.4 Conclusions

We have demonstrated experimentally that the conductivity allows to determine the state of wet granular matter and its internal capillary network. With the conductivity as an order parameter, the hysteretic solid/fluid transition could be measured in the bulk. This method allows, to the authors knowledge, the most precise observation of the fluidization transition. The fluctuation in the capillary network have been theoretically related to the granular temperature. Therefore the method enables the measurement of the mean connectivity in the bulk structure and the granular temperature in real-time. The fluidization was demonstrated experimentally to be a discontinuous nonequilibrium phase transition. Most significant in conjunction with the analytical predictions of a critical point for wet granular matter in the preceding Chaps. 6 and 7, is the experimental observation of this segregation transition as predicted. The values for the critical density and the critical temperature have been determined experimentally. The critical point was shown to be set by the capillary bridge length and the capillary bridge energy, confirming the preceding theoretical predictions quantitatively.

8.5 Appendix A: Analytic Solution of the Granular Heat Equation

The granular heat current

$$\mathbf{q} = -\kappa \nabla T - \mu \nabla n \quad (8.25)$$

has been derived for dilute (cf. [27] and references therein) and dense systems (Eq. (37) in [92]). The latter case is relevant to the present experimental system, since $\phi/\phi_J = 0.92$ is

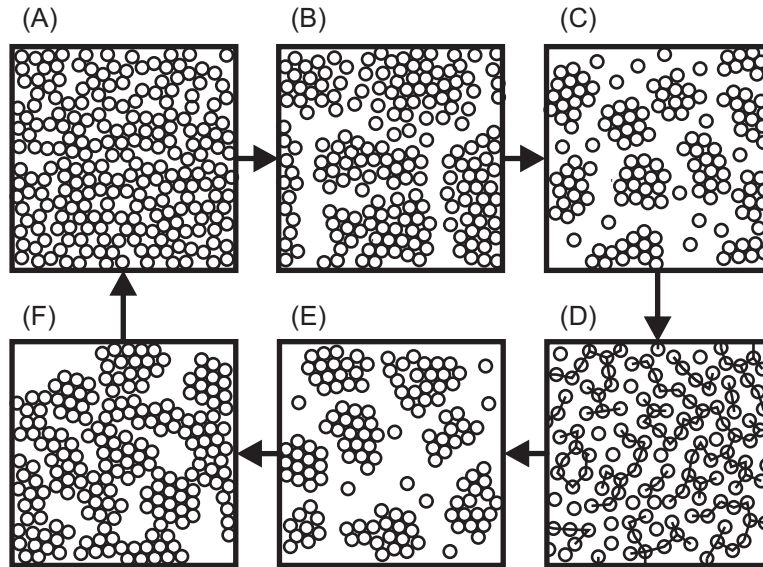


Figure 8.13: A highly simplified two-dimensional illustration of the states observed in wet granular matter. (A) The capillary network, made of liquid bridges between adjacent and close-by spheres, endues the solid state with rigidity against shear forces. (B) At the critical acceleration $\Gamma_{\text{SF}} \approx 9$ of the agitation, the network fractures with the breaking of capillary bonds along the local shear plains. For this reason the resistance instantly increases by almost a factor of three. This fracture is directly associated with the capillary bridge force, $F_{\text{cb}} = 2\pi\gamma R$, and the coordination number K of capillary bonds per sphere. The capillary network increases the critical acceleration $\Gamma_{\text{SF}} = \Gamma_{\text{dry}} + \Delta\Gamma$ as compared to the dry system. The increase $\Delta\Gamma \propto K\gamma$ of the acceleration is therefore proportional to the surface tension of the wetting liquid and the coordination number K . In the excited state of wet granular matter, the mean coordination number K is observable as the global resistance R , which is approximately inversely proportional to K . (D) When the granular temperature T is far above the capillary energy, $T \gg E_{\text{cb}}$ we have a homogeneous hard sphere fluid. This is a gas state (denoted by G in Fig. 8.9) in terms of the granular energy. The dense wet granular system has a dynamical capillary network of high connectivity in the state G, which lowers the resistance. At 94% of the jamming density and a liquid fraction $W = 1.6\%$, the resistance is as low as in the solid state, which indicates $K_{\text{G}} \approx 6$. With more wetting liquid even $K > 6$ is possible in this state. The theoretical maximum of Voronoï neighbors is approximately 15.5 in an ideal gas, and the kissing number is well-known to be 12 in the crystal state. Both values are never realized in a real system, because the capillary bridges are much shorter than the mean separation in the dilute ideal gas, and ordering is effectively prevented by the geometric frustration and the capillary network even for a monodisperse system. The homogeneous state shown in the panel (D) breaks up into dense granular droplets under the capillary attraction at the critical granular temperature $T = T_{\text{c}}$ as shown in (C) and (E). Because of the voids remaining between the droplets, the global resistance has a peak (denoted by P in Fig. 8.9) at this precipitation transition. The location of the peak, Γ_{P} , is linear in the driving frequency and the bond energy E_{cb} . (F) As the driving is further decreased, the granular system collapses in the solid state at $\Gamma_{\text{FS}} \approx 5$. Annealing eliminates inhomogeneities and leads to the more rigid configuration (A) as discussed in Sec. 8.2.2.

not small but close to unity. Heat transport due to density gradients, as described by the second term in (8.25), is a peculiarity caused by inelastic collisions. Since $\varepsilon_{\text{pp}} = 0.96$ in the experimental system, the second term is suppressed by more than one order of magnitude as compared to the first term (cf. the Figs. 1 and 4 in [92]). We can therefore neglect it, which allows for an analytic solution of the isochoric heat equation. The heat conductivity $\kappa(\varepsilon_{\text{pp}}, T) = \tilde{\kappa}(\varepsilon_{\text{pp}})\sqrt{T}$ depends on the particle restitution coefficient ε_{pp} and is proportional to the square root of the granular temperature. We can shift the temperature dependence to the right of the differentiation,

$$\mathbf{q} = -\frac{2}{3}\tilde{\kappa}\nabla T^{3/2}, \quad (8.26)$$

so that the stationary heat equation

$$\begin{aligned} 0 &= \text{div } \mathbf{q} + P_{\text{diss}} \\ &= -\frac{2}{3}\tilde{\kappa}\Delta T^{3/2} + P_{\text{diss}}, \end{aligned} \quad (8.27)$$

has the Laplace operator acting on the field $T^{3/2}$. The dissipation P_{diss} is derived easily. In each collision the normal component of the particle velocity is reduced by ε_{pp} . The initial kinetic energy of the normal velocity is $T/2$, so that the energy loss per particle is $T(1 - \varepsilon_{\text{pp}}^2)/2$ in each collision event. Multiplying with the particle density n and the particle collision frequency ν_{E} , we arrive at the dissipation power per volume element,

$$P_{\text{diss}} = \nu_{\text{E}} n T \frac{1 - \varepsilon_{\text{pp}}^2}{2}. \quad (8.28)$$

The particle density n and packing fraction are related by $\phi = \frac{\pi}{6} n d^3$. The Enskog collision frequency is

$$\nu_{\text{E}} = 2^D D g \phi \frac{v_{\text{th}}}{d}, \quad (8.29)$$

with the thermal velocity $v_{\text{th}} = \sqrt{\frac{T}{\pi m}}$. The contact correlation g rapidly grows with density. In the experimental system ($D = 3$, $\phi_{\text{J}} = 0.62$) we have (according to Chap. 7)

$$g = \frac{D}{2^{D-1}(\phi_{\text{J}} - \phi)} = 15.7. \quad (8.30)$$

From the Eqs. (8.29) and (8.28) we see that the energy sink P_{diss} in the heat equation (8.27) is proportional to $T^{3/2}$, as is well known [102]. Hence, the heat equation turns into a Helmholtz equation for $T^{3/2}$:

$$\left(\Delta - \frac{1}{\lambda^2}\right) T^{3/2} = 0, \quad (8.31)$$

with the intrinsic length scale $\lambda(n, \varepsilon_{\text{pp}})$,

$$\frac{1}{\lambda^2} = \frac{3}{4} \frac{\nu_{\text{E}}}{\kappa} n (1 - \varepsilon_{\text{pp}}^2), \quad (8.32)$$

which is independent of the granular temperature. The heat conductivity κ is altered by inelasticity [92]), $\varepsilon_{\text{pp}} < 1$,

$$\kappa = \kappa^*(g\phi, \varepsilon_{\text{pp}}) \kappa_{\text{E}}, \quad (8.33)$$

as compared to the equilibrium Enskog value κ_E , which is

$$\kappa_E = N \frac{v_{\text{th}}}{d^{D-1}g}, \quad (8.34)$$

with $N = 2$ in $D = 2$ and $N = 75/64$ in $D = 3$ dimensions. The effect of inelasticity (and excluded volume) is captured in the dimensionless factor κ^* of Eq. (8.33), which is for the three-dimensional experimental system (cf. Table 1 in [92]) equal to

$$\kappa^* = \frac{(1 + \frac{6}{5} g\phi (1 + \varepsilon_{\text{pp}}))}{\frac{1}{2}(1 + \varepsilon_{\text{pp}}) - \frac{7}{32}(1 - \varepsilon_{\text{pp}}^2)} + \frac{256}{25\pi} (g\phi)^2 (1 + \varepsilon_{\text{pp}}) \approx 539. \quad (8.35)$$

This yields for the length scale (8.32) of heat transport

$$\lambda = 3.41R = 852 \mu\text{m}. \quad (8.36)$$

The distribution of granular temperature arising according to the heat equation (8.31) and the boundary conditions leads to a mean granular temperature $\bar{T}(\lambda)$ in the system depending on the known heat penetration depth λ (8.36). We consider two limiting cases. The Dirichlet boundary condition (8.19), $T(\varphi) = T_{\text{max}} \sin^2(\varphi)$, allows for normal coupling between the boundary motion and the granular particles. This is regarded as the lower estimate of the granular temperature. Equally strong coupling of the granular motion to normal ($\propto \sin^2 \varphi$) and tangential ($\propto \cos^2 \varphi$) boundary motion defines a constant boundary temperature $T(\varphi) = T_{\text{max}}$, which provides us with an upper limit of \bar{T} . The analytic solution of the heat equation (8.31) in the cylindrical geometry is

$$T(r, \varphi) = T_{\text{max}} \left[\sum_{j=0}^{\infty} c_j \cos(2j\varphi) (A_j I_{2j}(r/\lambda) + B_j K_{2j}(r/\lambda)) \right]^{2/3} \quad (8.37)$$

$$\begin{aligned} \text{with } A_j &= (K_{2j}(R_1/\lambda) - K_{2j}(R_2/\lambda)) / N_j \\ B_j &= (I_{2j}(R_2/\lambda) - I_{2j}(R_1/\lambda)) / N_j \\ N_j &= I_{2j}(R_2/\lambda) K_{2j}(R_1/\lambda) - I_{2j}(R_1/\lambda) K_{2j}(R_2/\lambda). \end{aligned}$$

I and K are the modified Bessel functions of the first and second kind. The radii of the inner and outer electrode are $R_1 = 2$ mm and $R_2 = 8$ mm respectively. For the isotropic boundary condition there is only the zero term, ($c_0 = 1$, all other zero) in Eq. (8.37), while for the boundary condition with normal coupling (8.19), the coefficients are $c_0 = \frac{4}{3\pi}$ and $c_j = 24/(9 - 40j^2 + 16j^4)$ for $j > 1$. These solutions are plotted in Fig. 8.14. The resulting mean temperature is

$$\bar{T} = \begin{cases} 0.203 T_{\text{max}} & \text{for normal coupling only} \\ 0.396 T_{\text{max}} & \text{for normal and tangential coupling} \end{cases}, \quad (8.38)$$

in units of the ‘hottest’ location on the boundary,

$$T_{\text{max}} = \frac{\varepsilon_{\text{pw}}^2 m g^2 \Gamma_{\text{drive}}^2}{24\pi^2 f_{\text{drive}}^2}. \quad (8.39)$$

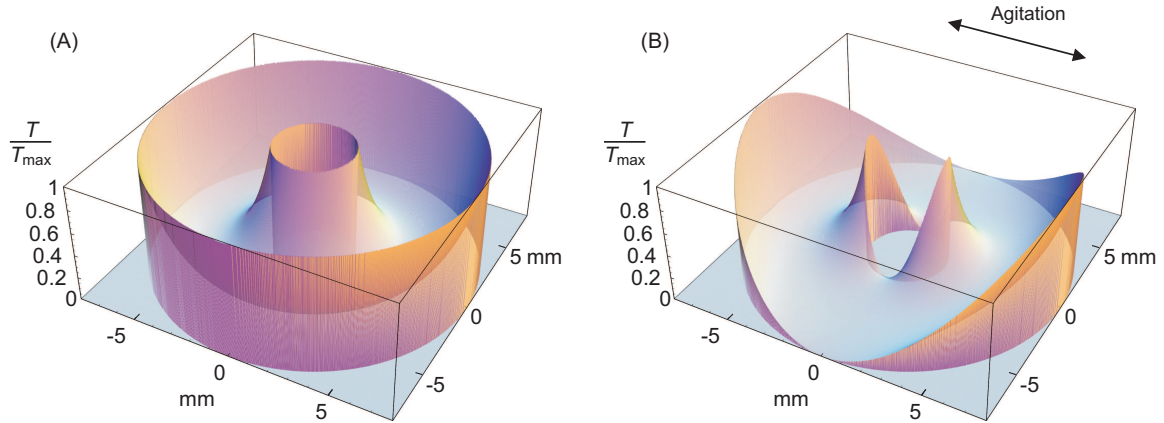


Figure 8.14: The solutions (8.37) of the heat equation (8.31). (A) Result for isotropic boundary conditions, which hold if the tangential coupling between granular motion and boundary motion is equal to the normal coupling. This provides us with an upper limit for the granular temperature. The radial section of this temperature profile is shown in Fig. 8.15A. (B) The lower limit and better estimate of the granular temperature follows from boundary conditions which assume perfectly flat surfaces, so that only the normal component of the boundary velocity drives the granular material.

8.6 Appendix B: Experimental Cross-Checks

8.6.1 Exclusion of Artifacts due to the Inelastic Heat Production

Nonequilibrium phase transitions have been clearly observed as changes in the resistance (or equivalently the conductivity) of wet granular matter. In order to compare the conductivity at different driving, we exclude the possibility of artifacts due to the change of the sample temperature. When the granulate enters the fluidized state, the dissipation of inelastic collisions and the ruptures of capillary bridges produces heat which increase the temperature of the sample. Since the ion mobility of the ionic solution is temperature dependent, such a temperature change could affect the measurement of the global conductivity.

The conductivity of the aqueous solution has a maximum at approximately 25 volume percent of the ionic liquid component. The full name of the ionic liquid reads 1-Butyl-3-methylimidazolium tetrafluoroborate (empirical formula $C_8H_{15}BF_4N_2$) and has density 1.1 g/cm^3 at 298 K. On a time scale of a few days, the conductivity of the solution increases significantly when left in contact with the steel granulate, since ferric ions enter the solution.

As is evident from the conductivity of the ionic solution we use in Fig. 8.16, and the measurement of the thermodynamic temperature in the cell, dissipation causes only percent effects, which can be easily corrected from the data.

8.6.2 Exclusion of Gravitational Artifacts

We made sure that the system does not expand under gravity. As mentioned in the introduction, the packing density of the dry randomly jammed state has been measured to be $\phi_J = 0.62$, while the mean density in the closed cell is lower by a factor 0.923: $\phi_{\text{sys}} = 0.57$. This allows for sufficient space for the capillary bridge dynamics. One might therefore think at first glance that the fluidized state would not fill the system volume completely, but leave a gap at the top. If this was the case, the resistance could fall off to the plateau level at high

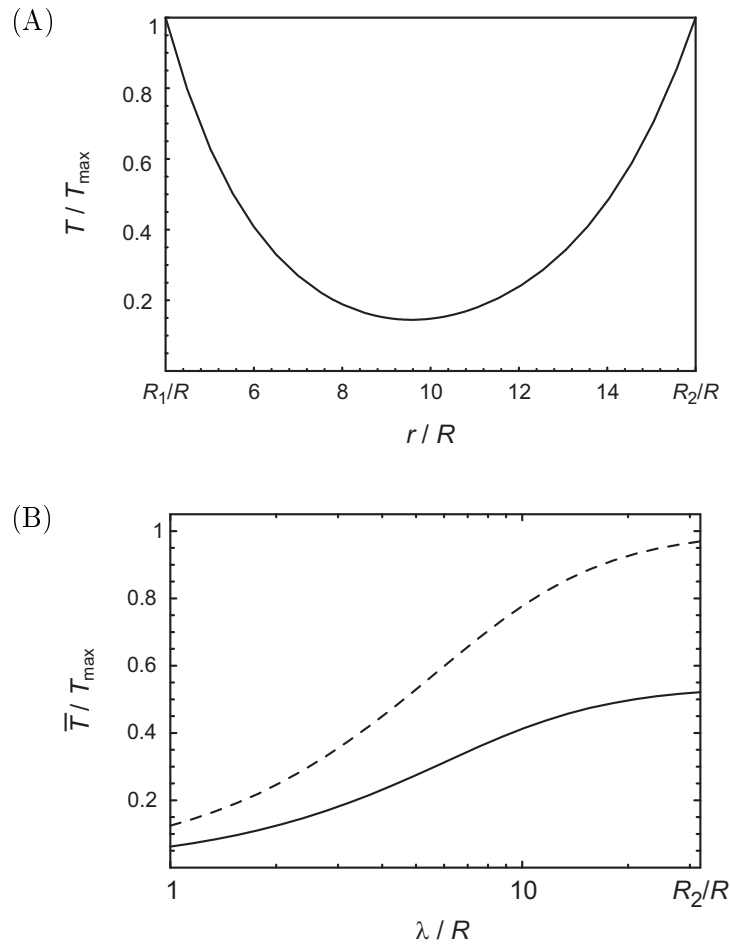


Figure 8.15: (A) Radial section of the granular temperature T for normal and tangential coupling to the driving walls. (B) The mean granular temperature as a function of the penetration depth λ . For full normal and tangential coupling results the dashed line. Due to the flatness of all surfaces in the experiment system the granular motion is expected to follow the normal motion and less closely the tangential motion. For pure normal coupling results the solid line. According to the revised Enskog theory [92] the length scale of penetration is $\lambda = 3.41R = 852 \mu\text{m}$ in the experimental system, for which the temperature profile shown in (A) is the solution (8.37) of the granular heat equation.

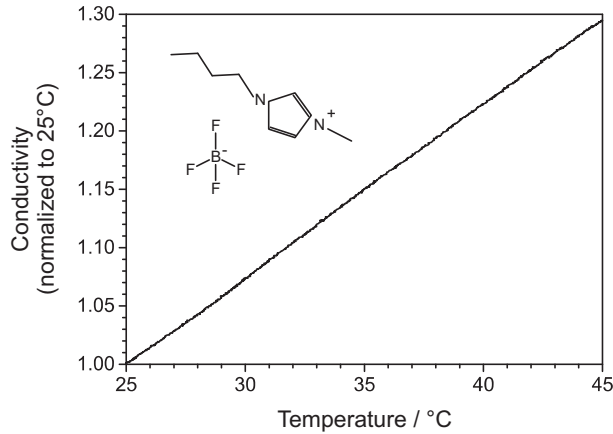


Figure 8.16: The increase of the conductivity of the ionic liquid dissolved in water as a function of temperature. The inset shows the structure formula of the ions. The conductivity of the solution shown here, as well as the conductivity of the wet granular sample, have been measured with AC currents at 1 to 5 kHz.

driving velocities because of a spurious expansion of the granular matter, which would increase the contact area of the granular matter with the outer electrode as the granular temperature is increased. Such an artifact can be excluded based on existing knowledge about wet granular matter, as well as directly with a modification of the experiment. From the theoretical point of view we compare the gravitational force mg of a particle with the capillary force of a bridge, $F_{cb} \approx 2\pi\gamma R$ (cf. Eq. (3.7)),

$$\frac{F_{cb}}{F_g} = \frac{3\gamma}{2\rho g R^2} \approx 22, \quad (8.40)$$

which shows the dominance of the capillary force for the small grains. The capillary forces are actually even more dominant than reflected by the ratio (8.40), because there are $K \approx 6$ bridges per sphere. Moreover, the density of volume-fluidized wet granular matter in an open system is equal or below the density of ‘random loose packing’, which is $\phi = 0.57$ [114]. Therefore the system fills the cell volume completely in the fluidized state, in both experiments at densities $0.923\phi_J$ and even more for $0.939\phi_J$. Ultimately, we masked 30% of the top area of the outer cylindrical electrode with an adhesive foil, so that this section of the electrode does not contribute to the conductivity, independent of the granular state. The segregation peak and the fall-off to the plateau were found unchanged⁴.

⁴Also the position of the segregation peak was found unchanged at frequencies up to 200 Hz. Furthermore, at high frequencies, the acceleration for the segregation grows faster than linear with frequency, due to the viscoelastic damping of the adhesive foil.

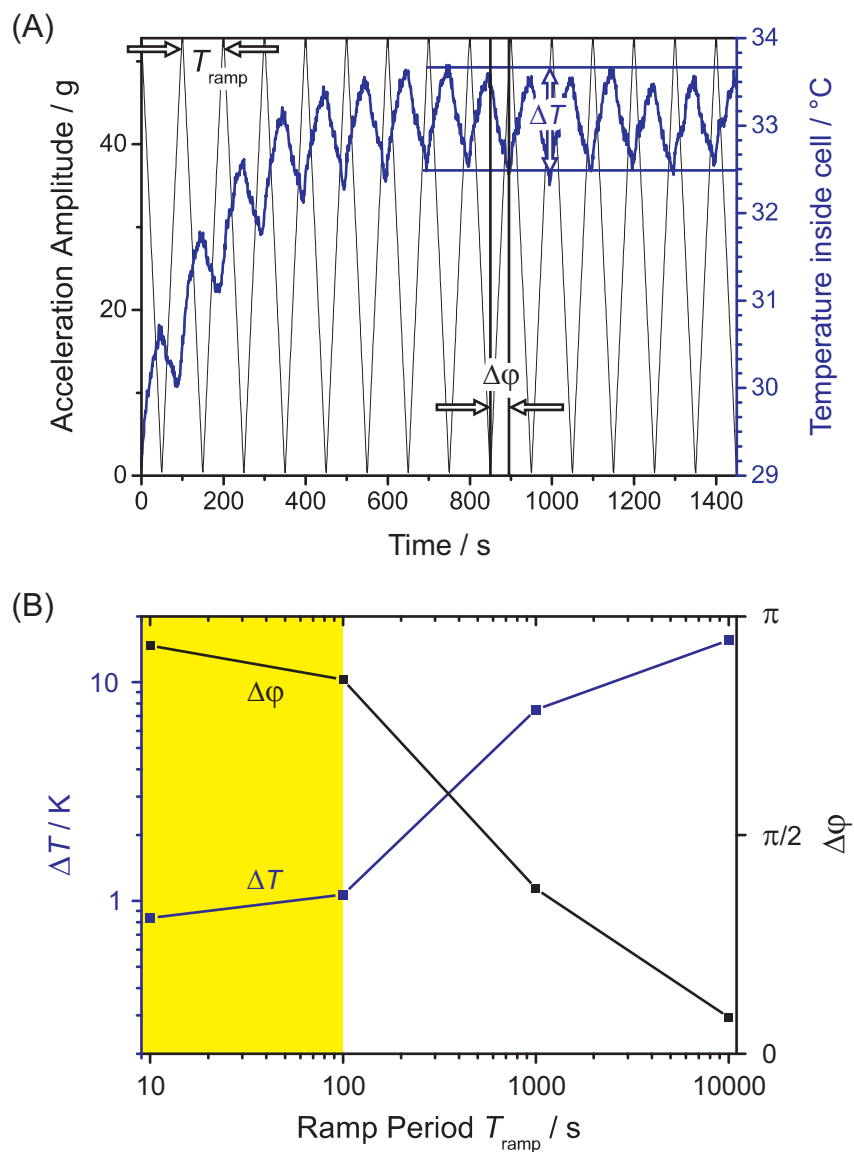


Figure 8.17: (A) Direct measurement of the change in the thermodynamic temperature due to the dissipation in the driven granular system. A platinum sphere, few times the mass of a granular particle, was placed in the cell to measure the thermodynamic temperature during the external driving. (B) Data for the critical point of wet granular matter are only taken in the highlighted region on the left for fast ramping, $T_{\text{ramp}} < 100$ s, where the change in temperature is a percent effect, which can be easily corrected.

Chapter 9

The Velocity Distribution of Granular Matter Measured by the Mössbauer Effect

The particle velocity distribution $P(v)$ is needed in many places, such as Eq. (5.43) in the computation of the Kolmogorov-Sinai entropy. In this chapter, a method to measure the velocity distribution in three-dimensional granular matter is put forward, which is at present absent in the literature. The method is developed theoretically and demonstrated experimentally. The experiment is based on the Mössbauer effect and demonstrated for the gas-like and fluidized state of granular matter. The central idea is that the resolution of nuclear resonance absorption suits perfectly the velocities in ‘granular’ fluids and gases, analogously to the optical Doppler broadening in ‘molecular’ gases. An exponentially shaped velocity distribution is found in the fluidized state. Future measurements that allow to detect the rotation states of particles are discussed.

9.1 The Mössbauer Effect from the Point of View of Granular Physics

Already in the year 1927, Werner Kuhn predicted nuclear resonance absorption, and visited Rutherford in Cambridge to perform experiments, yet with negative result [133]. The physical concept is analogous to (and was historically guided by) the fluorescence of atoms, excited by photons in the visible range. Kuhn suggested to establish the nuclear physics analogue, by replacing the light source by a radioactive source. Not until three decades later, Rudolf L. Mössbauer demonstrated the effect experimentally in 1957 [159]. He was the first to realize that the nuclei, as part of the harmonically bound crystal lattice, can only take up quantized energy and momentum in the creation and annihilation of phonons. The Mössbauer effect has been immediately appreciated as a powerful tool for material analysis and solid state physics, which awarded him the Nobel prize in 1961.

We want to measure the velocity distribution of a granular fluid or gas in the bulk, i.e. away from boundary effects where energy is injected and wall ordering dominates, and in three dimensions. The Doppler broadening of the ‘equilibrium’ gas of atoms points to a way of doing this in granular matter: the idea is to use the Doppler shift to measure velocities. As the speed of light is the reference velocity, high spectral resolution is needed. The speed of gas molecules at room temperature is three orders of magnitude higher than that of a typical granular particle, which can move at speeds of 100 mm/s in the granular gas state. Therefore

we are interested in frequency resolutions of $\Delta\omega/\omega = 10^{-11}$ or better, which correspond to a resolution in velocity space of 3 mm/s. Such resolutions are nowadays possible in the optical range by virtue of the ‘frequency comb’ developed in the group of T.W. Hänsch [223], and would be interesting to apply to a granulate of glass spheres to test the relativistic fluctuation theorem of Chap. 2¹. In contrast to the fluctuation theorem, in this chapter we are not interested in multiple scattering events, which would yield a Gaussian spectrum (according to the central limit theorem). To resolve the single particle velocity, the photon should interact only once with a granular particle. At this point the author appreciated the Mössbauer effect as a favorable method for granular physics, because the photon is absorbed in resonance with the desired spectral resolution ($\Delta\omega/\omega < 10^{-12}$). At present, experiments on the velocity distribution in granular matter use high speed cameras (cf. Chap. 3, [232]), x-ray tomographs [197], positron emission particle tracking (PEPT) [236], and nuclear magnetic resonance (NMR) methods [240]². It is the intention of this chapter to point out the advantages of the well-established Mössbauer effect as a reliable approach to the granular velocity distribution. This method measures velocity directly, while the methods mentioned above determine the particle velocity as the derivative of several position measurements. Aside from correction due to the hyperfine interaction, the Mössbauer spectrum taken from driven granular matter is directly the velocity distribution.

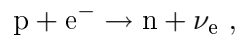
After summarizing briefly the principles of the Mössbauer spectroscopy in Sec. 9.2, the preparation of glass spheres with the Mössbauer isotope enclosed inside the glass is described in Sec. 9.3. The experimental properties of the glass spheres at rest are studied in Sec. 9.4. The effect of the granular motion on the measured spectrum is discussed analytically in Sec. 9.5. The reconstruction of the velocity distribution is derived in Sec. 9.6, where experimental examples are given. The possibility to measure the rotation of the granular particles, as well as the translation-rotation correlation is outlined in Sec. 9.7.

9.2 The Principal Effects for Mössbauer Spectroscopy

9.2.1 The Source of γ -Quanta

Mössbauer photons have to originate from a transition to the ground state, so that these photon can, in turn, be absorbed by a nucleus which is initially in the ground state. A Mössbauer source with ideal properties for the ‘recoilless emission’ of γ quanta is the decay cascade of the unstable isotope ^{57}Co . ^{57}Co decays to ^{57}Fe . These isotopes have been used in the present granular experiment.

^{57}Fe in the ground state can be born out of the ‘common’ ^{56}Fe by the nuclear reaction $^{56}\text{Fe}(\text{d},\text{p})^{57}\text{Fe}$ [47]. As a Mössbauer source providing ^{57}Fe in excited states serves ^{57}Co , which can be produced by the reaction $^{56}\text{Fe}(\text{d},\text{n})^{57}\text{Co}$. The decay scheme of ^{57}Co is shown in Fig. 9.1 with data taken from [195]. The source nucleus decays by K-electron capture (EC), i.e. an electron of principal quantum number $n = 1$ interacts with a proton of the nucleus according to the reaction



¹Such an experiment is suggested in the concluding paragraph of the Relativistic Fluctuation Theorem in Chap. 2.

²The Mössbauer effect had become extremely en vogue in the 1960s, when for instance lunar samples were analyzed. It is tempting to assume that the granular community, rising a generation of scientists later (mainly in the 1990s after the works of Goldhirsch, Jenkins and Haff around 1983, with the notable exception of Bagnold) therefore overlooked this method.

³The traditional notation for nuclear reaction is Target nucleus (Projectile, Ejectile) Final nucleus.

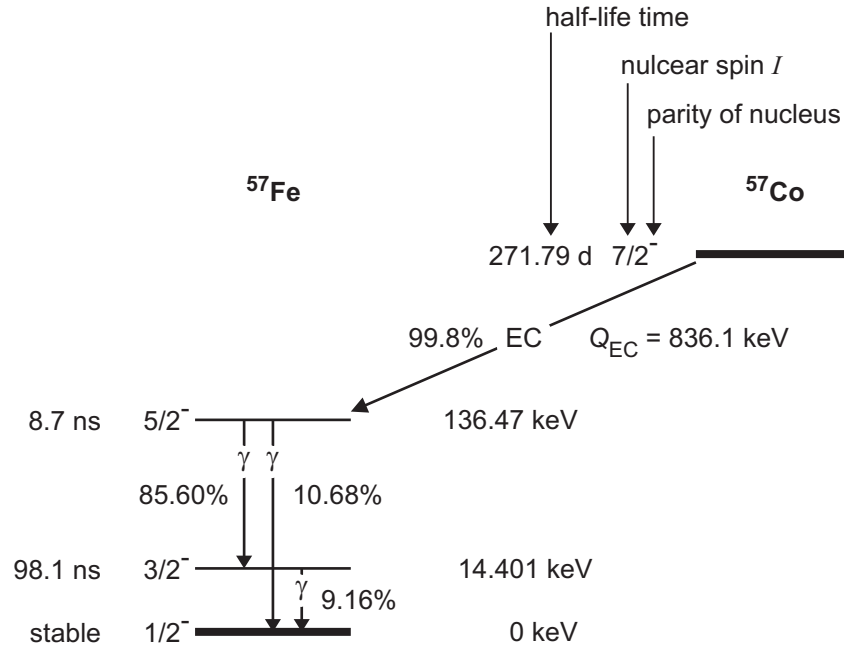


Figure 9.1: The decay of the radionuclide ^{57}Co and the nuclear term scheme of ^{57}Fe . The 14.4 keV photons serve as Mössbauer quanta.

which is the time-reversal of the beta decay. The energy released by this nuclear reaction is taken by the neutrino, while the vacant electronic state in the shell after EC is reoccupied under x-ray emission and the emission of Auger-electrons. EC has to take place whenever the energy, Q_{EC} , released is not sufficient to create an electron-positron pair (which would cost $2m_e c^2 = 1022$ keV). The lowest excitation of ^{57}Fe provides the 14.4 keV Mössbauer photons.

9.2.2 Phonons - The Quanta of Lattice Vibrations

The Hamiltonian describing the lattice vibrations has $3pN$ degrees of freedom, where N is the number of Bravais lattice sites, and p is number of nuclei forming one basis. Since there are N lattice momenta, $\mathbf{k}_n = \sum_{j=1}^3 n_j \mathbf{G}_j$, in reciprocal space, we have $3p$ eigenstates for each \mathbf{k} . Out of these, there are 3 ‘acoustic’ and $3(p-1)$ ‘optical’ normal modes. In the classical picture, the first represent coherent modes of the basis, while the latter correspond to oscillatory motion within the basis. The crucial difference is that the acoustic branches have zero energy $\Omega_A(0) = 0$ for zero momentum $\mathbf{k} = 0$, while the optical dispersion relation $\Omega_O(\mathbf{k})$ is bounded away from zero.

In ‘phonon coordinates’, $\mathbf{Q}_n = \sqrt{M/N} \sum_{\mathbf{m}} \mathbf{q}_m \exp\left(-2\pi i \sum_{j=1}^3 m_j n_j / N_j\right)$ ⁴, the Hamiltonian reads

$$H = \sum_{\mathbf{n},s} \left(\frac{P_{\mathbf{n},s}^\dagger P_{\mathbf{n},s}}{2} + \Omega^2(\mathbf{k}_{\mathbf{n},s}) \frac{Q_{\mathbf{n},s}^\dagger Q_{\mathbf{n},s}}{2} \right) \quad (9.1)$$

$$= \sum_{\mathbf{n},s} \hbar \Omega_s(\mathbf{k}_n) \left(a_{\mathbf{n},s}^\dagger a_{\mathbf{n},s} + \frac{1}{2} \right), \quad (9.2)$$

⁴where the \mathbf{R}_j span the Bravais lattice such that $\mathbf{r}_m = \sum_{j=1}^3 m_j \mathbf{R}_j$ are the Bravais lattice sites, and $\mathbf{r}_m + \mathbf{q}_m$ are the nuclei positions.

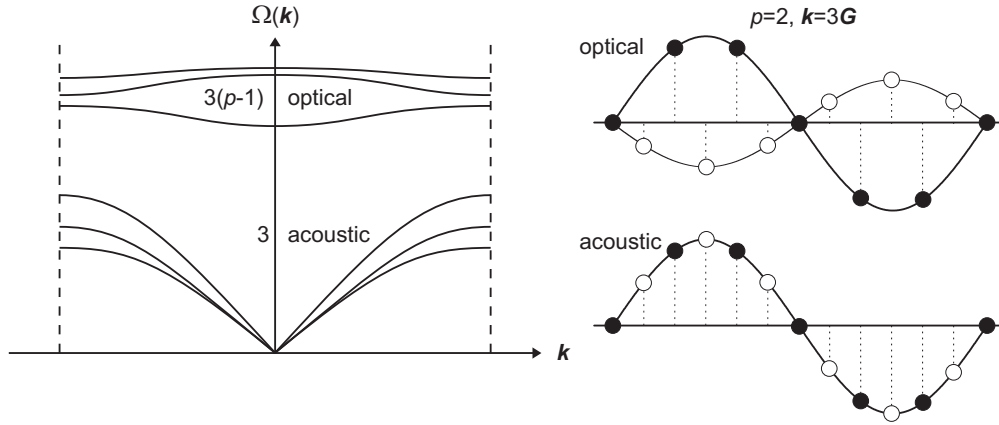


Figure 9.2: The phonon dispersion relation. The photons of the resonance frequency are emitted or absorbed with the simultaneous creation or annihilation of a phonon with energy $\hbar\Omega(\mathbf{k})$ and momentum $\hbar\mathbf{k}$.

where the index s denotes the phonon branch. The a^\dagger and a are the familiar bosonic creation and annihilation operators respectively. The creation and annihilation of phonons is the essential property of the solid emitter and absorber for the Mössbauer effect to work, as discussed in the following paragraph.

9.2.3 The Mössbauer - Lamb Factor

The spectra emitted out of the electronic shells of gas molecules suffer from two mechanisms of broadening: firstly, collisions reduce the life time of electronic states and hence give rise to a Lorentzian shaped spectral line (pressure broadening). Secondly, the Gaussian velocity distribution in conjunction with the Doppler shift (in first order) causes a Gaussian shaped spectral line (Doppler broadening). The absence of these familiar effects for nuclei embedded in the crystal lattice of a solid is the basis of the Mössbauer effect. Non of these broadening effects reduce the spectral resolution. Moreover, the emission is ‘recoilless’. This allows emission and absorption in resonance.

The principal line at ω_0 in Fig. 9.3 corresponds to the case of interest, when the momentum of the emitted photon, $\mathbf{p}_\gamma = \hbar\mathbf{k}$, is distributed over the entire crystal of mass NM , so that the emitted energy,

$$E_\gamma = \hbar\omega_0 - \frac{\mathbf{p}_\gamma^2}{2NM} = E_0 - \frac{E_\gamma^2}{2NMc^2} \quad (9.3)$$

is shifted by

$$\begin{aligned} \Delta E_{\text{recoil}} &= E_0 - NMc^2 \left(\sqrt{1 + \frac{2E_0}{NMc^2}} - 1 \right) \\ &= \frac{E_0^2}{2NMc^2} + \mathcal{O}(1/N^2), \end{aligned} \quad (9.4)$$

which is less than the natural line width, since even for a powder (as such shall be brought inside granular particles) is $N \gg 10^{12}$. For a free atom, $N = 1$, the recoil shift would largely exceed the natural line width, in the case of ^{57}Fe by more than five orders of magnitude.

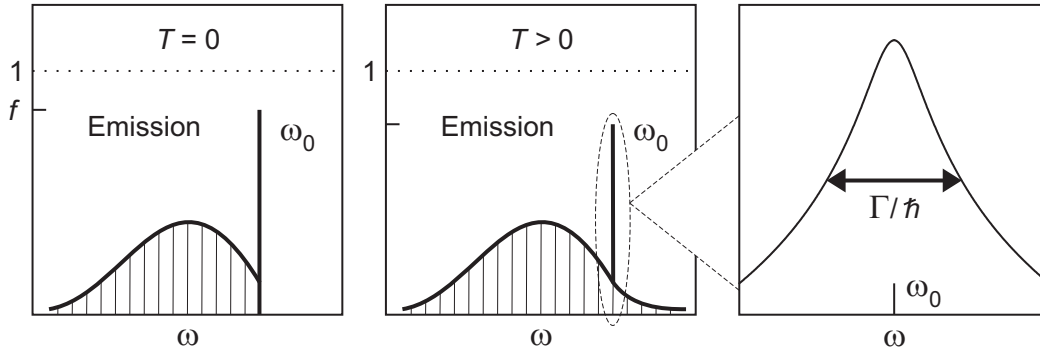


Figure 9.3: The photon spectrum emitted by a nucleus bound in a lattice. Emission events of the principal line at ω_0 do not create or annihilate phonons. The photon momentum is distributed over the entire lattice, so that the line is unshifted and has the natural line width Γ . The probability of such a recoilless emission is given by the Mössbauer -Lamb factor f_S of the source.

Now the crucial point is to understand why there is such a dominant principal line at ω_0 . The acoustic phonons can take up arbitrary small energies, however does the Debye density of state

$$Z(\Omega) = \frac{9N\hbar\Omega^2}{k_B\Theta^3}, \quad \Omega < \Omega_D \quad (9.5)$$

vanish quadratically for small energies. (Θ in (9.5) is the Debye temperature.) The optical phonons have an approximately constant dispersion relation, which corresponds to the Einstein model of solid state physics. Figure 9.3 outlines the distribution of photon energies, emitted by the source. For zero temperature there are no optical phonons to be annihilated in the emission process, whereas at positive temperature a photon with $\omega > \omega_0$ is possible.

The Mössbauer - Lamb factor f_{ML} gives the fraction of recoilless emissions among all transitions from the Mössbauer state to the ground state, i.e. the weight under the principal line in Fig. 9.3. The quantum mechanical probability for the photon momentum \mathbf{p}_γ to be absorbed or emitted by the solid, while the state vector $|L\rangle$ of the lattice is unchanged (no creation or annihilation of phonons), is given by the transition probability

$$f_{ML} = |\langle L | \exp i(\mathbf{p}_\gamma, \mathbf{q}_m) | L \rangle|^2, \quad (9.6)$$

where $\exp i(\mathbf{p}, \mathbf{q}_m)$ is the operator for the momentum transfer at the lattice site $\mathbf{m} = (m_1, m_2, m_3)^5$. The integration involved in the expectation value (9.6) results in

$$f_{ML} = \exp -k^2 \langle \mathbf{q}^2 \rangle / 3, \quad (9.7)$$

which has formal similarity with the Debye-Waller factor for scattering (of x-ray and neutrons), but physically Eq. (9.7) holds for emission and absorption events. The expectation value $\langle \mathbf{q}^2 \rangle$ involves in total three averaging steps: the quantum mechanical expectation value, the averaging over the thermodynamical ensemble, and for the Debye model the integration over the density of states $Z(\Omega)^6$. The exponent $\langle \mathbf{q}^2 \rangle$ increases quadratically with temperature T

⁵ \mathbf{q} is a vectorial operator and \mathbf{p}_γ a numerical vector.

⁶The Einstein approach yields $\langle \mathbf{q}^2 \rangle_E = \frac{\hbar}{M\Omega_E} \left[\frac{1}{\exp(\hbar\Omega_E)/(k_B T) - 1} + \frac{1}{2} \right]$, and the Debye result is $\langle \mathbf{q}^2 \rangle_D = \frac{3\hbar}{2M\Omega_D} \left[2 \left(\frac{T}{\Theta} \right)^2 \int_0^{\Theta/T} \frac{y}{\exp y - 1} dy + \frac{1}{2} \right]$.

below the Debye temperature Θ (which is 464 – 470 K for α -iron), and linearly above Θ . Typical values for the Mössbauer -Lamb factor of a ^{57}Co -source at room temperature are of the order of 75% [195, 138].

9.2.4 Natural Line Width

In the absence of phonon creation or annihilation, the remaining width of the Mössbauer line at ω_0 is the natural line width. The sharpness $\Delta\omega/\omega$ of the natural emission line (and for the time-reversed resonance absorption process) is extraordinarily high, and determined by the half-life time of the nuclear state, which is $T_{1/2} = 98.1$ ns for the Mössbauer level of ^{57}Fe : $\Gamma = \hbar/\tau = \hbar \ln 2/T_{1/2} = 4.7 \times 10^{-9}$ eV. The line shape is well-known to have Breit-Wigner⁷ form, $\propto 1/(1 + (2\Delta E/\Gamma)^2)$ as sketched in the right panel of Fig. 9.3. Resonance absorption is possible because the energy shift $E_\gamma^2/2NMc^2$ is far below the natural line width of

$$\frac{\Delta\omega}{\omega} = 3.3 \times 10^{-13} . \quad (9.8)$$

9.2.5 Longitudinal and Transverse Doppler Shift

The frequency is tuned by virtue of the Doppler effect. The source is brought in motion with respect to the lab frame. If one assumes that the local flow of time for the source equals the lab time, one arrives at the non-relativistic Doppler-shift:

$$\left. \frac{\omega}{\omega_0} \right|_{\text{L}} = \frac{1}{1 - \frac{v}{c}} \approx \left(1 + \frac{v}{c} \right) . \quad (9.9)$$

(v is positive for the source moving towards the sample). In order to take time dilatation into account, one simply has to multiply by the famous square root factor to arrive at the exact longitudinal Doppler effect:

$$\left. \frac{\omega}{\omega_0} \right|_{\text{L}} = \frac{\sqrt{1 - \frac{v^2}{c^2}}}{1 - \frac{v}{c}} = \sqrt{\frac{1 + \frac{v}{c}}{1 - \frac{v}{c}}} = 1 + \frac{v}{c} + \frac{v^2}{2c^2} + \dots . \quad (9.10)$$

In the transverse direction, there is only the quadratic time dilatation:

$$\left. \frac{\omega}{\omega_0} \right|_{\text{T}} = \sqrt{1 - \frac{v^2}{c^2}} = 1 - \frac{v^2}{2c^2} + \dots . \quad (9.11)$$

The linear term of the longitudinal effect (9.10) is used to tune the frequency in the range $v/c = -10^{-10} \dots 10^{-10}$. The natural line width (9.8) corresponds to the Doppler velocity

$$\Delta v = 0.1 \frac{\text{mm}}{\text{s}} . \quad (9.12)$$

Clearly, the quadratic term is *completely negligible* for this range of driving velocities. For this reason the Mössbauer effect measures the longitudinal velocity component only. This is favorable for nonequilibrium statistics as it allows to measure each component separately, and to detect a possible anisotropy of the granular temperature.

There is a well-known thermal shift due to the quadratic Doppler effect⁸, which is referred to as the second order Doppler shift (SOD) in the specialized literature. A simple calculation

⁷This distribution is also given the names of H.A. Lorentz and A.L. Cauchy.

⁸Due to thermal motion, which is isotropic, so that there is no thermal contribution by the linear term on average. In the quadratic order there are two negative transverse contributions and one positive longitudinal contribution. Hence the isotropic average yields a negative shift of ω with temperature.

for the present system with ^{57}Fe shows, that the source and the absorber would have to differ by more than 100 K for a measurable SOD effect, which is not the case for the granular sample.

9.2.6 The Chemical Isomer Shift

The energy levels of the nucleus can be perturbed due to hyperfine interactions. Expanding the local electric potential ϕ_E at the nucleus, yields the coulomb term in zero order, which is identical for all isotopes. The Mössbauer spectroscopy is sensitive to differences in the energy levels (between source and absorber), so that this term is irrelevant. The first order gives the dipole interaction. The nucleus state has defined parity, $P\psi_{N\pm} = \pm\psi_{N\pm}$, so that the charge distribution $\rho = Ze|\psi|^2$ is invariant under the spatial inversion P . Hence, there is no electric dipole moment. The second order of the spatial expansion, $E^{(2)} = \frac{1}{2} \int r_a r_b \rho \text{ dvol} (\partial_a \partial_b \phi_E)$ can be split up in an isotropic part, which is referred to in the literature as the monopole term E_C ⁹, and the traceless quadrupole term E_Q . The monopole term is

$$E_C = \frac{Ze^2}{6\epsilon_0} |\psi(0)|^2 \langle r^2 \rangle, \quad (9.13)$$

with the charge density $\epsilon_0(\Delta\phi_E)(0) = e|\psi(0)|^2$ at the nucleus due to the electronic state ψ . The squared radius of gyration of the nucleus with respect to its charge distribution is written as $\langle r^2 \rangle$ in Eq. (9.13). The state vector of a (single Schrödinger) electron with quantum numbers (n, l, m) is in polar coordinates

$$\begin{aligned} \psi(r, \theta, \varphi) &= \langle r, \theta, \varphi | n, l, m \rangle \\ &= \frac{1}{a_0^{3/2}} \frac{2}{n^2} \sqrt{\frac{(n-l-1)!}{(n+l)!}} \left(\frac{2r}{a_0 n}\right)^l e^{-\frac{r}{a_0 n}} L_{n-l-1}^{2l+1} \left(\frac{2r}{a_0 n}\right) Y_{lm}(\theta, \varphi). \end{aligned} \quad (9.14)$$

Since the Laguerre polynomials equal $\binom{n+l}{n-l-1} > 0$ at $r = 0$, we immediately see that $|\psi(0)|^2 > 0$ if and only if $l = 0$. Hence the monopole term is due to s-electrons, which have non-vanish probability at the nucleus. The monopole term is sensitive to the outer s- and also p-electrons, because the latter can shield the nuclear charge against the first. Therefore the monopole term is sensitive to the ionization state of the atom. It allows to determine the ratio of Fe^{2+} and Fe^{3+} .

9.2.7 The Electric Quadrupole Splitting

The quadrupole term is

$$E_Q = \frac{e}{6} \underline{\underline{Q}} : \underline{\nabla} \otimes \underline{\mathbf{E}}, \quad (9.15)$$

with the tensor contraction (denoted by the colon) between the electric field gradients and the quadrupole moment, $\underline{\underline{Q}}$, of the nucleus charge distribution. Rewritten in terms of the nucleus quantum numbers (I, M) , the quadrupole energy is

$$E_Q = \hbar\omega_Q (3M^2 - I(I+1)) \quad (9.16)$$

The ground state of ^{57}Fe has $I = 1/2$ (therefore $M = \pm 1/2$ and $E_Q = 0$), so that this level remains degenerated, whereas the Mössbauer state has $I = 3/2$ and therefore splits in two perturbed levels. This causes a doublet in the Mössbauer spectrum. The separation of the two lines is a measure for the local electric field gradients¹⁰.

⁹Although in electrostatics this usually denotes the zero order term mentioned before.

¹⁰Lattices with cubic symmetry have no field gradients and consequently no quadrupole splitting.

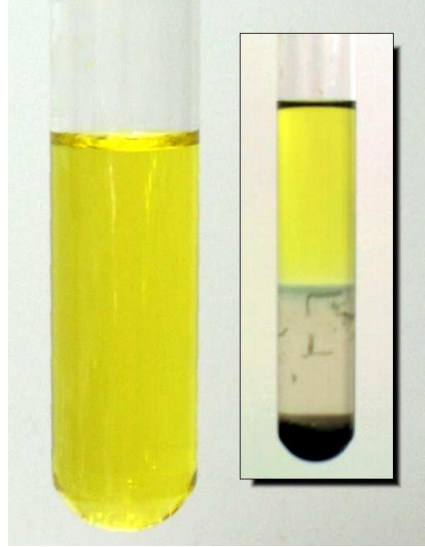


Figure 9.4: The solution of $^{57}\text{Fe}^{2+}$ ions and the precipitation reaction to obtain iron oxide as powder. The test tube contains 200 mg of ^{57}Fe .

9.2.8 Magnetic Splitting

The nuclear Zeeman effect breaks the degeneration with respect to the axial quantum number M of angular momentum (in the direction of the local magnetic flux \mathbf{B}):

$$E_m = -(\boldsymbol{\mu}, \mathbf{B}) = -g_N \mu_N B M, \quad (9.17)$$

where μ_N is the nuclear magneton $e\hbar/(2m_p)$ and g_N is the Landé factor. No magnetic splitting is found for the iron oxide used in the granular experiment.

9.3 Granular Glass Spheres with Highly Enriched ^{57}Fe

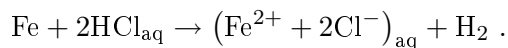
While iron is rank nine in cosmological abundance (with atomic fraction 1.4×10^{-5}), about 4.7% of the earth's mass is iron (rank four among all elements, and second most abundant metal), since our solar system descends from a mixture of later stellar generations [30], where heavier elements have been produced in consecutive supernovae. There are four stable isotopes of iron, among which ^{56}Fe dominates with 91.7%, because it is well-known for having the highest mean binding energy per nucleon of all nuclei. The rarer fractions are ^{54}Fe (5.8%), ^{57}Fe (2.2%) and ^{58}Fe (0.3%). For the resonance absorption of gamma quanta emitted by ^{57}Co we need the isotope ^{57}Fe , which has been provided by Chemotrade GmbH (Düsseldorf) with 95.70% enrichment in form of a porous chunk.

The iron is first brought in a fine powdered form. This allows to disperse the iron homogeneously within the glass phase. The size of the crystals in the powder has to be kept high enough for the Mössbauer effect to work, as emphasized before with Eq. (9.3). The powder is mixed with a fluid glass melt, out of which finally the glass spheres of the granular system are formed.

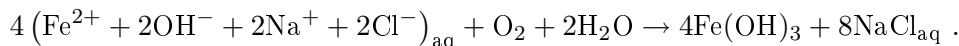
9.3.1 Production of $^{57}\text{Fe}_2\text{O}_3$ Powder

In order to disperse the iron in the spherical glass beads, the enriched iron cannot be used as delivered. The author decided to dissolve the iron in hydrochloric acid, to obtain an aqueous

solution of $^{57}\text{Fe}^{2+}$ as an intermediate step:



Adding the base of an alkali metal, such as sodium hydroxide (NaOH) or potassium hydroxide (KOH) causes precipitation:



The solution has been filtered to recover the iron oxide as powder. Being heated up at 150°C while exposed to air, the fraction of $^{57}\text{Fe}^{3+}$ increases as indicated by initial green color (for the oxidation state +2) which turned black (due to the unstable intermittent $\text{Fe}_3\text{O}_4 \cdot \text{aq}$) and eventually brown, indicating the end of the oxidation reaction. Weighing showed that the stoichiometric is precisely that of $^{57}\text{Fe}_2\text{O}_3$.

9.3.2 Production of Glass Melt with Enriched ^{57}Fe

A gas-fired melting furnace has been constructed which contained a vertical cylindrical crucible of graphite (2.8 ml total inner volume). The material graphite was chosen because test runs had shown that graphite has a high contact angle with molten glass. The crucible was filled at room temperature with the iron oxide powder (corresponding to 150 mg ^{57}Fe) and commercially available glass spheres as the raw material for the glass melt (2 g in mass). The crucible was closed and heated up to approximately 1500°C and kept at constant temperature for 15 minutes. The glass melt and the $^{57}\text{Fe}_2\text{O}_3$ powder are stirred with an titanium rod. After cooling, a homogeneous and dark-green glass was obtained.

9.3.3 Production of Spherically Shaped Particles

The following method for the production of glass spheres had been worked out by my colleague M. Scheel before. The glass block was mechanically broken in pieces which approximate the desired granular particle mass. Distributed on a charcoal surface, the pieces were reheated by the flame of a blowpipe. Above the glass transition temperature, the surface tension of the glass forms droplets. The surface tension and the zero contact angle of the molten glass droplets with the mildly burning charcoal surface produce spherical glass particles. In view of the high costs of the ^{57}Fe material, glass spheres of unwanted small size were remelted and those resulting from coalescence broken up again.

Finally three size fractions were separated by sieving (with the total granular mass indicated in brackets):

- $d=250\text{-}355\mu\text{m}$ (370 mg),
- $d=355\text{-}500\mu\text{m}$ (504 mg), and
- $d=500\text{-}710\mu\text{m}$ (543 mg).

The mass fraction of the ^{57}Fe nuclei, distributed homogeneously inside the glass spheres, is 6.0%. Due to the crucible and the charcoal, the glass spheres contain carbon with a mass fraction of at the most 3%.

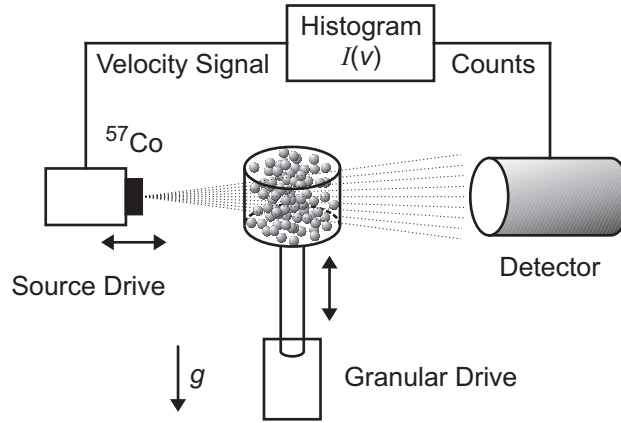


Figure 9.5: The granular Mössbauer setup. The absorber is replaced by the granular sample. The granular particles are glass beads, which contain a highly enriched fraction of the stable isotope ^{57}Fe . The granulate is driven by the vertical motion of its polycarbonate container.

9.4 The Granular Mössbauer Setup

Most measurements, including those reported here, are sensitive to the resonance absorption observed in transmission. Here the source of the photons, the granular sample, and the detector (a proportional counter in our case) are in line, as is shown by Fig. 9.5. It is mentioned in passing that one may as well observe with a scattering geometry the fluorescence photons resulting from the absorption. Furthermore, the relaxation of an excited Mössbauer state does not necessarily decay with the re-emission of a fluorescence photon. A certain fraction of decay events undergo internal conversion (IC), in which case the nucleus interacts directly with its electronic shell by emitting a conversion electron instead of a photon. This is actually the dominant decay branch of the 14.4 keV state of ^{57}Fe , for which approximately 85% of the relaxation processes to the ground state involve IC. Since IC leaves an electron state unoccupied, the electronic shell undergoes subsequent transitions [195], which gives rise to the emission of both, x-ray photons and Auger-electrons (similar as after EC). The high IC rate is favorable for the granular measurement, because the probability that a fluorescence photon is re-emitted from a granular particle (which could find its way in the detector, or cause multiple absorption and re-emission) is suppressed.

9.4.1 The Atomic Density and the Effective Absorber Thickness

Since the density of iron oxide is closely twice the density of glass, the volume fraction of $^{57}\text{Fe}_2\text{O}_3$ is 3% within the glass spheres. As throughout this thesis, the volume fraction of the spherical granular sample is denoted by ϕ . Hence the total molecular volume fraction of $^{57}\text{Fe}_2\text{O}_3$ is $a_A\phi = 0.03\phi$. Typical values at measurement are $\phi = 0.1$ for the strongly fluidized state and 10^{-2} for the gas state. The molecular number density of $^{57}\text{Fe}_2\text{O}_3$ is

$$N_A = 1.976 \times 10^{22} \frac{\text{molecules}}{\text{cm}^3}, \quad (9.18)$$

so that the number of ^{57}Fe -nuclei per volume is

$$n_A\phi = 2N_A a_A\phi = 1.2 \times 10^{21} \frac{\text{nuclei}}{\text{cm}^3} \phi. \quad (9.19)$$

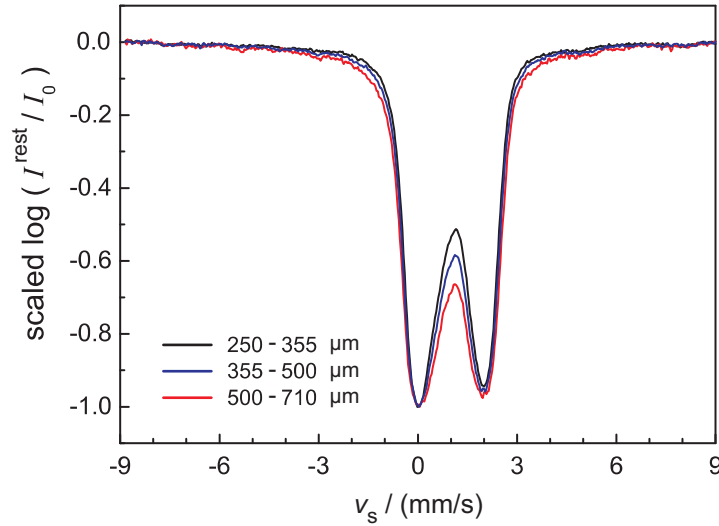


Figure 9.6: The Mössbauer spectrum of the ^{57}Fe -glass spheres at rest. The isomer shift is 1.03 mm/s and the quadrupole splitting is 1.84 mm/s.

With this information we compute the absorption length. The probability for a photon $\hbar\omega_0$ at the resonance frequency to penetrate into the absorber, reaching the depth x , decays exponentially, $\exp(-x/\lambda_A)$, since the probability for the photon being absorbed within a segment dx of its path is constant in the homogeneous absorber material. The resonance absorption length λ_A is given by the nuclear cross section σ_0 , the number density of nuclei n_A , and the recoilless fraction f_A (the Mössbauer - Lamb factor of the absorber): $1/\lambda_A = \sigma_0 n_A f_A$. For ^{57}Fe at room temperature we have $f_A \approx 0.75$ [195] and the resonance cross section is $\sigma_0 = 256.6 \times 10^{-20} \text{ cm}^2$, which yields

$$\lambda_A = 4.33 \mu\text{m} \quad (9.20)$$

for the glass material of our ^{57}Fe -enriched spheres. We compare this length scale (9.20), set by the nuclear resonance absorption, with the granular length scale of the particle diameter d , and the effective geometric depth $d_A = L\phi$ of the granular system, which is crossed by the ray with length L inside the sample. The dimensionless exponent of the resonance attenuation, $\tau_A = d_A/\lambda_A$, is called the effective absorber thickness, and assumes in the experimental system the values

$$\tau_A = \sigma_0 n_A f_A \begin{cases} d \\ d_A \end{cases} = \begin{cases} 58, & \text{diametrically for single particle } d = 250\mu\text{m} \\ 51, & \text{for the entire gas state.} \end{cases} \quad (9.21)$$

9.4.2 The Mössbauer Spectrum at Rest

The Mössbauer spectrum of the granular system at rest is already non-trivial, because of the chemical isomer shift and the electrostatic quadrupole splitting of iron oxide. Obviously, the full information about the detailed spectrum at rest is necessary, in order to uniquely extract the broadening of the Mössbauer spectrum due to the granular velocity distribution from the Mössbauer spectrum taken of driven granular matter.

A monolayer of the ^{57}Fe -enriched glass spheres was fixed between two plates (free of ^{57}Fe) and used as absorber material. The ray crossed the monolayer perpendicularly. The resulting spectrum $I^{\text{rest}}(v)$ is shown in Fig. 9.6 for monolayers of the three different size fractions (cf.

9.3.3). The source is ^{57}Co diffused into the metal matrix rhodium, which provides a single line, and the velocity axis has been calibrated with an $\alpha\text{-Fe}$ foil. We see a doublet due to the quadrupole splitting 9.2.7 of iron oxide, which is shifted towards positive velocities according to the isomer shift 9.2.6. The splitting is $\Delta v \approx 1.94$ mm/s. Typically, $^{57}\text{Fe}^{2+}$ has a quadrupole splitting close to $\Delta v=3$ mm/s, while $^{57}\text{Fe}^{3+}$ shows doublets with $\Delta v=0.5$ mm/s [233]. The position of the lines in Fig. 9.6 are similar but not identical with a recent study of iron oxide in glass [134]. There is no nuclear Zeeman splitting (which would cause a sextet according to the $\Delta M = \pm 1$ transition from $I = 3/2$ to $I = 1/2$) measurable at room temperature. The widths of the two dips is much larger than the theoretically possible values for a single iron oxidation state (as well as those widths found in [134]), which indicates that the $^{57}\text{Fe}_2\text{O}_3$ powder, brought initially in the glass melt, has been reduced to a large extent. While the positions of the doublet lines are independent of the particle diameter, the widths have a systematic dependence on the ratio d/λ_A of particle diameter and absorption length.

9.5 The Transmission Integral for the Granular Mössbauer Effect

The transmission intensity observed at the detector depends on the following three spectral distributions.

9.5.1 The Emission Distribution of the Source

The Mössbauer line, emitted by the decay cascade of the ^{57}Co source, has in its instantaneous inertial frame the Breit-Wigner shape

$$P_{\text{BW}}(E) = \frac{1}{2\pi} \frac{\Gamma}{(E - E_0)^2 + \Gamma^2/4}, \quad (9.22)$$

with $E_0=14.4$ keV and $\Gamma_S = 4.7 \times 10^{-9}$ eV. Boosted in the lab frame, the distribution is Doppler shifted, so that the probability for a photon entering the sample with energy in the interval between E and $E + dE$ is

$$P_S(E, v_S) dE = P_{\text{BW}}\left(E - \frac{v_S}{c}E_0\right) dE, \quad (9.23)$$

in the moment when the time dependent velocity of the source is v_S .

9.5.2 The Transmission Distribution of the Absorption

The resonance absorption length τ_A , as defined in Sec. 9.4 with the result (9.20), holds for photons of energy E_0 . When the photon energy is detuned, the cross section $\sigma(E)$ is reduced compared to σ_0 according to the Breit-Wigner line shape, $\sigma(E) \propto \sigma_0 P_{\text{BW}}(E)$. Therefore the absorption length is, as a function of energy E ,

$$\tau_A(E, \Gamma) = \frac{\tau_A}{1 + 4(E - E_0)^2/\Gamma^2}. \quad (9.24)$$

The corresponding transmission probability for a photon of energy E is

$$P_A(E, \Gamma) = e^{-\tau_A(E, \Gamma)}. \quad (9.25)$$

Equation (9.25) holds for a single line. The granular absorber has in general not only one absorption line. Rather, as seen in the last Sec. 9.4.2, the spectrum at rest is a non-trivial

intrinsic spectral function. The hyperfine splitting of the excited states shifts the energies by ΔE_j , so that the transmission probability becomes

$$P_A(E) = \prod_j e^{-\tau_{Aj}(E - \Delta E_j; \Gamma_j)} = \exp \left[- \sum_j \tau_{Aj}(E - \Delta E_j; \Gamma_j) \right] = e^{-\tau_A \text{ total}(E)}. \quad (9.26)$$

If the chemical environments of the ^{57}Fe in the sample were known, one could in principle compute the transmission probability theoretically. However, the most accurate and feasible approach *defines* the function $P_A(E)$ of the Mössbauer spectrum with the granular particles at rest by the experiment. In modifying the Mössbauer theory for driven granulates we use the relation between the absorption length and the transmission probability of the absorber (9.26):

$$\tau_A(E) = -\ln P_A(E). \quad (9.27)$$

9.5.3 The Granular Velocity Distribution

The distribution in which we are mainly interested from the point of view of granular and nonequilibrium physics, is the velocity distribution, which we want to denote by

$$P_{\text{gran}}(v_{\text{gran}}). \quad (9.28)$$

Given the three distribution functions (9.23), (9.26), and (9.28), we can write down the transmission intensity, $I(v_S)$. The transmission intensity is directly observed, and the final step of the analysis will be to reconstruct the granular velocity distribution, P_{gran} , from the measured intensity $I(v_S)$.

Let us begin with the standard case of an absorber at rest. We shall then modify the expression for the driven granular state. The activity $I(v_S)$ at the detector is due to recoilless photons emitted by the source with probability f_S , and the thermal background contribution $(1 - f_S)$. The intensity is attenuated by quantum electrodynamic interactions of the photons with the atomic shells¹¹ according to the Beer-Lambert law, $I \propto \exp(-\mu_A d_A)$. In addition to that, the recoilless photons have a probability $1 - P_{\text{trans}}$ for resonance absorption, so that the detected activity I obeys

$$\begin{aligned} \frac{I(v_S)}{I_S} &= f_S e^{-\mu_A d_A} P_{\text{trans}}(v_S) + (1 - f_S) e^{-\mu_A d_A} \\ &= e^{-\mu_A d_A} [1 - f_S (1 - P_{\text{trans}}(v_S))] . \end{aligned} \quad (9.29)$$

The source intensity in the solid angle of the detector is I_S . The probability P_{trans} in (9.29), that a photon (which originated from a recoilless emission) reaches the detector, is the product of the probability of the energy E under the emission line of the source, multiplied by the probability that the photon crosses the absorber. Finally we integrate over E , since the photon energy is not resolved by the detector at this level:

$$P_{\text{trans}}(v_S) = \int P_S(E, v_S) P_A(E) dE = \int P_{\text{BW}} \left(E - \frac{v_S}{c} E_0 \right) e^{-\tau_A(E)} dE . \quad (9.30)$$

Equation (9.30) is a convolution of the emission line shape and the transmission probability.

¹¹The Compton effect has a cross section $\sigma_c \propto Z/E_\gamma$ and the photoelectric effect has $\sigma_{\text{ph}} \propto Z^5/E_\gamma^{7/2}$. Rayleigh scattering is negligible at energies above 2keV.

Now we turn to the case of driven granular matter. Here the decisive physical point is that the photon with energy E does not ‘see’ the entire granulate as a resonance absorber, but only those particles which move at the velocity of the source within emission line width, so that resonance absorption is possible. Therefore the effective absorber thickness $\tau_A(E) = \sigma(E)n_A f_A d_A$ (Eqs. (9.21 and (9.27)), depends on the velocity distribution in the granular sample:

$$\begin{aligned}\tau_A^{\text{gran}}(E) &= \int \sigma\left(E - \frac{v_{\text{gran}}}{c}E_0\right) P_{\text{gran}}(v_{\text{gran}}) dv_{\text{gran}} n_A f_A d_A \\ &= \int \tau_A^{\text{rest}}\left(E - \frac{v_{\text{gran}}}{c}E_0\right) P_{\text{gran}}(v_{\text{gran}}) dv_{\text{gran}} .\end{aligned}\quad (9.31)$$

The convolution (9.31) relates the absorption length of the dynamical granular sample to the absorption at rest and the granular velocity distribution. We note that the latter convolution (9.31) appears in the exponent of the observable transmission probability, in contrast to the previous convolution with the source line (9.30). With Eqs. (9.30) and (9.31) we have the explicit effect of granular motion on the Mössbauer spectrum (9.29). We summarize this result using the convenient $*$ -notation for the convolution of functions.

$$I(v_S) = I_0 [1 - f_S (1 - P_{\text{trans}}(v_S))] \quad (9.32)$$

$$P_{\text{trans}}(v_S) = P_{\text{BW}} * \left[e^{-(\tau_A^{\text{rest}} * P_{\text{gran}})} \right] (v_S) \quad (9.33)$$

Energies and velocities are implicitly understood to be linearly related by $c \Delta E = E_0 \Delta v$. The maximal intensity of the Mössbauer spectrum is $I_0 = I_S e^{-\mu_A d_A}$.

9.6 Reconstruction of the Velocity Distribution

Aside from the neglect of multiple absorption and re-emission processes (causing resonance broadening), the result (9.32-9.33) does *not* involve an approximation (such as the wide-spread thin-absorber approximation, applicable for $\tau_A < 1$). We further simplify the analysis without significant error: the line width Γ_S of the source is of the order 0.1 mm/s, which is 20 times finer than the structures in the spectrum Fig. 9.6. We can therefore approximate the Breit-Wigner distribution P_{BW} by a delta distribution in the convolution (9.33). This yields

$$-\ln P_{\text{trans}} = \tau_A^{\text{rest}} * P_{\text{gran}} . \quad (9.34)$$

The transmission probability is related to the intensity Eq. (9.32):

$$-\ln P_{\text{trans}} = -\ln \left[1 - \frac{1 - I/I_0}{f_S} \right] \approx \frac{1 - I/I_0}{f_S} . \quad (9.35)$$

By virtue of the Eqs. (9.34) and (9.35), we arrive at the central formula for granular Mössbauer spectroscopy,

$$\tau_A^{\text{rest}} * P_{\text{gran}} = \frac{1 - I/I_0}{f_S} , \quad (9.36)$$

which relates intensity and velocity distribution. The measurement at rest (spectrum of Fig. 9.6) has $P_{\text{gran}}(v_{\text{gran}}) = \delta(v_{\text{gran}})$, so that the intrinsic resolution function τ_A^{rest} , which comprises the nuclear absorption properties of our sample, is known:

$$\tau_A^{\text{rest}} = \frac{1 - I^{\text{rest}}/I_0^{\text{rest}}}{f_S} . \quad (9.37)$$

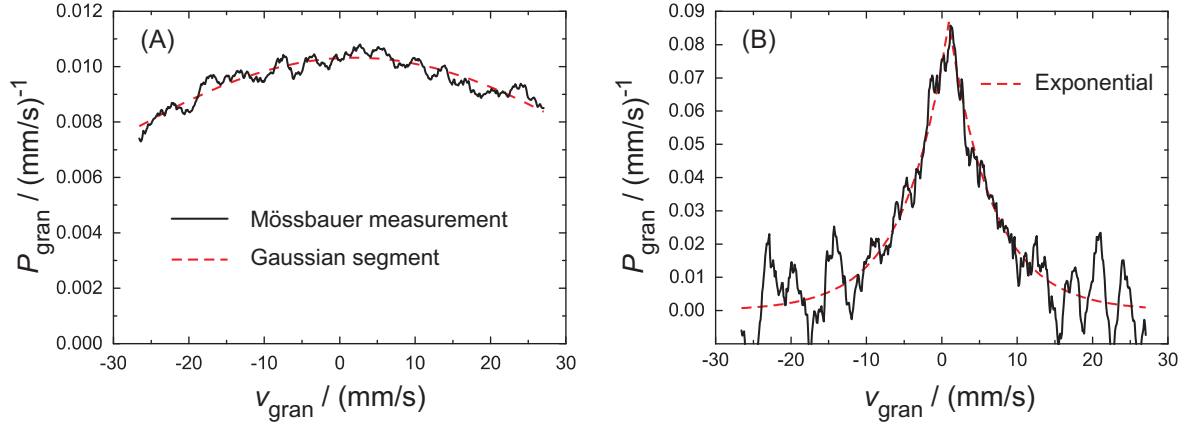


Figure 9.7: Preliminary experimental results on the granular velocity distribution. In the course of the deconvolution a Welch window was used to filter high frequency noise from the measurement. (A) The small particle fraction (250-355 μm , dry). Sinusoidal motion with peak acceleration 30 g drives the system in the gas state. The measured granular temperature is $T/m = \langle \Delta v^2 \rangle = (38 \pm 6 \text{ mm/s})^2$. The velocity distribution is on the narrow velocity range indistinguishable from a Gaussian. Deviations from the equilibrium distribution are theoretically expected for the high velocity tails at $v^2 > T/m$ [27]. The dotted curve is the best fit of a Gaussian segment. The velocities are significantly shifted with a convective drift of $\langle v \rangle = 2.0 \pm 0.4 \text{ mm/s}$ in the horizontal plane. (B) As we switch to the large particle fraction (500-710 μm) and reduce the driving amplitude to the acceleration 12 g , the full stationary velocity distribution enters the range of velocities, which are resolved by the drive of our Mössbauer source. For this vigorous fluid, the velocity distribution follows within experimental scattering an exponential $P_{\text{fluid}} \propto \exp(-|v - v_0|/\bar{v})$. The granular temperature is $T/m = 2\bar{v}^2 = (8.2 \pm 1.0 \text{ mm/s})^2$. A small drift, $v_0 = 0.93 \pm 0.20 \text{ mm/s}$, remains observable.

It is therefore a straightforward numerical procedure to deconvolute the ‘response function’ τ_A^{rest} out of the main formula (9.36) with Fourier transformation (denoted by $\widetilde{}$), to arrive at the granular velocity distribution:

$$\widetilde{P}_{\text{gran}} = \frac{\widetilde{(I_0 - I)}}{\widetilde{(I_0^{\text{rest}} - I^{\text{rest}})}} . \quad (9.38)$$

Some remarks are here in order. The functions I and I^{rest} result from the experiment with different discretizations in general. The wider velocity range of I has to be mapped carefully on the finer discretization of I^{rest} , and the narrower range of I^{rest} is to be continued with the constant I_0^{rest} . The deconvolution significantly increases the information gained from the measured signal I , because the resolution in velocity space is determined by the smallest dip structure of the rest spectrum, whereas the direct signal only reveals structures of the velocity distribution which are larger than the splitting of the dips. Of course, no information on velocities below the width of the dips in the rest spectrum is measurable. This physical limitation can be reflected mathematically by a zero (or very small value) of the denominator in (9.38), which is in reciprocal space located at the inverse dip width. In this case, the resummation of Fourier modes has to stop before this zero. If the Fourier transform of the rest spectrum has no zero (which is in practice the case for this complex valued function), the convolution can be completely undone. Noise in the signal I is then the only limitation. (Established techniques of optimal filtering in this context of deconvolution are nicely described in Sec. 13.3 of [175].)

Before transforming back to the velocity space, the Fourier transformed distribution (9.38) is conveniently used to extract the cumulants of the velocity distribution (in the case of a symmetric shape):

$$\ln \widetilde{P}_{\text{gran}}(s) = \sum_{k=1}^{\infty} c_{2k} \frac{(-1)^k}{(2k)!} s^{2k} . \quad (9.39)$$

The granular temperature $T = c_2$ is given by the second cumulant, and the fourth cumulant c_4 is the kurtosis, which indicates the deviation from a Gaussian. A preliminary experimental result is presented in Fig. 9.7. The range of velocities which can be resolved is set by the maximum speed of the Mössbauer source. Our driving mechanism allows up to 30 mm/s. On this velocity interval the gas state of the small particles cannot be distinguished from a Gaussian distribution (Fig. 9.7A). Here the peak acceleration is 30 g and the shaking frequency is 100 Hz. We therefore increase the particle mass and reduce the driving amplitude at constant frequency to the acceleration 12 g . The result is shown in (Fig. 9.7B), where the full distribution falls in the observed velocity range. The deviation from a Gaussian velocity distribution is obvious. Within the experimental scattering, the data agrees very well with an exponential distribution

$$P_{\text{fluid}} = \frac{1}{2\bar{v}} e^{-\frac{|v-v_0|}{\bar{v}}} . \quad (9.40)$$

Experimental values for the granular temperature and drift velocity are given in the caption of Fig. 9.7. While there are excellent experimental results on the velocity distribution for granular monolayers and surfaces [146], this is to the author’s knowledge the first experimental observation of exponential tails in the bulk, as predicted theoretically [3, 174].

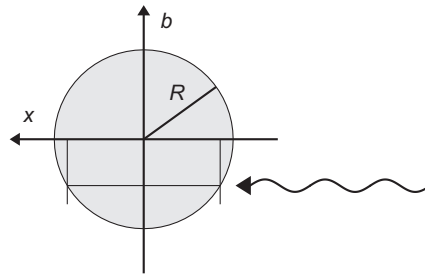


Figure 9.8: Section of a particle. A photon at impact parameter b has to cross the length $\sqrt{R^2 - b^2}$ through the particle. In general the particle will also rotate about its center of mass. For this reason, the velocities of the nuclei, which potentially absorb the photon as it crosses the particle, are not the equal.

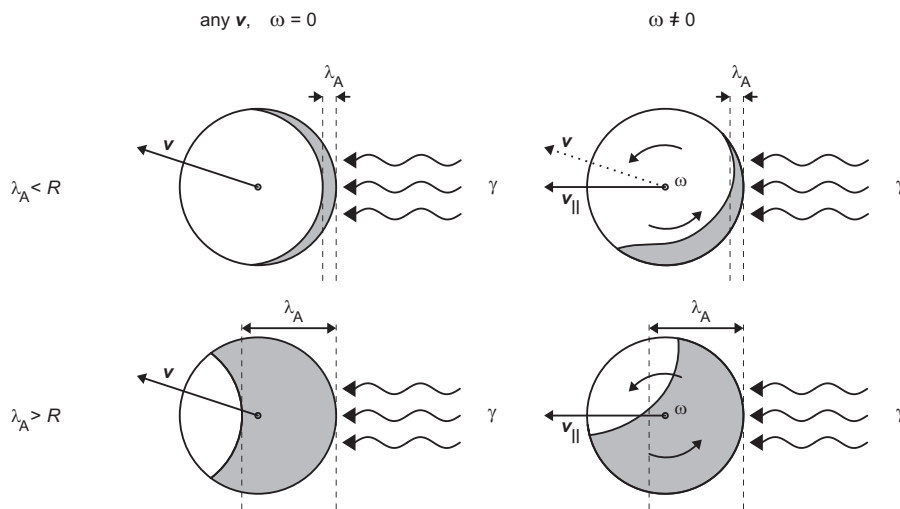


Figure 9.9: The rotation and translation state of the granular particle influences the preferred subvolume for absorption. Furthermore, the subvolume depends on the concentration of ^{57}Fe , which is inversely proportional to the absorption length λ_A . By taking the Mössbauer spectrum of different concentrations it is possible to extract information on the correlation between velocity and rotation.

9.7 How to Measure Translation and Rotation of Granular Particles

So far we treated the driven granulate as a spatially homogeneous system of (nucleus) density ϕn_A . That is, we distinguished the ^{57}Fe nuclei in velocity space, when writing (9.34)

$$P_{\text{trans}} = e^{-\tau_A^{\text{rest}} * P_{\text{gran}}} . \quad (9.41)$$

This implies that the velocity distribution $P_{\text{gran}}(v_{\text{gran}})$ is the distribution of the (horizontal) velocity component of the ^{57}Fe nuclei, which is *not* identical with the velocity of the granular particles.

In what follows it is outlined how particle velocity and particle rotation can be extracted from the granular Mössbauer experiment. There is substantial interest in the correlation of these quantities for nonequilibrium statistical physics [28]. The rigid body motion of the glass spheres is described by translation and rotation, so that the granular ensemble is described by the distribution $P_{\text{tr}}(\mathbf{v}_{\text{cm}}, \omega_{\text{rot}})$, where \mathbf{v}_{cm} is the velocity of the particle's center of mass, and the axial vector ω_{rot} describes the angular velocity and the rotation axis.

We consider the absorption of a glass sphere in detail. For this we need the energy dependent absorption length $\lambda_A(E)$, i.e. the resonance absorption length *inside* a ^{57}Fe -enriched sphere which is *at rest*. This function has been determined by the Mössbauer spectrum at rest, using the special case of Eq. (9.34) with $P_{\text{gran}} = \delta$, and the spatial intensity

$$\tau_A^{\text{rest}}(E) = d_A^{\text{rest}} / \lambda_A(E) \quad (9.42)$$

of the Poisson process describing the resonance absorption.

The transverse offset of the photons, which are uniformly distributed over the cross section, is described by the impact parameter b (cf. Fig. 9.8) relative to the position of the sphere. There is a crucial anisotropy in the physical transmission and detection process. The transverse directions are additive for the transmission probability, since the detector does not resolve where the photon enters its window. In contrast, the survival probability of a photon is multiplicative in the longitudinal direction. This is expressed by the x -integration in the exponent of the transmission probability:

$$P_{\text{trans}}(v_S) = \frac{1}{\pi R^2} \int_0^{2\pi} d\varphi \int_0^R db b \exp \left[\frac{\phi}{d_A^{\text{rest}}} \int_0^{\sqrt{R^2 - b^2}} dx \int d\mathbf{v}_{\text{cm}} \int d\omega_{\text{rot}} \tau_A^{\text{rest}}(v_S - v_{\parallel}) P_{\text{tr}}(\mathbf{v}_{\text{cm}}, \omega_{\text{rot}}) \right] \quad (9.43)$$

with the velocity

$$v_{\parallel} = [\mathbf{v}_{\text{cm}} + \omega_{\text{rot}} \times \mathbf{r}(x, b, \varphi)]_x \quad (9.44)$$

projected on the direction of the photon wave vector (longitudinal x -direction of the experiment). Aside from the trivial φ integration, the general expression (9.43) is, admittedly, complicated according to the generality of the joint distribution P_{tr} for translation and rotation. First one should motivate an ansatz for P_{tr} . The parameters of this ansatz are then determined by several measurements with different atomic densities n_A of ^{57}Fe in the glass spheres. We remind that in the integral (9.43), τ_A^{rest} is proportional to the concentration of ^{57}Fe . The numerical inversion of (9.43) is possible, because with different ^{57}Fe concentrations the absorption length λ_A is varied. This influences the preferred subvolume inside the glass spheres for absorption. The influence of the concentration is sketched in Fig. 9.9. Since this

subvolume also depends on the rotation state, the ω_{rot} -dependence of P_{tr} is probed. We finally remark that the spatial depth up to which the velocity distribution is measured inside a very large granular sample, is easily adjusted by substituting some pure glass spheres for ^{57}Fe -enriched spheres, to adapt the transparency for the Mössbauer photons.

9.8 Conclusions

In this chapter we discussed the application of the Mössbauer effect to the steady nonequilibrium states of granular matter. It was demonstrated analytically and experimentally, that the Mössbauer spectrum is directly related to the granular velocity distribution. The typical granular velocities and the resolution of the Mössbauer effect suit naturally, for which reason the method provides easy access to the nonequilibrium velocity distribution function. The effectiveness of the method has been demonstrated with a first experiment, and an exponential velocity distribution was observed *in the volume* of fluidized granular matter. The method is sensitive to the different spatial velocity components, so that an anisotropic velocity distribution can be measured.

This opens up interesting applications. The convective motion reported in this chapter can be studied by changing the horizontal position and the height at which the beam traverses the granulate. Measurements which include the particle rotations have been pointed out, and would allow the experimental observation of correlations predicted theoretically [28].

Chapter 10

Phase Transitions and Coexistence far from Equilibrium

While the physics of equilibrium phase transitions has meanwhile reached a state of mature textbook knowledge, similar phenomena observed in systems far from thermal equilibrium are still quite elusive. In particular transitions in wet granular matter, such as soil liquefaction due to earthquakes and fluidization by vibration, are still far from being understood [160, 191, 122, 98, 114]. In this thesis, the experiment in Chap. 8 demonstrated that the fluidization transition is discontinuous and a fluid/gas transition was discovered with simulations in Chap. 4 for one dimension. This chapter unifies these results and presents the nonequilibrium transitions of a vertically agitated wet granular medium in two and three dimensions.

Starting with the fundamental phase space dynamics, it is clarified why the logarithm of the phase space volume is not a measure for entropy production in granular matter. The phase space dynamics is extended by pseudo-Liouville operators for the capillary bridges, and a derivation of continuum equations for wet granular matter is discussed. Here the results about the chaoticity of wet granular matter and the hysteretic pair correlation of previous chapters are applied.

The global phase diagram is presented, both experimentally and by simulations, and quantitative agreement is found. The phase diagrams comprises the aforementioned transitions. Five nonequilibrium steady states are shown to exist: the solid, fluid, and gas phase, as well as the coexistences of solid/gas, and fluid/gas. For the latter, the interfacial profiles are computed with the continuum model, and qualitative agreement is found. Order parameters are defined and measured numerically.

Two principal mechanism for phase transitions far from equilibrium are revealed: The *solid/fluid transition* sets in when the characteristic force of the driving overcomes the intrinsic force of the liquid bridges. This transition is controlled by the acceleration of the driving. The *fluid/gas transition* is an energy-driven transition. The balance of power is shown analytically to have a subcritical instability with the driving velocity as the control parameter. This explains why the fluid/gas transition is discontinuous and determined by the capillary energy, as is confirmed experimentally.

All nonequilibrium states are explained solely by the hysteretic formation and rupture of capillary bridges, which provide the characteristic energy scale of the system. Other details of the interaction are shown to be remarkably irrelevant, suggesting considerable universality for the reported transitions far from equilibrium.

Finally, the coalescence dynamics of fluid droplets, embedded in a gas phase, is observed. This process is shown to be very distinct from the coarsening of ‘usual’ non-dissipative fluids. The dissipative coarsening is tightly accompanied by a self-organized increase of the granular temperature, which can give rise to abrupt configuration changes.

10.1 Balance Equations

Starting from the microscopic equations of motion, this section discusses the derivation of hydrodynamic equations by truncating the BBGKY-hierarchy with the extended *hysteretic* Enskog function derived in Chap. 7. The peculiarity of wet granular matter to increase entropy without phase space contraction is explained. A clarifying comment on an open issue [156] concerning phase space contraction in inelastic gases is given.

10.1.1 The Phase Space Flow of Wet Granular Matter

The dynamics of a classical N -particle system¹, not necessarily an energy conserving one, can be cast into the form

$$\dot{\mathbf{\Gamma}}(t) = \mathbf{F}(t, \mathbf{\Gamma}) , \quad (10.1)$$

which is a non-linear first-order system of differential equations. The canonical special case of the general system (10.1) are Hamiltonian systems, whose phase space flow is generated by the vector field \mathbf{F} with

$$\mathbf{F} = \mathbf{S} \nabla_{\mathbf{\Gamma}} H . \quad (10.2)$$

For the canonical dynamics the flow field \mathbf{F} is the gradient of the Hamiltonian function H , multiplied by the matrix \mathbf{S} of the symplectic form (as introduced in Chap. 4). The dependence of a solution $\mathbf{\Gamma}(t, \mathbf{\Gamma}_0)$ on its initial value $\mathbf{\Gamma}(0, \mathbf{\Gamma}_0) = \mathbf{\Gamma}_0$ is differentiable². As we have seen in Sec. 4.6.2 the corresponding map \mathbf{M} in tangent space,

$$(\delta \mathbf{x}_0, \delta \mathbf{p}_0) \rightarrow (\delta \mathbf{x}(t), \delta \mathbf{p}(t)) = \mathbf{M}(t) (\delta \mathbf{x}_0, \delta \mathbf{p}_0) , \quad (10.3)$$

is symplectic for wet granular matter:

$$\mathbf{M}^T(t) \mathbf{S} \mathbf{M}(t) = \mathbf{S} . \quad (10.4)$$

Wet granular matter is a dissipative piecewise Hamiltonian system. (The capillary bridges can be seen as ‘Maxwell-Demons’ which switch on and off the hysteretic forces, and give rise to a time-dependent Hamiltonian.) It is most convenient to describe the discrete bridge dynamics for the ensemble, which is the subject of Sec. 10.1.2. Here we construct the continuous phase space evolution for the ensemble from the solutions $\mathbf{\Gamma}(t, \mathbf{\Gamma}_0)$ of (10.1). The initial distribution of the ensemble be f_0 , which is convoluted with the initial state $\mathbf{\Gamma}_0$ of the general solution. This gives the phase space density

$$f(t, \mathbf{\Gamma}) = \int d\mathbf{\Gamma}_0 \delta(\mathbf{\Gamma}(t, \mathbf{\Gamma}_0) - \mathbf{\Gamma}) f_0(\mathbf{\Gamma}_0) =: (\hat{U}^{(t)} f_0) (\mathbf{\Gamma}) \quad (10.5)$$

at any later time t . Differentiating (10.5) with respect to time and using (10.1) yields

$$\partial_t f + \text{div} (\mathbf{F} f) = 0 . \quad (10.6)$$

This is the continuity equation in phase space. As with every classical probability current, from the continuity equation (10.6) follows that the phase space flow conserves the L^1 norm: $\int f(t, \mathbf{\Gamma}) d\mathbf{\Gamma} \equiv 1$ for all times t . In the special case of a Hamiltonian system (10.2), Eq. (10.6) reduces to the Liouville equation $\partial_t f + \{f, H\} = 0$. The conservation of the symplectic structure of phase space (10.4) by the dissipative liquid bridge interaction has the following two consequences.

¹Physically, collisions are differentiable w.r.t. time, albeit they may be approximated as discontinuity in phase space to simplify simulations. Moreover, the system (10.1) includes the phase space evolution $\mathbf{\Gamma} = (\mathbf{x}, \mathbf{p})$ of wet granular matter with discontinuous and finite forces. When we come to simulations, we will apply both time- and event-driven methods in this chapter.

²The tangent space dynamics is well-defined also for temporal discontinuities, such as instantaneous collisions or bridge rupture events.

Conservation of Phase Space Volume and Entropy Production

Entropy production is in the context of dynamical systems³ identified with the logarithmic rate at which phase space contracts [76, 41, 118, 75, 89] according to the Boltzmann formula for entropy⁴. Dry granulates modeled by inelastic collisions reduce their phase space volume in every collision. However, for such a dry model system with velocity-independent restitution coefficient (as discussed in Chap. 3) numerical results [156] showed no linear relation between dissipation (in the sense of energy loss) and the phase space contraction rate. The relation was found in simulations [156] to be quadratic. Since this quadratic relation was pointed out to be an open question in [156], it is briefly remarked that the analytic explanation for the quadratic relation between dissipation power and phase space contraction rate, observed numerically in [156], is as follows. The dissipation power is proportional to $\varepsilon^2 T f_{\text{coll}}(T)$ in dry granular matter with the restitution coefficient ε , while phase space shrinks linearly in the momentum direction according to the collisions: $d \ln \det M / dt = \varepsilon f_{\text{coll}}(T)$. Since the temperature was kept constant by a Gaussian thermostat in [156], the quadratic relation of dissipation power and phase space contraction was observed as ε was varied.

With wet granular matter according to the capillary model we have a striking counter example to the traditional expectation of a linear relation: *The hysteric liquid bridge interaction gives rise to well defined dissipation, while at the same time the phase space volume is exactly conserved.*

The conservation of phase space volume follows⁵ from the determinant of Eq. (10.4),

$$\det M(t) \equiv 1 , \quad (10.7)$$

so that a neighborhood of systems in phase space may be strongly deformed by the time evolution, but its volume remains constant. For the continuous dynamics (10.1), phase space conservation is equivalent to⁶

$$\operatorname{div} \mathbf{F} = 0 , \quad (10.8)$$

i.e. the phase space flow is incompressible. Therefore the traditional term $\dot{S}_{\text{flow}} = -\operatorname{div} \mathbf{F}$ in the general expression (5.61) for entropy production is absent in wet granular matter, and entropy production is exclusively due to the rupture and binding events⁷ (described by the terms in the second line of Eq. (5.61)).

³Systems which use a Gaussian thermostats thermostat to reach a steady state under an external driving, such as an electric field acting on a Lorentz gas, are the classical examples for phase space contraction. In such systems the phase space contraction is due to the action of the thermostat.

⁴ $\dot{S} = -\operatorname{div} \mathbf{F}$ follows also as the special case of formula (5.61) in the absence of capillary bridges.

⁵Eq. (10.4) implies $|\det M(t)| = 1$, and it is always $\det M > 0$.

⁶The tangent space dynamics follows from differentiating the solution $\Gamma(t, \Gamma_0)$ with respect to the initial state Γ_0 under usage of the evolution Eq. (10.1):

$$\dot{M} = (\nabla \otimes \mathbf{F}) \circ M ,$$

where the formal solution for the initial condition $M(0) = \mathbf{I}$ is

$$M(t) = T_t e^{\int_0^t dt' (\nabla \otimes \mathbf{F}(t', \Gamma))} .$$

The symbols \circ and \otimes stand for matrix multiplication and the tensor product respectively. The time ordering operator T_t has to be applied if the matrices $\nabla \otimes \mathbf{F}(t, \Gamma)$ do not commute for different times t . Taking the determinant, the time ordering operator drops out by virtue of the determinant multiplication theorem, $\det(\mathbf{A} \circ \mathbf{B}) = \det(\mathbf{A}) \det(\mathbf{B})$, yielding

$$\det M = e^{\operatorname{tr}(\nabla \otimes \mathbf{F})} = e^{\operatorname{div} \mathbf{F}} ,$$

so that (10.7) is equivalent to (10.8).

⁷Here we think for example of the freely cooling system in Chap. 6.

Unitarity of the Evolution in Phase Space

Furthermore, the time evolution of the phase space distribution, $f(t, \mathbf{\Gamma}) = \hat{U}^{(t)} f_0(\mathbf{\Gamma})$, is unitary, $\hat{U} = \hat{U}^\dagger$, because we can pull \mathbf{F} out of the div-operator in (10.6) by virtue of Eq. (10.8), which allows us to rewrite the ensemble evolution as

$$\partial_t f = i \hat{\mathcal{L}}_{\text{flow}}(t, \mathbf{\Gamma}) f, \quad (10.9)$$

with the Liouville operator $\hat{\mathcal{L}}_{\text{flow}}(t, \mathbf{\Gamma}) = i \mathbf{F}(t, \mathbf{\Gamma}) \circ \nabla$. The evolution operator

$$\hat{U}^{(t)} = \mathbb{T}_t e^{i \int_0^t dt' \hat{\mathcal{L}}_{\text{flow}}(t', \mathbf{\Gamma})}, \quad (10.10)$$

for the phase space distribution is unitary with the Hermitian⁸ Liouville operator in the exponent⁹.

10.1.2 The Pseudo-Liouville Operator for the Hysteretic Bridge Dynamics

The state $(\mathbf{\Gamma}, \mathbf{b}) = ((\mathbf{x}, \mathbf{p}), \mathbf{b})$ of wet granular matter is extended by the liquid bridge status $\mathbf{b} = (\dots, b_{ij}, \dots)$ for all pairs (i, j) of particles (cf. 5.8). The mean capillary coordination is $K = 2|\mathbf{b}|/N = 2 \sum_{i < j} b_{ij}/N$. The switching of the binary status of the capillary bridges is elegantly described by an additional term, $\hat{\mathcal{L}}_{cb}$, in the pseudo-Liouville operator:

$$\partial_t f = i \hat{\mathcal{L}} f = \left(i \hat{\mathcal{L}}_{\text{flow}} + i \hat{\mathcal{L}}_{cb} \right) f. \quad (10.11)$$

The explicit form of the capillary operator is

$$\hat{\mathcal{L}}_{cb} = \sum_{i < j} \left[\hat{\mathcal{L}}_{ij, \text{bind}} + \hat{\mathcal{L}}_{ij, \text{rupt}} \right], \quad (10.12)$$

wherein the bridge formation between particle i and j is triggered by

$$i \hat{\mathcal{L}}_{ij, \text{bind}} = \delta_{b_{ij}, 0} |(\mathbf{v}_{ij}, \tilde{\mathbf{r}}_{ij})| \theta(-\mathbf{v}_{ij}, \tilde{\mathbf{r}}_{ij}) \delta(r_{ij} - d_i/2 - d_j/2) \left(\hat{b}_{ij}^{(+)} - 1 \right). \quad (10.13)$$

(The superscript \sim denotes the unit vector, and (\cdot, \cdot) is the scalar product.) The bridge is broken by

$$i \hat{\mathcal{L}}_{ij, \text{rupt}} = \delta_{b_{ij}, 1} |(\mathbf{v}_{ij}, \tilde{\mathbf{r}}_{ij})| \theta(\mathbf{v}_{ij}, \tilde{\mathbf{r}}_{ij}) \delta(r_{ij} - d_i/2 - d_j/2 - s_{\text{crit}}) \left(\hat{b}_{ij}^{(-)} - 1 \right). \quad (10.14)$$

The creation and annihilation operators for capillary bridges, $\hat{b}_{ij}^{(\pm)}$, are defined by the action:

$$b_{ij}^{(\pm)} f \left(t, \mathbf{\Gamma}, (\dots, \begin{matrix} 0 \\ 1 \end{matrix}, \dots) \right) = f \left(t, \mathbf{\Gamma}, (\dots, \begin{matrix} 1 \\ 0 \end{matrix}, \dots) \right). \quad (10.15)$$

⁸With one partial integration, we readily see:

$$\langle g | \hat{\mathcal{L}}_{\text{flow}}^\dagger | h \rangle = -i \langle g | \overleftarrow{\nabla} \circ \mathbf{F}(t, \mathbf{\Gamma}) | h \rangle = i \langle g | \mathbf{F}(t, \mathbf{\Gamma}) \circ \overrightarrow{\nabla} + \text{div} \mathbf{F}(t, \mathbf{\Gamma}) | h \rangle = \langle g | \hat{\mathcal{L}}_{\text{flow}} | h \rangle.$$

⁹If one wants to recover unitarity for inelastic granular gases [228, 121, 244, 27], the author suggests to introduce an adapted scalar product $\langle g | h \rangle = \int \bar{g} h \gamma d\mathbf{\Gamma}$ with a positive weighting function γ . To compensate for the phase space contraction, $\text{div} \mathbf{F} < 0$, the weighting function γ has to fulfill the equation $\text{div} \mathbf{F} = -\mathbf{F} \circ \nabla \ln \gamma$. The existence of a solution γ is not obvious.

10.1.3 Projected Phase Space Density

As the first step towards a macroscopic or hydrodynamic description of wet granular matter in terms of local granular temperature, density, pressure, and flow in space, we are interested in the spatial density and velocity of single particles in the sample, instead of the detailed phase space distribution. The distribution of a single particle (or a pair of particles) derives from the full distribution, $f^{(N)} = f$, by integrating out $N - 1$ (respectively $N - 2$) particles. This is a projection of the high-dimensional N -particle phase space density, $f^{(N)}$, onto the one- and two-particle distribution¹⁰ (denoted by superscript indices):

$$f^{(N)}(t, \mathbf{\Gamma}, \mathbf{b}) \rightarrow \begin{cases} f^{(1)}(t, \mathbf{\Gamma}_1) \\ f^{(2)}(t, \mathbf{\Gamma}_1, \mathbf{\Gamma}_2, b_{12}) \\ \vdots \end{cases}, \quad (10.16)$$

Integrating the left- and right-hand side of the ensemble evolution (10.11) over the particles $2, \dots, N$, yields the evolution of the single particle density¹¹

$$\begin{aligned} & \left(\partial_t + \frac{\mathbf{P}_1}{m} \circ \nabla_{\mathbf{x}_1} + \mathbf{F}_{\text{ext}} \circ \nabla_{\mathbf{p}_1} \right) f^{(1)}(t, \mathbf{\Gamma}_1) \\ & + \sum_{b_{12}=0,1} \int d\mathbf{\Gamma}_2 \mathbf{F}_{\text{int}}(s_{12}, b_{12}) \circ \nabla_{\mathbf{p}_1} f^{(2)}(t, \mathbf{\Gamma}_1, \mathbf{\Gamma}_2, b_{12}) = 0. \end{aligned} \quad (10.17)$$

This equation is physically obvious: The first term represents the interactionless motion of a particle, which may be subject to some external force, \mathbf{F}_{ext} , typically gravity. The second term in (10.17) takes pair interaction into account, which is why it depends on the distribution $f^{(2)}$ for pairs of particles¹². The particle separation¹³ is denoted by s_{12} as the argument of the pair force \mathbf{F}_{int} . The evolution equation (10.17) for the one-particle distribution $f^{(1)}$ does not depend on higher dimensional distribution functions ($f^{(3)}, \dots$) provided 3- and many-body

¹⁰The projection of the detailed distribution $f^{(N)}(\mathbf{\Gamma})$ onto the N' -particle level is given by the expectation value of N' δ -distributions:

$$f^{(N')}(t, \mathbf{\Gamma}_1, \dots, \mathbf{\Gamma}_{N'}, \mathbf{b}') = \binom{N'}{N} \sum_{i_1 < i_2 < \dots} \left\langle \delta_{\mathbf{b}', \mathbf{b}'_{i'}} \delta(\mathbf{\Gamma}_1 - \mathbf{\Gamma}_{i_1}^*) \dots \delta(\mathbf{\Gamma}_{N'} - \mathbf{\Gamma}_{i_{N'}}^*) \right\rangle_{f^{(N)}}$$

with $\langle \dots \rangle_{f^{(N)}} := \sum_{\mathbf{b}^*} \int f^{(N)}(t, \mathbf{\Gamma}^*, \mathbf{b}^*) \dots d\mathbf{\Gamma}^*$, the binomial for the Gibbs factor, $\mathbf{b}' = (b'_{12}, b'_{13}, \dots)$ being the bridge status on the left-hand side, and the permutated status $\mathbf{b}'_{i'} = (b'_{i_1, i_2}, b'_{i_1, i_3}, \dots)$ which is summed on the right-hand side.

¹¹Eq. (10.17) for the one-particle distribution function is the first equation out of a series of N equations forming the BBGKY-hierarchy (Bogoliubov (1937), Born (1949), Green (1949), Kirkwood (1935) and Yvon (1935)). The full hierarchy is equivalent to the high-dimensional evolution (10.11). Using the one-particle Liouville operator $\hat{\mathcal{L}}^{(1)}$ to abbreviate the first term in (10.17), we have

$$(\partial_t - i\hat{\mathcal{L}}^{(1)})f^{(1)}(t, \mathbf{\Gamma}_1) + \sum_{b_{12}} \int d\mathbf{\Gamma}_2 \mathbf{F}_{2 \rightarrow 1} \circ \nabla_{\mathbf{p}_1} f^{(2)}(t, \mathbf{\Gamma}_1, \mathbf{\Gamma}_2, b_{12}) = 0.$$

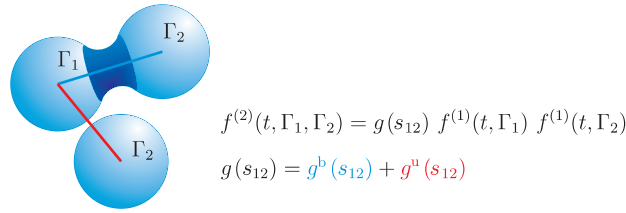
We write $\mathbf{F}_{2 \rightarrow 1} = \mathbf{F}_{\text{int}}$ for the two-body force acting on one particle. The N' -particle equation of the BBGKY-hierarchy has the analogous form,

$$(\partial_t - i\hat{\mathcal{L}}^{(n)})f^{(N')}(t, \mathbf{\Gamma}_1, \dots, \mathbf{\Gamma}_n, \mathbf{b}') + \sum \int d\mathbf{\Gamma}_{n+1} \mathbf{F}_{n+1 \rightarrow n} \circ \nabla_{(\mathbf{p}_1, \dots, \mathbf{p}_n)} f^{(N'+1)}(t, \mathbf{\Gamma}_1, \dots, \mathbf{\Gamma}_{n+1}, \mathbf{b}'') = 0$$

with $\mathbf{b}'' = (\mathbf{b}', b_{N'+1,1}, \dots, b_{N'+1, N'})$.

¹²In the limit case of hard-core potentials Eq. (10.17) reduces to the Boltzmann equation as the second term becomes the collision integral.

¹³As done throughout this thesis, it is appropriate to use the particle separation s instead of the center distance r , since s is the relevant length for the capillary bonds.



$$f^{(2)}(t, \Gamma_1, \Gamma_2) = g(s_{12}) f^{(1)}(t, \Gamma_1) f^{(1)}(t, \Gamma_2)$$

$$g(s_{12}) = g^b(s_{12}) + g^u(s_{12})$$

Figure 10.1: The contributions from neighbors with and without bridges to the two-particle distribution $f^{(2)}(t, \Gamma_1, \Gamma_2) = f^{(2)}(t, \Gamma_1, \Gamma_2, 0) + f^{(2)}(t, \Gamma_1, \Gamma_2, 1)$ give rise to two different pair correlation functions.

forces are absent. This is fulfilled because the amount of wetting liquid which we add to the granulate does not allow for objects more complex than ‘binary’ liquid bridges. Fluorescent microscopy and tomography studies of wet granular matter at rest show that the formation of capillary objects connecting three particles sets in when the local volume fraction of the liquid phase exceeds $W = 2\%$ w.r.t. the total jammed volume¹⁴ [197]. Three-particle interaction will be further suppressed in the fluidized or gas state. The experiments and simulations that will be discussed in this chapter were done with liquid volume fractions between $W = 0.15\%$ and $W = 1.0\%$. This is why there is no $f^{(3)}$ -term in (10.17).

10.1.4 Hysteretic Enskog Correlation for a Closed Evolution Equation

The second step to a continuum description uses the hypothesis of ‘molecular chaos’, which is the assumption that the initial velocities of colliding particles are independent,

$$f^{(2)}(t, \Gamma_1, \Gamma_2, b_{12}) = g(s_{12}, b_{12}) f^{(1)}(t, \Gamma_1) f^{(1)}(\Gamma_2) . \quad (10.18)$$

This classical assumption is frequently used for hard sphere fluids and granular systems (for instance p.134 in [27]). At the present stage in this thesis, we are in the beneficial situation that the computation of the Kolmogorov-Sinai entropy¹⁵ in Chap. 5 has shown that the time scale for correlations to be smeared out by chaos is indeed set by the collision frequency: the Kolmogorov-Sinai entropy h_{KS} was found to be greater than the particle collision frequency multiplied by the number of particles.

Furthermore, Chap. 7 was devoted to the computation of the isotropic pair correlation function¹⁶ $g(s_{12}, b_{12})$ by taking the bond status and the hysteretic interaction into account. Therewith, we have all information at hand to insert expression (10.18) for the pair distribution into the evolution equation (10.17), to arrive at a closed equation for the one-particle

¹⁴The range of the liquid content W for the capillary pair interaction is discussed in the introduction to the Equation of State in Chap. 7.

¹⁵The computation focused on the positive Lyapunov exponents in velocity space, which correlations are here considered.

¹⁶The hysteretic pair correlation derived for the Equation of State is actually more detailed: the sign of the radial relative velocity is a further argument of the function. This detailed correlation is necessary to compute binding and rupture frequencies.

distribution $f^{(1)}$:

$$\begin{aligned} & \left(\partial_t + \frac{\mathbf{p}_1}{m} \circ \nabla_{\mathbf{x}_1} \right) f^{(1)}(t, \mathbf{x}_1, \mathbf{p}_1) \\ & + \left(\mathbf{F}_{\text{ext}}(\mathbf{x}_1) + n(t, \mathbf{x}_1) \sum_{b_{12}=0,1} \int \text{dvol}(\mathbf{x}_2) \mathbf{F}_{\text{int}}(s_{12}, b_{12}) g(s_{12}, b_{12}) \right) \\ & \circ \nabla_{\mathbf{p}_1} f^{(1)}(t, \mathbf{x}_1, \mathbf{p}_1) = 0 . \end{aligned} \quad (10.19)$$

The hysteretic correlation function

$$g(s_{12}, b_{12}) = \delta_{b_{12},0} g^u(s_{12}) + \delta_{b_{12},1} g^b(s_{12}) \quad (10.20)$$

generalizes the Enskog factor, which accounts in the dry limiting case for excluded volume effects. We are concerned with a function over the capillary interaction length in wet granular matter, instead of the factor of the contact value. The local particle density

$$n(t, \mathbf{r}) = \int f^{(1)}(t, \mathbf{r}, \mathbf{v}) \, \text{d}\mathbf{v} \quad (10.21)$$

can be expressed equivalently by the dimensionless occupied volume fraction ϕ , and the functions $g^{u/b}(s_{12})$ depend on ϕ and the granular temperature T . The computation of the pair correlation in Chap. 7 covered the full density range.

10.1.5 The Hydrodynamic Fields

Local hydrodynamic fields follow by averaging over the particle velocities,

$$\langle \dots \rangle_{\mathbf{v}}(t, \mathbf{r}) := \frac{\int \text{d}\mathbf{v} f^{(1)}(t, \mathbf{r}, \mathbf{v}) \dots}{n(t, \mathbf{r})} . \quad (10.22)$$

Therewith, the nonequilibrium distribution function f defines the local flow \mathbf{u} and the local (granular) temperature T :

$$\mathbf{u}(t, \mathbf{r}) = \langle \mathbf{v} \rangle_{\mathbf{v}}(t, \mathbf{r}) \quad (10.23)$$

$$T(t, \mathbf{r}) = \frac{m}{D} \langle (\mathbf{v} - \mathbf{u})^2 \rangle_{\mathbf{v}}(t, \mathbf{r}) . \quad (10.24)$$

The local energy density $\epsilon(t, \mathbf{r})$ is the sum of the kinetic component, $\epsilon(t, \mathbf{r}) = n(t, \mathbf{r}) D T(t, \mathbf{r})/2$, and the capillary energy density

$$\epsilon_{\text{cb}}(t, \mathbf{r}) = \frac{n^2(t, \mathbf{r})}{2} F_{\text{cb}} \int_{0 < s < s_{\text{crit}}} s g^b(s) \, \text{dvol}(s) . \quad (10.25)$$

The detailed pair correlation functions g^u and g^b (which differentiate neighbors with and without capillary bond) have been derived in the Eqs. (7.58) and (7.59) in Chap. 7. There we computed analytically as well the isotropic stress tensor $\underline{\underline{\sigma}} = \underline{\underline{\sigma}}^{\text{kin}} + \underline{\underline{\sigma}}^{\text{force}} = -P\mathbb{I}$ in the absence of shear forces in Eq. (7.74).

The balance equations for mass, momentum, and energy follow from the evolution equation (10.17) of $f^{(1)}$ (cf. e.g. [26] or pp. 168-174 in [27]):

$$\text{mass} \quad \partial_t n + \text{div}(\mathbf{u}n) = 0 \quad (10.26)$$

$$\text{momentum} \quad \partial_t \mathbf{u} + \mathbf{u} \circ \nabla_{\mathbf{r}} \mathbf{u} = \frac{\text{div} \underline{\underline{\sigma}}}{nm} + \frac{\mathbf{F}_{\text{ext}}}{m} \quad (10.27)$$

$$\begin{aligned} \text{energy} \quad & \frac{Dn}{2} (\partial_t T + \mathbf{u} \circ \nabla_{\mathbf{r}} T) + \text{div} \mathbf{q} + (\partial_t + \mathbf{u} \circ \nabla_{\mathbf{r}}) \epsilon_{\text{cb}} \\ & = \underline{\underline{\sigma}}^{\text{kin}} : \nabla_{\mathbf{r}} \mathbf{u} + P_{\text{inj}} - P_{\text{diss}} \end{aligned} \quad (10.28)$$

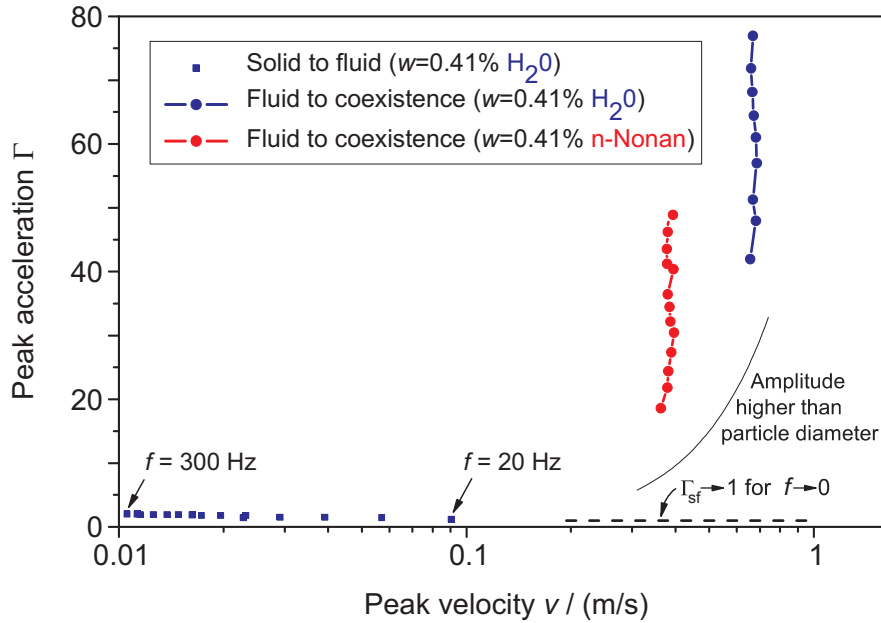


Figure 10.2: Unscaled experimental data. To reveal the influence of the surface tension of the wetting liquid, the author measured the onset of the coexistence with water and n-nonane as the wetting liquids. First, we see that the phase segregation is a vertical line corresponding to a defined energy scale $mv^2/2$ with the wall velocity v . Second, the transition is shifted to higher velocities as the surface tension is increased.

In the balance of energy (10.28) the bridge energy has been added. The colon denotes the product between second rank tensors (i.e. contracted twice), and the term where it appears describes shear induced heat.

10.2 Stationary States of Wet Granular Matter

The case of free cooling on the mean-field level¹⁷ was studied in Chap. 6:

$$\begin{aligned} \text{momentum:} & \quad \text{homogeneous pressure} \\ \text{energy:} & \quad \frac{Dn}{2} \partial_t T + \partial_t \epsilon_{cb} = -P_{\text{diss}} . \end{aligned}$$

In this chapter we are interested in the steady nonequilibrium states, so that all terms with time derivatives drop out in (10.26)-(10.28). Motivated by the numerical observation of the fluid/gas transition in 4.5, we pursue this prediction of a discontinuous nonequilibrium transition experimentally, as reported here. Simulation results are presented in the Secs. 10.3-10.5 The continuum model will be solved in 10.6 to follow the experimental setup.

As a well-defined granular system, spherical glass beads with 6% polydispersity in diameter were chosen. Different wetting liquids were added to the dry particles and well mixed. A wide cylindrical container (glass petri dish) was used to hold the granular material in order to eliminate side wall effects. In this geometry, energy is injected by the bottom and top plate and not by the tangential motion of side walls, which are effectively shifted ‘to infinity’. This

¹⁷The analytic model for the free cooling distinguished the gap lengths and bridge lengths as the only spatial dependencies.

emulates the driving by the two end points in 4.5, yet here we have the additional lateral dimensions. When the container was set in oscillatory vertical motion, $z(t) = A \cos(\omega t)$, the granulate was driven into a nonequilibrium state. The control parameter is the dimensionless peak acceleration, $\Gamma = A\omega^2/g$, where g is the acceleration. For Γ below and around one, the grains remained fixed at all frequencies, representing a solid condensed state. Fluidization occurs at a threshold acceleration, Γ_{sf} , which manifests itself by the onset of a mild movement of the grains, as revealed by direct visual inspection. Various wetting liquids (contact angle below 10 degrees) were used as additives. As it was shown before in [114], the attractive interaction exerted by capillary bridges between spheres gives rise to an increase of Γ_{sf} , which is proportional to the capillary force at contact, $F_0 = 2\pi R\gamma \cos\theta$. R is the radius of the grains, γ is the surface tension of the liquid, and θ is the contact angle [237, 196]. Confirming the measurements in Chap. 8 and [196] of the fluidization point in very different driving geometries, Γ_{sf} was found to be largely independent of frequency, as long as the latter was not too small. This is shown in Fig. 10.2 by the square data points, which form a horizontal line, with the highest and lowest frequency indicated.

At higher particle velocities, however, a completely different behavior was observed. When the amplitude was increased above a critical value, a situation as shown in Fig. 10.3A emerges. One clearly observes phase separation into a dense ‘fluid’ phase and a ‘gaseous’ bubble co-existing with it. The bubble is found to wander around in the container, which shows that this phenomenon is not driven by a lateral inhomogeneity in the excitation amplitude, but is intrinsic to the system under study. The color code in Fig. 10.3B, which was obtained by optical autocorrelation of the images, shows the large difference in the ‘granular temperature’ (i.e. 2/3 of the average kinetic energy of the grains) between the gaseous phase and the dense phase. If the amplitude is further increased, a homogeneous gas phase emerges which fills the container homogeneously.

It is enlightening to plot the loci of the observed transitions in the plane spanned by the peak acceleration, Γ , and the peak velocity, $v = A\omega$, of the container walls (bottom and lid). The container velocity v can be envisaged to set the scale for the kinetic energy injected into the system, and serves as a second control parameter. The experimental result is shown in Fig. 10.2. While the transition from the solid to the fluid phase is described by the almost *horizontal* sequence of blue squares, we see that the onset of the coexistence falls on *vertical* lines, depending on the wetting liquid chosen. The phase separation transition is therefore determined by a defined velocity v or energy $\frac{m}{2}v^2$ (where m is the mass of an individual glass bead). This is in clear contrast to the critical acceleration Γ_{sf} which is assigned to the fluidization transition. It is remarked that all data are taken for driving amplitudes well below the particle size, so that particle motion remains stochastic and couples closely to the velocity scale set by driving, instead of the ballistic decoupling which sets in at high amplitudes (cf. lower right corner in Fig. 10.2).

We scale the container velocity v in Fig. 10.4 with respect to the characteristic velocity at which the rupture energy of the liquid capillary bridges, $E_{\text{cb}} \propto R^2\gamma\sqrt{w}$ (cf. Eq. (3.10) in Chap. 3 and [144, 158, 203, 114]), equals the kinetic energy scale. w denotes the liquid content of the sample defined as the volume of the added liquid divided by the total volume of all glass spheres¹⁸. We thus used the quantity $v^* = v\sqrt{m/2E_{\text{cb}}}$ as the abscissa. The perfect matching of the data obtained for water (closed) and n-nonane (open), the surface tension of which is by a factor of three smaller¹⁹ than that of water, strongly suggests that

¹⁸In contrast to the capital W which is defined in this thesis and the literature on wet granular matter as the liquid volume divided by the total volume of the *jammed granulate*

¹⁹The surface tension of pure water at room temperature is 71.99 mN/m, and 22.85 mN/m for nonane, so that these significantly differ. In contrast their (shear) viscosities are low, very similar ($\eta \approx 0.8$ mN s/m²), and have been shown in Chap. 3 not to influence the wet granular dynamics.

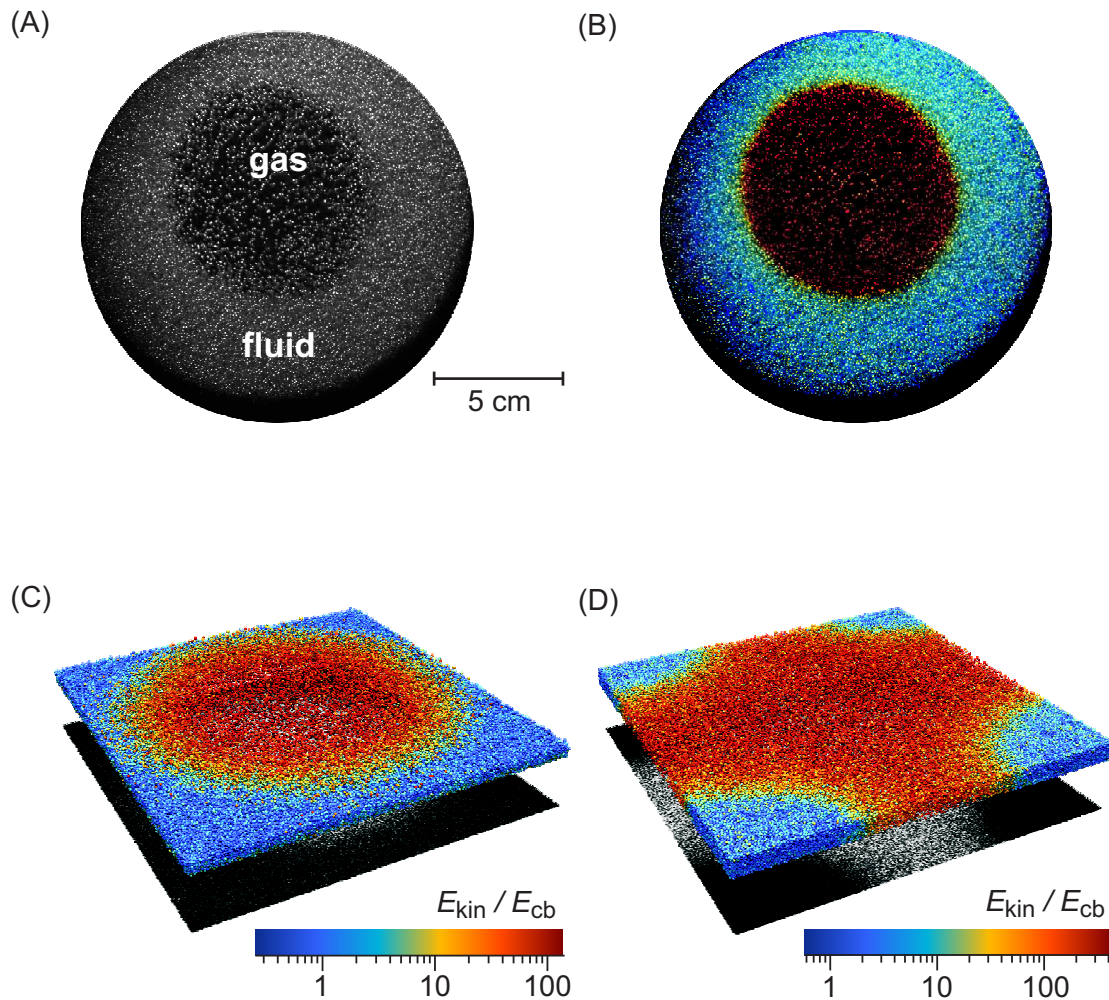


Figure 10.3: Gas bubble nucleation. (A) Top view of the experimental setup at high excitation. In the middle of the sample, a large gas bubble is clearly visible, while the outer part is filled with a condensed fluidized phase. (B) Same snapshot as in (A) but colored using temporal autocorrelation of the digital image. The color scale extends from blue (slow movement) to red (fast movement). (C) and (D) show snapshots of event-driven simulations in 3D, at early (C) and late (D) stages. The color codes the kinetic energy of the individual grains, similar to (B). The shadow accounts for the areal density of the particles.

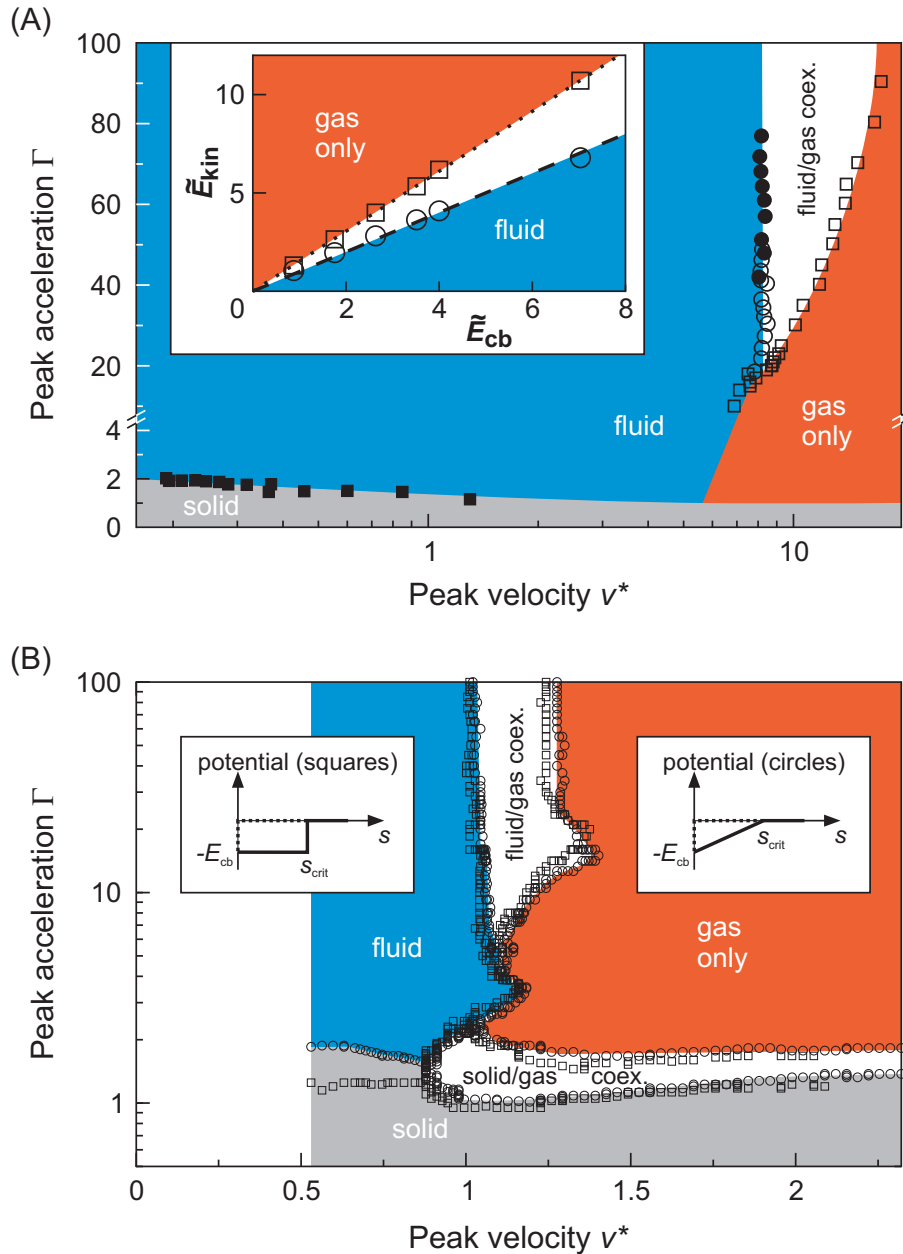


Figure 10.4: Phase diagram of wet granular matter far from equilibrium. (A) Experimental phase diagram of the system ($R = 850 \mu\text{m}$, $w = 0.41\%$, the spheres occupy one third of the container volume). The lower right is not accessible to our apparatus. The data for water (closed, $E_{cb} = 21 \text{ nJ}$) and nonane (open, $E_{cb} = 6.6 \text{ nJ}$) collapse when scaled with the capillary energy E_{cb} , which is proportional to the surface tension of the wetting liquid (Measurements of the single bridge energies are described in Chap. 3). The inset shows the dependence on the surface tension as a result from direct simulations. We observe that the transition lines scale precisely with the bridge energy E_{cb} . A best fit of the factors of proportionality yields $\frac{m}{2}v_c^2 = (1.52 \pm 0.02)E_{cb}$ for the transition to the pure gas (squares) and $\frac{m}{2}v_c^2 = (1.00 \pm 0.09)E_{cb}$ for the fluid/gas coexistence (circles). (B) Phase diagram out of simulations with 1200 particles in 2D. The horizontal boundary of the solid phase is clearly obtained, as well as the vertical fluid/gas boundaries which are also seen in the experiment. The insets show the hysteretic interaction ‘potentials’ chosen (dotted: approach; solid: retract).

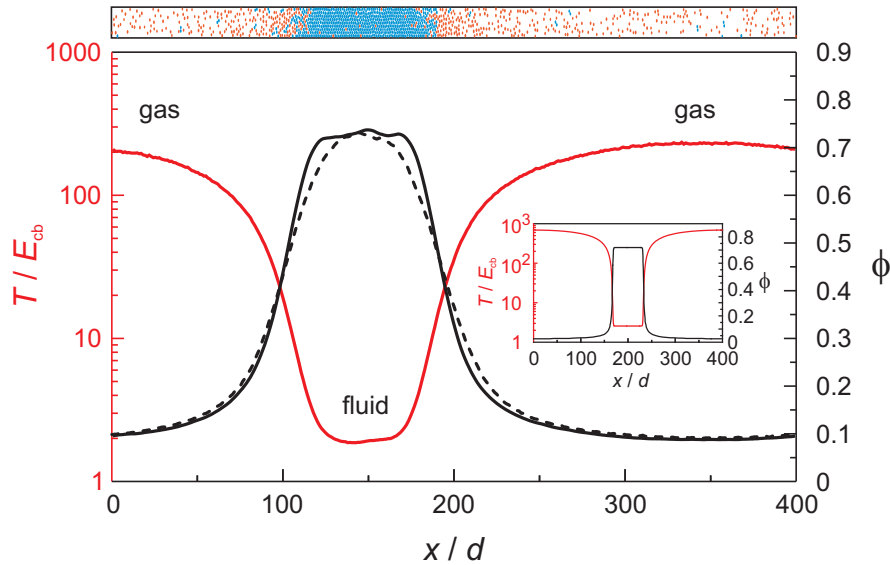


Figure 10.5: Snapshot of molecular dynamics type simulation of 1200 particles at parameters where fluid/gas coexistence occurs (box at the top). Blue grains have at least one liquid bridge, red grains have none. Main panel: Plot of the granular temperature (red curve) and the packing density (black curves) on the same scale as the simulation box above. The temperature varies laterally over two orders of magnitude, being high in the gas, but very low within the fluid plug. The density profile is also shown for event-driven simulations (dashed black curve). The inset shows the solution of the continuum model.

our scaling of v with respect to the rupture energy is appropriate. Figure 10.4 furthermore contains the transition line where the coexistence (white) terminates into the homogeneous gas (red). Solid states are indicated in gray and the domain of the fluid phase is shown in blue. In short, the solid/fluid transition is determined by the capillary bridge *force*, while the fluid/gas transition is determined by the capillary bridge *energy*.

10.3 Simulated Phase Diagram and the Hysteretic Interaction

In order to demonstrate the essential role of the capillary bridges, we perform molecular dynamics type simulations with ideally spherical, frictionless particles²⁰. The attractive pairwise *hysteretic* interaction ‘potential’²¹ illustrated in the right-hand inset of Fig. 10.4B models the capillary bridges (dotted: approach; solid: retract). A gravitational force acting in the vertical direction is included. The liquid content *per grain* was assumed to be the same everywhere. This is justified from the experimental observation in Chap. 3 that the liquid inside the capillary bridge redistributes quite evenly on each sphere after the rupture of the bridge. At the top of Fig. 10.5, a snapshot of a two-dimensional stationary state is shown. It is clearly seen that the simulation produces a dense plug as well as a gaseous region, which are in coexistence with each other. In the main panel of Fig. 10.5, the density as well as the granular temperature T in units of the rupture energy are plotted as a function of the lateral coordinate, on the same

²⁰Particle collisions are computed according to the Hertz force, Eq. (3.1), with the measured Young modulus of glass spheres inserted. Since the contact time and the time scale set by capillary oscillations differ by more than five orders of magnitude, the integration algorithm adapts the time-steps.

²¹The linear ‘potential’ is what is referred to as the Minimal Capillary model [114] throughout this thesis, as introduced in Chap. 3.

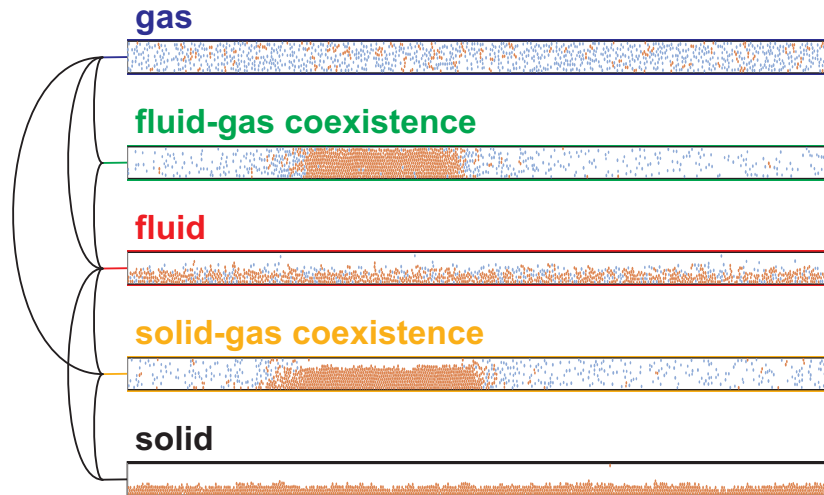


Figure 10.6: The five stationary states of wet granular matter under vertical agitation. Snap shots of 2D simulation (using the time-driven method) are shown. Particles without capillary bonds are shown in blue, those with at least one capillary bond (either shared with another particle, or to the wall) are given a red color. The lines to the left indicate the topology in the isochoric phase diagram for direct transitions. The two states of coexistence (fluid/gas and solid/gas) do not share a transition line in the plane spanned by the external driving parameters.

scale as the simulation box above. The granular temperature is found to vary over two orders of magnitude. This clearly demonstrates that the observed phenomenon is by no means akin to coexistence between thermodynamic phases, but is an intrinsically nonequilibrium state.

Figure 10.4B shows the phase diagram as obtained from the simulations, in the same plane as the experimental results in Fig. 10.4A, but on log/linear scale to better reveal the details. We clearly see the horizontal line separating the solid from the fluid phase, augmented by a solid/gas coexistence at higher v . This peculiar phase is related to the strength of the bridge force, which is in simulations and the experiment four times higher than the gravitational force F_g of a single particle. With the strength of the capillary force, the particles of the solid phase are virtually glued to the bottom plate. Snapshots of the five different stationary states of wet granular matter under vertical driving are collected in Fig. 10.6.

As found in the experiments, the vertical transition line delimiting the fluid state is very prominent, showing to its right the coexistence of a gas phase and a granular fluid. The coexistence region terminates abruptly at some larger critical velocity, giving way to a homogeneous gas-like state. In the corresponding transition line, a bulge is located where the excitation amplitude A equals the rupture length s_{crit} of the capillary bridges. It may be qualitatively understood that this leads to some extra dissipation at the container walls, and therefore shifts the transition to higher driving velocities. Unfortunately, scaling the simulation parameters according to the experimental conditions²² reveals that this bulge is slightly out of the range accessible to our experimental setup. It could therefore not be observed experimentally so far.

²²The position of the bulge is located at the intersection of the coexistence/gas transition line and the curve defined by the equivalence of the driving amplitude A and the rupture length s_{crit} . The latter condition, $A = s_c$ is a parabola in the Γ - v -plane. Since the coexistence/gas transition is shifted to higher driving velocities by the inelastic collisions, the bulge is shifted to accelerations beyond 100 g in the experimental system, which are unreachable for our equipment. Note the simulated phase diagram is for two dimensions.

In the inset of Fig. 10.4A, we replotted the coexistence region in the plane spanned by the ‘wall temperature’ and the capillary bridge energy. We rescaled them as $\tilde{E}_{\text{kin}} = \frac{1}{2}mv^2/(F_g s_{\text{crit}}) = v^2/(2gs_{\text{crit}})$ and $\tilde{E}_{\text{cb}} = E_{\text{cb}}/(F_g s_{\text{crit}})$, respectively. The accurate linear scaling of the transition points shows that this effect depends exclusively on the capillary interaction, while the gravitational energy scale naturally separates out, in contrast to dry granulates [103]. The only marked difference between the simulation and the experiment is that the energy-driven transition to coexistence occurs at a scaled velocity around one in the former, but around eight in the latter. This can be shown to be due to inelasticity of the glass beads used in the experiments. Their restitution coefficient, as determined experimentally for particle-wall collisions, was found to be $\varepsilon \approx 0.90 \pm 0.01$. Including this inelasticity ($\varepsilon < 1$) in the simulations, we observed that the transition lines are shifted to higher driving velocities by a factor of 2.7 in 2D, and a factor of 5.5 in 3D. Qualitatively, the phase diagram remained unchanged. In view of the neglect of tangential friction in simulations, the agreement between the simulation and the measurements is remarkable. In addition, the characteristic Y-shape at the coexistence region, as seen in the experiment, is very reminiscent of the structure found in the simulation results.

In earlier experiments, where agitation was applied to mixtures of glass beads in completely different settings, evidence was found for a qualitative transition in the dynamical behavior of the material [191, 98], which seemed to be driven by the energy injected into the sample rather than by acceleration. The corresponding energy scale was shown to be set by the rupture energy, E_{cb} [114, 98]. The present results strongly suggest to identify this transition with the vertical lines in Fig. 10.4A and B.

10.4 Order Parameters to Detect the Transition Lines

The position of the transition lines in the phase diagram 10.4B can be based on visual inspection, since the snap shots of the states (cf. Fig. 10.6) have a very distinct appearance. However it is preferable to define order parameters suited to this dynamical system.

10.4.1 An Order Parameter for Phase Coexistence

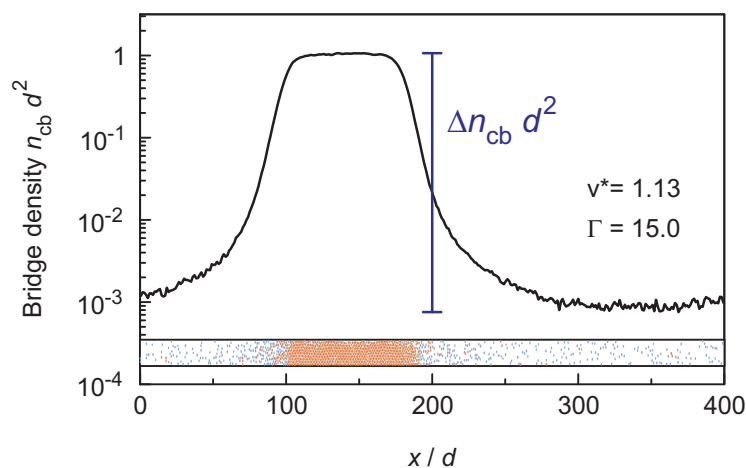


Figure 10.7: Bridge density as order parameter. Δn_{cb} is defined as the largest difference in the density of capillary bridges, occurring in the entire state. With $\Delta n_{\text{cb}} > 0$, an inhomogeneous state can be detected.

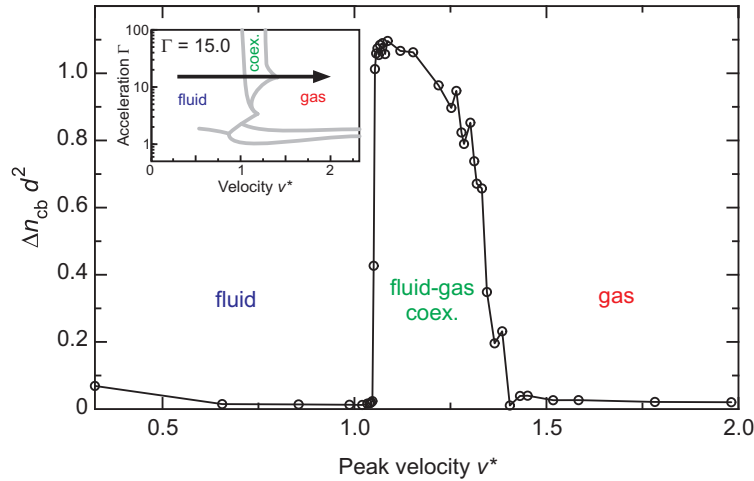


Figure 10.8: Order parameter Δn_{cb} in a section of the phase diagram. This order parameter clearly indicates the states of more than one phase.

Density differences are convenient to detect phase coexistences. It is favorable to use the capillary bridge density, n_{cb} , as it increases faster than the particle density in the dense regime, and therefore provides a sharper contrast between the phases. The bridge density varies by three orders of magnitude, as shown on log-scale in Fig. 10.7 for the state of fluid/gas coexistence. The order parameter to detect coexistences is then defined for a given density field²³ $n_{cb}(x, y)$ as the difference between the highest bridge density and the lowest:

$$\Delta n_{cb} = \max n_{cb} - \min n_{cb} . \quad (10.29)$$

Figure 10.8 shows its application within a section of the phase diagram (cf. the black arrow in the inset indicating the section). As we move from fluid to coexistence, the order parameter changes discontinuously. It is remarked that the granular temperature is also discontinuous upon crossing this transition line. A step in the temperature as function of the driving velocity was also found in Fig. 4.11 of Chap. 4 at the fluid/gas transition in the one-dimensional system. Of course a state of coexistence has been impossible in 1D where there is no lateral extent for phase separation. Here a remark on the typical granular temperatures of the wet granular fluid is in order. For the one-dimensional system we found (cf. Fig. 4.11) that the granular temperature is $T = (2.8 \pm 0.2)E_{cb}$ close to the fluid/gas transition. For the granular temperature in two dimensions, this limit at the transition line separating fluid to fluid/gas coexistence is remarkably independent of Γ with the value $T = (2.9 \pm 0.1)E_{cb}$. We therefore have also a remarkable independence with respect to the dimensionality. As the driving velocity is further increased in the two-dimensional system, we traverse the transition line to the pure gas state, where the order parameter Δn_{cb} rapidly drops to zero.

10.4.2 A Dynamical Order Parameter for Fluidization and Sublimation

Before melting, the mildly excited, still solid state has a high collision frequency with displacements far below the particle diameter. The breaking of the solid granular state (not necessarily but preferably in the case of wet granular matter) is characterized by the onset

²³The bridge density n is first averaged over the z -direction of gravity, so that $\Delta n_{cb} = 0$ for a laterally homogeneous system, which could without z -projection be perturbed away from zero by the vertical density gradient under gravity.

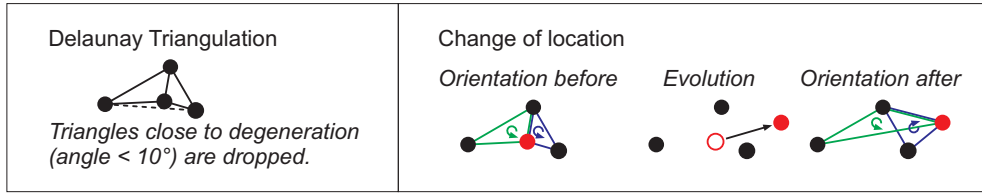


Figure 10.9: Delaunay triangulation defines a dynamical order parameter. First the particle positions are triangulated to have a valid set of Delaunay triangles. It is important that triangles close to degeneration (having an angle below 10°) are dropped. This prevents spurious contributions from the wall ordering. An event of location change is defined by the flipping of a triangle.

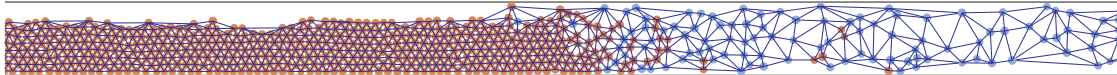


Figure 10.10: Example taken at the interface of the solid/gas coexistence for a Delaunay triangulation, which is sensitive to the local relative particle motion. (Particles are given a red color if they have a capillary bond.)

of particle motion, which is strong enough to allow the particles to reorder. The following method has been implemented to quantify this transition.

The center positions of the grains are Delaunay triangulated at time t_1 . The Delaunay triangulation captures information about the relative position of local groups of three²⁴ particles. Under the evolution of the dynamical system, the local order of the particles may change. This is precisely what we want to detect, for example, at the onset of fluidization. The local reordering causes a triangle, defined by the moving particle centers, to flip its orientation. This is illustrated in Fig. 10.9. The dynamical order parameter is defined as the frequency of these local reordering²⁵ events and denoted by f_{loc} . It gives us the rate of local configuration changes. Note that the Delaunay condition²⁶ for the triangulation is violated before the orientation of a triangle flips. After such an event, the triangulation bonds are updated to form again a valid Delaunay triangulation. Figure 10.10 gives an example of such a triangulation at the fluid interface when sublimation occurs (the fourth state in Fig. 10.6). The critical acceleration is clearly marked by the sudden rise of f_{loc} , which is shown in Fig. 10.11 for a section of constant driving velocity (indicated by the black arrow in the inset). As the sublimation of wet granular matter sets in, f_{loc} takes on positive values (with an apparently non-analytic dependence on the driving parameter Γ). Upon crossing the transition line to the homogeneous fluid, f_{loc} discontinuously drops to a constant value. The fact that f_{loc} is constant, while the shaking frequency f is increased, is due to the constancy of the granular temperature, $T \approx 3E_{cb}$, mentioned above for this fluid regime.

10.5 Universality with respect to the Force Law

In order to investigate whether the observed behavior is of appreciable universality, we varied the potential used in the simulations. In Fig. 10.4B, the circles represent simulations assum-

²⁴Indirectly, the existence of a Delaunay triangle also depends on a fourth particle, because of bond flipping.

²⁵It is noted, that in a dense glassy state, this frequency might be related to the cage breaking frequency.

²⁶A valid Delaunay triangulation has no particle center within the circumcircle of any triangle.

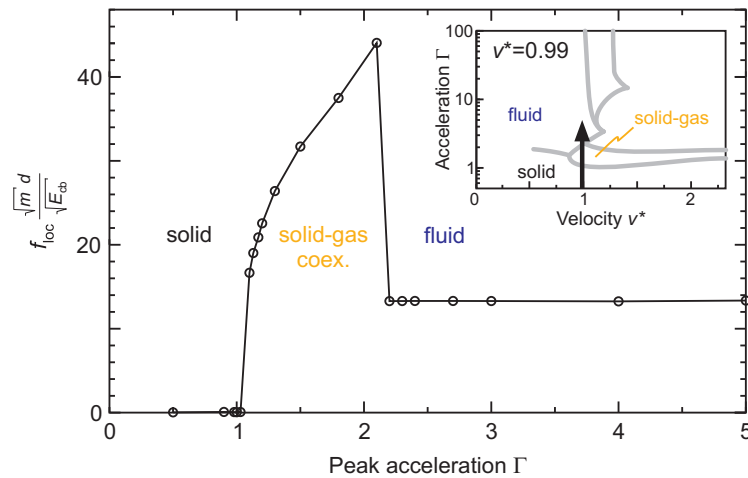


Figure 10.11: The order parameter f_{loc} derived from the dynamical Delaunay triangulation. This order parameter is sensitive to the breaking of a solid structure, so that it can detect fluidization and sublimation.

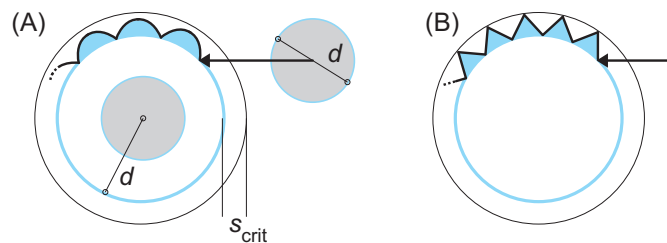


Figure 10.12: The difference of the potentials ((A) linear and (B) square well) applicable for the (A) time- and (B) event-driven simulation technique, is demonstrated for the motion of a bound 2-particle state. In the square-well potential, the mean particle separation is independent of the binding energy. Since particles at high densities move locally without binding forces, the solid state melts at lower driving force in Fig. 10.4B. This is the only marked difference compared to the Minimal Capillary model (A). In general, an event-driven technique requires the trajectory to be piecewise integrable, so that the time for the next event can be predicted analytically. This is not fulfilled for non-vanishing pair forces between more than two particles (cf. also the discussion in 5.7.1).

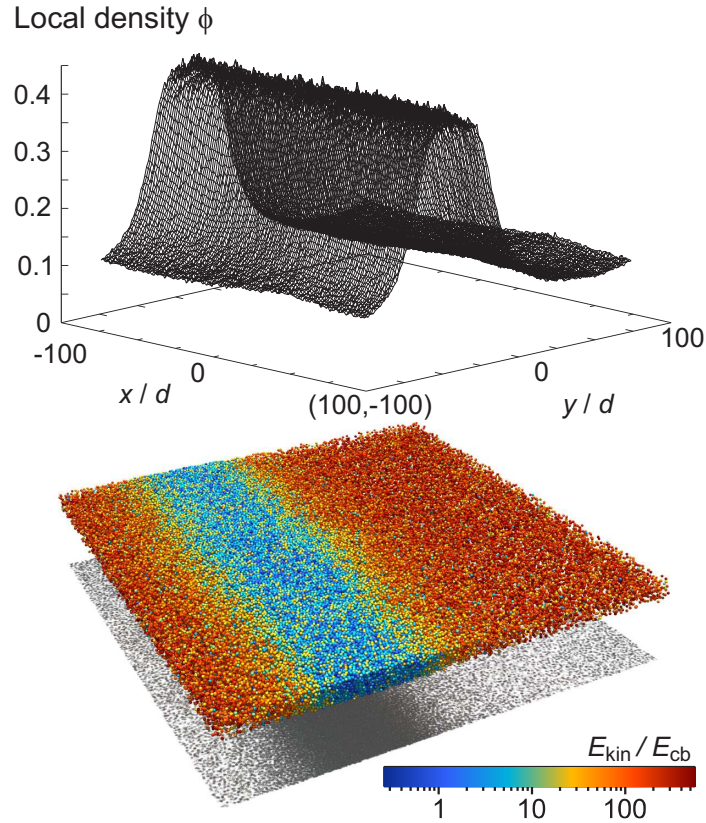


Figure 10.13: A second shape of the coexistence in the flat three-dimensional system. Instead of the circular shape (cf. Fig. 10.3C), the coexistence spontaneously breaks the four-fold symmetry of the simulation domain (with periodic boundaries). In about one out of three cases, starting with the homogeneous initial gas state, the system enters a stable stationary state as shown. The fluid phase (blue) is elongated across the system length. This behavior is very reminiscent to what one would expect in a description in terms of interfacial tension as a local minimum in configuration space. However it is emphasized that the notion of a free energy does not exist for such a state far from thermal equilibrium.

ing a constant capillary force upon retraction (right-hand inset), the squares were obtained assuming a box-like retraction potential, representing the limiting case of a delta-function force located at the rupture distance (left-hand inset). As the figure clearly shows, even these extreme cases give almost identical results. The only marked difference is in the position of the solid/fluid transition at small driving velocities, which is expected due to the vanishing contact force F_0 for the box-like potential. The difference in the pair dynamics is illustrated in Fig. 10.12. All other details do not depend crucially on the interaction characteristics, aside from their hysteretic dissipation with a defined intrinsic energy scale E_{cb} .

A particular significance of the square-well potential is that it leads to vanishing forces except for a set of zero measure on the time axis. This enables event-driven simulations, which are much more economic in computational power than the full integration of the equation of motion. For the square-well potential, we can thus perform simulations with very many particles, and in three dimensions. A three dimensional simulation at parameters corresponding to fluid/gas coexistence is shown in Fig. 10.3C. The similarity with the experimental results displayed in Fig. 10.3B is obvious. As we let the bubble of Fig. 10.3C expand to system size, it finally reaches the boundaries of the box. Due to the periodic boundary conditions, this

corresponds to a diamond-shaped condensed region centered at the corner between four adjacent replicas of the simulation boxes. Fig. 10.3D shows the situation somewhat later. Clearly, the diamond shaped condensate region has rounded to a circular spot, strongly suggesting the presence of an interfacial tension. Further evidence for the existence of an interfacial tension follows from a second stable shape of the coexistence far from equilibrium, which is shown in Fig. 10.13. The plot at the top presents the local density, with the corresponding snapshot of the granular bed underneath, and the energy color code for particles as before. Here the fluid phase happened to condense out of the initial gas state, such to interact with itself across the periodic boundaries in one direction. This configuration is very reminiscent to what one would expect as the local minimum of a free energy – if it existed. It appears therefore as an interesting future topic of research to investigate this, since interfacial tensions are usually defined as equilibrium free energies, which certainly does not apply here. Note also that the difference between the solid (full integration) and the dashed (event-driven) black curve in Fig. 10.5 shows that there is a minor influence of the force law on the structure of the interfacial profile.

10.6 The Continuum Solutions

Let us try to understand our findings in a more general framework. From the ‘traditional’ conditions invoked for the description of equilibrium phase transitions, only the homogeneity of the lateral pressure carries over to driven steady states, due to the required force balance at the phase boundaries. In contrast, the familiar uniformity of temperature was observed to break down. In what follows, we ask for the mechanism by which the lateral translation symmetry of the initially homogeneous system is broken, and how the system finds its steady state within the broken symmetry.

It is sufficient to consider one lateral section of the system. Let us denote the horizontal and vertical axes by x and z . Mechanical stability requires the lateral tension, σ_{xx} , to be constant across the phase boundary, because the force on each volume element vanishes in the steady state (cf. the balance equation (10.27)):

$$-f_x = \partial_x \sigma_{xx} + \partial_z \sigma_{zx} . \quad (10.30)$$

The stress tensor is diagonal because all forces act radially between the particle centers and there are no macroscopic (convective) flows that could give rise to shear forces in this system. Hence, $\sigma_{xx} = \text{const.}$ in the entire system, as confirmed directly by simulations. In the region $\Gamma \gg 1$ of the phase diagrams in Fig. 10.4, where the fluid/gas coexistence takes place, gravity is negligible so that the system is homogeneous in the z -direction. The simulations show indeed that the orthogonal component, σ_{yy} , closely follows σ_{xx} , so that we can use the isotropic Equation of State of Chap. 7 for the *global* (homogeneous) pressure $P(\phi, T) = (\sigma_{xx} + \sigma_{zz})/2$ to relate the *local* density

$$\phi(x) = \phi(T(x), P) \quad (10.31)$$

directly to the granular temperature $T(x)$ for a given system pressure P .

Based on the experimental and simulation results, we are interested in stationary solutions of the continuum description without convection, $\mathbf{u} = 0$, which dramatically simplifies the balance equations (10.26)-(10.28): the heat equation

$$\text{div } \mathbf{q} = P_{\text{inj}} - P_{\text{diss}} \quad (10.32)$$

remains to be solved. For simplicity we assume that heat transport (in the x -direction) is due to particle collisions described by the Fourier law

$$q = -\kappa_E \partial_x T \quad (10.33)$$

with the Enskog expression²⁷

$$\kappa_E = \frac{2v_{\text{th}}}{dg_c} \left(1 + 3g_c\phi + \left(\frac{9}{4} + \frac{4}{\pi} \right) (g_c\phi)^2 \right) \quad (10.34)$$

for the thermal conductivity $\kappa_E(\phi, T) = \kappa_E(\phi(T, P), T)$, where we insert the Equation of State to replace density in favor of pressure (10.31). When the velocity distribution is sufficiently close to a Gaussian we have the thermal velocity scale $v_{\text{th}} = \overline{v \theta(v)} = \sqrt{\frac{T}{\pi m}}$, which enters (10.34), as well as the frequencies for bridge binding and rupture. With such frequencies we evaluate the right-hand side of (10.32).

10.6.1 The Energetic Sinks

The power density of dissipation, P_{diss} in (10.32), is due to the local rupture events of capillary bridges. There are capillary bridges between particles, and furthermore bonds to the driving walls:

$$P_{\text{diss}} = P_{\text{diss}}^{(\text{pp})} + P_{\text{diss}}^{(\text{pw})} . \quad (10.35)$$

We assume in simulation as well as the continuum description, that the rupture of both kinds of bridges gives rise to a hysteretic loss E_{cb} in potential energy. The particle-particle dissipation is

$$P_{\text{diss}}^{(\text{pp})} = n E_{\text{cb}} f_{\text{rupt}} / 2 , \quad (10.36)$$

wherein f_{rupt} is the rupture frequency per particle. To find the rupture frequency per volume we have multiplied by the particle density n in (10.36), and there is a factor 1/2 since one bridge is shared by two particles. Explicit formulas for the particle frequencies under the hysteretic pinch-off dynamics were derived in the context of the Equation of State with the resulting Eqs. (7.44) and (7.43):

$$f_{\text{rupt}} = \left\langle \hat{\mathcal{L}}_{12, \text{rupt}} \right\rangle = 2^{D+1} D v_{\text{th}} \frac{\phi}{d} g_{\text{c} \rightarrow \text{c}}^{\text{b}} \gamma_{\text{vol}}(s_{\text{crit}}) . \quad (10.37)$$

The appearance of the pair correlation factors at rupture is also evident from the δ -functions in the corresponding pseudo-Liouville operator (10.14). The particle-wall dissipation follows analogously with the particle-wall pair correlation²⁸. Since particle-particle dissipation is quadratic in the density, the linear wall dissipation dominates in the gas state.

10.6.2 The Energetic Source

Energy is injected into the system by the wall motion in the vertical z -direction. The z -component of wall and particle velocity are denoted by v_w and v_j (with the particle index j), respectively. The particle-wall separation of the particle j is denoted by $s_{w,j}$. Then the

²⁷ κ_E is written for $D = 2$ so that we have an ordinary differential equation after averaging the z -direction, and can compare with the simulations.

²⁸Since we average over the z -direction, the units of particle-wall and particle-particle dissipation are equal after multiplying the latter with the system height.

pseudo-Liouville operator for the particle-wall collisions is (for the wall at the bottom and $v_{\text{rel},j} = v_j - v_w$):

$$i\mathcal{L}_w = \sum_j |v_{\text{rel},j}| \theta(-v_{\text{rel},j}) \delta(s_{w,j}) \left(\hat{b}_j(v_w) - 1 \right). \quad (10.38)$$

The operator $\hat{b}_j(v_w)$ reverses $v_{\text{rel},j} = v_j - v_w$ (the particle velocity in the instantaneous inertial frame of the wall), so that the energy of the particle changes by $\Delta E_j = \left(\hat{b}_j(v) - 1 \right) m\mathbf{v}_j^2/2 = 2mv_w(v_w - v_j)$, which is negative when the wall moves outwards as seen from the system, $v_w < 0$. The ensemble average gives the injected power per wall area:

$$P_{\text{inj}} = \langle i\mathcal{L}_w E \rangle = ng_{\text{wall}} \int_{-v}^v dv_w \varphi_w(v_w) \int_{-\infty}^{v_w} dv_j f(v_j) 2v_w(v_w - v_j)^2. \quad (10.39)$$

The upper integration limit in the second integral is due to the absence of a collision when the particle is faster than the wall. The first integral depends on our driving parameter v , which is the maximum wall velocity on the horizontal axis of the phase diagram. The particle-wall contact correlation originates from the δ -function in the Liouville operator and we approximately related it to the known particle-particle contact correlation g_c by Eq. (7.8). The particle and the wall velocities are assumed to be independent with Gaussian particle velocities. The wall velocity is distributed according to the sinusoidal motion with peak velocity v :

$$\varphi_w(v_w) = \frac{1}{\pi} \frac{1}{\sqrt{v^2 - v_w^2}}. \quad (10.40)$$

The double integral (10.39) can be performed analytically with the result

$$P_{\text{inj}} = \sqrt{\frac{2T}{\pi m}} \frac{ng_{\text{wall}}mv^2}{3} e^{-mv^2/4T} \times \left[(3 + mv^2/T) I_0\left(\frac{mv^2}{4T}\right) + (1 + mv^2/T) I_1\left(\frac{mv^2}{4T}\right) \right]. \quad (10.41)$$

(I_j are the modified Bessel functions.) The power injected into the system, $P_{\text{inj}} = P_{\text{inj}}(T, v)$, is a function of the granular temperature, after eliminating the density dependence with the Equation of State.

10.6.3 Stable Solutions

For a stable phase, the power injected into the system from the oscillating walls, P_{inj} , must be balanced at each lateral position within the sample by dissipation, P_{diss} . Assuming a certain velocity distribution for the grains both quantities can be evaluated as shown above. After eliminating density by virtue of the equation of state, the net power $\Delta P(T) = P_{\text{diss}} - P_{\text{inj}}$ can be obtained as a function of temperature.

Figure 10.14 shows the result obtained using the Gaussian velocity distribution (as described in Sec. 10.6.2), displayed for three values of the scaled peak velocity, v^* . For $v^* < 0.83$, we obtain just one stable (i.e. positive slope) zero, which is at low temperature. It corresponds to a moderately dense state, which has just enough free volume for the critical separation s_{crit} to be exceeded frequently enough to balance the injected power, P_{inj} . Any drop in the temperature would increase the density, implying a decrease in rupture frequency, such that the system would reheat. On the other hand, for $v^* > 1.49$, we have again only one stable zero,

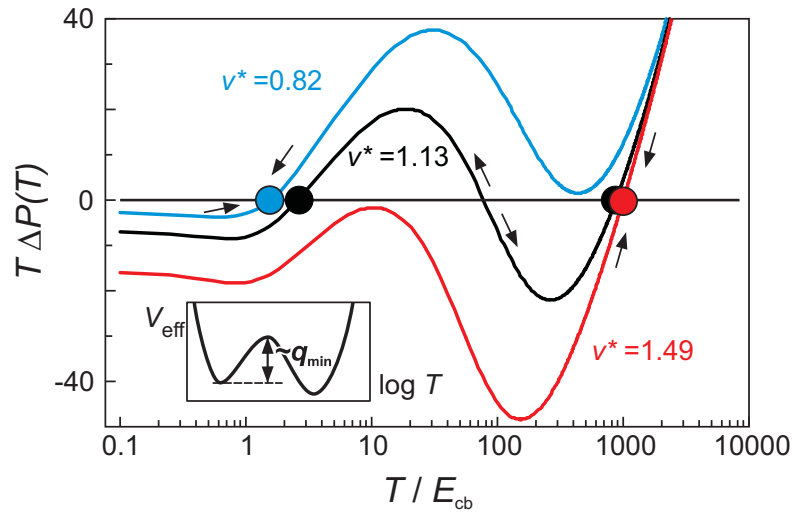


Figure 10.14: Plot of the net power, $\Delta P = P_{\text{diss}} - P_{\text{inj}}$, as a function of the granular temperature. Depending on the scaled peak velocity v^* of the container boundaries, we obtain either one (cases drawn in blue and red) or two (black curve) stable zeros, corresponding to a single phase or two-phase coexistence respectively. The arrows denote the response of the system to small fluctuations. The inset is the integrated effective nonequilibrium potential.

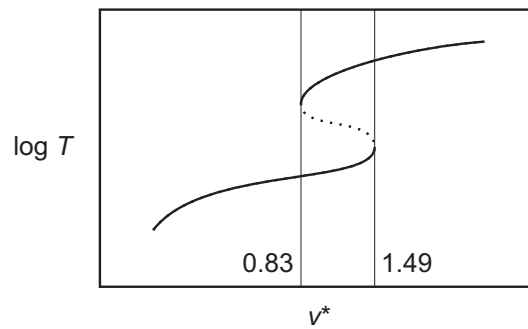


Figure 10.15: Sketch of the stable (solid) and unstable (dotted) solutions of $\Delta P(T) = 0$. According to this simplified description, the transition from the fluid to the coexistence state is subcritical and therefore discontinuous in the granular temperature T as a function of the control parameter v^* .

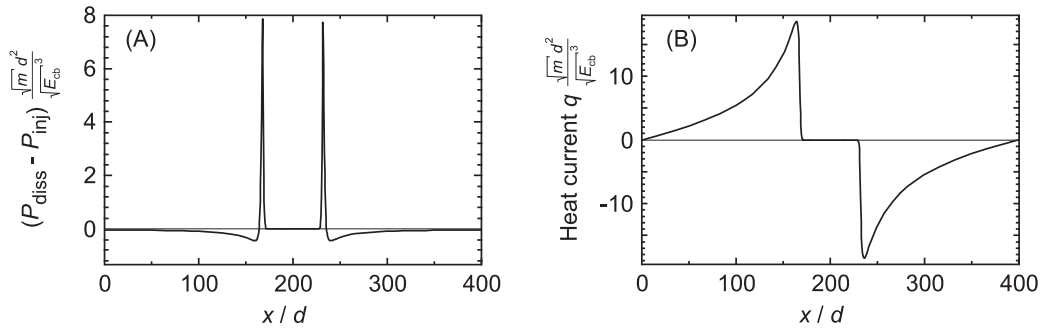


Figure 10.16: Stationary solution of the balance equations. (A) The net power as a function of space. Injection and dissipation is balanced inside the homogeneous phases. (B) The heat current in the system.

but this corresponds to a high temperature. It represents a dilute phase, the temperature of which is determined mainly by the balance of the energy uptake from the motion of the boundaries with the dissipation due to the ‘wet’ impacts with them.

At intermediate velocities (black curve in Fig. 10.14), two stable zeros (black circles) are obtained, one for low and one for high temperature. This is to be identified with the fluid/gas coexistence observed in the simulations as well as in the experiments for intermediate velocities. Since this continuum theory does not take gravity into account, it is intrinsically independent of the parameter Γ used in Fig. 10.4, and thus corresponds to the vertical lines in the phase diagram. The mean-field model predicts the coexistence in the stripe $0.83 < v^* < 1.49$ of the phase diagram, which compares quite favorably with Fig. 10.4B for $\Gamma \gg 1$ (where gravity is irrelevant) given the crudeness of the involved assumptions. Before we take the thermal coupling between the coexisting phases into account, it is remarked that the set of solutions of $\Delta P = 0$, sketched in Fig. 10.15, has the characteristic shape of a subcritical transition.

The solutions of the continuum model for the driving parameter in the range of coexistence, show that the net power is very closely balanced within each phase, but not at the fluid/gas phase interface, as we see in Fig. 10.16A. The corresponding heat current, from the gas into the fluid phase, is shown in Fig. 10.16B under periodic boundary conditions as in the simulation.

10.6.4 Comparison of Analytic and Simulation Results

From the solution of the heat equation $T(x)$, we can infer with the equation of state the local packing density $\phi(x)$. The result is included as inset in Fig. 10.5 and shown besides the time-driven simulation result in Fig. 10.17 (panel (A1) continuum model, (B1) simulation). The simulation shows broader phase boundaries because the stationary state exhibits some additional oscillatory motion of the fluid plug embedded in the granular gas atmosphere, and the simulation results are long time averages. In the second line in Fig. 10.17, the local dissipation is shown. From the bulk perspective, dissipation is highest within the fluid phase. This is expected since the high density of bridges leads to many rupture events. Note that the packing density is close but below the limit for the ordering transition ($\phi_o = 0.71$ discussed in detail in Chap. 7, Fig. 7.3), so that the particles stay mobile within the fluid phase while rapidly reforming the capillary network for dissipation. Dissipation is additionally increased at the interface when hot gas particles bombard the dense surface of the fluid, which gives rise to peaks in the continuum model. The breathing mode also broadens these peaks of dissipation in the simulation. The temperature is significantly overestimated by the continuum model.

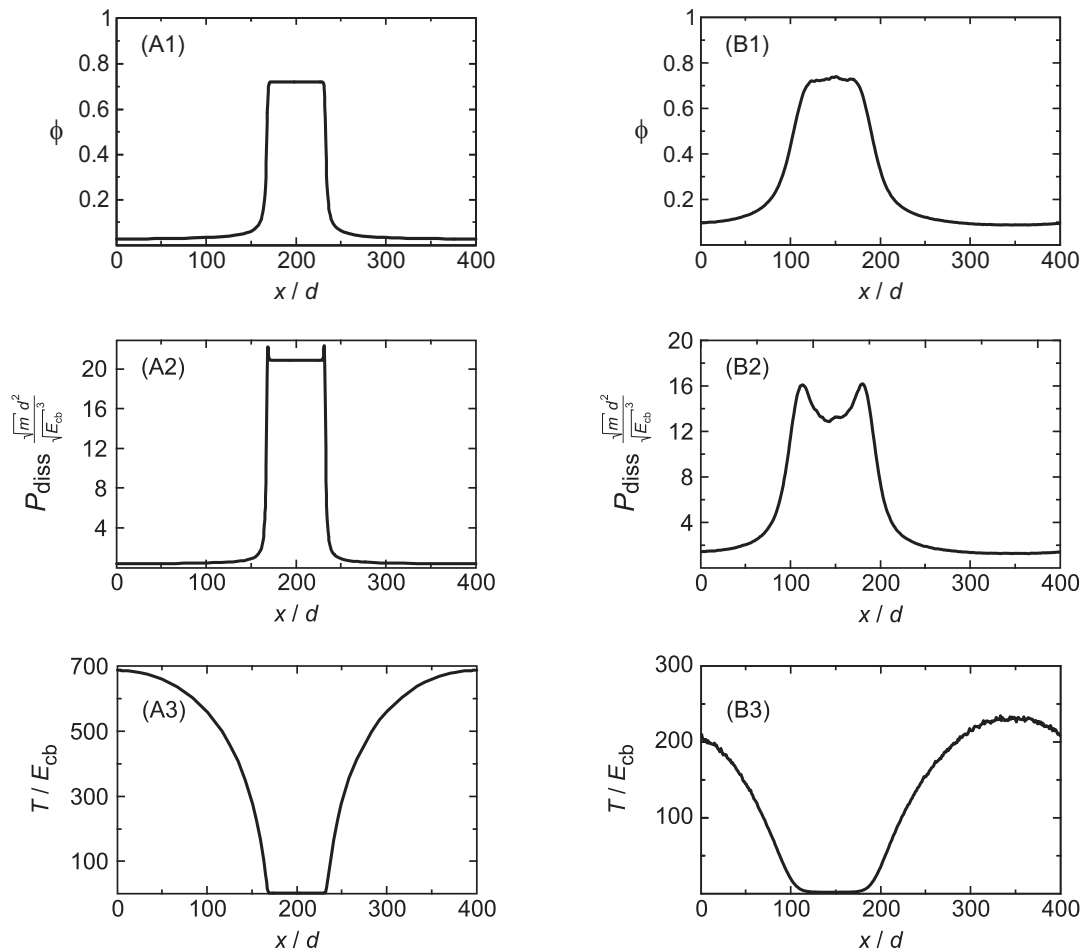


Figure 10.17: Comparison between the continuum theory and the simulation according to the Minimal Capillary Model. The profiles of density (1), dissipation power (2), and temperature (3) are qualitatively reproduced by the continuum model. The phase boundaries of all three fields are sharper in the continuum model. This is because the fluid phase in the full simulation has in addition a breathing mode weakly excited. The overshooting of the local dissipation power at the interface is due to the fast gas particles imposing their high kinetic energy on the dense capillary network of the fluid. (As the system is two-dimensional and we integrate over the vertical axis, dissipation has the units power per length.)

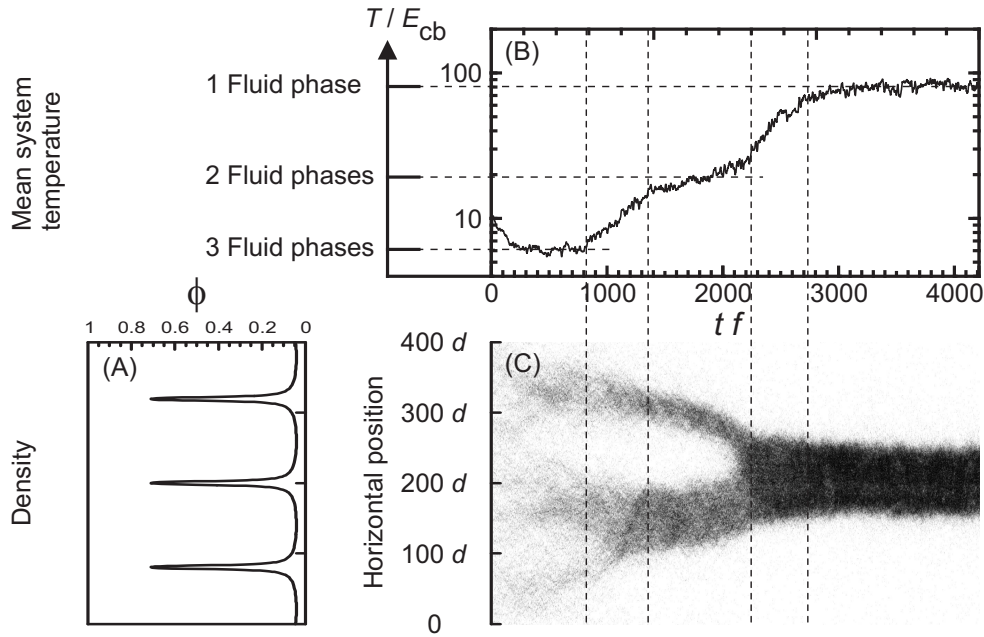


Figure 10.18: The relation between the number of fluid phases and the granular temperature in the sample. (A) The solutions of the heat equation are periodic. These stationary solution of the continuum theory explain the origin of the characteristic length scale due to heat conductivity and the effective potential V_{eff} (shown as inset in Fig. 10.14). The theoretical estimate discussed in the text expects that the length scale between the phases is set by the heat conductivity $\kappa_E \propto \sqrt{T}$. (B) Indeed we find in 2D-simulations (1200 particles, using the time-driven technique) that \sqrt{T} increases by a factor 1.7 (close to $3/2$, as the 3 phases rearranging into 2 phases), and 2.1 (close to 2, when the two-phase state rearranges into a single phase). (C) The bridge density as gray scale plot as a function of time (in units of the shaking frequency f).

This is so because we neglected correlation between particle and wall velocity in (10.39), which overestimates the injected power. Overall we can conclude that the interfacial profiles of the coexistence state are qualitative reproduced by the simple continuum model.

10.7 The Coarsening Dynamics of the Coexistence State

In this final section we discuss another peculiarity of the subcritical fluid/gas transition far from equilibrium, which distinguishes it from first order equilibrium transitions. We take a brief look at the onset of the fluid/gas coexistence as a homogeneous nucleation process.

In equilibrium situations we think of a Gibbs energy barrier which a fluid nucleus has to overcome in order to grow out of the gas. A later generic process for coarsening could be Ostwald ripening, where bigger droplets ‘eat up’ the smaller ones due to a size instability²⁹. A third, final regime is dominated by coalescence. The coarsening dynamics of wet granular matter is distinct from both.

A typical simulation of a two-dimensional system (under periodic boundary conditions), which is ten times wider than the previous ones, is shown in Fig. 10.19. At time t_0 the first fluid

²⁹Ostwald ripening gives rise to a self-similar evolution of the average droplet size.

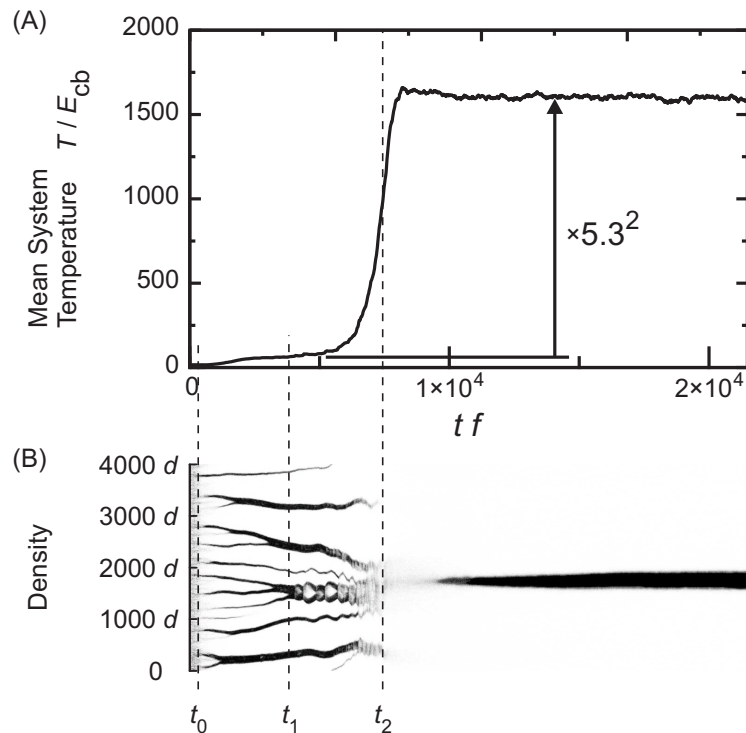


Figure 10.19: An approximate 5-to-1 transition in a system that is ten times as wide (12 000 particles, using the event-driven technique) as the preceding one in Fig. 10.18. The time evolution of temperature (A) and the bridge density (B) (projected on the lateral axis, where black represents the density maximum) are shown. Time on the horizontal axis is given in units of the shaking frequency f . At t_0 , fluid droplets nucleate out of the initially homogeneous gas state with a characteristic separation length, as in Fig. 10.18. This length scale bars the system from droplet coalescence. To minimizing its interfacial area, wet granular matter adapts its temperature in a self-organized manner. It heats up at t_2 until the temperature dependent separation length equals the system size, so that a single phase can condense out of the transient gas. The increase in temperature corresponds, according to the estimate in the text, to a change of 5.3 fluid phases (at time t_1) merging into one. (Giving half weight to the three thin phases at t_1 , and counting the four massive phases as full phases, yields in total 5.5 fluid phases.)

droplets precipitate out of the gas³⁰ and grow slowly. After the time t_1 we observe that the biggest droplet suddenly becomes unstable and starts to perform an ever increasing breathing-like oscillation (reminiscent to the oscillation reported in [242] for a one-dimensional system) which eventually leads to the burst of this fluid droplet. By the time t_2 , the shock front which goes out from this event³¹, has triggered the evaporation of all other fluid droplets. In the absence of the cooling fluid phases, the granular temperature rises rapidly. (\dot{T} is maximal at t_2 .) One might at first glance expect the system to settle in this gas state. Rather surprisingly, the system develops a single larger fluid phase embedded in the granular gas as the final nonequilibrium steady state.

Without resolving the complex detailed dynamics of this process, which is an interesting subject of future research, we can qualitatively understand the most striking property: the fluid phases do not coalesce, but abruptly evaporate and nucleate again to reach the stable final state. Figure 10.14 explains that the nonequilibrium steady states are determined by the balance of power. In the coexistence state, power is not only balanced locally. There is a heat current from the hot gas to the cold fluid phase as shown in Fig. 10.16B. This lateral coupling is due to the second order differential equation (10.32) for the nonequilibrium temperature $T(x)$ with the power currents of Fig. 10.14 as the driving forces. Hence, the nonequilibrium temperature changes in space according to the effective potential³² $V_{\text{eff}}(T) = \int^T \Delta P(T') dT'$. Fluctuations of the energy current \mathbf{q} that exceed the threshold q_{min} , push the system over the barrier into a state with two coexisting phases. Remarkably, the notion of a threshold is resumed in this nonequilibrium situation. Here it is a threshold for the energy current \mathbf{q} , and not an energetic barrier as for equilibrium nucleation. A corresponding solution for the density, shown in Fig. 10.18A, oscillates spatially between the fluid and the gas phase. States of multiple ‘drops’ are transient, so that there is no time for the ideal periodic order to develop. Therefore a preferred wave length λ is present but not easily seen in Fig. 10.19B. Clearly visible are the instability of the biggest fluid phase after t_1 and the complete evaporation at t_2 , by which the system rearranges its spatial structure globally, as if to minimize its interfacial area. The way by which wet granular matter reaches its final state without violating the length scale λ is rather elegant – and entirely self-organized: λ depends on temperature, which increases, as shown in the upper panel (A) of Fig. 10.19. For a rough theoretical estimate, we remind that the heat conductivity κ_E scales with the square root of temperature. We therefore expect that $\lambda \propto \sqrt{T}$, so that the number of fluid droplets, N_d , which share the lateral system size L , are related to the granular temperature according to

$$L/N_d = \lambda \propto \sqrt{T} . \quad (10.42)$$

Hence, as a rule of thumb, the mean granular temperature T is related to the number of droplets N_d by

$$T \propto \frac{1}{N_d^2} . \quad (10.43)$$

According to this idealized relation, wet granular system would assume a discrete temperature spectrum under isochoric conditions. On the level of its crude derivation, this is nicely

³⁰The initial temperature of the gas was chosen such that the mean kinetic energy per particle is twice the gravitational energy of the system height, and the particles were placed homogeneously in space. The driving conditions are constant with parameters well inside the fluid/gas coexistence regime ($\Gamma = 30$, $v^* = 1.13$).

³¹The author verified that its propagation speed is very close to the known speed of sound of the hard disc system at the present density.

³²In analogy to point mechanics, temperature plays here the role of position, position plays the role of time, and the heat current \mathbf{q} replaces the momentum. The potential arises from the net power ΔP and is sketched as inset in Fig. 10.14.

confirmed by the simulations, with few quantitative examples presented in the captions of the Figs. 10.18 (for the transitions $N_d = 3 \rightarrow 2 \rightarrow 1$) and 10.19 (for the abrupt transition of multiple phases into a single one).

10.8 Conclusions

This chapter presented the phase space evolution of the wet granular ensemble, and discussed the derivation of continuum equations on the basis of chaoticity and the extended hysteretic pair correlation. The global nonequilibrium behavior was mapped onto the plane spanned by acceleration and driving velocity in Fig. 10.4. This revealed two distinct mechanisms for phase transitions in wet granular matter: the solid/fluid transition ('fluidization') by force and the fluid/gas transition ('evaporation') which is determined by energy. The solid state generically terminates into a mobile phase by force-driven transitions, which include sublimation. The transitions located at critical driving energies, were explained as a subcritical instability of the power balance. The density profiles of the fluid/gas coexistence computed by the continuum theory reproduced all characteristics of the simulation results, including an overshooting of dissipation where the surface of the fluid is bombarded by fast gas particles. The dynamical order parameter f_{loc} was introduced as the rate at which local triangles flip their orientation. It was shown to precisely detect the nonequilibrium phase transitions of granular melting (by a discontinuity) and sublimation (with a sudden rise). The coalescence dynamics of wet granular droplets revealed a peculiar relation to the granular temperature: the squared number of fluid phases was found to be proportional to the inverse temperature.

The essential role of the hysteretic loss of energy in collisions was demonstrated by the quantitative comparison between experiments and simulations. With the replacement of the constant bridge force by a delta-force, the simulated phase diagram was shown to be remarkably independent of the actual force-distance characteristics. Hence the paradigm system can be viewed to represent a whole class of dissipative collective systems. Furthermore, wet granular matter is a particularly simple system with high experimental accessibility. It thus appears as a very promising system to achieve a deeper understanding of universal aspects of systems far from equilibrium.

Future analytic work will be devoted to the derivation of a coefficient of heat conductivity, which takes the transport of energy by the capillary bonds into account. The sharpness of the phase boundaries suggests to study non-linear gradients (Burnett order) of heat transport.

10.9 Appendix: Comment on Model Details

The square well potential models the force law of a rupturing 'thread' instead of a capillary bridge, which affects some dynamical details to change. Firstly the pair correlation function, whose logarithmic derivative $\partial \ln g / \partial s$ is the effective force, is discontinuous at the rupture length due to the delta force acting at rupture. Hence $g_{\text{sw}}(s)$ drops down at $s = s_{\text{crit}}$. The pair correlation has been reported [224] to have a peak rising from the lower side, s_{crit}^- . The reason for this is that the rupture shell in configuration space is equivalent to a partially reflecting wall, and at configuration boundaries there are generically peaks. Secondly, the vanishing contact force reduces the critical acceleration for fluidization as we discussed.

Furthermore a comment on the shear viscosity in both models is here in order. Shear viscosity describes the lateral flow of momentum, $\sigma_{xy} > 0$. A sheared granular system, $\tau = \gamma_{xy} = \partial_y u_x > 0$, has in its local center of mass two 'lanes' of particles streaming in opposite directions. The shear viscosity of dry granulates is due to the granular-thermal motion which causes particles to interchange the 'lanes'. This lateral exchange of momentum causes the resistance τ against the shearing γ . If shear bands form, typically occurring at high strain rates γ , this friction is strongly reduced because the particles follow the traffic rules. However in wet granular matter the lateral exchange of momentum is further enhanced by capillary bridges 'between the lanes'. Yet this lateral flow of momentum τ does not grow with the strain rate γ for the following reason. Under steady shearing, there is an average number of capillary bridges between the lanes depending on the

system density. If we increase the strain rate at fixed density, the frequency of bridge formation and rupture is increased, but the mean number of bridges between the lanes does not grow. Therefore the capillary bridges are responsible for the typical plasticity of wet granular τ_{crit} , while particle collisions similar to the dry case contribute to the viscous term in $\tau = \tau_{\text{crit}} + \eta\gamma$. This is correctly described by the minimal capillary model. In the square well model, the change in velocity is according to $v' = \sqrt{v^2 - 2E_{\text{cb}}/m}$, which is equal to an exchange of momentum $\Delta p = m(v' - v) = E_{\text{cb}}/v$ for a fluidized state with granular temperature $TD/2 = E_{\text{kin}} > E_{\text{cb}}$. There is also a geometric factor $\sin \varphi$ for the angle φ between the strain and the direction of the capillary bridge. The rupture frequency is proportional to v/d , so that the momentum exchanged via bridges is of the order $\Delta p v/d = (E_{\text{cb}}/d) \sin \varphi = \overline{F_{\text{cb}}} \sin \varphi s_{\text{crit}}/d$ with the effective bridge force $\overline{F_{\text{cb}}} = E_{\text{cb}}/s_{\text{crit}}$. Hence we find, as for the minimal capillary model, that the shear stress τ is independent of the shear rate $\gamma \propto v$ in the fluidized state. Yet there could be differences between the models when the shearing is at lower granular temperatures, analogously to the fluidization threshold for the solid/fluid transition mentioned above.

Finally, with time-driven simulations the author has verified that an interaction with more parameters, such as taking a finite time for the capillary bridges to grow into account, and the viscous damping of the liquid (similar to the force law in Eq. (3.3)), do not significantly influence the coexistence state for realistic parameters as those discussed in Chap. 3.

Chapter 11

Concluding Summary and Outlook

Nonequilibrium statistics and dynamics are very active fields of contemporary physics. The Fluctuation Theorem is among the few general results which we have for nonequilibrium systems so far. Since its initial formulation for dynamical systems in steady states [89], the Fluctuation Theorem has been fairly extended, e.g. to quantum [189] and relativistic (Chap. 2) systems. It is fascinating to see that under conditions where there is no First Law of thermodynamics (such as cosmic expansion discussed in Chap. 2 which slows down particle motion), the Second Law and, moreover, the Fluctuation Theorem hold. However we have shown (Chap. 4) that the Fluctuation Theorem does not apply to a tabletop system such as a granular gas. This observation is very clarifying since existing reports of confirmation [78, 10] cannot be explained by the derivations of the Fluctuation Theorem [90, 77], which require time-reversal symmetry. It was shown that the Fluctuation Theorem still holds for small fluctuations (with ‘small’ given a quantitative meaning in Chap. 4). By this, the contradiction is resolved as a mere consequence of the measurement range.

We have given reasons in this thesis why wet granular matter is – besides its applicational relevance – a paradigm system to investigate complex non-linear dynamics and dissipative collective phenomena such as nonequilibrium phase transitions. The breaking of time-reversal symmetry was shown (Chap. 3) to be exceptionally lucid in wet granular matter by the formation and rupture of capillary bridges. For wet granular matter it was shown (Chap. 4) that the violation of the functional form of the Fluctuation Theorem is directly related to the onset of the nonequilibrium fluid/gas transition. This was our initial observation pointing to the tight connection between dynamical system properties (here represented by the Fluctuation Theorem) and collective phenomena. Building upon this connection, the dynamical properties of wet granular matter have been investigated in this thesis with the physical objective to reveal and understand its collective nonequilibrium behavior. There are essentially two parameters which describe the particle interaction: the rupture length and the capillary energy. This simple but hysteretic interaction accounts for all macroscopic nonequilibrium properties reported in this thesis. The first qualitative observation (Chap. 3) resulted from a two-dimensional simulation, which showed the flocculent structures which condense out of the wet granular gas and form solid capillary networks, in contrast to the density clouds formed in dry granular matter assuming a restitution model.

For a quantitative theory, we are interested in a statistical and continuum description, which rests upon the chaoticity of the system [61, 64] to ensure the exponential decay of correlations and the convergence to defined local states. The dynamical chaos is quantified by the Kolmogorov-Sinai entropy which has been computed (Chaps. 4 and 5). We took advantage of the fluid/gas transition in one dimension (Chap. 4) to evaporate fluid clusters, which revealed the importance of capillary bonds for the chaotic dynamics: although the particle

motion is slower in the wet granular fluid, it was shown that in the fluid state with its many capillary bridges the Kolmogorov-Sinai entropy is approximately five times higher (so that correlations decay faster) as compared to the gas. This result was extended by the analytic computation of the Kolmogorov-Sinai entropy for $D > 1$ dimensions in the following Chap. 5. Also for the gas state it has been shown that the Kolmogorov-Sinai entropy rapidly rises as a function of the capillary energy. Another dynamical property is the symplectic tangent space evolution of wet granular matter. This is a consequence of the explicit hysteretic interaction (in sharp contrast to models where dissipation is hidden in the moment of collision) and equips the dissipative wet granular system with Hamiltonian properties, such as the symmetry of its Lyapunov spectrum (computed with the generalized Dellago-Posch formula in the Chaps. 4 and 5).

We applied the increased chaoticity and the piecewise Hamiltonian structure to compute the binding and rupture frequencies in freely cooling one-dimensional wet granular matter (Chap. 6). The resulting set of equations on the mean-field level could quantitatively reproduce the full simulations on logarithmic scales. In isochoric systems above a critical value of the density, the number of transient clusters is no longer monotonic in time: as the granular temperature falls below the capillary energy, dense granular droplets precipitate out of the homogeneous initial state. In the final regime these droplets coalesce as a sticky gas, in which the cluster size scales with time. As with the dynamical system description, the statistical description was extended to $D > 1$ dimensions in the following Chap. 7. We focused on the two-dimensional system which has already non-trivial¹ particle correlations described by the Enskog factor in the absence of the hysteretic capillary interaction. Due to the finite interaction length of the capillary bridges, the contact correlation (Enskog factor) is not sufficient to describe wet granular matter. The three main ideas of Chap. 7 which allow to extend the statistical description to the hysteretic interaction of wet granular matter are as follows: Firstly, explicit expressions for the near-contact pair correlation in the dry system have been derived. The expression for the dense regime describes in particular the formation of the delta-peak in the jamming limit, which corresponds to $2D$ exact contacts in D dimensions (in agreement with the accepted value for isostatic packings in existing simulations). For the dilute regime an expression has been derived based on the computation of correlated three-particle collision events. Secondly, the hysteretic interaction of wetted particles breaks detailed balance and gives rise to persistent microscopic probability fluxes. An equation system has been derived which describes these fluxes. Its steady state solution yields a set of six correlation factors, which generalize the single Enskog factor. Thirdly, at low temperatures many degrees of freedom are frozen within clusters. This has been described by a reciprocal two-fluid model. The theory includes the following results: We have explicit expressions for the near-contact pair correlation, the capillary coordination number (as confirmed numerically), and the pressure in wet granular matter over the full density and temperature range. Remarkably, the nonequilibrium isotherms of wet granular matter were shown to have a van-der-Waals-like mechanical instability. The critical density and the critical temperature of this instability for $D = 2$ (expressed in reduced variables using the capillary length and energy) are very close to those of the simulation in $D = 1$. These theoretical predictions for the existence of a critical point have been verified experimentally in Chap. 8. A granulate of steel spheres has been wetted with a conductive liquid. The particle segregation caused by the mechanical instability gives rise to a large increase in the global electrical resistance. The critical density and temperature were found to quantitatively agree with the theory. Since this segregation or unclustering transition is described by an instability of the isotherms of wet granular matter,

¹For example, as remarked in Chap. 7, the question of the existence of a Kosterlitz-Thouless transition is still open for this system.

it is emphasized that this transition occurs in excited states of wet granular matter when the temperature is (close to) homogeneous and the system is very dense (according to the critical value of density in Chap. 7).

An important property of nonequilibrium states of dissipative gases and fluids are deviation from the Maxwell velocity distribution. Over-occupied tails are frequently encountered, as we have seen in the free cooling simulation in Chap. 6, and have been reported for driven states [113]. The velocity distribution entered in virtually all analytical computations of this thesis, notably in the discussion of the Fluctuation Theorem (Chap. 4) and the computation of the Kolmogorov-Sinai entropy (Chap. 5). Therefore a method to measure the granular velocity distribution in steady nonequilibrium states has been suggested (Chap. 9). This method uses the Mössbauer effect. One advantage of nuclear resonance is that the velocity is measured directly, while other methods that detect particle positions have to derive the particle velocity indirectly from several measurements. The Mössbauer spectrum is a ‘velocity spectrum’ by virtue of the relativistic Doppler shift. The velocity scales of nuclear resonance fit naturally to the requirements in most granular experiments, so that the Mössbauer spectrum is directly related to the velocity distribution. The method is sensitive to anisotropies and the possibility to derive particle rotations has been discussed. For a vigorously driven granular fluid, a first experiment has been presented which showed an exponential velocity distribution in the volume.

We finally return to one of our main objectives: the nonequilibrium phase transitions. In the preceding experiment (Chap. 7) which used the conductive liquid to follow the dynamics of the capillary network in wet granular matter, the formation of a dilute gas phase was excluded due to the high density. It provided (besides the measurement of the critical point) the opportunity to observe the solid/fluid transition. This transition may be viewed as a strong physical idealization of the geological phenomenon of ground liquefaction caused by earthquakes, which can lead to land slides. While an optical detection of the fluidization transition is limited to particles on the surface, the conductivity method is sensitive to the bulk structure and allows to determine the transition point with remarkable precision. The experiment demonstrated clearly that the solid/fluid transition is discontinuous with respect to the driving acceleration. The last chapter unified and generalized the results on this solid/fluid transition and the previous fluid/gas transition of wet granular matter. Moderate overall densities provided space for large phase segregation. The global phase diagram of vertically agitated wet granular matter has been derived from experiments (in three dimensions) and simulations (in two and three dimensions), which agreed quantitatively. Two principal mechanisms for nonequilibrium transitions have been revealed: Firstly, there are force-driven transitions which are determined by the externally applied acceleration as compared to the capillary force. The solid/fluid transition and the discovered wet granular sublimation belong to this class. Secondly, there are energy-driven transitions, of which the fluid/gas transition is the most prominent one. Such transitions occur at a certain velocity of the driving. This wall velocity defines an energy scale which is to be compared with capillary energy. The balance of dissipated and injected power was shown analytically to have a subcritical instability with respect to the driving velocity, which explains the existence of the fluid/gas coexistence, and the final transition to the pure gas state. Marked as nonequilibrium states, the fluid and gas phase were shown to coexist at temperatures which differ by two orders of magnitude. Besides temperature and density differences, a dynamical order parameter has been defined, all of which demonstrated the discontinuity of these transitions as a function of the driving parameters. In view of these mechanisms for nonequilibrium phase transition, we can overall distinguish three of them: the mechanical instability which occurs in very dense systems (as described by the equation of state), the force-driven, and the energy-driven transitions. While

the first is an intrinsic mechanism (for which reason it occurs as well in the free cooling), the latter two cannot be considered independently of the boundary conditions defined by the driving. Based on the theoretical results concerning the dynamical chaos (Chap. 5) and the hysteretic pair correlation function (Chap. 7), a derivation of continuum equations has been discussed. Solutions for the states of fluid/gas coexistence showed qualitative agreement with the profiles of temperature, density, and dissipation power measured in the simulations. Furthermore, the details of the force law in the hysteretic interaction have been strongly varied in the simulations, which showed that the resulting phase diagram is remarkable independent of such details. This suggests that wet granular matter is truly a paradigm system representing a larger class of dissipative systems.

Future work will be concerned with the derivation of the coefficient of heat conductivity for wet granular matter. The presented results on the Kolmogorov-Sinai entropy and the generalization of the Boltzmann-Enskog kinematics established in this thesis for the hysteretic interaction, provide the starting point to derive such transport coefficients. The generalization of the Fluctuation Theorem for wet granular matter as a piecewise Hamiltonian system is tempting, because the wet granulate appears so closely related to a Hamiltonian system (for which derivations exist), while at the same time the system breaks time-reversal symmetry and is strongly dissipative. The construction developed in Chap. 3 to recover the Fluctuation Theorem may here serve as a lead. Finally, with the results presented in the last chapter, a very fundamental question of nonequilibrium systems arose: is there a ‘potential’ which determines the nonequilibrium steady state as its minimum? The simulation has shown different configurations for the fluid/gas coexistence, which are reminiscent of what one might expect to result from the minimization of the interfacial area. However, so far interfacial tensions can only be derived from the free energy as the appropriate thermodynamic potential in equilibrium. Furthermore, the last section in Chap. 10, presenting the coalescence dynamics in wet granular matter, has demonstrated clearly the influence of the global constraints imposed by heat currents. Therefore the quest for a nonequilibrium ‘potential’, if it exists, will have to take these nonlocal conditions into account.

References

- [1] M. Abramowitz and I. A. Stegun. *Handbook of mathematical functions*. Dover Publications, Inc., New York, 1965.
- [2] A. E. Allahverdyan and V. G. Gurzadyan. Arrows of time and chaotic properties of the cosmic background radiation. *J. Phys. A*, 35:7243–7254, 2002.
- [3] T. Antal, M. Droz, and A. Lipowski. Exponential velocity tails in a driven inelastic Maxwell model. *Phys. Rev. E*, 66(6):062301, Dec 2002.
- [4] S. Asakura and F. Oosawa. On interaction between 2 bodies immersed in a solution of macromolecules. *J. Chem. Phys.*, 22(7):1255–1256, 1954.
- [5] S. Asakura and F. Oosawa. Interaction between particles suspended in solutions of macromolecules. *J. Polymer Sci.*, 33:183–192, 1958.
- [6] T. Aste. Variations around disordered close packing. *J. Phys.: Cond. Mat.*, 17:S2361–S2390, 2005.
- [7] T. Aste and A. Coniglio. Cell theory for liquid solids and glasses: From local packing configurations to global complex behaviors. *Europhys. Lett.*, 67:165–171, 2004.
- [8] T. Aste, M. Saadatfar, A. Sakellariou, and T. J. Senden. Investigating the geometrical structure of disordered sphere packings. *Physica A*, 339:16–23, 2004.
- [9] T. Aste, M. Saadatfar, and T. J. Senden. The geometrical structure of disordered sphere packings. *Phys. Rev. E*, 71:061302, 2005.
- [10] S. Aumaître, J. Farago, S. Fauve, and S. McNamara. Energy and power fluctuations in vibrated granular gases. *Eur. Phys. J. B*, 42:255–261, 2004.
- [11] R. A. Bagnold. The movement of desert sand. *The Geographical Journal*, 85(4):342–365, 1935.
- [12] A. Baranyai, D. J. Evans, and E. G. D. Cohen. Field-dependent conductivity and diffusion in a 2-dimensional Lorentz gas. *J. Stat. Phys.*, 70:1085–1098, 1993.
- [13] J. A. Barker and D. Henderson. What is “liquid”? Understanding the states of matter. *Rev. Mod. Phys.*, 48(4):587–671, Oct 1976.
- [14] R. P. Behringer, K. E. Daniels, T. S. Majmudar, and M. Sperl. Fluctuations, correlations, and transitions in granular materials: Statistical mechanics for a non-conventional system. In *Proc. 9th Experimental Chaos Conference*. Sao Jose dos Campos, Brazil, 2006.

- [15] D. Beladjine, M. Ammi, L. Oger, and A. Valance. Collision process between an incident bead and a three-dimensional granular packing. *Phys. Rev. E*, 75:061305, 2007.
- [16] E. Ben-Naim, S. Y. Chen, G. D. Doolen, and S. Redner. Shocklike dynamics of inelastic gases. *Phys. Rev. Lett.*, 83:4069–4072, 1999.
- [17] G. Benettin, L. Galgani, A. Giorgilli, and J.-M. Strelcyn. Lyapunov characteristic exponents for smooth dynamical systems and for Hamiltonian systems - A method for computing all of them. I - Theory. II - Numerical application. *Meccanica*, 15:9–30, 1980.
- [18] C. L. Bennett. Cosmology from start to finish. *Nature*, 440:1126, 2006.
- [19] K. Binder, S. Sengupta, and P. Nielaba. The liquid-solid transition of hard discs: First-order transition or Kosterlitz-Thouless-Halperin-Nelson-Young scenario? *J. Phys.: Condens. Matter*, 14:2323–2333, 2002.
- [20] G. D. Birkhoff. Proof of the ergodic theorem. *Proc. Nat. Acad. Sci. USA*, 17:656–660, 1931.
- [21] N. D. Birrell and P. C. Davies. *Quantum fields in curved space*. Cambridge, 1994.
- [22] J. Blum, G. Wurm, S. Kempf, T. Poppe, H. Klahr, T. Kozasa, M. Rott, T. Henning, J. Dorschner, R. Schräpler, H. U. Keller, W. J. Markiewicz, I. Mann, B. A. S. Gustafson, F. Giovane, D. Neuhaus, H. Fechtig, E. Grün, B. Feuerbacher, H. Kochan, L. Ratke, A. El Goresy, G. Morfill, S. J. Weidenschilling, G. Schwehm, K. Metzler, and W.-H. Ip. Growth and form of planetary seedlings: Results from a microgravity aggregation experiment. *Phys. Rev. Lett.*, 85(12):2426–2429, Sep 2000.
- [23] G. N. Bochkov and Yu. E. Kuzovlev. Non-linear fluctuation-dissipation relations and stochastic-models in non-equilibrium thermodynamics: I. Generalized Fluctuation-Dissipation Theorem. *Physica*, 106A:443–479, 1981.
- [24] L. Boltzmann. Entgegnung auf die wärmetheoretischen Betrachtungen des Hr. E. Zermelo. *Ann. Phys.*, 57:773–784, 1896.
- [25] J. P. Boon and O. Decroly. Dynamical systems theory for music dynamics. *Chaos*, 5(3), 1995.
- [26] J. J. Brey, J. W. Dufty, and A. Santos. Dissipative dynamics for hard spheres. *J. Stat. Phys.*, 87(5–6):1051–1066, 1997.
- [27] N. V. Brilliantov and T. Pöschel. *Kinetic theory of granular gases*. Oxford University Press, Oxford, UK, 2004.
- [28] N. V. Brilliantov, T. Pöschel, W. T. Kranz, and A. Zippelius. Translations and rotations are correlated in granular gases. *Phys. Rev. Lett.*, 98:128001, 2007.
- [29] J. Buehler, R. H. Wentorf, J. O. Hirschfelder, and C. F. Curtiss. The free volume for rigid sphere molecules. *J. Chem. Phys.*, 19(1):61–71, 1962.
- [30] M. Busso, R. Gallino, and G. J. Wasserburg. Nucleosynthesis in asymptotic giant branch stars: Relevance for galactic enrichment and solar system formation. *Ann. Rev. Astron. Astrophys.*, 37:239–309, 1999.
- [31] N. F. Carnahan and K. E. Starling. Equation of state for nonattracting rigid spheres. *J. Chem. Phys.*, 51(2):635–636, 1969.

-
- [32] G. F. Carnevale, Y. Pomeau, and W. R. Young. Statistics of ballistic agglomeration. *Phys. Rev. Lett.*, 64:2913–2916, 1990.
- [33] O. Carvente and J. C. Ruiz-Suárez. Crystallization of confined non-Brownian spheres by vibrational annealing. *Phys. Rev. Lett.*, 95:018001, 2005.
- [34] M. Castagnino, O. Lombardi, and L. Lara. The global arrow of time as a geometrical property of the universe. *Found. Phys.*, 33:877–912, 2003.
- [35] N. Chernov. Entropy, Lyapunov exponents and mean free path for billiards. *Vienna, Preprint ESI*, page 410, 1996. <http://www.esi.ac.at>.
- [36] N. I. Chernov, G. L. Eyink, J. L. Lebowitz, and Ya. G. Sinai. Derivation of Ohm’s Law in a deterministic mechanical model. *Phys. Rev. Lett.*, 70:2209–2212, 1993.
- [37] N. I. Chernov, G. L. Eyink, J. L. Lebowitz, and Ya. G. Sinai. Steady-state electrical-conduction in the periodic Lorentz gas. *Commun. Math. Phys.*, 154:569–601, 1993.
- [38] M. Christensson, M. Hindmarsh, and A. Brandenburg. Inverse cascade in decaying three-dimensional magnetohydrodynamic turbulence. *Phys. Rev. E*, 64(5):056405, Oct 2001.
- [39] P. Cipriani, S. Denisov, and A. Politi. From anomalous energy diffusion to Levy walks and heat conductivity in one-dimensional systems. *Phys. Rev. Lett.*, 94:244301, 2005.
- [40] W. C. Clark and G. Mason. Tensile strength of wet granular materials. *Nature*, 216:826, 1967.
- [41] E. G. D. Cohen. Dynamical ensembles in statistical mechanics. *Physica A*, 240(1–2):43–53, 1997.
- [42] D. Collin, F. Ritort, C. Jarzynski, S. B. Smith, I. Tinoco, and C. Bustamante. Verification of the Crooks Fluctuation Theorem and recovery of RNA folding free energies. *Nature*, 437:231–234, 2005.
- [43] A. Coniglio, A. de Candia, A. Fierro, M. Nicodemi, M. P. Ciamarra, and M. Tarzia. On Edwards’ theory of powders. *Physica A*, 339:1–2, 2004.
- [44] R. Connelly. Generic global rigidity. *Discrete Comput. Geom.*, 33(4):549–563, 2005.
- [45] R. Connelly. Lecture on packings I-II: The basics of rigidity. Institut Henri Poincaré, <http://www.math.cornell.edu/~connelly/BasicsI.BasicsII.pdf>, 2005.
- [46] R. Connelly. Lecture on packings III-IV: Lecture on packings of circles and spheres. Institut Henri Poincaré, <http://www.math.cornell.edu/~connelly/PackingsIII.IV.pdf>, 2005.
- [47] B. Crasemann and D. L. Manley. Radioactivity of Co^{57} . *Phys. Rev.*, 98(1):66–68, Apr 1955.
- [48] G. E. Crooks. Entropy production Fluctuation Theorem and the nonequilibrium work relation for free energy differences. *Phys. Rev. E*, 60:2721–2726, 1999.
- [49] G. E. Crooks. Path-ensemble averages in systems driven far from equilibrium. *Phys. Rev. E*, 61:2361–2366, 2000.

- [50] A. S. de Wijn. Kolmogorov-Sinai entropy for dilute systems of hard particles in equilibrium. *Phys. Rev. E*, 71:046211, 2005.
- [51] F. Debbasch, K. Mallick, and J. P. Rivet. Relativistic Ornstein-Uhlenbeck process. *J. Stat. Phys.*, 88:945–966, 1997.
- [52] J. Y. Delenne, M. S. El Youssoufi, F. Cherblanc, and J. C. Benet. Mechanical behaviour and failure of cohesive granular materials. *Int. J. Num. Anal. Meth. Geom.*, 28:1577–1594, 2004.
- [53] Ch. Dellago and H. A. Posch. Lyapunov exponents of systems with elastic hard collisions. *Phys. Rev. E*, 52:2401–2406, 1995.
- [54] Ch. Dellago and H. A. Posch. Lyapunov instability, local curvature, and the fluid-solid phase transition in two-dimensional particle systems. *Physica A*, 230:364–387, 1996.
- [55] Ch. Dellago and H. A. Posch. Kolmogorov-Sinai entropy and Lyapunov spectra of a hard-sphere gas. *Physica A*, 240:68–83, 1997.
- [56] Ch. Dellago, H. A. Posch, and W. G. Hoover. Lyapunov instability in a system of hard disks in equilibrium and nonequilibrium steady states. *Phys. Rev. E*, 53:1485–1501, 1996.
- [57] A. Donev, F. H. Stillinger, and S. Torquato. Do binary hard disks exhibit an ideal glass transition? *Phys. Rev. Lett.*, 96:225502, 2006.
- [58] A. Donev, F. H. Stillinger, and S. Torquato. Configurational entropy of binary hard-disk glasses: Nonexistence of an ideal glass transition. *J. Chem. Phys.*, 2007.
- [59] A. Donev, S. Torquato, and F. H. Stillinger. Pair correlation function characteristics of nearly jammed disordered and ordered hard-sphere packings. *Phys. Rev. E*, 71(3):011105, 2005.
- [60] A. Donev, S. Torquato, F. H. Stillinger, and R. Connelly. Jamming in hard sphere and disk packings. *J. Appl. Phys.*, 95(3):989, 2004.
- [61] J. R. Dorfman. *An introduction to chaos in nonequilibrium statistical mechanics*. Cambridge University Press, 1999.
- [62] J. R. Dorfman and P. Gaspard. Chaotic scattering theory of transport and reaction-rate coefficients. *Phys. Rev. E*, 51:28, 1995.
- [63] J. R. Dorfman, A. Latz, and H. van Beijeren. Bogoliubov-Born-Green-Kirkwood-Yvon hierarchy methods for sums of Lyapunov exponents for dilute gases. *Chaos*, 8:444–454, 1998.
- [64] Y. Du, H. Li, and L. P. Kadanoff. Breakdown of hydrodynamics in a one-dimensional system of inelastic particles. *Phys. Rev. Lett.*, 74:1268–1271, 1995.
- [65] J. W. Dufty and J. J. Brey. Green-Kubo expressions for a granular gas. *J. Stat. Phys.*, 109:433–448, 2002.
- [66] J. Dunkel and P. Hänggi. Theory of relativistic Brownian motion: The (1+1)-dimensional case. *Phys. Rev. E*, 71:016124, 2005.

-
- [67] J. Dunkel and P. Hänggi. Theory of relativistic Brownian motion: The (1+3)-dimensional case. *Phys. Rev. E*, 72:036106, 2005.
- [68] J. Duran. *Sands, powders, and grains: An introduction to the physics of granular materials*. Springer, New York, 2000.
- [69] J.-P. Eckmann and D. Ruelle. Ergodic theory of chaos and strange attractors. *Rev. Mod. Phys.*, 57:617–656, 1985.
- [70] U. F. Edgal and D. L. Huber. Hard-particle-fluid equation of state and phase transition employing nearest-neighbor correlations. *Phys. Rev. E*, 48(4):2610–2621, 1993.
- [71] A. Einstein. Über die von der molekularkinetischen Theorie der Wärme geforderten Bewegung von in ruhenden Flüssigkeiten suspendierten Teilchen. *Ann. Phys.*, 17:549–560, 1905.
- [72] A. Einstein. Zur Elektrodynamik bewegter Körper. *Ann. Phys.*, 17:891–921, 1905.
- [73] A. Einstein. *Philosopher-scientist. Autobiographical notes*. P. A. Schlipp, editor, 1949 (sixth printing 1995).
- [74] B. J. Ennis, G. Tardos, and R. Pfeffer. A microlevel-based characterization of granulation phenomena. *Powder Technology*, 65:257–272, 1991.
- [75] D. J. Evans, E. G. D. Cohen, and G. P. Morriss. Probability of second law violations in shearing steady states. *Phys. Rev. Lett.*, 71:2401–2404, 1993.
- [76] D. J. Evans and G. P. Morriss. *Statistical mechanics of nonequilibrium liquids*. Advanced Series in Nonlinear Dynamics. Academic Press, London, 1990.
- [77] D. J. Evans and D. J. Searles. The Fluctuation Theorem. *Adv. Phys.*, 51:1529–1585, 2002.
- [78] K. Feitosa and N. Menon. Fluidized granular medium as an instance of the Fluctuation Theorem. *Phys. Rev. Lett.*, 92:164301, 2004.
- [79] A. Fingerle. Relativistic fluctuation theorems. *Comptes Rendus Phys.*, 8(5–6):696–713, 2007.
- [80] A. Fingerle and S. Herminghaus. Unclustering transition in freely cooling wet granular matter. *Phys. Rev. Lett.*, 97:078001, 2006.
- [81] A. Fingerle and S. Herminghaus. Equation of state of wet granular matter. *Phys. Rev. E*, 76(1), 2007.
- [82] A. Fingerle and S. Herminghaus. Mechanisms of dissipation in wet granular matter. *Submitted to Europhys. Lett.*, *arXiv:0708.2597*, 2007.
- [83] A. Fingerle, S. Herminghaus, and V. Yu. Zaburdaev. Kolmogorov-Sinai entropy of the dilute wet granular gas. *Phys. Rev. Lett.*, 95:198001, 2005.
- [84] A. Fingerle, S. Herminghaus, and V. Yu. Zaburdaev. Chaoticity of the wet granular gas. *Phys. Rev. E*, 75:061301, 2007.
- [85] A. Fingerle and K. Roeller. Efficient simulation techniques for dry and wet granular matter. In *Heinz-Billing-Preis*, 2007.

- [86] A. Fingerle, K. Roeller, K. Huang, and S. Herminghaus. Critical behavior far from equilibrium in wet granular matter. *Submitted to N. J. Phys.*, 2007.
- [87] Z. Fournier, D. Geromichalos, S. Herminghaus, M. M. Kohonen, F. Mugele, M. Scheel, M. Schulz, B. Schulz, Ch. Schier, R. Seemann, and A. Skudelny. Mechanical properties of wet granular materials. *J. Phys.: Condens. Matter*, 17:S477–S502, 2005.
- [88] L. Frachebourg. Exact solution of the one-dimensional ballistic aggregation. *Phys. Rev. Lett.*, 82(7):1502–1505, Feb 1999.
- [89] G. Gallavotti and E. G. D. Cohen. Dynamical ensembles in non-equilibrium statistical mechanics. *Phys. Rev. Lett.*, 74:2694–2697, 1995.
- [90] G. Gallavotti and E. G. D. Cohen. Dynamical ensembles in stationary states. *J. Stat. Phys.*, 80:931–970, 1995.
- [91] R. García-Rojo, S. Luding, and J. J. Brey. Transport coefficients for dense hard-disk systems. *Phys. Rev. E*, 74:061305, 2006.
- [92] V. Garzó and J. W. Dufty. Dense fluid transport for inelastic hard spheres. *Phys. Rev. E*, 59(5):5895–5911, May 1999.
- [93] P. Gaspard. Diffusion in uniformly hyperbolic one-dimensional maps and Appell polynomials. *Phys. Lett. A*, 168:13–17, 1992.
- [94] P. Gaspard. *Chaos, scattering and statistical mechanics*. Cambridge University Press, 1998.
- [95] P. Gaspard. Nonlinear dynamics and chaos in many-particle Hamiltonian system. *Prog. Theo. Phys., Suppl.*, 150:64–80, 2003.
- [96] P. Gaspard and G. Nicolis. Transport properties, Lyapunov exponents, and entropy per unit time. *Phys. Rev. Lett.*, 65:1693–1696, 1990.
- [97] P. Gaspard and H. van Beijeren. When do tracer particles dominate the Lyapunov spectrum? *J. Stat. Phys.*, 109:671–704, 2002. arXiv: nlin.CD/0112019.
- [98] D. Geromichalos, M. M. Kohonen, F. Mugele, and S. Herminghaus. Mixing and condensation in a wet granular medium. *Phys. Rev. Lett.*, 90:168702, 2003.
- [99] J. W. Gibbs. On the equilibrium of heterogeneous substances. *Trans. Conn. Acad.*, 3:227–229, 1875.
- [100] R. J. Glauber. Time-dependent statistics of the Ising model. *J. Math. Phys.*, 4:294, 1963.
- [101] I. Goldhirsch. Rapid granular flows. *Ann. Rev. Fluid Mech.*, 35:267–293, 2003.
- [102] I. Goldhirsch and G. Zanetti. Clustering instability in dissipative gases. *Phys. Rev. Lett.*, 70:1619–1622, 1993.
- [103] A. Götzendorfer, J. Kreft, C. A. Kruelle, and I. Rehberg. Sublimation of a vibrated granular monolayer: Coexistence of gas and solid. *Phys. Rev. Lett.*, 95, 2005.
- [104] D. Goulding and J. P. Hansen. Effects of size polydispersity on depletion interactions. *Molec. Phys.*, 99(10):865–874, 2001.

-
- [105] P. K. Haff. Grain flow as a fluid-mechanical phenomenon. *J. Fluid Mech.*, 134:401–430, 1983.
- [106] J.-P. Hansen and I. R. McDonald. *Theory of simple liquids*. Elsevier, 2nd ed. edition, 1986.
- [107] S. W. Hawking. Arrow of time in cosmology. *Phys. Rev. D*, 32:2489–2495, 1985.
- [108] S. W. Hawking, R. Laflamme, and G. W. Lyons. Origin of time asymmetry. *Phys. Rev. D*, 47:5342–5356, 1993.
- [109] E. Helfand, H. L. Frisch, and J. L. Lebowitz. Theory of the two- and one-dimensional rigid sphere fluids. *J. Chem. Phys.*, 34:1037–1042, 1961.
- [110] D. Henderson. Simple equation of state for hard disks. *Mol. Phys.*, 30:971–972, 1975.
- [111] D. Henderson, A. D. Trokhymchuk, and D. T. Wasan. Interaction energy and force for a pair of colloidal particles in a bidisperse hard-sphere solvent. *J. Mol. Liquids*, 112:21–28, 2004.
- [112] D. Henderson, D. T. Wasan, and A. Trokhymchuk. Effective interaction between large spheres immersed into a multicomponent hard-sphere fluid. *J. Chem. Phys.*, 119(22):11989–11997, 2003.
- [113] O. Herbst, P. Müller, M. Otto, and A. Zippelius. Local equation of state and velocity distributions of a driven granular gas. *Phys. Rev. E*, 70:051313, 2004.
- [114] S. Herminghaus. Dynamics of wet granular matter. *Adv. Phys.*, 54(3):221–261, 2005.
- [115] M. Heying and D. S. Corti. Scaled particle theory revisited: New conditions and improved predictions of the properties of the hard sphere fluid. *J. Phys. Chem. B*, 108:19756–19768, 2004.
- [116] H. Hinrichsen. Non-equilibrium phase transitions. *Physica A: Statistical Mechanics and its Applications*, 369(1):1–28, 2006.
- [117] J. Honerkamp. *Statistical physics*. Springer, 1998.
- [118] W. G. Hoover. *Time reversibility, computer simulation, and chaos*, volume 13 of *Advanced Series in Nonlinear Dynamics*. World Scientific, Singapore, 1999.
- [119] D. J. Hornbaker, R. Albert, I. Albert, A.-L. Barabási, and P. Schiffer. What keeps sandcastles standing? *Nature*, 387(4):765–765, 1997.
- [120] N. Huang, G. Ovarlez, F. Bertrand, S. Rodts, P. Coussot, and D. Bonn. Flow of wet granular materials. *Phys. Rev. Lett.*, 94:028301, 2005.
- [121] M. Huthmann and A. Zippelius. Dynamics of inelastically colliding rough spheres: Relaxation of translational and rotational energy. *Phys. Rev. E*, 56(6):R6275–R6278, Dec 1997.
- [122] S. M. Iveson, J. D. Litster, K. Hapgood, and B. J. Ennis. Nucleation, growth and breakage phenomena in agitated wet granulation processes: A review. *Powder Technol.*, 117:3, 2001.

- [123] H. M. Jaeger, S. R. Nagel, and R. P. Behringer. Granular solids, liquids, and gases. *Rev. Mod. Phys.*, 68:1259–1273, 1996.
- [124] C. Jarzynski. Equilibrium free-energy differences from nonequilibrium measurements: A master-equation approach. *Phys. Rev. E*, 56:5018–5035, 1997.
- [125] C. Jarzynski. Nonequilibrium equality for free energy differences. *Phys. Rev. Lett.*, 78:2690–2693, 1997.
- [126] C. Jarzynski. Hamiltonian derivation of a detailed Fluctuation Theorem. *J. Stat. Phys.*, 98:77–102, 2000.
- [127] A. Johansen, J. S. Oishi, M. M. Mac Low, H. Klahr, T. Henning, and A. Youdin. Rapid planetesimal formation in turbulent circumstellar disks. *Nature*, 448:1022–1025, 2007.
- [128] F. Jüttner. Das Maxwell'sche Gesetz der Geschwindigkeitsverteilung in der Relativitätstheorie. *Ann. Phys.*, 339:856–882, 1911.
- [129] H. Kantz and T. Schreiber. *Nonlinear time series analysis*. Cambridge University Press, 1997.
- [130] A. S. Keys, A. R. Abate, S. C. Glotzer, and D. J. Durian. Measurement of growing dynamical length scales and prediction of the jamming transition in a granular material. *Nat. Phys.*, 3(4):260–264, 2007.
- [131] M. M. Kohonen, D. Geromichalos, M. Scheel, C. Schier, and S. Herminghaus. On capillary bridges in wet granular materials. *Physica A*, 339:7–15, 2004.
- [132] R. Kubo. *Lectures in theoretical physics, Volume I*. Interscience Publishers, London, 1959.
- [133] W. Kuhn. Kernresonanzfluoreszenz von Gammastrahlung in Ir191. *Phil. Mag.*, 8:625, 1929.
- [134] R. K. Kukkadapu, G. L. Smith, H. Li, J. V. Crum, M. C. Weinberg, and H. Poisl. Mössbauer spectroscopy study of iron redox in silicate glasses. In *Annual Report 1999 Environmental Dynamics and Simulation*, pages 3–7, 1999.
- [135] S. Kullback. *Information theory and statistics*. Dover Publications, 1968.
- [136] S. Kullback and R. A. Leibler. On information and sufficiency. *Ann. Math. Stat.*, 22:79, 1951.
- [137] J. Kurchan. Fluctuation Theorem for stochastic dynamics. *J. Phys. A*, 31:3719, 1998.
- [138] E. Kuzmann, S. Nagy, and A. Vértes. Critical review of analytical applications of Mössbauer spectroscopy illustrated by mineralogical and geological examples. *Pure Appl. Chem.*, 75(6):801–858, 2003.
- [139] J. Lancaster, N. Lancaster, and M. K. Seely. Climate of the central Namib desert. *Madoqua*, 14(1):5–61, 1984.
- [140] H. H. Landolt and R. Börnstein. *Numerical data and functional relationships in science and technology*. Springer, New York, 1976.

-
- [141] M. Lenoble, P. Snabre, B. Pouligny, and C. Barentin. Shearing a granular paste in a Couette device: Flow and size segregation. In *Powders and Grains*, pages 621–625. Taylor & Francis, 2005.
- [142] Hongming Li and J. J. McCarthy. Phase diagrams for cohesive particle mixing and segregation. *Phys. Rev. E*, 71:021305, 2005.
- [143] G. Lian, C. Thornton, and M. J. Adams. A theoretical-study of the liquid bridge forces between 2 rigid spherical bodies. *J. Colloid Int. Sci.*, 161:138–147, 1993.
- [144] G. Lian, C. Thornton, and M. J. Adams. Discrete particle simulation of agglomerate impact coalescence. *Chem. Eng. Sci.*, 53:3381–3391, 1998.
- [145] J. Loschmidt. Über den Zustand des Wärmegleichgewichts eines Systems von Körpern mit Rücksicht auf die Schwerkraft. *Sitzungsber. Kais. Akad. Wiss. Wien, Math. Naturwiss. Klasse*, 73:128–142, 1876.
- [146] W. Losert, D. G. W. Cooper, J. Delour, A. Kudrolli, and J. P. Gollub. Velocity statistics in excited granular media. *Chaos*, 9(3):682–690, 1999.
- [147] B. D. Lubachevsky. Why hard disks pack easier. *Electronic Colloquium on Computational Complexity, Proceedings of the International Workshop on Randomized Algorithms*, pages 2610–2621, 1998.
- [148] S. Luding. Global equation of state of two-dimensional hard sphere systems. *Phys. Rev. E*, 63:042201, 2001.
- [149] S. Luding, M. Huthmann, S. McNamara, and A. Zippelius. Homogeneous cooling of rough, dissipative particles: Theory and simulations. *Phys. Rev. E*, 58:3416–3425, 1998.
- [150] C. Maes and K. Netočný. Time-reversal and entropy. *J. Stat. Phys.*, 110:269–310, 2003.
- [151] C. Maes and K. Netočný. Static and dynamical nonequilibrium fluctuations. In *Work, Dissipation and Fluctuations in Nonequilibrium Physics, Bruxelles*. Université Libre de Bruxelles, Center for Nonlinear Phenomena and Complex Systems, 2006.
- [152] C. Maes and M. H. van Wieren. Time-symmetric fluctuations in nonequilibrium systems. *Phys. Rev. Lett.*, 96:240601, 2006.
- [153] T. S. Majmudar, M. Sperl, S. Luding, and R. P. Behringer. Jamming transition in granular systems. *Phys. Rev. Lett.*, 98:058001, 2007.
- [154] C. H. Mak. Large-scale simulations of the two-dimensional melting of hard disks. *Phys. Rev. E*, 73:065104(R), 2006.
- [155] H. A. Makse and J. Kurchan. Testing the thermodynamic approach to granular matter with a numerical model of a decisive experiment. *Nature*, 415:614–617, 2002.
- [156] S. McNamara and M. Mareschal. Lyapunov spectrum of granular gases. *Phys. Rev. E*, 63:061306, 2001.
- [157] J. L. Meijering. Interface area, edge length, and number of vertices in crystal aggregates with random nucleation. *Philips Res. Rep.*, 8(4):270–290, 1953.
- [158] T. Mikami, H. Kamiya, and M. Horio. Numerical simulation of cohesive powder behavior in a fluidized bed. *Chem. Eng. Sci.*, 53:1927–1940, 1998.

- [159] R. L. Mössbauer. Kernresonanzfluoreszenz von Gammastrahlung in Ir191. *Zeitschr. Phys.*, 151:124–143, 1958.
- [160] S. R. Nagel. Instabilities in a sandpile. *Rev. Mod. Phys.*, 64:321, 1992.
- [161] Y. Nahmad-Molinari and J. C. Ruiz-Suárez. Epitaxial growth of granular single crystals. *Phys. Rev. Lett.*, 89(26):264302, Dec 2002.
- [162] O. Narayan and S. Ramaswamy. Anomalous heat conduction in one-dimensional momentum-conserving systems. *Phys. Rev. Lett.*, 89(20):200601, Oct 2002.
- [163] S. Nowak, A. Samadani, and A. Kudrolli. Maximum angle of stability of a wet granular pile. *Nature Physics*, 1:50–52, 2005.
- [164] V. I. Oseledec. *Trudy Mosk. Mat. Obsch.*, 19:179–210, 1968.
- [165] V. I. Oseledec. A multiplicative ergodic theorem. Lyapunov characteristic numbers for dynamical systems. *Trans. Moscow Math. Soc.*, 19:197–231, 1968.
- [166] D. N. Page. Will entropy decrease if the universe recollapses? *Phys. Rev. D*, 32:2496–2499, 1985.
- [167] D. Parker. Thermodynamic irreversibility: Does the big bang explain what it purports to explain? *Philosophy of Science*, 72(5):751–763, 2005.
- [168] E. J. R. Parteli and H. J. Herrmann. Saltation transport on Mars. *Phys. Rev. Lett.*, 98:198001, 2007.
- [169] J. A. Peacock. *Cosmological physics*. Cambridge University Press, 1999.
- [170] Ya. B. Pesin. *Usp. Mat. Nauk.*, 32(4):55–112, 1977.
- [171] Ya. B. Pesin. Characteristic Lyapunov exponents and smooth ergodic theory. *Russian Math. Surveys*, 32(4):55–114, 1977.
- [172] J. Piasecki, L. Bocquet, and J.-P. Hansen. Multiple time-scale derivation of the Fokker-Planck equation for 2 Brownian spheres suspended in a hard-sphere fluid. *Physica A*, 218:125–144, 1995.
- [173] R. Piazza, V. Peyre, and V. Degiorgio. “Sticky hard spheres” model of proteins near crystallization: A test based on the osmotic compressibility of lysozyme solutions. *Phys. Rev. E*, 58(3):R2733–R2736, Sep 1998.
- [174] T. Pöschel, N. V. Brilliantov, and A. Formella. Impact of high-energy tails on granular gas properties. *Phys. Rev. E*, 74:041302, 2006.
- [175] W. H. Press, S. A. Teukolsky, W. T. Vetterling, and B. P. Flannery. *Numerical recipes in Fortran 77, The art of scientific computing*. Cambridge University Press, 1992.
- [176] Y. P. Raizer. *Gas discharge physics*. Springer, Berlin, 1991.
- [177] F. H. Ree and W. G. Hoover. 5th + 6th virial coefficients for hard spheres + hard disks. *J. Chem. Phys.*, 40(4):939, 1964.
- [178] H. Reiss, H. L. Frisch, and J. L. Lebowitz. Statistical mechanics of rigid spheres. *J. Chem. Phys.*, 31:369–380, 1959.

-
- [179] F. Restagno, L. Bocquet, and E. Charlaix. Where does a cohesive granular heap break? *Eur. Phys. J. E*, 14:177–183, 2004.
- [180] O. Reynolds. On the theory of lubrication and its application to Mr. Beauchamp Tower’s experiments, including an experimental determination of the viscosity of olive oil. *Philosophical Transactions of the Royal Society of London*, 177:157–234, 1886.
- [181] V. Richefeu, M. S. El Youssoufi, and F. Radjaï. Shear strength properties of wet granular materials. *Phys. Rev. E*, 73:051304, 2006.
- [182] M. Rigotti and F. Debbasch. A H-Theorem for the general relativistic Ornstein-Uhlenbeck process. *J. Math. Phys.*, 46:103303, 2005.
- [183] H. Risken. *The Fokker-Planck equation*. Springer, Berlin, 2nd ed. edition, 1996.
- [184] Anthony Rosato, Katherine J. Strandburg, Friedrich Prinz, and Robert H. Swendsen. Why the brazil nuts are on top: Size segregation of particulate matter by shaking. *Phys. Rev. Lett.*, 58(10):1038–1040, Mar 1987.
- [185] B. S. Rothberg and K. L. Magleby. Testing for detailed balance (microscopic reversibility) in ion channel gating. *Biophys. J.*, 80:3025–3026, 2001.
- [186] J.-N. Roux. Geometric origin of mechanical properties of granular materials. *Phys. Rev. E*, 61(6):6802–6836, 2000.
- [187] D. Ruelle. Smooth dynamics and new theoretical ideas in nonequilibrium statistical mechanics. *J. Stat. Phys.*, 95:393, 1999.
- [188] H. Rumpf. The strength of granules and agglomerates. In W. A. Knepper, editor, *Agglomeration*, pages 379–418, New York, USA, 1962. AIME, Interscience.
- [189] K. Saito¹ and A. Dhar. Fluctuation theorem in quantum heat conduction. *Phys. Rev. Lett.*, 99:180601, 2007.
- [190] Z. W. Salsburg and W. W. Wood. Equation of state of classical hard spheres at high density. *J. Chem. Phys.*, 37(4):798–804, 1962.
- [191] A. Samadani and A. Kudrolli. Segregation transitions in wet granular matter. *Phys. Rev. Lett.*, 85:5102, 2000.
- [192] L. Santen and W. Krauth. Absence of thermodynamic phase transition in a model glass former. *Nature*, 405:550–551, 2000.
- [193] L. Santen and W. Krauth. Liquid, glass and crystal in two-dimensional hard disks. arXiv:cond-mat/0107459, 2001.
- [194] A. Santos, S. B. Yuste, and M. L. de Haro. Contact values of the radial distribution functions of additive hard-sphere mixtures in d dimensions: A new proposal. *J. Chem. Phys.*, 117(12):5785–5793, 2002.
- [195] P. Schaaf. Mössbauer spectroscopy. *Encyclopedia of Condensed Matter Physics*, 4:20–32, 2005.
- [196] M. Scheel, D. Geromichalos, and S. Herminghaus. Wet granular matter under vertical agitation. *J. Phys.: Condens. Matter*, 16:S4213, 2004.

- [197] M. Scheel, R. Seemann, M. Brinkmann, M. Di Michiel, A. Sheppard, B. Breidenbach, and S. Herminghaus. Morphological clues to wet granular pile stability. *Submitted to Nature Materials*, 2007.
- [198] M. Schulz, B. M. Schulz, and S. Herminghaus. Shear-induced solid-fluid transition in a wet granular medium. *Phys. Rev. E*, 67:052301, 2003.
- [199] U. Seifert. Entropy production along a stochastic trajectory and an integral Fluctuation Theorem. *Phys. Rev. Lett.*, 95:040602, 2005.
- [200] S. F. Shandarin and Ya. B. Zeldovich. The large-scale structure of the universe: Turbulence, intermittency, structures in a self-gravitating medium. *Rev. Mod. Phys.*, 61:185–220, 1989.
- [201] L. E. Silbert, D. Ertas, G. S. Grest, T. C. Halsey, and D. Levine. Geometry of frictionless and frictional sphere packings. *Phys. Rev. E*, 65:031304, 2002.
- [202] N. Simanyi. Ergodicity of hard spheres in a box. *Ergod. Theo. Dyn. Sys.*, 19:741–766, 1999.
- [203] S. J. R. Simons and R. J. Fairbrother. Direct observations of liquid binder-particle interactions: The role of wetting behavior in agglomerate growth. *Powder Technol.*, 110:44, 2000.
- [204] S. J. R. Simons and R. J. Fairbrother. Direct observations of liquid binder-particle interactions: The role of wetting behaviour in agglomerate growth. *Powder Technology*, 110:44–58, 2000.
- [205] S. J. R. Simons, J. P. K. Seville, and M. J. Adams. Mechanisms of agglomeration. *Sixth International Symposium on Agglomeration, Nagoya, Japan*, pages 117–122, 1993.
- [206] S. J. R. Simons, J. P. K. Seville, and M. J. Adams. An analysis of the rupture energy of pendular liquid bridges. *Chem. Eng. Sci.*, 49:2331–2339, 1994.
- [207] S. J. R. Simons, J. P. K. Seville, and M. J. Adams. An analysis of the rupture energy of pendular liquid bridges. *Chem. Eng. Sci.*, 49:2331, 1994.
- [208] R. J. Speedy. On the reproducibility of glasses. *J. Chem. Phys.*, 100(9):6684–6691, 1994.
- [209] D. N. Spergel, L. Verde, H. V. Peiris, E. Komatsu, M. R.olta, C. L. Bennett, M. Halpern, G. Hinshaw, N. Jarosik, A. Kogut, M. Limon, S. S. Meyer, L. Page, G. S. Tucker, J. L. Weiland, E. Wollack, and E. L. Wright. First year Wilkinson microwave anisotropy probe (WMAP) observations: Determination of cosmological parameters. *Astr. Phys. J. S. S.*, 148:175–194, 2003.
- [210] R. F. Streater and A. S. Wightman. *PCT, spin and statistics, and all that*. Princeton University Press, 1980.
- [211] S. Taibi, A. Alem, and J. M. Fleureau. Influence of capillary forces on the flow of granular materials: Experimental study and DEM modeling. In *Powders and Grains*, pages 605–609. Taylor & Francis, 2005.
- [212] H. Takana. Private communication, 2007.

-
- [213] M. L. Tan and I. Goldhirsch. Intercluster interactions in rapid granular shear flows. *Phys. Fluids*, 9:856–869, 1996.
- [214] F. M. Tao, Y. Song, and E. A. Mason. Derivative of the hard-sphere radial-distribution function at contact. *Phys. Rev. A*, 46(12):8007–8008, 1992.
- [215] C. Thornton. Interparticle sliding in the presence of adhesion. *J. Phys. D: Appl. Phys.*, 24:1942–1946, 1991.
- [216] C. Thornton and K. K. Yin. Impact of elastic spheres with and without adhesion. *Powder Technology*, 65:153–166, 1991.
- [217] C. Thornton, K. K. Yin, and M. J. Adams. Numerical simulation of the impact fracture and fragmentation of agglomerates. *J. Phys. D: Appl. Phys.*, 29:424–435, 1996.
- [218] A. G. Tomboulides and S. A. Orszag. Numerical investigation of transitional and weak turbulent flow past a sphere. *J. Fluid Mech.*, 416:45–73, 2000.
- [219] S. Torquato, T. M. Truskett, and P. G. Debenedetti. Is random close packing of spheres well defined? *Phys. Rev. Lett.*, 84:2064, 2000.
- [220] Sand World Travemünde. (cf. for instance: www.sandworld.de).
- [221] E. Trizac, A. Barrat, and M. H. Ernst. Boltzmann equation for dissipative gases in homogeneous states with nonlinear friction. *Phys. Rev. E*, 76:031305, 2007.
- [222] Ed. C. W. Tyler. *Human symmetry perception and its computational analysis*. L. Erlbaum, 2002.
- [223] Th. Udem, R. Holzwarth, and T. W. Hänsch. Optical frequency metrology. *Nature*, 416:233–237, 2002.
- [224] S. Ulrich. Private communication, 2007.
- [225] Paul B. Umbanhowar, Francisco Melo, and Harry L. Swinney. Umbanhowar, melo, and swinney. *Nature*, 382:793–796, 1996.
- [226] H. van Beijeren, J. R. Dorfman, H. A. Posch, and Ch. Dellago. Kolmogorov-Sinai entropy for dilute gases in equilibrium. *Phys. Rev. E*, 56:5272, 1997.
- [227] H. van Hees, V. Greco, and R. Rapp. Heavy-quark probes of the quark-gluon plasma and interpretation of recent data taken at the BNL Relativistic Heavy Ion Collider. *Phys. Rev. C*, 73:034913, 2006.
- [228] T. P. C. van Noije, M. H. Ernst, and R. Brito. Ring kinetic theory for an idealized granular gas. *Physica A*, 251:266–283, 1998.
- [229] R. van Zon and E. G. D. Cohen. Extension of the Fluctuation Theorem. *Phys. Rev. Lett.*, 91:110601, 2003.
- [230] L. Verlet and D. Levesque. Integral-equations for classical fluids: III. The hard disks system. *Mol. Phys.*, 46(5):969–980, 1982.
- [231] S. Viscardy and P. Gaspard. Viscosity in the escape-rate formalism. *Phys. Rev. E*, 68:041205, 2003.

- [232] S. Warr, J. M. Huntley, and G. T. H. Jacques. Fluidization of a two-dimensional granular system: Experimental study and scaling behavior. *Phys. Rev. E*, 52(5):5583–5595, Nov 1995.
- [233] H. Wegener. *Der Mössbauer-Effekt und seine Anwendungen in Physik und Chemie*. Bibliographisches Institut, Mannheim, Germany, 1965.
- [234] S. Weinberg. *Gravitation and cosmology*. Wiley, 1972.
- [235] S. Weinberg. “Living in the multiverse”, opening talk at the symposium “Expectations of a final theory”, Trinity College, Cambridge. In B. Carr, editor, *Universe or multiverse?* Cambridge University Press, Sep 2005.
- [236] R. D. Wildman, J. M. Huntley, and D. J. Parker. Granular temperature profiles in three-dimensional vibrofluidized granular beds. *Phys. Rev. E*, 63(6):061311, May 2001.
- [237] C. D. Willett, M. J. Adams, S. A. Johnson, and J. P. K. Seville. Capillary bridges between two spherical bodies. *Langmuir*, 16:9396–9405, 2000.
- [238] N. Xu, J. Blawdziewicz, and C. S. O’Hern. Random close packing revisited: Ways to pack frictionless disks. *Phys. Rev. E*, 71:061306, 2005.
- [239] H. L. Yang and G. Radons. Lyapunov instabilities of Lennard-Jones fluids. *Phys. Rev. E*, 71:036211, 2005.
- [240] X. Yang, C. Huan, D. Candela, R. W. Mair, and R. L. Walsworth. Measurements of grain motion in a dense, three-dimensional granular fluid. *Phys. Rev. Lett.*, 88(4):044301, Jan 2002.
- [241] V. Yu. Zaburdaev, M. Brinkmann, and S. Herminghaus. Free cooling of the one-dimensional wet granular gas. *Phys. Rev. Lett.*, 97:018001, 2006.
- [242] V. Yu. Zaburdaev and S. Herminghaus. Dry and wet granular shock waves. *Phys. Rev. E*, 75:031304, 2007.
- [243] H. D. Zeh. *The physical basis of the direction of time*. Springer, Heidelberg, 4th edition, 2001.
- [244] A. Zippelius. Granular gases. *Physica A: Statistical and Theoretical Physics*, 369(1):143–158, 2006.
- [245] L. Zitzler, S. Herminghaus, and F. Mugele. Capillary forces in tapping mode atomic force microscopy. *Phys. Rev. B*, 66:155436, 2002.

Acknowledgments

I wish to thank Prof. Dr. Stephan Herminghaus for supervising my work. Discussing results with Prof. Herminghaus always led to a tremendous clarification, and was for me great motivation. The scientific atmosphere which he creates, and the outreaching methodology and excellence he has created in his department are remarkable and a wonderful playground for the (re)search for “new answers to old questions”. There is no doubt that beyond physics this best experience will remain top influential for my life. I am honored that Prof. Dr. Annette Zippelius agreed to be referee of my thesis. I wish to thank her for initiating and organizing several interesting seminars at which I could present my ongoing work to her and her group. I gladly remember the fine discussions we had in these seminars. In particular I remember the discussions with Stephan Ulrich. It is a special pleasure for me to thank my colleague Dr. Vasily Zaburdaev, who came up with elegant suggestions in the challenging computation of the Kolmogorov-Sinai entropy of the wet granular gas (and I will never forget the sunny weeks we shared at the ICTP in Trieste when the reports of my first PRL arrived). In this context of the Kolmogorov-Sinai entropy, I remember interesting discussions with Prof. Dr. H. van Beijeren and Dr. H. Schanz on the relation between stochastic processes and dynamical systems, respectively on unstable manifolds. I guess without my wife and everlasting girlfriend Svenja, either this thesis would not have been possible, or my health would have severely suffered. Most probably both. More formally, I thank Svenja Hager for discussions on the three-particle collision events. The loving care of my families, Hiltrud and Hans, and Ute and Heinz, encouraged me throughout. I thank Klaus Röller for helping me with the automatization of data analysis, for sharing my mentality of ‘speed first’, especially for helping me with raytracing and good design style, for implementing my complicated ideas on the sinusoidal shaking in event-driven simulations, for teaching me much stuff about Linux, and the many interesting discussions we had in the Wilhelmsplatz Mensa. I am grateful that Dr. Kai Huang has meanwhile extended the data basis for the fluid/gas transition to further wetting liquids (other than water and nonane which I had originally applied) and thereby reconfirmed the observed scaling relation of Chap. 10. I want to thank Dr. Martin Brinkmann: there is a lot I learned when he spent time on having a look on my first manuscript, and in many later discussions. I thank Dr. Jürgen Vollmer for many interesting discussions, e.g. on dynamical systems. Mario Scheel is a remarkable physicist. What ever I asked him on granular matter, he could immediately confront me with the latest experimental facts. We shared an exciting time at the synchrotron in Grenoble, and he taught me how to melt glass spheres. In the context of the (relativistic) fluctuation theorem, I am grateful for the comments of J. Dunkel, Prof. Dr. P. Hänggi, Prof. Dr. C. Jarzynski, and Prof. Dr. U. Seifert. I am in particular grateful for the ongoing productive and joyful cooperation with Prof. P. Schaaf and S. Cusenza of the “Zweites Physikalisches Institut” at the Georg-August-University of Göttingen, which provided the Mössbauer facilities for the measurement of the granular velocity distribution. With Michael Schmiedeberg I had infinitely many ‘door conversations’. I remember one day I could not see why there are 12 neighbors but 14 simplexes in a close-packing surrounding each particle. He readily drew the geometry with his fingers in the air and started counting.

List of Publications and Meetings

Publications

A. Fingerle, S. Herminghaus and V. Yu. Zaburdaev, Kolmogorov-Sinai entropy of the dilute wet granular gas. *Phys. Rev. Lett.*, **95**, 198001 (2005).

A. Fingerle and S. Herminghaus, Unclustering transition in freely cooling wet granular matter. *Phys. Rev. Lett.*, **97**, 078001 (2006).

A. Fingerle, Relativistic fluctuation theorems. *Comptes Rendus Phys.*, **8**, 696 (2007).

A. Fingerle, S. Herminghaus, and V. Yu. Zaburdaev, Chaoticity of the wet granular gas, *Phys. Rev. E* **75**, 061301 (2007).

A. Fingerle and S. Herminghaus, Equation of state of wet granular matter, *Phys. Rev. E* **76** (2007).

A. Fingerle and S. Herminghaus, Mechanisms of dissipation in wet granular matter, *Submitted to Europhys. Lett.* (arXiv:0708.2597) (2007).

A. Fingerle, K. Roeller, K. Huang and S. Herminghaus, Critical behavior far from equilibrium in wet granular matter, *Submitted to the N. J. Phys.* (2007).

Meetings

- 2003 *Quantum Chaos on Hyperbolic Manifolds*, International School, Günzburg.
Dark Matter and Dark Energy, Bad Honnef.
- 2004 *Heidelberger Graduiertenkurse Physik*, Heidelberg.
- 2005 *Design and Control of Self-Organization in Physical, Chemical, and Biological Systems*, ICTP Summer School, Trieste (talk, poster).
DPG Frühjahrstagung, Berlin (poster).
6th Liquid Matter Conference, Utrecht (poster).
- 2006 *DPG Frühjahrstagung*, Dresden (talk, posters).
DPG Frühjahrstagung, München (talk).
Work, Dissipation, and Fluctuations in Nonequilibrium Physics, Brussels (talk).
- 2007 *DPG Frühjahrstagung*, Regensburg (posters).

Curriculum Vitae

Axel Hager-Fingerle, geb. Fingerle
Elbinger Str. 6
37083 Göttingen

E-Mail: axel.fingerle@ds.mpg.de

Persönlich Daten

Geboren am 7. 8. 1977 in Nürnberg
Deutsche Staatsangehörigkeit

Bildungsweg

1988-1997	Kreisgymnasium Riedlingen
Jun. 1997	<i>Allgemeine Hochschulreife</i>
1997-1998	Zivildienst Münsterklinik Zwiefalten
1998-2001, 2002-04	Universität Ulm
Sep. 2000	<i>Vordiplom Physik</i>
Nov. 2000	<i>Vordiplom Wirtschaftsphysik</i>
Okt. 2004	<i>Diplom Physik</i>
2002-2003	Wiss. Mitarbeiter
2001-2002	University of Oregon, Eugene
Jun. 2002	<i>Master of Science</i>
2004-2007	Promotion, Max-Planck-Institut für Dynamik und Selbstorganisation, Göttingen
2005-2007	Promotionsstudium Physik, Georg-August-Universität Göttingen
Nov. 2007	Vorlage der <i>Dissertation</i>

Göttingen, den 14. November 2007